Department of Chemical Engineering

University of Cambridge

Process Applications of NMR

A dissertation submitted for degree of Doctor of Philosophy

January 2001

Nora Ghaoui

New Hall

Supervisor: Prof. L.F. Gladden

for Elie and Ineke

Preface

The work described in this dissertation was undertaken at the Magnetic Resonance Research Centre, Department of Chemical Engineering, University of Cambridge, between October 1996 and January 2001.

This dissertation is the result of my own work and includes nothing which is the outcome of work done in collaboration, except where specifically stated in the text.

This dissertation is not substantially the same as any that I have submitted for a degree or diploma or other qualification at any other University. No part of this dissertation has already been or is being concurrently submitted for any such degree, diploma or other qualification.

This dissertation contains 64700 words and 127 figures.

Nora Ghaoui

January 2001

Abstract

This thesis describes applications of NMR techniques to flowing liquid streams to obtain quantitative information about the contents of the streams. The quantitative accuracy of NMR spectroscopy for composition measurement of liquid mixtures is measured as ±0.34 mol% and ±1 mol% for static and flowing mixtures respectively. The effects of flow on NMR spectroscopy are analysed using the residence time distributions of the streams in the magnet and the detection coil. Algorithms are developed for automated analysis of the NMR spectra of the mixtures, in which automatic phase and baseline correction are performed together. A peak-assignment algorithm is written that identifies components in a mixture based on the patterns observed in the pure-component spectra. Automated composition analysis of mixture spectra is performed using these algorithms in less than 4 minutes with an accuracy of ±0.66 mol%. A mathematical model is derived for the NMR spectrum of a mixture that considers the spectrum a weighted sum of pure-component spectra shifted in frequency. The experimental lineshape observed in an inhomogeneous magnetic field is poorly fitted by a Lorentzian lineshape, so a new model lineshape is developed based on the distribution of resonance frequencies across the sample. Volume-selective NMR spectroscopy using the STEAM and PROJSAT pulse sequences is optimised to give quantitative results from well-defined volumes with minimal signal contamination. The STEAM pulse sequence is modified to include flow-compensated slice selection gradients. The accuracy of the compositions measured from volume-selective spectra is measured as ±1 mol% and ±2 mol% for static and flowing mixtures respectively. Pulsed field gradient NMR sequences using double echoes for flow compensation are tested on flowing water, then used to determine the droplet size distributions of flowing emulsions. Flow images are acquired of a vertical liquid jets showing the narrowing and acceleration of the jet and the entrainment of the surrounding water.

Acknowledgements

My first thanks go to my supervisor, Prof. Lynn Gladden, for allowing me to join her excellent research group and for her guidance during my research and the writing of this thesis. Thanks also Malcolm McIvor and Alan Bunn of ICI, the sponsor of this project. The financial support of ICI and the Cambridge European Trust was gratefully received.

I am very grateful to Mick for keeping everything running and sorting out all problems, great and small, with endless amounts of patience and good humour. I am also grateful to the postdocs, Seders, Mike and Bertram, for their invaluable advice during my experiments, and helping me with the plumbing! Thanks to the gang at the MRRC for keeping the place lively: Sally, Mark, Boontham, Joe, Anuj, Farid, Gary, Andy D, Edwin, and Senthil; and to the other half of our research group for coming out to see us at the MRRC: Patrick, Alistair, Sunil, Dave, Fleming, Siva, Weibin and Liat.

Special thanks to Katherine and Ann for their friendship and support over the last four and a half years. I believe it's my turn to cook.

This past year that I have been working at Unilever Research Vlaardingen, I have been very thankful for the tolerance and support of my new colleagues while I finished writing this thesis. Thanks in particular to Irene, Remco and Kirsty for their encouragement.

Thanks to Lynn, Mick, Mike, Katherine and Prof. Mike Edwards for proof-reading chapters of this thesis.

And finally, thanks to my wonderful family for their love.

CONTENTS

1 INTRODUCTION

1.1 Objective

The aim of this work is the application of nuclear magnetic resonance (NMR) techniques to process streams to obtain quantitative information about the contents of the streams independently of the flow of the streams. The areas covered are on-line composition measurements of flowing liquid mixtures and on-line droplet distribution measurements of flowing emulsions. Monitoring a process stream on-line yields a quicker and more accurate result than sampling and off-line analysis, so it gives a direct means of monitoring and controlling the process to yield the desired product. An on-line measurement also allows monitoring of streams that cannot be sampled *e.g.* hot, pressurised, toxic or corrosive streams. Measurement time is another consideration: the delay between taking a sample and the result becoming available may make the measurement obsolete.

On-line measurement is often not possible because of the lack of suitable instrumentation. The potential exists for NMR to provide data for systems that are not amenable to other techniques. NMR has several advantages and disadvantages for on-line monitoring of process streams.

1.1.1 Advantages of using NMR

There are several reasons why NMR is suitable for on-line measurements and may be superior to optical or tomographic techniques.

1. Electromagnetic radiation is absorbed to the same extent by all nuclei of a given species. This has two consequences. Firstly, the intensity of the signal is linearly proportional to the number of nuclei giving rise to it, so NMR is quantitative. Secondly, it is not necessary to calibrate each component individually, so a mixture can be analysed without separation. In contrast, optical spectroscopy requires the absorption coefficient to be calibrated for each transition (Shoolery, 1996).

2. The NMR hardware – the magnet, coil and gradient set – is not in physical contact with the sample, it merely surrounds it. No probes or tracers need to be inserted in

the stream so the technique is non-invasive. This is a major advantage in a process environment where monitoring a flowing stream becomes possible without altering it. In addition, the performance of the instrument does not degrade over time because there is no contamination by the sample.

3. Opaque and solid-containing streams can be monitored as easily as clear liquids since no optical window is needed for light to pass through.

4. NMR has no directional preference, and both bulk and localised measurements are possible. The use of magnetic field gradients allows spatial selectivity in one, two or three dimensions. The highest spatial resolution is of the order of a few micrometers and is limited by the signal-to-noise ratio (Callaghan, 1991). In contrast, computed tomography techniques are restricted to a single imaging plane.

5. NMR is very versatile. NMR techniques exist to measure various parameters such as composition, diffusion, relaxation and velocity at different length and time scales. The measurements all use the same NMR apparatus – the difference lies in the programs used to drive the instrument and to analyse the results obtained.

6. NMR techniques can be applied to systems at a wide range of temperatures and pressures, although NMR performs better at lower temperatures (Harris, 1986).

7. The NMR measurement is non-destructive and does not generate any waste products because no sample is removed that would need to be disposed of after analysis. If a side stream is drawn off from the main process line for the NMR measurement, it can be returned to the process line after passing through the magnet.

1.1.2 Disadvantages of using NMR

NMR has several disadvantages, which contribute to its not being used for routine on-line analysis so far.

1. NMR has low sensitivity because the difference in energy between nuclear spin states in a magnetic field is very small and gives rise to very weak signals. The signal strength is dependent on the number of NMR-active nuclei present, the magnetic field strength and the gyromagnetic ratio of the nucleus (Harris, 1986).

^{1}H is the most useful of the NMR-active nuclei because of its high abundance and gyromagnetic ratio. The other commonly studied nucleus is ^{13}C, but it is only present in 1.1% natural abundance and has a lower gyromagnetic ratio, so the signal from ^{13}C is 1000 times less than that from ^{1}H. In this work, only ^{1}H nuclei are used.

2. The time scale of a single NMR measurement is of the order 10^{-6}-1 s, while optical measurements require 10^{-12}-10^{-9} s (Shoolery, 1996). Species with a lifetime below 10^{-6} s cannot be observed by NMR. In addition, since the signal strength is very weak, signal averaging over multiple scans is employed to increase the signal-to-noise ratio. This increases the total experiment time to a matter of minutes or hours. New techniques are being developed to decrease total experiment time, at the cost of signal-to-noise, such as Echo-Planar Imaging (Manz *et al.*, 1999).

3. NMR-active nuclei (such as ^{1}H or ^{13}C) must be present to produce a signal. This requirement is generally not difficult to satisfy for organic compounds.

4. Strong magnetic fields are required to generate a detectable signal. Therefore, NMR cannot be used with ferromagnetic materials that interfere with the field. The magnetic field attracts any nearby metallic objects, so an NMR on-line analyser cannot be located in the heart of a chemical plant, but must be placed some distance away from any metals.

5. NMR is very expensive because the magnet and associated electronics are precision instruments, which are not cheap to manufacture. The cost is a major investment that needs to be offset against the value of the information obtained using the instrument. NMR is unlikely to become a routine on-line tool. Rather, it would be applied in those cases where its specific capabilities are needed and no alternative is available.

6. A laboratory NMR instrument is complex and fragile and requires regular monitoring and maintenance (*e.g.* refilling with liquid nitrogen coolant for the superconducting coils). A low-field process instrument can be simpler and more rugged than a high-field laboratory instrument, but is unlikely to become a "black box" that can be bolted onto a process line and left to run.

7. The versatility of NMR has as drawback that operating the instrument and obtaining the desired results are not simple. Because NMR can be made sensitive to many parameters (*e.g.* composition, flow rate, physical environment) it can be difficult to arrange the apparatus so that the measurement reflects only the parameter of interest. The outcome of a measurement depends on many experimental settings that must be carefully chosen for the result to be valid. One of the aims of this work is to develop the necessary methods and programs for automated operation and composition analysis.

1.2 Literature Review: On-line NMR Spectroscopy

NMR spectroscopy is generally applied to composition measurements in non-flowing laboratory samples or *in vivo* experiments. There are few reports of on-line composition measurements using NMR in the literature. Any proprietary work carried out in industry is unreported, but some information is available from patents.

1.2.1 Process Applications

At the 35th Experimental NMR Conference Giammatteo *et al.* (1994) from Texaco R&D presented a design for a 1.3 T (^{1}H 55 MHz) gas-phase NMR analyser for quantitative composition measurements on hydrogen-containing species in natural gas. The design requirements for a process analyser at ambient temperature and pressure included on-site sampling, short analysis time (<30 s), accuracy (±2%) and low cost. Both stopped-flow and continuous-flow configurations were given. The gas composition was determined by comparison to an internal reference sample that was present in the sampling system. The composition was used to determine the BTU content of the stream, which was used to control a valve that adjusted the gas stream flow rate. The design has been patented (Giammatteo *et al.*, 1993), but no report of it has appeared in a peer-reviewed publication.

Auburn International in Danvers, MA (now part of Oxford Instruments) have patented Industrial Magnetic Resonance (IMR) technology (Dechene *et al.*, 1991, 1993). The technology was developed for on-line monitoring of chemical properties such as density, crystallinity and hydrogen content and is marketed under the trade name Magneflow (Oxford Instruments, 1999). The NMR measurement is performed under

stopped-flow conditions using a 0.47 T magnet (^{1}H 20 MHz) and the data are analysed by curve fitting to the FID. The ten parameters thus obtained are non-linearly transformed and regressed to correlate them to desired properties of the sample such as the tacticity of polypropylene (Dechene *et al.*, 1994). The technique relies on creating a calibration curve for the regression using samples of known properties.

Skloss *et al.* (1994) at Texas A&M University have designed an NMR system using a 1 T (^{1}H 42 MHz) permanent magnet to measure small concentrations of oxygenates in a liquid gasoline stream for process control of a gasoline blender. The total analysis time was 1 min for 12 scans under continuous flow conditions. The measurement relied on a calibration curve for MTBE (methyl tertiary-butyl ether) concentration using the integrated signal intensity of an isolated peak (OCH_3) in the ^{1}H spectrum.

1.2.2 Laboratory Applications

Several recent publications on laboratory-scale on-line NMR spectroscopy cover biological micro-reactor systems. In each case, selected peak intensities that were related to cell or product concentrations were observed to vary with time, hence providing information about the reaction under study. The effects of flow on the measurements were not considered.

Chen and Bailey (1993) circulated a continuously aerated sample of growing *Escherichia coli* through a flow loop into an NMR magnet and acquired ^{31}P spectra under continuous-flow. The intracellular metabolic state was monitored by assigning the peaks in the spectrum using an external reference sample. A single measurement took 3.5-14 min (300-1200 scans).

Hartbritch *et al.* (1996) developed a membrane cyclone reactor that fit wholly within a wide-bore magnet, to monitor aerobic fermentation at high cell densities. The fermentation broth was circulated through an NMR measuring chamber and spectra were acquired under continuous flow. In one experiment, the ^{31}P NMR signal intensity was used to monitor cell concentration with a time resolution of 60 min. In another experiment, ^{13}C spectra were acquired every 10 min to follow glucose uptake.

Neves *et al.* (1999) used ^{31}P and ^{13}C *in vivo* spectroscopy to follow the metabolism of glucose in *Lactococcus lactis* cells by measuring the time course of glycolitic

intermediates. The cells were circulated from a 50-ml bioreactor through an NMR magnet at a rate of 32 ml/min, with a mean residence time of 7 s in the magnet. Rapid pulsing was used for ^{13}C spectra to reduce the measurement time to 30 s. Correction factors for saturation and Overhauser effects were needed to infer accurate compositions from peak intensities. These factors were obtained from calibration runs and by use of a concentration standard.

Only one publication has been found relating to a laboratory-scale chemical reactor that was monitored using flowing NMR spectroscopy. Neudert *et al.* (1986) studied the kinetics of a semi-batch process for the synthesis of retinoic acid using ^{31}P NMR spectroscopy. A side stream from a 0.5-l reactor was circulated through an NMR magnet and spectra were acquired in stopped-flow mode. A single measurement took 135 s.

An emerging application in analytical chemistry is the coupling of on-line NMR spectroscopy to separation techniques such as capillary high-performance liquid chromatography (Behnke *et al.*, 1996), size exclusion chromatography (Ludlow *et al.*, 1999) and capillary zone electrophoresis (Schewitz *et al.*, 1998). Recent reviews have been written by Gfrörer *et al.* (1999) and Albert *et al.* (1999). For these techniques, the mixture is separated before NMR analysis and very dilute solutions (0.1%) in deuterated solvents are used. The measurements are performed under stopped-flow conditions, and the apparatus is miniaturised to improve resolution and sensitivity (Wu *et al.*, 1995). The analyses identify and characterise the components in a mixture, but the composition of the mixture is not determined by NMR.

1.3 Outline of Research

The research described in this thesis studies the strengths and limitations of various ^{1}H NMR techniques – bulk spectroscopy, volume-selective spectroscopy, diffusion measurement – for characterising multi-component flowing liquid streams. The approach taken is to develop principles and methods that are applicable to all flowing systems. Another outcome of this research is a methodology for automated data processing to enable on-line measurement of chemical composition without operator intervention.

The experimental conditions in this work deviate from ideal laboratory conditions for NMR spectroscopy in two respects. The first is a requirement for quantitative accuracy throughout. Acquisition parameters for NMR spectroscopy are usually optimised for maximum sensitivity, and the resulting signals are often weighted by parameters other than the sample composition. For each NMR technique used, the effect of each acquisition and processing parameter on the quantitative nature of the signal is studied. The procedures used to acquire and process the NMR signals are adjusted where necessary to ensure that the composition information is retained. The second non-ideal experimental condition is the presence of flow during signal acquisition. Although NMR flow imaging is a well-established field, NMR spectroscopy under flowing conditions has not been previously studied in detail. In this work, the properties of the flow are not being measured (except in chapter 8, see below). The flow is the means of transporting the sample through the apparatus, and its effects on the NMR signal must be understood and removed where necessary.

Chapter 2 of this thesis describes an assessment of the quantitative accuracy and reproducibility of NMR spectroscopy for measuring composition under non-flowing conditions. The test samples are liquid mixtures of water, methanol, toluene, cyclohexane, isooctane and ethyl acetate in various proportions. The compositions of the samples are measured from NMR spectra acquired and processed with the appropriate parameters. The accuracy of the NMR measurements is ±0.34 mol% and the reproducibility is ±0.08 mol%.

Automated processing of the NMR data is discussed in chapter 3, which describes the computer algorithms developed for automatic composition analysis of the NMR spectra of the liquid mixtures. Two algorithms are written for automatic phase and baseline correction based on two existing algorithms, numerical phasing and baseline optimisation. A novel peak-assignment algorithm is written that uses the spectral patterns of the components to identify them in the mixture spectra. The numerical phasing and peak-assignment algorithms are combined into a single program that performs the entire composition analysis in less than 4 minutes.

To improve accuracy, peak integration is replaced by model fitting in the data analysis procedure in chapter 4. A mathematical model is derived that describes the spectrum of a liquid mixture as a weighted sum of pure-component spectra. The model requires

a new lineshape model because of the non-ideal experimental lineshapes. The lineshape model is derived based on spherical harmonic functions. However, a least-squares fit of the model to the experimental lineshape fails to converge because it requires a better fitting algorithm.

Chapter 5 describes optimisation of volume-selective spectroscopy for quantitative measurements. Two pulse sequences, STEAM and PROJSAT, are implemented and adjusted to give spectra from accurately localised volumes. The PROJSAT spectra are the first reported, since PROJSAT is originally an imaging technique. The accuracy of the compositions of non-flowing samples determined using STEAM and PROJSAT is ±1 mol%.

In chapter 6, bulk and volume-selective NMR spectroscopy is applied to flowing liquid streams. The effect of flow on NMR signals is analysed in terms of residence time distributions and a new model is derived. The model gives better explanations of flow-induced peak broadening, sensitivity enhancement and apparent relaxation enhancement than the existing exponential model. Flow-compensated gradients are added to STEAM to minimise the loss of phase coherence caused by the velocity distribution. The accuracy of the measured composition is ±1 mol% using bulk spectroscopy and ±2 mol% using STEAM and PROJSAT. STEAM is also used to show heterogeneous flow of an emulsion of *o*-xylene in water.

Chapter 7 describes on-line droplet size determination of flowing emulsions using pulsed field gradient NMR. PFG pulse sequences using spin echoes and stimulated echoes are modified for volume selection and flow compensation. The sequences are tested by measuring the known diffusion coefficient of water under static and flowing conditions. The stimulated-echo sequences are more reliable than their spin-echo counterparts and are used to determine the droplet size distributions of static and flowing emulsions of *o*-xylene in water. Consistent droplet size distributions are measured using the flow-compensated sequences despite incomplete flow compensation. The droplet size distributions vary with the *o*-xylene content of the emulsion but are independent of flow rate.

Chapter 8 describes flow imaging of a vertically upward jet of octanol in water. No previous flow images of jet have been reported. The flow images are obtained despite

the instability of the jet. The images show the narrowing and acceleration of the jet downstream of the nozzle, and the entrainment and recirculation of water near the jet.

The conclusions of this thesis are given in chapter 9.

1.4 References

Albert, K., Dachtler, M., Glaser, T., Händel, H., Lacker, T., Schlotterbeck, G., Strohschein., S., Tseng, L.-H., & Braumann, U. (1999). On-line coupling of separation techniques to NMR. *HRC – Journal of High Resolution Chromatography, 22*, 135-143.

Behnke, B., Schlotterbeck, G., Tallarek, U., Strohschein, S., Tseng, L.-H., Keller, T., Albert, K., & Bayer, E. (1996). Capillary HPLC-NMR coupling: High-resolution ^{1}H NMR spectroscopy in the nanoliter scale. *Analytical Chemistry, 68*, 1110-1115.

Callaghan, P.T. (1991). *Principles of Nuclear Magnetic Resonance Microscopy*. p. 173. Clarendon Press, Oxford, UK.

Chen, R., & Bailey, J.E. (1993). Observation of aerobic, growing *Escherichia coli* metabolism using an on-line nuclear magnetic resonance spectroscopy system. *Biotechnology and Bioengineering, 42*, 215-221.

Dechene, R.L., Smith, T.B., & Marino, S.A. (1991). Magnetic resonance analysis in real time, industrial usage mode. Patent no. US5015954.

Dechene, R.L., Smith, T.B., Marino, S.A., Tache, R.J., & Roy, A.K. (1993). Improved magnetic resonance analysis in real time, industrial usage mode. Patent no. WO9310468.

Dechene, R.L., Smith, T.B., Marino, S.A., Tache, R.J., & Roy, A.K. (1994). Real time magnetic resonance analysis with non-linear regression means. Patent no. US5319308.

Gfrörer, P., Schewitz, J., Pusecker, K., & Bayer, E. (1999). On-line coupling of capillary separation techniques with ^{1}H NMR. *Analytical Chemistry, 71*, A315-A321.

Giammatteo, P.J., Trocino, R.J., & Marsh, G. (1993). Control means and method for controlling feed gases. Patent no. US5265635.

Giammatteo, P.J., Marsh, J.C., Marsh, G., Gordon, M., & Mooney, J.R. (1994). Process applications of NMR on flowing gaseous streams. Presented at the 35th Experimental NMR Conference, Pacific Grove, California, April 10-14, 1994.

Harris, R.K. (1986). *Nuclear Magnetic Resonance Spectroscopy: A Physicochemical View*. pp. 10-11. Longman, Harlow, UK.

Hartbrich, A., Schmitz, G., Weuster-Botz, D., de Graaf, A.A., & Wandrey, C. (1996). Development and application of a membrane cyclone reactor for *in vivo* NMR spectroscopy with high microbial cell densities. *Biotechnology and Bioengineering, 51*, 624-635.

Ludlow, M., Louden, D., Handley, A., Taylor, S., Wright, B., & Wilson, I.D. (1999). Size exclusion chromatography with UV detection coupled to on-line ^{1}H NMR and on-line collection via a dedicated interface for subsequent off-line FT-IR. *Analytical Communications, 36*, 85-87.

Manz, B., Chow, P.S., & Gladden, L. F. (1999). Echo-planar imaging of porous media with spatial resolution below 100 μm. *Journal of Magnetic Resonance, 136*, 226-230.

Neudert, R., Ströfer, E., & Bremser, W. (1986). On-line NMR in process engineering. *Magnetic Resonance in Chemistry, 24*, 1089-1092.

Neves, A.R., Ramos, A., Nunes, M.C., Kleerebezem, M., Hugenholtz, J., de Vos, W.M., Almeida, J., & Santos, H. (1999). *In vivo* nuclear magnetic resonance studies of glycolytic kinetics in Lactococcus lactis. *Biotechnology and Bioengineering, 64*, 200-212.

Oxford Instruments, plc. (1999). *Industrial Analysis – Magneflow*. Web page retrieved July 17, 1999 from the World Wide Web: http://www.oxinst.com/iag/magneflow.htm

Schewitz, J., Gfrörer, P., Pusecker, K., Tseng, L.-H., Albert, K., Bayer, E., Wilson, I.D., Bailey, N.J., Scarfe, G.B., Nicholson, J.K., & Lindon, J.C. (1998). Directly coupled CZE-NMR and CEC-NMR spectroscopy for metabolite analysis: paracetamol metabolites in human urine. *Analyst, 123*, 2835-2837.

Shoolery, J.N. (1996). Quantitative measurements. In D.M. Grant & R.K. Harris (Eds.), *Encyclopedia of Nuclear Magnetic Resonance, vol. 6*, pp. 3907-3916. John Wiley & Sons, Chichester, UK.

Skloss, T.W., Kim, A.J., & Haw, J.F. (1994). High-resolution NMR process analyzer for oxygenates in gasoline. *Analytical Chemistry, 66*, 536-542.

Wu, N., Webb, A., Peck, T.L., & Sweedler, J.V. (1995). On-line detection of amino acids and peptides in microbore LC. *Analytical Chemistry, 67*, 3101-3107.

2 COMPOSITION MEASUREMENTS USING QUANTITATIVE NMR SPECTROSCOPY

2.1 Introduction

Nuclear magnetic resonance (NMR) is the phenomenon whereby some atomic nuclei behave like magnets when placed in a magnetic field. This is due the inherent angular momentum of the nuclei, which is commonly called nuclear spin. Electromagnetic radiation in the radio-frequency (r.f.) region of the spectrum can induce transitions between nuclear energy levels, and this forms the basis of NMR spectroscopy. The NMR signal intensity is proportional to the number of nuclei giving rise to it, so NMR is a quantitative technique. The aim of the work presented in this thesis is to apply NMR spectroscopy to automated on-line determination of the composition of a flowing liquid process stream. As a first step, the accuracy of quantitative NMR spectroscopy was assessed under normal laboratory conditions, since no studies of this topic have been reported in the literature. The compositions of liquid mixtures were measured by NMR spectroscopy and compared to the known compositions, in order to assess the extent to which the inherent quantitative nature of NMR is retained in the spectra. This provided a reference for assessing the accuracy of NMR when the laboratory conditions were replaced by process conditions: firstly, by replacing manual data analysis by automated data processing algorithms (chapters 3 and 4); secondly, by acquiring volume-selective spectra (chapter 5); and thirdly, by acquiring the spectra in the presence of flow (chapter 6).

This chapter describes the theory of NMR and the procedure used to acquire and process NMR spectra to retain as much quantitative information as possible. The composition results for non-flowing mixtures of up to five components are presented and discussed. It is shown that NMR spectroscopy is quantitative provided that appropriate acquisition and processing parameters are used.

2.2 Theory

NMR was discovered independently by Purcell *et al.* (1946) at Harvard and Bloch *et al.* (1946a) at Stanford. The early continuous-wave NMR experiments were

performed by sweeping through either the r.f. irradiation frequency or the strength of the magnetic field to find the resonance condition (Bloch *et al.*, 1946b). A few years later, Proctor and Yu (1950) discovered that nuclei in different chemical environments had slightly different resonance frequencies, a phenomenon known as chemical shift. The pulsed NMR experiment was suggested by Bloch (1946) as a quicker means of exciting all frequencies simultaneously and was first performed by Hahn (1950). Lowe and Norberg (1957) showed that the transient response to an r.f. pulse was the Fourier transform of the continuous-wave spectrum. Pulsed NMR spectroscopy (Ernst and Anderson, 1966) came into common use with the publication of the fast Fourier transform algorithm (Cooley and Tukey, 1965), which greatly shortened data processing times. Pulsed NMR has now completely superseded continuous-wave spectroscopy.

This section follows the presentations of NMR theory by Fukushima and Roeder (1981), Harris (1983), Derome (1987), Friebolin (1993) and Gladden (1994).

2.2.1 Nuclear Spin in a Magnetic Field

Protons, neutrons and electrons have an inherent angular momentum called "spin" associated with a magnetic dipole moment. The numbers of protons and neutrons in a nucleus determine the overall spin of the nucleus, given by the nuclear spin quantum number, I, that can have values of 0, 1/2, 1, 3/2, 2…. The nuclear spin angular momentum, **P**, is a quantized vector whose magnitude is given by:

$$P = \hbar\left[I(I+1)\right]^{1/2}, \tag{2.1}$$

where $\hbar = h/2\pi$ and h is Planck's constant. The magnetic dipole moment, $\boldsymbol{\mu}$, is proportional to the angular momentum,

$$\boldsymbol{\mu} = \gamma \mathbf{P}. \tag{2.2}$$

This relationship defines the parameter γ, called the gyromagnetic ratio of the nucleus. For ^{1}H, the nucleus used in this work, $\gamma = 2.67519\times10^8$ rad T^{-1} s^{-1}.

In the absence of a magnetic field, **P** can have any orientation, and all orientations have equal energy. Inside a static magnetic field, **P** orients itself such that its component P_z along the direction of the field is given by:

$$P_z = m_I \hbar, \tag{2.3}$$

where m_I is the magnetic quantum number and can have values I, I-1…0,…-I. Since **P** is quantized, only certain values of P_z and their associated orientations are allowed. Each orientation has a different energy, so a nucleus in a magnetic field has (2I+1) discrete energy levels corresponding to different values of m_I. The energy, E, of each orientation, or spin state, is given by:

$$E = -\boldsymbol{\mu} \cdot \mathbf{B_0} = -\gamma \hbar m_I B_0, \tag{2.4}$$

where B_0 is the magnitude of the applied magnetic field.

Nuclei with spin $I = 0$ have no magnetic moment and do not align themselves in a magnetic field. For ^{1}H, the spin quantum number is $I = ½$, so $m_I = \pm ½$ and two orientations of **P**, parallel and anti-parallel to the field, are allowed, labelled α and β respectively (figure 2.1). These orientations lie at an angle, ϑ, relative to the field, given by (Harris, 1983):

$$\cos \vartheta = \frac{m_I}{\left[I(I+1)\right]^{1/2}}. \tag{2.5}$$

ϑ equals 54°44' for a spin-½ nucleus.

Transitions between spin states α and β can be induced by applying an amount of energy equal to the difference between the energy levels,

$$\Delta E = \gamma \hbar B_0, \tag{2.6}$$

which can be supplied using electromagnetic radiation at the resonance frequency,

$$\nu_0 = \frac{\Delta E}{h} = \left|\frac{\gamma}{2\pi}\right| B_0. \tag{2.7}$$

The magnetic field strengths used in this work were 4.7 T and 7.05 T, which correspond to ^{1}H resonance frequencies of 200 MHz and 300 MHz respectively. These frequencies lie in the radio-frequency range of the electromagnetic spectrum.

2.2.2 Bulk Magnetisation

In a sample containing many nuclei, the total magnetic moment or bulk magnetisation, **M**, is the vector sum of the individual magnetic moments. Spin-½ nuclei form a double cone along the magnetic field direction (z) with half-angle 54°44'. **M** is oriented parallel to the magnetic field, because there are more spins

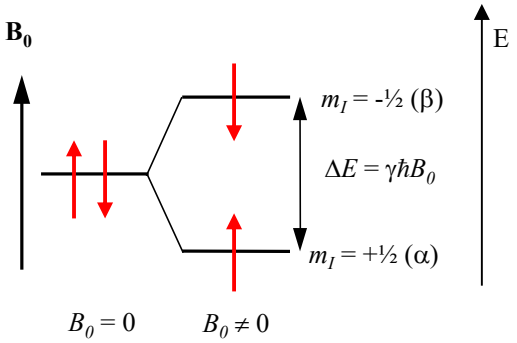

Figure 2.1 Energy level diagram for spin-½ nuclei inside a static magnetic field. The arrows denote the direction of P_z relative to $\mathbf{B_0}$.

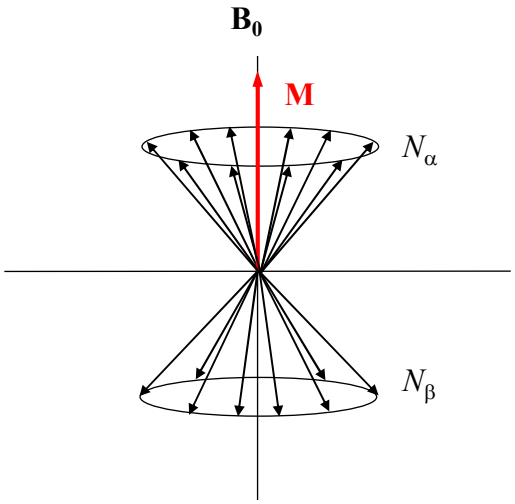

Figure 2.2 Bulk magnetisation **M** along $\mathbf{B_0}$ for a macroscopic sample of spin-½ nuclei inside a magnetic field with $N_\alpha > N_\beta$.

aligned with the field than against it and the x and y components average out to zero (figure 2.2). For spin-½ nuclei the magnitude of **M** along z is given by:

$$M_z = N_\alpha \mu_\alpha + N_\beta \mu_\beta , \tag{2.8}$$

where N_i is the number of nuclei in spin state i and μ_i is the magnetic moment of spin state i. At thermal equilibrium, there is a Boltzmann distribution of nuclei over the available spin states. Hence,

$$\frac{N_\beta}{N_\alpha} = e^{-\Delta E/kT} = e^{-\gamma\hbar B_0/kT}, \tag{2.9}$$

where k is Boltzmann's constant and T is the absolute temperature. Combining equations (2.2), (2.3), (2.8) and (2.9) gives:

$$M_z = \frac{\gamma\hbar}{2} N_\alpha \left(1 - e^{-\gamma\hbar B_0/kT}\right). \tag{2.10}$$

For ambient temperatures, equation (2.10) can be simplified to give:

$$M_z = \frac{(\gamma\hbar)^2}{4kT} N_{total} B_0 , \tag{2.11}$$

where $N_{total} = N_\alpha + N_\beta$, and is the total number of nuclei. Thus, the net magnetisation is directly proportional to the number of nuclei in the sample. This proportionality is the origin of the quantitative nature of NMR. The net magnetisation increases linearly with field strength; hence the use of strong fields to increase the strength of the NMR signal.

2.2.3 Larmor Precession and the Rotating Frame

The effect of the magnetic field on the bulk magnetisation is given by classical mechanics as:

$$\frac{d\mathbf{M}}{dt} = -\gamma \mathbf{B}_0 \times \mathbf{M} . \tag{2.12}$$

This results in a torque acting on **M** that causes the precession of **M** about $\mathbf{B_0}$ at an angular frequency, called the Larmor frequency, given by:

$$\omega_0 = \gamma B_0 = 2\pi\nu_0 . \tag{2.13}$$

Transitions between energy levels only occur when the frequency of the applied electromagnetic radiation matches the Larmor frequency, *i.e.* at resonance.

The electromagnetic radiation that induces these transitions is applied by using an oscillating electric current to induce a magnetic field, $\mathbf{B_1}$, perpendicular to $\mathbf{B_0}$, oscillating at frequency $\omega_1 = \gamma B_1$. The $\mathbf{B_1}$ field can be decomposed into two equal vectors rotating at ω_1 and $-\omega_1$ respectively (figure 2.3). In the presence of both fields $\mathbf{B_0}$ and $\mathbf{B_1}$, $\mathbf{M}$ precesses simultaneously about two perpendicular axes. This motion is difficult to visualise and to treat mathematically. To simplify matters, a frame of reference is used that rotates at frequency ω_1 in step with one component of $\mathbf{B_1}$ (Hahn, 1950), making $\mathbf{B_1}$ appear stationary relative to $\mathbf{B_0}$. The other component of $\mathbf{B_1}$ rotates at $2\omega_1$ in this frame and does not interact with the magnetisation because its frequency is too high. The axes of the rotating frame are defined as (x', y', z') with $\mathbf{B_1}$ along x' and $\mathbf{B_0}$ along z'. In the rotating frame, the effective magnetic field is given by:

$$\mathbf{B_{eff}} = \left(B_0 - \frac{\omega_1}{\gamma} \right) \mathbf{k} + B_1 \mathbf{i} \,, \tag{2.14}$$

where $\mathbf{k}$ and $\mathbf{i}$ are the unit vectors in the z' and x' directions respectively (figure 2.4). At resonance, $\omega_1 = \omega_0$, so $\mathbf{B_{eff}} = \mathbf{B_1}$ and $\mathbf{M}$ precesses about $\mathbf{B_1}$, which causes it to rotate away from $\mathbf{B_0}$. If the $\mathbf{B_1}$ field is applied for a short time, τ, using a radio-frequency (r.f.) pulse, then the angle by which $\mathbf{M}$ is rotated away from $\mathbf{B_0}$ is given by:

$$\varphi = \omega_1 \tau = \gamma B_1 \tau \,. \tag{2.15}$$

The duration of the r.f. pulse is chosen so that it rotates $\mathbf{M}$ by a known angle, *e.g.* a "90° pulse" rotates $\mathbf{M}$ by 90° onto the x'-y' plane and a "180° pulse" rotates $\mathbf{M}$ by 180° onto the $-z'$ axis (figure 2.5). The direction of rotation follows the right hand rule: for $\mathbf{B_0}$ along z', a 90° pulse applied along x' rotates the magnetisation clockwise onto the y' axis. In energy terms, the transitions induced by the absorption of energy from the $\mathbf{B_1}$ field alter the populations of the α and β states in the sample, thus changing the orientation of the net magnetisation $\mathbf{M}$ relative to $\mathbf{B_0}$. A 90° pulse provides enough energy to equalise N_α and N_β and a 180° pulse inverts N_α and N_β.

2.2.4 The NMR Signal

The signal that is detected in an NMR experiment is an oscillating electric current induced in the receiver coils by the oscillating magnetic field created by the precession of $\mathbf{M}$ about $\mathbf{B_0}$. The current is proportional to the rate of change of $\mathbf{M}$. The receiver coils are perpendicular to $\mathbf{B_0}$, so they detect the transverse magnetisation

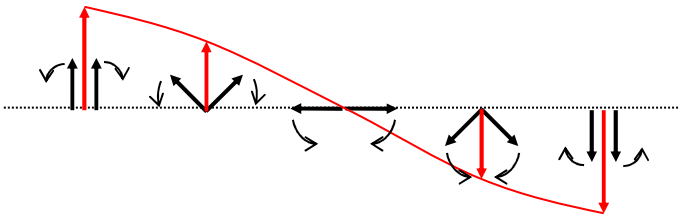

Figure 2.3 Decomposition of the oscillating magnetic field into two counter-rotating vectors of equal magnitude.

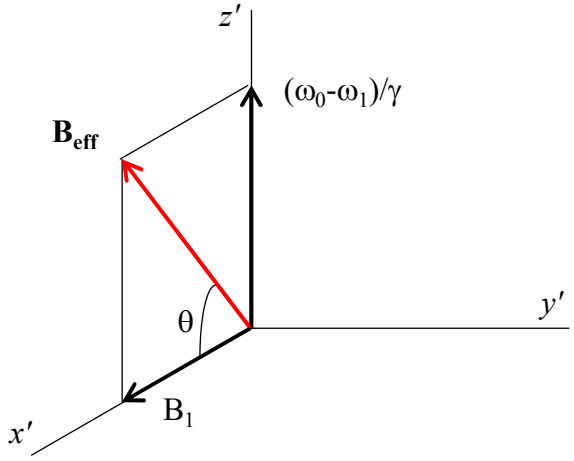

Figure 2.4 The effective magnetic field in the rotating frame, resulting from the static field $\mathbf{B_0}$ and the applied field $\mathbf{B_1}$.

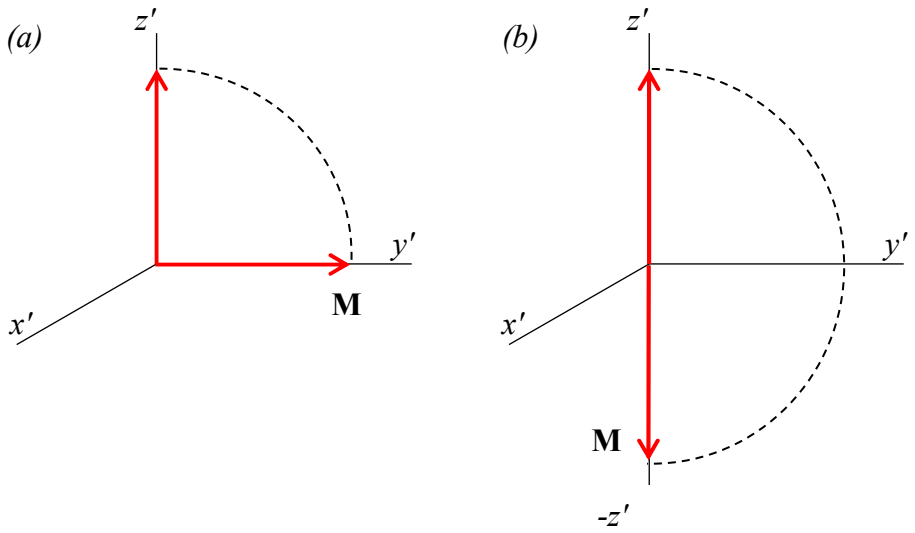

Figure 2.5 The effect of *(a)* a 90° pulse and *(b)* a 180° pulse on a magnetisation vector originally aligned along *z′*.

present after an r.f. pulse using separate receiver channels for the x' and y' components. The use of two receiver channels, called quadrature detection, is to allow correct measurement of the signal frequency relative to the receiver reference frequency. It is impossible to distinguish between frequencies above and below the reference frequency unless both components of the magnetisation are detected (Fukushima and Roeder, 1981).

The time-domain NMR signal is a sum of decaying sinusoids (figure 2.6(a)) and is called a Free Induction Decay (FID). The oscillations in the FID are caused by the difference between the signal frequency and the receiver reference frequency, and the decay is caused by the loss of magnetisation coherence over time. The x' and y' (real and imaginary) components of the signal detected in quadrature are Fourier transformed into a real and an imaginary spectrum. After phase correction (section 2.3.5.2), the real spectrum contains absorption lineshapes (figure 2.6(b)) that show the absorption of energy at each frequency and the imaginary spectrum contains dispersion lineshapes (figure 2.6(c)), which are phase shifted by 90° relative to the absorption lineshapes. The integrals of the absorption lineshapes are proportional to the number of nuclei, so they are used to calculate the composition of the sample.

2.2.5 Relaxation

Once the nuclei in the sample have been excited by the r.f. pulse, they will relax back to equilibrium. The relaxation can be divided into two components, transverse and longitudinal. The transverse component is associated with the decay of the FID over time, and the longitudinal component is associated with the recovery of the equilibrium magnetisation.

Transverse relaxation refers to relaxation that alters the transverse components of magnetisation ($\mathbf{M_x}$ and $\mathbf{M_y}$) without affecting the longitudinal component ($\mathbf{M_z}$). We consider two mechanisms of transverse relaxation. The first is spin-spin relaxation, which has an exponential time constant T_2. Spin-spin relaxation is caused by the exchange of energy between nuclear spins in the sample without energy loss to the surroundings. This process randomises the phases of the spins, so the net magnetisation decreases with time. The equation that describes spin-spin relaxation is given by (Bloch, 1946):

(a)

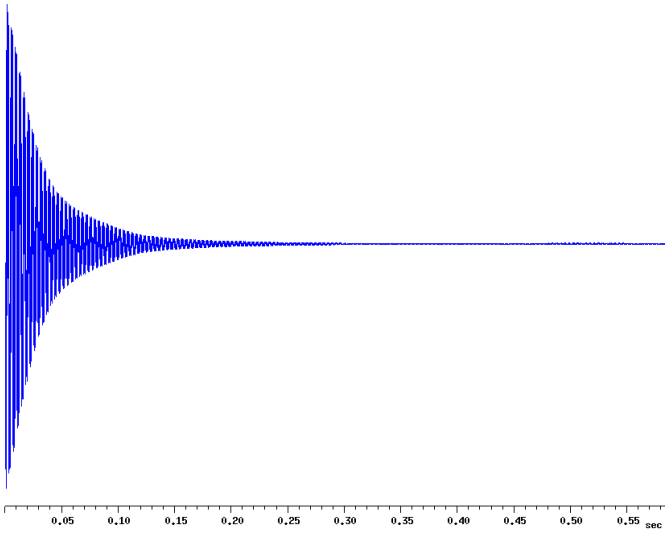

(b)

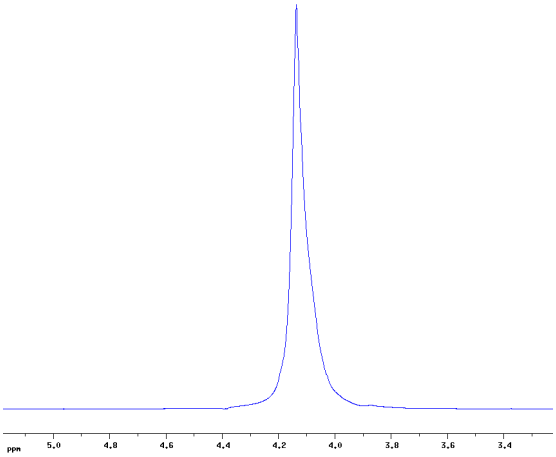

(c)

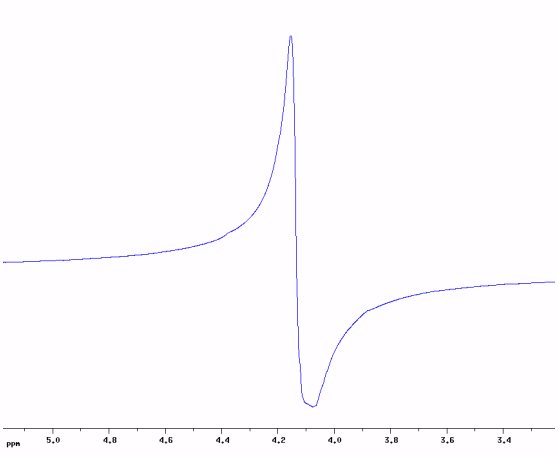

Figure 2.6 *(a)* a ^{1}H Free Induction Decay (FID) recorded for water at 200 MHz, *(b)* the ^{1}H absorption spectrum of water at 200 MHz, *(c)* the ^{1}H dispersion spectrum of water at 200 MHz. The chemical shift axis for the spectra is relative to the resonance frequency of TMS.

$$\frac{dM_x}{dt} = \frac{-M_x}{T_2}, \tag{2.16}$$

with solution:

$$M_x(t) = M_x(0)\exp\left(-t/T_2\right). \tag{2.17}$$

The equations for M_y are equivalent.

The second cause of transverse relaxation is magnetic field inhomogeneity. $\mathbf{B_0}$ is never perfectly homogeneous, so nuclei at different positions have slightly different Larmor frequencies ($\omega_0 = \gamma B_0$). Directly after an r.f. pulse, all spins are in phase and start precessing at their respective Larmor frequencies. Some spins precess faster and some slower than others do, so the spins fan out and lose phase coherence over time (figure 2.7), and the transverse magnetisation decreases with exponential time constant T_2'.

An important difference between decay due to $\mathbf{B_0}$ inhomogeneity and that due to spin-spin relaxation is that the former is reversible whereas the latter is not. Spin-spin relaxation is a random process, but $\mathbf{B_0}$ inhomogeneity is constant over the course of the experiment, so its effect can be reversed by using a spin echo (section 5.2.4).

An observed relaxation time constant, T_2^*, can be defined that combines both relaxation processes, and is given by:

$$\frac{1}{T_2^*} = \frac{1}{T_2} + \frac{1}{T_2'}. \tag{2.18}$$

Longitudinal relaxation refers to the recovery of the magnetisation $\mathbf{M_z}$ parallel to $\mathbf{B_0}$. This occurs when the nuclei that were excited to a higher spin state by the r.f. pulse fall back to their ground state, thereby re-establishing thermal equilibrium. The time constant for longitudinal relaxation, T_1, is different for nuclei in different physical and chemical environments. The relaxation process is described by the equation (Bloch, 1946):

$$\frac{dM_z(t)}{dt} = \frac{-(M_z - M_0)}{T_1} \tag{2.19}$$

whose solution is:

$$M_z(t) = M_0\left[1 - \exp(-t/T_1)\right] + M_z(0)\exp(-t/T_1). \tag{2.20}$$

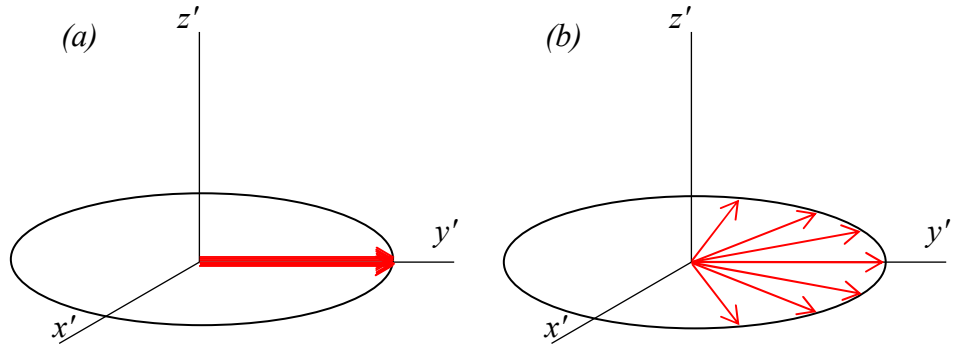

Figure 2.7 *(a)* After a 90° pulse, the nuclei are all in phase but have different precession frequencies.
(b) Over time the nuclei fan out as some of them precess faster than others do.

Longitudinal relaxation is slower than transverse relaxation because it requires the presence of suitable acceptors for the energy emitted by the nuclei when they fall to their ground state. It is also called spin-lattice relaxation because the energy is transferred from the spins to the surroundings (lattice) through randomly fluctuating magnetic fields arising from molecular motion. There are several sources of fluctuating fields, among them magnetic dipole-dipole interactions, spin-rotation interactions, chemical shift anisotropy, scalar interactions and paramagnetic interactions (Traficante, 1996). The rate of transverse relaxation governs how quickly the magnetisation recovers after a pulse, and hence how long the delay between experiments must be to allow complete recovery.

2.2.6 Chemical Shift

Nuclei in different chemical environments, *e.g.* at different positions in a molecule, have different resonance frequencies (Proctor and Yu, 1950). The differences in the frequencies are very small and are called chemical shifts. Chemical shifts arise because nuclei in different environments experience differences in the local magnetic field due to small secondary magnetic fields generated by the motion of electrons surrounding the nuclei. The magnetic fields induced by the electrons oppose the primary applied field, so a nucleus with a higher electron density is more strongly "shielded" from the primary field and has a lower chemical shift. Chemical shifts are expressed on a dimensionless scale, δ, defined as:

$$\delta = \frac{\nu - \nu_{ref}}{\nu_{ref}} \times 10^6 \ \ (ppm). \tag{2.21}$$

The chemical shift scale is useful because it is independent of $\mathbf{B_0}$, enabling comparison of spectra acquired at different field strengths. For ^{1}H spectra, the reference frequency, ν_{ref}, is often taken to be that of the ^{1}H nuclei in tetramethylsilane (TMS), $Si(CH_3)_4$.

2.2.7 Spin-Spin Coupling

The local magnetic field experienced by a nucleus is affected by the spin states of other nearby nuclei, particularly those with which the nucleus shares electrons. This spin-spin coupling between nuclei causes a splitting of the peaks in the NMR spectrum. The magnitude of the peak splitting is independent of $\mathbf{B_0}$ and is called the coupling constant, J_{AB}, measured in Hz.

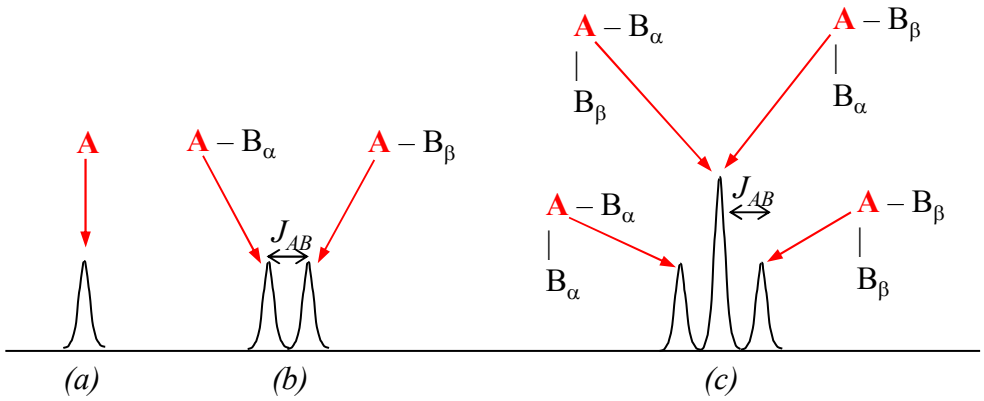

Figure 2.8 Peak splitting of the signal for nucleus A observed for
(a) no coupling,
(b) coupling to a single spin-½ B nucleus,
(c) coupling to two equivalent spin-½ B nuclei.

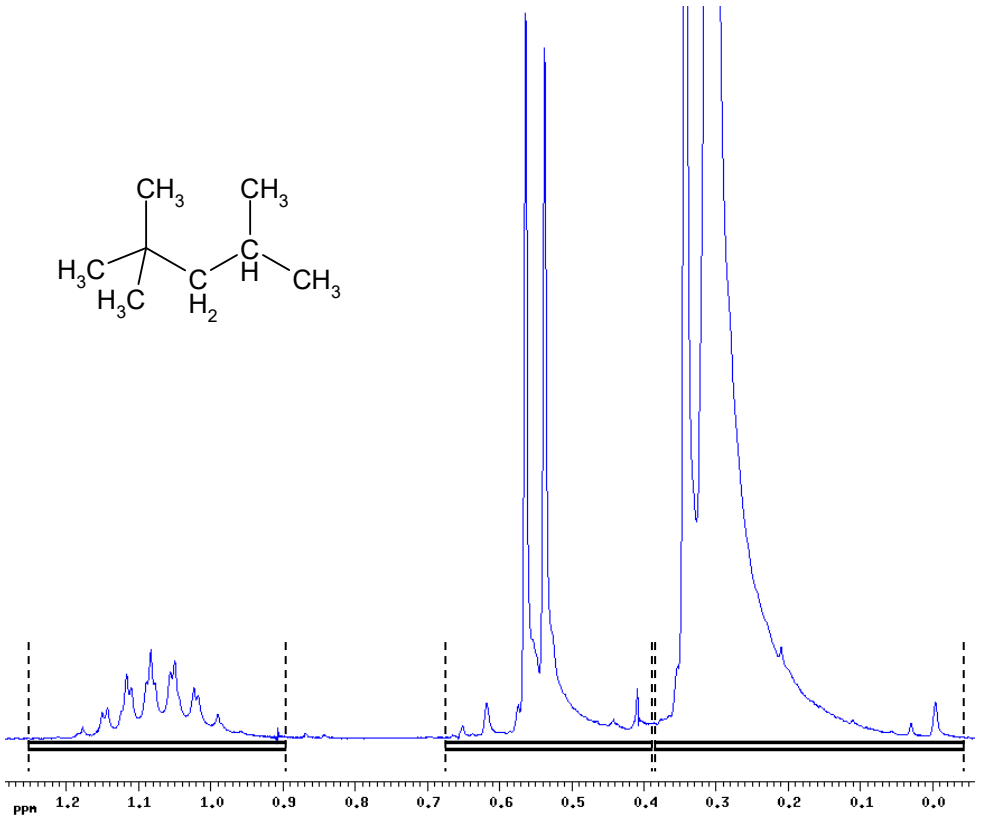

Figure 2.9 High-resolution 200 MHz ^{1}H NMR spectrum of pure liquid isooctane (2,2,4-trimethyl pentane) at 293 K. The chemical shift axis is relative to the resonance frequency of TMS. The asymmetric lineshapes were caused by magnetic field inhomogeneity. The dashed lines show the limits for peak integration.

δ (ppm)	**multiplicity**	**assignment**	**coupled to**	**J_{AB} (Hz)**	**J_{CH} (Hz)**	**number of ^{1}H nuclei**
0.314	singlet	$(CH_3)_3$	---	---	61.35	9
0.328	doublet	$(CH_3)_2$	CH	6.65	61.65	6
0.553	doublet	CH_2	CH	5.30	60.73	2
1.085	septet of triplets	CH	$(CH_3)_2$, CH_2	6.65,5.30	*	1

* ^{13}C satellites were not observed because they were too small

Table 2.1 Peak assignments for isooctane.

No coupling is observed for magnetically equivalent nuclei, *i.e.* those in identical electronic environments with identical coupling to all other nuclei. For a nucleus, A, coupled to one spin-½ nucleus, B, the peak for A is split into two equal peaks (a doublet) arising from the two spin states of B, α or β. For A coupled to two equivalent B nuclei, a binomial triplet is seen (figure 2.8). The multiplicity of a peak from a coupled nucleus is $2nI+1$, where n is the number and I is the spin quantum number of the neighbouring nuclei.

Spin-spin coupling often occurs between bonded ^{1}H and ^{13}C nuclei. Since ^{13}C occurs with 1.1% natural abundance, all hydrocarbon samples contain ^{13}C nuclei. The ^{1}H peak consists of a singlet arising from 98.9% of ^{1}H nuclei that are attached to a ^{12}C nucleus ($I = 0$), and a much smaller doublet arising from 1.1% of ^{1}H nuclei that are attached to a ^{13}C nucleus ($I = ½$). The coupling constant J_{CH} is ~60 Hz. The two small peaks on either side of the main peak are called ^{13}C satellites.

The ^{1}H spectrum of isooctane (figure 2.9) shows extensive spin-spin coupling, including ^{13}C satellites. The peak assignments for this spectrum are listed in table 2.1.

2.3 Experimental

2.3.1 Materials and Method

The composition of liquid mixtures measured from ^{1}H NMR spectra was compared with the composition determined by weight when preparing the mixtures. Six liquid components were chosen that were non-reactive and gave distinctive NMR peaks: water (H_2O), methanol (CH_3OH), cyclohexane (C_6H_{12}), toluene ($C_6H_5CH_3$), isooctane ($CH_3C(CH_3)_2CH_2CH(CH_3)_2$) and ethyl acetate ($CH_3CH_2OCOCH_3$). The water was deionised tap water and the other liquids were 99.9% HPLC grade supplied by the Aldrich Chemical Company and used without further purification. Liquid mixtures were made up with two, three, four and five components, using the combinations of liquids shown in table 2.2. For each combination in the table, two to six mixtures were made with different compositions. The mixtures were prepared by weight, with an accuracy of ±0.003 g. The volatility of the liquid components caused some of the added liquids to evaporate during preparation, leading to an average error in the made-up mixture compositions of ±0.023 mol%.

mixture	**water**	**methanol**	**toluene**	**cyclohexane**	**isooctane**	**ethyl acetate**
2A	■	■				
2B		■	■			
2C		■				■
2D			■	■		
2E			■		■	
2F			■			■
2G				■	■	
2H				■		■
2I					■	■
3A	■	■				■
3B		■	■	■		
3C		■	■		■	
3D		■	■			■
3E		■		■		■
3F		■			■	■
3G			■	■	■	
3H			■	■		■
3I			■		■	■
3J				■	■	■
4A		■	■	■	■	
4B		■	■	■		■
4C		■	■		■	■
4D			■	■	■	■
4E		■		■	■	■
5A		■	■	■	■	■

Table 2.2 Combinations of liquids in mixture samples. A ■ indicates the presence of a component in a mixture.

The ^{1}H NMR spectra were acquired using a Bruker MSL 200 spectrometer equipped with a 4.7 T, 89-mm bore, vertical superconducting magnet. A high-resolution probe was used with a 5-mm saddle coil tuned to a ^{1}H resonance frequency of 200.130 MHz. Eight scans were acquired using the pulse sequence shown in figure 2.12 with a four-scan phase cycle (+*x* -*x* +*y* -*y*). After a pre-scan delay of 100 μs, the FID was sampled every 100 μs for 32,768 data points. The acquisition parameters were chosen to ensure that the integrals in the spectra were strictly proportional to the number of nuclei in the sample. They are explained in more detail in section 2.3.4 below.

Two series of spectra were acquired. Series I contained spectra of mixtures 2A, 2B, 2D, 2G, 3G and 4A acquired at temperatures of 293 K, 313 K and 333 K. Following common practice in NMR spectroscopy, a small tip angle (3.00 μs r.f. pulse for 40°) and a short repetition time (3.2778 s) were used. However, the T_1 values of the liquid components were measured later and found to be in the range of 1-6 s for the pure liquids. In the mixtures, the T_1 values varied quite strongly with sample composition but remained within the same range. Therefore, a second series of spectra were acquired with a 90° tip angle (6.80 μs r.f. pulse duration) and a repetition time of 30 s to allow for full relaxation between scans. Series II contained spectra of all the mixtures listed in table 2.2 acquired at 293 K.

The reproducibility of the NMR composition measurement was tested by acquiring 10 spectra of the same sample (methanol-toluene-cyclohexane-ethyl acetate) and comparing the compositions calculated from them. The limits of detection were tested by acquiring spectra of very dilute solutions of isooctane in toluene. The solutions were measured twice: immediately after preparation and after three weeks' storage at room temperature in vials sealed with parafilm.

The data were processed using the Bruker software, *xwinnmr 1.3*. The first point of the FID was halved to remove baseline offset prior to Fourier transformation. After manual phase and baseline correction, the peaks were integrated using fixed integration ranges (table 2.3 and figure 2.9). The composition was calculated from the integrals manually at first, later using the *nmrquant* module of *xwinnmr*. These processing operations are explained in more detail in section 2.3.5 below.

component	peak	integration range (Hz either side)	number of ^{1}H nuclei in peak
water	H_2O	150	2
cyclohexane	C_6H_{12}	150	12
methanol	OH	65	1
methanol	CH_3	100	3
toluene	CH_3	80	3
toluene	C_6H_5	120	5
isooctane	CH	40	1.0110
isooctane	CH_2	minima	2.0715
isooctane	$(CH_3)_2$ & $(CH_3)_3$	80 or minimum	14.9175
ethyl acetate	CH_2	100	2
ethyl acetate	$COCH_3$	100 or minimum	3
ethyl acetate	CH_3	100 or minimum	3

Table 2.3 Frequency ranges for peak integrals in multi-component mixture spectra. "minimum": integrate until minimum between overlapping peaks. Non-integral values in the last column are caused by ^{13}C satellites hidden under neighbouring peaks.

2.3.2 Apparatus

2.3.2.1 Magnet

The static magnetic field of 4.7 T was produced using a 89-mm bore, vertical superconducting magnet. The homogeneity of the field over the sample volume was crucial, since an inhomogeneous field broadened the peaks in the spectrum and increased peak overlap. The homogeneity of the field was improved by adding small corrective fields generated by electric coils called shims (Golay, 1958; Anderson, 1961). The magnet was "shimmed" at the start of the experiments by adjusting the currents in the shim coils (Conover, 1984; Chmurny and Hoult, 1990) to give a ^{1}H linewidths at half-maximum of 1-3 Hz in the mixture spectra.

2.3.2.2 Spectrometer

The spectrometer contains the electronic hardware that controls the excitation and detection of the NMR signal. The Bruker MSL 200 spectrometer used in these experiments is shown schematically in figure 2.10. An r.f. pulse was synthesised, converted to the desired frequency and transmitted to the coil inside the probe. The signal was detected using the same coil as an oscillating electric current, which was amplified in the pre-amplifier and sent to the receiver. The receiver converted the analogue signal from radio frequency to audio frequency, then the quadrature phase detector separated the signal into real and imaginary components. The audio band-pass filter only passed the frequency range selected by the operator, to prevent noise from all frequencies appearing in the spectrum. Finally, the signal was digitised in the analogue-to-digital converter (ADC) and stored in the computer as a series of integers. The ADC had 16 bits, so its dynamic range was limited to a factor of $2^{16} = 65536$.

2.3.3 Sample Preparation

Spectroscopists often dilute samples with deuterated solvents (all ^{1}H replaced with ^{2}H, $I = 1$). In a 4.7 T magnetic field, the resonance frequencies of ^{1}H and ^{2}H are 200 MHz and 30.7 MHz respectively, so the ^{2}H signals lie outside the frequency range of the ^{1}H spectrum, typically 5 kHz either side of 200 MHz. Deuterated solvents increase the resolution by reducing the ^{1}H spin density so that the lines in the spectrum are narrower, because samples with a high ^{1}H spin density exhibit magnetisation

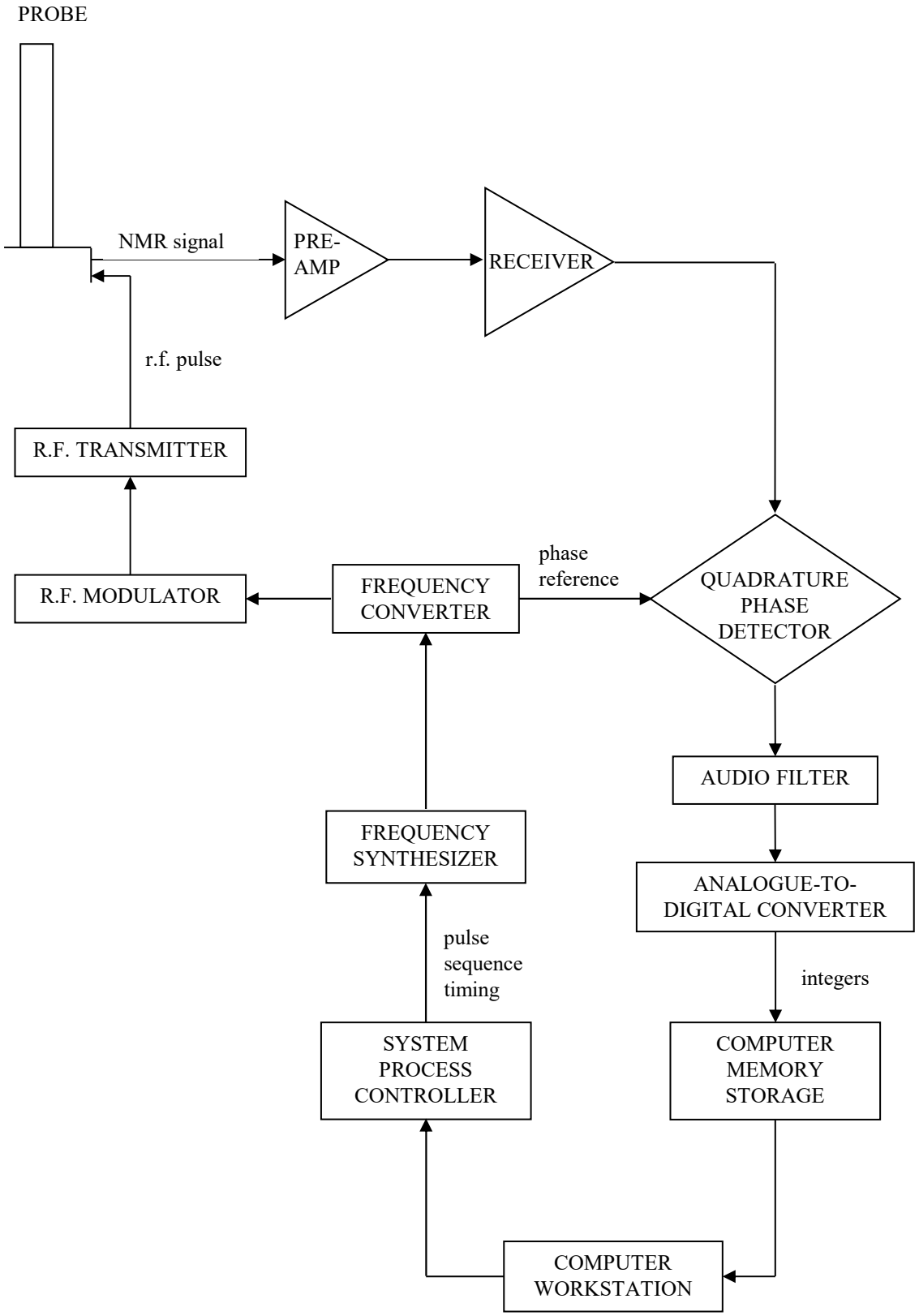

Figure 2.10 Schematic of NMR spectrometer operation for high-resolution spectroscopy.

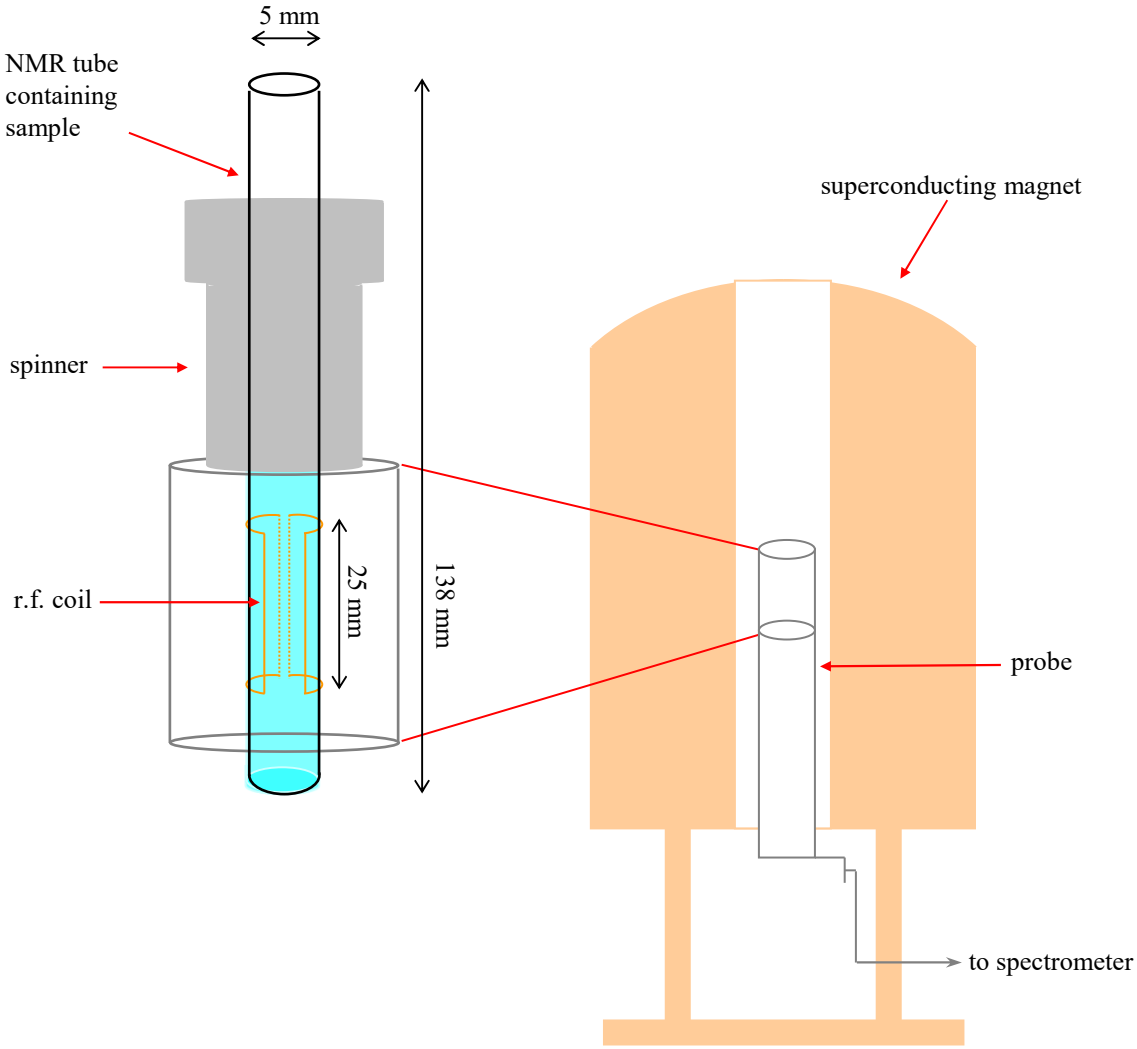

Figure 2.11 Experimental set-up for high-resolution NMR spectroscopy of liquid samples inside NMR tubes.

anisotropy and line broadening due to radiation damping (Warren and Richter, 1996). Radiation damping is caused by a secondary magnetic field opposing the original field, which is generated by the current induced in the receiver coil by a large transverse magnetisation. The secondary field causes non-exponential decay and provides another mechanism for relaxation (Traficante, 1996). However, the liquid mixtures in this work were undiluted to mimic process conditions, so significant radiation damping was present and the lines in the spectrum were relatively broad.

The liquid mixtures were introduced into the magnetic field inside glass tubes (4.1 mm i.d., 5 mm o.d., 138 mm length) that did not produce an NMR signal. A tube was placed inside a sample holder called a spinner, which was then placed inside the bore of the magnet such that the liquid inside the tube completely filled the active region of the r.f. coil (figure 2.11). During the experiments, the sample was spun at 20 Hz to average out radial magnetic field inhomogeneity. This improved resolution by narrowing the lines in the spectrum.

2.3.4 Signal Acquisition

The pulse sequence used to acquire the spectra (figure 2.12) consisted of a single r.f. pulse followed by acquisition of the FID. After a delay to allow longitudinal relaxation, the sequence was repeated. Electronic noise is associated with all frequencies and is generally assumed to be uncorrelated. The NMR signal is weak compared to the noise, so the signals from several scans were co-added to increase the signal-to-noise ratio. For N_S measurements, the signal intensity increased as N_S but the r.m.s. noise increased as $\sqrt{N_S}$, so the signal-to-noise ratio increased as $\sqrt{N_S}$ (Derome, 1987). The pulse sequence also contained an eight-scan phase cycle to reduce artefacts in the spectrum caused by the receiver. In theory, phase cycling consists of switching r.f. pulses and receiver channels between different axes of the rotating frame on successive scans. In practice, it was achieved by electronically altering the phases of the r.f. pulse and the receiver reference frequency.

The energy required for the r.f. pulse depends on the desired tip angle, but the operator is free to choose a combination of pulse power and duration to supply that energy. For quantitative spectroscopy, a “hard pulse” is required with a high power level and a short duration to uniformly excite a wide frequency range (Fukushima and Roeder, 1981). For a 90° tip angle, the r.f. pulse duration was 6.8 μs.

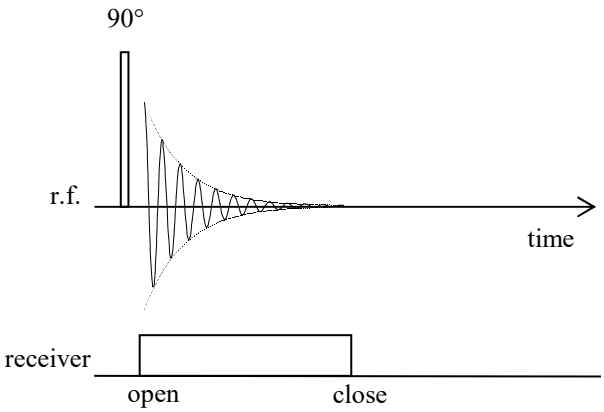

Phase Cycle

90° pulse	$+x$	$-x$	$-x$	$+x$	$+y$	$-y$	$-y$	$+y$
receiver	$+x$	$-x$	$+x$	$-x$	$+y$	$-y$	$+y$	$-y$

Figure 2.12 R.F. pulse sequence and phase cycle for ^{1}H NMR spectroscopy. The receiver is opened after the pulse to acquire the FID and is closed at the end of acquisition. After a repetition time T_R, the sequence is repeated with the pulse and receiver phases set to the next value in the phase cycle.

Since the same coil was used for excitation and detection, the receiver was opened after a short pre-scan delay (100 μs) to allow the ringing in the coil caused by the pulse to die away. If the receiver was opened immediately, it was overloaded by the intense signal from the pulse. The pulse "breakthrough" signal carried over into the first few points of the FID, especially if the pre-scan delay is short. However, if the pre-scan delay was long then the initial part of the FID is lost. The corruption of the start of the FID caused baseline distortions in the spectrum (section 2.3.5.3).

The delay between scans, T_R, had to be long enough to allow the longitudinal magnetisation to recover fully, otherwise a pulse applied to a partially recovered magnetisation gave a relaxation-weighted signal. Different nuclei in the sample had different T_1 values, so they had relaxed to different extents when the next pulse was applied, unless the delay was long enough for all nuclei to have relaxed fully. Relaxation-weighted signals are not proportional to the number of nuclei, so they cannot give composition information unless the T_1 values are known exactly (Derome, 1987). However, T_1 values depend on the surroundings of the sample, so they vary with magnetic field strength, sample composition, physical environment, temperature and pressure (Jonas and Lee, 1991). Measuring T_1 values is very time-consuming, so it was quicker to select a value of T_R large enough to give full relaxation. T_R can be calculated from equation (2.20) by setting $M_z(0)$ to zero after a 90° pulse and rearranging to give:

$$\frac{M_z(t)}{M_0} = 1 - \exp\left(-T_R/T_1\right). \qquad (2.22)$$

For 99% magnetisation recovery $T_R = 4.61T_1$. The longest T_1 value measured in the liquid mixtures was 6 s, so T_R was set to 30 s.

2.3.5 Post-Acquisition Data Processing

There were several stages in obtaining the sample composition from the digitised FID: Fourier transformation, phase and baseline correction, peak integration and assignment, and composition calculation.

2.3.5.1 The Fourier Transform

The time-domain signal was converted to the frequency domain by applying a Fourier transform to the FID. The discrete Fourier transform was performed using the Fast Fourier Transform (FFT) algorithm (Cooley and Tukey, 1965).

For liquids, the FID can be considered a sum of exponentially damped sinusoids that is sampled in the time domain with an interval of Δt. A single frequency component in the FID is given by:

$$\hat{S}(t) = \begin{cases} S(0)e^{-k\Delta t/T_2^*}e^{i(2\pi\nu_0 k\Delta t+\phi)} & t \geq 0 \\ 0 & t < 0 \end{cases}, \tag{2.23}$$

where ν_0 is the frequency and ϕ is the phase of the oscillating component, k is the data point index and T_2^* is the decay time constant. The application of the r.f. pulse defines $t = 0$, so the signal is zero for negative time before the pulse.

The discrete Fourier transform (DFT) into the frequency domain is defined as (Bracewell, 1978):

$$\hat{s}(\nu) = \frac{1}{\sqrt{N}} \sum_{k=0}^{N-1} \hat{S}(t) e^{-i2\pi j\Delta\nu k\Delta t/N}. \tag{2.24}$$

The DFT of equation (2.23) is the sum of a finite geometric progression given by (Hoch and Stern, 1996):

$$\hat{s}(\nu) = \frac{S(0)e^{i\phi}}{\sqrt{N}} \cdot \frac{1 - e^{-N\left(\Delta t/T_2^* + i2\pi\Delta t\left(j\Delta\nu/N - \nu_0\right)\right)}}{1 - e^{-\left(\Delta t/T_2^* + i2\pi\Delta t\left(j\Delta\nu/N - \nu_0\right)\right)}}. \tag{2.25}$$

Assuming complete sampling of the FID, so that $N\Delta t >> T_2^*$ and $\Delta t << 1$, equation (2.25) can be simplified to give (Abildgaard *et al.*, 1988; Gesmar *et al.*, 1990):

$$\hat{s}(\nu) = \frac{S(0)e^{i\phi}}{\sqrt{N}} \left[\frac{\Delta t/T_2^* - i2\pi\Delta t\left(j\Delta\nu/N - \nu_0\right)}{\left(\Delta t/T_2^*\right)^2 + 4\pi^2\Delta t^2\left(j\Delta\nu/N - \nu_0\right)^2} \right] + \frac{S(0)e^{i\phi}}{2\sqrt{N}}. \tag{2.26}$$

The first term in equation (2.26) is the discrete Lorentzian lineshape centred at frequency ν_0 (figure 2.13). The half-width, λ, at half the maximum intensity of the lineshape is given by:

$$\lambda = \frac{1}{2\pi T_2^*}, \tag{2.27}$$

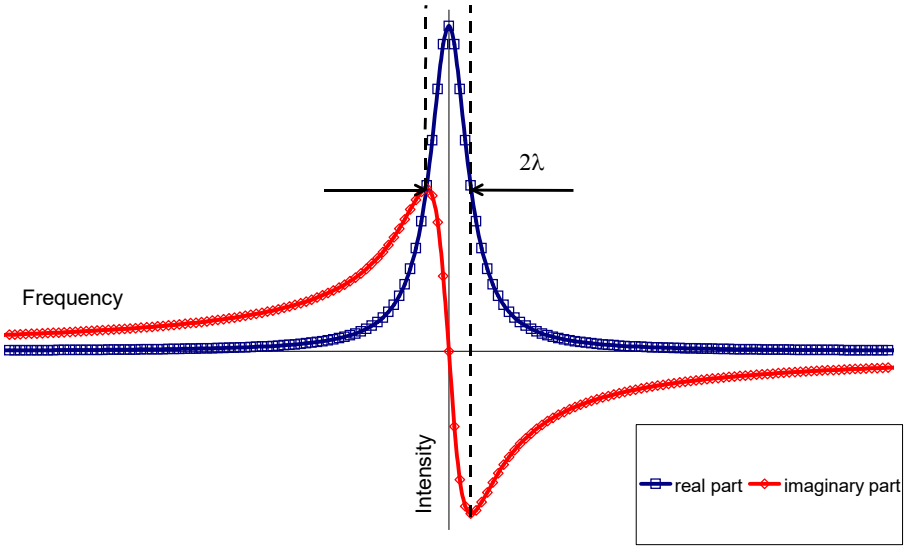

Figure 2.13 The real and imaginary parts of a Lorentzian lineshape. 2λ equals the width of the real part at half its maximum intensity and difference in frequency between the minimum and maximum of the imaginary part.

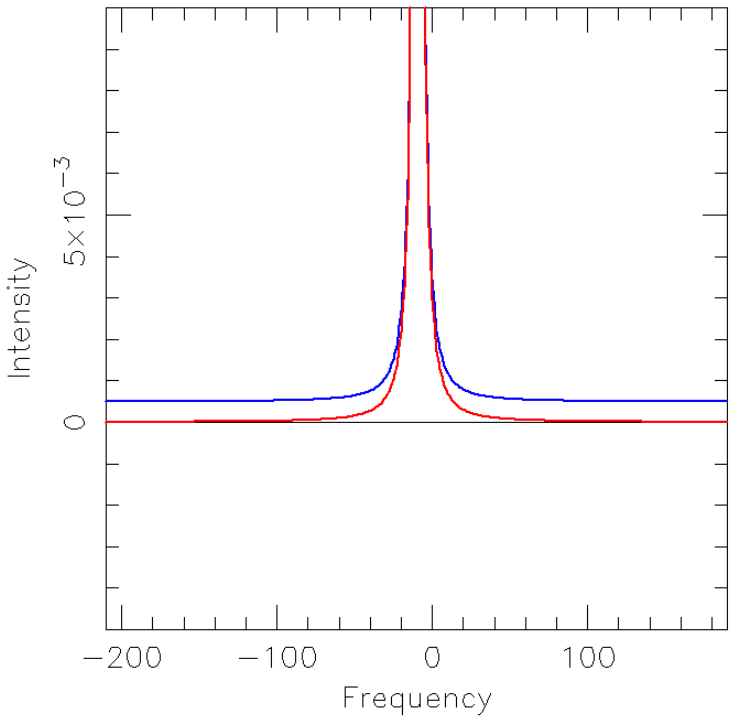

Figure 2.14 The baseline offset caused by the discrete Fourier transform (blue line) can be removed by halving the first point in the FID (red line).

so the linewidth can be used to determine the value of T_2^* for each peak in the spectrum. The second term in equation (2.26) is frequency-independent and causes a constant baseline offset in the spectrum (figure 2.14). This offset is undesirable because it causes integration errors, and it was removed by halving the value of the first point in the FID before applying the DFT (Tang, 1994).

If $\phi = 0$, then the integral of the real part of the Lorentzian equals $S(0)$ and the integral of the imaginary part equals zero. $S(0)$ is proportional to the spin density, so the composition is determined from the real part of the lineshape, which corresponds to the absorption lineshape of section 2.2.4.

2.3.5.2 Phase Correction

The acquired real and imaginary components of the FID did not correspond directly to the absorption and dispersion components due to the phase offset between the reference frequency and the signal. This offset is given by the $e^{i\phi}$ term in equation (2.26). The pure absorption and dispersion signals, s_A and s_D, were recovered by applying a phase correction to the real and imaginary signals, s_R and s_I, using (Derome, 1987):

$$\begin{aligned} s_A(\nu) &= s_R(\nu)\cos\phi - s_I(\nu)\sin\phi \\ s_D(\nu) &= s_R(\nu)\sin\phi + s_I(\nu)\cos\phi \end{aligned} . \qquad (2.28)$$

The pre-scan delay introduced an additional frequency-dependent phase offset. The application of the r.f. pulse defines $t = 0$, but sampling only began a short time, t_{in}, later to avoid pulse breakthrough. The digitised FID with delayed sampling is given by:

$$\hat{S}(t) = \begin{cases} S(0)e^{-(k\Delta t + t_{in})/T_2^*} e^{i\phi} e^{i2\pi\nu_0(k\Delta t + t_{in})} & t \geq 0 \\ 0 & t < 0 \end{cases}, \qquad (2.29)$$

which has a spectrum given by (Gesmar *et al.*, 1990):

$$\hat{s}(\nu) = \frac{S(0)e^{-t_{in}/T_2^*}}{\sqrt{N}} e^{i(2\pi\nu_0 t_{in} + \phi)} \left[\frac{1}{2} + \frac{1}{\frac{\Delta t}{T_2^*} + i2\pi\Delta t\left(\frac{j\Delta\nu}{N} - \nu_0\right)} \right]. \qquad (2.30)$$

The phase offset now contains the term $2\pi\nu_0 t_{in}$ that depends on the resonance frequency of the peak in the spectrum and the pre-scan delay, t_{in}. Off-resonance

excitation also caused a linear frequency-dependent phase shift in the spectrum (Fukushima and Roeder, 1981) and higher-order phase shifts were caused by the non-linear phase behaviour of the frequency filter (Daubenfeld *et al.*, 1985). These phase shifts were all corrected together using a phase angle that varied linearly with frequency, given by:

$$\phi(\nu) = \phi_0 + \phi_1 \nu, \tag{2.31}$$

which was a good approximation provided that non-linear phase shifts were small. Manual phase correction was performed by altering the parameters ϕ_0 and ϕ_1, while viewing the spectrum, until all the peaks had absorption lineshapes.

2.3.5.3 Baseline Correction

The pre-scan delay distorted the baseline of the spectrum because the first point was not sampled at $t = 0$. The initial value of the FID equals the integral over the entire spectrum (Anderson, 1996) and is given by:

$$\hat{S}(t_{in}) = S(0) e^{-t_{in}/T_2^*} e^{i(2\pi\nu_0 t_{in} + \phi)} \neq S(0). \tag{2.32}$$

The incorrect initial value of the FID alters the integral of the spectrum by distorting the baseline from zero. This distortion is minimised when t_{in} equals 0, Δt or $\Delta t/2$ (Tang, 1994). A spectrum acquired with $t_{in} = \Delta t$ (figure 2.15(a)) had a fairly flat baseline, in contrast to the undulating baseline obtained when $t_{in} = 5\Delta t$ (figure 2.15(b)). Linear phase correction also caused undulations in the baseline because the phase offset $2\pi\nu_0 t_{in}$ was incompletely removed and the wings of the dispersion spectrum were folded into the absorption spectrum (Marion and Bax, 1988) through improper re-sampling of the signal (Starcuk *et al.*, 1994). The baseline distortions were removed in the frequency domain by fitting a function (e.g. a polynomial) through the regions in the spectrum that were devoid of signal. The function was then subtracted from the data to give an artificially flattened baseline (Daubenfeld *et al.*, 1985). This form of baseline correction has widespread use even though it has no theoretical justification, because it is easy to implement and does not cause large errors in the peak integrals provided the original baseline distortions were small.

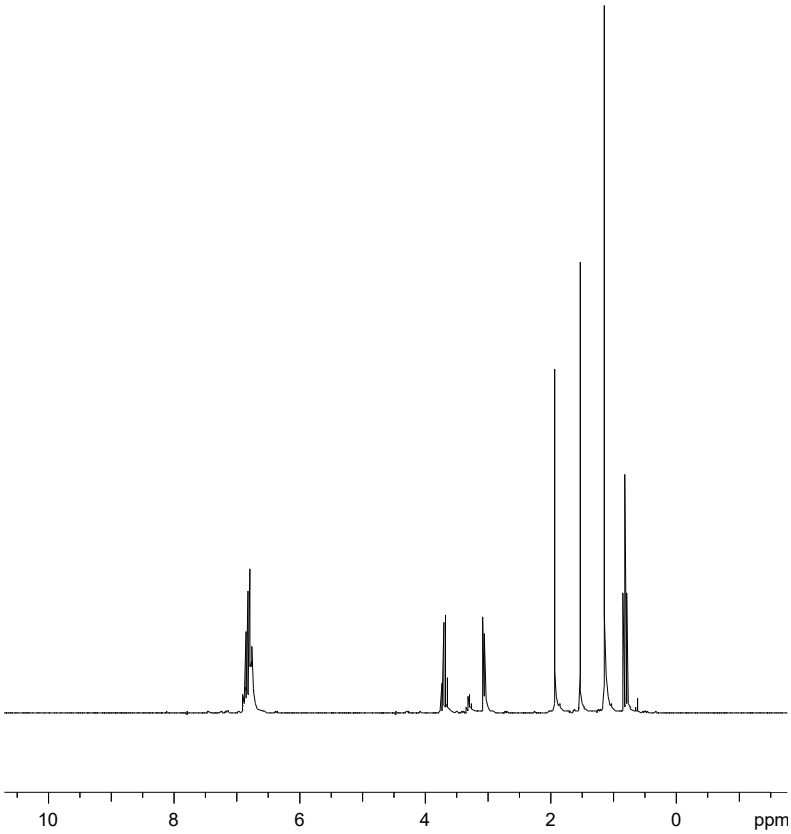

(a)

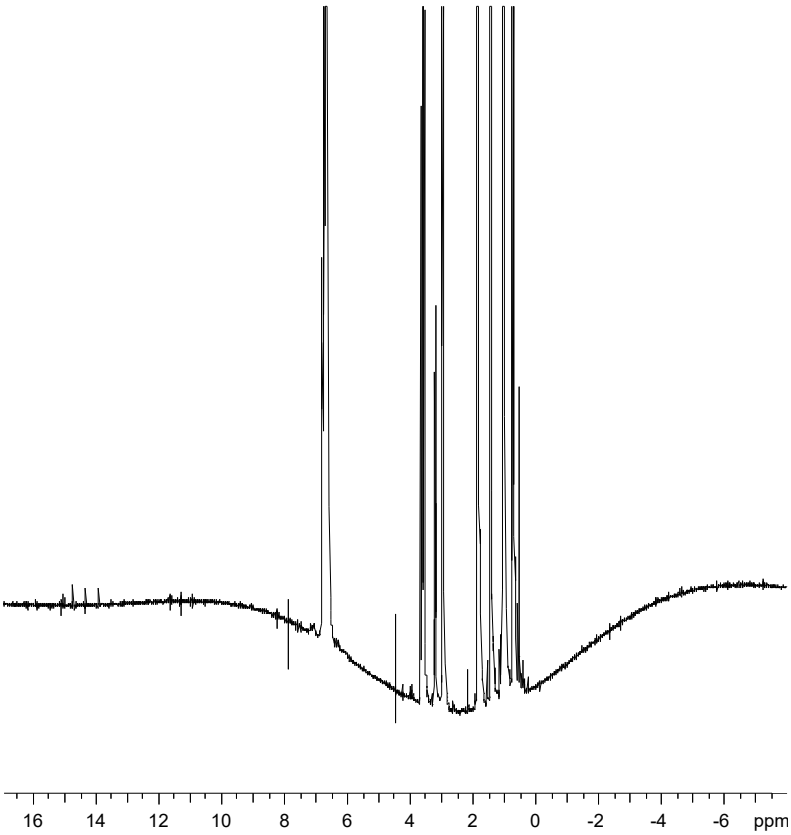

(b)

Figure 2.15 200 MHz ^{1}H NMR spectra at 293K of a mixture of methanol-toluene-cyclohexane-ethyl acetate showing the effect of the pre-scan delay on the baseline: *(a)* $t_{in} = \Delta t$, *(b)* $t_{in} = 5\Delta t$.

2.3.5.4 Peak Integration

Accurate integrals of the absorption peaks were required to allow the composition of the samples to be calculated. The integral was taken to be the sum of the intensities of the points defining each peak, since this was more precise than the trapezoid rule and Simpson's rule when integrating sharp lines (Hoch and Stern, 1996). For single peaks, the integration range covered the whole peak down to the noise level. For overlapping peaks, the total integral, which was the sum of the individual peak integrals, was partitioned at the minimum between the peaks. This "perpendicular drop" method is most commonly used because it is reliable and simple, but it is inherently inaccurate (Westerberg, 1969; Hancock *et al.*, 1970; Foley, 1987). The peak integration ranges are given in table 2.3.

2.3.5.5 Peak Assignment

The peaks in the spectrum of a single component were assigned to specific ^{1}H nuclei in the molecule based on their chemical shifts, multiplicities, coupling constants and relative integrals. The chemical shifts of the peaks were determined relative to the resonance frequency of TMS by measuring the resonance frequency of TMS in a separate sample under identical conditions. It was not possible to add TMS directly to the mixtures because it was immiscible with water and the resulting two-phase samples exhibited distorted lineshapes. Tables of chemical shifts and rules for estimating their values (Williams and Fleming, 1989), and the spectra of common molecules found in catalogues of NMR spectra (Pouchert and Behnke, 1992) were used to aid peak assignment. The spectra of multi-component samples were considered, as a first approximation, as the sum of pure component spectra. The pattern of peaks from each component was unchanged, but the peak positions shifted slightly depending on the sample composition.

2.3.5.6 Composition Calculation

The composition of a multi-component mixture was calculated manually from its spectrum as follows:

1. For each component, the integrals of all the peaks assigned to that component were added, then the sum was divided by the number of ^{1}H nuclei in that component to give the weighted integral.

2. The weighted integrals were added to give the total spin density in the sample.
3. Each weighted integral was divided by the total spin density to give the mole fraction of each component.

The compositions of the mixtures in Series I were calculated using this procedure. For Series II, the *nmrquant* module of the *xwinnmr* software was used because it was faster. The details of *nmrquant* are not available, but it gave results identical to those obtained manually, so it must operate along similar lines.

2.4 Results and Discussion

The spectra of pure water, methanol, cyclohexane, toluene, isooctane and ethyl acetate at 293 K are shown in figure 2.16 with their peak assignments. The chemical shifts for all spectra presented in this chapter are relative to TMS.

2.4.1 Quantitative Measurements

For each mixture, the difference between the composition measured by NMR and the composition by weight was calculated to give the measurement error for each component. The overall error for the mixture was calculated as the average of the absolute values of the component errors. The individual mixture errors were further averaged for each type of mixture to see if the mixture type had a significant influence on accuracy. The average error over all mixtures in a series was also calculated.

The average errors for the mixture types in Series I (2A, 2B, 2D, 2G, 3G and 4A) at 293 K, 313 K and 333 K are given in table 2.4. The errors were in the range of 1-2 mol% and generally increased with temperature. The errors showed no dependence on mixture type or number of components in the mixture. The largest source of error was relaxation weighting because the repetition time between scans was too short for full recovery of the magnetisation. The volatility of the liquids also caused errors because the mixtures were prepared one day in advance and the composition had changed slightly by the time the spectra were acquired. NMR spectroscopy is sufficiently sensitive that these small changes were observed in the spectra.

The average errors for the mixture types in Series II at 293 K are given in table 2.5. These errors were much smaller than those for Series I (with a few exceptions) because relaxation weighting was eliminated by the 30-s repetition time. The errors

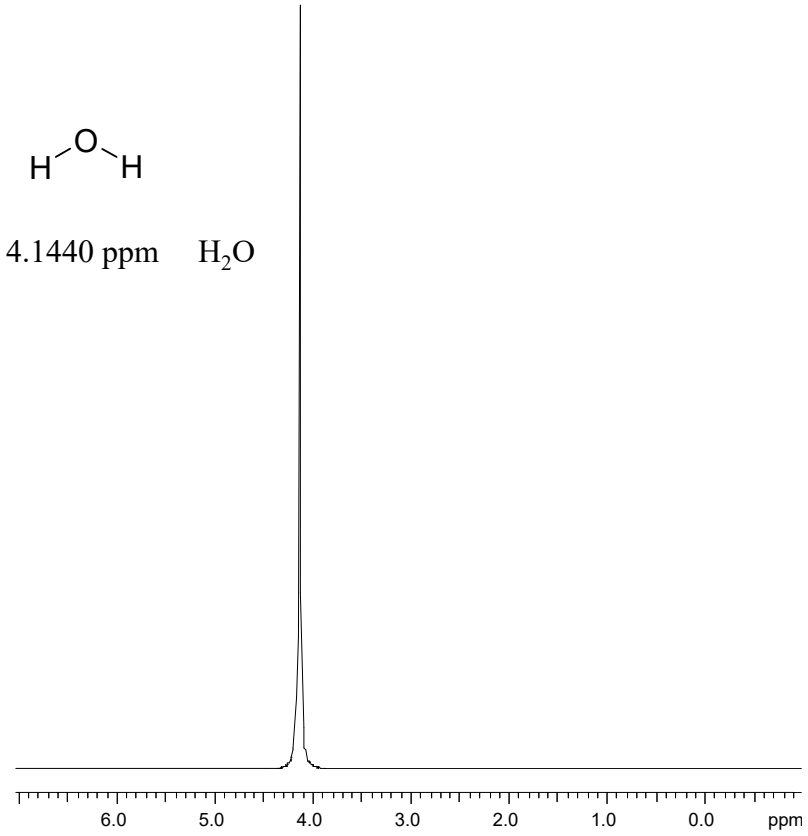

(a)

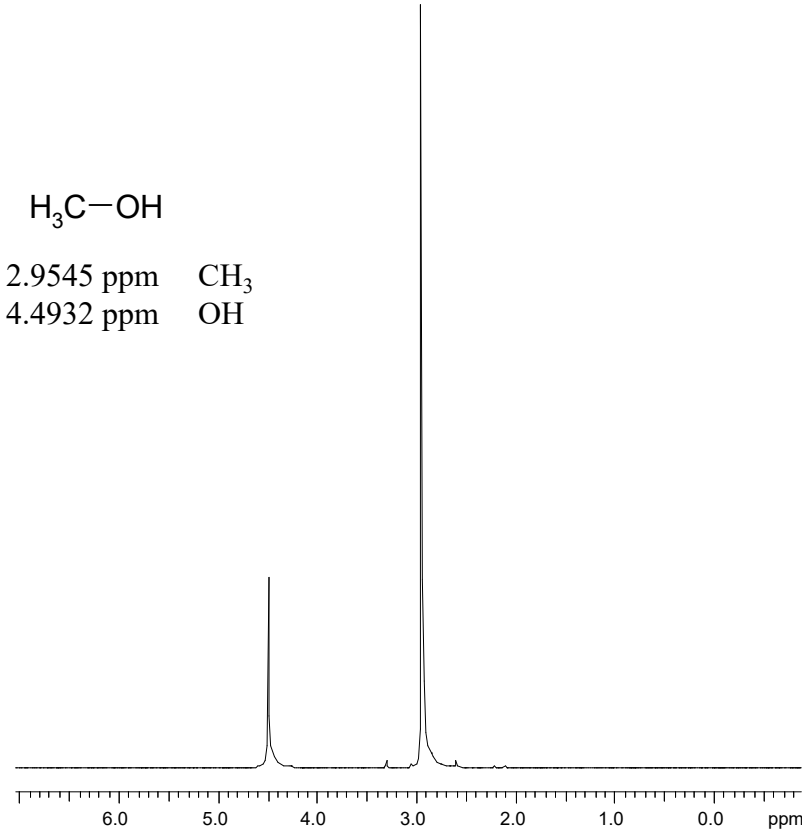

(b)

Figure 2.16 200 MHz ^{1}H NMR spectra at 293K *(a)* water *(b)* methanol

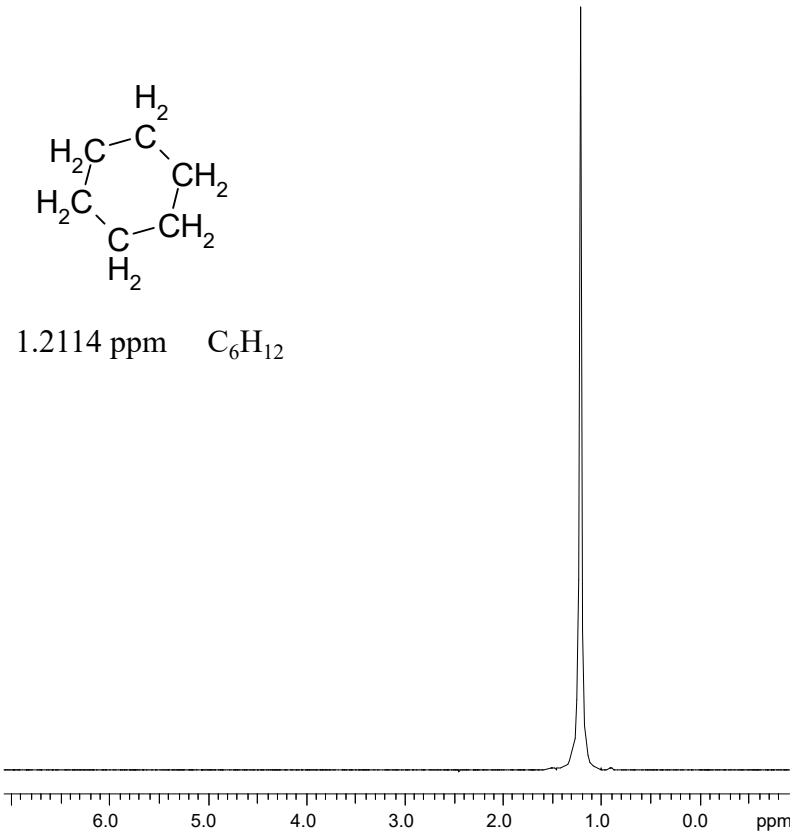

(c)

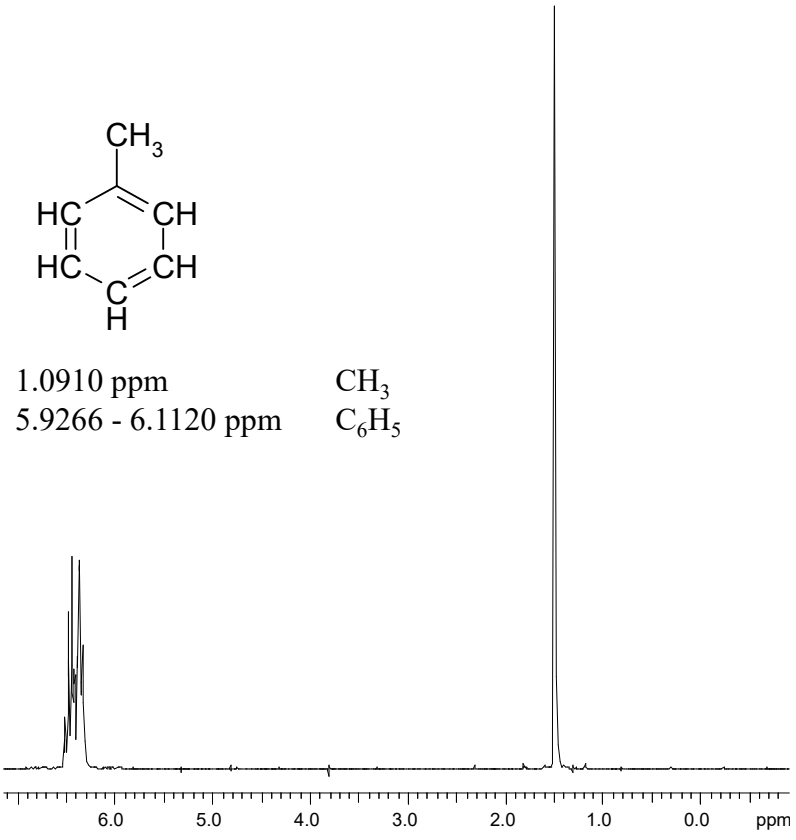

(d)

Figure 2.16 200 MHz ^{1}H NMR spectra at 293K *(c)* cyclohexane *(d)* toluene

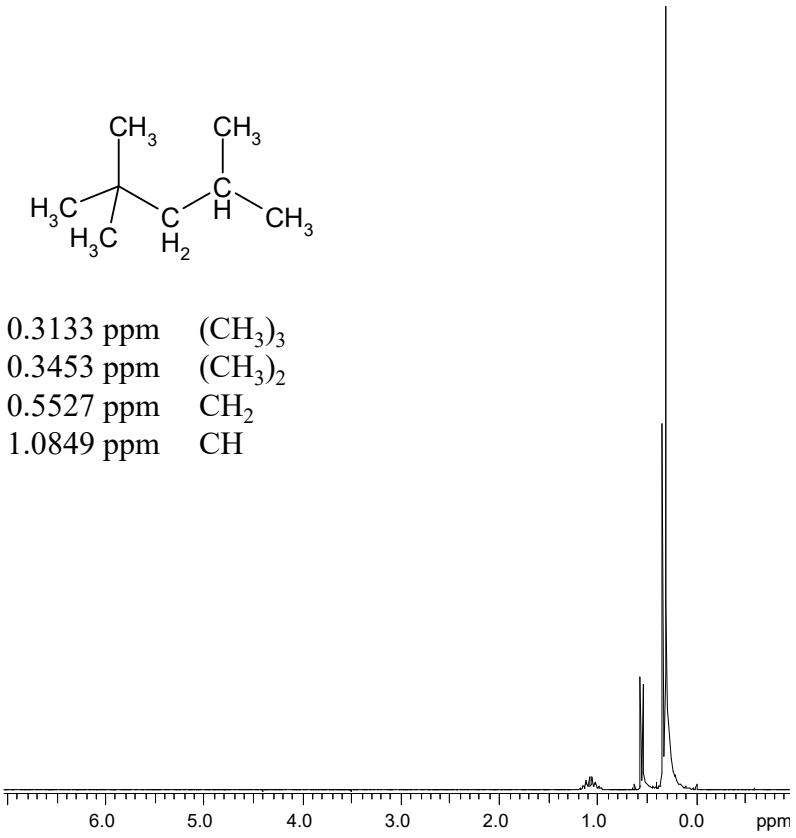

(e)

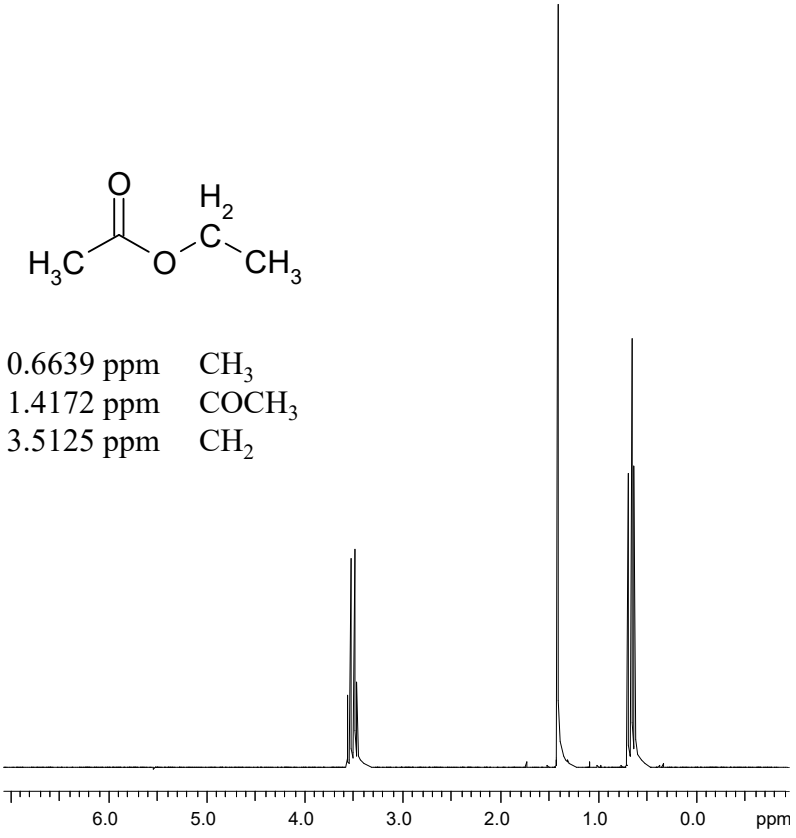

(f)

Figure 2.16 200 MHz ^{1}H NMR spectra at 293K *(e)* isooctane *(f)* ethyl acetate

Average composition error in Series I (mol%)			
mixture	293 K	313 K	333 K
2A	1.82	1.08	0.65
2B	1.23	1.15	2.75
2D	0.77	0.97	0.79
2G	1.05	0.42	1.28
3G	1.04	1.06	1.62
4A	0.64	1.49	5.15
all	*1.12*	*1.01*	*2.00*

Table 2.4 Errors in the compositions measured by ^{1}H NMR spectroscopy for the liquid mixtures in Series I at 293, 313 and 333 K, listed by mixture type.

Average composition error in Series II (mol%)			
mixture	error (mol%)	mixture	error (mol%)
2A	0.52	**3E**	2.13
2B	1.46	**3F**	0.58
2C	0.05	**3G**	0.19
2D	4.36	**3H**	0.41
2E	0.59	**3I**	0.15
2F	0.40	**3J**	1.45
2G	2.46	**4A**	0.22
2H	0.69	**4B**	0.22
2I	0.36	**4C**	0.47
3A	1.56	**4D**	0.60
3B	0.21	**4E**	0.88
3C	0.20	**5A**	1.04
3D	0.44	*all*	*0.79*

Table 2.5 Errors in the compositions measured by ^{1}H NMR spectroscopy for the liquid mixtures in Series II at 293 K, listed by mixture type.

from composition changes were also eliminated by preparing the mixtures immediately before acquiring the NMR spectra. The remaining errors in Series II were caused by artefacts in the spectra that distorted the peak integrals, especially baseline distortions. The errors in the peak integrals limited the accuracy of the composition measured by NMR to ±0.50 mol% averaged over all spectra, which was lower than the average difference with the composition by weight of 0.79 mol%. The mixture preparation error of ±0.023 mol% was negligible in comparison. If the spectra with severe baseline artefacts (7 out of 45 spectra) were excluded, the average NMR measurement error was ±0.34 mol% and the average difference with the composition by weight was 0.35 mol%. Therefore, the two compositions agreed within the range of experimental error.

The reproducibility was tested with ten measurements of the sample methanol-toluene-cyclohexane-ethyl acetate, which gave an average composition of 16.28 ± 0.53 mol% methanol, 40.67 ± 0.28 mol% toluene, 18.70 ± 0.14 mol% cyclohexane and 24.36 ± 0.36 mol% ethyl acetate. One of the ten spectra is shown in figure 2.15(a). The error values quoted are the averages of the errors from each measurement. The variation between measurements was no more than 0.08 mol% for any component, demonstrating a very high reproducibility for quantitative NMR measurements.

The sensitivity was tested by acquiring spectra of dilute solutions of isooctane in toluene (figure 2.17). For the lowest isooctane content (0.05 mol%), 32 scans were needed for the peaks to become visible in the spectrum. The compositions measured immediately after preparation were within 5% of the nominal composition (table 2.6). After three weeks' storage, the second measured compositions showed an increase in isooctane content caused by the lower volatility of isooctane compared to toluene. These results again demonstrate the sensitivity of NMR measurements to small changes in composition.

2.4.2 Effects of Composition and Temperature on Chemical Shifts

The chemical shifts of the peaks in the spectra varied with composition and with temperature. For example, the spectrum of a mixture of methanol (48.57 mol%), toluene (16.29 mol%), cyclohexane (14.98 mol%), isooctane (10.61 mol%) and ethyl acetate (9.61 mol%) is shown in figure 2.18. The chemical shifts of the peaks in this

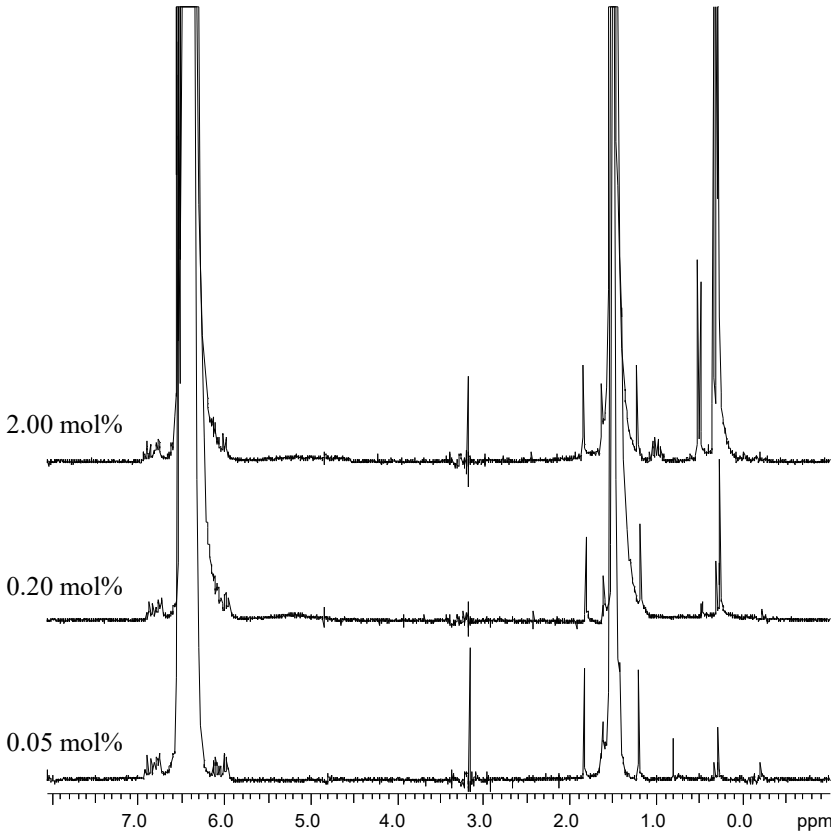

Figure 2.17 A series of high-resolution ^{1}H NMR spectra of dilute solutions of isooctane in toluene acquired at 293 K.

Prepared (mol%)	**Measured I (mol%)**	**Measured II (mol%)**
2.00	1.90±0.05	2.26±0.04
0.20	0.19±0.04	0.29±0.05
0.05	0.048±0.04	0.07±0.05

Table 2.6 Compositions of dilute solutions of isooctane in toluene used to test limits of detection in NMR spectra. The error ranges quoted are based on the errors in the relative peak integrals.

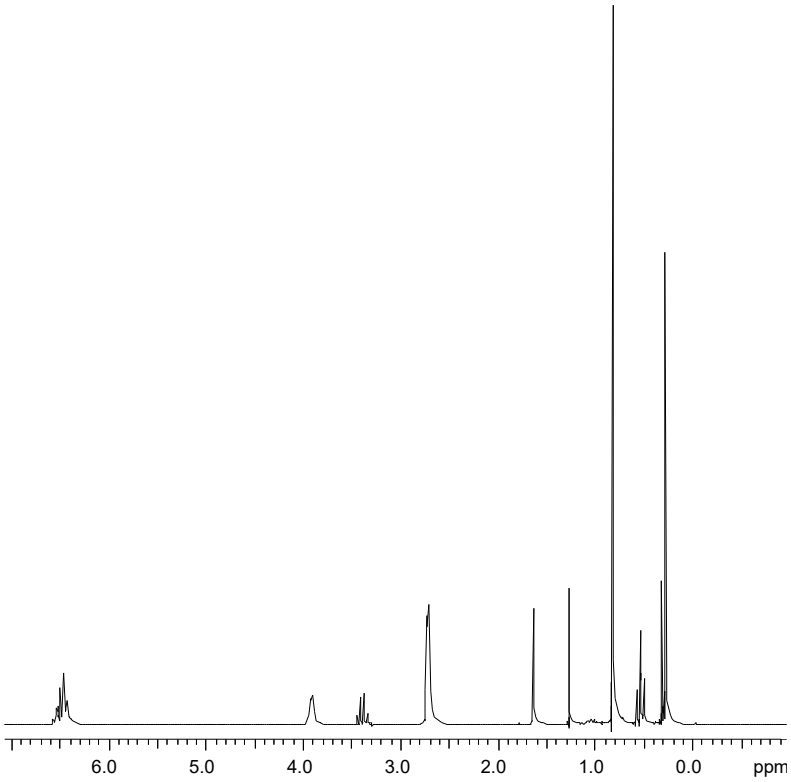

Figure 2.18 200 MHz ^{1}H NMR spectrum at 293K of a five-component mixture with molar composition: methanol 48.57%, toluene 16.29%, cyclohexane 14.98%, isooctane 10.61% and ethyl acetate 9.61%.

component	peak	δ in mixture (ppm)	δ pure (ppm)	change (ppm)
methanol	CH_3	2.7232	2.9545	-0.2313
methanol	OH	3.9224	4.4932	-0.5708
toluene	CH_3	1.6439	1.0910	+0.5529
toluene	C_6H_5	6.5007	6.0349	+0.4658
cyclohexane	C_6H_{12}	0.8195	1.2114	-0.3919
isooctane	$(CH_3)_3$	0.2798	0.3133	-0.0335
isooctane	$(CH_3)_2$	0.2998	0.3453	-0.0455
isooctane	CH_2	0.5147	0.5527	-0.0380
isooctane	CH	1.0443	1.0849	-0.0406
ethyl acetate	CH_3	0.5346	0.6639	-0.1293
ethyl acetate	$COCH_3$	1.2692	1.4172	-0.1480
ethyl acetate	CH_2	3.3977	3.5125	-0.1148

Table 2.7 Chemical shifts of the peaks in the spectrum shown in figure 2.18, and changes in chemical shifts relative to pure-component values.

spectrum were different from the pure-component values (table 2.7). The variation of chemical shifts with composition was seen most strongly for water-methanol mixtures where hydrogen bonding was present (figure 2.19(a)), but was less pronounced in mixtures without hydrogen bonding such as toluene-cyclohexane (figure 2.19(b)). The variation with temperature was strongest for water (figure 2.20(a)) and weakest cyclohexane (figure 2.20(b)). These variations in chemical shift were due to the changes in the chemical environments of the nuclei in the mixtures, particularly changes in hydrogen bonding or polarity of the molecules. Some changes were very consistent, *e.g.* an increase in the toluene content of a mixture moved all peaks to lower chemical shifts due to local magnetic fields induced by the circulation of the delocalised electrons in the aromatic ring of toluene (Harris, 1983) while an increase in the methanol content of a sample moved all peaks to higher chemical shifts due to the polarity of methanol (Harris, 1983). The non-polar molecules (cyclohexane, isooctane, ethyl acetate) often moved peaks to lower chemical shifts, but these effects were not consistent. None of the changes in chemical shift was linearly proportional to composition. This was consistent with reports in the literature of non-linear changes in the chemical shift with composition for mixtures of 2-propanol-cyclohexane (Karachewski *et al.*, 1989), halogenoalcohol-water (Mizuno *et al.*, 1995), and tri-*n*-butyl phosphate-chloroform (Choi and Tedder, 1995).

Another interesting effect was observed for the methanol peaks, which has not been found reported in the literature. The spectrum of pure methanol contained a narrow peak with ^{13}C satellites from the CH_3 protons and a broad peak from the OH protons. The OH peak is broad due to hydrogen bonding and intermolecular proton exchange (Friebolin, 1993). The exchange also prevents scalar coupling between the two types of protons, so both peaks are singlets. However, a spectrum of 37.76 mol% methanol in ethyl acetate (figure 2.21) contained a doublet with ^{13}C satellites from the CH_3 protons and a quartet from the OH protons. This indicated that hydrogen bonding and intermolecular exchange were not taking place, i.e. each methanol molecule was surrounded by ethyl acetate molecules. A series of spectra of methanol-toluene (figure 2.22) showed the transition from hydrogen-bonded to non-bonded methanol with decreasing methanol content.

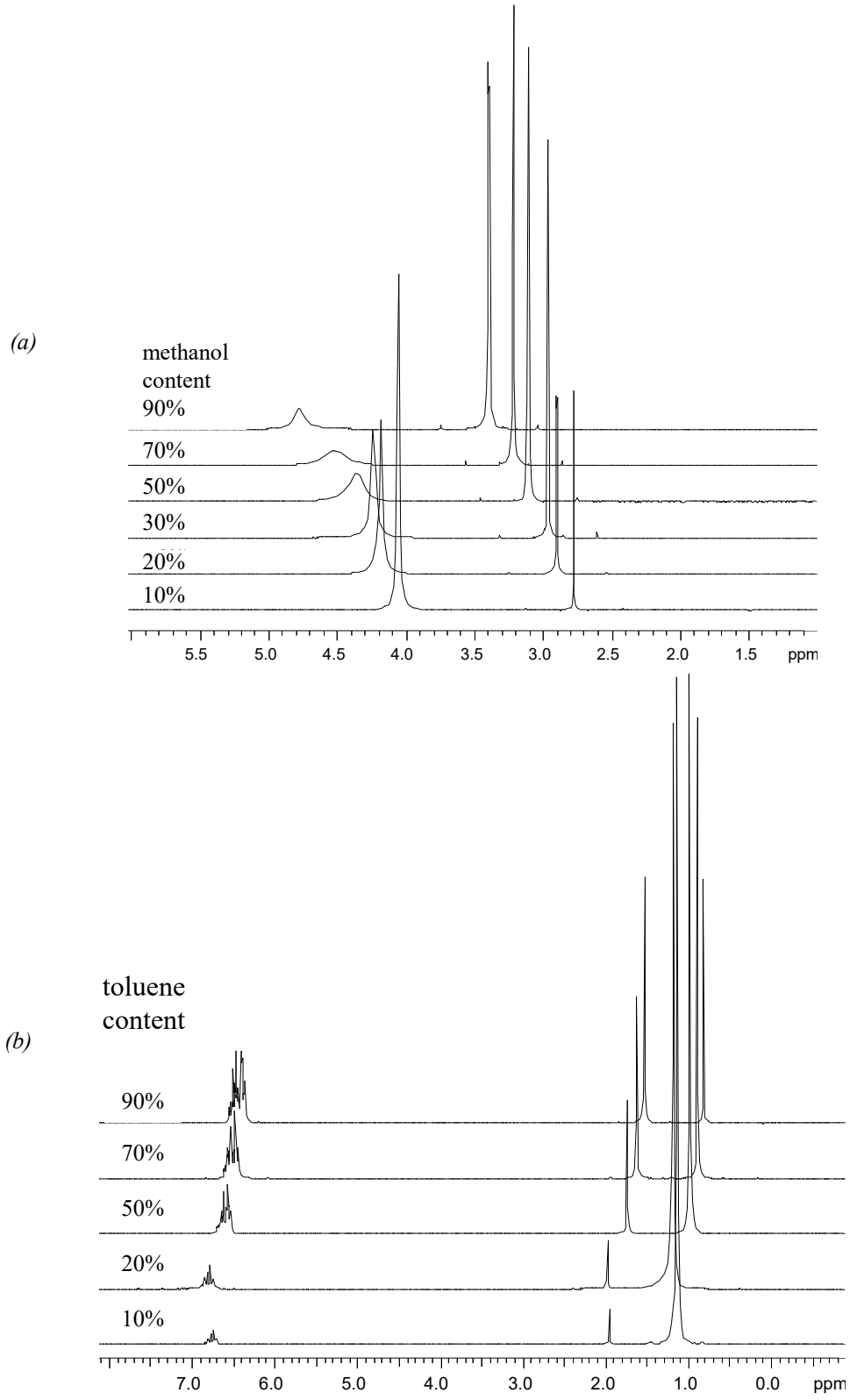

Figure 2.19 The effect of composition on chemical shift in ^{1}H NMR spectra of mixtures: *(a)* Methanol-water peaks move to higher chemical shift with increasing methanol content. *(b)* Toluene-cyclohexane peaks move to lower chemical shift with increasing toluene content.

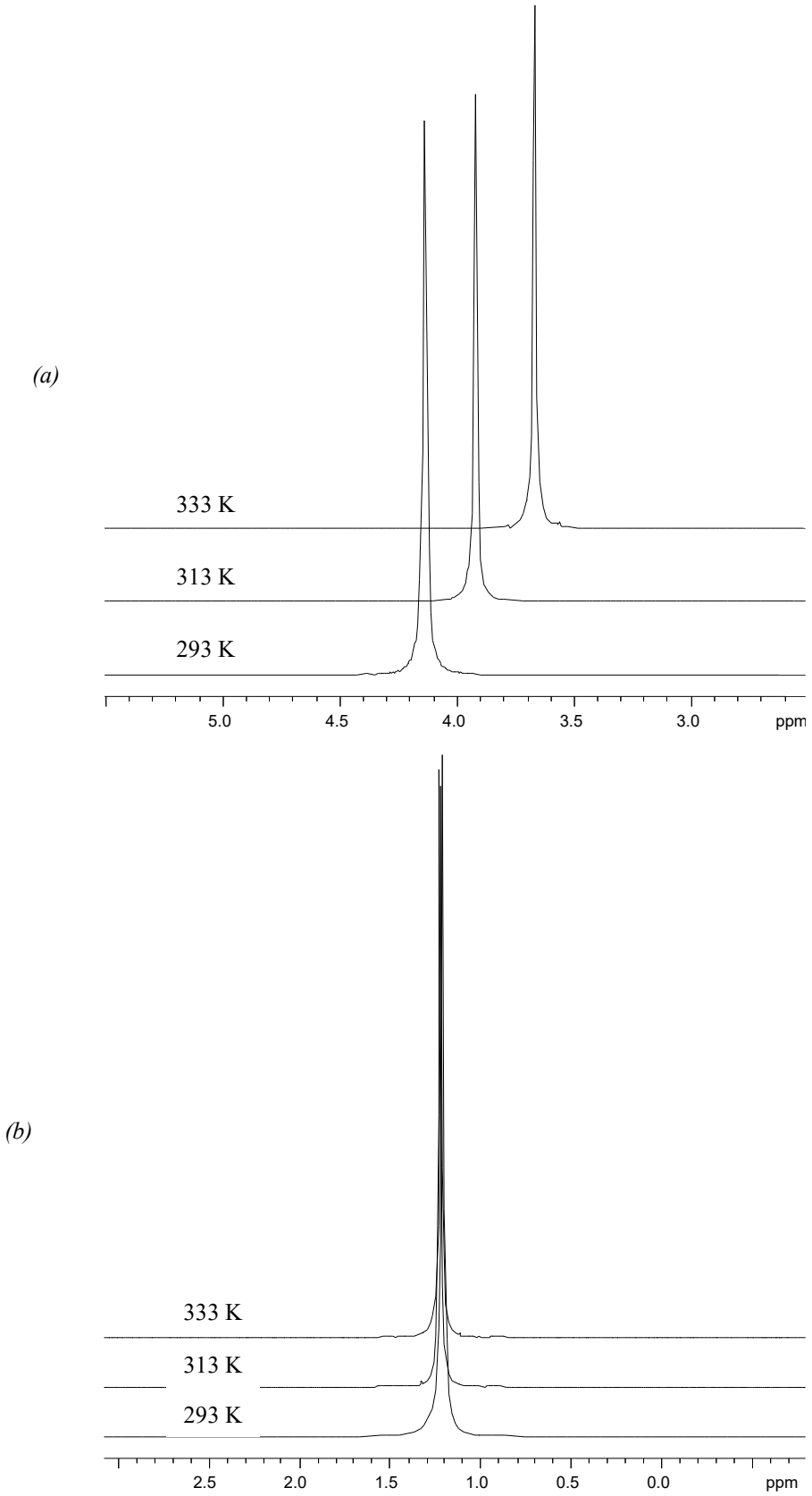

Figure 2.20 The effect of temperature on chemical shift in ^{1}H NMR spectra: *(a)* Water peaks move to lower chemical shift with increasing temperature. *(b)* Cyclohexane peaks do not move with increasing temperature.

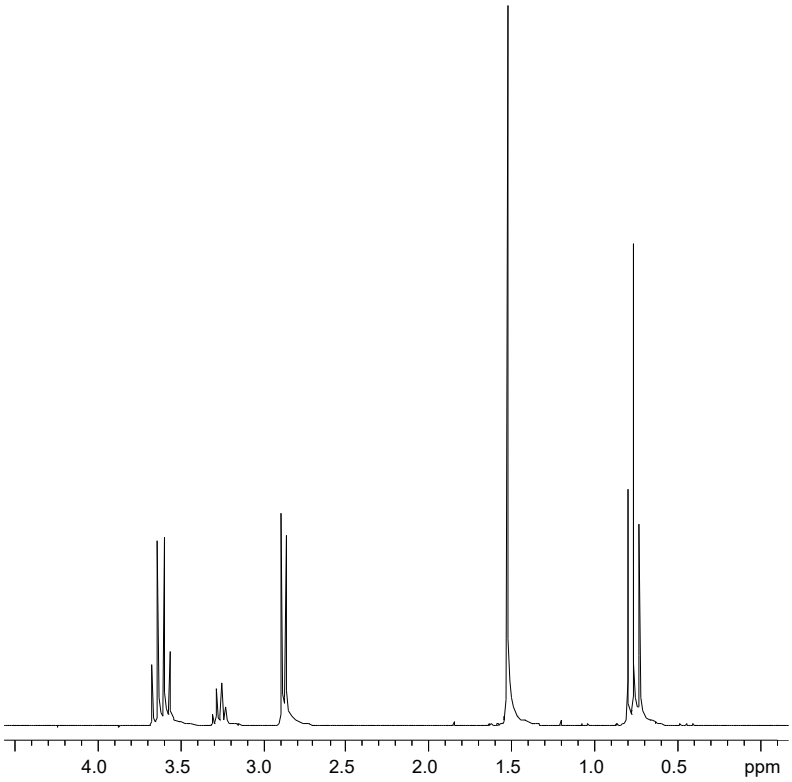

Figure 2.21 A high-resolution ^{1}H NMR spectrum of 37.76 mol% methanol in ethyl acetate at 293 K. The methanol peaks exhibit spin-spin coupling because there is no intermolecular exchange of protons.

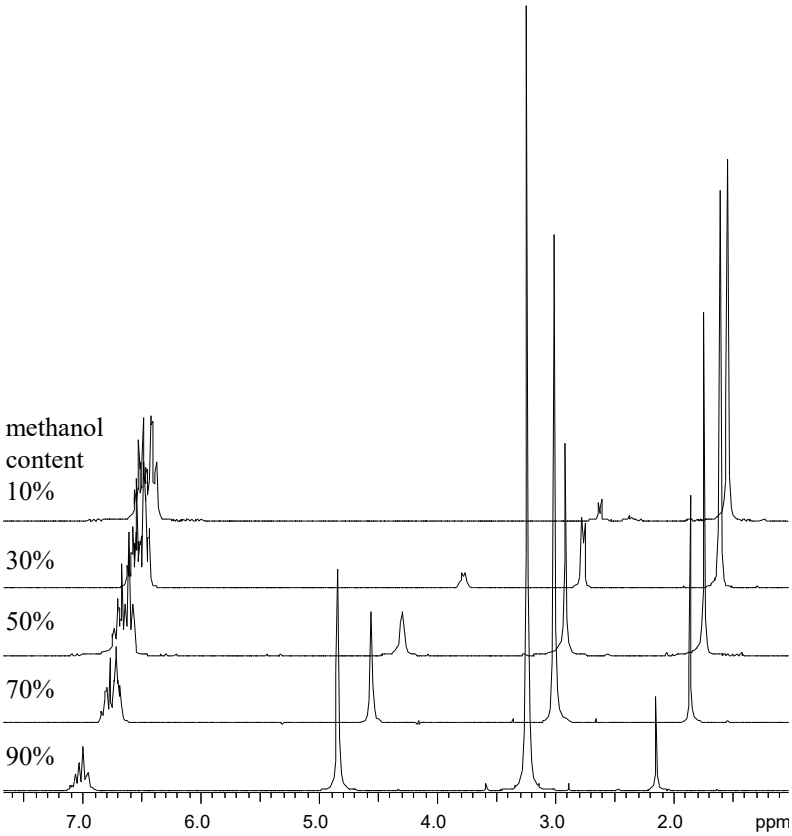

Figure 2.22 A series of high-resolution ^{1}H NMR spectra of methanol in toluene at 293 K. The methanol peaks move to lower chemical shift and intermolecular exchange of protons is reduced as the methanol content decreases.

2.5 Conclusion

The overall accuracy of the NMR composition measurement was tested on a series of liquid mixtures and was found to be ±0.34 mol% once relaxation weighting and baseline distortions were eliminated. The reproducibility of the NMR composition measurements was ±0.08 mol%. Dilute components were measured accurately at 0.05-mol% concentration once the peaks were visible in the spectrum. Based on this study, it can be concluded that NMR spectroscopy can give accurate quantitative composition measurements of liquids if the spectra are acquired correctly. The sensitivity of NMR is such that the differences between the compositions by weight and the compositions by NMR were often due small changes in the sample composition before acquisition of the NMR data.

The chemical shifts of the peaks in the spectra of mixtures were observed to vary with composition and temperature. The polar molecules (water, methanol, toluene) exhibited larger variations than the non-polar molecules (cyclohexane, isooctane, ethyl acetate). These variations were related to changes in the local chemical environment in the mixtures, notably changes in polarity and hydrogen bonding. The variations in chemical shifts had a significant effect on the development of a peak assignment algorithm, which is discussed in the next chapter on automated data analysis of these spectra.

2.6 References

Abildgaard, F., Gesmar, H., & Led, J.J. (1988). Quantitative analysis of complicated Fourier transform NMR spectra. *Journal of Magnetic Resonance, 79*, 78-89.

Anderson, W.A. (1961). Electrical current shims for correcting magnetic fields. *The Review of Scientific Instruments, 32*, 241-250.

Anderson, W.A. (1996). Fourier transform spectroscopy. In D.M. Grant & R.K. Harris (Eds.), *Encyclopedia of Nuclear Magnetic Resonance, vol. 3*, pp. 2126-2136. John Wiley & Sons, Chichester, UK.

Bloch, F., Hansen, W.W., & Packard, M. (1946a). Nuclear induction. *The Physical Review, 69*, 127.

Bloch, F., Hansen, W.W., & Packard, M. (1946b). The nuclear induction experiment. *The Physical Review, 70*, 474-487.

Bloch, F. (1946). Nuclear induction. *The Physical Review, 70*, 460-474.

Bracewell, R.N. (1978). *The Fourier Transform and its Applications, second edition*, pp. 77-79. McGraw-Hill International Book Company, Singapore.

Chmurny, G.N., & Hoult, D.I. (1990). The ancient and honourable art of shimming. *Concepts in Magnetic Resonance, 2*, 131-149.

Choi, K., & Tedder, D.W. (1995). Nuclear magnetic resonances of tri-*n*-butyl phosphate-diluent mixtures. *Spectrochimica Acta Part A, 51*, 2301-2305.

Conover, W.W. (1984). Practical guide to shimming superconducting NMR magnets. *Topics in Carbon-13 NMR Spectroscopy, 4*, 37-51.

Cooley, J.W., & Tukey, J.W. (1965). An algorithm for the machine calculation of complex Fourier series. *Mathematics of Computation, 19*, 297-301.

Daubenfeld, J.M., Boubel, J.C., Delpuech, J.J., Neff, B., & Escalier, J.C. (1985). Automatic intensity, phase, and baseline corrections in quantitative carbon-13 spectroscopy. *Journal of Magnetic Resonance, 62,* 195-208.

Derome, A.E. (1987). *Modern NMR Techniques for Chemistry Research*, pp. 63-97, 164-172. Pergamon Press, Oxford, UK.

Ernst, R.R., & Anderson, W.A. (1966). Application of Fourier transform spectroscopy to magnetic resonance. *The Review of Scientific Instruments, 37*, 93-102.

Foley, J.P. (1987). Systematic errors in the measurement of peak area and peak height for overlapping peaks. *Journal of Chromatography, 384*, 301-313.

Friebolin, H. (1993). *Basic One- and Two-Dimensional NMR Spectroscopy, Second, enlarged edition,* pp.1-36, 58. VCH, Weinheim, Germany.

Fukushima, E., & Roeder, S.W. (1981). *Experimental Pulse NMR: A Nuts and Bolts Approach*. pp. 1-92. Addison-Wesley, New York, USA.

Gesmar, H., Led, J.J., & Abildgaard, F. (1990). Improved methods for quantitative spectral analysis of NMR data. *Progress in Nuclear Magnetic Resonance Spectroscopy, 22*, 255-288.

Gladden, L.F. (1994). Nuclear magnetic resonance applications in chemical engineering: principles and applications. *Chemical Engineering Science, 49*, 3339-3408.

Golay, M.J.E. (1958). Field homogenizing coils for nuclear spin resonance instrumentation. *The Review of Scientific Instruments, 29*, 313-315.

Hahn, E.L. (1950). Nuclear induction due to free Larmor precession. *The Physical Review, 77*, 297-298.

Hancock, H.A. Jr., Dahm, L.A. and Muldoon, J.F. (1970). A new computer program for the resolution of fused chromatographic peaks. *Journal of Chromatographic Science, 8*, 57-63.

Harris, R.K. (1983). *Nuclear Magnetic Resonance Spectroscopy: A Physicochemical View*, pp. 1-19, 189-214. Longman, Harlow, UK.

Hoch, J.C., & Stern, A.S. (1996). *NMR Data Processing*, pp. 9-65, 172-180. Wiley-Liss, New York, USA.

Jonas, J., & Lee, Y.T. (1991). NMR and laser Raman scattering studies of fluids at high pressure. *Journal of Physics: Condensed Matter,3*, 305-338.

Karachewski, A.M., McNiel, M.M., & Eckert, C.A. (1989). A study of hydrogen bonding in alcohol solutions using NMR spectroscopy. *Industrial and Engineering Chemistry Research, 28*, 315-324.

Lowe, I.J., & Norberg, R.E. (1957). Free-induction decays in solids. *The Physical Review, 107*, 46-61.

Marion, D., & Bax, A. (1988). Baseline distortion in real-Fourier-transform NMR-spectra. *Journal of Magnetic Resonance, 79*, 352-356.

Mizuno, K., Oda, K., Maeda, S., Shindo, Y., & Okumura, A. (1995). ^{1}H-NMR study on water structure in halogenoalcohol-water mixtures. *Journal of Physical Chemistry, 99*, 3056-3059.

Pouchert, C.J., & Behnke, J. (1992). *The Aldrich Library of ^{13}C and ^{1}H FT-NMR Spectra*. Aldrich Chemical Company, Milwaukee, Wisconsin, USA.

Proctor, W.G., & Yu, F.C. (1950). The dependence of a nuclear magnetic resonance frequency upon chemical compound. *The Physical Review, 77*, 717.

Purcell, E.M., Torrey, H.C., & Pound, R. (1946). Resonance absorption by nuclear magnetic moments in a solid. *The Physical Review, 69*, 37-38.

Starcuk, Z.Jr., Bartušek, K., & Starcuk, Z. (1994). First-data-point problem and baseline distortion in Fourier-transform NMR spectroscopy with simultaneous sampling. *Journal of Magnetic Resonance, Series A, 108*, 177-188.

Tang, C. (1994). An analysis of baseline distortion and offset in NMR spectra. *Journal of Magnetic Resonance, Series A, 109*, 232-240.

Traficante, D.D. (1996). Relaxation: an introduction. In D.M. Grant & R.K. Harris (Eds.), *Encyclopedia of Nuclear Magnetic Resonance, vol. 6*, pp. 3988-4003. John Wiley & Sons, Chichester, UK.

Warren, W.S., & Richter, W. (1996). Concentrated solution effects. In D.M. Grant & R.K. Harris (Eds.), *Encyclopedia of Nuclear Magnetic Resonance, vol. 3*, pp. 1417-1423. John Wiley & Sons, Chichester, UK.

Westerberg, A.W. (1969). Detection and resolution of overlapped peaks for an on-line computer system for gas chromatographs. *Analytical Chemistry, 41*, 1770-1777.

Williams, D.H., & Fleming, I. (1989). *Spectroscopic methods in organic chemistry, fourth edition, revised*, pp.63-149. McGraw-Hill Book Company, London, UK.

2.7 Nomenclature

(symbol)	(description)	(value or unit)
Constants		
h	Planck's constant	6.62620×10^{-34} J s
$\hbar$	$h/2\pi$	1.054592×10^{-34} J s
k	Boltzmann's constant	1.38062×10^{-23} J K^{-1}
Vector Variables		
$\mathbf{B_0}$	static magnetic field	T
$\mathbf{B_1}$	oscillating magnetic field perpendicular to $\mathbf{B_0}$	T
$\mathbf{B_{eff}}$	effective magnetic field in the rotating frame	T
i	unit vector in x direction	-
k	unit vector in z direction	-
M	bulk magnetisation in a macroscopic sample	J s
$\mathbf{M_x}$, $\mathbf{M_y}$, $\mathbf{M_z}$	net magnetisation along x, y, z direction	J s
P	nuclear spin angular momentum	J s
$\boldsymbol{\mu}$	magnetic dipole moment	J T^{-1}
Scalar Variables		
A, B	labels for coupled nuclei	-
B_0, B_1	magnitude of magnetic field $\mathbf{B_0}$, $\mathbf{B_1}$	T
E	energy	J
i	label for spin state	-
I	nuclear spin quantum number	-
j	index of data point in frequency domain	-
J_{AB}	scalar coupling constant for nuclei A and B	s^{-1}
J_{CH}	heteronuclear coupling constant ^{13}C-^{1}H	s^{-1}
k	index of data point in time domain	-
m_I	magnetic quantum number	-
M_0	magnitude of bulk magnetisation at equilibrium	J s
M_x, M_y, M_z	component of magnetisation along x, y, z direction	J s
n	number of equivalent coupled nuclei	-
N	number of points in FID	-
N_S	number of scans	-
N_{total}	total number of nuclei in sample	-
N_α	number of nuclei in spin state α	-
N_β	number of nuclei in spin state β	-
P_z	component of angular momentum along field direction	J s
$s_A(\nu)$	pure absorption signal	-

$s_D(\nu)$	pure dispersion signal	-
$s_I(\nu)$	imaginary component of signal	-
$s_R(\nu)$	real component of signal	-
$\hat{s}(\nu)$	digitised frequency-domain signal	-
$\hat{S}(t)$	digitised time-domain signal	-
$S(0)$	signal intensity at $t = 0$	-
t	time	s
t_{in}	delay between r.f. pulse and start of sampling	s
T	absolute temperature	K
T_1	longitudinal relaxation time constant	s
T_2	spin-spin relaxation time constant	s
T_2'	inhomogeneity relaxation time constant	s
T_2^*	observed transverse relaxation time constant	s
T_R	inter-scan delay, or repetition time	s
x, y, z	axes in laboratory frame	-
x', y', z'	axes in rotating frame	-
α	spin-½ state parallel to the magnetic field	-
β	spin-½ state anti-parallel to the magnetic field	-
γ	gyromagnetic ratio	rad T^{-1} s^{-1}
δ	chemical shift	ppm
ϑ	vertical angle between magnetic field and spin orientation	rad
λ	half-width at half maximum of peak in spectrum	s^{-1}
μ_i	magnetic moment of spin state i	J T^{-1}
ν	frequency	s^{-1}
ν_0	resonance frequency in static magnetic field $\mathbf{B_0}$	s^{-1}
ν_{ref}	reference frequency for chemical shift measurements	s^{-1}
τ	duration of radio-frequency pulse	s
ϕ	phase offset of FID	rad
$\phi(\nu)$	phase correction applied to spectrum	rad
ϕ_0	zero order phase correction term	rad
ϕ_1	linear phase correction term	rad s
φ	tip angle of radio-frequency pulse	rad
ω_0	Larmor frequency in static magnetic field $\mathbf{B_0}$	rad s^{-1}
ω_1	angular frequency of oscillating magnetic field $\mathbf{B_1}$	rad s^{-1}

3 AUTOMATED ANALYSIS OF NMR SPECTRA OF LIQUID MIXTURES

3.1 Introduction

For implementation of an NMR analyser in a process environment, it is necessary to automate data acquisition and, more importantly, data analysis. Automated data acquisition is already possible with current NMR hardware, but automated data analysis requires algorithms that reproduce the procedure used by trained operators to produce reliable composition measurements. Furthermore, for the on-line monitoring of a time-varying system the analysis must be completed in a short time, say a few minutes. The data analysis procedure consists of (section 2.3.5):

1. First point correction,
2. Fourier transformation,
3. Phase correction,
4. Baseline correction,
5. Peak picking,
6. Peak integration,
7. Peak assignment,
8. Composition calculation.

Of these, steps 1, 2, 5, 6 and 8 are mathematical operations that are easily carried out by a computer. Steps 3 and 4, phase and baseline correction, involve the judgement and experience of the operator, so they do not have well-established procedures. Although many proposed algorithms are described in the literature, none performs well in all cases because there are many possible phase and baseline distortions, and any single algorithm can only deal with a subset of these. Step 7, peak assignment, is less subjective than phase and baseline correction, but it requires prior knowledge about the sample that is being measured.

This chapter describes the algorithms developed to automate the analysis procedure, particularly phase correction, baseline correction and peak assignment. The existing algorithms for phase and baseline correction are reviewed and two algorithms, numerical phasing and baseline optimisation, are tested on spectra of liquid mixtures.

It is found that phase and baseline correction cannot be performed separately, so the two algorithms are modified to perform phase and baseline correction together. For peak assignment, an entirely novel algorithm is described that uses prior knowledge about the component spectra to identify the liquids in the mixture and calculate their relative amounts. These algorithms are then combined into a single program that covers all eight steps in the analysis procedure, whose performance is evaluated on its running time and the accuracy of the composition results.

3.2 Automatic Phase and Baseline Correction

In the literature, phase and baseline correction have always been considered separately. Previous workers have only tackled phase correction of spectra with perfect baselines and baseline correction of pure absorption spectra. In this case, phase and baseline correction algorithms were required for spectra of liquid mixtures obtained on a Bruker MSL 200 spectrometer (section 2.3). The spectra were acquired using sequential acquisition, and the first imaginary point was acquired before the first real point. The baseline curvature increases with length of the time delay between the pulse and the first sampled point, so the baselines of the real spectra were more strongly curved than those of the imaginary spectra (figure 3.1). The spectra had neither perfect baselines nor pure absorption peaks, and it became evident while testing several algorithms that phase and baseline correction had to be performed together, since the existing separate algorithms were unsuccessful.

3.2.1 Review of Existing Algorithms

Many algorithms have been published for automatic phase correction of NMR spectra. They all make use of the linear phase function given by:

$$\phi(\nu) = \phi_0 + \phi_1 \nu , \tag{3.1}$$

and aim to find the optimum values of ϕ_0 and ϕ_1 to give the pure absorption and dispersion spectra, s_A and s_D, from the real and imaginary spectra, s_R and s_I, using:

$$\begin{aligned} s_A(\nu) &= s_R(\nu)\cos\phi - s_I(\nu)\sin\phi \\ s_D(\nu) &= s_R(\nu)\sin\phi + s_I(\nu)\cos\phi \end{aligned} . \tag{3.2}$$

The difficulty lies in determining when the observed spectrum corresponds to a pure absorption spectrum. The algorithms can be divided into two groups, depending on the method used to determine ϕ_0 and ϕ_1.

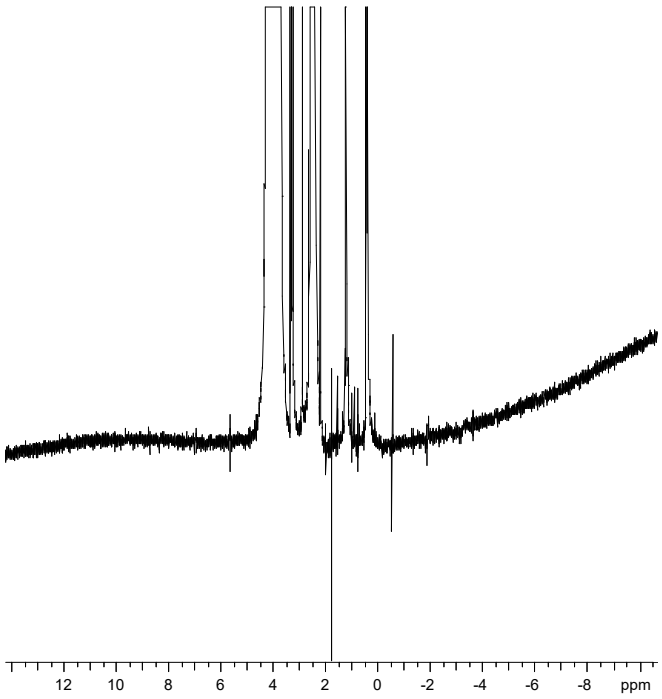

(a)

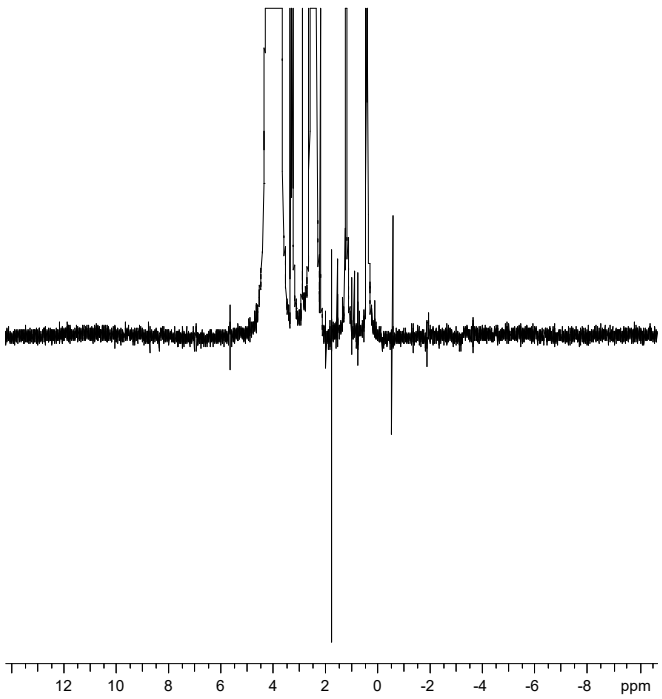

(b)

Figure 3.1 The real part of a ^{1}H NMR spectrum *(a)* before and *(b)* after baseline correction. The real spectrum has a curved baseline because the initial real point is delayed during sequential acquisition.

The first group of algorithms adjust ϕ_0 and ϕ_1 iteratively to optimise a phase-dependent target function. The first published algorithm (Ernst and Anderson, 1966) maximised the ratio of the areas above and below a continuous-wave spectrum. The same target function was used by Chen and Kan (1988), who optimised ϕ_0 and ϕ_1 separately. Ernst (1969) maximised the ratio of the most positive point to the most negative point in the spectrum, using the Hilbert transform to obtain the imaginary part of a continuous-wave spectrum. Gladden and Elliott (1986) adjusted ϕ_0 and ϕ_1 to obtain a wholly positive real spectrum, while Brown *et al.* (1989) maximised the number of points in the baseline. Sterna and Tong (1991) mimicked a trained operator by equalising the baseline level either side of a group of peaks, and using two well-separated groups in the spectrum to find the two parameters. Balacco (1994) devised a zero-order equality (ZOE) criterion to find the optimum value of ϕ_1 such that ϕ_0 was constant across the spectrum.

The second group of algorithms determine the phases of some or all peaks in the spectrum, then fit the phases to equation (3.1) to obtain the parameters for the entire spectrum. The key difference between these algorithms is the method used to determine the phases of the individual peaks. Craig and Marshall (1988) used a DISPA plot of dispersion vs. absorption signal intensity for a Lorentzian lineshape, and obtained the phase of a peak from the centre of a rotated DISPA circle. Montigny *et al.* (1990) found an approximate phase by maximising the signal in the real spectrum, then refined the estimate by fitting a Lorentzian lineshape to the peak. Van Vaals and van Gerwen (1990) found the phase from the ratio of imaginary and real signal intensities at the peak central frequency. Heuer (1991) determined the phase from the asymmetry of the peak, by comparing the integrals of the two halves of the peak either side of the central frequency.

The performance of these phase correction algorithms depends on the original appearance of the spectrum before correction. All assume that the baseline is flat, in some cases allowing for a constant offset from zero, so they cannot phase-correct spectra with baseline distortions. In addition, the algorithms in the second group assume that the peaks are Lorentzian, and fail if the peaks are non-Lorentzian. The algorithms in the first group do not contain assumptions about the lineshape.

There are fewer baseline correction algorithms in the literature, because most workers simply use a polynomial fit (section 2.3.5.3). Heuer and Haeberlen (1989) fitted to the real baseline a function, $B(j)$, that is the cosine Fourier transform of m initial data points of the FID assumed to be missing or corrupted:

$$B(j) = \sum_{k=0}^{m-1} S(k) \cos\left(\frac{\pi}{N} j \Delta\nu (k\Delta t + \phi_1) + \phi_0 \right). \qquad (3.3)$$

Equation (3.3) requires the phase correction parameters to be known, *i.e.* the phase correction must already have been carried out. Starcuk *et al.* (1990) proposed correcting the baseline by estimating the values of the initial points of the FID from an inverse Fourier transform of a model spectrum with a zero baseline. The model spectrum was created by zeroing all points in the spectrum below a threshold level, and the estimate was improved over several iterations. This method also implicitly required the phase correction to have been already performed.

3.2.2 Experimental

Phase correction and baseline correction are mutually dependent, so none of the algorithms that perform only one correction will be successful on spectra that require both. Therefore, an algorithm is required that performs both corrections together. Two such combined algorithms were written by adding baseline fitting to two phase-correction algorithms: numerical phasing (Gladden and Elliott, 1986) and baseline optimisation (Brown *et al.*, 1989). These algorithms were chosen because they did not require Lorentzian lineshapes, since our spectra contained non-Lorentzian lineshapes due to magnetic field inhomogeneity. The algorithms were coded in the Tcl language to run as part of our in-house image and data analysis (IDA) software, written by Dr Paul Alexander of the Department of Physics, University of Cambridge.

3.2.2.1 Numerical Phasing

The numerical phasing algorithm of Gladden and Elliott (1986) estimated the optimal values of the phase-correction parameters ϕ_0 and ϕ_1 using a "self-calibration" procedure. This algorithm was chosen because its target – a wholly positive spectrum – was obeyed by our data. In this context, "positive" translates as "above the baseline", since the "positive" model spectrum was constructed by reflecting all data points that fell below the baseline about the baseline level. The model was fitted to

the data using a Bayesian approach: analytical expressions for the optimal values of ϕ_0 and ϕ_1 were obtained by maximising the joint probability distribution of ϕ_0, ϕ_1, and ε_j, the complex spectral noise. For each iteration of the algorithm, a model spectrum was constructed from the experimental spectrum and the values of ϕ_0 and ϕ_1 were calculated. These values were used to adjust the experimental spectrum, and the procedure was repeated until the values of ϕ_0 and ϕ_1 were below a chosen convergence limit.

Numerical phasing is described mathematically as follows: If the experimental spectrum to be phased, containing N complex data points, is denoted by s_j, $j = 1, 2, \ldots, N$, and the model (phased) spectrum is denoted by $\tilde{s}_j$, both are given by:

$$\begin{aligned} s_j &= |s_j| e^{i\theta_j} \\ \tilde{s}_j &= |\tilde{s}_j| e^{i\tilde{\theta}_j} \end{aligned}, \tag{3.4}$$

and the expressions for the phase-correction parameters ϕ_0 and ϕ_1 are given by (Gladden and Elliott, 1986):

$$\phi_0 = \frac{\kappa_2''\Delta_0 - \kappa_1\Delta_1}{\kappa_0'\kappa_2'' - \kappa_1^2} \tag{3.5}$$

and

$$\phi_1 = \frac{\kappa_0'\Delta_1 - \kappa_1\Delta_0}{\kappa_0'\kappa_2'' - \kappa_1^2}, \tag{3.6}$$

where the additional parameters are given by:

$$\kappa_i = \sum_{j=1}^{N} \frac{\nu_j^i |s_j| |\tilde{s}_j|}{\sigma_j^2}, \tag{3.7}$$

$$\Delta_i = \sum_{j=1}^{N} \frac{\nu_j^i |s_j| |\tilde{s}_j| \left(\theta_j - \tilde{\theta}_j\right)}{\sigma_j^2}, \tag{3.8}$$

$$\kappa_i' = \kappa_i + 1/\sigma_0^2, \tag{3.9}$$

$$\kappa_i'' = \kappa_i + 1/\sigma_1^2. \tag{3.10}$$

The parameters σ_0 and σ_1 are the standard deviations of the Gaussian probability distributions of ϕ_0 and ϕ_1 respectively.

A Tcl computer program was written by the author to implement the original algorithm of Gladden and Elliott, labelled NUM1, as follows:

1. Enter the maximum number of iterations, convergence limits, and values for σ_0 and σ_1.
2. Calculate the mean baseline level (μ) and the standard deviation of the noise (σ_j) for the real and imaginary spectra separately, from the first 20% and last 20% regions of the spectrum, which are assumed to contain no signal.
3. Construct model spectrum: if the j^{th} real data point, $s_{R,j}$, has a value lower than the real baseline (μ_R - $3\sigma_R$), the j^{th} real and imaginary points are transformed using:

$$\begin{aligned} s_{R,j} &\rightarrow -s_{R,j} + 2\sigma_R \\ s_{I,j} &\rightarrow -s_{I,j} + 2\sigma_I \end{aligned} \quad . \tag{3.11}$$

4. Calculate ϕ_0 and ϕ_1 using equations (3.5) - (3.10).
5. If the values of both ϕ_0 and ϕ_1 are smaller than the convergence limit, go to step 8.
6. Adjust experimental spectrum using equation (3.2).
7. Return to step 2 if the maximum number of iterations has not been reached.
8. Output phased experimental spectrum.

The performance of NUM1 depended on the validity of the reflected "positive" spectrum as a model for the correctly phased spectrum. The model was generally poor because reflection was performed about a flat baseline that did not match the curved baselines in the spectra. Therefore, a new numerical phasing algorithm, labelled NUM2, was written by the author to perform simultaneous phase correction and baseline fitting by including curved baselines in the model spectrum. The baseline was estimated using prior knowledge about the data, as follows:

1. For the spectra in our data set, all the peaks appeared in the range 0 to 8 ppm. Therefore, all points outside this range were assigned to the baseline, B_1.
2. The mean (μ_{B1}) and standard deviation (σ_{B1}) of B_1 were determined for the real and imaginary spectra separately.
3. Inside the range 0 to 8 ppm, all points inside the range ($\mu_{B1} \pm 2\sigma_{B1}$) were added to B_1 give a second baseline, B_2, for each of the real and imaginary spectra.
4. The data points in B_2 were fitted using a third order polynomial for the real spectrum and a linear function for the imaginary spectrum. The polynomials matched the different curvatures of the two baselines.
5. The two polynomials were output as the estimated baseline of the spectrum, B_3.

The standard deviation of the noise was obtained from the outer 20% of the spectrum as before. With the improved baseline estimate, the points falling below (μ_R - 1σ_R) were reflected to speed up convergence. After phase correction, the final fitted baseline was subtracted from the spectrum to improve its appearance and allow peak integration.

3.2.2.2 Baseline Optimisation

Brown *et al.* (1989) developed an algorithm for automatic phase correction by optimising the baseline of the real spectrum, *i.e.* by maximising the number of points inside the range ($\mu_R \pm nsd\ \sigma_R$), where the parameter *nsd* was the number of noise standard deviations used to define the baseline region, typically $3 \le nsd \le 6$. The standard deviation of the noise, σ_R, was determined from the first *N*/32 and last *N*/32 points in the spectrum. They used a Simplex optimiser to maximise the function:

$$f = \sum_{p=1}^{q} p^2 , \qquad (3.12)$$

where *q* was the number of points in the spectrum found to lie in the range ($\mu_R \pm nsd\ \sigma_R$). In order to speed up computation, they only considered 1 in every 16 points in the spectrum, which did not alter the results.

A Tcl computer program was written by the author to implement this algorithm, labelled BCM1, as follows:

1. Calculate the mean baseline level (μ_R) and the standard deviation of the noise (σ_R) for the real spectrum from the first 20% and last 20% regions of the spectrum, which are assumed to contain no signal.
2. Initialise the starting guess for ϕ_0 and ϕ_1.
3. Adjust the phase of the trial spectrum with the current values of ϕ_0 and ϕ_1 using equation (3.2).
4. Sample the spectrum every n^{th} point to give a reduced spectrum of approximately 1000 points for optimisation. The value of *n* was *N*/1000, rounded down to the nearest integer.
5. Count the number of points, *q*, in the reduced spectrum that lie in the range ($\mu_R \pm 3\sigma_R$) and calculate the function *f* using equation (3.12).

6. Use Simplex optimisation to maximise *f* by adjusting ϕ_0 and ϕ_1 and repeating steps 2 to 4 for each iteration.

The Simplex optimisation was carried out using an algorithm based on the subroutine "amotry" of Press *et al.* (1992).

Like NUM1, BCM1 had a flat model baseline, so it could not deal with the curved baselines of our spectra. BCM1 was modified by the author to include baseline fitting, as follows:

1. The spectral region outside -2 to 10 ppm was used to determine the mean and standard deviation of the baseline. A wider region was selected than 0 to 8 ppm to allow for some baseline region either side of the peaks.
2. The data points outside -2 to 10 ppm were fitted using a third order polynomial for the real spectrum and a linear function for the imaginary spectrum, to give a better baseline estimate than simply the mean value across the spectrum.
3. The trial spectrum was sampled only inside the region -2 to 10 ppm to optimise the baseline in the region where peaks are present. Optimising the baseline outside this region was not relevant to accurate phase correction of the spectrum.

In addition, if the algorithm converged to a solution that was "upside down", *i.e.* all negative peaks, then the spectrum was inverted. The new algorithm was labelled BCM2.

3.2.3 Results

The numerical phasing and baseline optimisation algorithms were tested on several high-resolution ^{1}H spectra of liquid mixtures. The spectra were read in and Fourier transformed using the IDA software, and the phase corrections were performed in IDA using the four Tcl programs NUM1, NUM2, BCM1 and BCM2. About ten different spectra were used to test the phasing algorithms, but only two are shown due to space constraints. The first spectrum, labelled N9, is of a five-component mixture of methanol-toluene-cyclohexane-isooctane-ethyl acetate, with peaks covering a large frequency range (figure 3.2). The second spectrum, labelled N34, is of a four-component mixture of methanol-toluene-cyclohexane-ethyl acetate, with fewer overlapping peaks than N9 (figure 3.3).

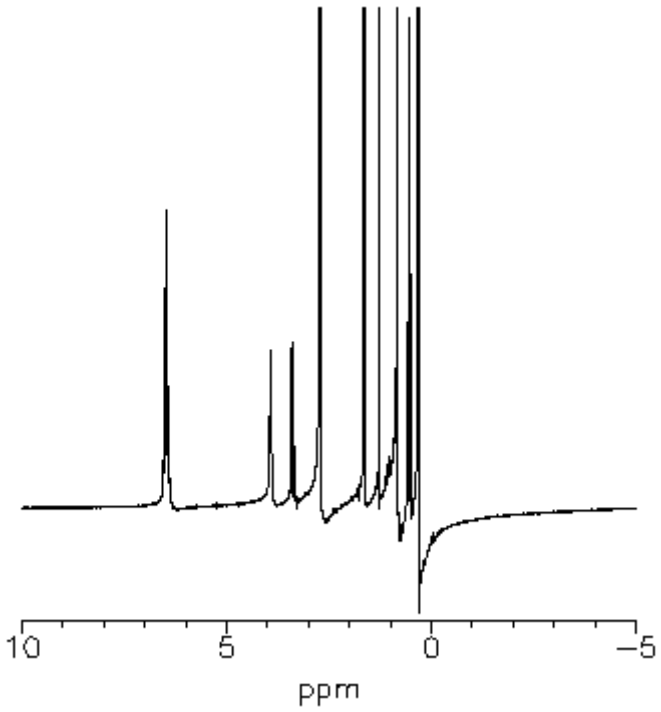

(a)

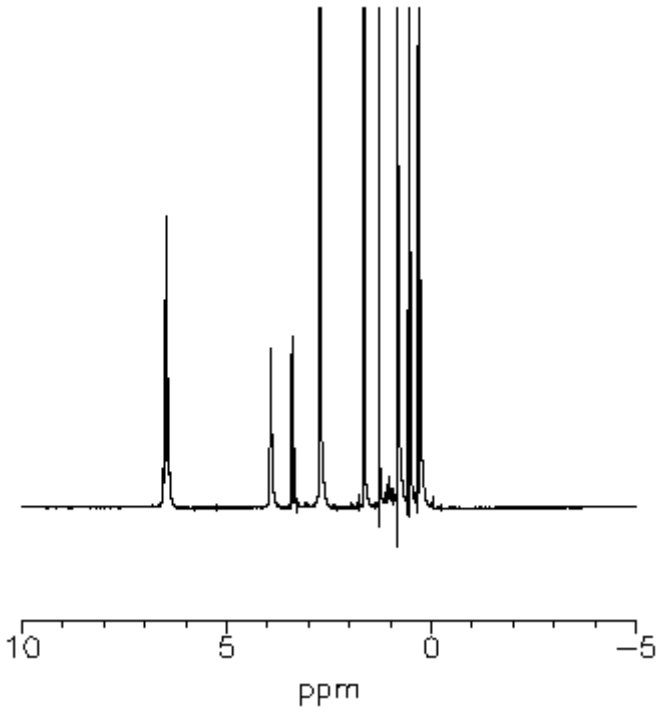

(b)

Figure 3.2 Spectrum N9 of a five-component mixture, used for testing automatic phase correction algorithms *(a)* before phase correction *(b)* corrected manually: ϕ_0 = -0.4726, ϕ_1 = 1.7345.

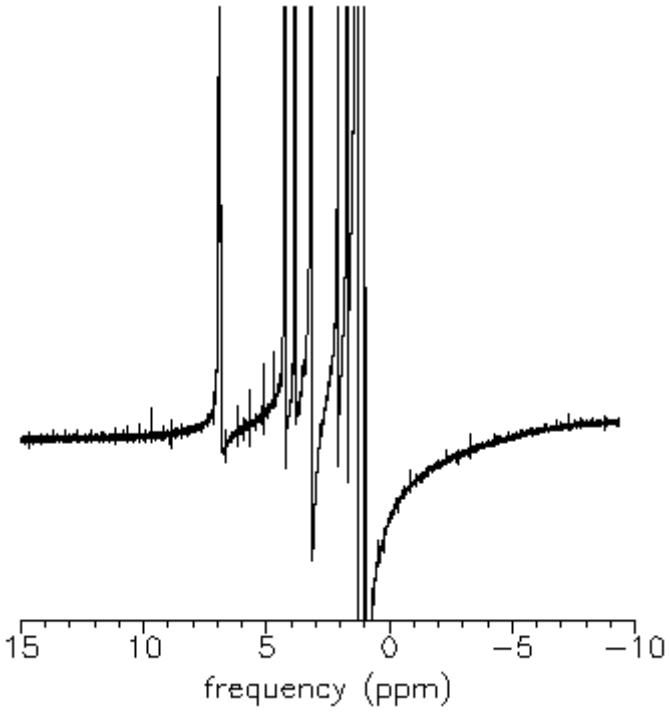

(a)

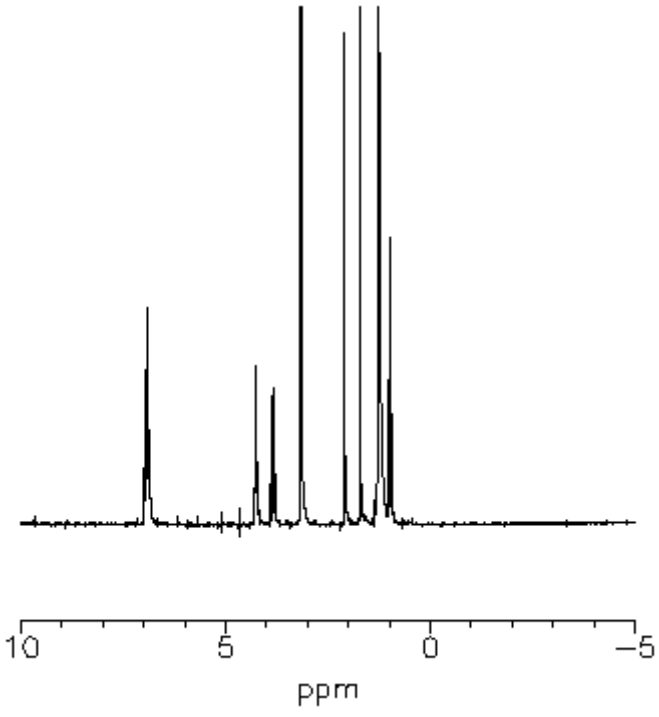

(b)

Figure 3.3 Spectrum N34 of a four-component mixture, used for testing automatic phase correction algorithms *(a)* before phase correction *(b)* corrected manually: ϕ_0 = -0.3203, ϕ_1 = 1.7977.

3.2.3.1 Numerical Phasing

Numerical phasing was very consistent and ran without any operator input. As expected, NUM2 with the curved baseline model phased more spectra correctly than NUM1 with the linear baseline model did. NUM2 phased both N9 and N34 correctly (figure 3.5) where NUM1 did not (figure 3.4). The difference between the two algorithms was most evident near convergence when fine adjustments required a very accurate model spectrum. NUM2 was much slower than NUM1 because of the two baseline fits per iteration and the large number of iterations needed to converge. NUM1 took 2-3 minutes to run, but NUM2 usually took at least 5 minutes. The total number of iterations to converge depended on the step size, controlled by σ_0/σ_1. NUM1 failed to converge in several cases for which NUM2 converged with $\sigma_0/\sigma_1 \leq 0.01$ after 10 or more iterations.

The overall performance of numerical phasing was strongly dependent on the values used for its five parameters: the maximum number of iterations, the convergence limits for ϕ_0 and ϕ_1 and the standard deviations σ_0 and σ_1. For both NUM1 and NUM2, the maximum number of iterations was set to 20 and the convergence limits for ϕ_0 and ϕ_1 to 5.0×10^{-3}. The convergence limits were set to the level below which phase adjustment caused no visible changes in the spectra. The standard deviations σ_0 and σ_1 were a measure of the (lack of) knowledge of the true values of ϕ_0 and ϕ_1 and were set equal to each other because they were both equally unknown. Several values of σ_0 and σ_1 were tried, and were found to determine the magnitudes of ϕ_0/ϕ_1 applied at each iteration, but not the overall values of ϕ_0 and ϕ_1 at convergence. The non-linear dependence of ϕ_0/ϕ_1 on σ_0/σ_1 for the first iteration of NUM2 on spectrum N9 is shown in table 3.1 and figure 3.6. Small values of σ_0/σ_1 (10^{-5} for NUM1, 0.001 - 0.01 for NUM2) gave small step sizes for ϕ_0/ϕ_1, so that many iterations (20 or more) were needed to converge. For larger values of σ_0/σ_1 (10^{-3} for NUM1, 0.05 - 1.0 for NUM2) the algorithms would reach near-optimal phasing, but then "overshoot" and fail to converge. The optimal values of σ_0/σ_1 were near 10^{-4} for NUM1 and 0.01 for NUM2. For all test spectra, NUM2 consistently converged the same solution with different values of $\sigma_0/\sigma_1 \leq 0.01$, and overshot at the same point for $\sigma_0/\sigma_1 > 0.01$.

Thus, the new algorithm NUM2 succeeded at simultaneous phase correction and baseline fitting of experimental NMR spectra without operator intervention. Its main

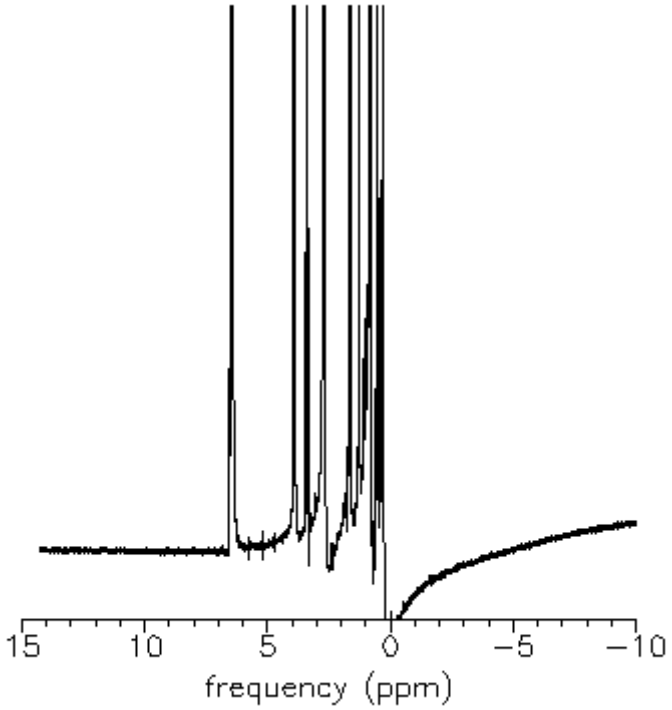

(a)

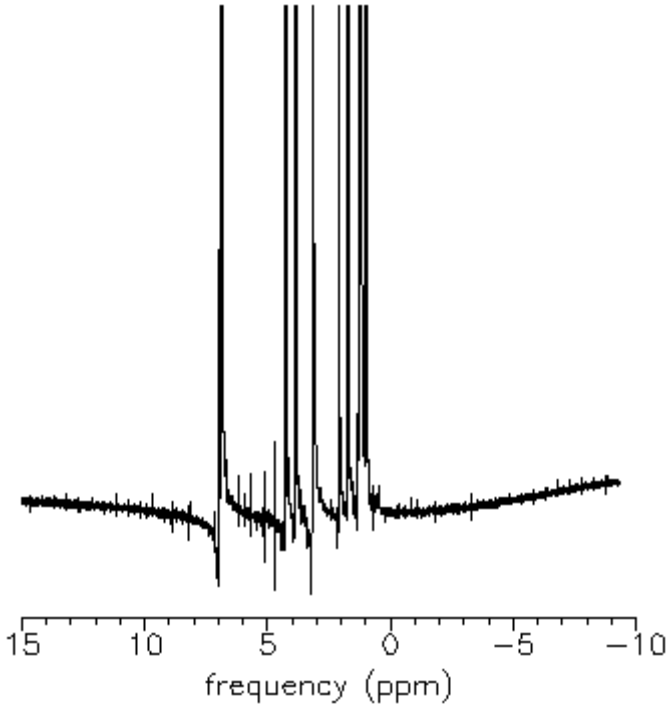

(b)

Figure 3.4 Test spectra automatically phase corrected using NUM1 *(a)* N9: ϕ_0 = 0.16570, ϕ_1 = 0.09352, *(b)* N34: ϕ_0 = 0.52069, ϕ_1 = 0.35713.

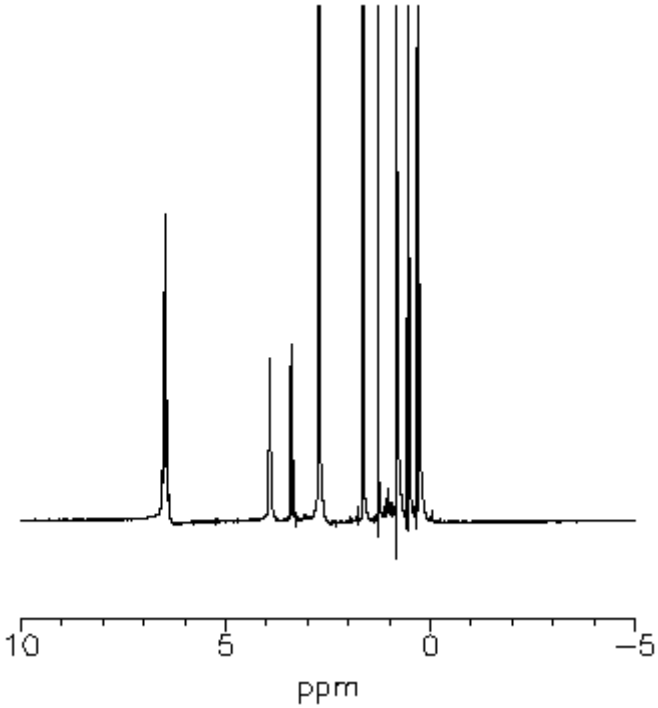

(a)

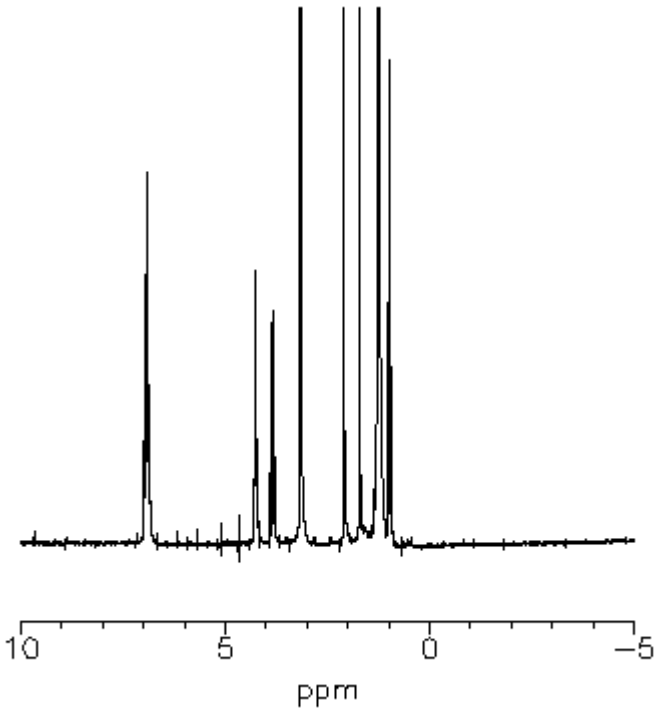

(b)

Figure 3.5 Test spectra automatically phase corrected using NUM2 *(a)* N9: ϕ_0 = -0.83695, ϕ_1 = 2.5517, *(b)* N34: ϕ_0 = -0.35846, ϕ_1 = 1.80922.

σ_0 / σ_1	ϕ_0	ϕ_1
1.0	-1.4140	3.2440
0.5	-1.4139	3.2439
0.1	-1.4109	3.2831
0.05	-1.4015	3.2204
0.01	-1.1481	2.7433
0.005	-0.6965	1.8924

Table 3.1 Phase correction parameters ϕ_0 and ϕ_1 calculated in the first iteration of the numerical phasing algorithm NUM2 for test spectrum N9 using different values of σ_0 / σ_1.

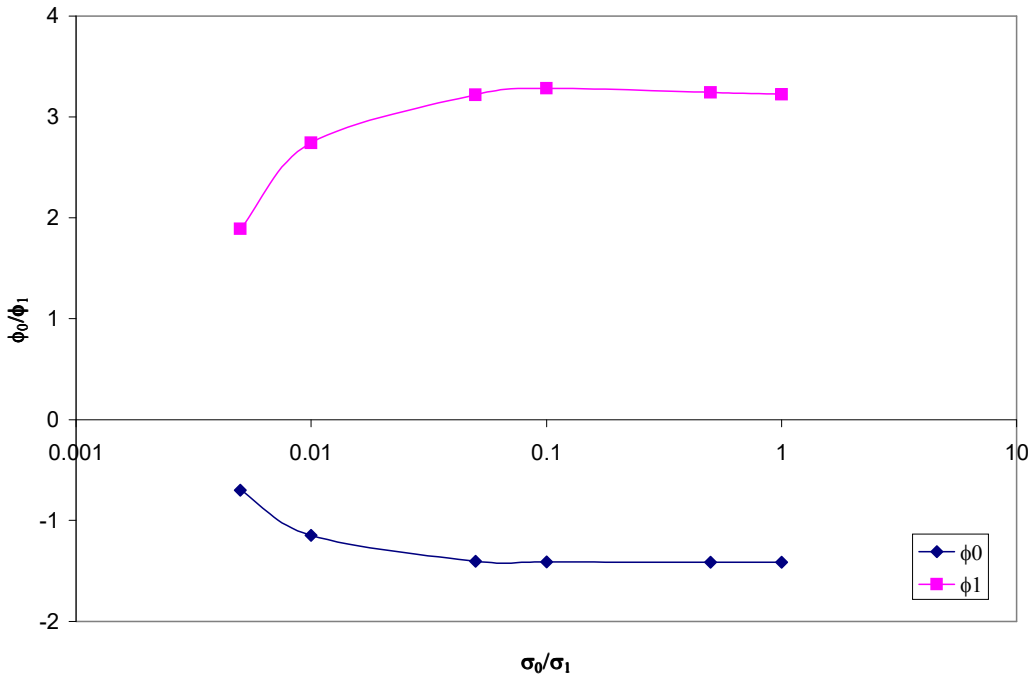

Figure 3.6 Plot of the data in table 3.1 showing the non-linear dependence of ϕ_0 / ϕ_1 on σ_0 / σ_1. Note σ_0 / σ_1 is shown on a logarithmic scale.

drawback was execution time, which can be reduced by better programming, especially a faster algorithm to calculate the baseline fits. Further speed can be gained by starting with large values of σ_0 and σ_1 so that the first two iterations rapidly approach the solution, and then reducing σ_0 and σ_1 so that later iterations have smaller step sizes and do not overshoot the solution. A linear scaling of σ_0/σ_1 with iteration number had no effect, but stronger scaling may be successful.

3.2.3.2 Baseline Optimisation

The baseline optimisation algorithms were less reliable than numerical phasing because the results depended strongly on the starting values of (ϕ_0, ϕ_1). For both BCM1 and BCM2, these values were set to (-0.374, 1.662), (-0.692, 1.866) and (-1.271, 2.612), based on typical phase parameters obtained during manual phasing, so that the algorithms started their search in the right direction. The convergence limit was set to a fractional tolerance of 0.01, *i.e.* the best and worst guesses had to give values of the objective function *f* within 1% of each other, and the maximum number of iterations was set to 20.

Good results were obtained for the test spectra N9 and N34 using BCM1 (figure 3.7) and BCM2 (figure 3.8), but different starting values and many iterations (20 or more) were required for convergence. Changing the starting values gave different solutions or no convergence. No single set of starting values gave convergence within 20 iterations for all spectra tested, nor was there a reliable method to determine such a set that would work for all spectra. BCM2 performed better than BCM1 for all test spectra, because the baseline model was better and optimisation of the baseline regions between the peaks was more important for accurate phase correction than optimising the baseline in the outer regions of the spectra. However, in some cases, the solution – a spectrum with the highest number of baseline points – was not the desired accurately phased spectrum because broad peaks contributed more points to the "baseline" when they were incorrectly phased.

The baseline optimisation algorithms may be improved by replacing Simplex optimisation with a different search algorithm, but since the phasing criterion was not obeyed by some of the test spectra, this was not pursued.

The performance of all four automatic phase correction algorithms on the test spectra N9 and N34 is compared to manual phasing in table 3.2. NUM1 and NUM2 gave

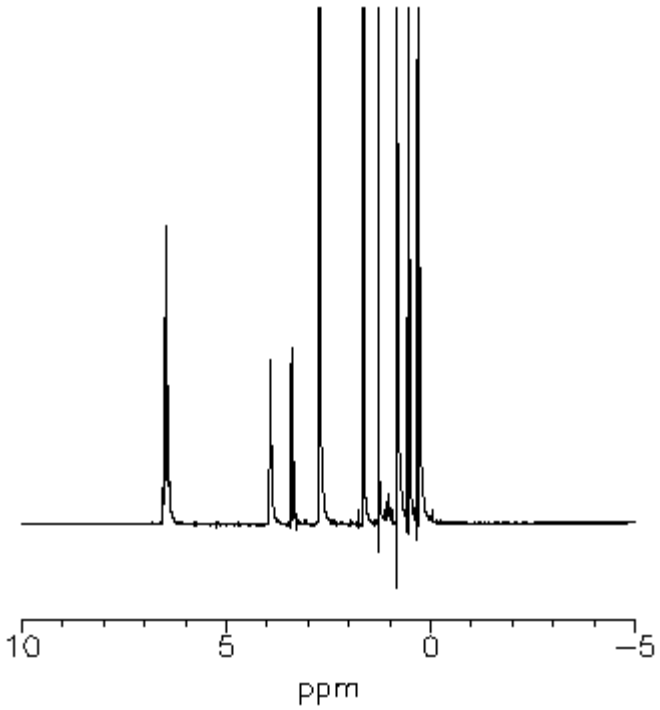

(a)

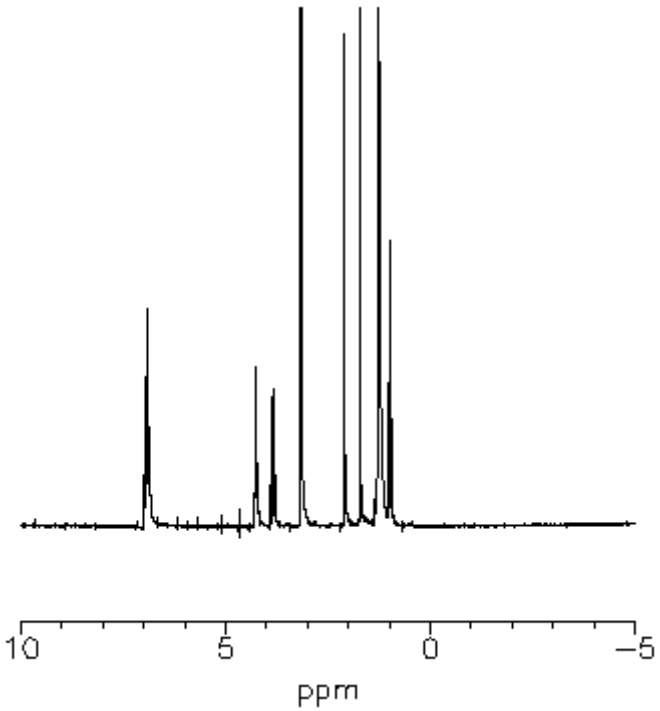

(b)

Figure 3.7 Test spectra automatically phase corrected using BCM1 *(a)* N9: ϕ_0 = -0.37790, ϕ_1 = 1.79692, *(b)* N34: ϕ_0 = -0.11933, ϕ_1 = 1.43516.

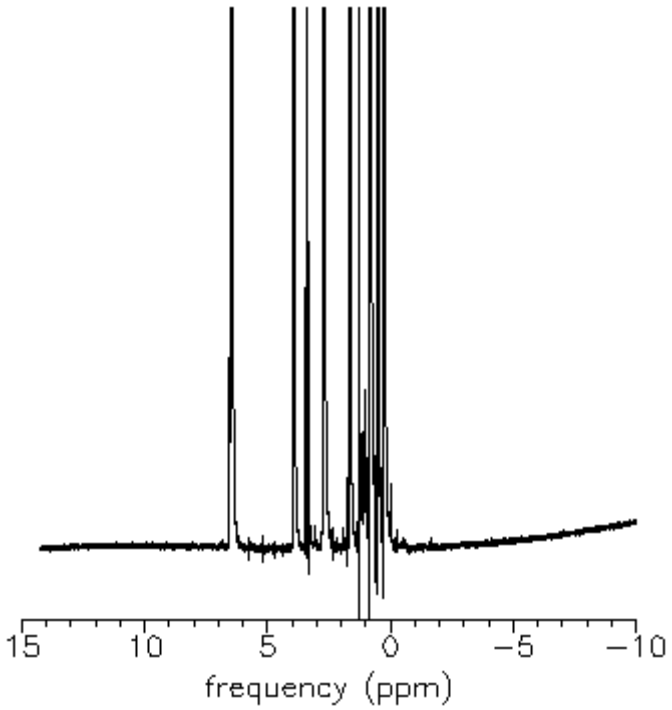

(a)

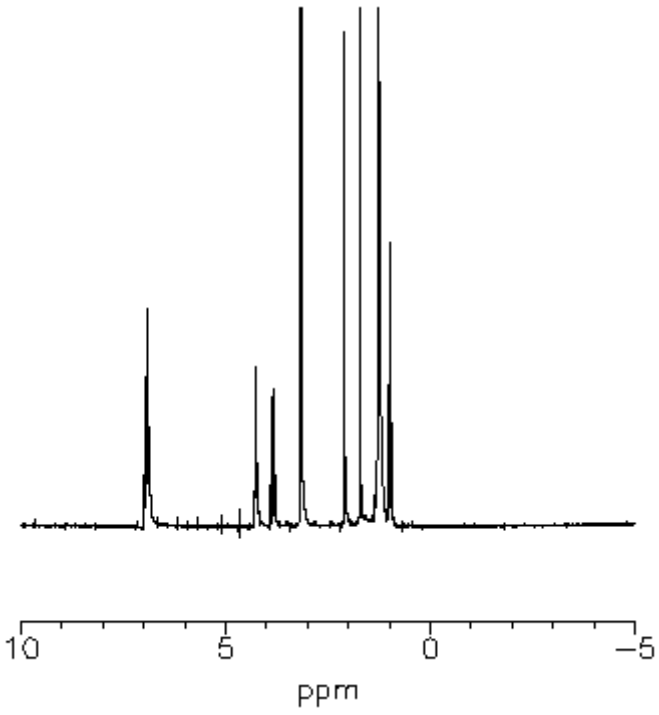

(b)

Figure 3.8 Test spectra automatically phase corrected using BCM2 *(a)* N9: ϕ_0 = -0.38440, ϕ_1 = 1.76821, *(b)* N34: ϕ_0 = -0.09458, ϕ_1 = 1.35984.

phase-correction algorithm	**spectrum N9**		**spectrum N34**	
	ϕ_0	**ϕ_1**	**ϕ_0**	**ϕ_1**
manual	-0.47260	1.73450	-0.32030	1.7977
NUM1	0.16570	0.09352	0.52069	0.35713
NUM2	-0.83695	2.5517	-0.35846	1.80922
BCM1	-0.37790	1.79692	-0.11933	1.43516
BCM2	-0.38440	1.76821	-0.09458	1.35984

Table 3.2 Phase correction parameters ϕ_0 and ϕ_1 obtained for test spectra N9 and N34 by manual phasing and automatic phase correction algorithms.

different values of ϕ_0 and ϕ_1 than manual phasing while BCM1 and BCM2 gave similar values. The values returned by NUM2, BCM1 and BCM2 yielded correctly-phased spectra, but those returned by NUM1 did not. The closest match to manual phasing was observed for NUM2 on spectrum N34. It should be noted that spectra can be correctly phased using many different combinations of ϕ_0 and ϕ_1.

3.3 Assigning Peaks in Spectra of Liquid Mixtures

After phase and baseline correction of the spectra, the next algorithm required for the composition analysis was one to find and assign peaks, steps 5 to 7 of the analysis procedure. Peak assignment was performed very efficiently by using the prior knowledge that was available about the system. The system consisted of spectra of mixtures containing components drawn from the following list: water, hydrogen-bonded methanol, methanol without hydrogen bonding, toluene, cyclohexane, isooctane and ethyl acetate. The algorithm described here assumed that only the listed components were present, but algorithms can be written for other systems using the same approach. This algorithm is entirely novel and not based on the work of anyone else. No similar algorithm has been described in the literature to the author's knowledge.

3.3.1 Experimental

3.3.1.1 Prior Knowledge

The prior knowledge used in the peak assignment algorithm was obtained by analysing all available spectra of liquid mixtures to obtain the frequency ranges, relative integrals, relative heights, separation, order in the spectrum and coupling constants of the peaks. The results are summarised here:

- All the peaks were in the range of 7.5 ppm to -0.25 ppm.
- Inside this range, another division was made into three regions:
  1. Region 1, from -0.25 ppm to 2.35 ppm, contained peaks from cyclohexane, isooctane, toluene (CH_3) and ethyl acetate (CH_3 singlet and CH_3 triplet).
  2. Region 2, from 2.35 ppm to 5.25 ppm, contained peaks from water, methanol (H-bonded and not H-bonded) and ethyl acetate (CH_2 quartet).
  3. Region 3, from 5.25 ppm to 7.5 ppm, contained the aromatic peaks of toluene.

- The peak resonance frequencies changed with composition and temperature, but the peaks did not move between regions. For each peak, the range of frequencies where it was found is given in table 3.3.
- The change in resonance frequency with composition and temperature was different for each peak.
- The order of the peaks in the spectrum did not change with composition and temperature. Therefore, it was always possible to distinguish between *e.g.* the toluene CH_3 peak and the ethyl acetate CH_3 peak. Even when they both shifted in frequency by different amounts, the toluene CH_3 peak always had a higher resonance frequency.
- The peaks from each component had fixed integral ratios given by the number of nuclei producing each peak.
- Peaks that formed part of a multiplet had a fixed integral ratio and a fixed separation given by the coupling constant.
- ^{13}C satellites were separated from the main peak by ~65 Hz, and had intensities of ~0.011 times the main peak.
- Spinning sidebands were separated from the main peak by 20 Hz.

By combining these properties, a spectral pattern was defined for each component consisting of the number, relative positions, multiplicities, coupling constants and relative integrals of all the peaks from that component. The parameters for these spectral patterns are given in table 3.4.

3.3.1.2 Peak Picking Procedure

Peak picking was performed on the real spectrum, which contained the absorption spectrum after phase correction. A peak in the absorption spectrum was identified by having higher signal intensity than the baseline. This definition was slightly circular because the baseline was everything in the spectrum that was not a peak. However, the range of frequencies where peaks were present was known (1500 Hz to -50 Hz), so the regions devoid of peaks were used to estimate the baseline. (Throughout this section, frequency in Hz is used to measure peak position instead of chemical shift in ppm for consistency, because coupling constants in Hz are used to identify multiplets.) The baseline was estimated by fitting a linear function to all the points in

Component	Peak	Frequency in Pure Component (Hz)	Frequency Range in Mixtures (Hz)
Toluene	CH_3	218	251 - 467
	C_5H_5	1208	1101 - 1501
Methanol	CH_3	591	481 - 687
	OH	899	538 - 1003
Water	OH_2	829	829 - 937
Ethyl Acetate	CH_3 (t)	133	32 - 235
	CH_3 (s)	284	177 - 388
	CH_2	703	613 - 807
Cyclohexane	C_6H_{12}	243	128 - 272
Isooctane	$C(CH_3)_3$	63	35 - 174
	$C(CH_3)_2$	66	42 - 180
	CH_2	111	82 - 222
	CH	217	191 - 329

Table 3.3 Range of frequencies in which peaks were observed in pure component and mixture spectra. Frequencies are quoted in Hz for ^1H spectra acquired at 200.13 MHz.

Peak	*Frequency* ν_{0l} *(Hz)*	*Peak Width* λ_{0l} *(Hz)*	*Number of* ^{1}H *nuclei*	*Multiplet Order*	*Coupling Constant (Hz)*
Toluene					
CH_3	218.45	1.10	2.967	1	0
^{13}C-CH_3	217.94	0.80	0.033	2	125.93
Methanol (hydrogen bonded)					
CH_3	591.37	1.00	2.967	1	0
^{13}C-CH_3	590.74	0.55	0.033	2	140.58
OH	899.10	1.30	1.000	1	0
Methanol (no hydrogen bonding)					
CH_3	641.13	0.53	2.967	2	5.05
^{13}C-CH_3	640.68	0.43	0.033	2 & 2	140.05 & 5.05
OH	850.33	0.70	1.000	4	5.05
Water					
OH_2	829.34	1.70	2.000	1	0
Ethyl Acetate					
CH_3 (t)	132.72	0.25	2.967	3	7.13
^{13}C-CH_3 (t)	132.315	0.23	0.033	2 & 3	126.63 & 7.13
CH_3 (s)	283.52	0.41	2.967	1	0
^{13}C-CH_3 (s)	283.12	0.25	0.033	2	129.02
CH_2	702.97	0.35	1.978	4	7.13
^{13}C-CH_2	702.425	0.35	0.022	2 & 4	146.91 & 7.13
Cyclohexane					
C_6H_{12}	242.75	1.60	11.868	1	0
Isooctane					
$(CH_3)_3$	62.80	0.60	8.901	1	0
^{13}C- $(CH_3)_3$	62.00	0.65	0.099	2	124.30
$(CH_3)_2$	65.68	0.40	5.934	2	6.65
^{13}C- $(CH_3)_2$	65.25	0.60	0.066	2 & 2	124.25 & 6.65
CH_2	110.63	0.45	1.978	2	5.30
^{13}C-CH_2	110.63	0.50	0.022	2 & 2	121.80 & 5.30
CH	217.12	0.60	0.989	7 & 3	6.65 & 5.30

Table 3.4 Parameters defining spectral patterns observed for each component in the liquid mixtures studied in this work. (s): singlet, (t): triplet.

the real spectrum lying outside the range of 1500 Hz to -50 Hz. For peak assignment, the spectrum was divided into the three regions described above:

1. -50 Hz to 470 Hz,
2. 470 Hz to 1050 Hz,
3. 1050 Hz to 1500 Hz.

Since the actual signal intensities varied from one spectrum to another, the peak intensities in the spectrum were normalised by setting the point with the highest intensity equal to 100. Both real and imaginary spectra were normalised using the same scale factor.

Peak picking was performed separately in each of the three regions. If all the components were present in the spectrum, the number of peaks present (excluding ^{13}C satellites) would be 17, 11 and 6 for regions 1, 2 and 3 respectively, so these values were used to limit the number of peaks selected in each region. In addition, only peaks with normalised intensities above 0.5 (*i.e.* 0.5% of the largest peak) were picked so that ^{13}C satellites would not be picked as independent peaks. A "top-down" approach to peak picking was used. The largest peak was found by locating the point of maximum intensity in the spectrum, then expanding the peak region to include the points with decreasing signal intensity at higher and lower frequencies either side of the maximum. The peak limits were reached when the signal intensity either reached the fitted baseline level or started to increase due to an overlapped neighbouring peak. The peak region was then blanked out and the process was repeated to find the next largest peak. For each peak the position, integral, maximum intensity and phase were stored in a parameter file. The peak integral was obtained from a sum of the signal intensities in the peak region, and the phase was obtained from the ratio of the imaginary integral to the real integral. If the peak integral was below 1, the peak was not stored because it was a single-point "spike" and not of interest. At the end of this process, the parameter file contained the peaks sorted by intensity, but the peaks were then re-sorted by resonance frequency because the order of the peaks in the spectrum was an important parameter in assigning them.

3.3.1.3 Peak Assignment Procedure

The first stage of peak assignment was a preliminary determination of the components that were present based on the number of peaks in each region.

- The presence of peaks in region 3 indicated the presence of toluene.
- The presence of peaks in region 2 indicated the possible presence of water, methanol and ethyl acetate.
- The presence of several peaks in region 1 indicated the possible presence of cyclohexane and isooctane.
- The presence of only one peak in region 1 in combination with peaks in region 3 indicated that the peak in region 1 was the toluene CH_3 peak, so cyclohexane and isooctane were absent.

The second stage of peak assignment was a detailed search for each component starting with the component with the fewest overlapping peaks. The peaks in the parameter files were matched to the assignment criteria in the order listed in table 3.5 until there were no unassigned peaks remaining or until all the possible components had been unambiguously determined. It was not necessary to find all the peaks, and allowances were made for overlapping peaks and low-intensity peaks below the peak picking limit.

3.3.2 Results

The peak picking algorithm was applied to 6 pure-component spectra and 47 mixture spectra. The spectra were manually phase and baseline corrected to give pure absorption spectra for peak picking. The mixture composition was calculated from the weighted integrals of characteristic peaks from each component (table 3.6). The algorithm was run using the IDA software, and took under 15 s to analyse a spectrum. The algorithm correctly assigned all 6 pure component spectra and 29 out of 47 mixture spectra. The incorrectly assigned spectra contained peaks that fell outside the range of parameters coded in the algorithm. Incorrect peak integrals due to baseline distortions or peak overlap were the most common source of assignment errors. Widening the range of acceptable integrals to "catch" these spectra was considered unwise because it would have reduced the reliability of the peak assignment. In such cases, it was better to improve the data acquisition and obtain better spectra that fell within the expected range. Some spectra included spurious assignments to cyclohexane, since any peak in the range 120 - 320 Hz still unassigned at the end was assumed to be cyclohexane. However, the assignment of cyclohexane could not be made foolproof because its spectral pattern consisted of a single peak.

Component	*Peak*	*Assignment*	*Region*	*Characteristics*
Toluene	T1	C_6H_5 (m)	3	all peaks in region 3
	T2	CH_3 (s)	1	$\nu > 240$ Hz, $\int = (0.6\pm0.2)\times\int_{T1}$
	T3	^{13}C-CH_3 (d)	1	$\nu = \nu_{T2}\pm(63.0\pm1)$ Hz, $I < 0.015\times I_{T2}$
Ethyl Acetate	E1	CH_2 (q)	2	$\nu > 600$ Hz, $J_{AB} = 7.5\pm0.7$ Hz
	E2	CH_3 (s)	1	$\int = (1.5\pm0.5)\times\int_{E1}$
	E3	^{13}C-CH_3 (d)	1	$\nu = \nu_{E2}\pm(64.5\pm1)$ Hz, $I < 0.015\times I_{E2}$
	E4	CH_3 (t)	1	$\nu < \nu_{E2}$, $J_{AB} = 7.13\pm0.25$ Hz, $\int = (1.5\pm0.5)\times\int_{E1}$
	E5	^{13}C-CH_2 (q)	2	$\nu = \nu_{E1}\pm(73.0\pm1)$ Hz, $I < 0.015\times I_{E1}$
Methanol (no H-bonds)	M1	CH_3 (d)	2	$J_{AB} = 5.5\pm1.6$ Hz, $\nu < 670$ Hz
	M2	OH (q)	2	$J_{AB} = 5.5\pm1.6$ Hz, $\int = (0.31\pm0.05)\times\int_{M1}$
	M3	^{13}C-CH_3 (d)	2	$\nu = \nu_{M1}\pm(70.0\pm1)$ Hz, $I < 0.015\times I_{M1}$
Methanol (H-bonded)	MH1	CH_3 (s)	2	$\nu < 750$ Hz
	MH2	OH (s)	2	$\int = (0.33\pm0.05)\times\int_{MH1}$
	MH3	^{13}C-CH_3 (d)	2	$\nu = \nu_{MH1}\pm(70.0\pm1)$ Hz, $I < 0.015\times I_{MH1}$
Water	W1	OH_2 (s)	2	$\nu > 750$ Hz
Methanol & Water	MW1	Combined OH (s)	2	$\int > 0.40\times\int_{MH1}$ OR $\nu > 750$ Hz
Isooctane	I1	$(CH_3)_3$ (d)	1	$\nu < 182$ Hz, $J_{AB} = 6.5\pm0.8$ Hz
	I2	$(CH_3)_2$ (d)	1	$\nu < 182$ Hz, $\nu > \nu_{I1}$, $J_{AB} = 6.5\pm0.8$ Hz
	I3	^{13}C-$(CH_3)_3$ (d)	1	$\nu = \nu_{I1}\pm(62.0\pm1)$ Hz, $I < 0.015\times I_{I1}$
	I4	CH (s-t)	1	$J_{AB} = (6.65\pm0.5$ OR $5.3\pm0.5)$ Hz, $\nu > (\nu_{I1}+120)$ Hz, $I < I_{I1}/54$
	I5	CH_2 (d)	1	$J_{AB} = (5.30\pm0.25)$ Hz, $\nu > \nu_{I2}$
Cyclohexane	C1	C_6H_6 (s)	1	120 Hz $< \nu <$ 320 Hz
--	--	spinning sideband (s)	any	$\nu = 20\pm1$ Hz from nearest peak, $I <$ I of nearest peak

Table 3.5 Peak characteristics used by the peak assignment algorithm to identify peaks in liquid mixture spectra. ν: frequency, $\int$: integral, I: intensity, J_{AB}: coupling constant, (m): multiple peaks, (s): singlet, (d): doublet, (t): triplet, (q): quartet, (s-t): septet of triplets.

Component	Peak	Number of ^{1}H nuclei
toluene	CH_3 (s)	2.967
ethyl acetate	CH_3 (s)	2.967
methanol (H-bonded)	CH_3 (s)	2.967
methanol (not H-bonded)	CH_3 (d)	2.967
water	OH_2 (s)	2.000
cyclohexane	C_6H_{12} (s)	12.000
isooctane	$(CH_3)_2$ & $(CH_3)_3$	11.868

Table 3.6 Characteristic peaks used in calculating the mixture compositions after peak assignment. The peak integrals are divided by the number of ^{1}H nuclei giving rise to them. (s): singlet, (d): doublet.

The mixture compositions were calculated for the 29 correctly assigned spectra with average error ±2.69 mol%. For comparison, the average error for the same spectra analysed manually was ±0.50 mol% (section 2.4). The source of the error was automatic integration of overlapped peaks using the perpendicular drop method, which did not partition the overlapped integrals correctly between the components (Foley, 1987). The least reliable compositions were measured for mixtures containing components whose characteristic peaks were partially overlapped by other peaks: water, isooctane and toluene.

These results showed that an algorithm incorporating prior knowledge about spectral characteristics succeeded at assigning peaks in a series of mixture spectra rapidly and reliably. The composition results were only accurate within ±2-3 mol% because of error-prone integration of overlapping peaks. In order to improve accuracy, peak integration can be replaced by lineshape fitting, as will be discussed in chapter 4.

3.4 Combined Algorithm for Composition Analysis

3.4.1 Experimental

After separate optimisation of phase and baseline correction and peak assignment, the algorithms were combined into a single Tcl program to carry out the entire composition analysis procedure. The program performed first point correction and Fourier transformation of the FID followed by phase correction using NUM2 with the polynomial baseline fit. For later iterations of NUM2, the peak picking procedure was used to distinguish peak and baseline regions, instead of distinguishing them only by signal intensity. This combined approach allowed more baseline points between peaks to be included in the baseline fit and prevented the low-intensity wings of the peaks from being assigned to the baseline. This gave a better estimate of the baseline underneath the peaks and more accurate peak integrals. After NUM2 had converged, a final iteration of peak picking and assignment was performed to calculate the composition.

3.4.2 Results

The test spectra N9 and N34 analysed using this program are shown in figure 3.9. The measured composition of N9 had an average error of ±2.15 mol% due to the incorrect assignment of non-hydrogen bonded methanol peaks to hydrogen-bonded

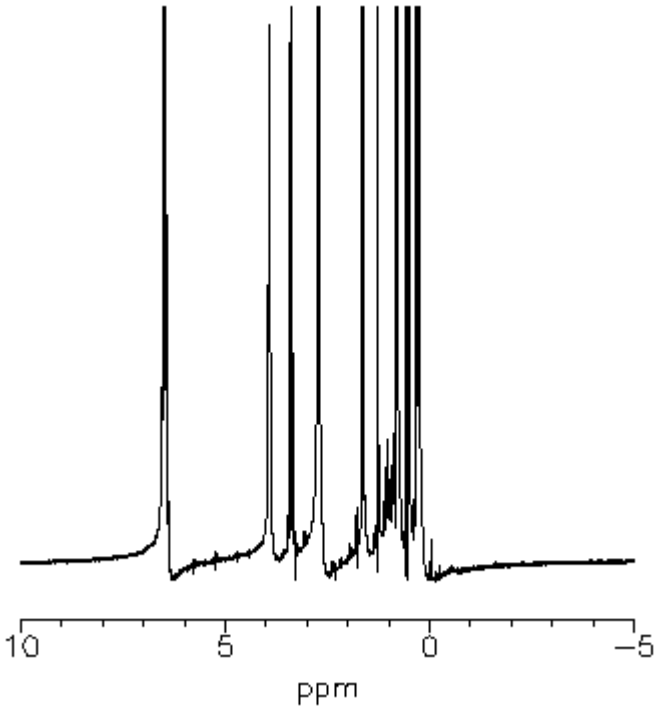

(a)

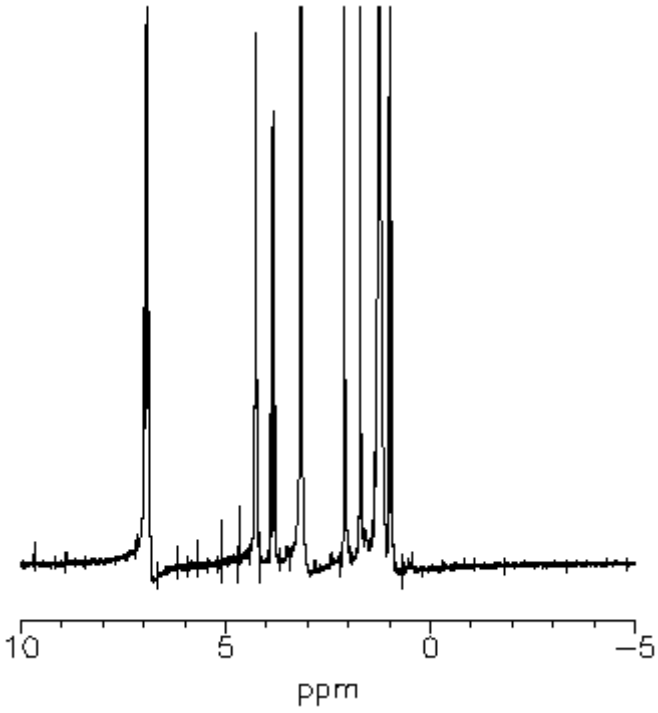

(b)

Figure 3.9 Test spectra processed using a fully automatic phase and baseline correction algorithm including peak picking *(a)* N9: $\phi_0 = 4.0509$, $\phi_1 = -4.0603$ *(b)* N34: $\phi_0 = 4.0712$, $\phi_1 = -4.3085$.

methanol and water. The measured composition of N34 had an average error of ±0.66 mol% with all peaks correctly assigned, due to imperfect phase correction altering the peak integrals. The values of ϕ_0 and ϕ_1 obtained were larger than necessary because large values of σ_0/σ_1 were needed for the first few iterations of NUM2. For later iterations, the ϕ_0/ϕ_1 step size did not decrease fast enough to prevent the accumulation of a large overall phase. A more sophisticated algorithm employing adaptive values of σ_0/σ_1 may give better results.

The execution time for each step in the algorithm was measured. Reading in the FID and performing the Fourier transform took 30 - 40 s. NUM2 took 20 s per iteration without peak picking, and 23 s per iteration with peak picking. A good overall result was obtained using 5 iterations of NUM2 without peak picking ($\sigma_0/\sigma_1 = 5.0\times10^{-4}$) followed by 5 iterations of NUM2 including peak picking ($\sigma_0/\sigma_1 = 5.0\times10^{-3}$), giving a total execution time for the whole algorithm of 201 s. This time was short enough for a hypothetical on-line analyser to process a spectrum within a few minutes.

3.5 Conclusion

Procedures and computer algorithms were successfully developed for automated analysis of NMR spectra of liquid mixtures, including algorithms for phase and baseline correction and peak assignment. In a departure from other workers, phase and baseline correction were performed together in two algorithms based on numerical phasing and baseline optimisation respectively. The algorithms were updated with more sophisticated baseline models and performed better than the originals at the expense of longer running times. Numerical phasing was more suitable for fully automated analysis than baseline optimisation because it was less dependent on the starting parameters and converged to sensible solutions more consistently. Its long execution time can be reduced by using an adaptive scheme for the parameters σ_0 and σ_1. An entirely novel algorithm was written to identify the peaks in the spectrum of a mixture based on prior knowledge of the component spectra. Peaks were assigned using their frequencies, intensities, integrals, coupling constants, separation and order in the spectrum. The algorithm correctly assigned 29 out of 47 mixture spectra and required peak integrals and resonance frequencies within expected ranges. The phase correction, baseline fitting and peak assignment algorithms were combined into a single program that performed the entire

composition analysis in less than 4 minutes and gave a result with accuracy ±0.66 mol% for a correctly-assigned test spectrum.

3.6 References

Balacco, G. (1994). A new criterion for automatic phase correction of high-resolution NMR spectra which does not require isolated or symmetrical lines. *Journal of Magnetic Resonance, Series A, 110*, 19-25.

Brown, D.E., Campbell, T.W., & Moore, R.N. (1989). Automated phase correction of FT NMR spectra by baseline optimisation. *Journal of Magnetic Resonance, 85*, 15-23.

Chen, C.N., & Kan, L.S. (1988). An iterative phase correction program for nuclear magnetic resonance (NMR) spectra. *Computer Methods and Programs in Biomedicine, 26*, 81-84.

Craig, E.C., & Marshall, A.G. (1988). Automated phase correction of FT NMR spectra by means of phase measurement based on dispersion versus absorption relation (DISPA). *Journal of Magnetic Resonance, 76*, 458-475.

Ernst, R.R. (1969). Numerical Hilbert transform and automatic phase correction in magnetic resonance spectroscopy. *Journal of Magnetic Resonance, 1*, 7-26.

Ernst, R.R., & Anderson, W.A. (1966). Application of Fourier transform spectroscopy to magnetic resonance. *The Review of Scientific Instruments, 37*, 93-102.

Foley, J.P. (1987). Systematic errors in the measurement of peak area and peak height for overlapping peaks. *Journal of Chromatography, 384*, 301-313.

Gladden, L.F., & Elliott, S.R. (1986). A numerical phasing technique for application to one-dimensional NMR spectra. *Journal of Magnetic Resonance, 68*, 383-388.

Heuer, A. (1991). A new algorithm for automatic phase correction by symmetrizing lines. *Journal of Magnetic Resonance, 91*, 241-253.

Heuer, A., & Haeberlen, U. (1989). A new method for suppressing baseline distortions in FT NMR. *Journal of Magnetic Resonance, 85*, 79-94.

Montigny, F., Elbayed, K., Brondeau, J., & Canet, D. (1990). Automatic phase correction of Fourier transform nuclear magnetic resonance spectroscopy data and estimation of peak area by fitting to a Lorentzian shape. *Analytical Chemistry, 62*, 864-867.

Press, W.H., Teukolsky, S.A., Vetterling, W.T., & Flannery, B.P. (1992). *Numerical Recipes in C: The Art of Scientific Computing, Second Edition*. p. 409-412. Cambridge University Press, Cambridge, UK.

Starcuk, Z., Starcuk, Z. Jr., & Halámek, J. (1990). Correction of baseline and lineshape distortions in Fourier transform NMR spectroscopy by estimation of missing signals. *Journal of Magnetic Resonance, 86*, 30-38.

Sterna, L.L., & Tong, V.P. (1991). Automated method of phasing difficult nuclear magnetic resonance spectra with application to unsaturated carbon analysis of oils. *Fuel, 70*, 941-945.

Vaals, J.J. van, & Gerwen, P.H.J. van (1990). Novel methods for automatic phase correction of NMR spectra. *Journal of Magnetic Resonance, 86*, 127-147.

3.7 Nomenclature

(symbol)	(description)	(unit)

Scalar Variables

$B(j)$	baseline function	-
B_i	estimate of baseline, i = 1, 2, 3	-
f	object function maximised in algorithm of Brown *et al.*	-
j	index of data point in frequency domain	-
k	index of data point in time domain	-
m	number of corrupted data points (Heuer & Haeberlen)	-
n	= N / 1000 rounded down to the nearest integer	-
nsd	number of noise standard deviations in baseline region	-
N	number of points in spectrum	-
p	index of points in baseline region (Brown *et al.*)	-
q	number of points in baseline region (Brown *et al.*)	-
$s_A(\nu)$	pure absorption spectrum	-
$s_D(\nu)$	pure dispersion spectrum	-
$s_I(\nu)$	imaginary spectrum	-
$s_R(\nu)$	real spectrum	-
s_j	j^{th} data point in measured spectrum	-
$\tilde{s}_j$	j^{th} data point in model spectrum	-
t	time	s
Δ_i	parameter for numerical phasing, i = 1, 2	-
θ_j	phase of j^{th} complex point in measured spectrum	rad
$\tilde{\theta}_j$	phase of j^{th} complex point in model spectrum	rad
$\kappa_i, \kappa_i', \kappa_i''$	parameters for numerical phasing, i = 0, 1, 2	-
μ	mean baseline level	-
ν	frequency	s^{-1}
σ_j	standard deviation of the noise in spectrum	-
σ_0, σ_1	standard deviations of the Gaussian probability distributions of ϕ_0, ϕ_1	-
$\phi(\nu)$	phase correction applied to spectrum	rad
ϕ_0	zero order phase correction term	rad
ϕ_1	linear phase correction term	rad s

4 MATHEMATICAL MODELLING OF NMR SPECTRA OF LIQUID MIXTURES

4.1 Introduction

The simplest method to obtain quantitative composition data from NMR signals is to integrate the absorption peaks in the FT spectrum as described in chapters 2 and 3. However, the presence of overlapping peaks in the mixture spectra causes integration errors because the integral of the non-overlapped part of a peak gives a biased estimate of the integral of the entire peak (Foley, 1987). The resulting compositions are not accurate enough even when the spectra are correctly phased. The alternative method is to fit a model to the spectrum and use the parameters of the fit to determine the composition. Model fitting is expected to be more accurate than peak integration and less sensitive to peak overlap, phase errors and baseline distortions. In model fitting there are two things to consider: which model is appropriate to describe the data, and which fitting procedure gives the best fit to the data. This chapter discusses the development of new mathematical models for the mixture spectra and the non-Lorentzian lineshapes present in the spectra, and the results obtained. The emphasis is on the development of better models, which may be used with any model fitting procedure. The models are based on an analysis of the physical conditions under which the NMR signal is acquired and the effect of the data processing operations, and incorporate prior knowledge about the sample to give meaningful results.

4.2 Mathematical Model of NMR Spectrum

A mathematical model of the NMR spectrum must give the best possible representation of the signal that is consistent with the known properties of the system. It must also be correctly fitted to the data to obtain unbiased estimates of the spectral parameters.

4.2.1 Model Fitting Procedures

For this application, a model fitting procedure is required that gives accurate estimates of the signal intensities in the NMR data. Of the procedures that abound, least-

squares fitting, linear prediction, maximum entropy fitting and Bayesian analysis have been most often applied to NMR data.

Least-squares fitting of a model to time-domain and frequency-domain NMR data has been used by several groups (Abildgaard *et al.*, 1988; van den Boogaart *et al.*, 1994) and was proven mathematically to be the most accurate quantitative method (Martin, 1994). Least-squares fitting requires starting values for the model parameters (Joliot *et al.*, 1991), but it can incorporate prior knowledge about the data in the model or the starting values for the fit.

Time-domain fitting using linear prediction (LP) is often chosen to avoid the errors in the spectrum introduced by the Fourier transform (Led and Gesmar, 1991). LP is non-iterative and does not require starting values for the model parameters (Barkhuijsen *et al.*, 1985; de Beer and van Ormondt, 1992), but it requires long computing times, and a large amount of computing effort is spent on solutions that are discarded (Joliot *et al.*, 1991; Gesmar *et al.*, 1990). In practice, LP methods give biased estimates of the spectral parameters from noisy data and are only useful when the FID is severely truncated (Joliot *et al.*, 1991; Stephenson, 1988).

The maximum entropy method (MEM) selects the spectrum with the least structure from several spectra that represent the noisy data equally well (Laue *et al.*, 1985). Mathematically, this consists of constrained optimisation of a non-linear entropy function over all possible spectra (Hore, 1985). The drawback of MEM is that it is inherently non-linear and strongly dependent on the parameters used during the reconstruction (Schmieder *et al.*, 1997). The MEM spectrum is a non-linear amplification of the FT spectrum where the baseline noise is selectively suppressed (Jones and Hore, 1991a). More accurate quantitative results were obtained by fitting lineshapes to the FT spectrum than by integrating the MEM spectrum (Jones and Hore, 1991b). Another maximum entropy technique, Burg MEM, is an auto-regressive technique that computes a maximum-entropy power spectral estimator. It was developed for non-decaying signals so it is not strictly valid for NMR (Stephenson, 1988; Hoch and Stern, 1996), and it gives inaccurate results because information about the peak intensities is lost (Kauppinen and Saario, 1993).

The maximum entropy principle comes from Bayesian probability theory, which uses Bayes' theorem to calculate the probability that a model fits the data (Sivia, 1996).

Bayesian analysis has been applied to NMR time-domain data to estimate the frequencies, amplitudes, phases and decay rate constants of damped sinusoids (Bretthorst, 1990a, 1990b, 1992). The required calculations are computationally intensive because each parameter is calculated separately. The results depend strongly on the prior information used in the model (Bretthorst, 1991) but can be more accurate than those obtained by Fourier analysis (Kotyk *et al.*, 1992).

Of these fitting methods, least-squares fitting is most appropriate for quantitative composition analysis, due to its accuracy and speed. The maximum entropy methods are not quantitative, and the computationally intensive linear prediction and Bayesian techniques are too slow. Following Martin (1994), least-squares model fitting is performed in the frequency domain because it is easier to determine the quality of fit for individual peaks.

4.2.2 Model Derivation

The model of the NMR spectrum was developed by describing mathematically the effect of each stage of data acquisition and analysis on the NMR signal. The model in this section (4.2.2) was derived in collaboration with Dr Paul Alexander of the Department of Physics, University of Cambridge. The analysis resembles those of Abildgaard *et al.* (1988) and Martin (1994) with one important exception: The mixture spectrum is a weighted sum of the pure-component spectra, so the pattern of peaks in the spectrum is fixed. The number, frequency and multiplicity of the peaks are not independent variables and cannot be varied to give the best fit.

In any spectrum, the apparent number of peaks may not match the actual number present. Some peaks may be lost in the noise or hidden under other peaks, and extra peaks may appear from instrumental artefacts or contaminants in the sample. Fitting each apparent peak separately is computationally intensive because of the large number of independent variables. It is also physically meaningless, since the peaks are not independent of each other. Instead, this model uses the pattern of peaks for each mixture component, allowing hidden peaks to be included and spurious peaks to be excluded. The peak assignment algorithm of section 3.3 identifies the components present and gives starting values for the least-squares fit. The peak patterns used in this model are listed in table 3.4. All peaks and ^{13}C satellites for each component are included except the aromatic peaks of toluene because their exact number and spacing

was not known. This model can also be used with other fitting procedures such as Bayesian analysis.

4.2.2.1 Time-Domain Signal

Consider a mixture containing N_c components, each component i having a proportion X_i. Each component produces an NMR signal in the time domain corresponding to one or more peaks in the frequency domain. This signal is represented by the function $C_i(t, \nu_{0i}, \lambda_i, \phi_i)$ where t is time, ν_{0i} is the spectral reference frequency, λ_i is the linewidth and ϕ_i is the phase for that component. The total signal from the mixture is given by:

$$S(t) = \sum_{i=1}^{N_c} X_i C_i(t, \nu_{0i}, \lambda_i, \phi_i). \tag{4.1}$$

During acquisition, the signal is altered in the following manner:

1. The signal contains noise, E:

$$S(t) = \sum_{i=1}^{N_c} X_i C_i(t, \nu_{0i}, \lambda_i, \phi_i) + E. \tag{4.2}$$

2. The signal is sampled digitally with interval Δt:

$$\hat{S}_k = \Psi(t, k, \Delta t) \cdot S(t), \tag{4.3}$$

where the sampling function, Ψ, is given by (Bracewell, 1978):

$$\Psi(t, k, \Delta t) = \sum_{-\infty}^{\infty} \delta(t - k\Delta t), \tag{4.4}$$

and δ is the Dirac delta function.

3. The signal is acquired for a finite time period between $t = 0$ and $t = t_{max} = N_t \Delta t$, where N_t is the total number of points in the FID. The FID is set equal to zero (zero-filled) at all other times. This corresponds to multiplying the FID with a rectangle (top-hat) function, Π, given by:

$$\Pi(0, t_{\max}) = \begin{cases} 1 & 0 < t \le N_t \Delta t \\ 0 & \text{otherwise} \end{cases}. \tag{4.5}$$

4. The discrete Fourier transform is periodic (Stephenson, 1988), so the signal is replicated with a spacing of $2N_t \Delta t$ when the FID is zero filled once. This

corresponds to convolution of the signal with the replication function, Θ, given by:

$$\Theta = \sum_{j=-\infty}^{\infty} \delta\left(t - j \cdot 2N_t \Delta t\right). \tag{4.6}$$

Combining all four effects, the experimental signal is related to the ideal signal by:

$$\hat{S}_k = \left(\Pi \cdot \Psi \cdot S(t)\right) \otimes \Theta. \tag{4.7}$$

4.2.2.2 Frequency-Domain Signal

The equation for the experimental spectrum, $\hat{s}_j$, is obtained by Fourier transforming equation (4.7) to give:

$$\hat{s}_j = \widetilde{\Theta} \cdot \left[\widetilde{\Psi} \otimes \left(\widetilde{\Pi} \otimes s(\nu)\right)\right], \tag{4.8}$$

where

$$s(\nu) = FT\left[S(t)\right] = \sum_{i=1}^{N_c} X_i c_i\left(\nu, \nu_{0i}, \lambda_i, \phi_i\right) + \varepsilon \tag{4.9}$$

is the signal in the frequency domain. The Fourier transform converts convolution into multiplication and vice versa. The spectral noise, ε, is the Fourier transform of the time-domain noise, E. The function $c_i(\nu, \nu_{0i}, \lambda_i, \phi_i)$ is the Fourier transform of $C_i(t, \nu_{0i}, \lambda_i, \phi_i)$ and contains the spectral pattern of peaks from component i. The signal is sampled in the frequency domain by the Fourier transform of the replication function, given by:

$$\widetilde{\Theta} = \sum_{j=-\infty}^{\infty} \delta(\nu - j\Delta\nu), \tag{4.10}$$

where the sampling frequency is given by:

$$\nu_j = j\Delta\nu = \frac{j}{2N_t \Delta t}. \tag{4.11}$$

The Fourier transform of the sampling function Ψ is a replication function in the frequency domain given by:

$$\widetilde{\Psi} = \sum_{k=-\infty}^{\infty} \delta\left(\nu - \frac{k}{\Delta t}\right), \tag{4.12}$$

which replicates the spectrum with a spacing $1/\Delta t$. If Δt is small enough that $\nu_{max} << 1/\Delta t$, no aliasing is observed and the replication can be neglected. The

Fourier transform of the window function Π is the sinc function given by (Bracewell, 1978):

$$\widetilde{\Pi} = \frac{\sin(\pi j \Delta\nu)}{\pi j \Delta\nu}. \tag{4.13}$$

If t_{max} is large enough for complete signal decay, then the sinc function can be neglected as well.

There are two terms in the model that describe the phases of the signals in the spectrum. Firstly, each peak has its own phase, so a phase term is included in the function c_i (see below). Secondly, the pre-scan delay, t_{in}, shifts the start of signal acquisition from $t = 0$ to $t = t_{in}$. In the model, the time-domain window function is shifted from $\Pi(0, t_{max})$ to $\Pi(t_{in}, t_{in}+t_{max})$ by convolution with a delta function at $t = t_{in}$. The sinc function in equation (4.13) is replaced by:

$$FT\left[\Pi(t_{in}, t_{in}+t_{\max})\right] = FT\left[\Pi(0, t_{\max}) * \delta(t-t_{in})\right] = \widetilde{\Pi}\cdot e^{i2\pi\nu t_{in}}. \tag{4.14}$$

The exponential term in equation (4.14) is the Fourier transform of the delta function and causes a frequency-dependent phase across the spectrum.

If the initial points of the FID are corrupted by pulse breakthrough in the receiver, the spectrum contains a non-zero baseline (section 2.3.4). The k_1 corrupted points in the FID are corrected by adding a complex error term, given by:

$$\sum_{k=1}^{k_1} B_k e^{i\beta_k}, \tag{4.15}$$

whose Fourier transform is the spectral baseline function given by:

$$\sum_{k=1}^{k_1} B_k e^{i(\beta_k + 2\pi k \Delta t j \Delta\nu)}. \tag{4.16}$$

Combining equations (4.8) to (4.16), the frequency-domain model of the NMR spectrum is given by:

$$\hat{s}_j = e^{i\phi_1 j\Delta\nu}\left[\sum_{i=1}^{N_c} X_i c_i(\nu, \nu_{0i}, \lambda_i, \phi_i) + \sum_{k=1}^{k_1} B_k e^{i(\beta_k + 2\pi k\Delta t j\Delta\nu)} + \varepsilon\right]. \tag{4.17}$$

The model requires a function to define the spectral pattern, $c_i(\nu, \nu_{0i}, \lambda_i, \phi_i)$, of each component i. The pattern in the pure component spectrum is a series of peaks with parameters ν_{0l}, λ_{0l} and ϕ_l for the frequency, linewidth and phase respectively for each peak, l, in the pattern. In the mixture spectrum, the peaks are shifted in frequency and

have different linewidths, so the parameters in the pattern become ($\nu_{0l} + \nu_l$), ($\lambda_{0l} + \lambda_l$) and ϕ_l. The subscript $_{0l}$ refers to the pure component value and the subscript $_l$ refers to the difference between the pure component and mixture values for each parameter. The parameters ν_l and λ_l are adjusted to fit the model to the mixture spectrum. Their starting values are determined by the peak picking algorithm.

4.2.3 Least-Squares Fitting using Lorentzian Lineshapes

4.2.3.1 Lineshape Model

The spectral pattern needs a lineshape function for the peaks in the spectrum. Theoretically, the correct function is the Lorentzian lineshape, given by:

$$L(\nu) = \frac{S(0)e^{i\phi}}{2\pi} \cdot \frac{\lambda - i(\nu - \nu_0)}{\lambda^2 - (\nu - \nu_0)^2}, \tag{4.18}$$

which is the Fourier transform of a single exponentially damped sinusoid of amplitude $S(0)$, frequency ν_0, phase ϕ and decay constant $(2\pi\lambda)^{-1}$. The real part of this function has a maximum intensity of $(2\pi\lambda)^{-1}$ at $\nu = \nu_0$. To speed up the least-squares fit, a normalised Lorentzian function, $L'(\nu)$, was used that had a maximum intensity of 1 at $\nu = \nu_0$:

$$L'(\nu) = \frac{S(0)e^{i\phi}\left(1 - i\left(\frac{\nu - \nu_0}{\lambda}\right)\right)}{1 + \left(\frac{\nu - \nu_0}{\lambda}\right)^2}. \tag{4.19}$$

Using this lineshape, the spectral function $c_i(\nu, \nu_{0l}+\nu_l, \lambda_{0l}+\lambda_l, \phi_l)$ was written as:

$$c_i(\nu, \nu_{0l} + \nu_l, \lambda_{0l} + \lambda_l, \phi_l) = \sum_{l=1}^{N_l} \frac{s_l e^{i\phi_l}\left(1 - i\left(\frac{j\Delta\nu - (\nu_{0l} + \nu_l)}{\lambda_{0l} + \lambda_l}\right)\right)}{1 + \left(\frac{j\Delta\nu - (\nu_{0l} + \nu_l)}{\lambda_{0l} + \lambda_l}\right)^2}, \tag{4.20}$$

where N_l is the number of peaks in the pattern for component i, s_l is the relative intensity and ϕ_l is the phase of the l^{th} peak in the pattern and the other parameters are defined above. The relative intensity s_l was fixed for each peak and depended on the number of ^{1}H nuclei producing the peak and the multiplicity of the peak. For example, in the hydrogen-bonded methanol pattern $s_l = 2.967$ for the CH_3(s) peak and

$s_l = 1.000$ for the OH(s) peak. The mole fraction of component i, X_i, was used to scale the entire pattern c_i to fit the peaks in the spectrum.

4.2.3.2 Experimental

The model was fitted to the data using a least-squares algorithm that minimised the sum of squared differences between the data points and the model function for both the real and imaginary spectra. A program was written in FORTRAN 77 that used the subroutine E04FDF from the NAG Fortran Library Mark 17. The subroutine found the unconstrained minimum of a sum of squares of m non-linear functions in n variables ($m \geq n$). The m non-linear functions were the data points and the n variables were $\{X_i, 1 \leq i \leq N_i\}$, ϕ_1, $\{B_k, \beta_k, 1 \leq k \leq k_1\}$, $\{\phi_l, \nu_l, \lambda_l, 1 \leq l \leq N_l\}$.

The input to the program was a spectrum of a liquid mixture truncated to 3605 complex data points covering the frequency range from -50 Hz to 1050 Hz. Frequencies outside this range were excluded because they contained no peaks. The program received starting values for the variables X_i, ν_l, ϕ_l from the peak-assignment program, and the other variables were initialised to zero values. The components included in the model were toluene, ethyl acetate, cyclohexane, isooctane, water, hydrogen-bonded methanol and methanol without hydrogen bonding. The OH peak of methanol (both forms) was treated as a separate "component" because its frequency separation from the CH_3 multiplet was not constant and it required its own ν_l parameter.

For each component present, a spectral pattern was produced consisting of a fixed number of multiplets, with fixed relative intensity and relative position. The variable X_i was used to scale the pattern, while ν_l shifted the frequency of the pattern and λ_l altered the linewidths of the peaks in the pattern. Each peak in the pattern had its own phase, ϕ_l. For example, the pattern for hydrogen-bonded methanol consisted of a CH_3 singlet of intensity X_{MeOH} at frequency $(591.37+\nu_{MeOH})$ Hz with a FWHM of $(2.0+\lambda_{MeOH})$ Hz, CH_3 ^{13}C satellites of intensity of $0.075X_{MeOH}$ at 70.29 Hz either side of the singlet with FWHM of $(1.05+\lambda_{MeOH})$ Hz, and an OH singlet of intensity $0.58X_{MeOH}$ at $(899.10+\nu_{OH})$ Hz with a FWHM of $(2.6+\lambda_{OH})$ Hz. A baseline was added using three terms ($k_1 = 3$) to match the third-order baseline used in the baseline-fitting algorithms.

The residuals were calculated separately for the real and imaginary spectra, so that the vector to be minimised consists of 7210 points. The output of the program was a complex model spectrum and a list of the optimum values of the model parameters. The composition of the mixture was calculated by normalising the X_i values to add up to 1.

4.2.3.3 Results

The least-squares fit was applied to six test spectra containing 2 to 4 components. Each fit took about half an hour to run. The calculated compositions had an average error of 5.46 mol% (table 4.1), which was larger than that obtained using the data analysis program of chapter 3 (2.69 mol%) or by manual processing (0.50 mol%). The cause of the errors was apparent from the fits, *e.g.* spectra N4 and N17 in figure 4.1: The experimental peaks were non-Lorentzian, so the Lorentzian lineshapes in the model were incorrectly phased to fit the low-frequency shoulder on the peaks, because the main peak contributed less to the total error than the shoulder did. This resulted in X_i values that were too low. Therefore, the mathematical model of the spectrum was valid, but the Lorentzian lineshape was not a good model for the experimental peaks. To improve the fit and obtain more accurate composition results, a better model lineshape is required.

4.3 Modelling NMR Lineshapes

The experimental NMR lineshapes are not well-represented by a Lorentzian function because the decay in the FID is non-exponential. Firstly, the high concentration of ^{1}H nuclei produces radiation damping effects that give non-exponential decay behaviour (Warren and Richter, 1996). Secondly, the magnetic field is not perfectly homogeneous, so instead of a single resonance frequency across the sample giving a single exponential decay, there is a distribution of resonance frequencies that depends on the distribution of magnetic field strengths over the sample. This leads to a superposition of exponential decays for each signal giving a non-Lorentzian peak. Both of these conditions can occur in a process environment. If a process stream is to be monitored non-invasively, it cannot be diluted using a deuterated solvent. Perfect magnetic field homogeneity is difficult to achieve in a laboratory and even harder in a process environment. Therefore, it is worthwhile studying non-Lorentzian lineshapes so that quantitative results can be obtained even under non-ideal conditions.

spectrum	component	composition by weight (mol%)	composition from model fit with Lorentzians (mol%)	error (mol%)
N4	toluene	17.74	22.43	+4.69
	cyclohexane	82.26	77.57	-4.69
N17	methanol	37.76	36.84	-0.92
	ethyl acetate	62.24	63.16	+0.92
N18	toluene	25.98	23.11	-2.87
	isooctane	74.02	76.89	+2.87
N21	ethyl acetate	21.05	28.00	+6.95
	cyclohexane	78.95	72.00	-6.95
N22	ethyl acetate	41.99	35.08	-6.91
	isooctane	58.01	64.92	+6.91
N34	toluene	13.35	15.87	+2.52
	ethyl acetate	11.19	16.52	+5.33
	methanol	38.56	17.78	-20.78
	cyclohexane	36.90	49.83	+12.93
average error over all spectra				*5.46*

Table 4.1 Composition results obtained by fitting the model in equation (4.17) to experimental spectra using Lorentzian lineshapes. The compositions by weight were measured when the mixtures were prepared.

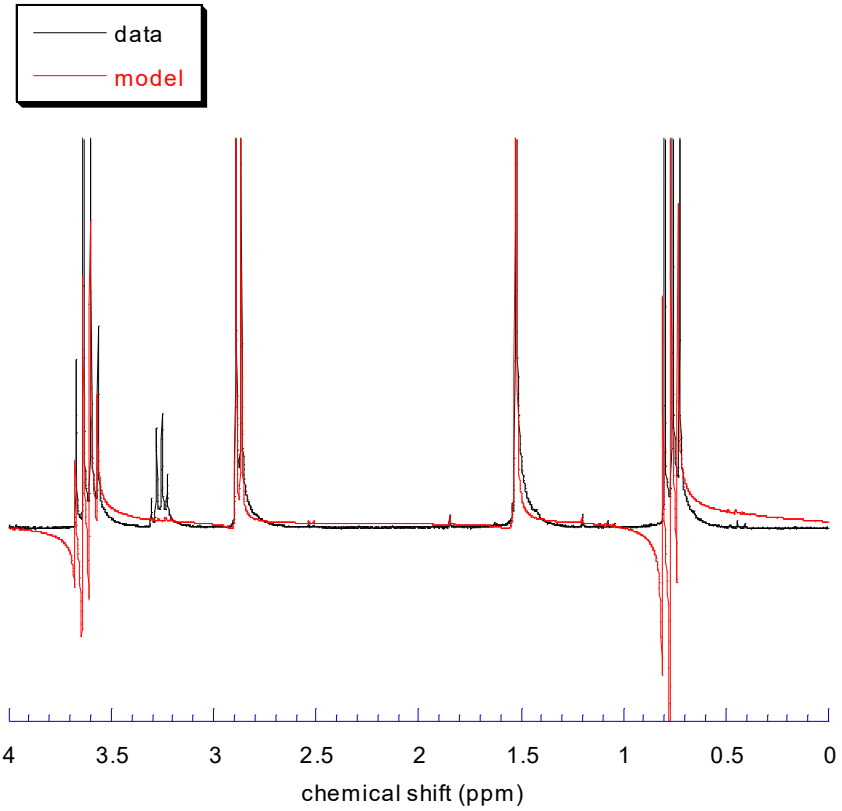

(a)

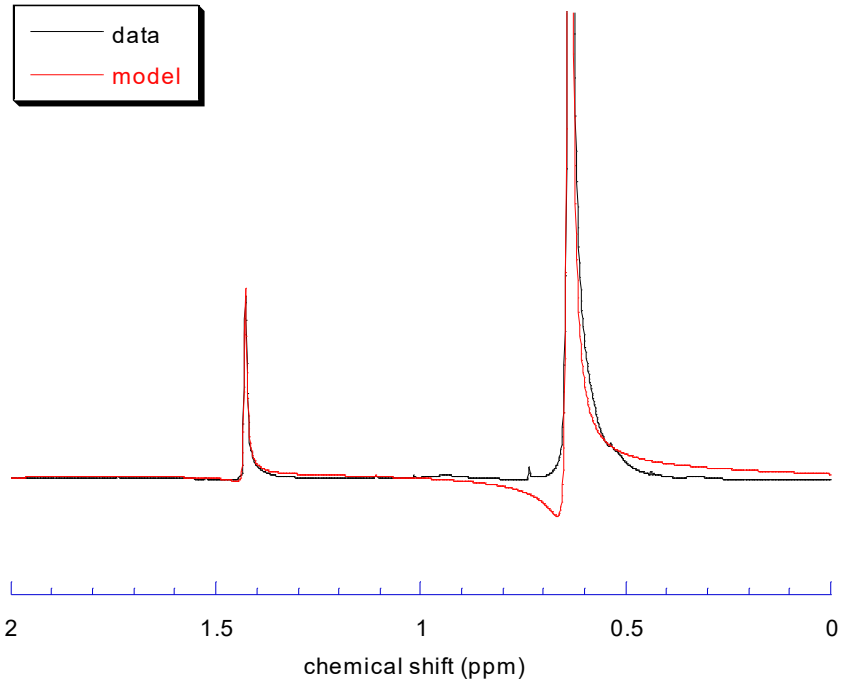

(b)

Figure 4.1 Model fits to experimental spectra using Lorentzian lineshapes *(a)* N17 (methanol-ethyl acetate), *(b)* N4 (toluene-cyclohexane).

4.3.1 Reference Deconvolution

If a non-Lorentzian lineshape cannot be improved experimentally, it may be possible to correct it numerically. For example, the FIDDLE algorithm attempts to convert non-Lorentzian lineshapes to Lorentzian or Gaussian by "reference deconvolution" (Morris, 1988; Gibbs and Morris, 1991; Morris *et al.*, 1997). A single reference peak is converted into a Lorentzian, then the same deconvolution is applied to all peaks in the spectrum.

The FIDDLE algorithm in AcornNMR's NUTS software was tested on a ^{1}H spectrum of undiluted ethyl acetate with slightly asymmetric peaks that suffered from both radiation damping and magnetic field inhomogeneity. The peaks in the spectrum had different linewidths in the range 0.5 - 0.9 Hz. For the CH_2 quartet, CH_3 singlet and CH_3 triplet, the peak integral ratio was expected to be 2:3:3 and was found by integration to be 2.00:3.01:3.05 in the original spectrum. The CH_3 singlet without ^{13}C satellites was used for reference deconvolution. After deconvolution with an ideal Lorentzian peak of 0.5 Hz linewidth, the peak integral ratio was 2.00:3.33:2.99. Increasing the ideal linewidth to 1.0 Hz gave an integral ratio of 2.00:2.99:2.66. Both deconvolved spectra contained baseline distortions that caused the large errors in the integrals.

The poor performance of FIDDLE is caused by several factors. The extraction of the reference lineshape by selecting a portion of the spectrum is very sensitive to overlap with other peaks, ^{13}C satellites, baseline errors and truncation of the reference peak (Gibbs and Morris, 1991). FIDDLE treats the noise in the reference region as part of the lineshape and convolves it with the rest of the spectrum, leading to a lower signal-to-noise ratio and distorted lineshapes in the deconvolved spectrum (Morris *et al.*, 1997). The deconvolution is performed in the time domain by dividing the ideal signal by the reference signal, and is highly unreliable for those points in the FID where the signal is comparable to the noise and indeterminate when the signal drops to zero (Barjat *et al.*, 1995). And finally, FIDDLE is an entirely arbitrary replacement of one lineshape for another. Therefore, FIDDLE is unsuitable for accurate quantitative analysis of the liquid mixture spectra.

4.3.2 Model Lineshapes

The non-Lorentzian lineshapes are asymmetric, so asymmetric model lineshapes are required to replace the Lorentzian function in the model. Two asymmetric lineshapes are described in the literature. The first is based on a hyperbolic secant curve (Losev, 1994). The second is an asymmetric form of the Voigt lineshape, which is the convolution product of Gaussian and Lorentzian functions (Jiménez-Domínguez *et al.*, 1996, 1997).

4.3.2.1 Losev Lineshape

A purely phenomenological lineshape was defined by Losev (1994) as a simple mathematical function with a minimum number of parameters. The lineshape is defined by the normalised function:

$$h_0(x) = \frac{A}{\eta} \cdot \frac{1}{e^{-a_L(x-c+\xi)} + e^{b_L(x-c+\xi)}}, \tag{4.21}$$

with

$$\xi = \frac{\ln(a_L/b_L)}{a_L + b_L} \tag{4.22}$$

and

$$\eta = \frac{a_L^{\,a_L/(a_L+b_L)} b_L^{\,b_L/(a_L+b_L)}}{a_L + b_L}. \tag{4.23}$$

The function has four parameters A, a_L, b_L and c. The maximum amplitude A of the lineshape occurs at frequency c, while a_L and b_L determine the shape of the left-hand and right-hand sides of the peak respectively. If $a_L = b_L$, the lineshape is a symmetric hyperbolic secant, which has a shape intermediate between Lorentzian and Gaussian. If $b_L = 0$, the lineshape is a scaled Fermi function. The function describes an absorption peak, but lacks an equivalent expression for the dispersion peak. The dispersion function can be obtained from the Hilbert transform of equation (4.21) (Bracewell, 1978).

4.3.2.2 Asymmetric Voigt Lineshape

Jiménez-Domínguez *et al.* (1996, 1997) have generalised the Voigt lineshape to an asymmetric form using its relation to the plasma dispersion function (PDF). The PDF is given by:

$$Z(z) = \frac{1}{\sqrt{\pi}} \int_{-\infty}^{\infty} \frac{e^{-y^2}}{y - z} dy, \tag{4.24}$$

which cannot be evaluated analytically. The symmetric Voigt absorption and dispersion lineshapes are associated with the imaginary and real parts of the PDF respectively, and are approximately written as:

$$h_{abs}(\vartheta, a_V) = \frac{a_V}{\sqrt{\pi}} \frac{1}{\vartheta^2 + {a_V}^2} + \frac{a_V}{2\sqrt{\pi}} \frac{3\vartheta^2 - {a_V}^2}{\left(\vartheta^2 + {a_V}^2\right)^3} \tag{4.25}$$

and

$$h_{disp}(\vartheta, a_V) = \frac{-1}{\sqrt{\pi}} \frac{\vartheta}{\vartheta^2 + {a_V}^2} - \frac{1}{2\sqrt{\pi}} \frac{\vartheta\left(\vartheta^2 - 3{a_V}^2\right)}{\left(\vartheta^2 + {a_V}^2\right)^3}, \tag{4.26}$$

where

$$a_V = \frac{\Gamma_L}{\Gamma_G}(\ln 2)^{1/2} \tag{4.27}$$

is the ratio of Lorentzian full width at half maximum (FWHM), Γ_L, to Gaussian FWHM, Γ_G. The parameter ϑ, defined by:

$$\vartheta = \frac{2(\nu - \nu_0)(\ln 2)^{1/2}}{\Gamma_G} \tag{4.28}$$

measures the distance from the centre of the peak. The lineshapes are made asymmetric by adding an asymmetry parameter $e^{b_V \vartheta}$ that has no physical meaning. The asymmetric Voigt lineshapes are written approximately as:

$$h'_{abs}(\vartheta; a_V, b_V) = \frac{a_V}{\sqrt{\pi}} \frac{e^{b_V \vartheta}}{\vartheta^2 + {a_V}^2} + \frac{a_V e^{b_V \vartheta}}{4\sqrt{\pi}} \times \left[\frac{{b_V}^2\left(\vartheta^2 + {a_V}^2\right)^2 - 4b_V\vartheta\left(\vartheta^2 + {a_V}^2\right) + 2\left(3\vartheta^2 - {a_V}^2\right)}{\left(\vartheta^2 + {a_V}^2\right)^3} \right] \tag{4.29}$$

and

$$h'_{disp}(\vartheta; a_V, b_V) = \frac{-1}{\sqrt{\pi}} \frac{\vartheta\cos(a_V b_V) - a_V \sin(a_V b_V)}{\vartheta^2 + {a_V}^2} - \frac{1}{2\sqrt{\pi}} \times \left[\frac{{a_V}^3 \sin(a_V b_V) + \vartheta\left(\vartheta^2 - 3{a_V}^2\right)\cos(a_V b_V) - 3a_V\vartheta^2 \sin(a_V b_V)}{\left(\vartheta^2 + {a_V}^2\right)^3} \right] \tag{4.30}$$

when $a_V >> 1/\sqrt{2}$ and $|b_V| \leq 0.08$. For other values of a_V and b_V, the plasma dispersion function must be evaluated exactly.

4.3.2.3 Comparison of Lineshapes

The Lorentzian, Losev and asymmetric Voigt lineshapes were fitted to the asymmetric CH_3 singlet in the ^1H spectrum of toluene. Both absorption and dispersion peaks were fitted (absorption only for the Losev lineshape) using the subroutine E04FDF from the

NAG Fortran Library. The fit was constrained to pure absorption and dispersion functions by setting the peak phase to 0.

The least-squares fit of the Lorentzian lineshape to the test peak is shown in figure 4.2(a). The residual sum of squares of the fit equals 6.8375×10^{11} for 7210 data points. A good match is seen on the right hand side, leading to an overshoot on the left hand side because the experimental lineshape is not symmetric. The least-squares fit of the Losev absorption lineshape to the test peak is shown in figure 4.2(b). The residual sum of squares of the fit equals 1.0920×10^{11} for 3605 data points. This lineshape shows a perfect fit to the left hand side and most of the right hand side, but the shoulder on the right is too large to be fitted correctly. The least-squares fit of the asymmetric Voigt lineshape to the test peak is shown in figure 4.2(c). The residual sum of squares of the fit equals 1.3764×10^{13} for 7210 data points. This fit is very close to the Lorentzian, but there is an additional mismatch at the top of the peak because the approximate expression for the lineshape is being used. Of the three functions, the Losev lineshape gives the best fit to the test peak. However, none of these lineshapes gave a fit that would give a good estimate of the peak integral, so a better lineshape is still needed.

4.3.3 Analysis of Non-Lorentzian Lineshape

Since none of the existing model lineshapes match the actual non-Lorentzian lineshapes observed in the spectra, a new lineshape must be derived, preferably in the form of an algebraic expression that can be used in the model of the NMR spectrum. The analysis of the non-Lorentzian lineshape presented here is entirely novel and not based on the work of anyone else.

The non-Lorentzian lineshape is caused by the distribution of resonance frequencies in the sample, so it depends on the magnetic field inside the sample, which in turn depends on the external magnetic field and the magnetic susceptibility of the sample. In a homogeneous liquid, the magnetic susceptibility is constant across the sample, so the external magnetic field is the determining factor. The external magnetic field is never perfectly homogeneous, and can be considered as the sum of many smaller homogeneous fields, each with its own resonance frequency. The resulting lineshape is a sum of Lorentzians, with each Lorentzian generated by a homogeneous field region and weighted by the volume of the region giving rise to it. This is expressed

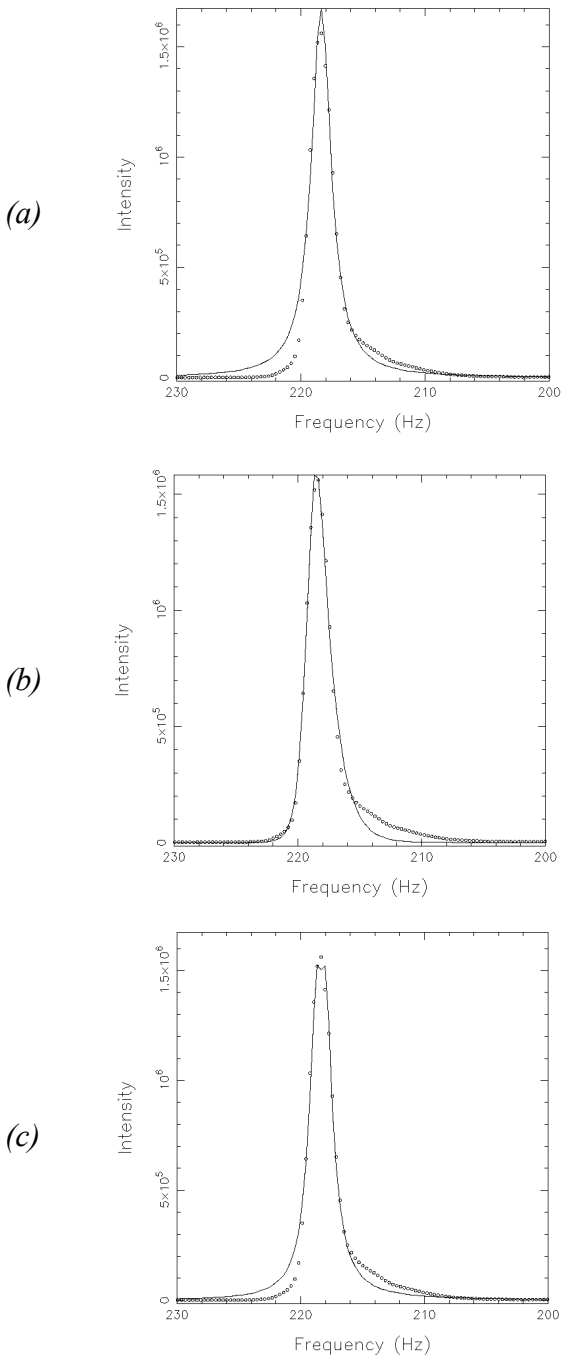

Figure 4.2 Least-squares fits of model lineshapes to a test peak. The circles represent the NMR data and the solid lines represents the lineshapes. *(a)* Lorentzian lineshape with parameters $\nu_0 = 218.364$ Hz, $\lambda = 0.9592$ Hz and $s_k = 1.674\times10^6$, *(b)* Losev lineshape with parameters $A = 1.606\times10^6$, $a_L = 0.8577$ Hz, $b_L = 1.912$ Hz and $c = 218.520$ Hz, *(c)* asymmetric Voigt lineshape with parameters $s_k = 1.500\times10^6$, $\Gamma_L = 1.534$ Hz, $\Gamma_G = 0.8587$ Hz, $b_V = -0.01079$ and $\nu_0 = 218.375$ Hz.

mathematically as a convolution of the Lorentzian function with a resonance frequency distribution function. In order to describe the lineshape accurately, the resonance frequency distribution function is required.

The static magnetic field obeys Laplace's equation, which is written in spherical polar co-ordinates as (Paul and Nasar, 1987):

$$\nabla^2\Phi = \frac{1}{r^2}\frac{\partial}{\partial r}\left(r^2\frac{\partial\Phi}{\partial r}\right)+\frac{1}{r^2\sin\theta}\frac{\partial}{\partial\theta}\left(\sin\theta\frac{\partial\Phi}{\partial\theta}\right)+\frac{1}{r^2\sin^2\theta}\frac{\partial^2\Phi}{\partial\phi^2}=0, \quad (4.31)$$

where Φ is the vector potential that describes the magnetic field, and (r, θ, ϕ) are the spherical polar co-ordinates. The vector potential Φ is a real function that can be expressed mathematically using a series expansion over an orthogonal basis set such as the spherical harmonic functions defined by (Riley *et al.*, 1997):

$$Y_l^m(\theta,\phi)\equiv(-1)^m\sqrt{\frac{2l+1}{4\pi}\frac{(l-m)!}{(l+m)!}}P_l^m(\cos\theta)e^{im\phi}, \quad (4.32)$$

where m = -l,-l+1, ..., 0, ..., l and $P_l^m(\cos\theta)$ is an associated Legendre polynomial. The full solution to Laplace's equation in terms of spherical harmonics is given by:

$$\Phi(r,\theta,\phi)=\sum_{l=0}^{\infty}\sum_{m=0}^{l}a_l^m r^l Y_l^m(\theta,\phi)=\sum_{l=0}^{\infty}\sum_{m=0}^{l}r^l P_l^m(\cos\theta)\left(C_l^m\cos m\phi+S_l^m\sin m\phi\right). \quad (4.33)$$

There are other possible basis sets for describing the magnetic field potential, but the spherical harmonics were chosen by Golay (1958) and others when designing shim coils (Anderson, 1961; Konzbul and Švéda, 1995). Shim coils are electric coils that generate secondary magnetic fields used to improve the overall magnetic field homogeneity by locally counteracting the main field inhomogeneity. Shim coils are designed to generate one spherical harmonic function each, to enable them to be adjusted independently of each other, but practical imperfections make shimming a magnet to high homogeneity rather difficult (Chmurny and Hoult, 1990). The twelve shim coils present on the Bruker MSL 200 and DMX 200 magnets in our laboratory are listed in table 4.2 with their corresponding spherical harmonic functions (Conover, 1984; Gruelter and Boesch, 1992). Incomplete shimming occurred in our laboratory because the equipment was shared between different users, so only a few days could be spent setting up the magnet for each experimental session. For a static magnetic field that is incompletely shimmed, the residual inhomogeneity can also be expressed using spherical harmonics.

Spherical Harmonics $r^l Y_l^m(\theta,\phi)$				
name	*l*	*m*	*Spherical Co-ordinates*	*Cartesian Co-ordinates*
Z	1	0	$r\cos\theta$	z
Z^2	2	0	$r^2\left(3\cos^2\theta-1\right)$	$2z^2-\left(x^2+y^2\right)$
Z^3	3	0	$r^3\left(5\cos^3\theta-3\cos\theta\right)$	$z\left[2z^2-3\left(x^2+y^2\right)\right]$
Z^4	4	0	$r^4\left(35\cos^4\theta-30\cos^2\theta+3\right)$	$8z^2\left[z^2-3\left(x^2+y^2\right)\right]+3\left(x^2+y^2\right)^2$
X	1	1	$r\sin\theta\cos\phi$	x
Y	1	1	$r\sin\theta\sin\phi$	y
XZ	2	1	$r^2\sin\theta\cos\theta\cos\phi$	xz
YZ	2	1	$r^2\sin\theta\cos\theta\sin\phi$	yz
XY	2	2	$r^2\sin^2\theta\sin 2\phi$	xy
X^2-Y^2	2	2	$r^2\sin^2\theta\cos 2\phi$	x^2-y^2
XZ^2	3	1	$r^3\sin\theta\left(5\cos^2\theta-1\right)\cos\theta$	$x\left[4z^2-\left(x^2+y^2\right)\right]$
YZ^2	3	1	$r^3\sin\theta\left(5\cos^2\theta-1\right)\sin\theta$	$y\left[4z^2-\left(x^2+y^2\right)\right]$

Table 4.2 Spherical harmonic functions for the twelve shim coils present on our Bruker MSL 200 and DMX 200 magnets, in spherical polar and Cartesian co-ordinates.

4.3.4 Derivation of Resonance Frequency Distributions

The distribution of resonance frequencies causing the non-Lorentzian lineshape is derived by converting the spatial distribution of resonance frequencies in the inhomogeneous magnetic field into a frequency distribution of resonance frequencies. Just as the total spatial distribution is a weighted sum of spherical harmonics, the total frequency distribution is a weighted sum of the frequency distributions of the spherical harmonics. These spherical harmonic frequency distributions are not available in the literature, so they are derived here by changing the independent variables in the spherical harmonic functions from (x, y, z) to ν.

For the derivation, the sample space is taken as a cylinder of radius a and length $2L$, corresponding to the region inside a radio-frequency coil. The z-axis points along the length of the cylinder, and has its origin in the centre of the sample (figure 4.3). The sample is static within this region. The change of variables is performed by treating x, y, z, and ν as random variables and calculating their probabilities. The normalised probabilities of x, y, z and r (where $r^2 = x^2 + y^2$) in the cylindrical sample are given by:

$$\begin{aligned} f_1(x) &= \frac{2}{\pi a^2}\sqrt{\left(a^2 - x^2\right)} \quad && -a \le x \le a \\ f_1(y) &= \frac{2}{\pi a^2}\sqrt{\left(a^2 - y^2\right)} \quad && -a \le y \le a \\ f_1(z) &= \frac{1}{2L} && -L \le z \le L \\ f_1(r) &= \frac{2r}{a^2} && 0 \le r \le a \end{aligned} \quad . \tag{4.34}$$

Each spherical harmonic function is treated as a definition of ν in terms of x, y, z and r, from which the probability of ν can be calculated. The probability of a function of one random variable is calculated by inverting the function and applying the transformation law of probabilities given by (Port, 1994):

$$\begin{aligned} Y &= \Phi(X) \\ f_2(Y) &= f_1\left(\Phi^{-1}(Y)\right)\left|\frac{\partial}{\partial Y}\left(\Phi^{-1}(Y)\right)\right| \end{aligned} \quad . \tag{4.35}$$

This transformation law always holds, but its usefulness is limited in practice to the functions $\Phi(X)$ that can be inverted to yield $\Phi^{-1}(Y)$. For the sum of two independent random variables, $Z=X+Y$, the probability of Z is conditional on the probabilities of both X and Y, and is calculated from (Pugachev, 1984):

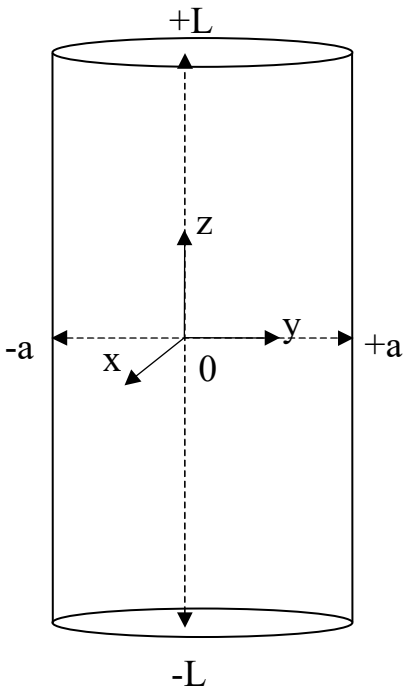

Figure 4.3 Definition of Cartesian axes for cylindrical sample used in simulation of spherical harmonic functions.

$$f_2(Z) = \int_{-\infty}^{\infty} f_1(X) f_1(Z - X) dX \,, \tag{4.36}$$

which is the convolution integral of $f_1(X)$ and $f_1(Y)$. The convolution integral can be evaluated using Fourier transforms: the convolution of two functions equals the inverse Fourier transform of the product of their Fourier transforms (Springer, 1979). For the product of two independent random variables, $Z=XY$, the conditional probability of Z is calculated from a similar integral (Port, 1984):

$$f_2(Z) = \int_{-\infty}^{\infty} f_1(X) f_1\left(\frac{Z}{X}\right) \cdot \frac{1}{X} dX \,, \tag{4.37}$$

which can be evaluated using Mellin transforms (Springer, 1979).

In principle, the frequency distribution of each spherical harmonic function can be derived using equations (4.34) to (4.37). In practice, it was only possible to derive analytically the frequency distributions for the Z^2 and XZ/YZ functions. The distributions for the Z^3 and XZ^2/YZ^2 functions could not be derived because the functions could not be factored into a sum or product of independent variables. The functions Z^4, XY and X^2-Y^2 could be inverted to give convolution integrals, but these integrals could not be evaluated analytically. The derivation of the frequency distribution for the Z^2 function is as follows:

Two independent variables were defined as $x = 2z^2$ and $y = -r^2$ in order to rewrite the Z^2 function $\nu = 2z^2 - r^2$ as $\nu = x + y$. Using equations (4.34) and (4.35), the probability density functions for x and y were given by:

$$f_1(x) = \frac{1}{4L\sqrt{x}} \quad 0 \le x \le 2L^2 \tag{4.38}$$

and

$$f_1(y) = \frac{1}{a^2} \quad -a^2 \le y \le 0 \,. \tag{4.39}$$

Using equation (4.36), the probability density function for ν was given by:

$$f_2(\nu) = \int \frac{dy}{4a^2 L\sqrt{\nu - y}} \,. \tag{4.40}$$

The integration limits had to be considered carefully. Since the variable of integration was y, the limits were determined by the range of values of x. This gave three integration ranges for equation (4.40):

$$\begin{array}{lll} x \geq 0 \quad \rightarrow & -a^2 \leq y \leq \nu & -a^2 \leq \nu \leq 0 \\ & -a^2 \leq y \leq 0 & 0 \leq \nu \leq 2L^2 - a^2 \\ x \leq 2L^2 \quad \rightarrow & \nu - 2L^2 \leq y \leq 0 & 2L^2 - a^2 \leq \nu \leq 2L^2 \end{array} . \qquad (4.41)$$

Substituting these limits into the integral gave the following probability density function for ν:

$$\begin{aligned} f_2(\nu) &= \frac{1}{2a^2 L}\sqrt{\nu + a^2} && -a^2 \leq \nu \leq 0 \\ f_2(\nu) &= \frac{1}{2a^2 L}\left[\sqrt{\nu + a^2} - \sqrt{\nu}\right] && 0 \leq \nu \leq 2L^2 - a^2 \\ f_2(\nu) &= \frac{1}{2a^2 L}\left[\sqrt{2L^2} - \sqrt{\nu}\right] && 2L^2 - a^2 \leq \nu \leq 2L^2 \end{aligned} . \qquad (4.42)$$

This function is shown graphically in figure 4.4(a). A similar derivation for the XZ/YZ function, using *x*/*y* and *z* as the independent variables, gave the following probability density function for ν:

$$f_2(\nu) = \frac{1}{\pi a^2 L}\left[-\sqrt{a^2 - \left(\frac{\nu}{L}\right)^2} + a \ln\left|\frac{\sqrt{(aL)^2 - \nu^2} + aL}{\nu}\right|\right] \qquad -aL \leq \nu \leq aL , \qquad (4.43)$$

which is shown in figure 4.4(b). Approximate expressions were obtained for the distributions of the Z^3 and Z^4 spherical harmonics by considering only the first term of each function, which is a simple power of *z*. These expressions are given by:

Z^3
$$f_2(\nu) \approx \frac{1}{6L\nu^{2/3}} , \qquad (4.44)$$

Z^4
$$f_2(\nu) \approx \frac{1}{4L\nu^{3/4}} . \qquad (4.45)$$

By analogy with the distribution for XZ, the distribution for XY was approximated by:

$$f_2(\nu) \approx \ln\left|\frac{\sqrt{a^2 - (2\nu)^2} + a^2}{2\nu}\right| . \qquad (4.46)$$

which is shown in figure 4.4(c).

Since analytical expressions could not be obtained for all the resonance frequency distributions, the distributions were simulated numerically and approximated using Chebyshev polynomials.

(a)

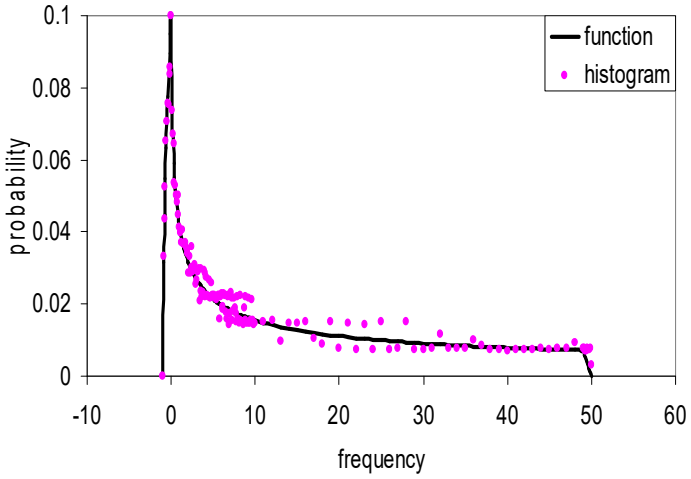

(b)

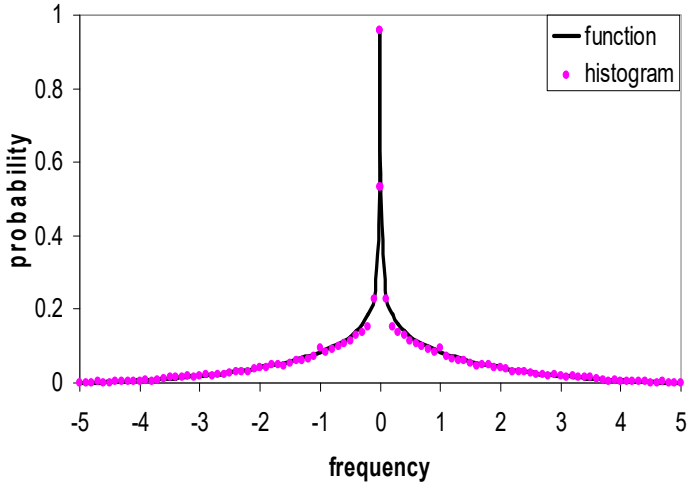

(c)

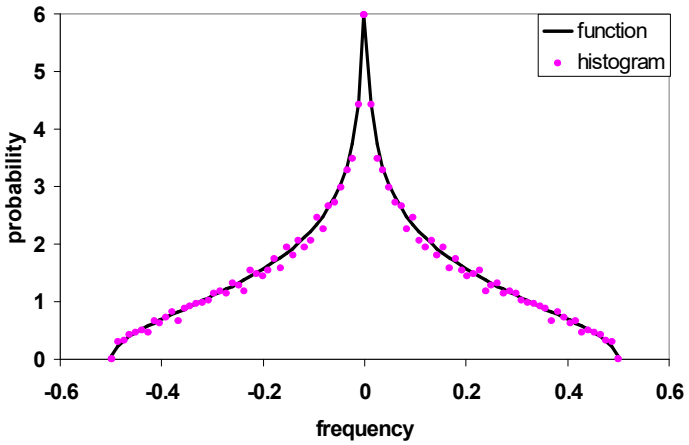

Figure 4.4 Plots of resonance frequency distributions for spherical harmonic functions, generated analytically (function) and numerically (histogram) *(a)* Z^2 (equation 4.42), *(b)* XZ/YZ (equation 4.43), *(c)* XY (equation 4.46).

4.3.5 Numerical Simulations

4.3.5.1 Resonance Frequency Distributions

Three-dimensional arrays were defined to simulate a cylindrical sample with (101, 101, 201) elements in the (x, y, z) directions. Setting $a = 1$ and $L = 5$ gave a resolution of 0.02 in the x and y directions and 0.05 in the z direction. The values of the spherical harmonic functions were calculated for each (x, y, z) co-ordinate in the cylinder and stored in the arrays. The resonance frequency distributions were approximated by calculating histograms of the frequency values in the arrays. The histograms of the spherical harmonic functions are shown in figure 4.5. The ripples in the histograms were due to the finite resolution of the array. The histograms had a single maximum at $\nu = 0$, except that for Z which was flat, and dropped off to zero at the limits of the sample. The histograms for X and Y, XZ and YZ, XZ^2 and YZ^2 were identical by symmetry. The limits of the distributions and the positions in the sample at which they occurred are listed in table 4.3. The histograms matched the analytical frequency distributions (figure 4.4).

4.3.5.2 Lineshapes

Each spherical harmonic function gives a characteristic lineshape that is the convolution of the resonance frequency distribution with a Lorentzian function. The lineshape was obtained by Fourier transforming a simulated FID consisting of a sum of sinusoids with the frequencies in the cylindrical sample array multiplied by an exponentially decaying function (Conover, 1998). The array used in the simulation contained (21, 21, 101) elements in the (x, y, z) directions for a cylinder with $a = 1$ and $L = 5$. The simulated FID contained 1024 points spaced at 0.1 (arbitrary units) for a spectral width of 50. The exponential decay constant gave a Lorentzian linewidth (FWHM) of 2.0, except for Z^2 and Z^4 which had linewidths of 1.0 and 0.2 respectively to avoid aliasing. The weighting of the spherical harmonic function relative to the Lorentzian was 10.0, except for Z^2 and Z^4 which were weighted by 5.0 and 0.05 respectively. The simulated lineshapes are shown in figure 4.6 to match the frequency distributions in figure 4.5. The lineshapes were symmetric about zero frequency, except for Z^2 and Z^4. These lineshapes were simulated with positive weightings; for negative weightings the lineshapes were mirrored (results not shown). The ripples in the lineshapes were due to the finite resolution of the array.

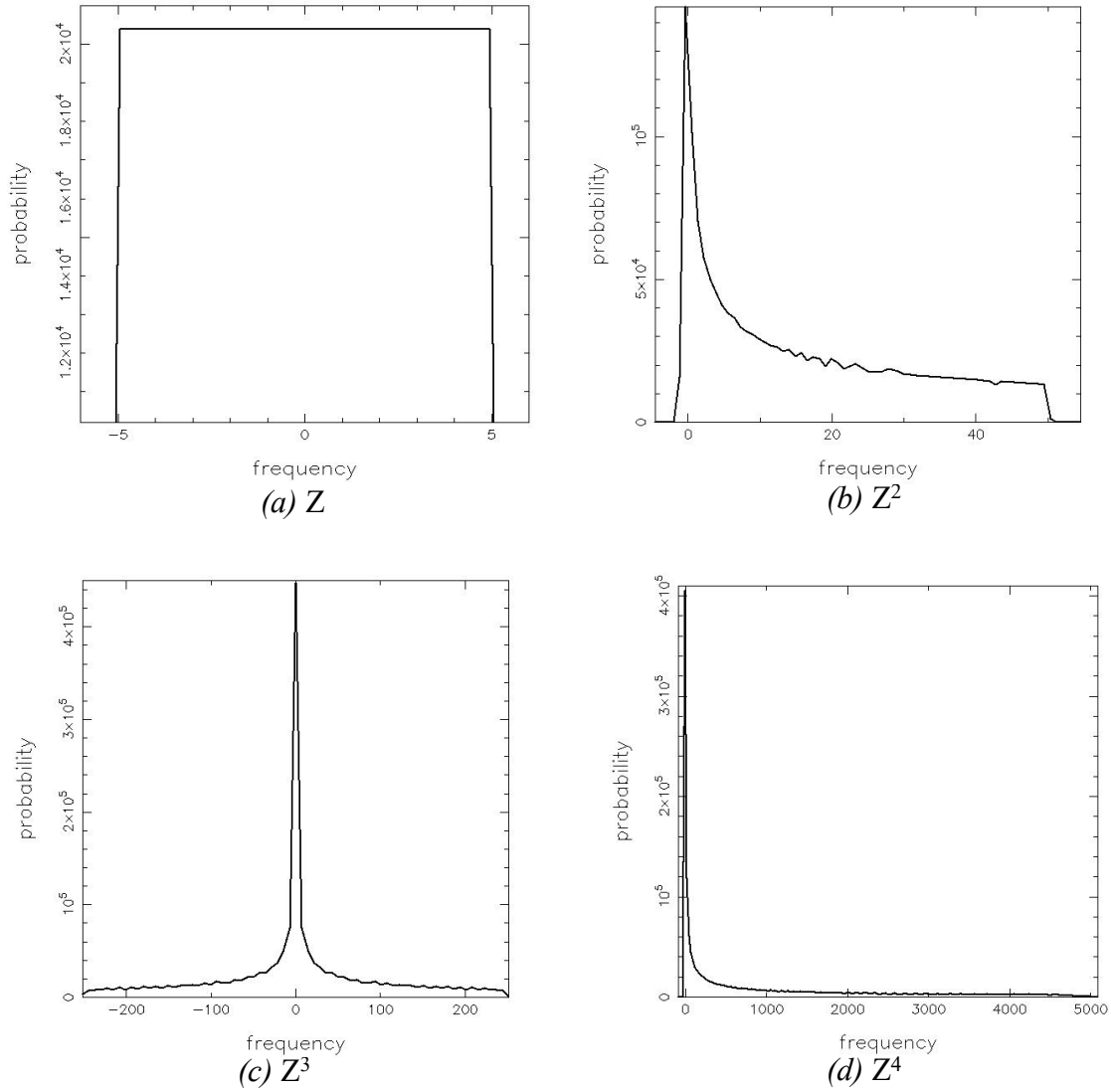

Figure 4.5 Histograms of resonance frequencies in a cylindrical sample with a = 1 and L = 5, simulated numerically for spherical harmonic functions *(a)* Z, *(b)* Z^2, *(c)* Z^3, *(d)* Z^4.

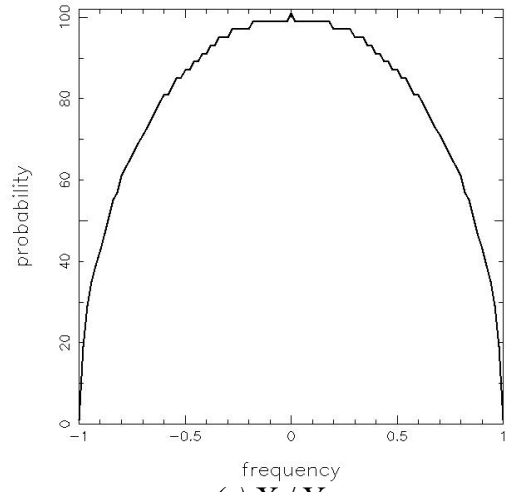

(e) X / Y

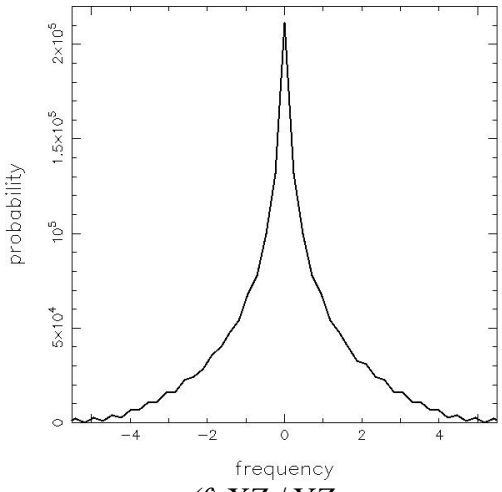

(f) XZ / YZ

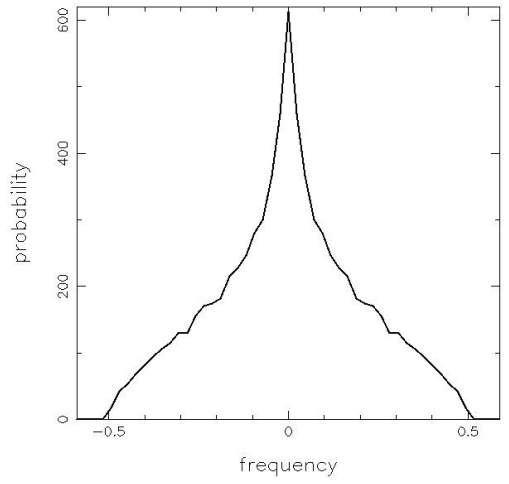

(g) XY

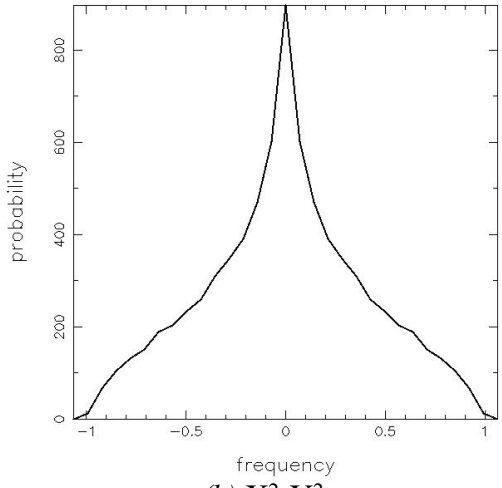

(h) X^2-Y^2

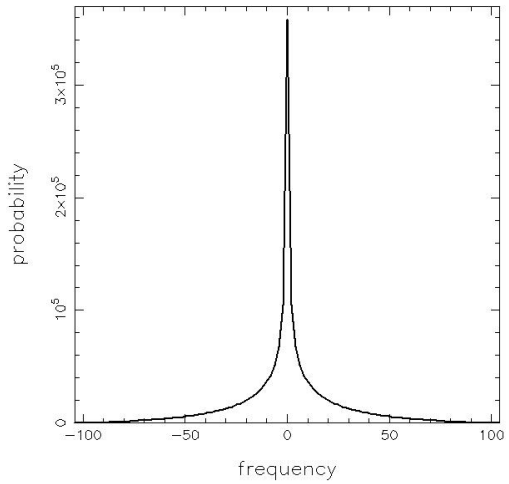

(i) XZ^2 / YZ^2

Figure 4.5 Histograms of resonance frequencies in a cylindrical sample with a = 1 and L = 5, simulated numerically for spherical harmonic functions *(e)* X / Y, *(f)* XZ / YZ, *(g)* XY, *(h)* X^2-Y^2, *(i)* XZ^2 / YZ^2.

shim	minimum	min. at	maximum	max. at
Z	$-L$	$z = -L$	L	$z = L$
Z^2	$-a^2$	$z = 0, r = a$	$2L^2$	$z = L, r = 0$
Z^3	$-2L^3$	$z = -L, r = 0$	$2L^3$	$z = L, r = 0$
Z^4	$-15a^4$	$z = \sqrt{3/2}a, r = a$	$8L^4$	$z = L, r = 0$
X	$-a$	$x = -a$	a	$x = a$
Y	$-a$	$y = -a$	a	$y = a$
XZ	$-aL$	$x = -a, z = L$ $x = a, z = -L$	aL	$x = a, z = L$ $x = -a, z = -L$
YZ	$-aL$	$y = -a, z = L$ $y = a, z = -L$	aL	$y = a, z = L$ $y = -a, z = -L$
XY	$-a^2/2$	$x = -a/\sqrt{2}, y = a/\sqrt{2}$ $x = a/\sqrt{2}, y = -a/\sqrt{2}$	$a^2/2$	$x = a/\sqrt{2}, y = a/\sqrt{2}$ $x = -a/\sqrt{2}, y = -a/\sqrt{2}$
X^2-Y^2	$-a^2$	$x = 0, y = a$	a^2	$x = a, y = 0$
XZ^2	$-4aL^2+a^3$	$x = -a, y = 0, z = \pm L$	$4aL^2-a^3$	$x = a, y = 0, z = \pm L$
YZ^2	$-4aL^2+a^3$	$x = 0, y = -a, z = \pm L$	$4aL^2-a^3$	$x = 0, y = a, z = \pm L$

Table 4.3 Limits of frequency distributions for spherical harmonic functions in a cylindrical sample of radius a and length $2L$.

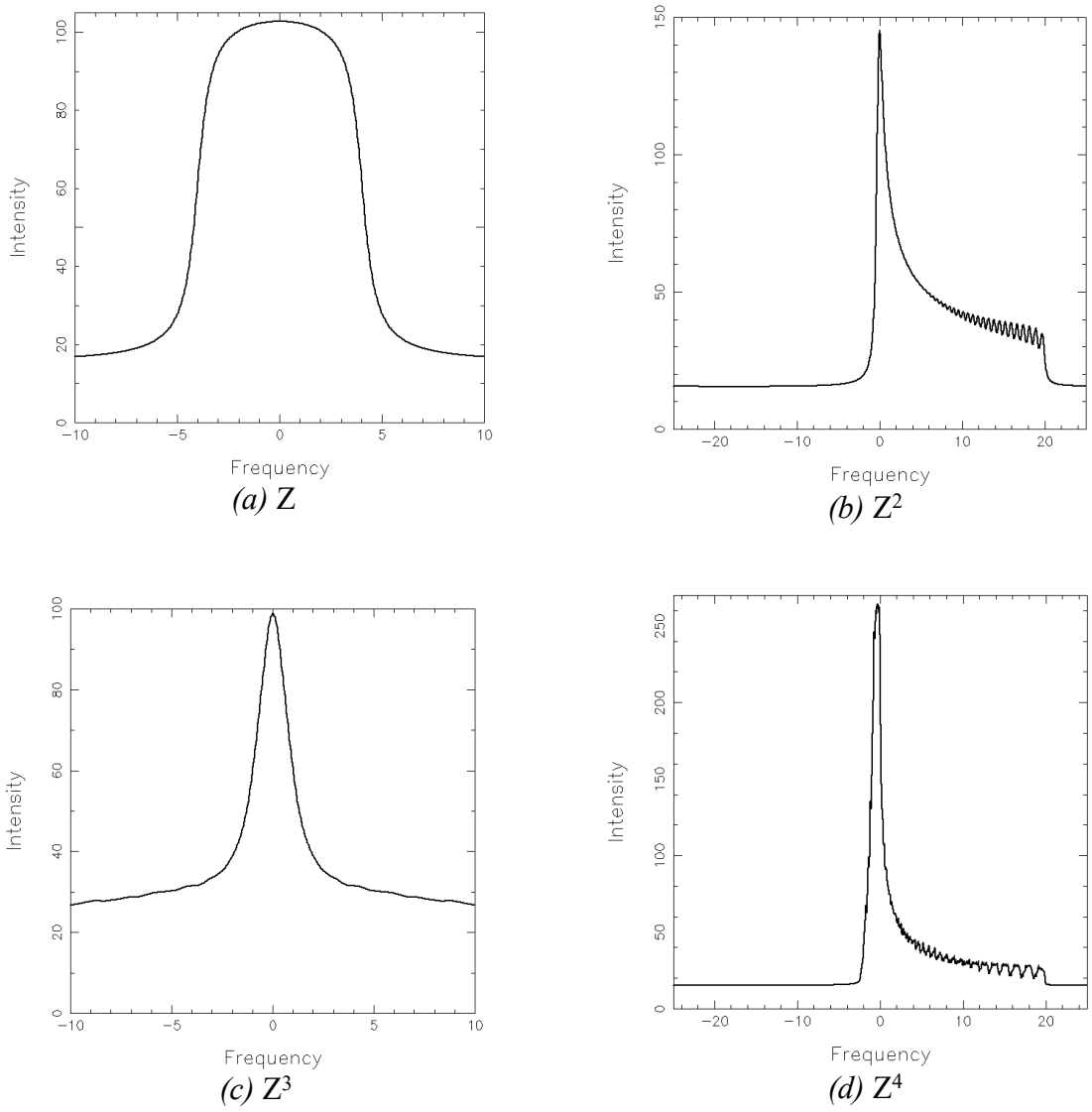

Figure 4.6 Lineshapes resulting from distribution of resonance frequencies in a cylindrical sample with a = 1 and L = 5, simulated numerically for spherical harmonic functions *(a)* Z, *(b)* Z^2, *(c)* Z^3, *(d)* Z^4.

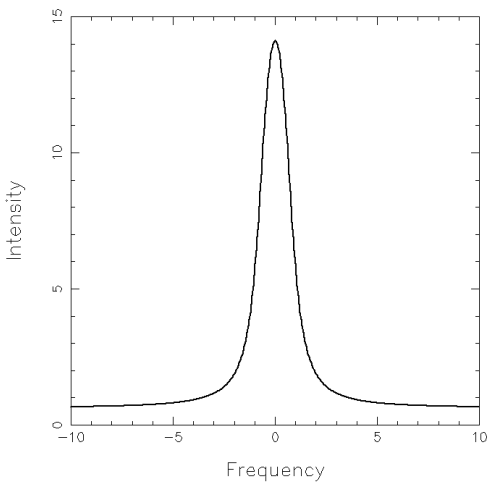

(e) X / Y

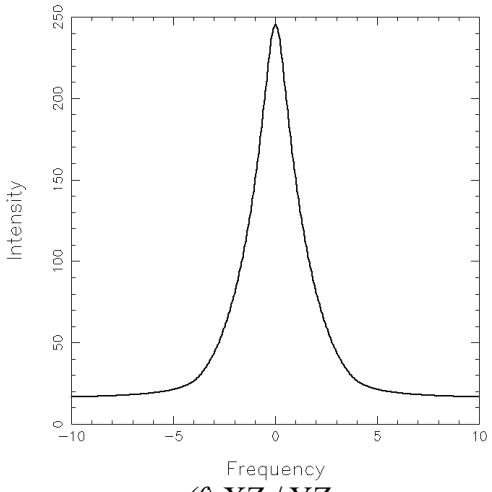

(f) XZ / YZ

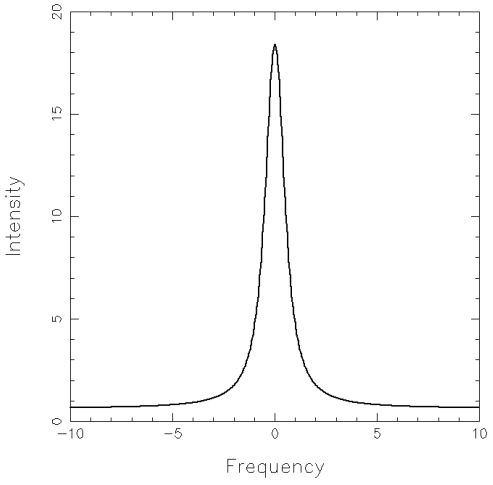

(g) XY

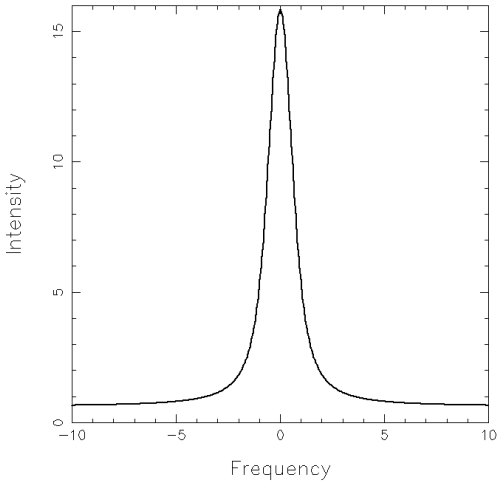

(h) X^2-Y^2

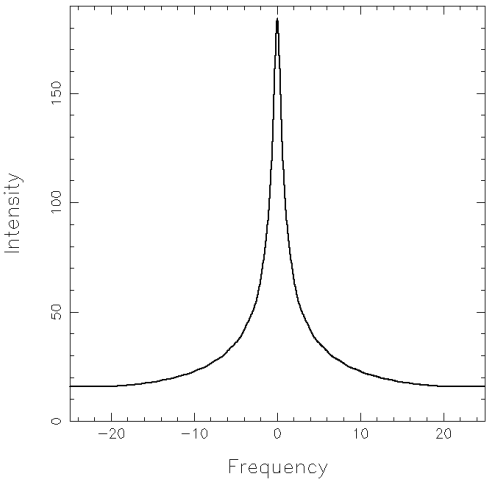

(i) XZ^2 / YZ^2

Figure 4.6 Lineshapes resulting from distribution of resonance frequencies in a cylindrical sample with a = 1 and L = 5, simulated numerically for spherical harmonic functions *(e)* X / Y, *(f)* XZ / YZ, *(g)* XY, *(h)* X^2-Y^2, *(i)* XZ^2 / YZ^2.

4.3.6 Chebyshev Polynomial Approximations

The resonance frequency distributions of the spherical harmonic functions were approximated by a Chebyshev series fit to the frequency histograms. A Chebyshev series has the form:

$$f(x) = \frac{1}{2}a_0 T_0(x) + a_1 T_1(x) + a_2 T_2(x) + \ldots + a_p T_p(x), \tag{4.47}$$

where $T_i(x)$ is the Chebyshev polynomial of the first kind of degree i (NAG, 1997). The Chebyshev polynomials are defined by:

$$T_i(x) = \cos(i \arccos(x)), \tag{4.48}$$

and are orthogonal over the interval [-1, 1] (Kreyszig, 1988). The Chebyshev polynomial fit to the histograms was performed using the subroutine E02ADF from the NAG Fortran Library Mark 17. The histograms were smoothed to remove the ripples caused by the simulation. Since the histograms were symmetric (except Z^2 and Z^4, see below), only the negative half of each histogram was used in the fit. The frequency range of the histogram was normalised to [-1, 1] as follows:

1. The frequency variable ν: [ν_{min}, ν_{max}] was normalised to a variable x: [-100, 0] with a fixed range by the transformation given by:

$$x = \frac{\nu - \nu_{max}}{\nu_{max} - \nu_{min}} \times 100. \tag{4.49}$$

2. The data points were required in non-decreasing order, so the variable x: [-100, 0] was transformed to y: [101^{-1}, 1] using:

$$y = \frac{1}{1 + |x|}. \tag{4.50}$$

3. The subroutine E02ADF normalised the variable y: [101^{-1}, 1] to z: [-1, 1] using the transformation given by:

$$z = \frac{(y - y_{min}) - (y_{max} - y)}{y_{max} - y_{min}}. \tag{4.51}$$

The purpose of the transformation $\nu \rightarrow y$ was to make the independent variable similar to the shape of the distribution. Without it the Chebyshev polynomial approximation was very poor. After the transformation, good fits were obtained with Chebyshev polynomial series of order 8 for Z^3 and XZ/YZ, order 9 for XY, order 11

for X^2-Y^2 and order 5 for XZ^2/YZ^2. The distributions for X/Y and Z did not need fitting.

The asymmetric histograms of Z^2 and Z^4 were divided into positive and negative halves and each half was smoothed and approximated by a separate Chebyshev polynomial series. The frequency range was normalised to x: [1, 1001] for the positive halves and to x: [-101, -1] for the negative halves. The transformation of x to y was given by:

$$y = |x|^{-m}, \tag{4.52}$$

where $m = ½$ for Z^2 and $m = ¾$ for Z^4. Good fits were obtained with Chebyshev polynomial series of order 5 for the positive half of Z^2 and both halves of Z^4, and order 11 for the negative half of Z^2. The Chebyshev polynomial coefficients for all the fits are listed in table 4.4. The fits are shown in figure 4.7.

4.3.7 Lineshape Fitting

4.3.7.1 Experimental

A model lineshape with appropriate parameters for the width and height of the resonance frequency distributions could give a very accurate representation of the experimental lineshapes, and allow the model in equation (4.17) to give accurate composition information. Since all the peaks in the spectra had the same lineshape, the lineshape parameters for one peak could be used for all peaks in the spectrum. To obtain these parameters, a model lineshape was fitted to the asymmetric CH_3 singlet in the ^1H spectrum of toluene using the subroutine E04FDF from the NAG Fortran Library. The lineshape was obtained numerically from the convolution of a Lorentzian function with the Chebyshev series for the spherical harmonic frequency distributions. By the convolution theorem, convolution in one Fourier domain corresponds to multiplication in the other domain. Thus the convolution of the Lorentzian and Chebyshev frequency-domain functions was obtained by inverse Fourier transforming both functions into the time domain, multiplying the two time-domain functions and Fourier transforming the product back into the frequency domain.

Since the experimental lineshapes were asymmetric, the Lorentzian function was convolved with the Chebyshev functions of the asymmetric Z^2 and Z^4 distributions

coefficient	Z^2 (negative)	Z^2 (positive)	Z^3	Z^4 (negative)	Z^4 (positive)
a_0	-4.034e+06	8.079e+04	2.184e+05	1.110e+05	4.982e+04
a_1	-3.641e+06	3.768e+04	1.675e+05	4.810e+04	3.764e+04
a_2	-2.282e+06	7.891e+03	7.583e+04	-6.008e+03	2.089e+04
a_3	-4.982e+05	9.673e+03	-8.200e+02	-1.728e+03	1.144e+04
a_4	1.008e+06	3.423e+03	-4.497e+04	1.267e+03	4.255e+03
a_5	1.917e+06	9.460e+02	-4.942e+04	2.939e+03	8.710e+02
a_6	2.062e+06		-3.221e+04		
a_7	1.687e+06		-1.319e+04		
a_8	1.077e+06		-2.895e+03		
a_9	5.430e+05				
a_{10}	1.956e+05				
a_{11}	4.391e+04				

coefficient	XY	XZ / YZ	$X^2 - Y^2$	XZ^2 / YZ^2
a_0	-3.449e+08	6.026e+04	-4.847e+11	1.755e+05
a_1	-2.559e+08	3.371e+04	-3.780e+11	1.026e+05
a_2	-5.816e+07	1.104e+04	-1.299e+11	2.496e+04
a_3	1.091e+08	4.087e+03	1.062e+11	1.053e+04
a_4	1.634e+08	-7.763e+03	2.196e+11	2.827e+03
a_5	1.253e+08	-1.106e+04	2.057e+11	2.541e+03
a_6	6.294e+07	-1.086e+04	1.312e+11	
a_7	2.103e+07	-5.608e+03	6.103e+10	
a_8	4.315e+06	-1.806e+03	2.069e+10	
a_9	4.164e+05		4.900e+09	
a_{10}			7.303e+08	
a_{11}			5.188e+07	

Table 4.4 Coefficients for Chebyshev polynomial fits to histograms of resonance frequencies shown in figure 4.7.

(a) Z^2

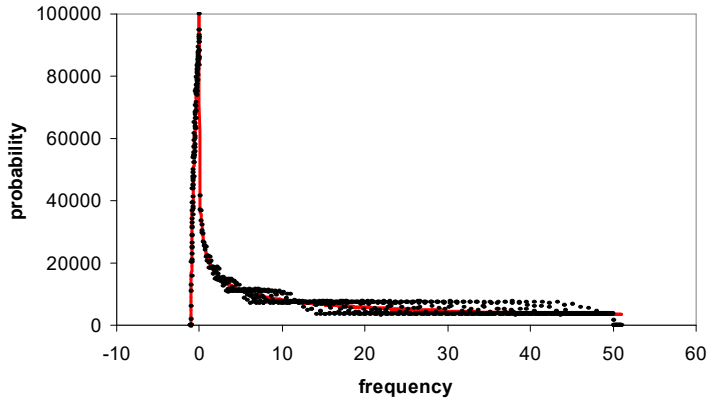

(c) Z^3

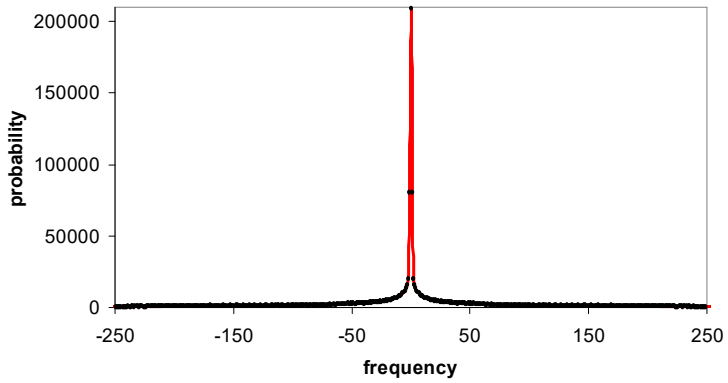

(b) Z^4

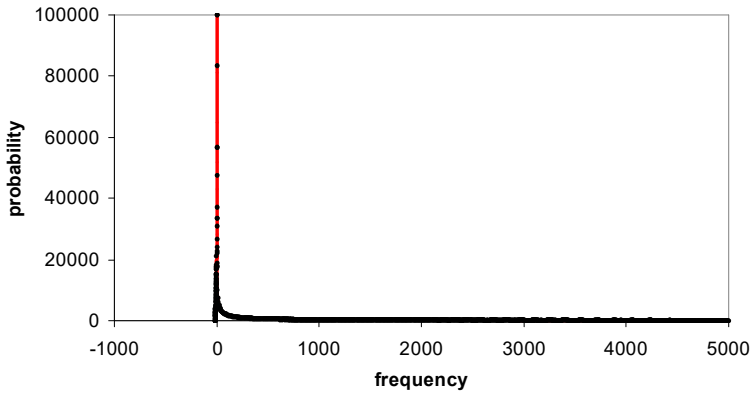

Figure 4.7 Chebyshev polynomial fits to histograms of resonance frequencies for spherical harmonic functions *(a)* Z^2, *(b)* Z^3, *(c)* Z^4. The histograms are represented by dots and the Chebyshev fits by solid lines.

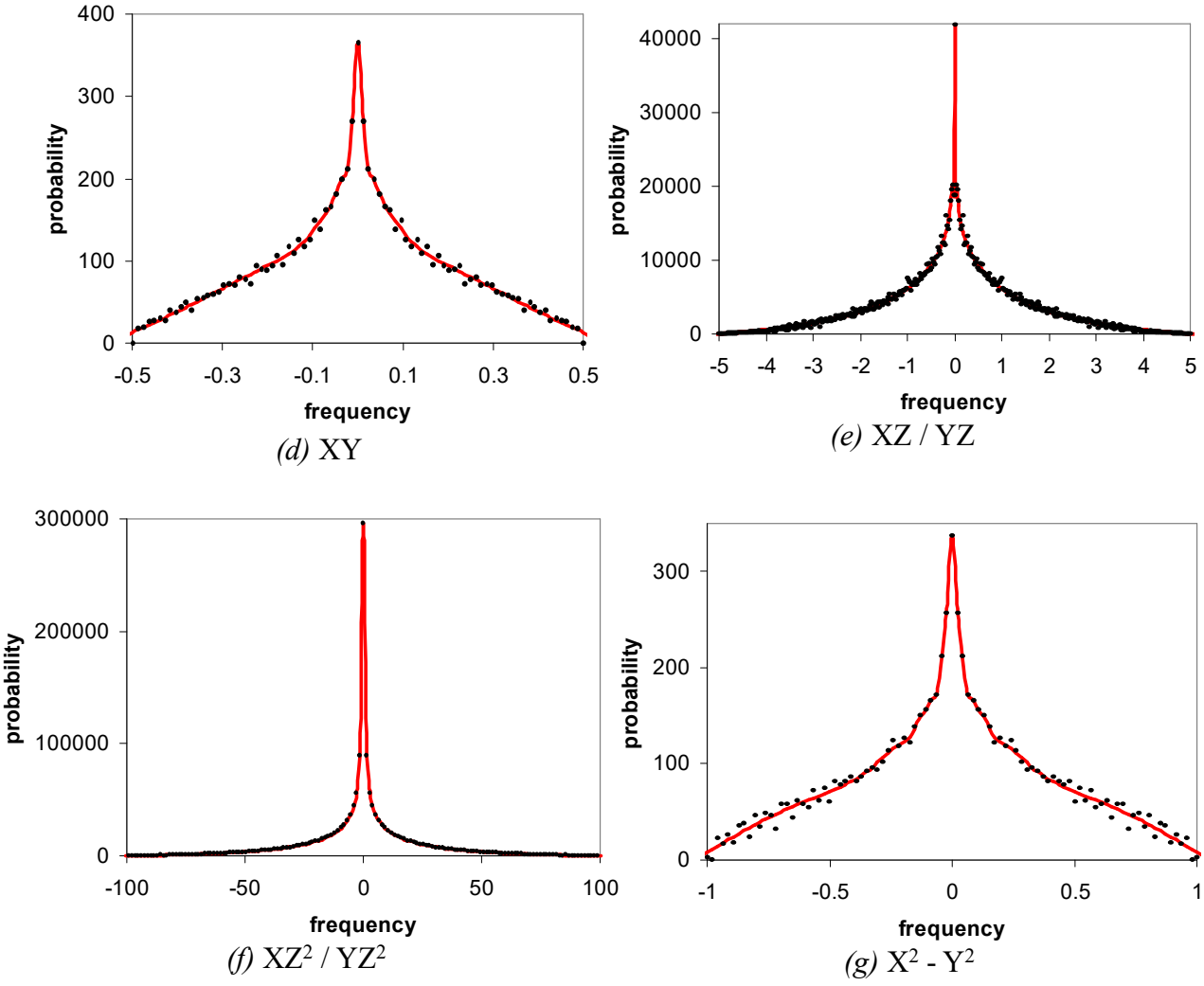

(d) XY *(e)* XZ / YZ

(f) XZ^2 / YZ^2 *(g)* X^2 - Y^2

Figure 4.7 Chebyshev polynomial fits to histograms of resonance frequencies for spherical harmonic functions *(d)* XY, *(e)* XZ / YZ, *(f)* XZ^2 / YZ^2, *(g)* X^2 - Y^2. The histograms are represented by dots and the Chebyshev fits by solid lines.

only. The symmetric distributions were not expected to improve the fit to the experimental lineshapes and were excluded to reduce the amount of computation. The model lineshape had ten parameters: four for the Lorentzian component – height h, centre ν_0, width λ, phase ϕ – and three for each frequency distribution – negative frequency range x, positive frequency range y, and height s – that determined the width and height of the shoulders either side of the central peak. The fit was constrained to pure absorption and dispersion functions by setting the peak phase to 0.

4.3.7.2 Results and Discussion

The best fit of the model lineshape with only Z^2 and Z^4 distributions did not match the test lineshape regardless of the parameters used (figure 4.8(a)), so the Z and Z^3 frequency distributions were added to the model. Manual scaling of the parameters showed that the model lineshape now qualitatively matched the test peak (figure 4.8(b)), but E04FDF could not fit test peak, despite repeatedly changing the scaling of the parameters and fitting the Lorentzian and Chebyshev functions separately. The model lineshape was very sensitive to changes in the Lorentzian parameters but relatively insensitive to changes in the Chebyshev parameters. The model lineshape is a convolution product, so any particular shape can be described by many different sets of parameters, just as the number 24 can be obtained from the multiplication products 2×12, 3×8, and 4×6. The least-squares fit could not converge to a global minimum because there were too many local minima in the parameter space. Therefore, fitting the model lineshape requires a more sophisticated fitting algorithm and more programming skill and effort than was available.

Additional work is also required to translate the final lineshape into a template for use with the spectral model since there is no analytical function to describe it. This requires a method to scale the lineshape in both height and width. Height scaling is easily performed by multiplication with a scaling factor, but width scaling would require some form of resampling or interpolation. An alternative would be to fit the entire lineshape with a new set of Chebyshev polynomials, since width scaling of Chebyshev polynomials is possible and was used in the lineshape fit.

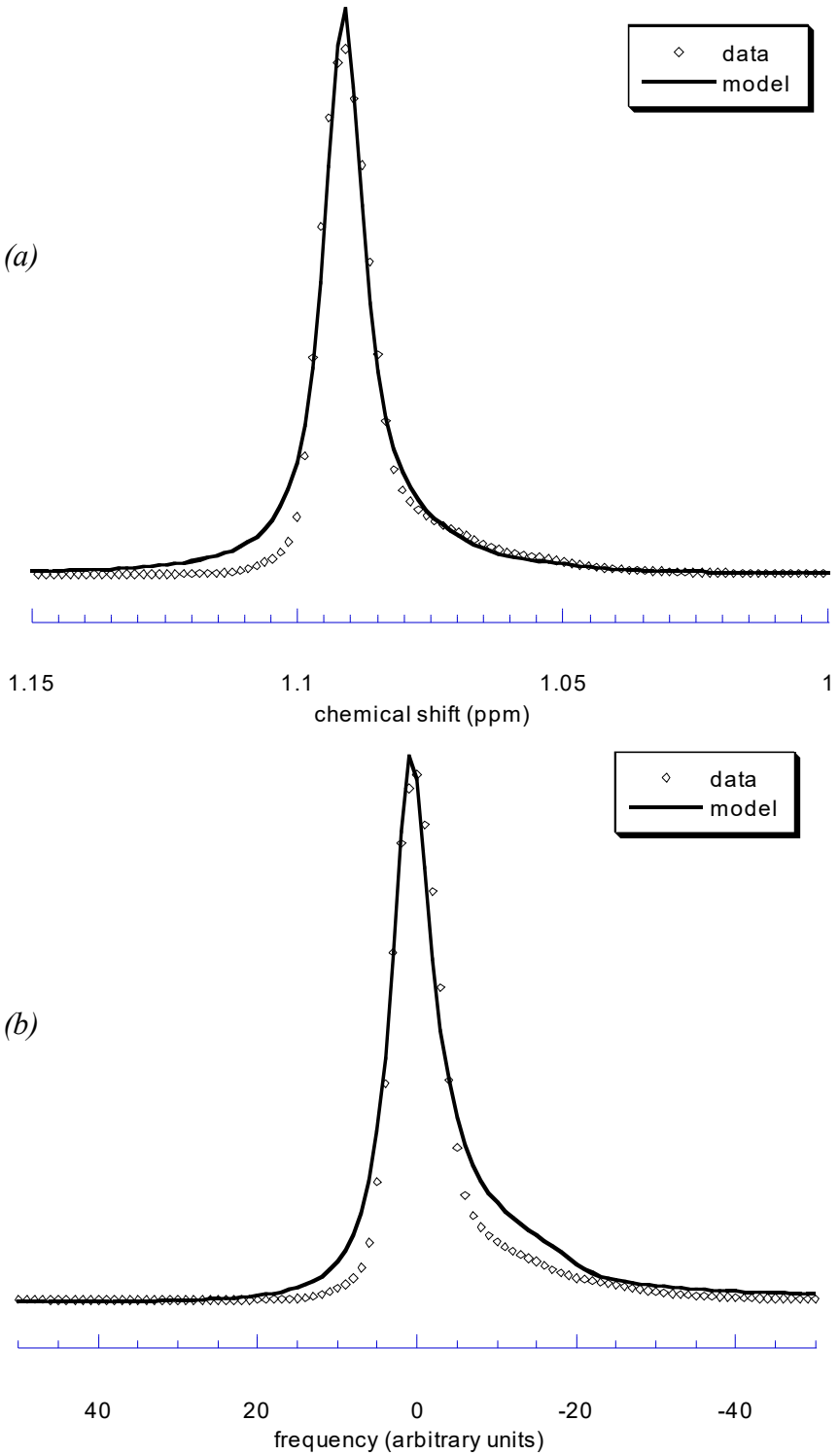

Figure 4.8 Fitting of new model lineshape to toluene CH_3 test peak. *(a)* Best fit by E04FDF of model with Z^2 and Z^4 distributions, $h = 1.004$, $\nu_0 = 219.115$ Hz, $\lambda = 0.8605$ Hz, $\phi = 0$, $x_2 = 2$, $y_2 = 30$, $s_2 = 1.055\times10^{-6}$, $x_4 = 2$, $y_4 = 16$, $s_4 = 1.009\times10^{-5}$. *(b)* Qualitative manual fit of model with Z, Z^2, Z^3 and Z^4 distributions, $h = 1.8\times10^{-3}$, $\nu_0 = 0.0$, $\lambda = 3.0$, $\phi = 0$, $x_1 = 2$, $s_1 = 0.70$, $x_2 = 2$, $y_2 = 20$, $s_2 = 0.80$, $x_3 = 2$, $s_3 = 0.70$, $x_4 = 2$, $y_4 = 10$, $s_4 = 1.0$.

4.4 Conclusion

A new mathematical model was derived to describe the spectrum of a liquid mixture as a weighted sum of pure-component spectra. The model used a series of peak patterns instead of individual peaks to ensure that the parameters of the fit were meaningful. Fitting the model using Lorentzian lineshapes gave inaccurate composition results (±5.46 mol%) because the experimental lineshapes were non-Lorentzian. A more suitable model lineshape was expected to improve the fit and give more accurate composition results.

Converting the experimental lineshapes to Lorentzian peaks using reference deconvolution was unsuccessful, and existing asymmetric model lineshapes did not match the experimental lineshapes. Consequently, a new model lineshape was developed based on the distribution of resonance frequencies in an inhomogeneous magnetic field. The mathematical derivation was analytically intractable in many cases, so the frequency distributions and resulting lineshapes were simulated numerically and approximated by Chebyshev series. The new model lineshape was a convolution of a Lorentzian function with the Chebyshev series, and was shown to be qualitatively similar to the experimental lineshape. A least-squares fit of the model lineshape to a test peak failed to converge, so it could not be used in the model of the spectrum. To fit the lineshape requires more sophisticated algorithms, or rewriting the model using a smaller number of independent variables to make it mathematically better-behaved. Further development of the model lineshape includes considering the effects of spinning and flow, which cause averaging of the magnetic field homogeneity in the radial and axial directions respectively.

4.5 References

Abildgaard, F., Gesmar, H., & Led, J.J. (1988). Quantitative analysis of complicated Fourier transform NMR spectra. *Journal of Magnetic Resonance, 79*, 78-89.

Anderson, W.A. (1961). Electrical current shims for correcting magnetic fields. *The Review of Scientific Instruments, 32*, 241-250

Barjat, H., Morris, G.A., Swanson, A.G., Smart, S., & Williams, S.C.R. (1995). Reference deconvolution using multiplet reference signals. *Journal of Magnetic Resonance, Series A, 116*, 206-214.

Barkhuijsen, H., Beer, R. de, Bovée, W.M.M.J., & Ormondt, D. van (1985). Retrieval of frequencies, amplitudes, damping factors, and phases from time-domain signals using a linear least-squares procedure. *Journal of Magnetic Resonance, 61*, 465-481.

Beer, R. de, & Ormondt, D. van (1992). Analysis of NMR data using time domain fitting procedures. *NMR Basic Principles and Progress, 26*, 201-248.

Boogaart, A. van den, Alakorpela, M., Jokisaari, J., & Griffiths, J.R. (1994). Time and frequency domain analysis of NMR data compared: an application to 1D ^{1}H spectra of lipoproteins. *Magnetic Resonance in Medicine, 31*, 347-358.

Bracewell, R.N. (1978). *The Fourier Transform and its Applications, second edition*, pp. 77-79, 98, 267. McGraw-Hill International Book Company, Singapore.

Bretthorst, G.L. (1990a). Bayesian analysis. I. Parameter estimation using quadrature NMR models. *Journal of Magnetic Resonance, 88*, 533-551.

Bretthorst, G.L. (1990b). Bayesian analysis. III. Applications to NMR signal detection, model selection, and parameter estimation. *Journal of Magnetic Resonance, 88*, 571-595.

Bretthorst, G.L. (1991). Bayesian analysis. IV. Noise and computing time considerations. *Journal of Magnetic Resonance, 93*, 369-394.

Bretthorst, G.L. (1992). Bayesian analysis. V. Amplitude estimation for multiple well-separated sinusoids. *Journal of Magnetic Resonance, 98*, 501-523.

Chmurny, G.N., & Hoult, D.I. (1990). The ancient and honourable art of shimming. *Concepts in Magnetic Resonance, 2*, 131-149.

Conover, W.W. (1984). Practical guide to shimming superconducting NMR magnets. *Topics in Carbon-13 NMR Spectroscopy, 4*, 37-51.

Conover, W.W. (1998). Private communication following from description of simulation on web page: http://www.acornnmr.com/Sam/samprog.htm

Foley, J.P. (1987). Systematic errors in the measurement of peak area and peak height for overlapping peaks. *Journal of Chromatography, 384*, 301-313.

Gesmar, H., Led, J.J., & Abildgaard, F. (1990). Improved methods for quantitative spectral analysis of NMR data. *Progress in Nuclear Magnetic Resonance Spectroscopy, 22*, 255-288.

Gibbs, A., & Morris, G.A. (1991). Reference deconvolution. Elimination of distortions arising from reference line truncation. *Journal of Magnetic Resonance, 91*, 77-83.

Golay, M.J.E. (1958). Field homogenizing coils for nuclear spin resonance instrumentation. *The Review of Scientific Instruments, 29*, 313-315.

Gruelter, R., & Boesch, C. (1992). Fast, noniterative shimming of spatially localized signals. In vivo analysis of magnetic field along axes. *Journal of Magnetic Resonance, 96*, 323-344.

Hoch, J.C., & Stern, A.S. (1996). *NMR Data Processing*, pp. 78-122. Wiley-Liss, New York, USA.

Hore, P.J. (1985). NMR data processing using the maximum entropy method. *Journal of Magnetic Resonance, 62*, 561-567.

Jiménez-Domínguez, H., Cruz-Jiménez, S, & Cabral-Prieto, A. (1996). Spectroscopic applications of the plasma dispersion function. *Spectrochimica Acta Part B, 51*, 165-174.

Jiménez-Domínguez, H., Cruz-Jiménez, S, & Cabral-Prieto, A. (1997). Spectroscopic applications of the plasma dispersion function. II: An asymmetric lineshape model and complex susceptibility. *Spectrochimica Acta Part B, 52*, 1113-1124.

Joliot, M., Mazoyer, B.M., & Huesman, R.H. (1991). In vivo spectral parameter estimation: a comparison between time and frequency domain methods. *Magnetic Resonance in Medicine, 18*, 358-370.

Jones, J.A., & Hore, P.J. (1991a). The maximum entropy method and Fourier transformation compared. *Journal of Magnetic Resonance, 92*, 276-292.

Jones, J.A., & Hore, P.J. (1991b). The maximum entropy method. Appearance and reality. *Journal of Magnetic Resonance, 92*, 363-376.

Kauppinen, J.K., & Saario, E.K. (1993). What is wrong with MEM? *Applied Spectroscopy, 47*, 1123-1127.

Konzbul, P., & Švéda, K. (1995). Shim coils for NMR and MRI solenoid magnets. *Measurement Science and Technology, 6*, 1116-1123.

Kotyk, J.J., Hoffman, N.G., Hutton, W.C., Bretthorst, G.L., & Ackerman, J.J.H. (1992). Comparison of Fourier and Bayesian analysis of NMR signals. I. Well-separated resonances (the single-frequency case). *Journal of Magnetic Resonance, 98*, 483-500.

Kreyszig, E. (1988). *Advanced Engineering Mathematics, sixth edition*, p. 234. John Wiley & Sons, New York, USA.

Laue, E.D., Skilling, J., Staunton, J., Sibisi, S., & Brereton, R.G. (1985). Maximum entropy method in nuclear magnetic resonance spectroscopy. *Journal of Magnetic Resonance, 62*, 437-452.

Led, J.J., & Gemar, H. (1991). Application of the linear prediction method to NMR spectroscopy. *Chemical Reviews, 91*, 1413-1426.

Losev, A. (1994). On a model line shape for asymmetric spectral peaks. *Appied. Spectroscopy, 48*, 1289-1290.

Martin, Y.L. (1994). A global approach to accurate and automatic quantitative analysis of NMR spectra by complex least-squares curve fitting. *Journal of Magnetic Resonance, Series A, 111*, 1-10.

Morris, G.A. (1988). Compensation of instrumental imperfections by deconvolution using and internal reference signal. *Journal of Magnetic Resonance, 80*, 547-552.

Morris, G.A., Barjat, H., & Horne, T.J. (1997). Reference deconvolution methods. *Journal of Progress in Nuclear Magnetic Resonance Spectroscopy, 31*, 197-257.

NAG (1997). Chapter E02 - Introduction. *NAG Fortran Library Manual*. Numerical Algorithms Group, Oxford, UK.

Paul, C.R., & Nasar, S.A. (1987). *Introduction to Electromagnetic Fields, second edition*, pp. 590-594. McGraw-Hill Book Company, New York, USA.

Port, S.C. (1994). *Theoretical Probability for Applications*, p. 454. Wiley-Interscience, New York, USA.

Pugachev, V.S. (1984). *Probability Theory and Mathematical Statistics for Engineers*, pp. 157-199. Pergamon Press, Oxford, UK.

Riley, K.F., Hobson, M.P., & Bence, S.J. (1997). *Mathematical Methods for Physics and Engineering*, p. 565. Cambridge University Press, Cambridge, UK.

Schmieder, P., Stern, A.S., Wagner, G., & Hoch, J.C. (1997). Quantification of maximum-entropy spectrum reconstructions. *Journal of Magnetic Resonance, 125*, 332-339.

Sivia, D.S. (1996). *Data Analysis. A Bayesian Tutorial.* p 1-12. Clarendon Press, Oxford, UK.

Springer, M.D. (1979). *The Algebra of Random Variables*, pp. 47-64, 91-100. John Wiley & Sons, New York, USA.

Stephenson, D.S. (1988). Linear prediction and maximum entropy methods in NMR spectroscopy. *Progress in Nuclear Magnetic Resonance Spectroscopy, 20*, 515-626.

Warren, W.S., & Richter, W. (1996). Concentrated solution effects. In D.M. Grant & R.K. Harris (Eds.), *Encyclopedia of Nuclear Magnetic Resonance, vol. 3*, pp. 1417-1423. John Wiley & Sons, Chichester, UK.

4.6 Nomenclature

(symbol)	(description)	(unit)

Scalar Variables

a	radius of cylindrical sample space	m
a_i	coefficient of Chebyshev polynomial of order i	-
a_L	parameter for left-hand side of Losev lineshape function	-
a_V	ratio of Lorentzian to Gaussian linewidths for Voigt lineshape function	-
A	maximum intensity of Losev lineshape function	-
b_L	parameter for right-hand side of Losev lineshape function	-
b_V	asymmetry parameter for Voigt lineshape function	-
B_k	modulus of complex error at point k	-
c	central frequency of Losev lineshape function	s^{-1}
c_i	pattern of peaks from component i in spectrum	-
C_i	pattern of sinusoids from component i in FID	-
C_l^m , S_l^m	coefficients of cosine, sine terms in solution to Laplace's equation in spherical polar co-ordinates	-
E	complex noise in FID	-
$f_1(x)$	primary probability of variable x	-
$f_2(x)$	derived probability of variable x	-
h	height of Lorentzian component in model lineshape	-
$h_{abs}(\vartheta, a)$	symmetric Voigt absorption lineshape function	-
$h_{disp}(\vartheta, a)$	symmetric Voigt dispersion lineshape function	-
$h'_{abs}(\vartheta; a, b)$	asymmetric Voigt absorption lineshape function	-
$h'_{disp}(\vartheta; a, b)$	asymmetric Voigt dispersion lineshape function	-
$h_0(\mathrm{x})$	Losev lineshape function	-
i	index of component in mixture	-
j	index of data point in frequency domain	-
k	index of data point in time domain	-
k_1	number of corrupted data points	-
l	index of peak in pattern for component i	-
L	length of cylindrical sample space	m
$L(\nu)$	Lorentzian lineshape function	-
$L'(\nu)$	Lorentzian lineshape function normalised to $I_0 = 1$	-
N_c	number of components in mixture	-
N_l	number of peaks in pattern for component i	-
N_t	number of points in FID	-
$P_l^m(\cos\theta)$	Legendre polynomial	-

r, θ, ϕ	spherical polar co-ordinates	-
$s(\nu)$	frequency-domain signal (spectrum)	-
$\hat{s}_j$	frequency-domain signal (spectrum) at j^{th} data point	-
s_l	scale factor for peak l	-
s_1, s_2, s_3, s_4	scale factors for resonance frequency distributions	-
$S(t)$	time-domain signal (FID)	-
$S(0)$	signal intensity at $t = 0$	-
$\hat{S}_k$	time-domain signal (FID) at k^{th} data point	-
t	time	s
t_{in}	pre-scan delay	s
t_{max}	maximum sampling time	s
$T_i(x)$	Chebyshev polynomial of first kind of degree i	-
x, y, z	Cartesian co-ordinates	-
x_1, x_2, x_3, x_4	width factors for resonance frequency distributions	-
X_i	proportion (mole fraction) of component i in mixture	-
y_2, y_4	width factors for resonance frequency distributions	-
$Y_l^m(\theta,\phi)$	spherical harmonic function	-
$Z(z)$	Plasma dispersion function for complex variable z	-
β_k	argument of complex error at point k	-
Γ_G	Gaussian full-width at half-maximum	s^{-1}
Γ_L	Lorentzian full-width at half-maximum	s^{-1}
δ	Dirac delta function	-
ε	complex noise in spectrum	-
η	parameter for Losev lineshape function	-
ϑ	frequency parameter for Voigt lineshape function	s^{-1}
Θ	replicating function in time domain	-
$\widetilde{\Theta}$	sampling function in frequency domain	-
λ	peak linewidth (half-width at half maximum)	s^{-1}
λ_l	change in linewidth of peak l in mixture spectrum	s^{-1}
λ_{0l}	pure component linewidth of peak l	s^{-1}
ν	frequency	s^{-1}
ν_l	shift in frequency of peak l in mixture spectrum	s^{-1}
ν_{max}	highest frequency in signal	s^{-1}
ν_0	resonance frequency	s^{-1}
ν_{0i}	spectral reference frequency for component i	s^{-1}
ν_{0l}	pure component frequency of peak l	s^{-1}
ξ	parameter for Losev lineshape function	-

Π	rectangle function	-
$\widetilde{\Pi}$	sinc function	-
ϕ_i	reference phase for component *i*	rad
ϕ_l	phase of peak *l*	rad
ϕ_1	linear phase correction term	rad s
Φ	magnetic field potential	-
Ψ	sampling function in time domain	-
$\widetilde{\Psi}$	replicating function in frequency domain	-

5 VOLUME-SELECTIVE NMR SPECTROSCOPY

5.1 Introduction

The NMR spectra used for composition measurements so far have been bulk spectra that gave the average composition of a sample. For a heterogeneous sample, spatially resolved composition information can be obtained using volume-selective NMR spectroscopy. This chapter describes spatially resolved NMR techniques that allow the acquisition of volume-selective spectra, 1D profiles and 2D images. Two methods of volume selection are presented: STEAM, which selectively excites the signal from the volume of interest, and PROJSAT, which saturates the signal outside the volume of interest so that only the desired signal remains. STEAM and PROJSAT are optimised for quantitative spectroscopy and used to acquire volume-selective spectra from different locations in a static sample. The PROJSAT spectra are the first reported, since PROJSAT had previously only been used for imaging. In the next chapter, STEAM and PROJSAT are applied to flowing liquid samples.

5.2 Theory

Spatially resolved NMR is performed by selectively exciting part of the sample in the presence of magnetic field gradients, then spatially encoding the signal during acquisition by making the signal frequency or phase (or both) position-dependent. The signal is Fourier transformed into an image that shows the spatial distribution of the nuclei in the sample. Depending on the number of encoding dimensions, profiles and images can be obtained that are selective in one, two or three dimensions.

5.2.1 Magnetic Field Gradients

Magnetic field gradients are used to link resonance frequency with position. The Larmor relation states that the resonance frequency, ω_0, of a nucleus (or "spin") in a magnetic field is a proportional to the field strength, B_0:

$$\omega_0 = \gamma B_0 . \tag{5.1}$$

By varying B_0 with position in a known manner, the resonance frequency of a nucleus becomes a function of its position inside the field; it is said to be "spatially encoded".

The variation in B_0 is obtained by adding a small magnetic field gradient, **g**, to the main field, so that the Larmor frequency has the dependence:

$$\omega(\mathbf{r}) = \gamma(B_0 + \mathbf{g}\cdot\mathbf{r}), \tag{5.2}$$

where **r** is the position vector of the nucleus (Callaghan, 1991). Three-dimensional spatial encoding is obtained by using three orthogonal linear gradients, one along the main field direction (g_z) and two perpendicular to it (g_x and g_y).

5.2.2 Selective Excitation

A rectangular radio-frequency pulse of constant amplitude and duration t_p excites a range of frequencies in a sinc pattern whose main peak has a width of $2/t_p$. Conversely, an r.f. pulse modulated in a sinc pattern of width t_p excites a rectangular frequency pattern of width $2/t_p$, and a Gaussian-shaped r.f. pulse of duration t_p excites frequencies in a Gaussian pattern with half-width $4/\pi t_p$ (Callaghan, 1991). The pulses and frequency patterns are shown in figure 5.1. A narrow frequency range is excited by a long pulse with sufficiently low power to give the desired flip angle, and in the presence of a slice selection gradient the excited frequency range corresponds to a narrow slice perpendicular to the gradient direction.

5.2.3 Spatial Encoding

There are two methods for spatially encoding the signal received from different locations in the sample. The first method is frequency encoding, which consists of acquiring the signal in the presence of a "read" gradient so that the frequency of the signal corresponds to its position. The second method is phase encoding, which consists of applying a "phase" gradient for a short time while the magnetisation is in the transverse plane, then switching it off before signal acquisition. A phase gradient, g_x, applied along the x axis for a time t_x induces a phase shift given by (Crooks, 1996):

$$\phi_x = \gamma x g_x t_x, \tag{5.3}$$

which is proportional to position, x, and the gradient strength. The read and slice gradients also induce phase shifts that must be refocused to maximise the signal intensity since those phase shifts are not used for spatial encoding. The refocusing is achieved by applying a gradient equal in magnitude but opposite in sign to the gradient that dephased the spins.

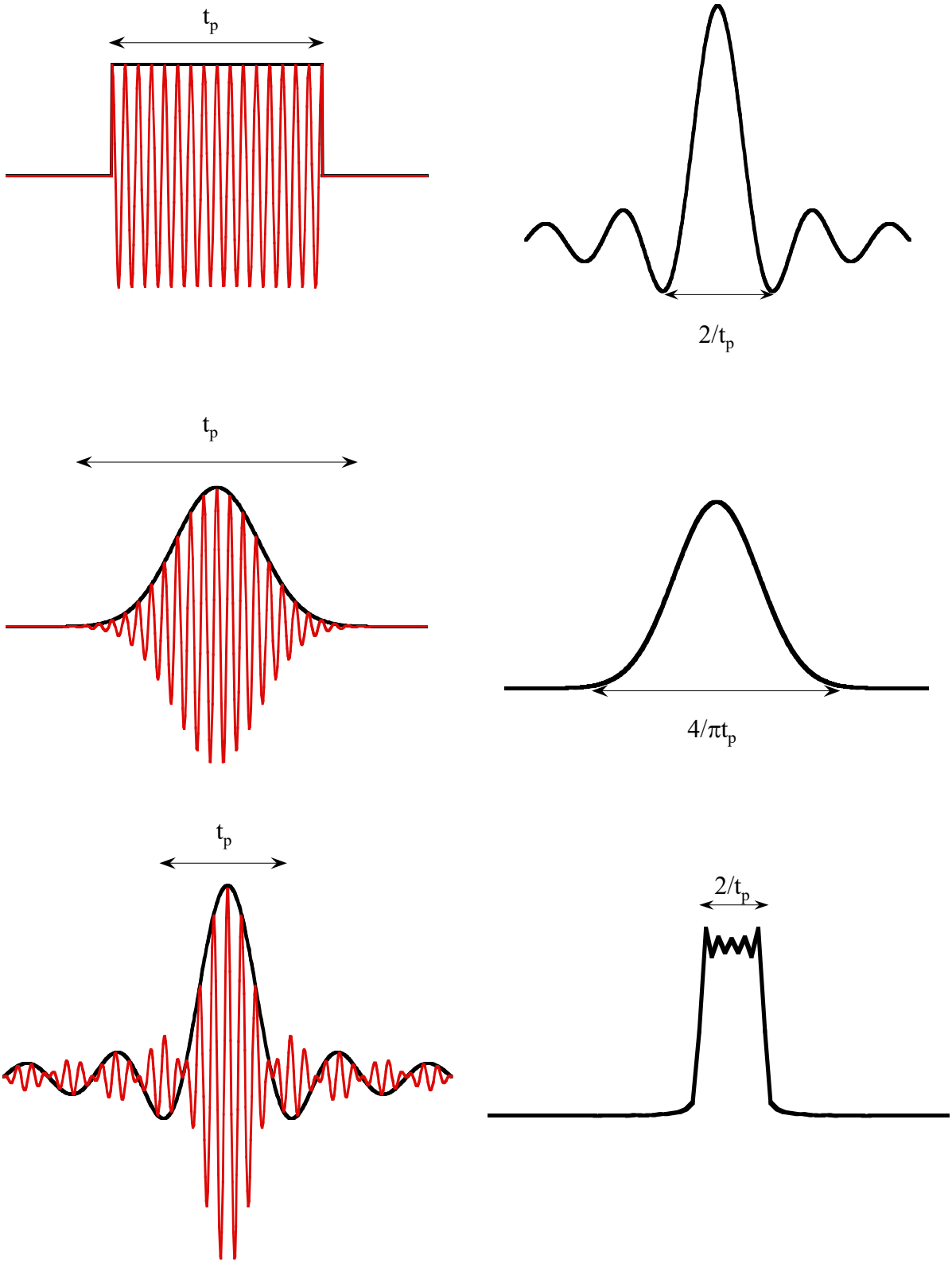

Figure 5.1 Three different radio-frequency pulses (left) with their frequency responses (right): top, a rectangular pulse with a sinc response; middle, a Gaussian pulse with a Gaussian response; bottom, a sinc pulse with a near-rectangular response (after Gladden, 1994).

5.2.4 Echoes

As discussed in section 2.2.5, the transverse magnetisation dephases over time with time constant T_2^* due to magnetic field inhomogeneity and spin-spin relaxation. The dephasing leads to a significant loss of signal intensity in imaging pulse sequences due to the delay between the first pulse and the start of acquisition. Since the magnetic field inhomogeneity does not vary during the experiment, its dephasing effect can be reversed by using a "spin echo" (Hahn, 1950). The echo results from a 180° pulse applied at a time τ after a 90° pulse. The 180° pulse reverses the phases of the spins but leaves their frequencies unaltered, so they refocus and form an echo at time 2τ (figure 5.2(a)). The signal now decays due to spin-spin relaxation only, with the longer time constant T_2.

Another echo is the "stimulated echo" produced by a train of three 90° pulses: 90°-τ_1-90°-τ_2-90°-τ_1-echo (Hahn, 1950). The advantage of the stimulated echo is that the magnetisation is stored along the longitudinal axis during the delay τ_2, where it undergoes longitudinal relaxation (figure 5.2(b)). For systems with $T_1 > 2T_2$, a stimulated echo has higher signal intensity and less relaxation contrast than a spin echo.

A refocusing gradient produces a "gradient echo" when the spins are back in phase (Callaghan, 1991). For maximum signal intensity, the spin and gradient echoes are timed to coincide. Unwanted echoes are removed using "homospoil" gradients that dephase the transverse magnetisation, for example, after the second 90° pulse in the stimulated echo sequence (Granot, 1986).

5.2.5 Signal Reconstruction

In a volume element dV at position $\mathbf{r}$ with a local nuclear spin density of $\rho(\mathbf{r})$, there are $\rho(\mathbf{r})dV$ spins present that give a signal (Callaghan, 1991):

$$dS(\mathbf{g},t) = \rho(\mathbf{r})dV e^{i\omega(\mathbf{r})t}. \tag{5.4}$$

The spatially resolved signal from the sample is given by:

$$S(t) = \iiint \rho(\mathbf{r}) e^{i\gamma \mathbf{g}\cdot\mathbf{r}t} d\mathbf{r}, \tag{5.5}$$

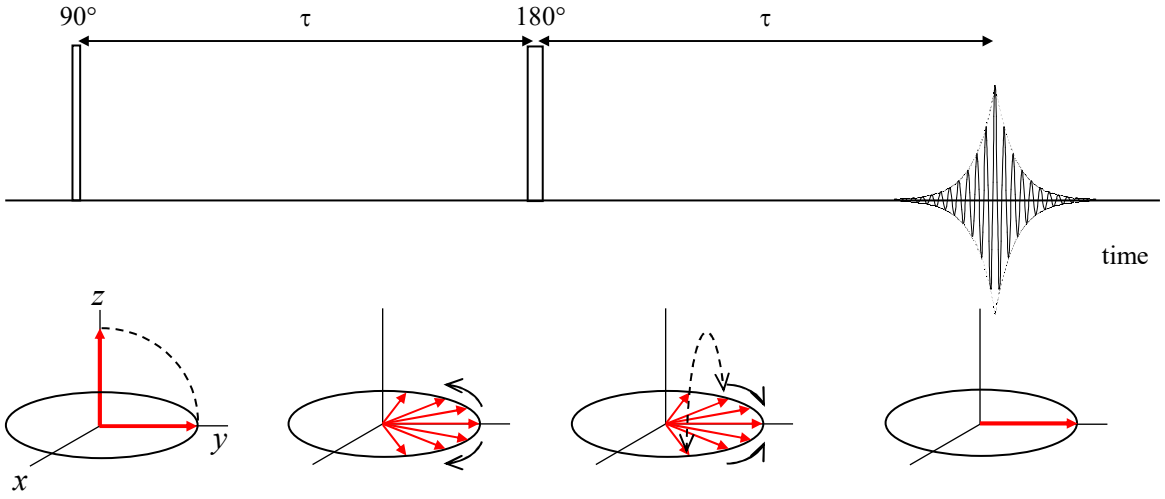

(a)

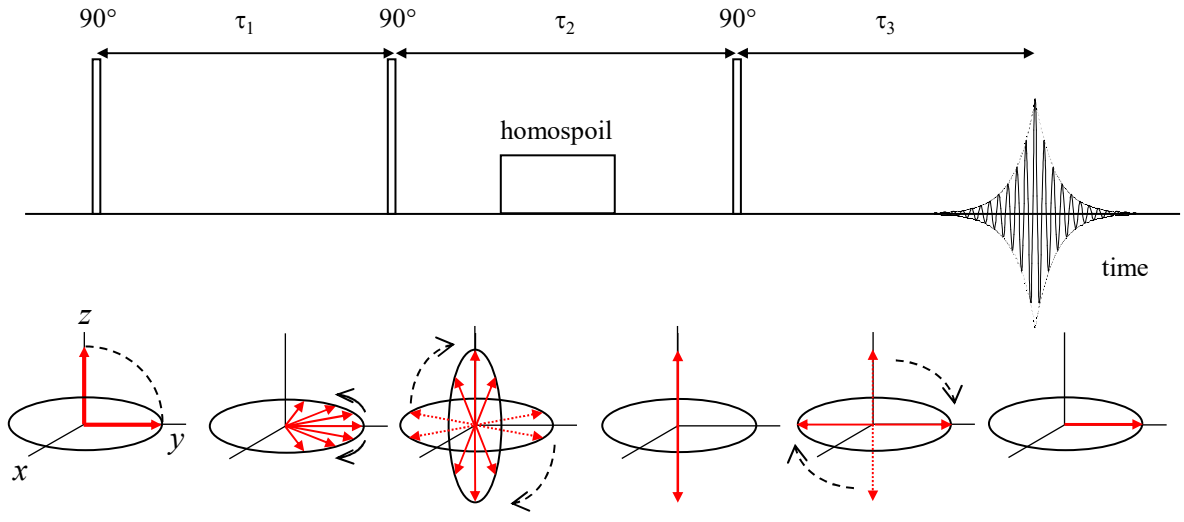

(b)

Figure 5.2 *(a)* Evolution of the magnetisation during a spin echo pulse sequence. A 90º pulse rotates the magnetisation onto the transverse plane where it dephases, then a 180º pulse inverts the phase of the magnetisation, which refocuses to form an echo. *(b)* During a stimulated echo pulse sequence a 90º pulse rotates the magnetisation onto the transverse plane where it dephases, then a second 90º pulse rotates half the magnetisation onto the *z* axis and the remaining transverse magnetisation is dephased by the homospoil gradient. A third 90º pulse rotates the magnetisation back onto the transverse plane where it refocuses to form an echo (after Callaghan, 1991).

where the signal at the reference frequency $\omega = \gamma B_0$ has been excluded. The spin density is recovered from the signal using a Fourier transform,

$$\rho(\mathbf{r}) = \iiint S(t) e^{-i\gamma \mathbf{g}\cdot\mathbf{r}t}\, dt\,. \tag{5.6}$$

The Fourier transform is used to construct images from both frequency-encoded and phase-encoded signals.

5.2.6 Spin-Echo Pulse Sequences

A profile in one dimension is produced by the pulse sequence shown in figure 5.3. A hard 90° pulse is used to rotate all the magnetisation into the transverse plane. A 180° pulse applied at time τ produces a spin echo at time 2τ. A dephasing read gradient is applied that equals the read gradient applied up to the time 2τ, so that the gradient echo coincides with the spin echo at 2τ, in the middle of the acquisition time. The dephasing read gradient has the same sign as the read gradient because the 180° pulse between them inverts the phases of all the spins. A one-dimensional Fourier transform gives a profile of spin density along the read gradient direction. Resonance frequency is converted to position by:

$$r = \frac{\omega - \omega_0}{\gamma g}\,, \tag{5.7}$$

where ω_0 is the resonance frequency at $r = 0$.

A two-dimensional slice-selective image is produced by the pulse sequence shown in figure 5.4. A hard 90° pulse is followed at time τ by a soft 180° pulse in the presence of a slice gradient, giving a spin echo from spins in the selected slice only. A negative slice gradient is applied after the 180° pulse to refocus the spins dephased by the slice gradient. A dephasing read gradient and a phase gradient are applied during the interval between the pulses. The spin and gradient echoes coincide at 2τ in the centre of the acquisition. The pulse sequence is repeated while incrementing the phase gradient to give the signal in the phase direction. This is the spin warp method (Hutchison, 1996). A two-dimensional Fourier transform gives a 2D image that shows the spatial distribution of spins, in the *xy* plane in this case.

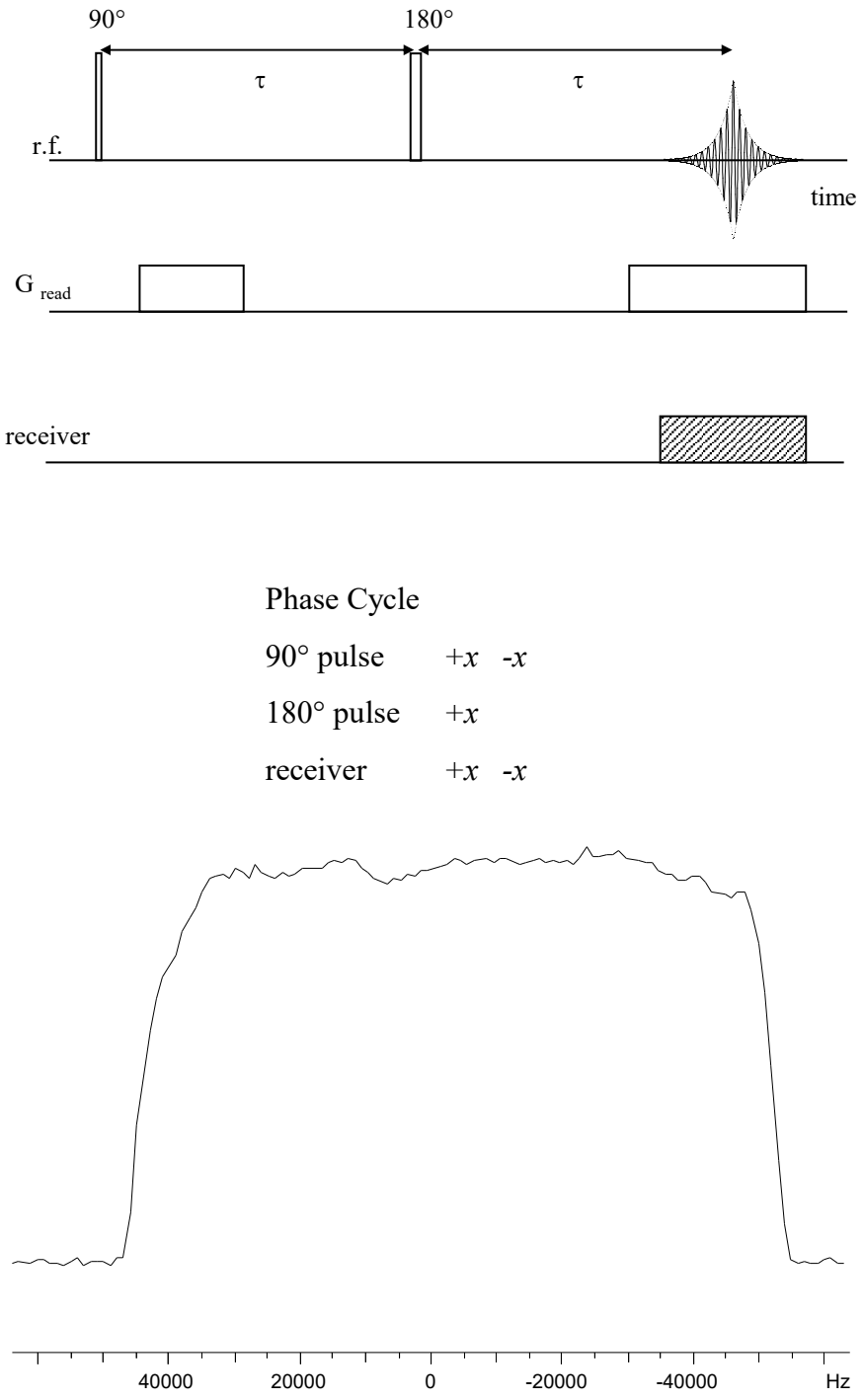

Figure 5.3 Pulse sequence for the acquisition of a one-dimensional profile of a sample using a spin echo. Two non-selective pulses are used to form the echo, which is acquired in the presence of a read gradient. The ^{1}H profile acquired using this pulse sequence shows the signal intensity along the *z* axis of a 10-mm sample of hydrogel. The profile resolution is 10 kHz/mm.

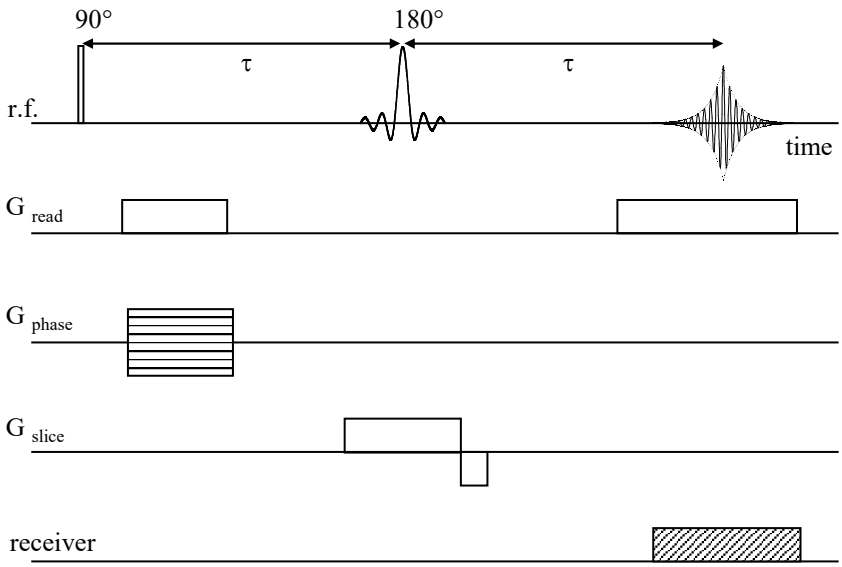

Phase Cycle

90° pulse	+*x*	-*x*
180° pulse	+*x*	
receiver	+*x*	-*x*

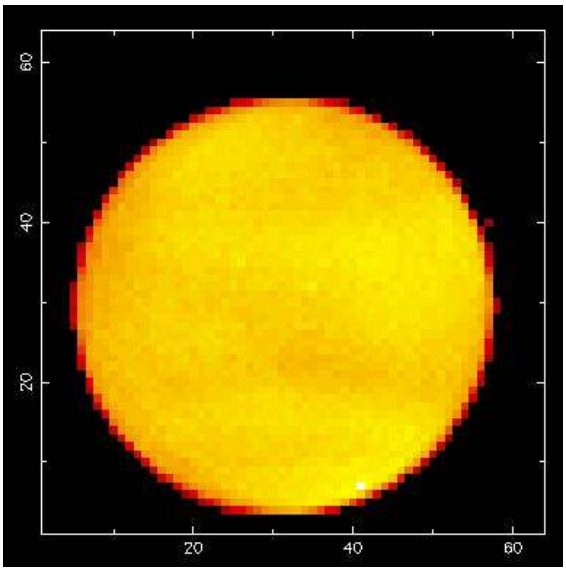

Figure 5.4 Pulse sequence for the acquisition of a two-dimensional image of a sample using a spin echo. A non-selective 90º pulse is followed by a slice-selective 180º pulse to form the echo, which is acquired in the presence of a read gradient. The sequence is repeated as many times as there are steps in the phase gradient. The ^{1}H image acquired using this pulse sequence is of water inside a tube of inner diameter 4.1 mm. The field of view is 5×5 mm^2.

5.3 STEAM Spectroscopy

This section describes volume-selective spectroscopy using STEAM. The pulse sequence and acquisition parameters are optimised for obtaining quantitative spectra, and composition results are presented for non-flowing liquid mixtures. STEAM spectroscopy of flowing liquids is described in chapter 6.

5.3.1 Historical Overview

The STEAM (*st*imulated *e*cho *a*cquisition *m*ode) technique was developed in the mid-1980's (Frahm *et al.*, 1985). It is a single-shot volume selection technique that excites the desired signal directly instead of saturating or subtracting unwanted signals (Frahm and Hänicke, 1996). The pulse sequence consists of three 90° pulses, which produce a stimulated echo (Hahn, 1950). One, two or three of these pulses can be made slice-selective, leading to a stimulated echo from a selected volume of interest at the intersection of the slices (figure 5.5). STEAM was first applied to rapid multi-slice imaging due to its ability to store the magnetisation along the z axis during the interval between the second and third 90° pulses. Later, a pulse sequence for STEAM spectroscopy was published (Frahm *et al.*, 1987).

An identical pulse sequence for stimulated echo imaging – without an acronym – was published almost simultaneously with STEAM (Sattin *et al.*, 1985a; Sattin *et al.*, 1985b). The pulse sequence includes a four-step phase cycle and a homospoil gradient between the second and third pulses to reduce image artefacts. Another identical pulse sequence for imaging and spectroscopy was published under the name of VEST (*v*olume *e*xcitation using *st*imulated echoes) the following year (Granot, 1986). The listed advantages of VEST were the use of conventional imaging hardware, easy adjustment of the size and location of the selected volume, good definition of the volume of interest, and a reduced T_2-dependence of the stimulated echo relative to a spin echo. The same pulse sequence was introduced under yet another name one year later: VOSY, for *vo*lume *s*elective spectroscop*y* (Kimmich and Hoepfel, 1987). Three 90° pulses produce eight signals: three one-pulse FIDs from selected slice planes, three two-pulse spin echoes from selected lines, one three-pulse spin echo and one three-pulse stimulated echo, both from the selected cube (figure 5.6). The selection of different signals is achieved by different gradient schemes that refocus the desired signals only and dephase the other signals.

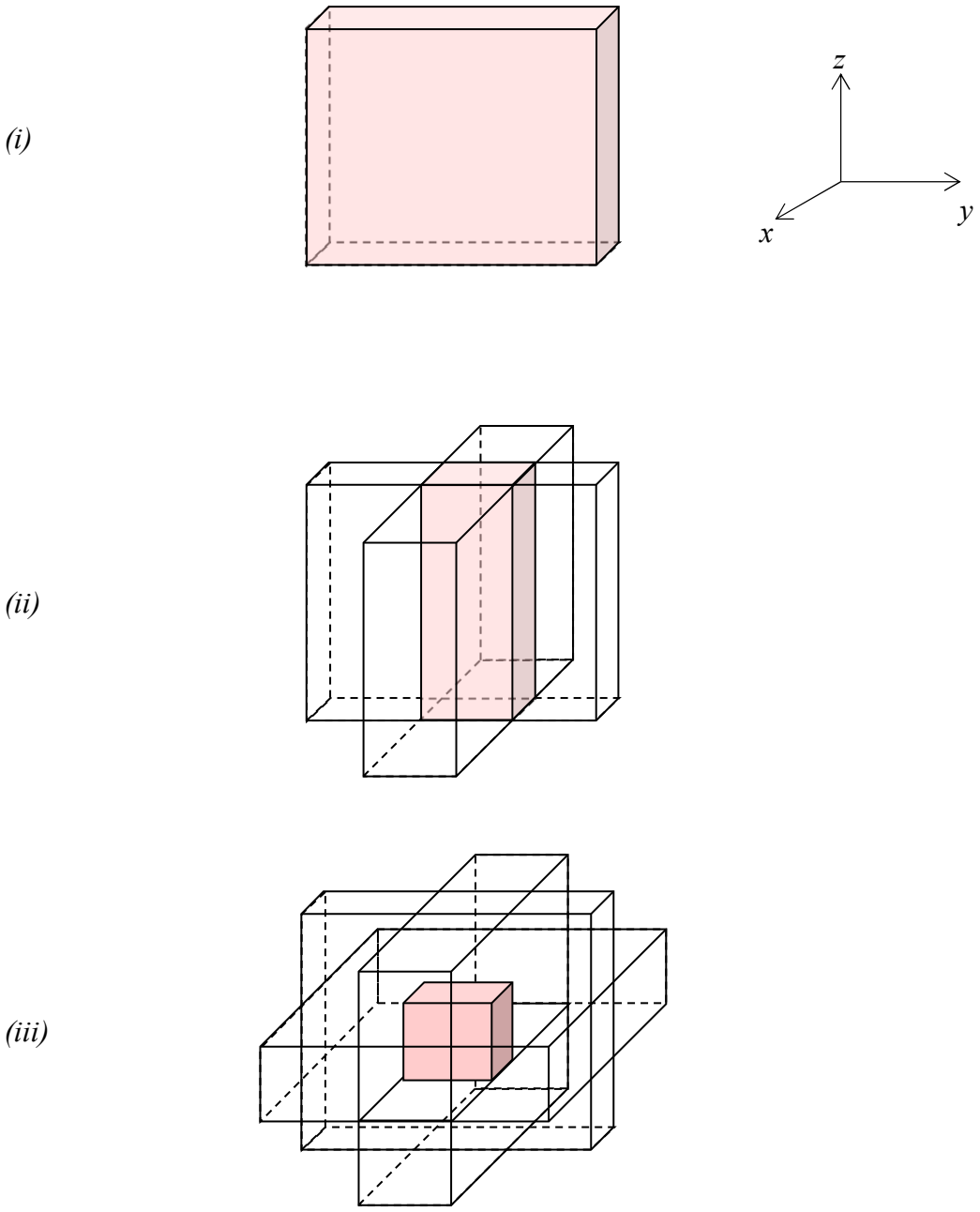

Figure 5.5 STEAM volume selection by selective excitation. *(i*) The first 90º pulse excites a slice along the *x* axis which then has its magnetisation in the transverse plane. *(ii)* The second 90º pulse excites a slice along the *y* axis so that half the magnetisation in the line of intersection is back along the longitudinal direction. *(iii)* The third 90º pulse excites a slice along the *z* axis so that the magnetisation in the volume of intersection is back in the transverse plane. The stimulated echo is formed only in the volume at the intersection of the three slices.

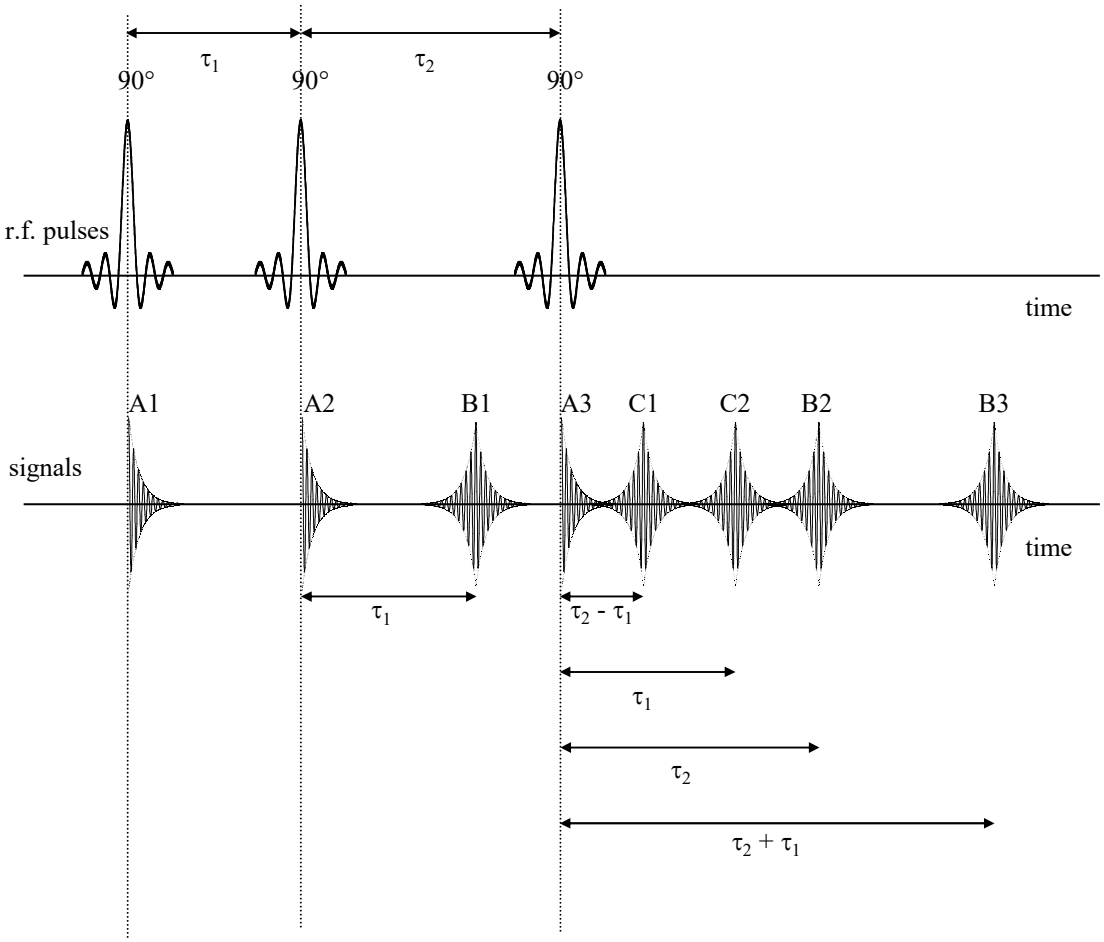

Figure 5.6 Overview of signals excited by three soft 90º pulses. A1, A2, A3: slice-selective one-pulse FIDs. B1, B2, B3: line-selective two-pulse spin echoes. C1: volume-selective three-pulse secondary spin echo. C2: volume-selective three-pulse stimulated echo (after Kimmich and Hoepfel, 1987).

Comparing STEAM, VOSY, VEST and the Sattin sequence, it is evident that the same pulse sequence for volume selection using stimulated echoes was developed near-simultaneously by several groups. The acronym STEAM is used throughout this work to refer to this pulse sequence.

5.3.2 STEAM Pulse Sequences

The STEAM pulse sequences used in this work (figure 5.7) are based on those of Frahm *et al.* and were implemented on our Bruker DMX 200 spectrometer equipped with a 4.7 T magnet and a 5 mm micro-imaging coil tuned to a ^{1}H resonance frequency of 199.700 MHz. Three sinc-modulated soft 90° pulses are applied with three orthogonal slice selection gradients, in order to select a box-shaped volume. The location of the volume is altered by changing the frequency offset of the soft pulses. Each slice gradient leads to some dephasing of the signal, which is rephased using a refocusing gradient. The refocusing gradients cannot be placed in the second interval, because the phase of the magnetisation along the *z* axis is not affected by the gradients. The homospoil gradient before the third 90° pulse dephases the remaining transverse magnetisation that has not been stored by the second pulse. Without the homospoil gradient, additional spin echoes would form after the third pulse (Burstein, 1996).

The stimulated echo sequence is followed by one of three sequences, depending on whether a spectrum, a profile or an image is required. For a spectrum, no further gradients are needed and the receiver is timed to start signal acquisition at the echo maximum ($\tau_3 = \tau_1$). Only the second half of the echo is acquired for a spectrum; the first half of the echo is truncated by the pulse sequence itself. For a 1D profile, the entire echo is acquired in the presence of a read gradient. For a 2D image, a read defocusing gradient and a ramped phase gradient are applied before acquiring the entire echo in the presence of a read gradient and the entire pulse sequence is repeated for each value of the phase gradient. Examples of a STEAM spectrum, profile and image are shown in figure 5.8.

For STEAM spectroscopy at high field with strong slice selection gradients, different magnetic susceptibilities across the sample can make accurate volume selection difficult (van Zijl *et al.*, 1989). Interference from unwanted echoes and inaccurate rephasing of the slice selection gradients shifts the echo maximum and gives

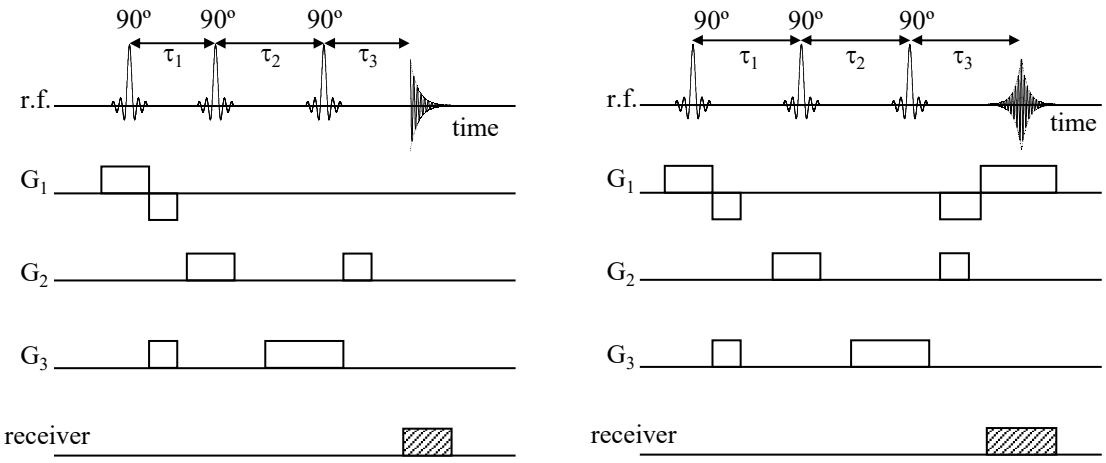

(a) *(b)*

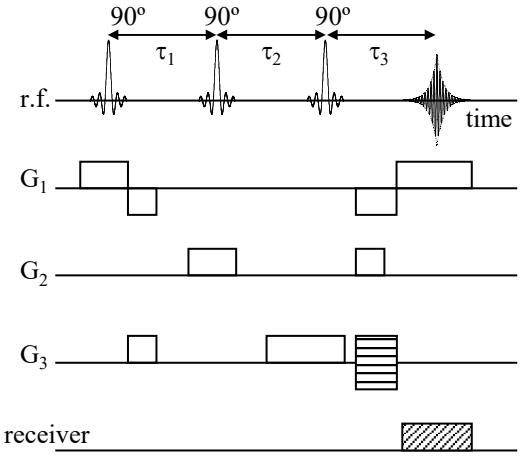

(c)

Phase Cycle																
1st 90° pulse	+x	+x	+x	+x	+x	+x	+x	+x	-x	-x	-x	-x	-x	-x	-x	-x
2nd 90° pulse	+x	+x	-x	-x	+x	+x	-x	-x	+x	+x	-x	-x	+x	+x	-x	-x
3rd 90° pulse	-x	+x	-x	+x	-y	+y	-y	+y	-x	+x	-x	+x	-y	+y	-y	+y
receiver	+x	-x	-x	+x	+y	-y	-y	+y	-x	+x	+x	-x	-y	+y	+y	-y

Figure 5.7 STEAM pulse sequences for acquisition of *(a)* a spectrum, *(b)* a 1D profile, *(c)* a 2D image. Three soft 90º pulses excite a stimulated echo from a volume at the intersection of three slices. The sixteen-scan phase cycle removes interference from unwanted echoes.

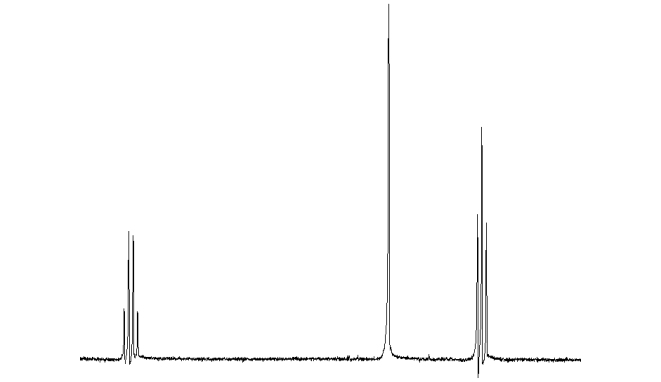

(a)

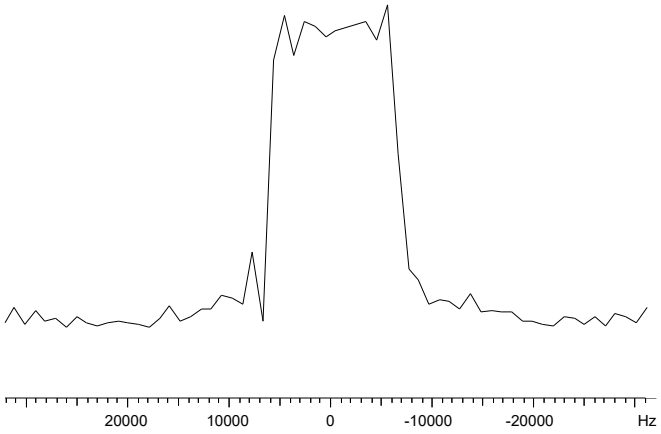

(b)

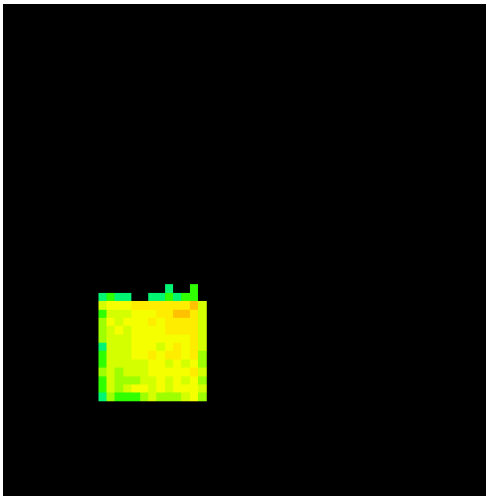

(c)

Figure 5.8 *(a)* 200 MHz ^{1}H STEAM spectrum of ethyl acetate from a 1×1×1 mm^3 volume showing higher resolution but lower signal-to-noise than a typical ZG spectrum.
(b) 200 MHz ^{1}H STEAM profile of the four-component test mixture showing a 1-mm selected slice along the *z* axis.
(c) 200 MHz ^{1}H STEAM image of ethyl acetate from a 1×1×1 mm^3 volume. The image field of view is 5×5 mm^2.

asymmetric and distorted lineshapes. The distortions were removed by van Zijl by adding balanced homospoil gradients after the first and third 90° pulses and using a four-scan phase cycle. The modified STEAM sequence (figure 5.9) suggested by van Zijl was also implemented on our system for comparison with the original version. This pulse sequence is referred to as STEAMQR (*q*uick *r*efocus) throughout this work.

5.3.3 Optimisation of STEAM for Quantitative Spectroscopy

Ideally, STEAM would give perfect volume selection and uniform excitation of the nuclei inside the selected volume, and interference from unwanted echoes and relaxation contrast would be non-existent. This would allow accurate measurement of the composition of the sample inside the volume of interest. In practice, STEAM can give good spectra from a well-defined volume of interest if care is taken to refocus the dephased magnetisation and minimise interference by unwanted echoes. The important parameters are the refocusing and homospoil gradients and phase cycling.

5.3.3.1 Gradients

A magnetic field gradient dephases the transverse magnetisation (equation 5.3). To form an echo, this dephasing is reversed by applying a refocusing gradient that is theoretically equal and opposite to the original gradient. In practice, the refocusing gradient is manually adjusted ("trimmed") slightly from its theoretical value to give the optimum signal. It was found on our system that the main effect of trimming refocusing gradients was to reduce the signal-to-noise ratio of the spectrum, with occasional improvements in lineshapes.

Gradients do not affect longitudinal magnetisation, so refocusing gradients must be applied during τ_1 or τ_3. For STEAM, the second slice gradient is refocused after the third 90° pulse and the third slice gradient is pre-focused before the second 90° pulse. Additional "homospoil" gradients are applied during τ_2 to dephase the remaining transverse magnetisation, which interferes with the stimulated echo. The gradients can also be refocused immediately before or after they are applied, but this refocusing causes unwanted gradient echoes. For STEAMQR, additional homospoil gradients dephase the gradient echoes formed by the immediate refocusing of the slice gradients.

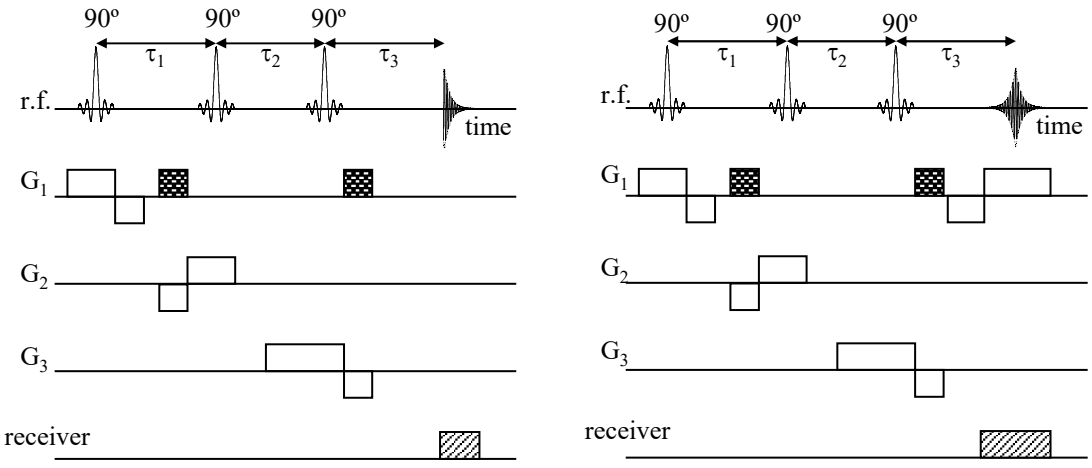

(a) *(b)*

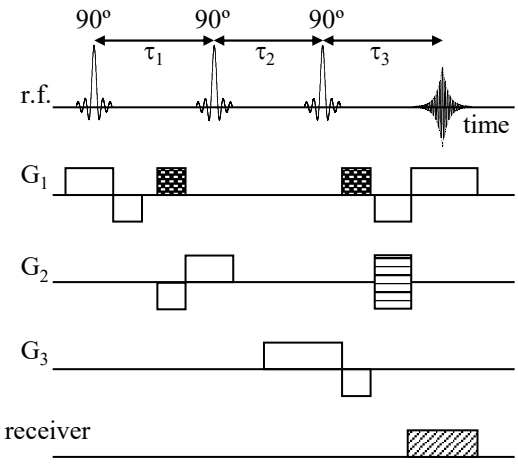

(c)

Phase Cycle																
1st 90° pulse	+x	+x	+x	+x	+x	+x	+x	+x	-x	-x	-x	-x	-x	-x	-x	-x
2nd 90° pulse	+x	+x	-x	-x	+x	+x	-x	-x	+x	+x	-x	-x	+x	+x	-x	-x
3rd 90° pulse	-x	+x	-x	+x	-y	+y	-y	+y	-x	+x	-x	+x	-y	+y	-y	+y
receiver	+x	-x	-x	+x	+y	-y	-y	+y	-x	+x	+x	-x	-y	+y	+y	-y

Figure 5.9 STEAMQR pulse sequences for acquisition of *(a)* a spectrum, *(b)* a 1D profile, *(c)* a 2D image. Three soft 90º pulses excite a stimulated echo from a volume at the intersection of three slices. The sixteen-scan phase cycle removes interference from unwanted echoes.

5.3.3.2 Phase Cycling

Phase cycling is applied in STEAM spectroscopy to remove interference from the other echoes present besides the stimulated echo (figure 5.6). The phase cycling scheme was developed by observing the effects on the spectrum of altering the phases of the pulses. It was found that incorrect pulse phases caused ripples to appear in the spectrum. The ripples could be avoided by alternately matching and opposing the phase of two successive pulses. A full implementation of this scheme requires a sixteen-scan cycle (figure 5.7), which requires long acquisition times. In practice, only the first half of the cycle was used because it gave identical spectra to the full cycle.

5.3.3.3 Phase Artefacts

For quantitative spectroscopy, the volume-selective spectra must be analysed in phase sensitive mode where the integrals of the absorption peaks are proportional to spin density. Many published STEAM spectra are presented in magnitude mode as can be seen from the wide dispersion wings of the peaks (Granot, 1986; Frahm *et al.*, 1987). The magnitude spectrum is the modulus of the real and imaginary parts of the phase-sensitive spectrum. It is used because it is difficult to phase the spectra to pure absorption mode, due to the complex phase evolution of the magnetisation during the pulse sequence. The phase shifts induced by the selection, refocusing and homospoil gradients are not entirely balanced out, although they are minimised by gradient trimming. Phase artefacts that appear in STEAM spectra include phase twists that can be eliminated by phase cycling and negative dips and "spikes" (figure 5.10(a)) caused by imperfect gradient refocusing (van Zijl *et al.*, 1989). The negative dips near the peaks complicate phase correction because there is no unambiguous absorption lineshape. All spectra in this chapter are presented in phase-sensitive mode and were phased manually to give a flat baseline either side of each peak. Since the FIDs were acquired as the second half of an echo instead of directly after a pulse, there was no ringing in the receiver. No data points were corrupted and the spectral baselines were perfectly flat.

Phase correction can be avoided by acquiring a full echo, which contains more information than a FID – it is equivalent to sampling a FID at negative time, and satisfies the Fourier requirement for periodicity. The magnitude spectrum of the echo

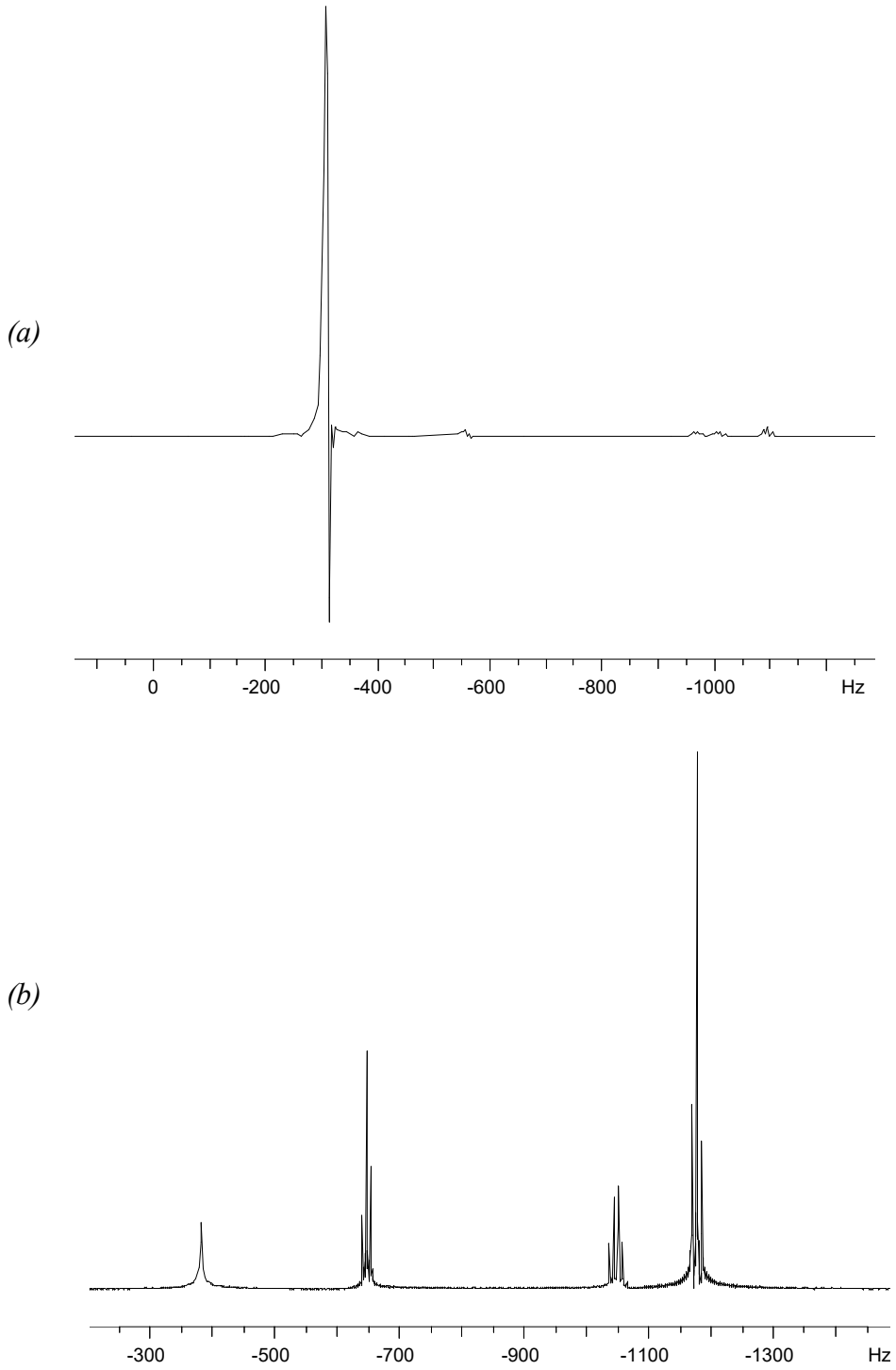

Figure 5.10 *(a)* 200 MHz ^{1}H STEAM spectrum of 1.5 mol% butanol in water from a 1×1×10 mm^3 volume (10 mm along *z*) showing a large negative dip near the water peak and a flat baseline. *(b)* 200 MHz ^{1}H magnitude spectrum of 5.9 mol% propanol in water, acquired using a secondary echo generated by applying a hard 180° pulse after a STEAM sequence. This magnitude spectrum does not require phase correction but exhibits strong T_2 weighting: the water peak (far left) is almost completely dephased.

is equivalent to the pure absorption spectrum of the FID (Callaghan, 1991). The full stimulated echo cannot be acquired because its negative half is truncated by the pulse sequence, but the stimulated echo can be refocused to form a secondary echo by adding a 180° pulse to the end of the pulse sequence. However, the echo time is very long in a highly homogeneous magnetic field, so the resulting spectrum is heavily T_2-weighted. In a spectrum of water and propanol obtained using a secondary echo (figure 5.10(b)), the water peak is almost entirely lost. Therefore, a full echo is unsuitable for quantitative spectroscopy.

5.3.3.4 Diffusion Attenuation

A side effect of asymmetric refocusing or balanced homospoil gradients is the loss of signal due to self-diffusion of the nuclei during the delay between the two gradients. The gradients act as position-encoding pairs, and the remaining signal, S, is given by:

$$\frac{S}{S_0} = e^{-\gamma^2 g^2 \delta^2 (\Delta - \delta/3) D}, \tag{5.8}$$

where S_0 is the original signal, g is the applied gradient strength, δ is the gradient duration, Δ is the time delay, γ is the gyromagnetic ratio and D is the self-diffusion coefficient of the nuclei in the sample (Stejskal and Tanner, 1965). Diffusion is covered in more detail in chapter 7. Assuming the diffusion coefficient of water ($D = 2.0\times10^{-9}$ m^2/s), the three slice gradient pairs in STEAM reduce the signal to $S = (1.0 \times 0.8648 \times 0.9864)S_0 = 0.8530S_0$. For STEAMQR, the balanced homospoil gradients reduce the signal to $S = 0.8481S_0$. STEAM and STEAMQR spectra of the same four-component sample are shown in figure 5.11. The STEAM spectrum has a signal-to-noise ratio of 301 vs. 410 for STEAMQR at twice the receiver gain, so STEAM gives more signal. The STEAMQR sequence is not useful for a homogenous sample because there are no susceptibility differences in the sample that require compensation, so there are no benefits to offset the loss of signal.

5.3.3.5 Relaxation Contrast

The entire pulse sequence must be as short as possible to minimise relaxation during the delay between the first pulse and the start of acquisition, which alters the peak intensities and causes quantification errors. For STEAM, the shortest delay is 13.045 ms during which the magnetisation decays due to both transverse and

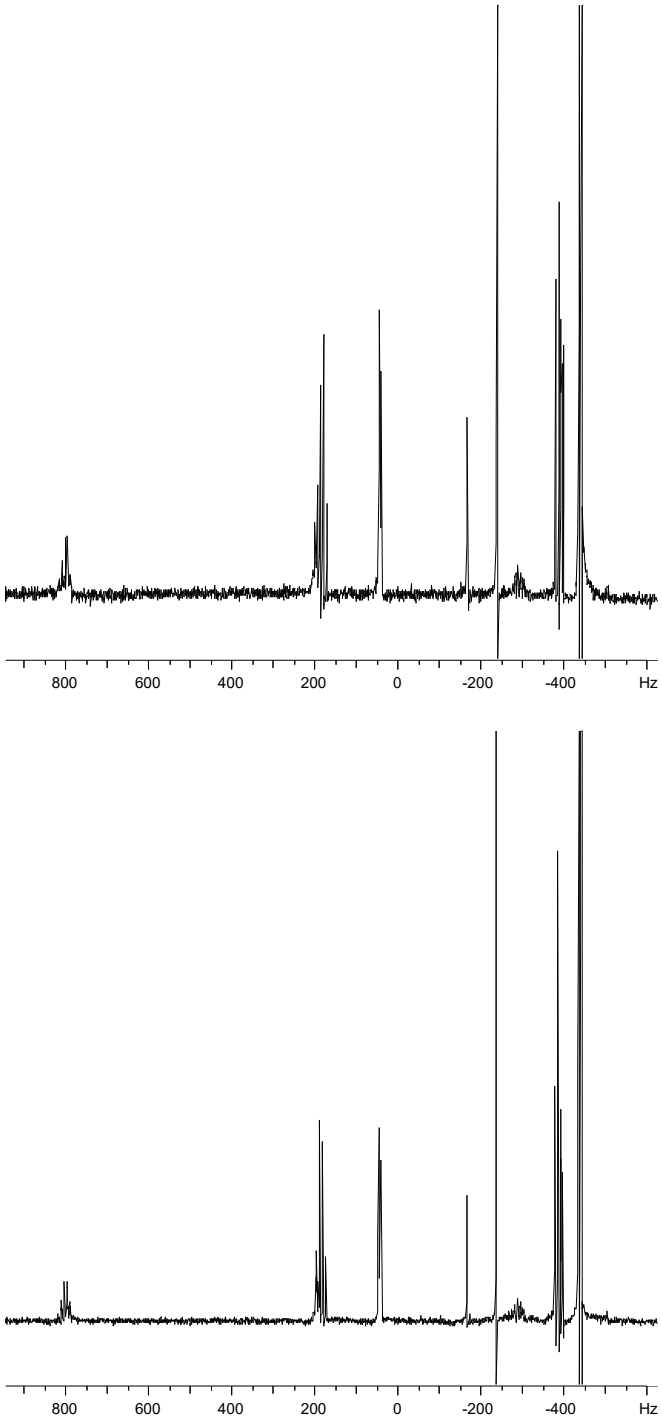

Figure 5.11 200 MHz ^{1}H spectra of a mixture of toluene, methanol, ethyl acetate and isooctane acquired using STEAM (top) and STEAMQR (bottom). The STEAMQR spectrum has a larger signal-to-noise ratio (410 vs 301) but it was acquired with twice the receiver gain to compensate for signal loss.

longitudinal relaxation. Transverse relaxation governed by T_2 occurs for 7.035 ms ($\tau_1+\tau_3$) and longitudinal relaxation governed by T_1 occurs for 6.01 ms (τ_2). For STEAMQR, the shortest delay is 14.04 ms with $\tau_2 = 6.01$ ms as STEAM, but $\tau_1+\tau_3 = 8.03$ ms due to the extra homospoil gradients. For liquids, T_1 is longer than T_2, so T_2 contrast will influence the spectrum more strongly and STEAMQR will have more contrast than STEAM. This is reflected in the composition results given below.

5.3.3.6 Accuracy of Volume Selectivity

Signal-selection efficiency is reduced by relaxation losses, imperfect gradient refocusing, motion and non-rectangular slice selection profiles. Contamination with signal from outside the volume of interest occurs by inadvertent signal excitation or refocusing, or from the side lobes excited by the truncated r.f. pulses. Spectroscopy suffers more strongly from contamination than imaging because the contaminant signal in an image is spatially resolved and can be ignored, but the contaminant signal in a spectrum is unresolved. STEAM imaging has been found to give near its maximum theoretical selection efficiency, low contamination and good volume-of-interest delineation (Yongbi *et al.*, 1995).

The slice selection profile depends on the soft pulse used for excitation. The soft 90° pulse used here is sinc-modulated to give a rectangular profile. The larger the number of zero-crossings in the sinc envelope, the closer the excitation profile approaches a perfect rectangle. This pulse has a duration of 1 ms and is truncated at the fifth zero-crossing (figure 5.12(a)) so it excites the nuclei inside a 10-kHz frequency range fairly uniformly and it partially excites nuclei outside the 10-kHz range (figure 5.12(b)). The partially excited signal is unwanted and is the main source of contamination. Here it equals 5% of the main signal.

To assess the relative contribution of contaminant signal, STEAM profiles were acquired using the pulse sequence in figure 5.7(b). Three profiles were acquired with read gradients along the *x*, *y* and *z* directions respectively. The echoes were Fourier transformed to give magnitude representations of the profiles (figure 5.13). The baselines were set to zero and the profiles were integrated in three regions: left side lobe, central slice and right side lobe. The integral of the central slice was normalised to 1. For a nominal slice thickness of 1.00 mm, the actual slice thickness was 1.06 mm along *x*, 1.09 mm along *y* and 1.25 mm along *z* and was the same for both

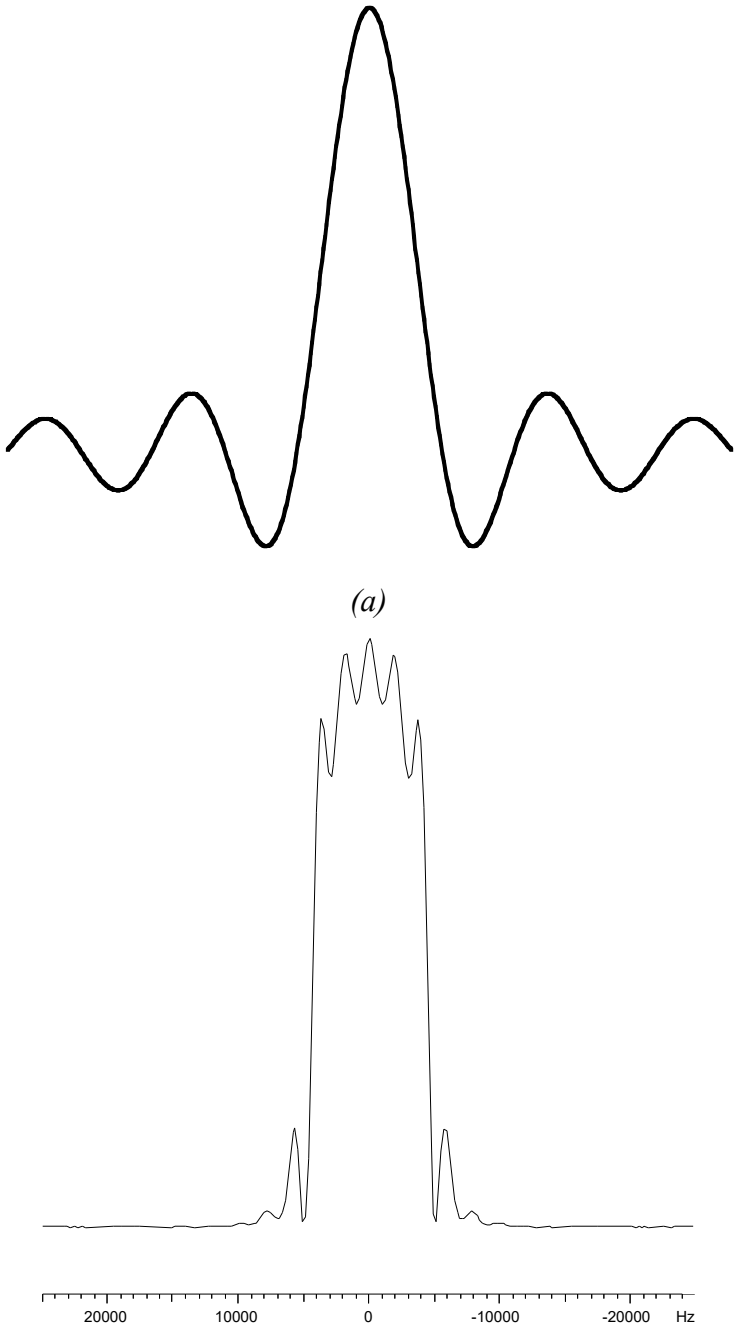

Figure 5.12 *(a)* Sinc-modulated pulse for rectangular excitation. The sinc function is defined using 1024 points and is truncated at the fifth zero-crossing. *(b)* Experimental excitation profile resulting from the pulse shown in (a). The slice is not excited uniformly and there is some extra-slice excitation.

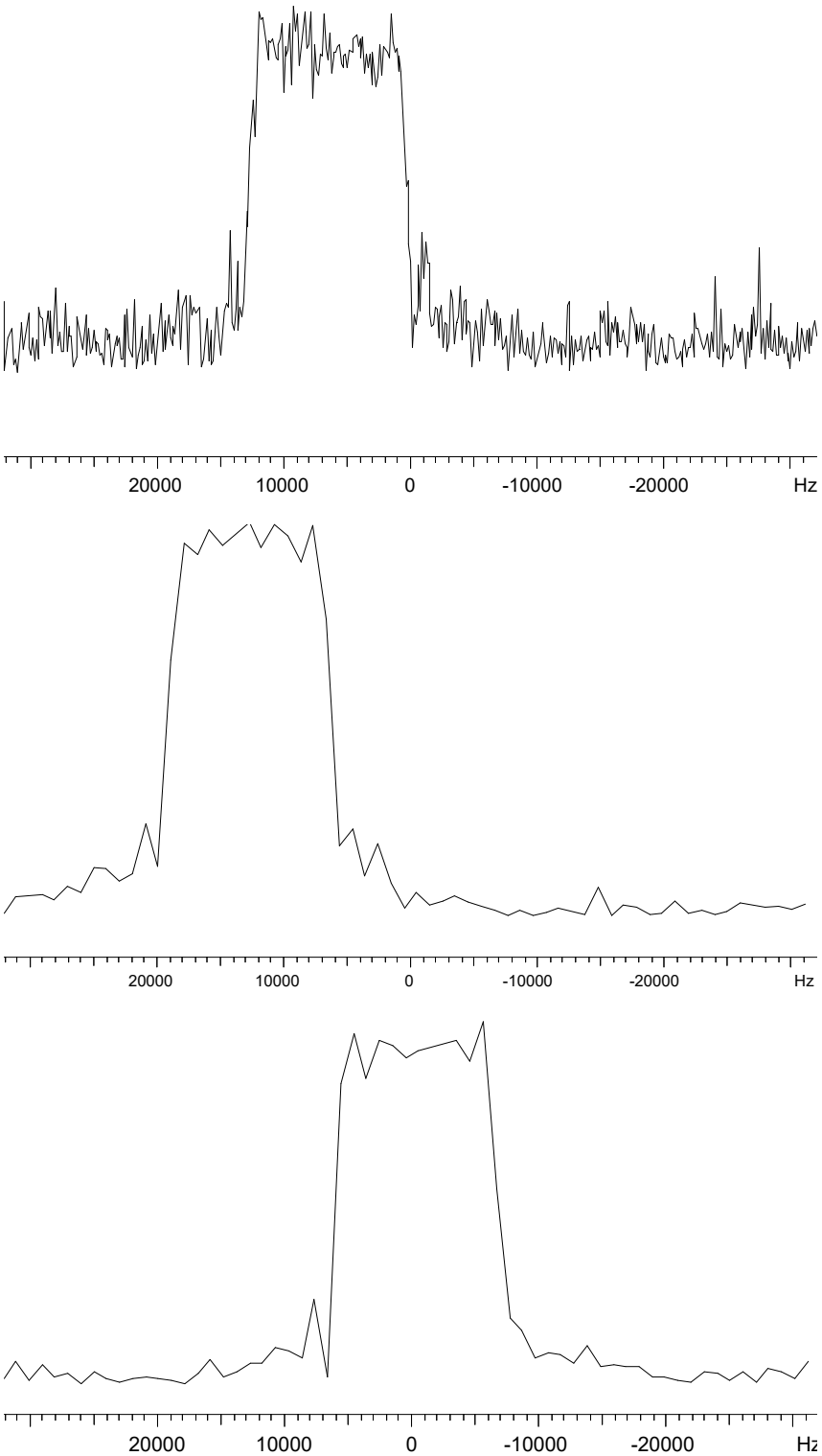

Figure 5.13 Experimental STEAM profiles of ^{1}H at 200 MHz along the *x*, *y*, and *z* axes (top to bottom) for a 1×1×1 mm^3 selected volume in a liquid mixture sample containing methanol, toluene, isooctane and ethyl acetate. The top profile has a poor signal-to-noise because the receiver gain was set too low.

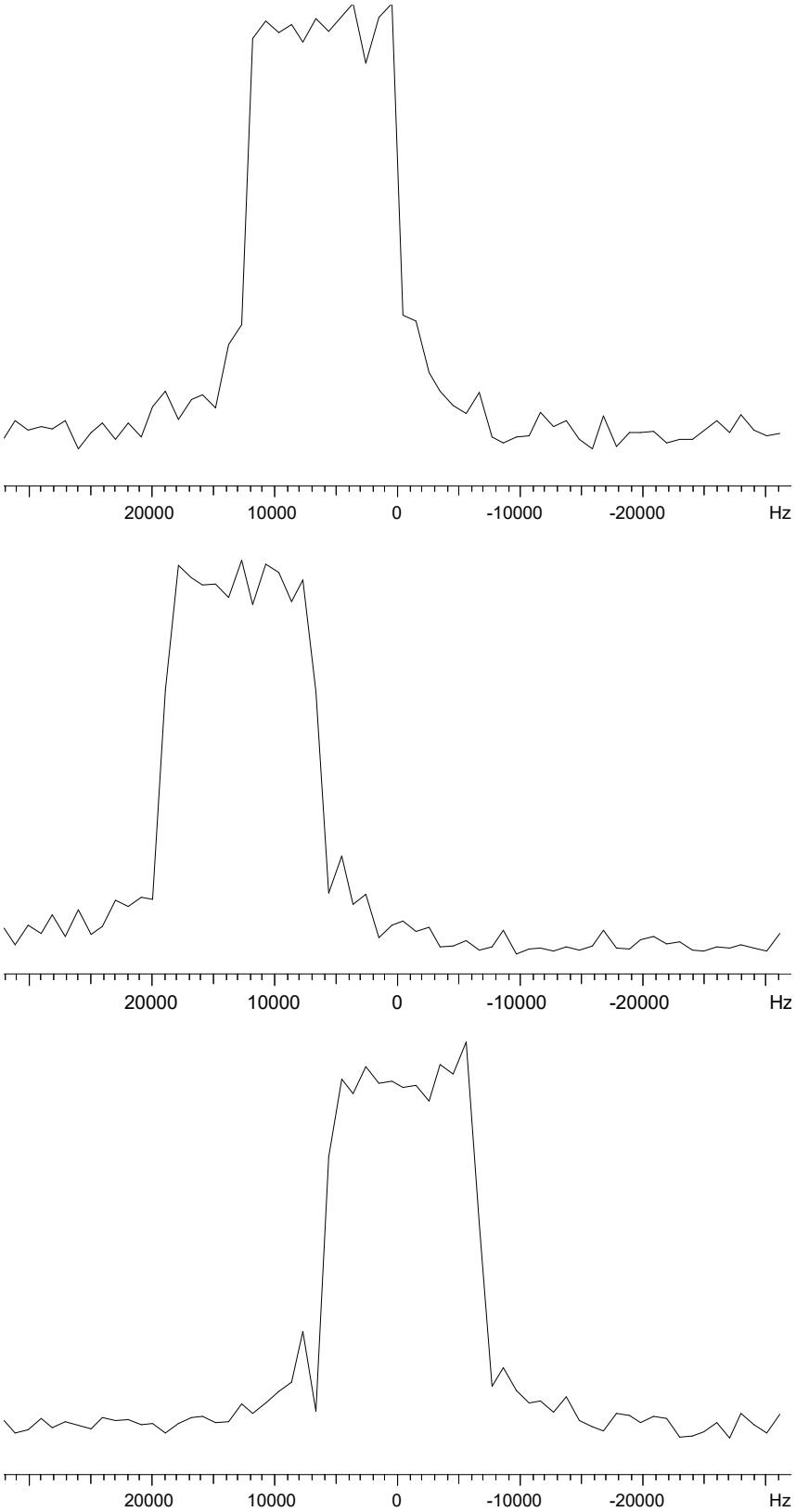

Figure 5.14 Experimental STEAMQR profiles of ^{1}H at 200 MHz along the *x*, *y*, and *z* axes (top to bottom) for a 1×1×1 mm^3 selected volume in a liquid mixture sample containing methanol, toluene, isooctane and ethyl acetate

the untrimmed and trimmed slice refocusing gradients. The actual selected volume of 1.44 mm^3 was larger than the nominal volume of 1.00 mm^3. The contaminant signal equalled 7.4% of the main signal, averaged over the three slices. STEAMQR profiles (figure 5.14) were similarly acquired using the pulse sequence in figure 5.9(b). For a nominal slice thickness of 1.00 mm, the actual slice thickness was 1.17 mm along *x*, 1.09 mm along *y* and 1.10 mm along *z*. The actual selected volume was 1.40 mm^3 and the contaminant signal equalled 10.4% of the main signal, averaged over the three slices. The contaminant signal for STEAMQR was proportionately higher with stronger homospoil gradients, because the homospoil gradients reduced the main signal more than the unwanted signals. The STEAMQR *x*, *y* and *z* profiles also had lower signal intensities of 0.68, 0.83 and 0.72 relative to the STEAM profiles, leading to an overall signal of 0.41 relative to STEAM. The additional signal loss can be attributed to stronger diffusion and relaxation effects than for STEAM.

Overall, STEAM has higher signal intensity and lower contamination from unwanted signal than STEAMQR, so it is better suited to quantitative applications. The actual selected volume is larger than the nominal volume but signal contamination is not too severe, since the contaminant signal arises near the selected volume where the composition of a heterogeneous sample is likely to be similar to that of the volume of interest.

5.3.4 Compositions of Liquid Mixtures

The ultimate purpose of STEAM in this work is to measure the composition of flowing liquid mixtures, but the performance of STEAM spectroscopy on non-flowing mixtures is considered first.

5.3.4.1 Experimental

A test sample for quantitative STEAM spectroscopy was prepared containing four components: methanol (35.71 mol%), toluene (8.88 mol%), ethyl acetate (30.61 mol%) and isooctane (24.80 mol%). The composition of the test sample was determined using ZG, STEAM and STEAMQR. Several spectra were acquired for each pulse sequence with the following acquisition parameters:

ZG 8 scans, 16384 data points, spectral width 5000 Hz, hard 90° pulse duration 3.65 μs, repetition time 15 s, receiver gain 4.

STEAM 1×1×1 mm^3 selected volume, 8 scans, 32768 data points, spectral width 5000 Hz, soft 90° pulse sinc5.1000 duration 1 ms, soft pulse power 36 dB, gradient stabilisation delay 1 ms, homospoil gradient duration 2 ms, refocusing gradient duration 0.5 ms, repetition time 15 s, receiver gain 256.

STEAMQR as STEAM, except balanced homospoil gradients duration 1.5 ms, receiver gain 512.

The volume-selective spectra contained narrower peaks than the bulk spectra did because the magnetic field was more homogeneous across a small selected volume. The narrow peaks did not overlap much, so they were easily integrated separately to determine the sample composition. Automatic phase correction was not possible because the negative dips and spikes in the spectra violated the "wholly positive" rule used in the numerical phasing algorithm. The baselines did not need correction.

5.3.4.2 Results

The composition results are shown in table 5.1. The composition obtained from ZG had the lowest error (±0.52 mol%), followed by STEAM (±0.96 mol%), then STEAMQR (±1.63 mol%). For the volume-selective spectra, the largest factor influencing the errors was signal-to-noise ratio. The STEAM spectra were acquired using 32768 data points in the FID, most of which had a very low signal-to-noise ratio. When all the data points were Fourier transformed, the spectral signal-to-noise ratio was 187, but when only the first 8192 points were Fourier transformed the signal-to-noise ratio increased to 243 because the discarded data points were mostly noise. The composition errors for STEAM using 8192 data points were ±0.96 mol% on average, increasing to ±1.28 mol% when 32768 data points were used. The STEAMQR spectra were acquired with a higher receiver gain to compensate for the inherently lower signal than STEAM, so all spectra had similar signal-to-noise ratios. The larger errors for STEAMQR were caused by the stronger relaxation weighting that was inherent in the pulse sequence.

Trimming the slice refocusing gradients reduced the artefacts in STEAM spectra at the expense of signal-to-noise ratio. The composition results were improved slightly by small adjustments, but if carried too far the reduction in signal-to-noise outweighed the improvements. The composition of the test mixture obtained using

	Composition by weight (mol%)	ZG	STEAMQR	STEAM	STEAM (8K points)
Methanol	35.71	35.80	33.77	36.40	36.43
Toluene	8.88	7.85	7.57	6.33	7.48
Ethyl acetate	30.61	31.54	31.89	32.27	31.81
Isooctane	24.80	24.81	26.77	25.00	24.28
Average error	---	*0.52*	*1.63*	*1.28*	*0.96*

Table 5.1 Composition of four-component test mixture (in mol%) by weight and as determined from several bulk and volume-selective NMR spectra using the pulse sequences ZG, STEAM and STEAMQR. The average error is calculated relative to the composition by weight. The uncertainty of the NMR values is ±0.5 mol% for ZG and ±1.5 mol% for STEAM.

Refocusing Gradient (G/mm)	Signal-to-Noise Ratio	Average Composition Error (mol%)	Average Measurement Uncertainty (mol%)
2.349	458	2.32	2.21
2.312	393	1.88	1.48
2.303	363	1.18	1.65
2.254	226	1.00	1.88
2.205	187	2.98	1.97

Table 5.2 Effect of the refocusing gradient strength on the signal-to-noise ratio, composition error and measurement uncertainty for a STEAM spectrum of the mixture shown in table 5.1. The selected volume was 1×1 ×1 mm^3 and the slice selection gradient strength was 2.349 G/mm.

Volume	Propanol content (mol%)
all	5.18
$(3.33\ mm)^3$	5.22
$(1.00\ mm)^3$	5.40
$(0.72\ mm)^3$	6.80

Table 5.3 Effect of size of selected volume on apparent propanol content as measured by STEAM spectroscopy for a mixture of 5 mol% propanol in water.

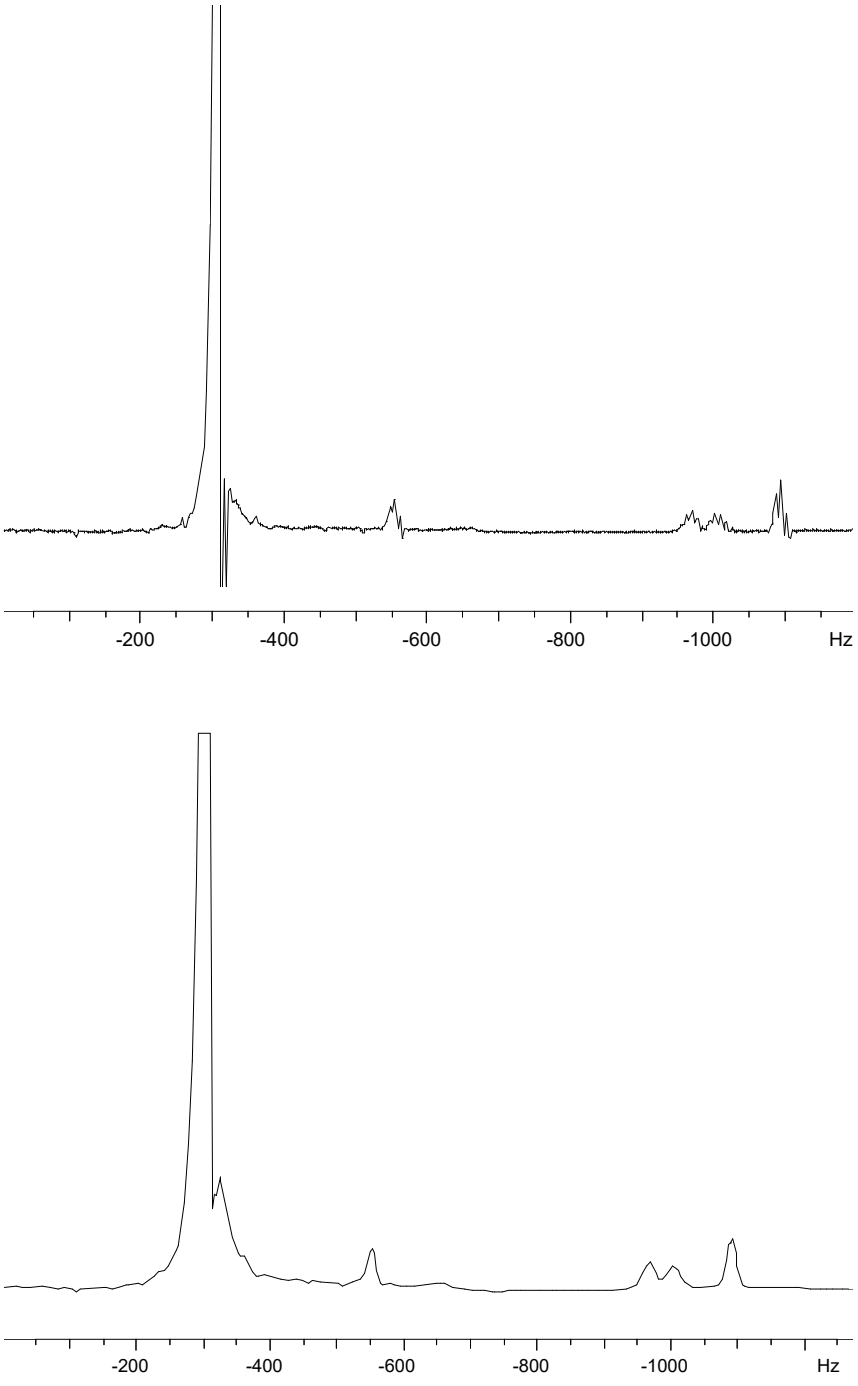

Figure 5.15 *(a)* A 200 MHz ^{1}H STEAM spectrum of 1.5 mol% butanol in water showing negative dips near the peaks. *(b)* The same spectrum after application of 6.5 Hz line broadening. The negative dips are eliminated at the expense of a degraded resolution, but the measured composition is 1.79 mol% for both spectra.

STEAM while trimming the slice selection gradient of 2.349 G/mm is shown in table 5.2. The more the refocusing gradient deviated from the selection gradient, the lower the signal-to-noise ratio and the larger the uncertainty of the results. The average composition error was initially reduced, then increased.

The size of the selected volume also affected the accuracy of the composition results. The smaller the selected volume the lower the number of nuclei producing a stimulated echo, so the lower the signal-to-noise ratio. In addition, selecting smaller volumes required stronger gradients, leading to more dephasing of the signal. For a mixture of 5 mol% propanol in water, the composition obtained from STEAM spectra for different volumes is shown in table 5.3. As the selected volume decreased, the apparent concentration of propanol increased due to increased dephasing of the water signal.

Negative dips and spikes prevented the STEAM spectra from being processed automatically, but they did not influence the quantitative results. A STEAM spectrum of 1.5 mol% butanol in water that contained artefacts was cosmetically improved by multiplying the FID with an exponential function. The exponential function removed the negative dips, broadened the peaks to 6.5 Hz and increased the signal-to-noise ratio from 1702 to 4639 (figure 5.15), but both the original and the apodised spectrum gave the same composition: 1.79 mol% butanol in water.

5.4 Projection Presaturation

This work on volume-selective spectroscopy ultimately aims to acquire spectra from well-defined regions inside flowing liquid streams. A circular pipe has radial symmetry, so a sensible region of interest would be cylindrical (*e.g.* at the centre of the pipe) instead of cuboid. An imaging technique called "projection presaturation" (PROJSAT) can select a volume of arbitrary shape. PROJSAT is optimised for quantitative spectroscopy and composition results are presented for non-flowing liquid mixtures. PROJSAT spectroscopy of flowing liquids is described in chapter 6.

5.4.1 Pulse Sequence

PROJSAT is a single-shot method for isolating a region of interest (ROI) of arbitrary shape and position by saturating the magnetisation outside the ROI while leaving the magnetisation inside the ROI along the longitudinal axis (Singh *et al.*, 1990a; Singh *et*

al., 1990b). The magnetisation outside the ROI is tipped into the transverse plane by multiple repetitions of short, selective, small-tip-angle r.f. pulses and continually dephased by a constant-amplitude rotating gradient. This gradient is formed by vectorially summing two identical sinusoidal gradients with a 90° phase shift between them. The saturation pulse shape is tailored to excite only the outer region by taking the inverse Fourier transform of the desired response profile, which is the projection of the vertices of the polygonal ROI onto the direction of the rotating gradient. The profile consists of a series of rectangles with gaps for the ROI, so the pulse shape is a frequency-modulated sinc function, where the modulation frequencies determine the size of the gaps. The actual saturation profile does not have sharp edges due to the truncation of the sinc function, and the transition regions between the rectangles and the gaps scale with the size of the outer volume (Singh *et al.*, 1992).

The advantages of PROJSAT are that the quality of the outer volume signal saturation is not susceptible to tip-angle errors, the single-shot approach does not rely on accurate subtraction of signals, and the magnetisation inside the ROI does not undergo any relaxation during the saturation train (Singh *et al.*, 1990a). The single-shot localisation is fast and can be used on systems with short T_2 values although T_1 must be longer than the saturation time to avoid recovery of the saturated magnetisation. An alternate pulse sequence combines the saturation train with hard 180° inversion pulses to null the residual magnetisation outside the ROI (Singh and Brody, 1993), but the magnetisation inside the ROI is also inverted and undergoes T_1 relaxation during the nulling period, so the resulting signal is T_1-weighted.

The pulse sequences used in this work are based on the original PROJSAT sequence without 180° inversion pulses (Singh *et al.*, 1990a). The pulse sequences for producing localised spectra, 1D profiles and 2D images are shown in figure 5.16. The saturation train consists of a series of *n* soft pulses tailored to excite the outer volume and leave the ROI unperturbed. The rotating gradient is created by the simultaneous application of stepped gradients along the *x* and *y* axes, so that the ROI is parallel to the longitudinal axis of the sample. After each saturation pulse, an additional homospoil gradient is applied along the *z* axis that rapidly dephases the transverse magnetisation. After a short delay for eddy currents to die down, the saturation train is followed by a hard 90° pulse that generates a FID from the magnetisation inside the ROI. A localised spectrum is obtained without any additional gradients, and a 1D

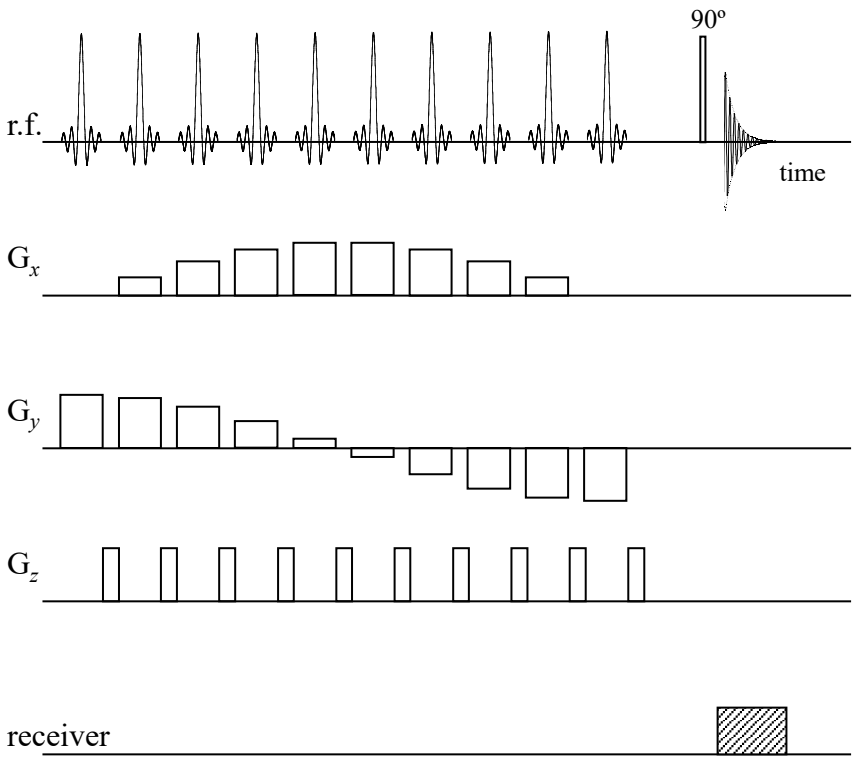

Phase Cycle								
saturation pulses	+*x*							
hard 90° pulse	+*x*	-*x*	-*x*	+*x*	+*y*	-*y*	-*y*	+*y*
receiver	+*x*	-*x*	+*x*	-*x*	+*y*	-*y*	+*y*	-*y*

Figure 5.16 *(a)* Pulse sequence for PROJSAT spectroscopy based on Singh *et al.*, 1990a. A train of tailored soft pulses and homospoil gradients (G_z) saturates the outer volume magnetisation so that the hard 90º pulse gives a spectrum from the selected volume. The number of saturation pulses is variable. Ten have been shown for illustrative purposes.

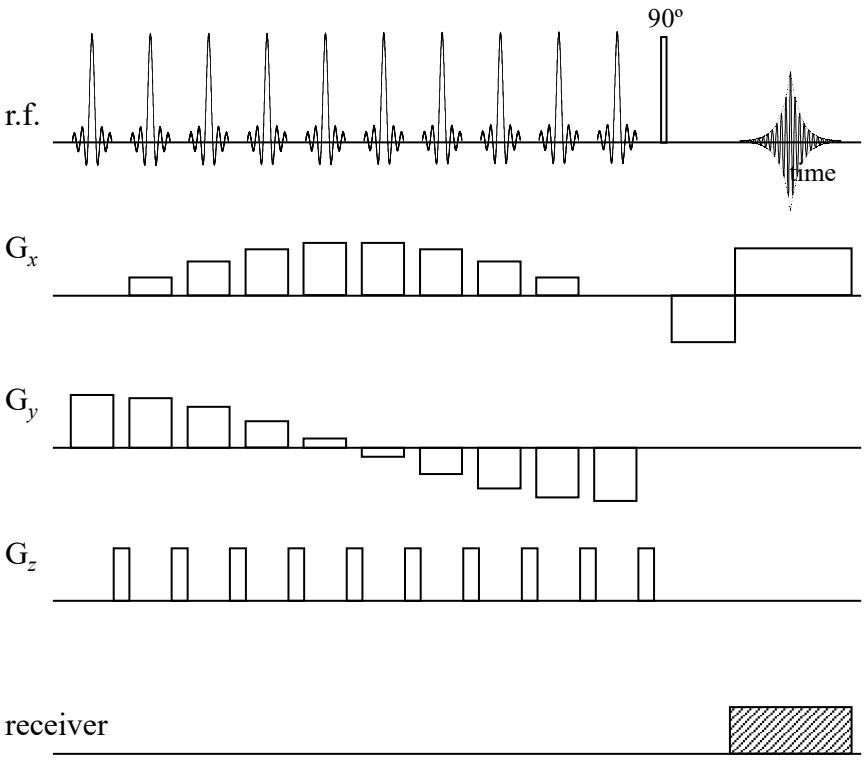

Phase Cycle								
saturation pulses	$+x$							
hard 90° pulse	$+x$	$-x$	$-x$	$+x$	$+y$	$-y$	$-y$	$+y$
receiver	$+x$	$-x$	$+x$	$-x$	$+y$	$-y$	$+y$	$-y$

Figure 5.16 *(b)* Pulse sequence for a one-dimensional PROJSAT profile based on Singh *et al.*, 1990a. A train of tailored soft pulses and homospoil gradients (G_z) saturates the outer volume magnetisation. After the hard 90º pulse excites the selected volume, the read gradient spatially encodes the signal. The number of saturation pulses is variable. Ten have been shown for illustrative purposes.

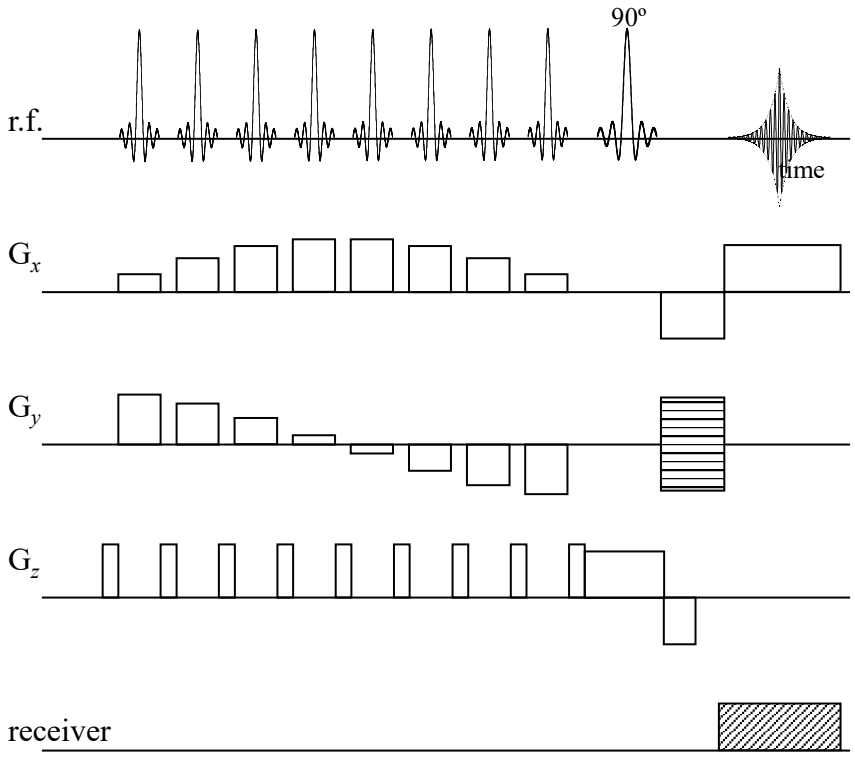

Phase Cycle								
saturation pulses	+*x*							
soft 90° pulse	+*x*	-*x*	-*x*	+*x*	+*y*	-*y*	-*y*	+*y*
receiver	+*x*	-*x*	+*x*	-*x*	+*y*	-*y*	+*y*	-*y*

Figure 5.16 *(c)* Pulse sequence for a two-dimensional PROJSAT image based on Singh *et al.*, 1990a. A train of tailored soft pulses and homospoil gradients (G_z) saturates the outer volume magnetisation. After the soft 90º pulse excites a slice within the selected volume, the read and phase gradients spatially encode the signal. The number of saturation pulses is variable. Eight have been shown for illustrative purposes. The pulse sequence is repeated as many times as there are steps in the phase gradient.

profile is obtained with an additional read gradient after the hard 90° pulse. A 2D image is obtained by adding a soft 90° pulse with a slice selection gradient after the saturation train and using read and phase gradients to encode the two spatial dimensions of the image.

5.4.2 Design of Saturation Pulses

The shape of the r.f. saturation pulse is derived from the desired saturation profile by the linear Fourier transform method (Singh *et al.*, 1990b). The excitation profile at each angle of the rotating gradient is the projection of the vertices of the polygonal ROI onto the direction of the gradient. For a ROI that is symmetric about the centre of the rotating gradient, the profile is the same for all gradient directions so only a single tailored r.f. pulse is needed. For an asymmetric or off-centre ROI, a different pulse is needed for each gradient direction. This is a serious drawback of PROJSAT, because the design of 32 or more tailored r.f. pulses is very tedious, and the spectrometer driver software is limited to 16 pulse waveforms per pulse program.

In this work two centred, symmetric ROIs were used: a cylinder of diameter d_i inside a cylindrical outer volume of diameter d_o, and an annulus of thickness t_a at a diameter d_i inside a cylindrical outer volume of diameter d_o. These ROIs are interesting for studying liquids undergoing laminar flow, where the cylinder selects the fastest-flowing nuclei and the annulus selects nuclei with a specific velocity range.

5.4.2.1 Cylinder

For a cylindrical ROI, the saturation profile consists of two rectangles of base b and centre c (figure 5.17(a)), which are related to d_i and d_o by:

$$b = \frac{d_o - d_i}{2} \qquad c = \frac{d_o + d_i}{4}. \tag{5.9}$$

The saturation profile is described by the function given by:

$$f(x) = \begin{cases} 1 & -c - \frac{b}{2} \le x \le -c + \frac{b}{2} \\ 1 & c - \frac{b}{2} \le x \le c + \frac{b}{2} \\ 0 & \text{otherwise} \end{cases}, \tag{5.10}$$

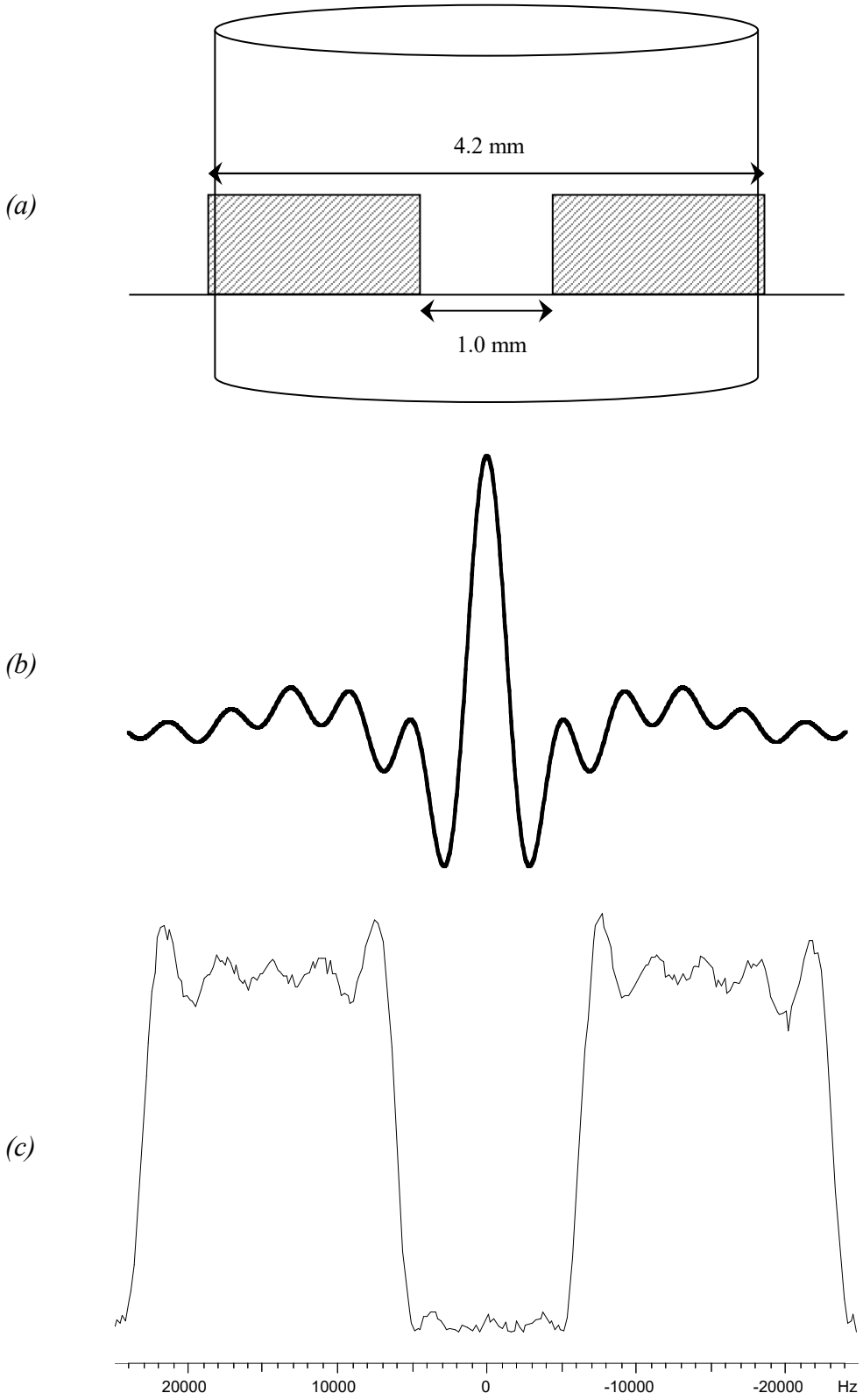

Figure 5.17 *(a)* Theoretical excitation profile for localisation of a cylindrical ROI using PROJSAT. *(b)* Tailored r.f. pulse shape obtained by Fourier transformation of the profile shown in (a). *(c)* Experimental saturation profile resulting from the r.f. pulse shown in (b).

and the r.f. excitation function is obtained by Fourier transforming equation (5.10) to give:

$$F(s) = 2b\cos(2\pi sc)\mathrm{sinc}(sb). \tag{5.11}$$

On our system, d_o = 4.2 mm and d_i = 1.0 mm, so b = 1.6 mm and c = 1.3 mm. The applied rotating gradient, g, had an amplitude of 4.41 G/mm. Inverting equation (5.7) gives:

$$\nu = \frac{x\gamma g}{2\pi}, \tag{5.12}$$

from which b_ν = 30038 Hz and c_ν = 24405 Hz. The r.f. pulse waveform was created using 1024 points for a duration of 500 μs, so the time between points was 488 ns. Inserting these parameters into equation (5.11), the p^{th} point in the waveform, labelled "cossinc1", is given by:

$$F(p) = \cos(0.074875p)\mathrm{sinc}(0.014667p). \tag{5.13}$$

The waveform is shown in figure 5.17(b) and the experimental saturation profile is shown in figure 5.17(c). Some excitation occurs inside the central region due to the truncation of the sinc function after 7 zero-crossings.

5.4.2.2 Annulus

For an annular ROI, the saturation profile consists of three rectangles (figure 5.18(a)), one central rectangle of base b_1 and centre c_1 and two outer rectangles of base b_2 and centre c_2, which are related to d_i, d_o and t_a by:

$$\begin{aligned} b_1 &= d_i - t_a & c_1 &= 0 \\ b_2 &= \frac{d_o - d_i - t_a}{2} & c_2 &= \frac{d_o + d_i + t_a}{4} \end{aligned}. \tag{5.14}$$

The saturation profile is described by the function given by:

$$f(x) = \begin{cases} 1 & -c_2 - \frac{b_2}{2} \le x \le -c_2 + \frac{b_2}{2} \\ 1 & -\frac{b_1}{2} \le x \le \frac{b_1}{2} \\ 1 & c_2 - \frac{b_2}{2} \le x \le c_2 + \frac{b_2}{2} \\ 0 & \text{otherwise} \end{cases}, \tag{5.15}$$

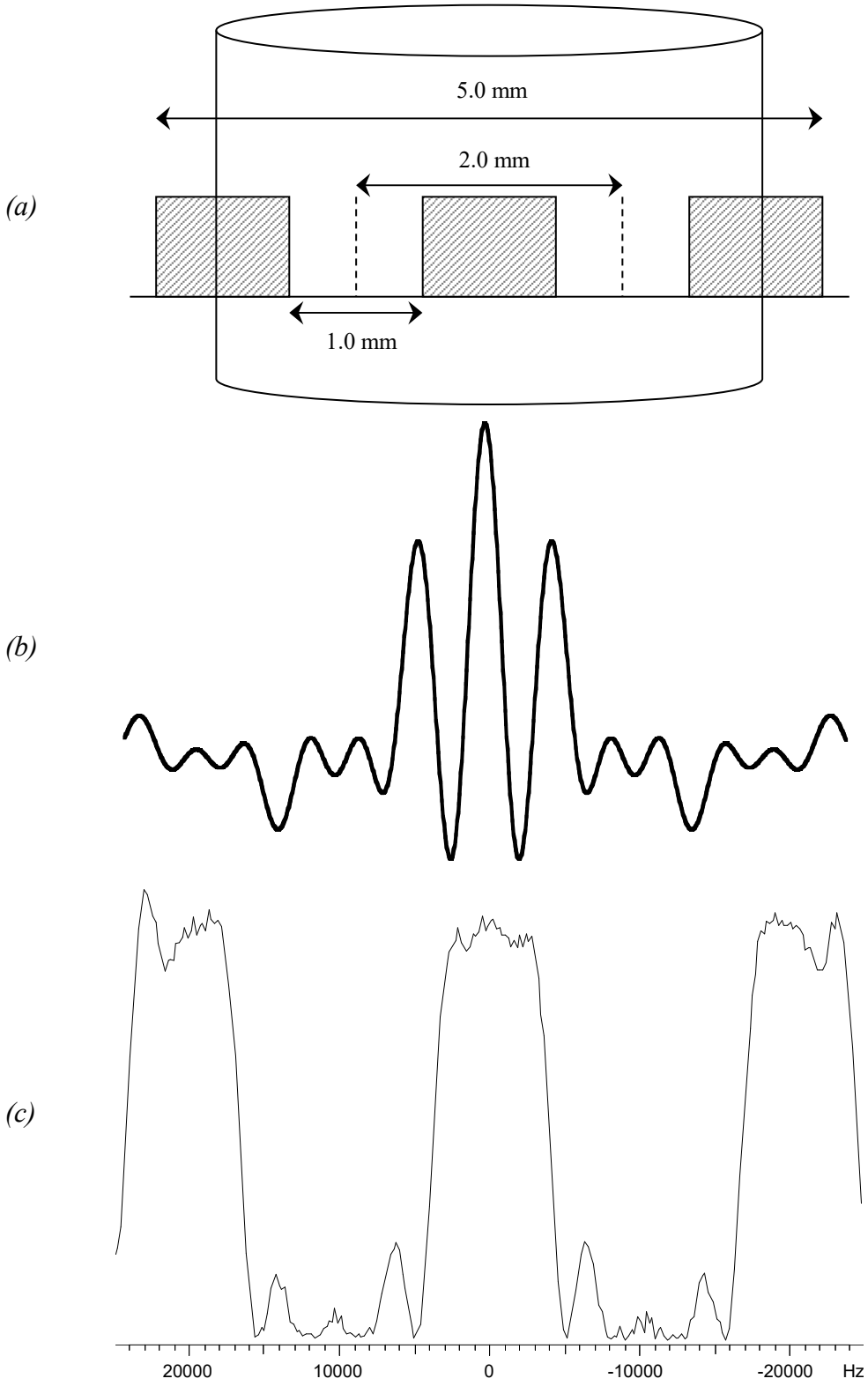

Figure 5.18 *(a)* Theoretical excitation profile for localisation of an annular ROI using PROJSAT. *(b)* Tailored r.f. pulse shape obtained by Fourier transformation of the profile shown in (a). *(c)* Experimental saturation profile resulting from the r.f. pulse shown in (b).

and the r.f. excitation function is obtained by Fourier transforming equation (5.15) to give:

$$F(s) = b_1 \mathrm{sinc}(sb_1) + 2b_2 \cos(2\pi sc_2)\mathrm{sinc}(sb_2). \qquad (5.16)$$

For this ROI, d_o = 5.0 mm, d_i = 2.0 mm and t_a = 1.0 mm, so b_1 = 1.0 mm, b_2 = 1.0 mm and c_2 = 2.0 mm. The applied rotating gradient, g, had an amplitude of 2.45 G/mm. Using equation (5.12), $b_{1\nu}$ = 10430 Hz, $b_{2\nu}$ = 10430 Hz and $c_{2\nu}$ = 20859 Hz. The r.f. pulse waveform was created using 1024 points for a duration of 500 μs, so the time between points was 488 ns. Inserting these parameters into equation (5.16), the p^{th} point in the waveform, labelled "cossinc2" is given by:

$$F(p) = \mathrm{sinc}(0.00509261p) + 2\cos(0.0639955p)\mathrm{sinc}(0.00509261p). \quad (5.17)$$

The waveform is shown in figure 5.18(b) and the experimental saturation profile is shown in figure 5.18(c). There is significant excitation inside the annular region due to the truncation of the sinc functions after only 3 zero-crossings.

5.4.3 Optimisation of Saturation Parameters

The degree of signal suppression is usually measured as the average intensity of the outer volume signal relative to the average signal inside the ROI (Singh *et al*., 1990a). However, for localised spectroscopy, a more relevant parameter is the degree of signal contamination, which is the total signal from the outer volume relative to the total signal from inside the ROI. Measuring the contamination accurately requires integrating the signal intensities from a 2D image, but the acquisition of images is very time-consuming, so the signal intensity of a 1D profile was used instead. The outer-volume saturation achieved by PROJSAT depends on the following parameters: the rotating gradient cycle, number of saturation pulses (*n*), saturation pulse power level (*sp*0), homospoil gradient strength, gradient switching delay (d2), homospoil gradient duration (d3) and dead time (d4) before the hard 90° pulse. These parameters were individually adjusted to minimise the signal contamination.

5.4.3.1 Experimental

A test sample of tap water in an NMR tube of o.d. 5 mm, i.d. 4.1 mm was placed inside a Bruker DMX 200 spectrometer equipped with a 4.7 T magnet and a 5 mm micro-imaging coil tuned to a ^{1}H resonance frequency of 199.700 MHz. A cylindrical

ROI was isolated at the centre of the sample using a train of r.f. pulses with the "cossinc1" waveform, and a profile was acquired using the pulse sequence in figure 5.16(b). The acquisition parameters were: 8 scans, repetition time 10 s, 256 FID points, spectral width 50 kHz for 5 mm field of view, hard 90° pulse duration 3.70 μs and soft pulse duration 500 μs. When they were not being optimised, the saturation parameters were held constant at the following values unless stated otherwise: rotating gradient 4.41 G/mm, 180° cycle, $n = 83$, $sp0 = 30$ dB, homospoil gradient 4.9 G/mm along the z direction, d2 = 1 ms, d3 = 2 ms, and d4 = 3 ms.

Each profile was integrated as shown in figure 5.19. The integral of the central peak, resulting from the magnetisation inside the ROI, was normalised to 1. The integrals of the low-intensity regions either side, resulting from the residual outer volume magnetisation, were taken as the degree of contamination.

5.4.3.2 Results

The optimum vales of the saturation parameters were found to be: 360° gradient cycle, $n = 95$, $sp0 = 28$ dB, homospoil gradient 7.35 G/mm, d2 = 1 ms, d3 = 1 ms, and d4 = 2 ms. A profile obtained with these parameters has 40% contamination for a cylindrical ROI with $d_i = 0.86$ mm and $d_o = 4.53$ mm (figure 5.20(a)). For a larger cylindrical ROI with $d_i = 1.33$ mm and $d_o = 4.53$ mm, the contamination is reduced to 9% (figure 5.19). Some saturation parameters are discussed in more detail below.

5.4.3.2.1 Rotating Gradient Cycle

In the original PROJSAT sequence, the rotating gradient only covers a single half-cycle of 180° so that each part of the outer volume is saturated once, but a longer gradient cycle with repeated saturation could improve outer volume signal suppression. Keeping $n = 64$ throughout, profiles were acquired where the gradient cycle was increased from 180° to 360°, 720° and 1440°. Little difference was found between the cycles larger than 360° (figure 5.21(a)), so repeated saturation did not improve signal suppression for the same number of saturation pulses.

5.4.3.2.2 Number of Saturation Pulses

A series of profiles was acquired with variable n (figure 5.22(a)). The signal suppression improved with the number of pulses and reached an optimum at $n = 83$ for a 180° gradient cycle and at $n = 95$ for a 360° gradient cycle (figure 5.21(b)).

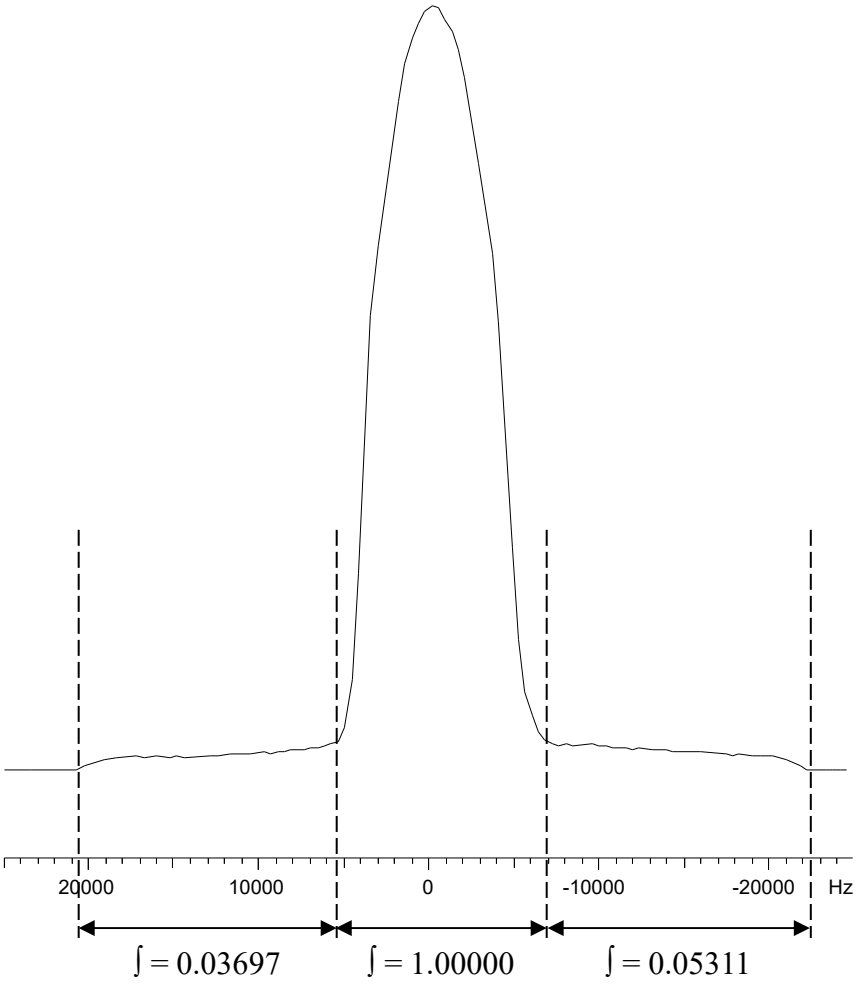

Figure 5.19 One-dimensional profile of a cylindrical VOI obtained using the PROJSAT sequence. The profile is integrated in three regions and the integral of the central region is normalised to 1.

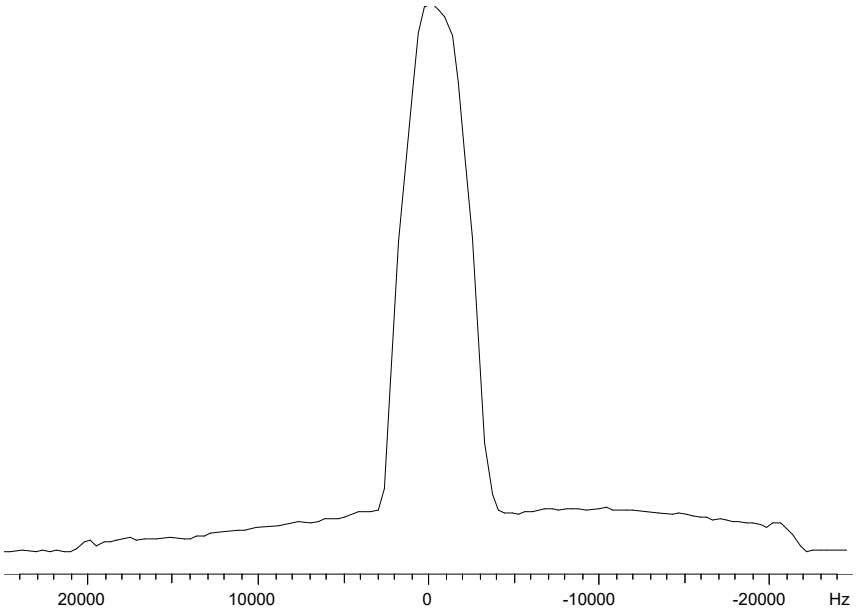

(a)

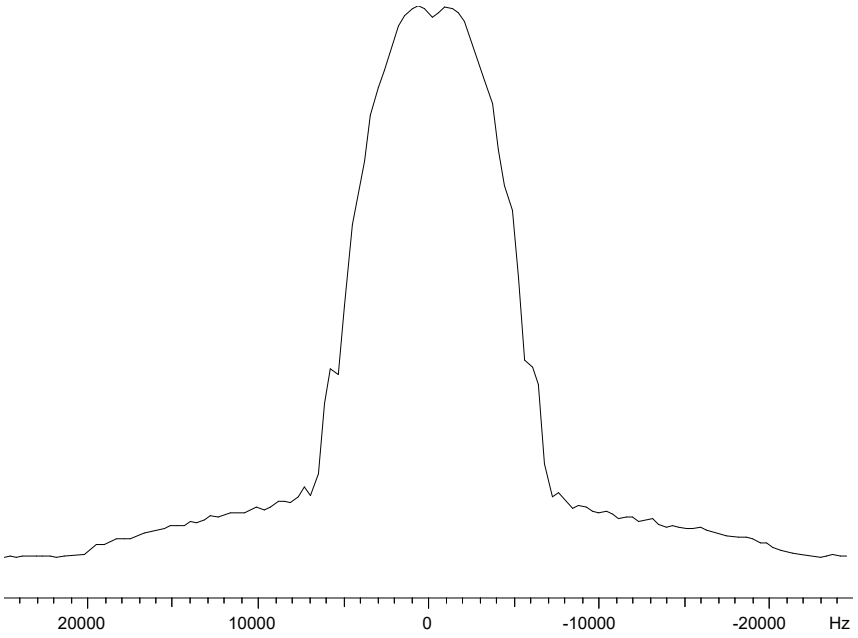

(b)

Figure 5.20 PROJSAT profiles acquired with optimised saturation parameters. *(a)* Original PROJSAT sequence with 180º cycle, *n* = 83, *sp*0 = 28 dB, d2 = 1 ms, d3 = 1 ms, d4 = 1 ms, homospoil gradient 4.9 G/mm along the *z* direction. *(b)* Modified PROJSAT sequence with 180º cycle, *n* = 83, *sp*0 = 28 dB, d2 = 0.2 ms, d3 = 0.1 ms, d4 = 1 ms, no homospoil gradient.

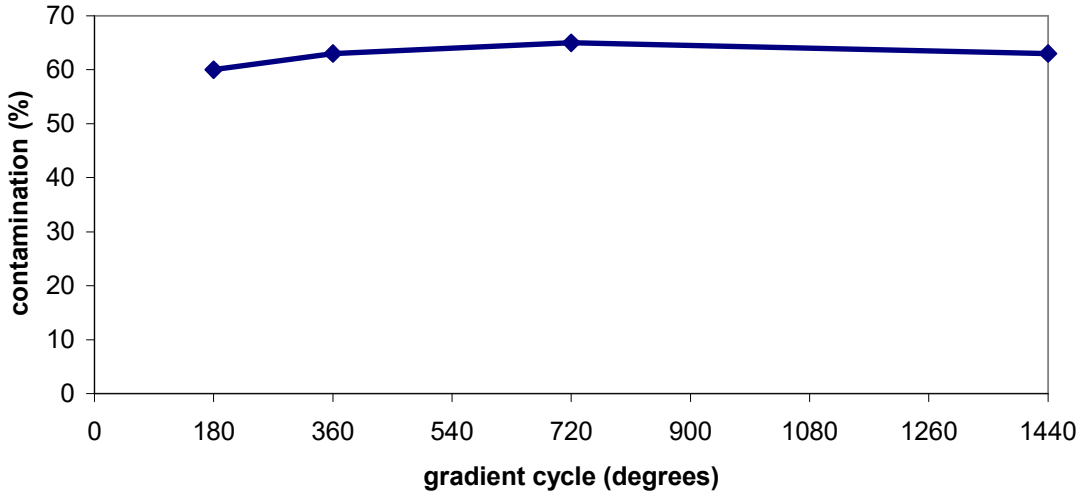

(a)

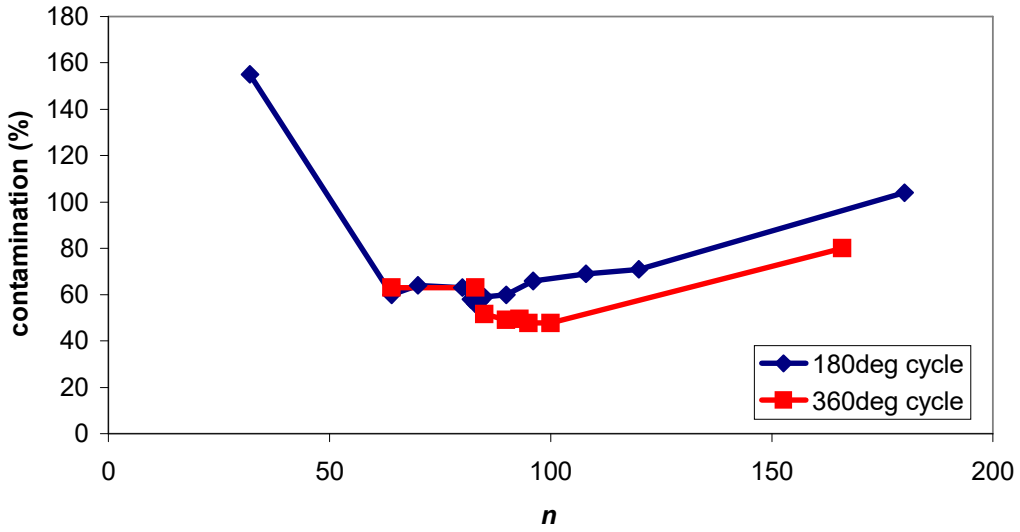

(b)

Figure 5.21 Effect of PROJSAT saturation parameters on signal contamination. *(a)* Variation of contamination with gradient cycle. *(b)* Variation of contamination with number of saturation pulses, *n*.

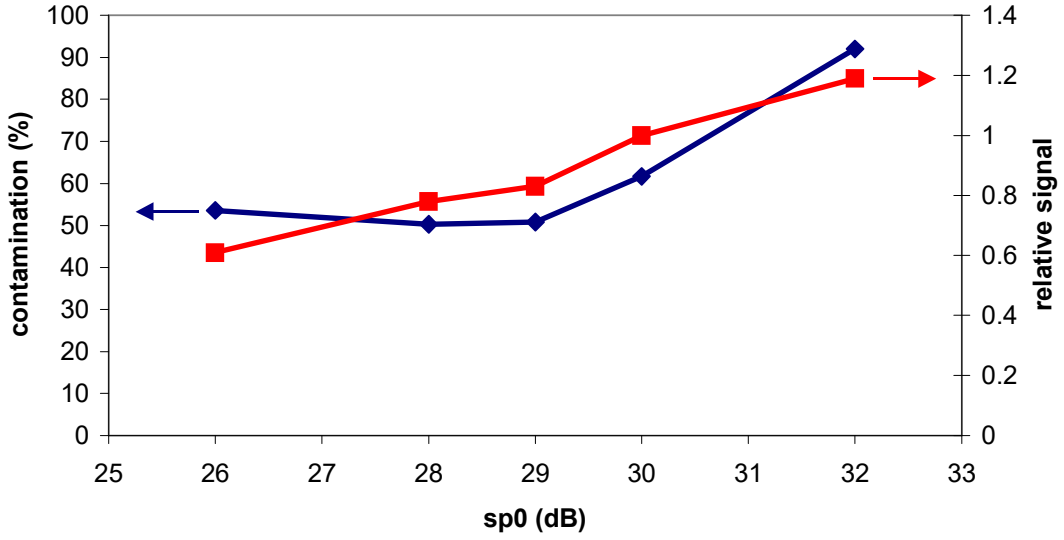

(c)

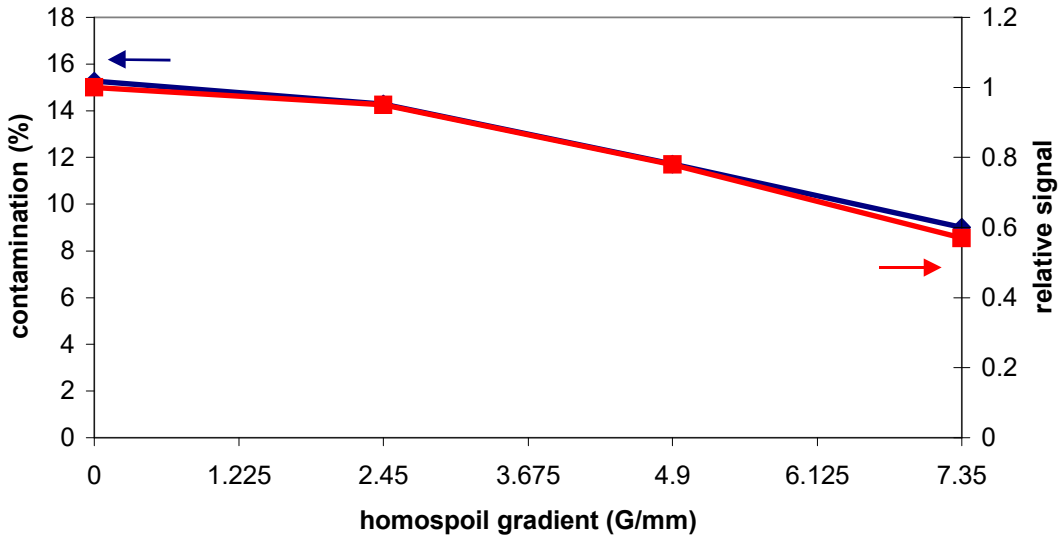

(d)

Figure 5.21 Effect of PROJSAT saturation parameters on signal contamination. *(c)* Variation of contamination and relative signal with soft pulse attenuation, *sp*0. *(d)* Variation of contamination and soft pulse signal with strength of homospoil gradient.

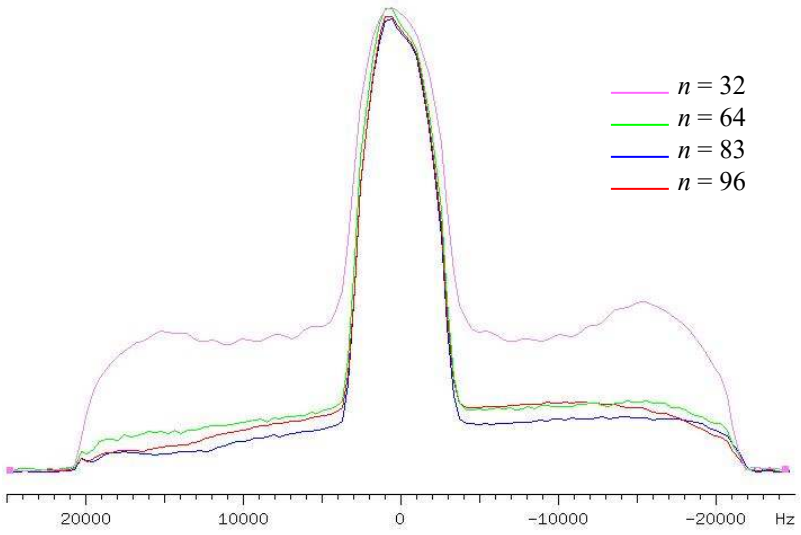

(a)

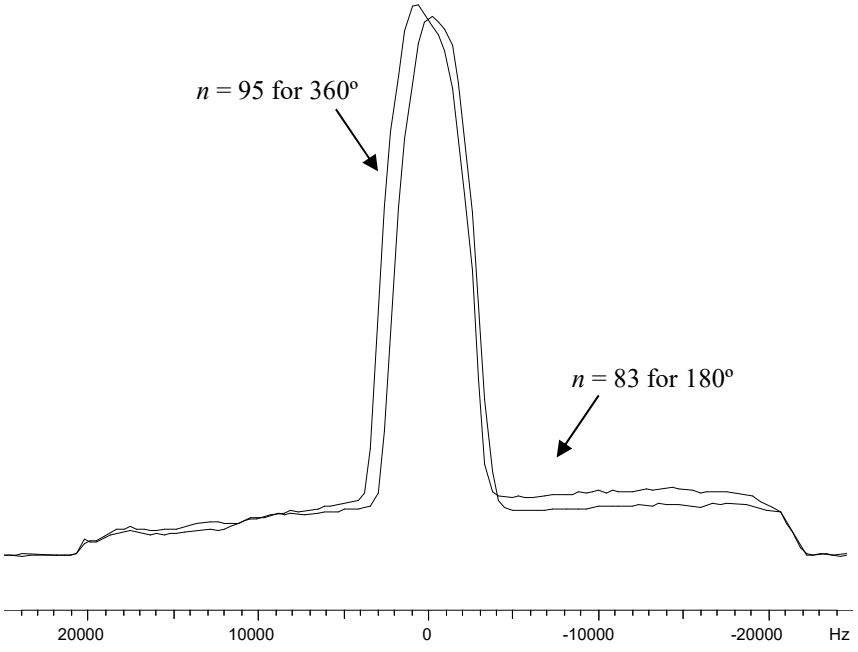

(b)

Figure 5.22 Optimisation of PROJSAT saturation parameters. *(a)* Increasing saturation is observed with increase in *n* for a 180º cycle. *(b)* The best saturation profiles with *n* = 83 for a 180º cycle and *n* = 95 for a 360º cycle (lower profile). The difference between them is very small.

With more pulses, the saturation train became long enough for partial longitudinal recovery of the magnetisation saturated by earlier pulses. The 360° cycle gave better signal suppression than the 180° cycle for $n \geq 85$, and the 360° optimum had less contamination (48%) than the 180° optimum (56%). The profiles obtained using a 360° cycle were also more symmetric (figure 5.22(b)).

5.4.3.2.3 Saturation Pulse Power Level

The r.f. saturation pulse duration was held constant at 500 μs so the pulse power level determined the tip angle (equation 2.15). The power attenuation level (in dB) for a tip angle of 180° was determined experimentally, then the attenuation level for a tip angle of 30° was calculated using:

$$sp0(\theta) = sp0(180) + 20\log_{10}\left(\frac{180}{\theta}\right), \qquad (5.18)$$

where $sp0(180)$ is the attenuation level for a 180° pulse and $sp0(\theta)$ is the attenuation level for a pulse of tip angle θ in degrees. A 180° pulse using the "cossinc1" waveform had $sp0(180) = 18$ dB, so for a 30° pulse $sp0(30) = 33.56$ dB. In practice, slightly lower attenuation levels gave better single-pulse excitation profiles.

A series of profiles was acquired where $sp0$ was varied between 26 dB and 32 dB for a 180° cycle with $n = 83$. The total signal in the ROI decreased as the pulse power (tip angle) increased, due to partial excitation of the magnetisation inside the ROI. The profile acquired with $sp0 = 28$ dB had the lowest contamination of 50% (figure 5.21(c)). The optimum power level was balanced between the reduction in signal inside the ROI at higher power and the reduction in saturation outside the ROI at lower power, both of which caused higher contamination.

5.4.3.2.4 Homospoil Gradient Strength

The homospoil gradient that was applied between the saturation pulses rapidly dephased the transverse magnetisation and improved the signal suppression. Various profiles were acquired with different homospoil gradient strengths (0 to 7.35 G/mm) with a 360° cycle, $n = 95$, $sp0 = 28$ dB, d3 = 1 ms, d4 = 2 ms, rotating gradient 2.45 G/mm and the other parameters as above. There was an inverse correlation between gradient strength and contamination and an identical correlation with relative signal inside the ROI (figure 5.21(d)) because the homospoil gradients dephased the

partially excited signal from both inside and outside the ROI. For the lowest contamination, the strongest homospoil gradient was used and the signal loss was compensated by increasing the receiver gain and acquiring more scans.

5.4.3.2.5 Continuous Gradients

The PROJSAT sequence caused the gradients to overheat due to the frequent gradient on and off switching, so a modified pulse sequence was written where the gradients were switched on at the beginning of the saturation train, ramped through the different values and only switched off at the end of the train (figure 5.23). The delays between pulses were reduced to d2 = 0.2 ms and d3 = 0.1 ms, so the saturation train was shorter, but the homospoil gradient was removed because it could not be applied for the entire train. The profile obtained using the modified PROJSAT sequence with optimum saturation parameters (figure 5.20(b)) had a more jagged shape and more contamination (18% versus 9%) than that from the original PROJSAT sequence.

5.4.4 PROJSAT Images

PROJSAT images were acquired with the optimum saturation parameters to verify that the tailored r.f. pulses selected the correct ROI. The image parameters were: field of view 5×5 mm^2, 64×64 pixels, 10 kHz/pixel and slice thickness 1 mm. The slice-selective pulse of duration 1 ms had a sinc waveform truncated after 5 zero-crossings, with *sp*0 = 36 dB for a 90° tip angle. The images required less outer-volume signal suppression than the profiles, so 32 saturation pulses were sufficient. Increasing the number of saturation pulses reduced the signal-to-noise ratio due to partial saturation inside the ROI. As expected, "cossinc1" excited a cylinder at the centre of the sample (figure 5.24(a)) and "cossinc2" excited an annulus (figure 5.24(b)). Both the original and modified PROJSAT sequences gave good outer volume suppression. The images showed little dependence on homospoil gradient strength or dead time.

5.4.5 PROJSAT Spectroscopy

There are no PROJSAT spectra published in the literature, although localised spectroscopy is mentioned as a possible application of PROJSAT (Singh and Brody, 1993). PROJSAT spectra were acquired of the water test sample using the "cossinc1" and "cossinc2" saturation pulses with optimised saturation parameters (figure 5.25). The spectra contained a single water peak with a broad, unusual lineshape, which was

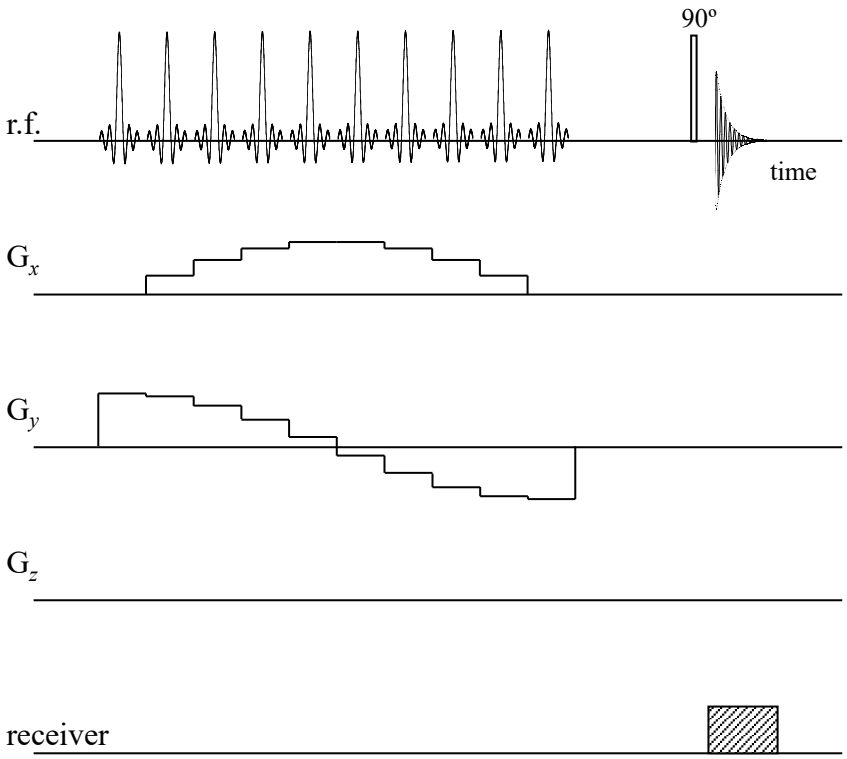

Phase Cycle								
saturation pulses	+*x*							
hard 90° pulse	+*x*	-*x*	-*x*	+*x*	+*y*	-*y*	-*y*	+*y*
receiver	+*x*	-*x*	+*x*	-*x*	+*y*	-*y*	+*y*	-*y*

Figure 5.23 Modified pulse sequence for PROJSAT spectroscopy. A train of tailored soft pulses and continuous rotating gradients saturates the outer volume magnetisation so that the hard 90º pulse gives a spectrum from the selected volume. The number of saturation pulses is variable. Ten have been shown for illustrative purposes.

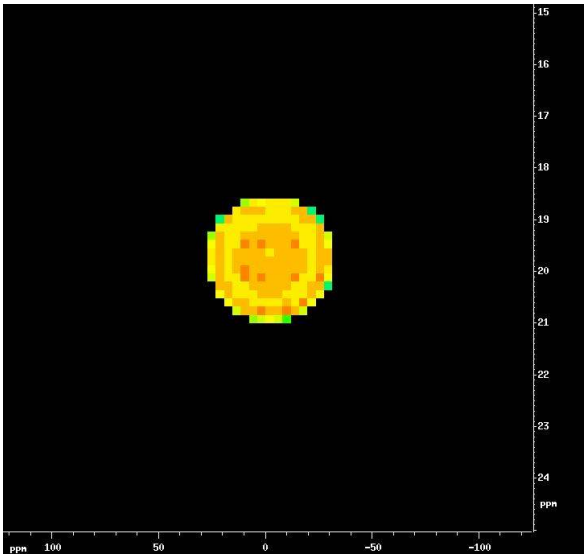

(a)

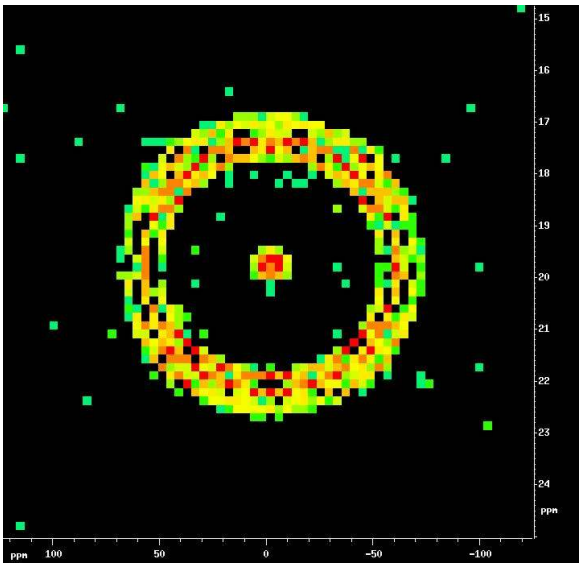

(b)

Figure 5.24 200 MHz ^{1}H PROJSAT images acquired to verify shapes of selected volumes. *(a)* Image of a cylindrical ROI of diameter 1.2 mm using "cossinc1" saturation pulse in a 180º cycle, $n = 32$. The image field of view is 5×5 mm^2. *(b)* Image of an annular ROI of thickness 0.7 mm using "cossinc2" saturation pulse in a 180º cycle, $n = 32$. The image field of view is 5×5 mm^2. Note the unsaturated magnetisation at the centre of the sample and the poor signal-to-noise ratio.

improved on removal of the homospoil gradient (figure 5.25(b)). The lineshape arose from the unsaturated magnetisation inside the entire sample, not just the ROI. The complex shape resulted from the uneven distribution of unsaturated magnetisation across the sample, but there was no clear correlation between specific parts of the lineshape and specific regions in the sample. A PROJSAT spectrum and a ZG spectrum on the same scale (figure 5.26(a)) revealed that the PROJSAT lineshape was much smaller and narrower than the Lorentzian lineshape in the ZG spectrum. The outer wings of the Lorentzian lineshape were suppressed most by PROJSAT, since they arose from the outer regions of the sample with slightly different resonance frequencies than the centre. The PROJSAT central peak was smaller than the ZG peak, indicating partial saturation of the magnetisation inside the ROI.

5.4.5.1 Effect of Saturation Parameters

Various spectra were acquired to study the effect of the saturation parameters on the PROJSAT lineshape. Increasing *sp*0 led to higher signal-to-noise ratios and larger high-frequency humps because the smaller tip angle reduced signal suppression. This also indicated that the hump arose from the unsuppressed magnetisation in the outer volume. The application of a homospoil gradient caused baseline oscillations and a negative dip in the lineshape reminiscent of those seen in STEAM spectra (figure 5.25(b)). Increasing the number of saturation pulses in a 180° cycle decreased the signal-to-noise ratio without decreasing the size of the high-frequency hump (figure 5.26(b)) because the increased signal suppression was accompanied by increased longitudinal recovery as the length of the saturation train increased. Increasing the dead time, d4, between the saturation train and the 90° pulse increased the signal-to-noise ratio, due to longitudinal recovery, and changed the pattern of baseline oscillations, due to the changing phase coherence of the incompletely saturated magnetisation with time.

Thus, it appears that the odd lineshape obtained using PROJSAT is inherent in the technique because it arises from the residual magnetisation after the saturation train. The outer-volume magnetisation is incompletely dephased, so it interferes with the FID from the ROI. Increasing the saturation, by adding a homospoil gradient or increasing the number of saturation pulses, does not improve the lineshape because a larger proportion of the magnetisation inside the ROI is saturated as well.

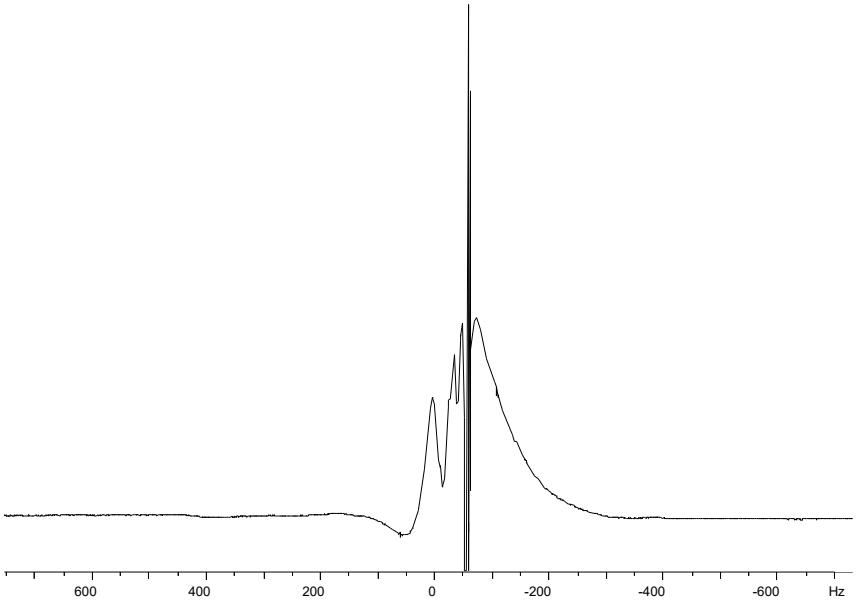

(a)

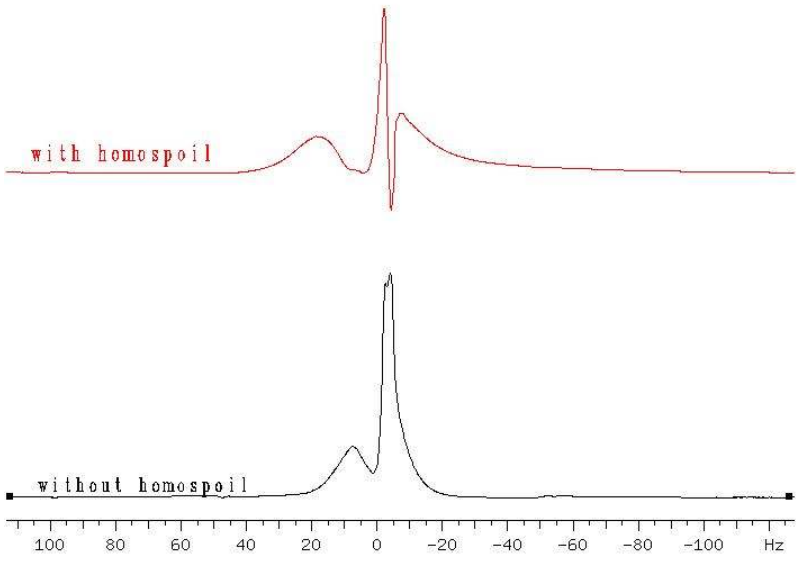

(b)

Figure 5.25 200 MHz ^{1}H PROJSAT spectra of water from two different selected volumes. *(a)* Spectrum of a cylindrical ROI of diameter 1.0 mm using "cossinc1" saturation pulse in a 180º cycle, n = 48, with homospoil gradient. *(b)* Spectra of an annular ROI of thickness 1.0 mm using "cossinc2" saturation pulse in a 180º cycle, n = 83, showing the effect of the homospoil gradient on the lineshape.

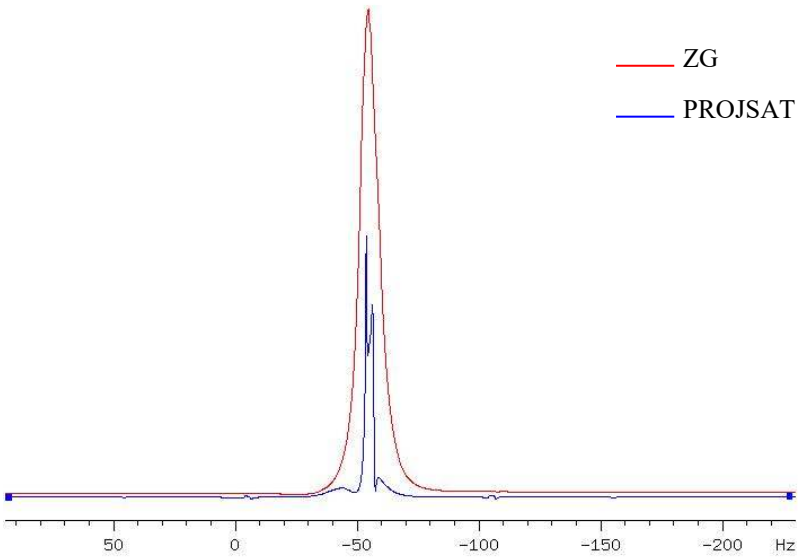

(a)

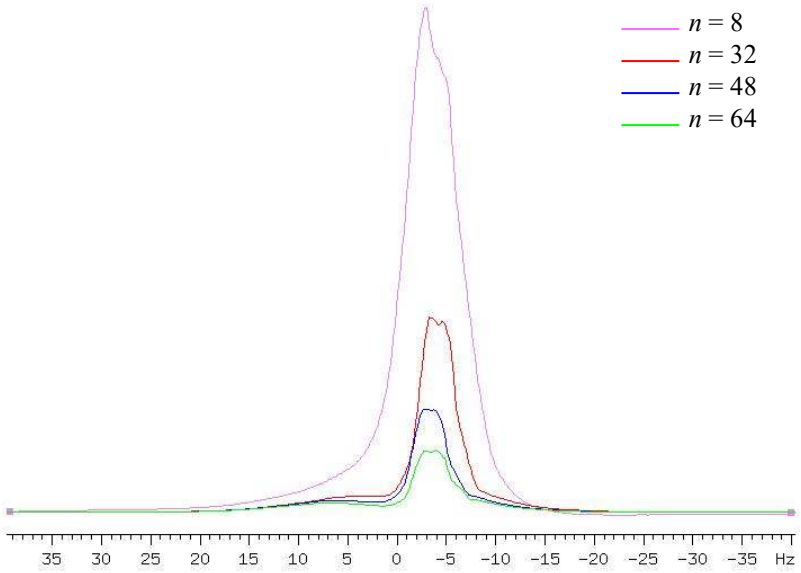

(b)

Figure 5.26 200 MHz ^{1}H spectra of water. *(a)* ZG spectrum and PROJSAT spectrum of a cylindrical ROI of diameter 1.0 mm. *(b)* PROJSAT spectra of an annular ROI of thickness 1.0 mm using "cossinc2" saturation pulses in a 180º cycle, showing the decrease in signal with n.

5.4.5.2 Compositions of Liquid Mixtures

Two liquid mixtures were used to test quantitative PROJSAT spectroscopy. The first was a four-component mixture containing methanol (35.71 mol%), toluene (8.88 mol%), ethyl acetate (30.61 mol%) and isooctane (24.80 mol%). The second was a five-component mixture containing methanol, toluene, cyclohexane, isooctane and ethyl acetate. The PROJSAT pulse sequence with continuous gradients was used with 32 "cossinc1" saturation pulses in a 180° cycle, no homospoil gradients, *sp*0 = 28 dB, d2 = 0.2 ms, d3 = 0.1 ms and d4 = 2 ms. Some outer-volume saturation was sacrificed for more manageable lineshapes. The spectra were processed manually due to the unusual lineshapes, and the compositions were determined from the integrals of the peaks including the high-frequency humps.

Nine different spectra of the four-component mixture were acquired, each with one parameter slightly different from those listed above (*sp*0 = 28 or 32 dB, *n* = 32, 64 or 96, cycle 180° or 360°, d2 = 0.2 or 0.4 ms, d4 = 2 or 5 ms). The composition results were very similar for all nine because the sample was homogenous, so the suppression quality did not affect the apparent composition. The mean composition from five PROJSAT spectra with *n* = 96 is shown in table 5.4, with the compositions measured from two ZG spectra and two STEAM spectra for comparison (acquisition parameters in section 5.3.4.1). Each technique gave a slightly different composition and the STEAM results were slightly closer to the ZG composition than the PROJSAT results. For the five-component mixture, the compositions measured using ZG, STEAM and PROJSAT also agreed with each other (table 5.5). However, in both cases the compositions measured by NMR differed slightly from those measured by weight due to evaporative losses during the experiments.

5.5 Conclusion

Two different approaches to volume-selective spectroscopy have been presented. STEAM is a selective excitation technique that uses a stimulated echo to localise the volume of interest (VOI) at the intersection of three orthogonal slices. PROJSAT is a presaturation technique that suppresses the unwanted signal from outside the VOI so that the spectrum only contains signals from inside the selected volume. Both techniques were optimised for quantitative high-resolution spectroscopy, in particular the parameters for accurate localisation and minimum signal contamination. These

	Composition by weight (mol%)	ZG	STEAM	PROJSAT
Methanol	35.71	33.67	33.91	35.60
Toluene	8.88	8.64	8.49	7.98
Ethyl acetate	30.61	30.39	28.94	30.40
Isooctane	24.80	27.30	28.66	26.02
Average error	---	*1.25*	*1.93*	*0.61*

Table 5.4 Composition of a four-component liquid mixture (in mol%) determined from several bulk and volume-selective NMR spectra using the pulse sequences ZG, STEAM and PROJSAT. The average error is calculated relative to the composition by weight. The uncertainty of the NMR values is ±0.5 mol% for ZG and ±1.5 mol% for STEAM and PROJSAT.

	Composition by weight (mol%)	ZG	STEAM	PROJSAT
Methanol	31.16	29.39±0.90	30.02±1.79	29.03±1.74
Toluene	22.69	26.14±0.49	27.03±0.96	26.67±0.94
Ethyl acetate	26.32	21.92±0.61	20.53±1.21	20.17±1.19
Cyclohexane	12.43	13.97±0.23	13.64±0.47	15.27±0.45
Isooctane	7.40	8.57±0.19	8.77±0.37	8.85±0.36
Average error	---	*2.47*	*2.77*	*3.31*

Table 5.5 Composition of five-component test mixture (in mol%) determined from three NMR spectra using the pulse sequences ZG, STEAM and PROJSAT respectively. The average error is calculated relative to the composition by weight. The quoted uncertainty values are based on the errors in the peak integrals.

parameters had not been considered in detail previously because STEAM and PROJSAT were originally developed for imaging.

STEAM gave good localisation of the VOI with low levels of signal contamination (10%) near the edges of the VOI. The composition measurements suffered from relaxation weighting, but they agreed with the compositions from bulk spectroscopy to within 1 mol%. A modified pulse sequence, STEAMQR, with balanced homospoil gradients, was inferior to the original sequence.

PROJSAT was better suited to imaging than spectroscopy. With optimum saturation parameters, the signal contamination was 40% from the entire sample. This form of contamination is more severe than the edge contamination of STEAM because it causes larger composition errors in heterogeneous samples. PROJSAT spectra did not contain any relaxation weighting but they contained very unusual lineshapes from the unsaturated magnetisation in the sample. The compositions determined from PROJSAT spectra had similar accuracy to STEAM and agreed with the compositions from bulk spectroscopy to within 1 mol%. A drawback of PROJSAT is its inability to change the position of the VOI inside the sample without designing a new set of tailored pulses. In comparison, the VOI selected using STEAM can be moved by merely changing the offset frequencies of the soft 90° pulses.

Both STEAM and PROJSAT can be improved by the use of better soft pulses tailored to minimise unwanted excitation. The partially excited signals from outside the VOI cause signal contamination in STEAM, and signal loss from the partially saturated signals from inside the VOI in PROJSAT increases the relative contribution of the contaminant signal from outside the VOI. There is a pulse sequence called ROISTER, similar to PROJSAT, that uses optimised noise pulses to randomise the phase of the magnetisation outside the VOI (de Crespigny *et al.*, 1989), but we could not test it because insufficient detail was provided to duplicate the pulse optimisation procedure.

5.6 References

Callaghan, P.T. (1991). *Principles of Nuclear Magnetic Resonance Microscopy*, pp. 75, 93-105. Clarendon Press, Oxford, UK.

Crespigny, A.J.S. de, Carpenter, T.A., & Hall, L.D. (1989). Region-of-interest selection by outer-volume saturation. *Journal of Magnetic Resonance, 85*, 595-603.

Crooks, L.E. (1996). Image formation methods. In D.M. Grant & R.K. Harris (Eds.), *Encyclopedia of Nuclear Magnetic Resonance, vol. 4*, pp. 2439-2450. John Wiley & Sons, Chichester, UK.

Frahm, J., Merboldt, K.D., Hänicke, W., & Haase, A. (1985). Stimulated echo imaging. *Journal of Magnetic Resonance, 64*, 81-93.

Frahm, J., Merboldt, K.D., & Hänicke, W. (1987). Localized proton spectroscopy using stimulated echoes. *Journal of Magnetic Resonance, 72*, 502-508.

Frahm, J., & Hänicke, W. (1996). Single voxel proton NMR: human subjects. In D.M. Grant & R.K. Harris (Eds.), *Encyclopedia of Nuclear Magnetic Resonance, vol. 7*, pp. 4407-4423. John Wiley & Sons, Chichester, UK.

Gladden, L.F. (1994). Nuclear magnetic resonance applications in chemical engineering: principles and applications. *Chemical Engineering Science, 49*, 3339-3408.

Granot, J. (1986). Selected volume excitation using stimulated echoes (VEST). Applications to spatially localized spectroscopy and imaging. *Journal of Magnetic Resonance, 70*, 488-492.

Hahn, E.L. (1950). Spin echoes. *The Physical Review, 80*, 580-594.

Hutchison, J.M.S. (1996). Spin warp data acquisition. In D.M. Grant & R.K. Harris (Eds.), *Encyclopedia of Nuclear Magnetic Resonance, vol. 7*, pp. 4535-4541. John Wiley & Sons, Chichester, UK.

Kimmich, R., & Hoepfel, D. (1987). Volume-selective multipulse spin-echo spectroscopy. *Journal of Magnetic Resonance, 72*, 379-384.

Sattin, W., Mareci, T.H., & Scott, K.N. (1985a). Exploiting the stimulated echo in nuclear magnetic resonance imaging. I. Method. *Journal of Magnetic Resonance, 64*, 177-182.

Sattin, W., Mareci, T.H., & Scott, K.N. (1985b). Exploiting the stimulated echo in nuclear magnetic resonance imaging. II. Applications. *Journal of Magnetic Resonance, 65*, 298-307.

Singh, S., Rutt, B.K., & Henkelman, R.M. (1990a). Projection presaturation: a fast and accurate technique for multidimensional spectral localization. *Journal of Magnetic Resonance, 87*, 567-683.

Singh, S., Rutt, B.K., & Napel, S., (1990b). Projection presaturation. II. Single-shot localisation of multiple regions of interest. *Journal of Magnetic Resonance, 90*, 313-329.

Singh, S., Taylor, C.P.S., & Rutt, B.K. (1992). Application of projection presaturation to localized proton relaxomtry. *Journal of Magnetic Resonance, 98*, 49-61.

Singh, S., & Brody, W.R. (1993). Projection presaturation. III. Accurate selective excitation or presaturation of the regions of tailored shape in the presence of short-T_1 species. *Journal of Magnetic Resonance, Series B, 101*, 52-62.

Stejskal, E.O., & Tanner, J.E. (1965). Spin diffusion measurements: spin echoes in the presence of a time-dependent field gradient. *The Journal of Chemical Physics, 42*, 288-292.

Yongbi, N.M., Payne, G.S., Collins, D.J., & Leach, M.O. (1995). Quantification of signal selection efficiency, extra volume suppression, and contamination for ISIS, STEAM and PRESS localized ^{1}H NMR spectroscopy using an EEC localization test object. *Physics in Medicine and Biology, 40*, 1293-1303.

Zijl, P.C.M. van, Moonen, C.T.W., Alger, J.R., Cohen, J.S., & Chesnick, S.A. (1989). High field localized proton spectroscopy in small volumes: greatly improved localization and shimming using shielded strong gradients. *Magnetic Resonance in Medicine, 10*, 256-265.

5.7 Nomenclature

(symbol)	(description)	(unit)
Vector Variables		
g	magnetic field gradient	T m^{-1}
r	position	m
Scalar Variables		
b	base of rectangle in saturation profile for cylinder	m
b_1	base of inner rectangle in saturation profile for annulus	m
b_2	base of outer rectangle in saturation profile for annulus	m
b_ν	frequency range of rectangle in saturation profile	s^{-1}
$b_{1\nu}$	frequency range of inner rectangle in saturation profile	s^{-1}
$b_{2\nu}$	frequency range of outer rectangle in saturation profile	s^{-1}
B_0	magnitude of static magnetic field $\mathbf{B_0}$	T
c	centre of rectangle in saturation profile for cylinder	m
c_1	centre of inner rectangle in saturation profile for annulus	m
c_2	centre of outer rectangle in saturation profile for annulus	m
c_ν	central frequency of rectangle in saturation profile	s^{-1}
$c_{1\nu}$	central frequency of inner rectangle in saturation profile	s^{-1}
$c_{2\nu}$	central frequency of outer rectangle in saturation profile	s^{-1}
d2	delay between gradient switching and soft pulse	s
d3	duration of homospoil gradient	s
d4	dead-time between end of saturation train and 90° pulse	s
d_i	diameter of inner, unsaturated volume	m
d_o	diameter of outer, saturated volume	m
D	self-diffusion coefficient	$m^2\ s^{-1}$
g_x, g_y, g_z	strength of magnetic field gradient along x, y, z axes	T m^{-1}
n	number of pulses in PROJSAT saturation train	-
p	point index in waveform for tailored r.f. pulse	-
S	time-domain signal	-
S_0	signal before diffusion attenuation	-
*sp*0	soft pulse power attenuation level	dB
t	time	s
t_a	thickness of annulus	m
t_p	duration of radio-frequency (r.f.) pulse	s
t_x	duration of gradient applied along x axis	s
T_1	longitudinal relaxation time constant	s
T_2	spin-spin relaxation time constant	s
T_2*	observed transverse relaxation time constant	s

V	volume	m^3
x, y, z	Cartesian axes: z is parallel to static magnetic field $\mathbf{B_0}$	-
γ	gyromagnetic ratio	rad T^{-1} s^{-1}
δ	duration of pulsed magnetic field gradient	s
Δ	delay between two pulsed magnetic field gradients	s
θ	tip angle of soft r.f. pulse	deg
ν	frequency	s^{-1}
$\rho(\mathbf{r})$	local spin density at position $\mathbf{r}$	m^{-3}
τ	delay between 90° and 180° pulses in spin-echo sequence	s
τ_1	delay between first and second 90° pulses in stimulated echo sequence	s
τ_2	delay between second and third 90° pulses in stimulated echo sequence	s
τ_3	delay between third 90° pulse and stimulated echo	s
ϕ	gradient-induced phase shift	rad
ω	angular frequency	rad s^{-1}
ω_0	resonance frequency in static magnetic field $\mathbf{B_0}$	rad s^{-1}

6 NMR SPECTROSCOPY OF FLOWING STREAMS

6.1 Introduction

The NMR techniques for high-resolution spectroscopy using ZG, STEAM and PROJSAT have been optimised to give accurate, quantitative compositions of non-flowing liquid mixtures. In this chapter, their application is extended to cover liquid mixtures that are flowing along the direction of the magnetic field. The flowing mixtures are models for an industrial set-up in which a process line is passed through an NMR apparatus for measuring its composition, *e.g.* a sideline from a reaction vessel used to monitor the extent of reaction. Previous applications of NMR spectroscopy to flowing samples have included monitoring chemical reactions (Dorn, 1996) or the growth of bacteria (Chen and Bailey, 1993).

Due to the motion of the nuclei in the magnetic field, the NMR signal acquired from a flowing sample differs from that of a static sample. NMR spectra of flowing samples exhibit increased sensitivity (signal-to-noise per unit time) relative to those of static samples because the flowing sample is continually refreshed, so the inter-scan delay for longitudinal relaxation is not needed (Laude *et al.*, 1984; Sudmeier *et al.*, 1996). "Lifetime" broadening of the peaks is caused by the motion of excited nuclei out of the detection coil during signal acquisition (Laude *et al.*, 1985b; Dorn, 1996). Several analyses have been published to explain the effects of flow on NMR signals (Laude *et al.*, 1984, 1985a; Sudmeier *et al.*, 1996; Lee *et al.*, 1999). However, they are all incorrect, probably due to ignorance of fluid mechanics among NMR spectroscopists. Some principles of fluid mechanics are presented and used to derive a correct description of the flowing NMR signal, which is a convolution of the static NMR signal with the residence time distribution of the nuclei in the detection coil. Experimental results are presented to support this new description and show the effect of increasing flow rate on the quantitative composition measurement of a single-phase multi-component stream.

Volume-selective spectroscopy of multi-component flowing liquid streams is then considered. The interaction of moving nuclei with magnetic field gradients is well studied as part of NMR flow visualisation and measurement techniques that use magnetic field gradients to encode higher derivatives of position (Caprihan and

Fukushima, 1990; Fukushima, 1999). A flow-compensated STEAM pulse sequence (STEAM_FC) is used to acquire volume-selective spectra from a flowing sample. Experimental results are presented to show the accuracy of quantitative composition measurements from volume-selective spectra obtained from multi-component flowing liquid streams – single-phase mixtures and emulsions – using STEAM, STEAM_FC and PROJSAT at various flow rates.

6.2 The Effect of Flow on NMR Spectroscopy

Flow NMR experiments typically consist of flowing a liquid through the magnet inside a cylindrical pipe. A long section of pipe upstream of the detection coil allows the flow to stabilise and the nuclei to spend enough time in the magnet to align themselves with the magnetic field. The velocity profiles for laminar, turbulent and plug flow are used to derive residence time distributions for the nuclei inside the flow loop, the magnet and the detection coil. The residence time distributions are then used to explain lifetime broadening, sensitivity enhancement and apparent relaxation enhancement. These effects were observed by various groups, but were explained incorrectly (Laude *et al.*, 1984, 1985a, 1985b; Sudmeier *et al.*, 1996; Dorn, 1996; Lee *et al.*, 1999). No previous analysis in the literature of NMR spectroscopy under flowing conditions has discussed residence time distributions.

6.2.1 Theory

For a liquid flowing through a cylindrical pipe at a constant flow rate, there are two possible flow regimes (Reynolds, 1883). At low flow rates, the flow is steady and the fluid velocity at a fixed position does not vary with time. This is the laminar flow regime where viscous effects dominate. At higher flow rates, the flow contains random eddies and the fluid velocity at a fixed position fluctuates about a well-defined mean. This is the turbulent flow regime where momentum effects dominate. The transition between laminar and turbulent flow takes place at a fixed value of the Reynolds number, Re, which is defined as:

$$\mathrm{Re} = \frac{\rho u d}{\mu}, \tag{6.1}$$

where ρ and μ are respectively the density and viscosity of the fluid, u is the fluid velocity and d is the diameter of the pipe. Reynolds observed the laminar-turbulent transition at Re = 2200.

For both laminar and turbulent flow, the fluid velocity varies with radial position in the pipe. It is described by a function called the velocity profile. The velocity profile for laminar flow is a parabola (figure 6.1(a)) and is given by (Kay and Nedderman, 1985):

$$\frac{u_r}{u_0} = 1 - \frac{r^2}{a^2}, \tag{6.2}$$

where u_r is the velocity at radius r, u_0 is the centreline velocity and a is the radius of the pipe. This parabolic profile has been observed in numerous NMR flow visualisation experiments (Kose *et al.*, 1985; Callaghan, 1991). An experimental velocity profile for water flowing at 20 ml/min in a 4.1-mm diameter tube, Re = 104, is shown in figure 6.1(b).

The volumetric flow rate, Q, is obtained by integrating the velocity profile over the cross-section of the pipe:

$$Q = \int_0^a u_r \cdot 2\pi r \, dr = \frac{u_0}{2} \pi a^2 . \tag{6.3}$$

The mean velocity is defined by:

$$\bar{u} = \frac{Q}{\pi a^2}, \tag{6.4}$$

so the laminar mean velocity is given by:

$$\bar{u} = \frac{u_0}{2}. \tag{6.5}$$

The "1/7th power law" velocity profile (figure 6.1(c)) is an approximation to the actual velocity profile in turbulent flow and is given by (Kay and Nedderman, 1985):

$$\frac{u_r}{u_0} = \left(1 - \frac{r}{a}\right)^{1/7}. \tag{6.6}$$

The volumetric flow rate is given by:

(a)

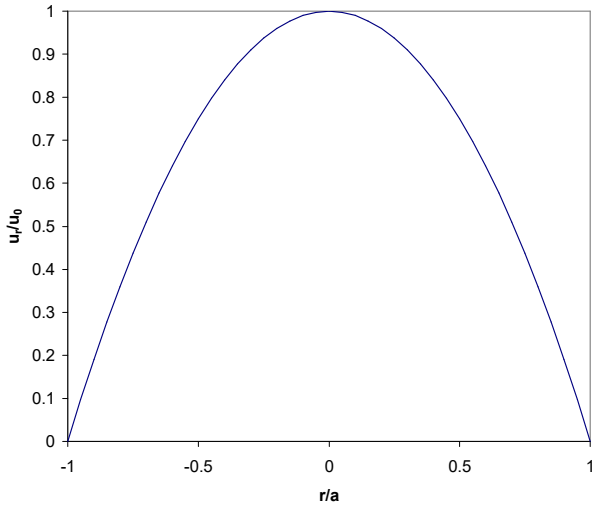

(b)

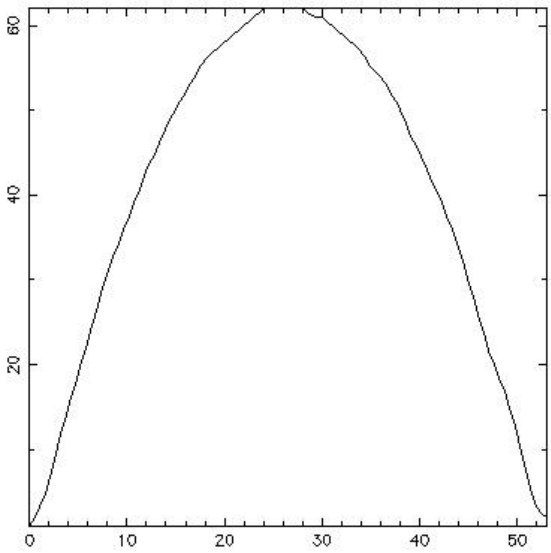

(c)

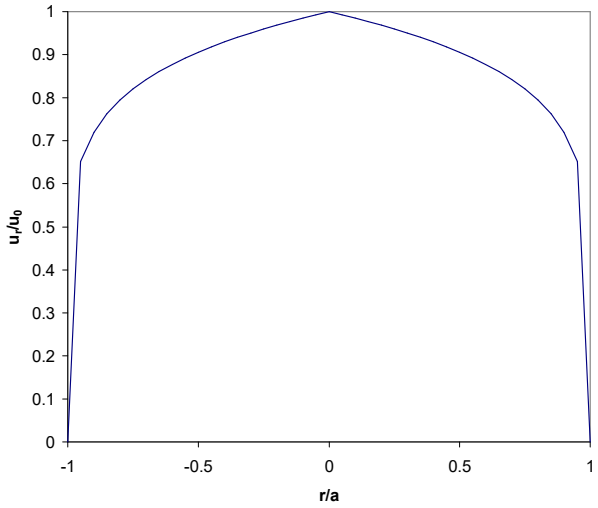

Figure 6.1 *(a)* Parabolic velocity profile for laminar flow. *(b)* Experimental laminar velocity profile for water flowing at 20 ml/min through a 4.1-mm diameter pipe. The spatial resolution is 78 μm/pixel. *(c)* $1/7^{th}$ power law velocity profile for turbulent flow.

$$Q = \int_0^a u_r \cdot 2\pi r \, dr = \frac{49}{60} u_0 \pi a^2 , \tag{6.7}$$

and the turbulent mean velocity is given by:

$$\bar{u} = \frac{49}{60} u_0 . \tag{6.8}$$

Plug flow is a hypothetical flow regime with a flat velocity profile such that:

$$\frac{u_r}{u_0} = 1, \quad Q = u_0 \pi a^2, \quad \bar{u} = u_0 . \tag{6.9}$$

The term "plug flow" refers to a type of chemical reactor in which "fluid flows through the reactor with no mixing of earlier and later entering fluid and with no overtaking" (Levenspiel, 1979). The plug flow model applies to packed bed or tubular reactors only. Laude, Sudmeier, Dorn, Lee and others think that liquids flowing in pipes undergo plug flow, but they are wrong. It will be shown below that the plug flow assumption is the reason why all published analyses of the effect of flow on NMR signals are incorrect.

6.2.2 Derivation of Residence Time Distributions

A useful concept in the analysis of flow behaviour is the residence time, which is the length of time a fluid element spends in a vessel or pipe section. Consider the flow apparatus shown in figure 6.2, where a sampling stream from a vessel circulates continuously through a magnet with a r.f. probe. The composition of the sampling stream is obtained from the NMR spectrum of the stream as it flows through the r.f. coil. In this apparatus, there are three important residence times:

1. The time to flow from the vessel being monitored to the detection coil: This determines the "age" of the measurement.
2. The residence time inside the magnet: This determines the build-up of net magnetisation before the r.f. pulse.
3. The residence time inside the detection coil after the r.f. pulse: This determines the decay of the NMR signal due to the flow of nuclei out of the coil.

Since the fluid velocity varies with radial position, there is a distribution of residence times in each case instead of a single value. The shape of the distribution depends on the flow regime.

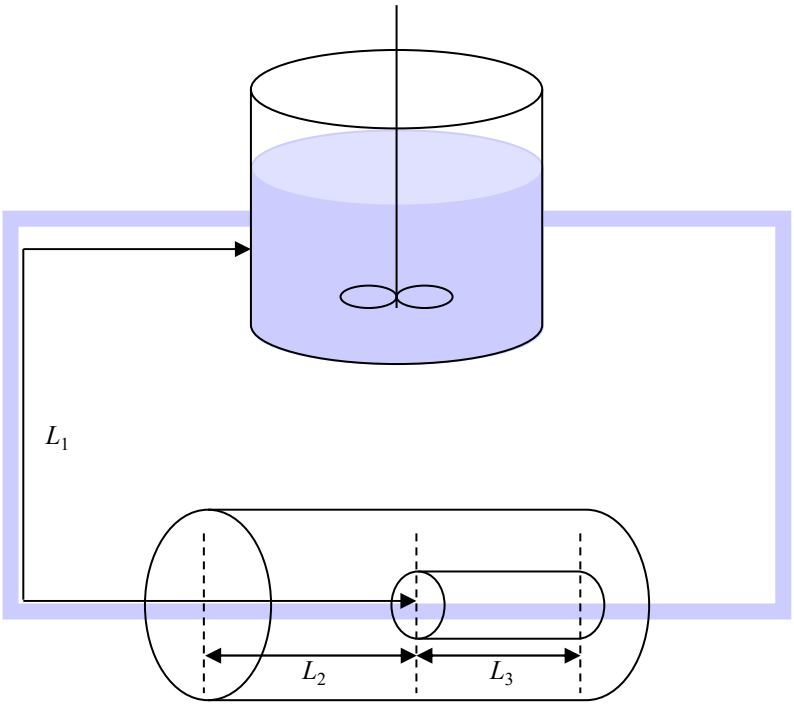

Figure 6.2 Flow loop for monitoring vessel contents by passing a sampling stream through a magnet and r.f. detection coil. The distance from the vessel to the detection coil is L_1, the length of the magnet upstream of the detection coil is L_2 and the length of the detection coil is L_3.

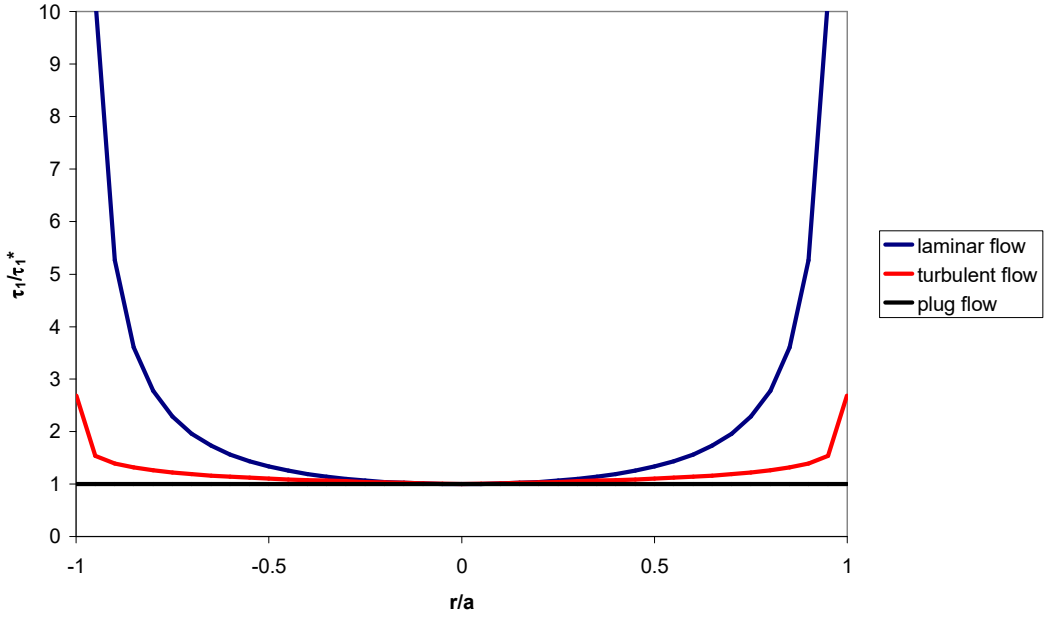

Figure 6.3 Variation of exit age (τ_1/τ_1^*) with radial position (r/a) for laminar, turbulent and plug flow inside a circular pipe.

6.2.2.1 Exit Age Distributions

A fluid element flowing at a velocity u_r travels a distance L_1 from the vessel to the detection coil in a time τ_1 given by:

$$\tau_1 = \frac{L_1}{u_r}. \tag{6.10}$$

τ_1 is called the exit age of the fluid element; it represents the delay before a sample from the vessel reaches the monitoring apparatus, so a change in composition inside the vessel is not detected until a time τ_1 later. At any position along the pipeline, the radial distribution of velocities gives an equivalent distribution of exit ages. The shortest exit age belongs to the fastest-moving fluid at the centre of the stream and is given by:

$$\tau_1^* = \frac{L_1}{u_0}. \tag{6.11}$$

The radial distribution of exit ages is the inverse of the velocity profile and is given by:

$$\frac{\tau_1}{\tau_1^*} = \frac{L_1/u_r}{L_1/u_0} = \frac{u_0}{u_r}. \tag{6.12}$$

Therefore, the exit age distribution for laminar flow is given by:

$$\frac{\tau_1}{\tau_1^*} = \left(1 - \frac{r^2}{a^2}\right)^{-1}, \tag{6.13}$$

and for turbulent flow by:

$$\frac{\tau_1}{\tau_1^*} = \left(1 - \frac{r}{a}\right)^{-1/7}. \tag{6.14}$$

For plug flow, the exit age is τ_1^* over the entire cross-section of the coil. The three radial exit age distributions are shown in figure 6.3.

The radial exit age distribution means that at any one time the detector coil contains fluid elements that left the vessel at different times. Since an NMR spectrum of the stream gives the average composition of the stream inside the detector coil, the composition measured by NMR is a time-average of the composition of the vessel

during the period $-\infty \le t \le -\tau_1^*$ before the measurement at $t = 0$. The weighting function for the time averaging of the vessel composition is the histogram of exit age values across the pipe. This histogram, or probability distribution, is obtained by using the method of random variables outlined in section 4.3.4. The independent variable is the radius r, which has a normalised probability given by:

$$f_1(r) = \frac{2r}{a^2} \qquad 0 \le r \le a \,. \tag{6.15}$$

The two dependent variables are u_r and τ_1. The probabilities of both dependent variables are calculated using the transformation law of probabilities given by (Port, 1994):

$$\begin{aligned} Y &= \Phi(X) \\ f_2(Y) &= f_1\left(\Phi^{-1}(Y)\right)\left|\frac{\partial}{\partial Y}\left(\Phi^{-1}(Y)\right)\right| \end{aligned} \,. \tag{6.16}$$

For laminar flow, the inverted functions $X=\Phi^{-1}(Y)$ are given by:

$$\begin{aligned} r &= a\left(1-\frac{u_r}{u_0}\right)^{1/2} \\ r &= a\left(1-\frac{\tau_1^*}{\tau_1}\right)^{1/2} \end{aligned} \,, \tag{6.17}$$

so $f_2(u_r)$ and $f_2(\tau_1)$ are given by:

$$\begin{aligned} f_2(u_r) &= \frac{1}{u_0} \\ f_2(\tau_1) &= \frac{\tau_1^*}{\tau_1^{\,2}} \end{aligned} \,. \tag{6.18}$$

The equivalent expressions for turbulent flow are given by:

$$\begin{aligned} f_2(u_r) &= 14\left(\frac{u_r^{\,6}}{u_0^{\,7}} - \frac{u_r^{\,13}}{u_0^{\,14}}\right) \\ f_2(\tau_1) &= 14\left(\frac{\tau_1^{*7}}{\tau_1^{\,8}} - \frac{\tau_1^{*14}}{\tau_1^{\,15}}\right) \end{aligned} \,. \tag{6.19}$$

The probability distributions for u_r and τ_1 are shown in figure 6.4.

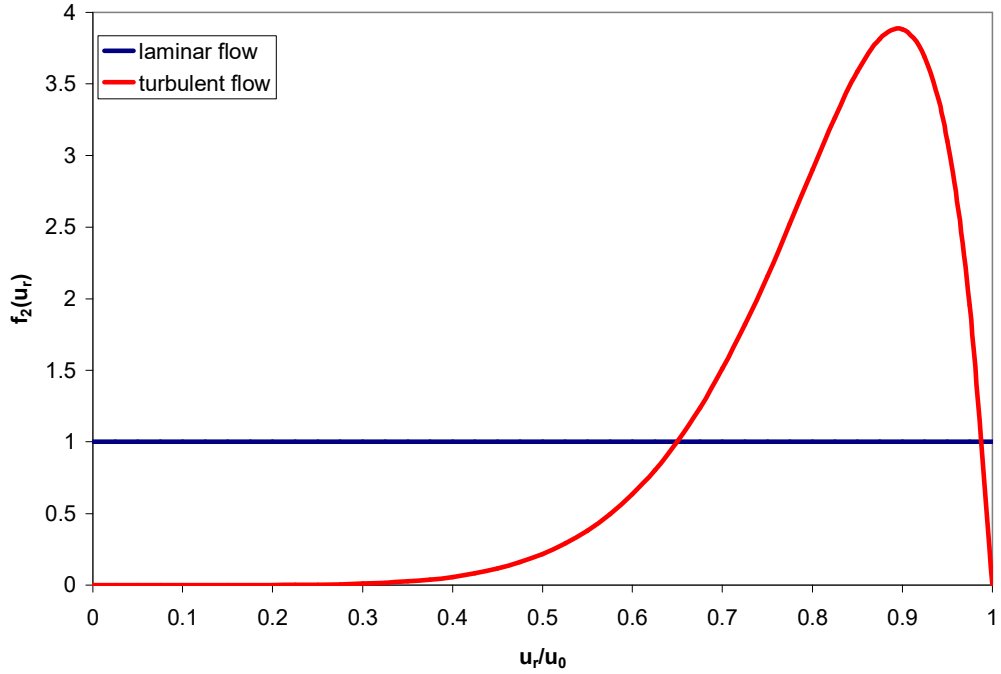

(a)

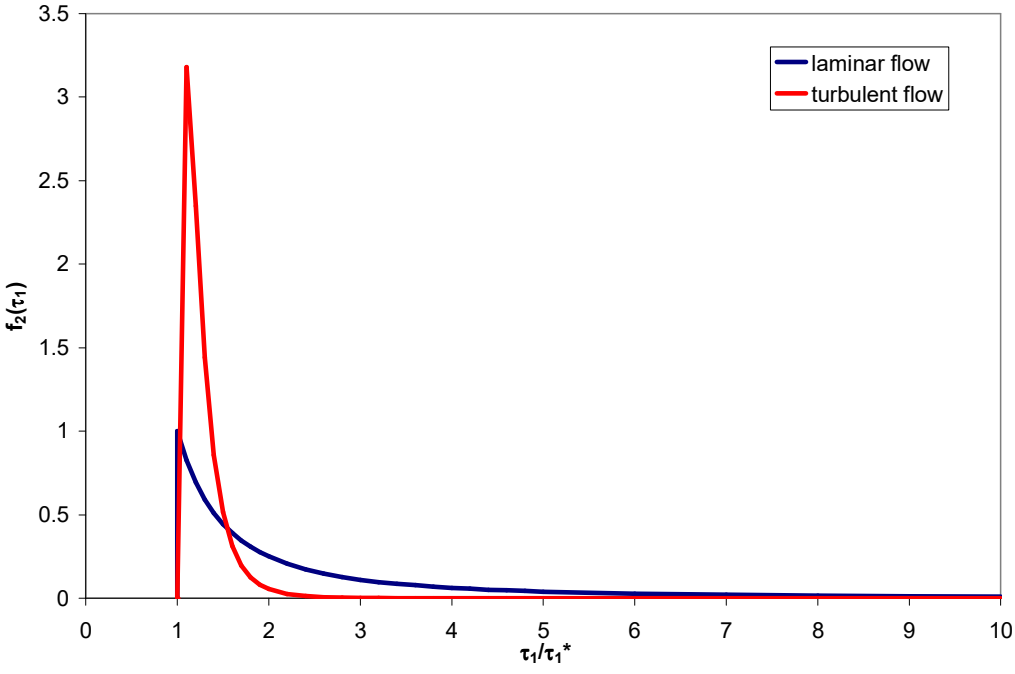

(b)

Figure 6.4 *(a)* Normalised probability distribution for velocity u_r for laminar and turbulent flow.
(b) Normalised probability distribution for exit age τ_1 for laminar and turbulent flow.

Measuring the vessel composition by means of a sample stream is therefore subject to a delay due to the pipe length L_1, and time averaging due to the velocity distribution. Both the delay and the averaging period depend on the minimum exit age τ_1^*, so they are shorter when the pipe length L_1 is small or the velocity u_0 is large, or both. The averaging period can also be reduced by measuring the composition of the fluid at the centre of the stream only, so that the fluid elements with long exit ages do not contribute to the measurement. For a cylinder of radius r at the centre of the pipe, the period for which the average composition is measured is $-\tau_1^* u_0/u_r \le t \le -\tau_1^*$ for a measurement at $t = 0$. For example, if the radius of the cylinder is $r = a/2$, then the period is $-1.33\tau_1^* \le t \le -\tau_1^*$ for laminar flow and $-1.10\tau_1^* \le t \le -\tau_1^*$ for turbulent flow. The mean exit age of the fluid inside a central cylinder of radius r is calculated using the formula:

$$\bar{\tau}_1 = \frac{\int_0^r 2\pi r \tau_1 \, dr}{\int_0^r 2\pi r \, dr}. \tag{6.20}$$

For laminar flow this yields:

$$\bar{\tau}_1 = -\tau_1^* \left(\frac{r}{a}\right)^{-2} \ln\left(1 - \left(\frac{r}{a}\right)^2\right), \tag{6.21}$$

and for turbulent flow:

$$\bar{\tau}_1 = \frac{7}{39}\tau_1^* \left\{ 7\left(\frac{r}{a}\right)^{-2}\left[1 - \left(1 - \frac{r}{a}\right)^{6/7}\right] - 6\left(\frac{r}{a}\right)^{-1}\left(1 - \frac{r}{a}\right)^{6/7} \right\}. \tag{6.22}$$

For example, the mean exit age for a cylinder of radius $r = a/2$ is $1.15\tau_1^*$ for laminar flow and $1.06\tau_1^*$ for turbulent flow. Therefore, monitoring the centre of a sampling stream can reveal short-term changes – of the order of the minimum exit age – in the process vessel. Volume-selective NMR spectroscopy is ideally suited to this task, and shows the unique advantage of NMR for rapid on-line monitoring of a time-varying sample. However, it should be noted that the acquisition of several scans, needed for a good signal-to-noise ratio, is another time-averaging factor in the measurement.

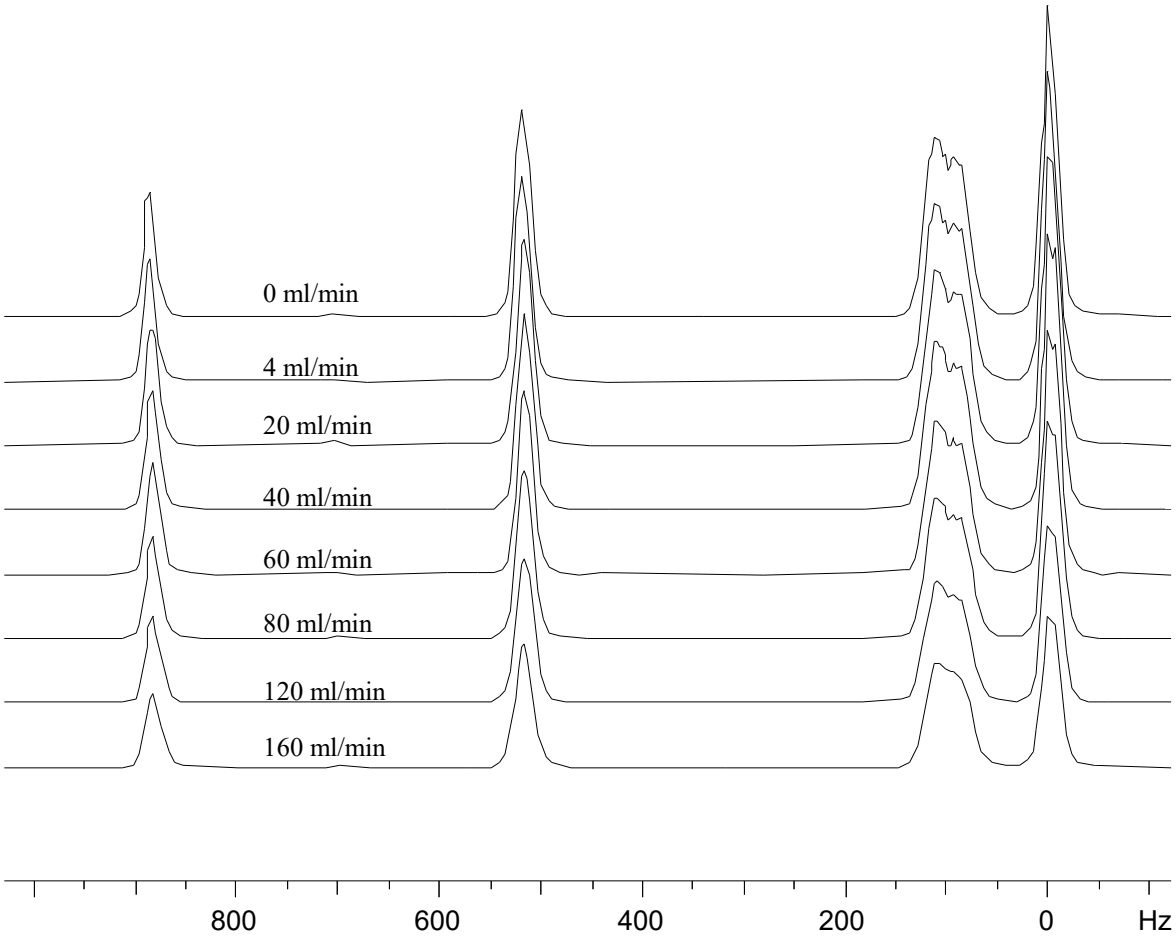

Figure 6.5 ^{1}H NMR spectra of butan-1-ol acquired under flowing conditions. The flow-induced peak broadening and intensity reduction is visible. The frequency axis is in Hz instead of ppm because there was no TMS present to give a chemical shift reference.

Peak	***T_1 (s)***
OH	1.655±0.089
CH_2	1.962±0.098
$(CH_2)_2$	1.998±0.020
CH_3	3.030±0.049

Table 6.1 T_1 values for the peaks in the ^{1}H NMR spectrum of butan-1-ol.

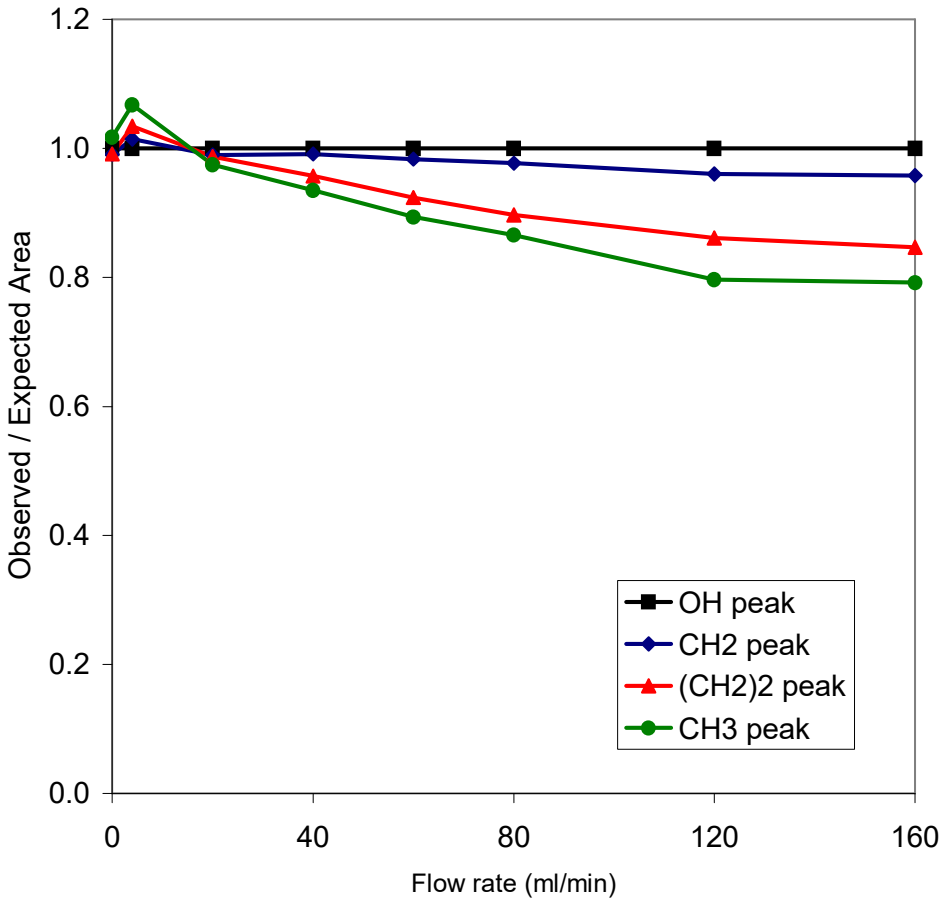

Figure 6.6 Variation of peak area with flow rate for spectra of flowing butan-1-ol. The errors in the ratios are roughly ±0.005. The systematic reduction in peak area indicates insufficient residence time in the magnet to build up an equilibrium magnetisation.

Peak	***T_1 (s)***
OH	1.768±0.275
CH_2 a	2.112±0.020
CH_2 b	2.347±0.131
CH_3	2.388±0.012

Table 6.2 T_1 values for the peaks in the ^{1}H NMR spectrum of a water/propan-1-ol mixture.

6.2.2.2 Magnet Residence Time Distributions

The sample stream entering the magnet has no net magnetisation, but as it flows through the magnet, the nuclear spins align themselves with the magnetic field through the process of longitudinal relaxation (section 2.2.5). The build-up of a net magnetisation is exponential with a time constant T_1, so the spins must spend a period of at least $5T_1$ inside the magnetic field for the magnetisation to reach 99% of its equilibrium value. For a multi-component sample containing spins with several different T_1 values, full relaxation requires a period of at least five times the longest T_1 value. If the magnetisation is not fully relaxed when the sample reaches the detection coil, then the acquired spectrum will exhibit T_1 weighting.

As described above, the flowing sample has a spread of velocities and thus residence times. For full relaxation before the sample reaches the detection coil, the *shortest* residence time should be at least five times the *longest* T_1 time. If the length of the pipe section upstream of the detection coil and inside the magnet is L_2, then the shortest residence time, τ_2^*, is defined as:

$$\tau_2^* = \frac{L_2}{u_0}. \qquad (6.23)$$

The residence time distribution inside the magnet is the inverse of the velocity profile, and is given by equations (6.13) and (6.14) on substituting τ_2 for τ_1. If $\tau_2^* \geq 5T_{1,\,max}$, the shape of the distribution has no influence on the measurement.

For example, T_1 weighting was observed in spectra of flowing butan-1-ol at flow rates of 0 to 160 ml/min (figure 6.5). The T_1 values for the four observed peaks in the butan-1-ol spectrum – OH, CH_2, $(CH_2)_2$, CH_3 – are given in table 6.1. The peak integrals deviated from their expected values for flow rates above 20 ml/min (figure 6.6) with the strongest deviation observed for the CH_3 peak with the largest T_1 (3.03 s). At 20 ml/min, taking L_2 = 1 m, τ_2^* = 19 s and $5T_{1,\,max}$ = 15.2 s, so there was no weighting. At higher flow rates, τ_2^* became less than 15.2 s, so T_1 weighting was observed.

To increase the residence time of the spins inside the magnetic field, a cylindrical equilibration chamber was added to the flow loop upstream of the detection coil. The chamber had an i.d. of 13.42 mm and a length of 535 mm, so its volume was 7.57×10^{-5} m^3. The addition of the chamber successfully eliminated relaxation

(a)

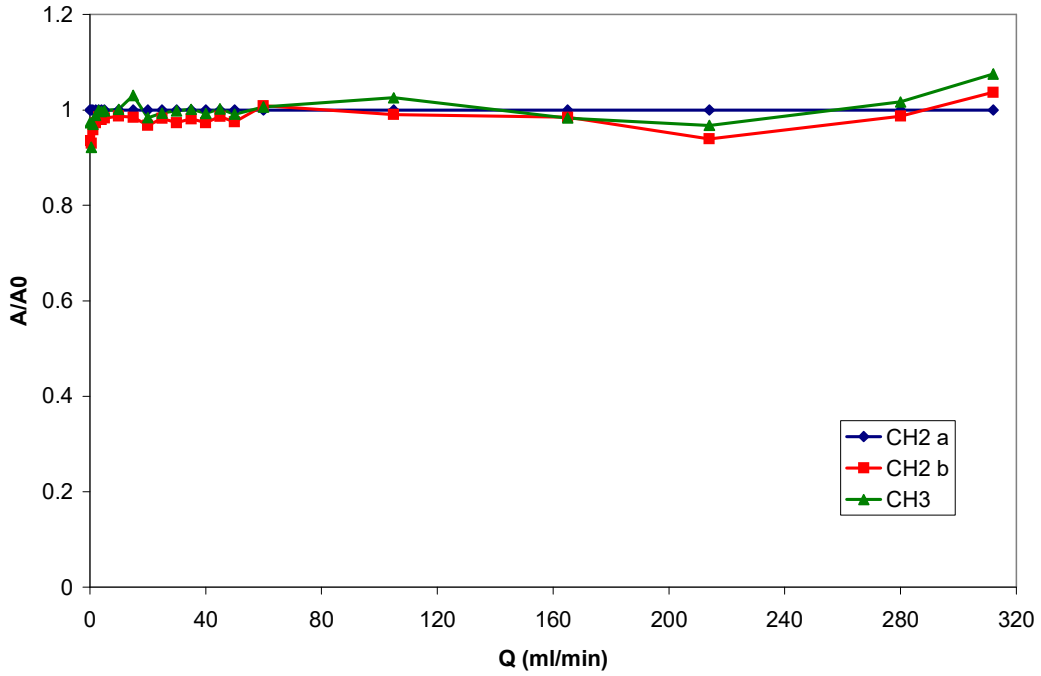

(b)

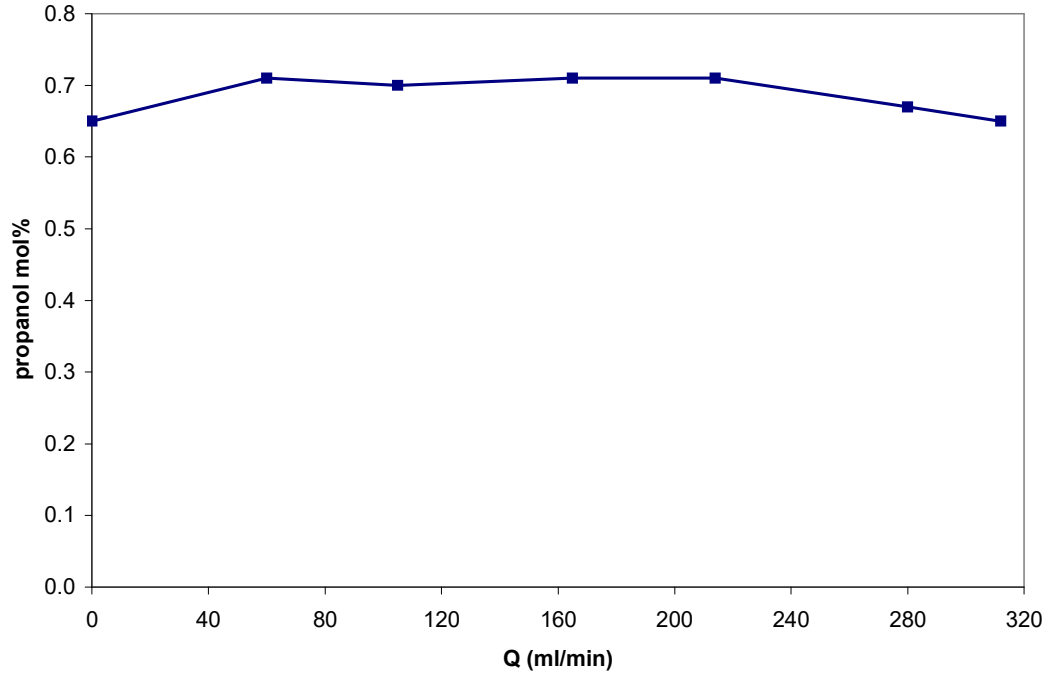

Figure 6.7 *(a)* Variation with flow rate of the areas of the aliphatic peaks of propan-1-ol for a flowing water/propan-1-ol mixture. The errors in the peak ratios are roughly ±0.005.
(b) Variation of measured propan-1-ol content (mol%) with flow rate for a flowing water/propan-1-ol mixture. The measurement error is roughly ±0.05 mol%.

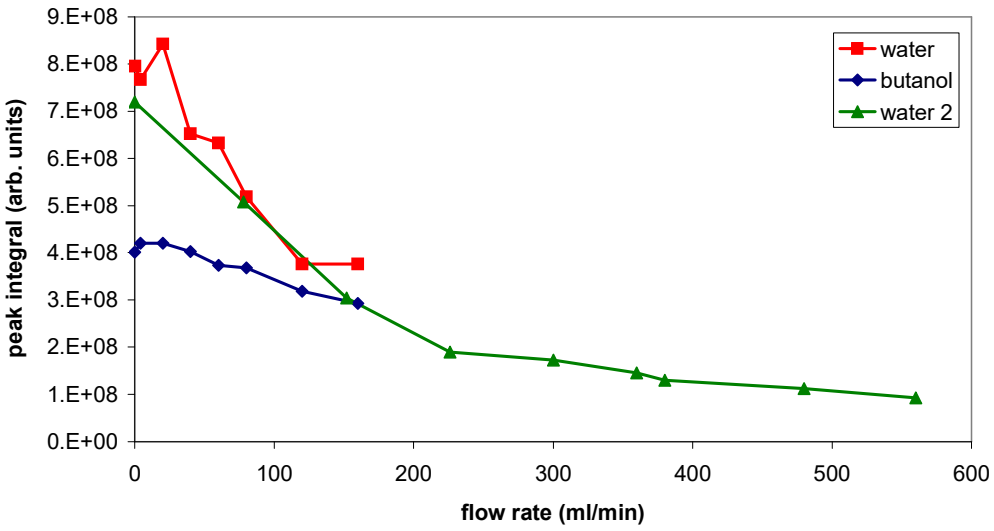

Figure 6.8 Decrease of peak integrals with flow rate due to the flow of excited spins out of the coil during the pre-scan delay. The chart shows results from two sets of experiments: flow of a water/butan-1-ol mixture (up to 160 ml/min) and flow of water (up to 560 ml/min).

weighting for flow rates up to 300 ml/min, for which the minimum residence time of the spins inside the equilibration chamber was 7.57 s. For a mixture of water and propan-1-ol flowing at rates up to 300 ml/min, the relative integrals of the aliphatic propan-1-ol peaks – CH_2, CH_2, CH_3 – did not deviate significantly from their expected values (figure 6.7(a)). This result was partly due to the similar T_1 values of the aliphatic peaks (table 6.2), but further support came from the composition data. The measured propan-1-ol content did not decrease systematically with flow rate (figure 6.7(b)), as would occur if the peaks were T_1-weighted, since the OH spins with the shortest T_1 value would have a larger net magnetisation than the aliphatic spins.

6.2.2.3 Coil Residence Time Distributions

The NMR signal of the sample stream is acquired while the nuclear spins flow continuously through the r.f. coil. When a 90° pulse is applied, it excites the spins that are inside the coil at that instant, but the spins can only provide a detectable signal while they remain in the coil. The flow of the excited spins out of the coil is another mechanism of signal decay in addition to the free-induction decay (FID). The acquired signal is thus the product of the FID and a flow-induced residence-time decay (RTD) function that is related to the residence time distribution of the spins in the coil. The form of the RTD function determines the observed lifetime broadening, sensitivity enhancement and apparent relaxation enhancement.

At any time after the 90° pulse, the signal detected in the r.f. coil is proportional to the number of excited nuclei present in the coil. Neglecting relaxation, the signal intensity decreases with time as the excited nuclei flow out of the detection region. The peak integrals to decrease with increasing flow rate (figure 6.8) because some excited nuclei leave the coil during the pre-scan delay between the pulse and the start of acquisition.

At a time t after the pulse, a fluid element at a radial position r with a velocity u_r will have travelled a distance $u_r t$ since the pulse (figure 6.9(a)). In a coil of length L_3, the fraction of excited spins that has left the coil is given by:

$$f_{out}(r,t) = \frac{u_r t}{L_3}. \tag{6.24}$$

The spins that leave the coil fastest are those at the centreline that have a minimum residence time given by:

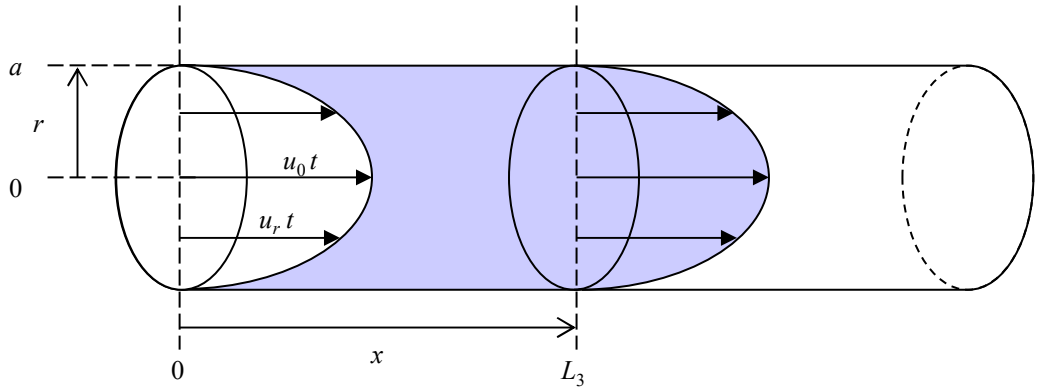

(a)

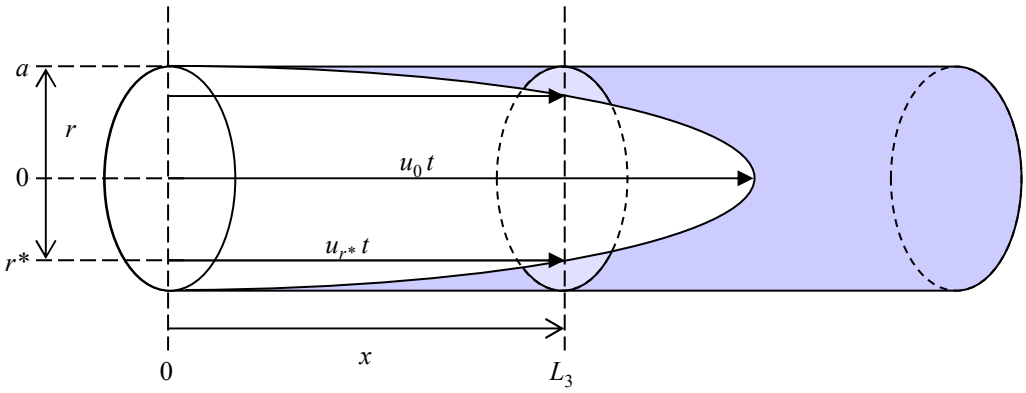

(b)

Figure 6.9 *(a)* Diagram showing the flow of excited spins with local velocity u_r out of the detection coil of length L_3 after the application of an excitation pulse.
(b) Diagram showing the excited spins remaining inside the detection coil after the spins at the centre up to a radius r^* have flowed out.

$$t_0 = \frac{L_3}{u_0} . \tag{6.25}$$

Combining equations (6.24) and (6.25), the fraction of spins remaining in the coil at each radius is given by:

$$f_{in}(r,t) = 1 - \frac{u_r t}{u_0 t_0} . \tag{6.26}$$

The total fraction of excited spins remaining in the coil at time t is obtained by substituting a velocity profile for u_r/u_0 and integrating equation (6.26) over the cross-section of the coil:

$$F_{in}(t) = \int_0^a 2\pi r \left(1 - \frac{u_r t}{u_0 t_0} \right) dr . \tag{6.27}$$

This integral is only valid for $t \le t_0$, when $f_{out} \le 1$ for all radial positions. After t_0, the centre of the sample will be entirely devoid of excited spins, up to a radius r^* for which $u_{r^*} t = L_3$. The coil then "hollows out" with time (figure 6.9(b)), with the remaining excited spins present near the walls of the pipe. In this period, the total fraction of excited spins remaining in the coil is given by:

$$F_{in}(t) = \int_0^{r^*} 2\pi r(0) dr + \int_{r^*}^a 2\pi r \left(1 - \frac{u_r t}{u_0 t_0} \right) dr . \tag{6.28}$$

For laminar flow, the velocity profile from equation (6.2) gives r^* as:

$$r^* = a \left(1 - \frac{t_0}{t} \right)^{1/2} , \tag{6.29}$$

and the fraction of excited spins over time as:

$$F_{in}(t) = \begin{cases} 1 - \dfrac{t}{2t_0} & 0 \le t \le t_0 \\ \dfrac{t_0}{2t} & t \ge t_0 \end{cases} . \tag{6.30}$$

A similar procedure for turbulent flow gives:

$$F_{in}(t)=\begin{cases}1-\dfrac{49t}{60t_0} & 0\le t\le t_0\\ \dfrac{t_0^{\,7}}{4t^7}-\dfrac{t_0^{\,14}}{15t^{14}} & t\ge t_0\end{cases}, \tag{6.31}$$

and for plug flow:

$$F_{in}(t)=\begin{cases}1-\dfrac{t}{t_0} & 0\le t\le t_0\\ 0 & t\ge t_0\end{cases}. \tag{6.32}$$

The three RTD functions (figure 6.10(a)) exhibit the same linear decay for $t \le t_0$ due to constant outflow at the mean velocity, but they diverge for $t > t_0$. For the same mean velocity, the turbulent RTD function is close to the plug flow function while the laminar function has a much slower decay.

6.2.3 Flow-Induced Peak Broadening

The time-domain signal acquired from a flowing sample is the product of the free induction decay function and the flow-induced decay function, since both decay mechanisms occur simultaneously (figure 6.11(a)). By the convolution theorem, the resulting lineshape (figure 6.11(b)) is the convolution product of a Lorentzian function with the Fourier transform of the RTD function. This lineshape is not Lorentzian, but there is no simple function to describe it. In principle, if the Lorentzian function is known, the RTD function can be deconvolved from the lineshape.

The FID of a flowing sample decays more rapidly with increasing flow rate, so the peak widths increase because the width is inversely proportional to the FID decay rate. This phenomenon is known as "lifetime broadening" in the literature (Sudmeier *et al.*, 1996). A commonly held model treats flow as an exponential relaxation process whereby the FID of a flowing sample decays with an observed time constant, $T_2^*{}_{obs}$, given by (Laude *et al.*, 1984; Dorn, 1996):

$$\left(\frac{1}{T_2^*}\right)_{obs}=\left(\frac{1}{T_2^*}\right)_{static}+\frac{1}{\bar{\tau}}, \tag{6.33}$$

where $\bar{\tau}$, the mean residence time in the coil, is inversely proportional to the flow rate ($\bar{\tau}=V/Q$). This model predicts that the peak width increases linearly with flow rate,

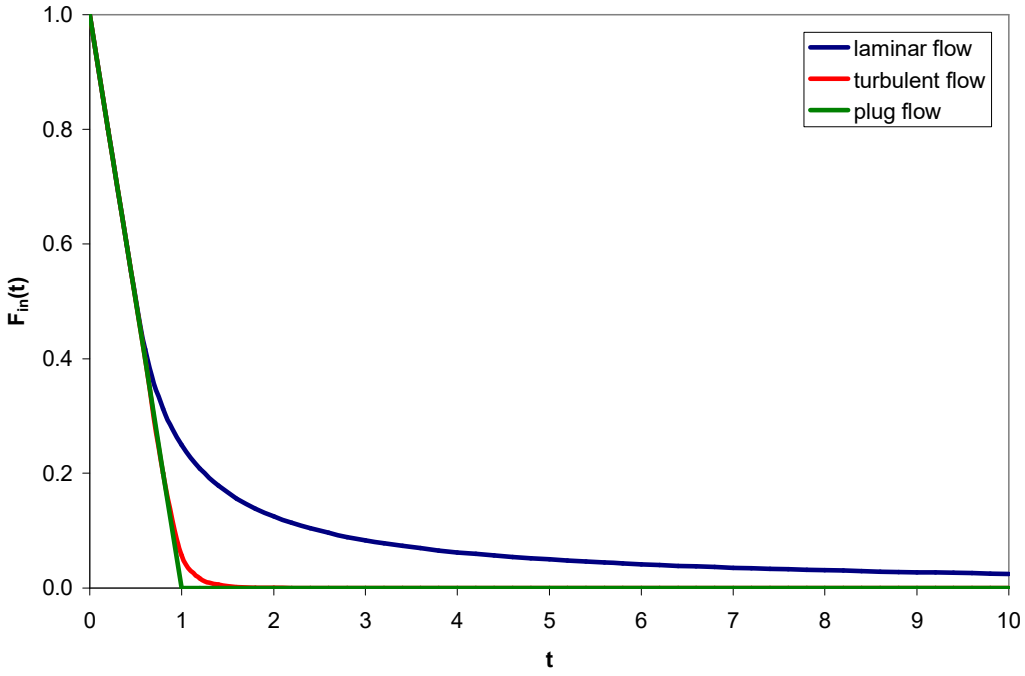

(a)

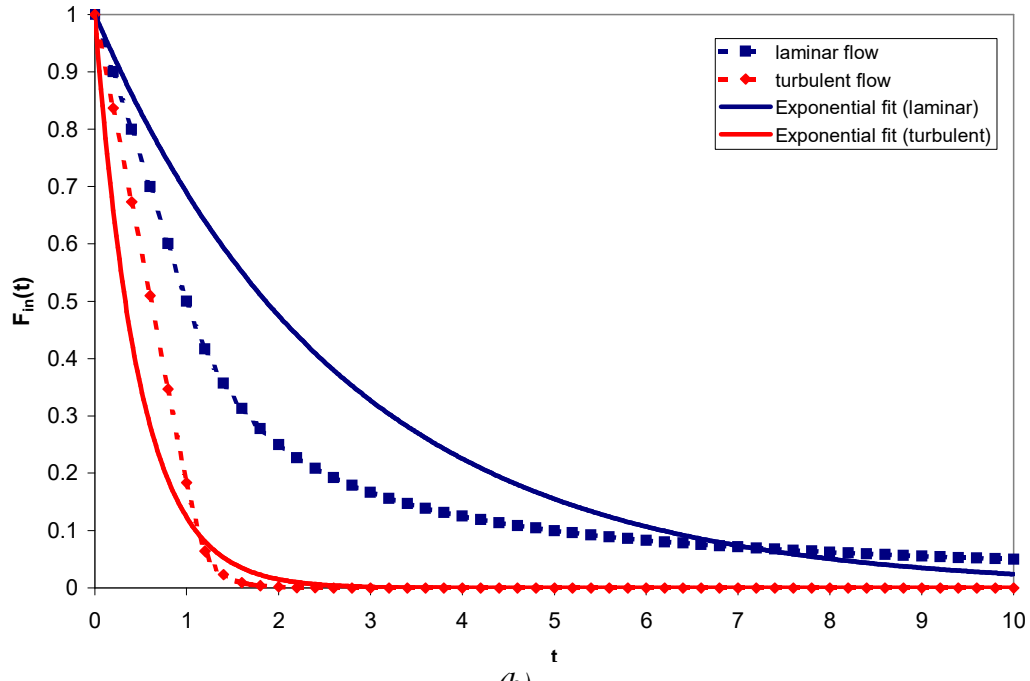

(b)

Figure 6.10 *(a)* Residence time decay functions showing the fraction of excited spins remaining in the coil for a liquid flowing out of the detection coil at the same mean velocity in the laminar, turbulent and plug flow regimes. *(b)* Least-squares fits of exponential decay functions to the laminar and turbulent RTD functions. The fits are very poor, showing that an exponential model is not appropriate for flow-induced signal decay.

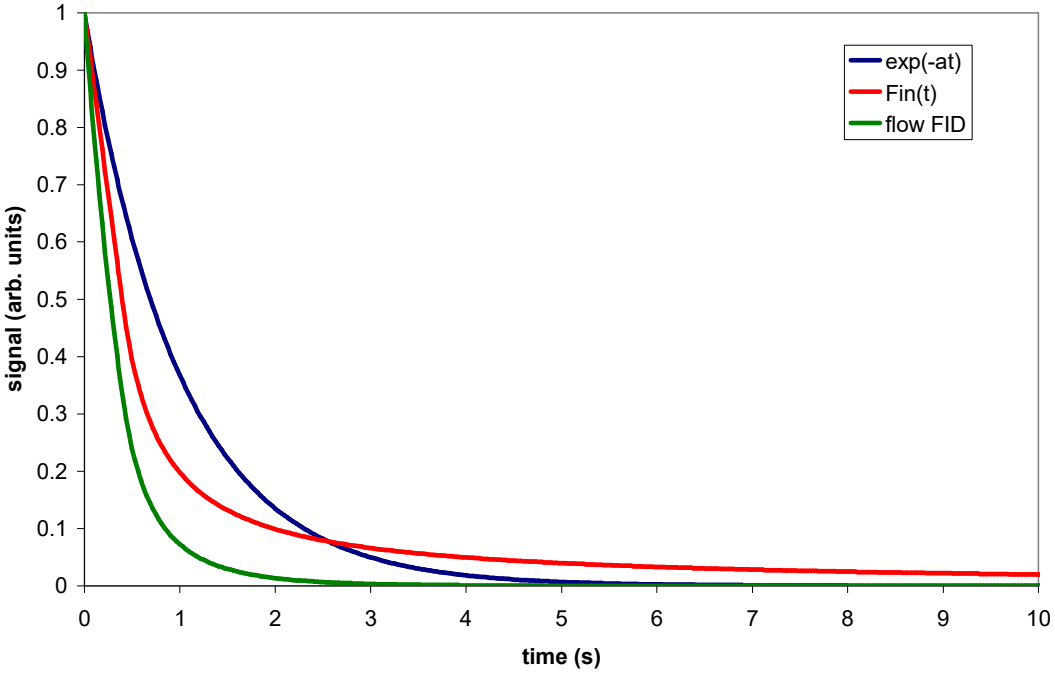

(a)

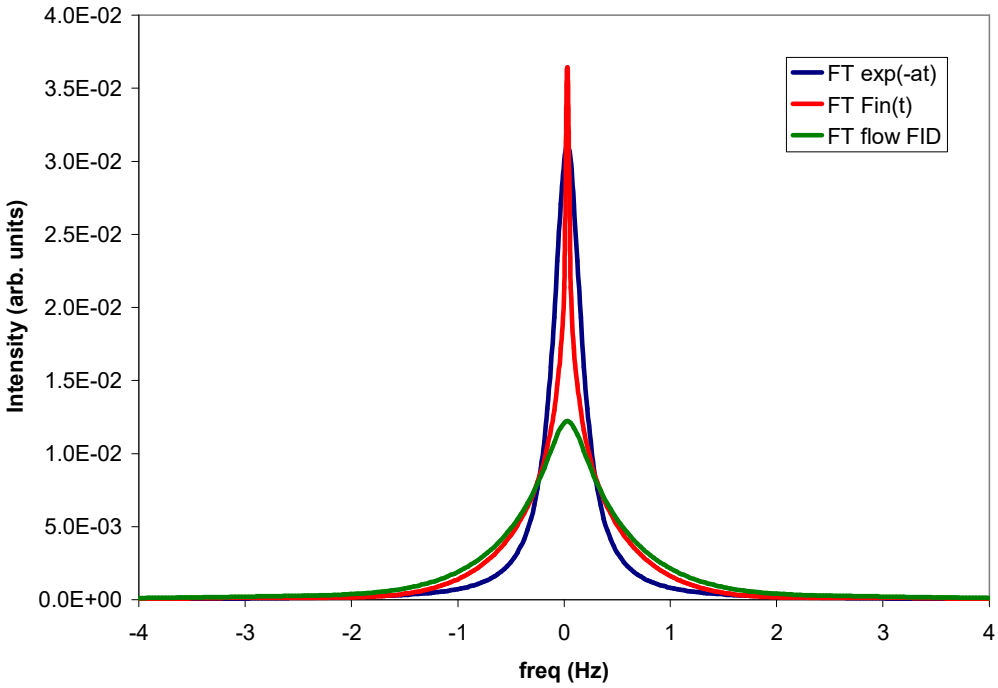

(b)

Figure 6.11 *(a)* The time-domain NMR signal obtained from a flowing sample is the product of free induction decay (e^{-at}) and flow-induced decay ($F_{in}(t)$) functions. The function shown here is for laminar flow. *(b)* The corresponding frequency-domain signal is the convolution product of the Fourier transforms of the two decay functions.

but experimental results do not support this prediction. Lifetime broadening was observed experimentally in ^{1}H NMR spectra of flowing liquid mixtures. At low flow rates, each peak in the spectrum had its own linewidth, but at higher flow rates the flow-induced broadening caused all peaks to have the same linewidth. The variation of peak widths with flow rate was non-linear, and was fitted empirically using cubic polynomials (figure 6.12(a)).

The model in equation (6.33) is incorrect because the assumptions that it is based on are false and incompatible. The first assumption is that the outflow from the coil is analogous to relaxation, *i.e.* a first-order process that can be described using an exponential function and an appropriate time constant. However, the RTD functions derived above are clearly not exponential and are very poorly approximated by an exponential function (figure 6.10(b)), so the analogy does not hold. The second assumption is that flow-induced "relaxation" depends only on the mean residence time in the coil, *i.e.* that the flow is uniform. However, uniform flow gives constant decay (equation 6.32), which is a zero-order process that is not described by an exponential function either. Finally, this model assumes that the two "relaxation" mechanisms are independent, so that $T_2^*{}_{obs}$ is calculated from two independent constants.

Flow-induced broadening was simulated numerically using the RTD functions derived above. A series of FIDs was generated using the equation:

$$S(t) = S(0)F_{in}(t)e^{-t/T_2^*}, \qquad (6.34)$$

with different flow rates, T_2^* values and flow regimes. The FIDs were Fourier transformed and the peak widths were measured. The results of the simulation in figure 6.12 show the peak broadening, $\Delta\lambda = \lambda(Q) - \lambda(0)$, versus flow rate for laminar, turbulent and plug flow with $T_2^* = 0.1$, 1.0 and 10 s. $\Delta\lambda$ increased with Q as expected, but also depended on the flow regime. Laminar flow gave the least broadening and plug flow the most, reflecting the shapes of the RTD functions. $\Delta\lambda$ also decreased as T_2^* decreased, so the two "relaxation" mechanisms were not independent. The dependence of $\Delta\lambda$ on both Q and T_2^* is caused by the lineshape being the convolution of (the Fourier transforms of) the two decay functions. The variation of $\Delta\lambda$ with Q at constant T_2^* was fitted with a cubic polynomial, where the form of the polynomial depended on T_2^*. For large T_2^*, the polynomial had the form

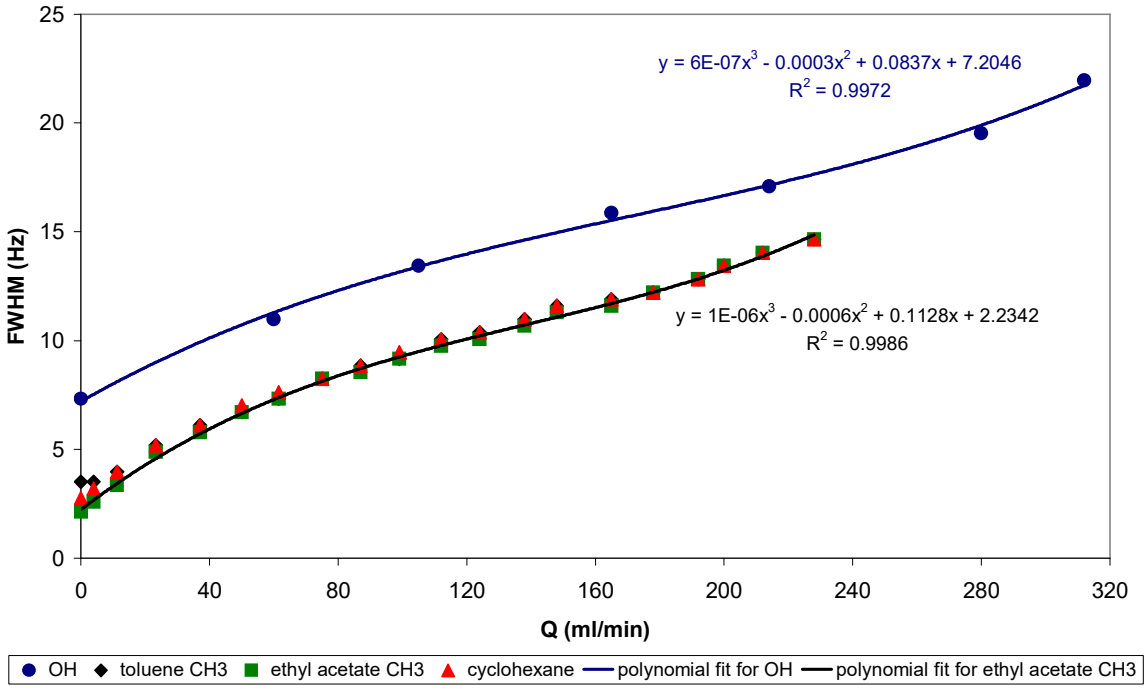

(a)

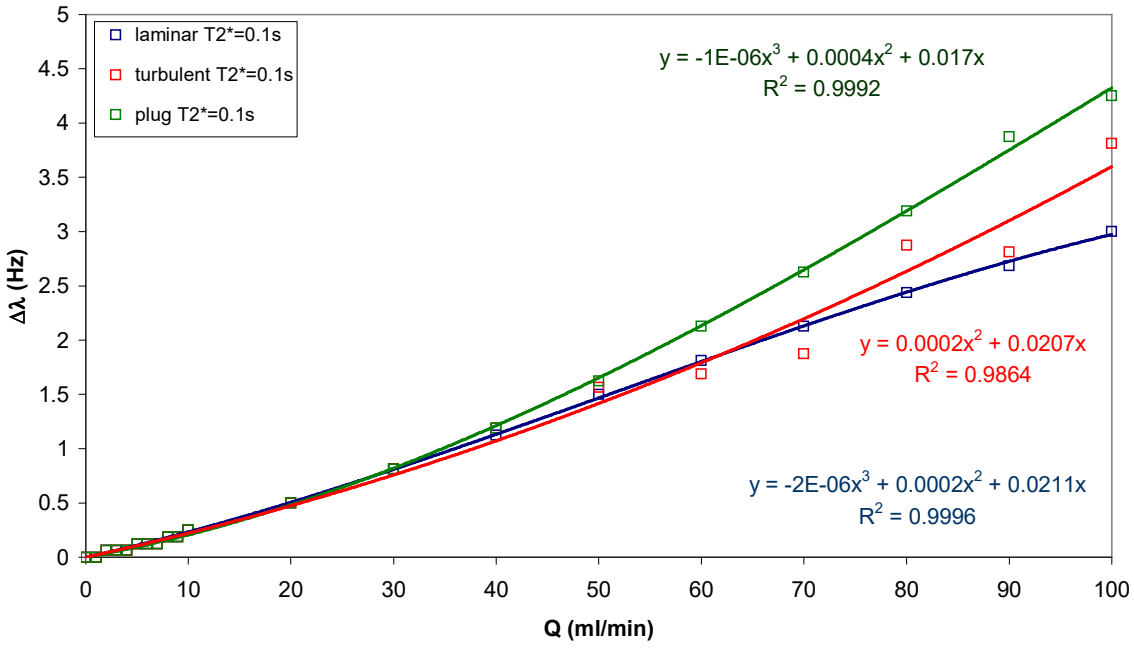

(b)

Figure 6.12 *(a)* Flow-induced peak broadening observed experimentally in the spectra of a mixture of methanol, toluene, cyclohexane, isooctane and ethyl acetate. *(b)* Flow-induced peak broadening simulation results for laminar, turbulent and plug flow with $T_2^* = 0.1$ s. The lines show the polynomial fits to the data points.

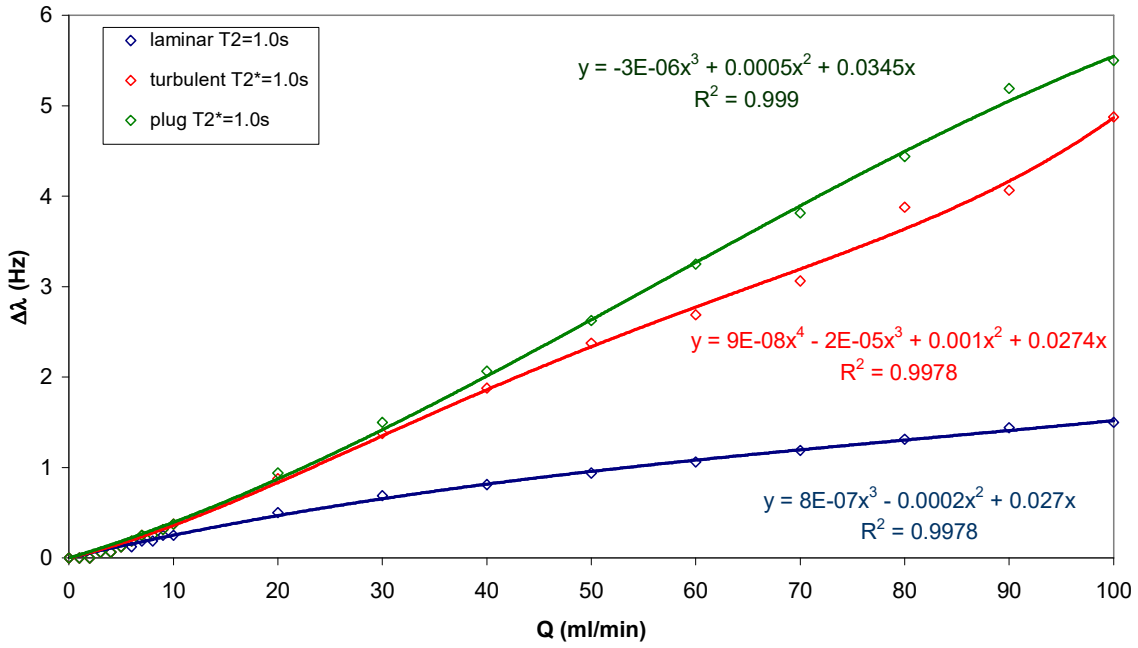

(c)

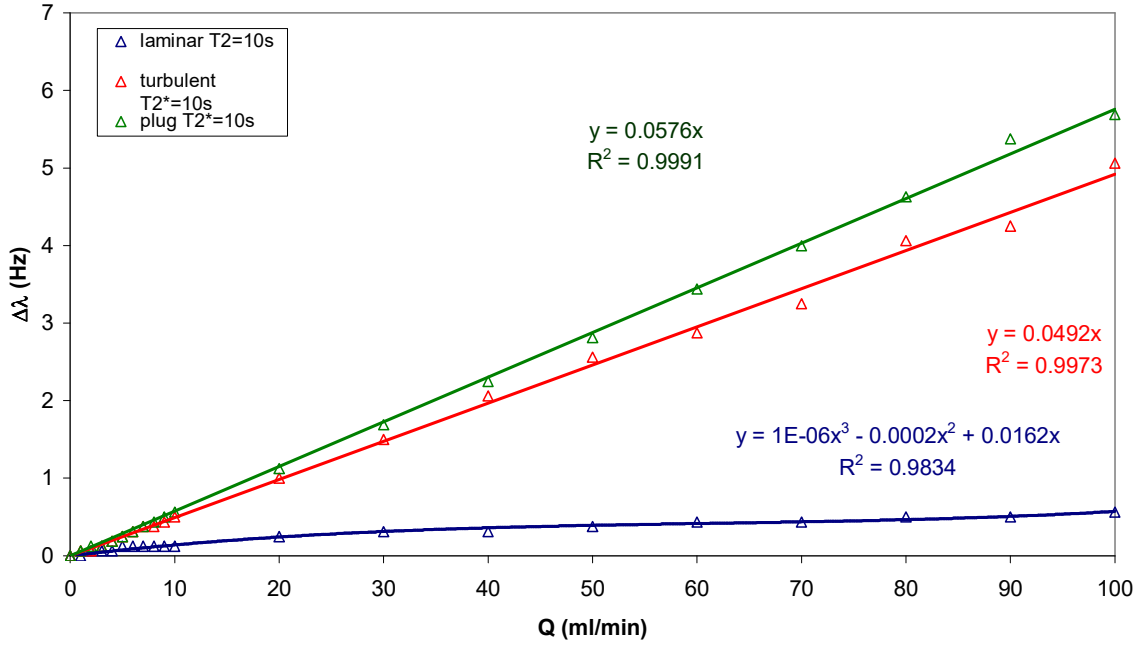

(d)

Figure 6.12 *(c)* Flow-induced peak broadening simulation results for laminar, turbulent and plug flow with $T_2^* = 1.0$ s. The lines show the polynomial fits to the data points.
(d) Flow-induced peak broadening simulation results for laminar, turbulent and plug flow with $T_2^* = 10$ s. The lines show the polynomial fits to the data points.

aQ^3-bQ^2+cQ, which was the form used to fit the broadening of initially narrow experimental peaks. For small T_2^*, the polynomial had the form -aQ^3+bQ^2+cQ, which was the form used to fit the broadening of initially broad water peaks. This qualitative agreement between the simulation and the experimental data shows that the residence-time model explains flow-induced peak broadening better than the relaxation model.

6.2.4 Sensitivity Enhancement

Laude *et al.* have attempted to determine the optimal acquisition parameters for obtaining maximum sensitivity (signal-to-noise ratio per unit time) from a flowing sample (Laude *et al.*, 1984, 1985a, 1985b). They observed that sensitivity increased with pre-magnetisation volume at constant flow rate, but the increase was small for short-T_1 signals. At constant pre-magnetisation volume and inter-scan delay, sensitivity increased with flow rate up to a maximum then decreased, and the flow rate with maximum sensitivity increased with pre-magnetisation volume. Laude concluded that "sensitivity in a flow FT-NMR experiment is a complicated function of pre-magnetisation volume, observation volume, flow rate, T_1, observation pulse width and delay times" (Laude *et al.*, 1985a). Sudmeier *et al.* modelled Laude's results by simulating the steady-state magnetisation in the coil using a classical vector model (Sudmeier *et al.*, 1996). They assumed plug flow, so the model did not match Laude's results. They improved the fit by arbitrarily adding an extra 4 ml of pre-magnetisation volume and changing the pulse angle from 90° to 70°, but they could not justify the changes to their model. Sudmeier concluded that "it may be that nonplug flow has an effect similar to reduced pulse angle".

In fact, Laude's results are very simple. At constant flow rate, sensitivity increased with pre-magnetisation volume because the spins had a longer residence time in the magnet, so the magnetisation built up closer to equilibrium. The exponential build-up was more rapid for short-T_1 signals, so the sensitivity rapidly reached its maximum and stopped increasing with pre-magnetisation volume. Laude's plot of sensitivity vs. pre-magnetisation volume clearly shows the exponential build-up of magnetisation (sensitivity) with pre-magnetisation volume (residence time) for different T_1 values (Laude *et al.*, 1985a). At constant pre-magnetisation volume and inter-scan delay, sensitivity initially increased with flow rate because more saturated spins in the coil

were refreshed between scans. At high flow rates, sensitivity decreased as more spins left the coil before the end of signal acquisition. The maximum sensitivity occurred when sample refreshment and outflow were balanced.

Sudmeier's model of the build-up of magnetisation as a function of flow rate and pre-magnetisation volume failed because it did not consider the distribution of residence times in the pipe. The correct model is given here. At any position (x, r) inside the pipe section upstream of the coil, the spins will have spent a time, t_r, inside the magnetic field given by:

$$t_r = \frac{x}{u_r}, \tag{6.35}$$

and built up a partial magnetisation, M_r, given by:

$$M_r = M_0\left(1 - e^{-t_r/T_1}\right) = M_0\left(1 - e^{-x/u_r T_1}\right). \tag{6.36}$$

The two-dimensional surface plot in figure 6.13(a) shows the magnetisation inside a pipe section for laminar flow. Along the length of the pipe, the magnetisation builds up exponentially because the spins flow at constant velocity. Across the diameter of the pipe, the magnetisation builds up slowly in the centre and steeply near the outer edges. The total magnetisation built up inside the pipe section of radius a and length L_2 is given by the integral:

$$M = \int_0^a \int_0^{L_2} 2\pi r M_r \, dr \, dx. \tag{6.37}$$

This integral is very difficult to evaluate analytically because of the complex dependence of u_r on r (equations (6.2) and (6.6)), so it was integrated numerically using Simpson's rule. For the three flow regimes, figure 6.13(b) shows the net magnetisation as a function of a non-dimensional residence time given by:

$$\frac{\tau_2}{T_1} = \frac{Q}{\pi a^2 L_2 T_1}. \tag{6.38}$$

The three curves have different shapes that reflect the underlying velocity profiles. For short residence times ($\tau_2 < 1.6T_1$), the net magnetisation builds up more rapidly for laminar flow than for turbulent or plug flow because the laminar velocity profile has a larger proportion of low velocities. This difference explains why the plug flow

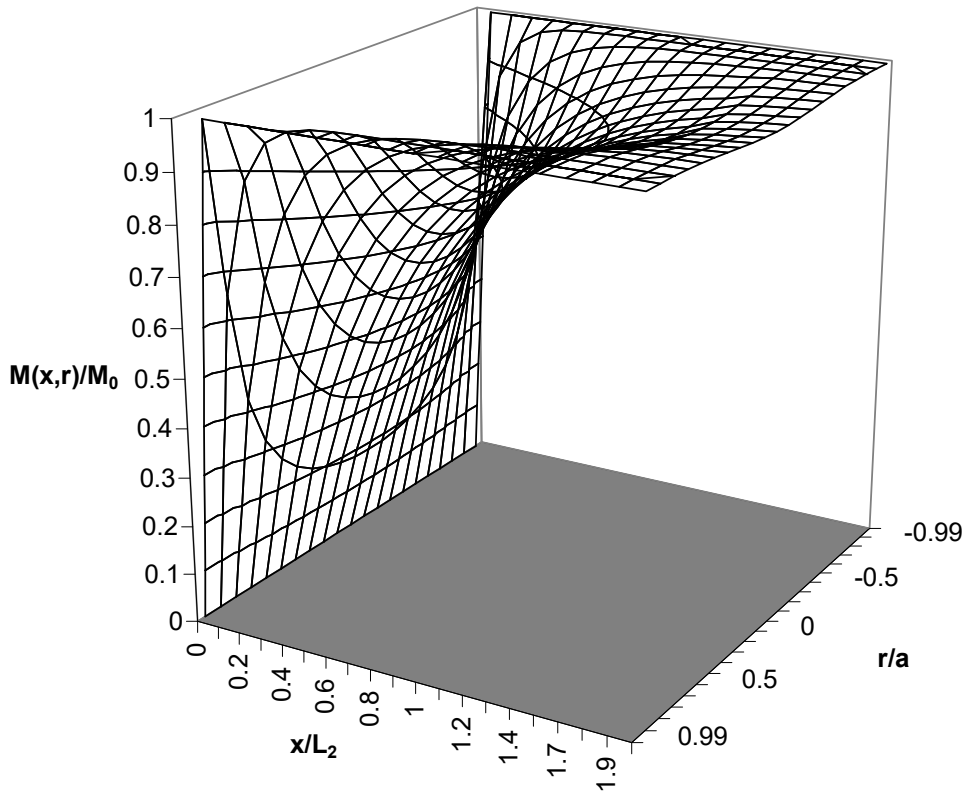

(a)

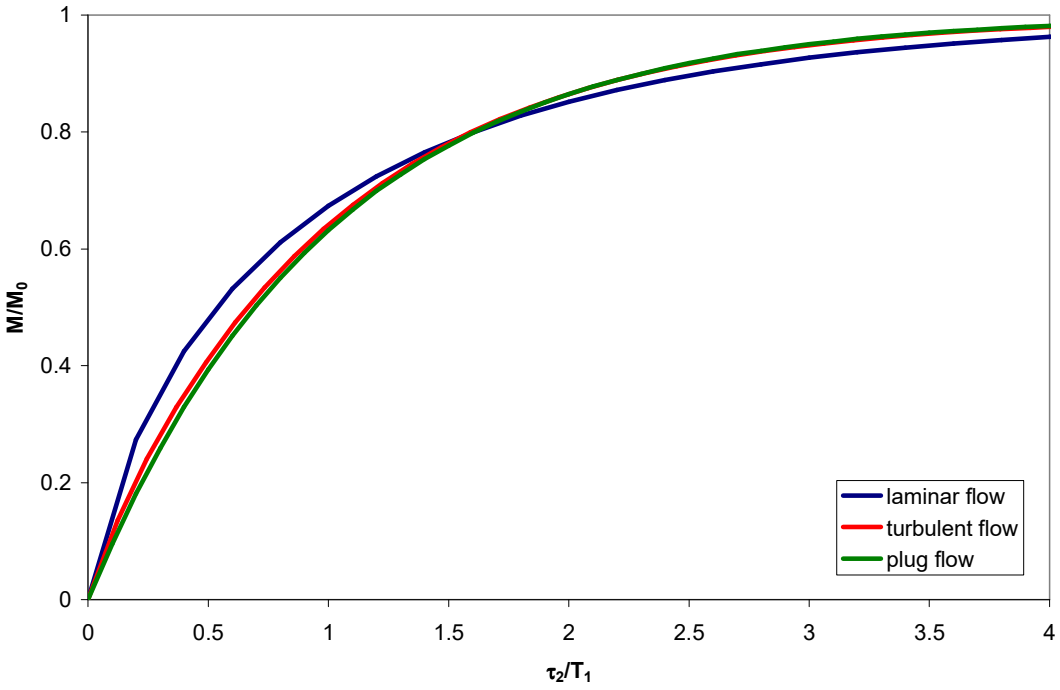

(b)

Figure 6.13 *(a)* Two-dimensional surface plot showing the local magnetisation at various axial (x/L_2) and radial (r/a) positions in a stream flowing inside a magnetic field in the laminar flow regime.
(b) Net magnetisation built up in a flowing stream with various residence times inside the magnet for laminar, turbulent and plug flow.

model of Sudmeier *et al.* needed a larger pre-magnetisation volume and reduced pulse angle to fit Laude's data: for the same pre-magnetisation volume, laminar flow gives a higher net magnetisation than plug flow.

6.2.5 Relaxation

Lee *et al.* have investigated the dependence of the apparent longitudinal relaxation constant, T_1^*, on flow rate (Lee *et al.*, 1999). They inverted the magnetisation in a wide slice of length L_i (volume V_i), then detected the recovery of the magnetisation inside various narrow slices of length L_o (volume V_o) at the centre of L_i (figure 6.14(a)). They modelled the dependence of T_1^* on flow rate using an exponential model given by:

$$\frac{1}{T_1^*} = \frac{1}{T_1} + \frac{1}{t_F}, \tag{6.39}$$

where t_F was the time required for the trailing edge of the irradiated plug to reach the point (1-1/e) of the way through the detection volume. t_F was related to the flow rate by:

$$t_F = \frac{V^*}{Q}, \tag{6.40}$$

where V^* was the "effective volume" defined as:

$$V^* = \left(1 - \frac{1}{e}\right) V_o + \frac{1}{2}\left(V_i - V_o\right). \tag{6.41}$$

In Lee's experiments, which were in the laminar flow regime, $1/T_1^*$ increased with flow rate as expected. At constant flow rate, $1/T_1^*$, and hence $1/V^*$, was proportional to V_i and independent of V_o, instead of depending linearly on both volumes as defined in equation (6.41). Lee did not explain the discrepancies between his model and experiments, nor did he mention laminar flow as the cause.

As explained in section 6.2.3, the exponential model is unsuitable for modelling flow. A better model for the recovery of the magnetisation after inversion must include the velocity profile explicitly. After an inversion pulse, the magnetisation aligned along the $-z$ axis recovers by longitudinal relaxation, given by (equation 2.20):

$$M(t) = M_0\left(1 - 2e^{-t/T_1}\right). \tag{6.42}$$

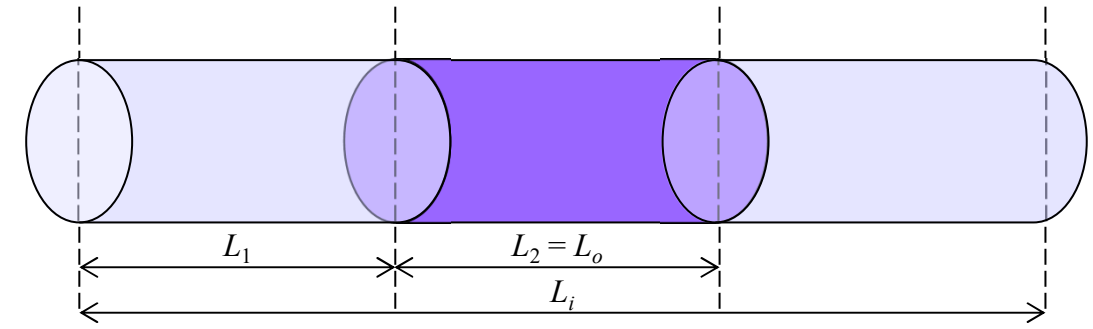

(a)

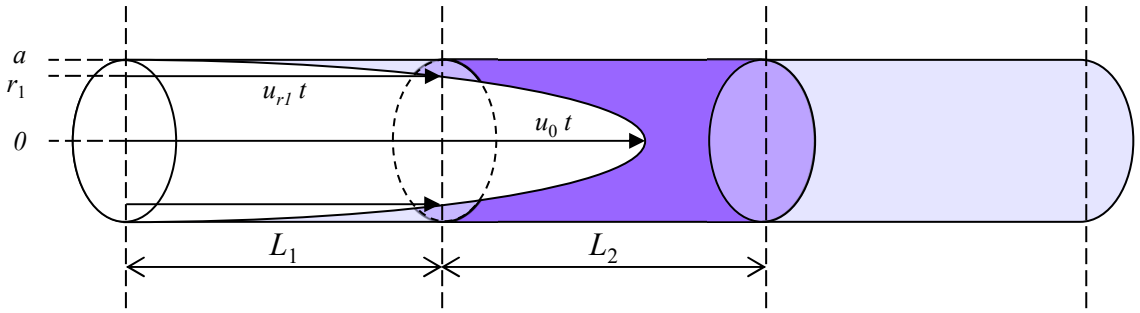

(b)

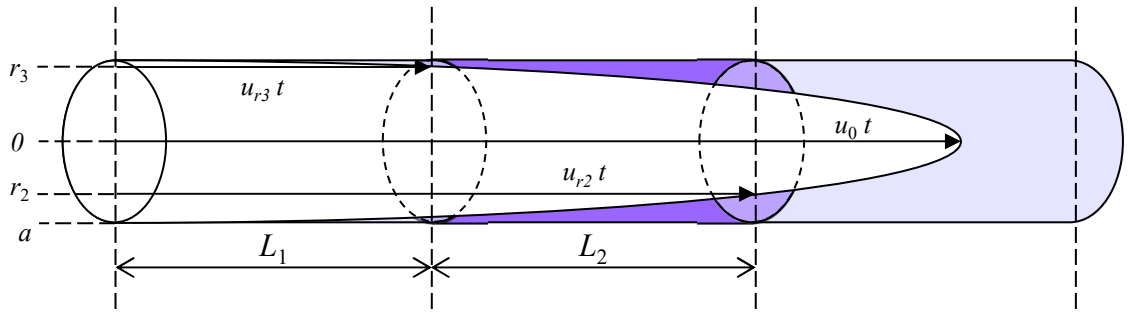

(c)

Figure 6.14 *(a)* The flow relaxivity experiment of Lee *et al.* (1999) with an inversion slice of length L_i and a narrower observation slice of length L_o. *(b)* The inflow of unsaturated spins with local velocity u_r into the observation region of length L_2 after travelling a length L_1, up to a limiting radius r_1. *(c)* as (b), with limiting radii r_2 and r_3 for the flow of unsaturated spins through the observation slice.

The flow of the sample causes apparent relaxation because some inverted spins leave the coil and fresh spins aligned along the $+z$ axis replace them. If the fraction of fresh spins present in the observation volume V_o at time t is denoted as $F_{in}(t)$, then the magnetisation in the observation volume is given by:

$$M(t) = F_{in}(t)M_0 + (1 - F_{in}(t))M_0\left(1 - 2e^{-t/T_1}\right) = M_0\left(1 - 2e^{-t/T_1}(1 - F_{in}(t))\right). \quad (6.43)$$

The derivation of the inflow function $F_{in}(t)$ is analogous to that of the RTD functions in section 6.2.2.3, except that the fresh spins must travel a distance L_1 before reaching the observation volume of length L_2 (figure 6.14(b)). If the inversion pulse defines $t = 0$, then at time t a fluid element at a radial position r with a velocity u_r will have travelled a distance $u_r t$. The fraction of fresh spins inside V_o at each radial position is given by:

$$f_{in}(r,t) = \frac{u_r t - L_1}{L_2}. \quad (6.44)$$

The times for the fastest spins at the centreline to cross the distances L_1 and L_2 are τ_1 and τ_2 given by:

$$\tau_1 = \frac{L_1}{u_0}, \quad \tau_2 = \frac{L_2}{u_0}. \quad (6.45)$$

The centreline spins reach V_o at $t = \tau_1$, so for $0 \le t \le \tau_1$, $F_{in}(t) = 0$. For $\tau_1 \le t \le \tau_1+\tau_2$, the inflow of fresh spins into V_o is limited to a radius r_1 for which $u_{r1}t = L_1$ (figure 6.14(b)) because the slower spins at $r > r_1$ will have travelled a distance shorter than L_1 at time t. During this period, the total fraction of fresh spins is given by:

$$F_{in}(t) = \int_0^{r_1} 2\pi r f_{in}(r,t)dr + \int_{r_1}^{a} 2\pi r(0)\,dr \quad \tau_1 \le t \le \tau_1 + \tau_2. \quad (6.46)$$

For $t \ge \tau_1+\tau_2$, the centre of the tube is completely filled with fresh spins up to a radius r_2 for which $u_{r2}t = L_1+L_2$. The inflow of fresh spins is limited to a radius r_3 for which $u_{r3}t = L_1$ (figure 6.14(c)). Now the total fraction of fresh spins is given by:

$$F_{in}(t) = \int_0^{r_2} 2\pi r(1)dr + \int_{r_2}^{r_3} 2\pi r f_{in}(r,t)dr + \int_{r_3}^{a} 2\pi r(0)dr \quad t \ge \tau_1 + \tau_2. \quad (6.47)$$

$F_{in}(t)$ was calculated for laminar, turbulent and plug flow by inserting the appropriate expression for u_r in equation (6.44) before substituting it into the integrals (6.46) and (6.47). For laminar flow, this gave the expression:

$$F_{in}(t)=\begin{cases}0 & 0\le t\le \tau_1\\ \dfrac{(t-\tau_1)^2}{2t\tau_2} & \tau_1\le t\le \tau_1+\tau_2\\ 1-\dfrac{\tau_1-\tau_2/2}{t} & t\ge \tau_1+\tau_2\end{cases}, \tag{6.48}$$

while the expression for turbulent flow was given by:

$$F_{in}(t)=\begin{cases}0 & 0\le t\le \tau_1\\ \dfrac{49}{60}\dfrac{(t-\tau_1)}{\tau_2}-\dfrac{11}{60}\dfrac{\tau_1}{\tau_2}+\dfrac{{\tau_1}^8}{4\tau_2 t^7}-\dfrac{{\tau_1}^{15}}{15\tau_2 t^{14}} & \tau_1\le t\le \tau_1+\tau_2\\ 1-\dfrac{(\tau_1+\tau_2)^8-{\tau_1}^8}{4\tau_2 t^7}+\dfrac{(\tau_1+\tau_2)^{15}-{\tau_1}^{15}}{15\tau_2 t^{14}} & t\ge \tau_1+\tau_2\end{cases}, \tag{6.49}$$

and that for plug flow by:

$$F_{in}(t)=\begin{cases}0 & 0\le t\le \tau_1\\ \dfrac{t-\tau_1}{\tau_2} & \tau_1\le t\le \tau_1+\tau_2\\ 1 & t\ge \tau_1+\tau_2\end{cases}. \tag{6.50}$$

These three functions are shown in figure 6.15(a). The differences between laminar and plug flow are very clear: with laminar flow the spread of velocities leads to earlier inflow of fresh spins, but at later times the inflow slows down considerably. The magnetisation recovery in the presence of flow, equation (6.43), depends on the relative values of T_1, τ_1 and τ_2. For small T_1 values, the flow regimes hardly influence the magnetisation (figure 6.15(b)), but when T_1 is large the magnetisation recovery follows the inflow curves and is not exponential (figure 6.15(c)).

This model was compared with the results of Lee *et al.* by considering the flow decay time t_F, which was defined as:

$$F_{in}(t_F)=1-\frac{1}{e}=0.63212\ldots. \tag{6.51}$$

Expressions were obtained for t_F in terms of τ_1 and τ_2 from equations (6.48) - (6.50), and for V^* in terms of V_o and V_i from equation (6.40). For plug flow, V^* was given by:

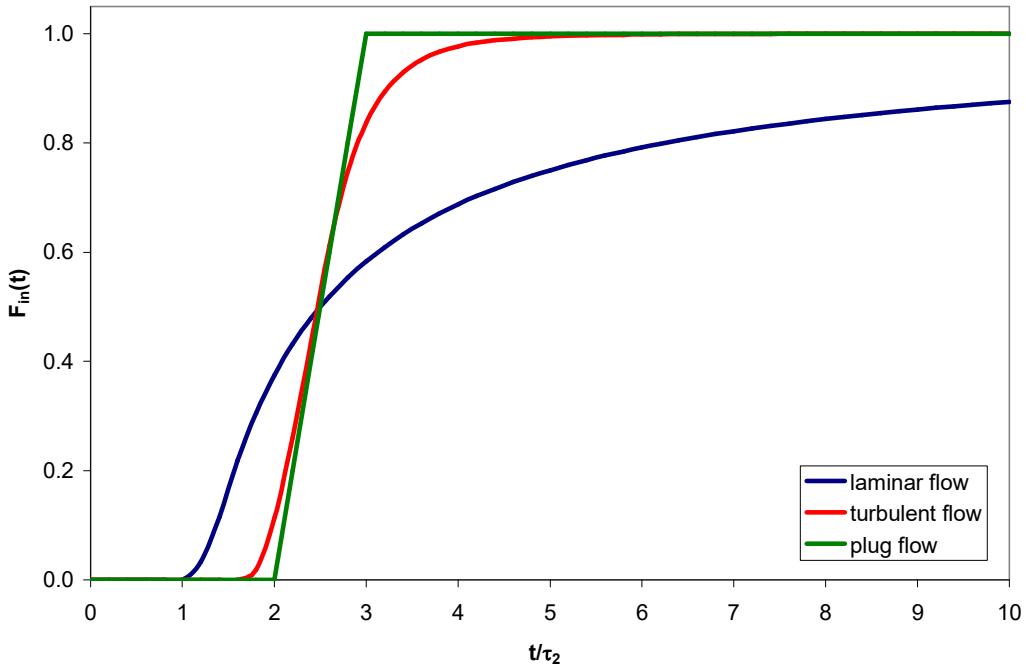

(a)

Figure 6.15 *(a)* Inflow function $F_{in}(t)$ showing the fraction of unsaturated spins present inside the observation region in a flow relaxivity experiment of Lee *et al.* The curves show the results for $\tau_1 = 2\tau_2$ in the laminar, turbulent and plug flow regimes with the same mean flow velocity.

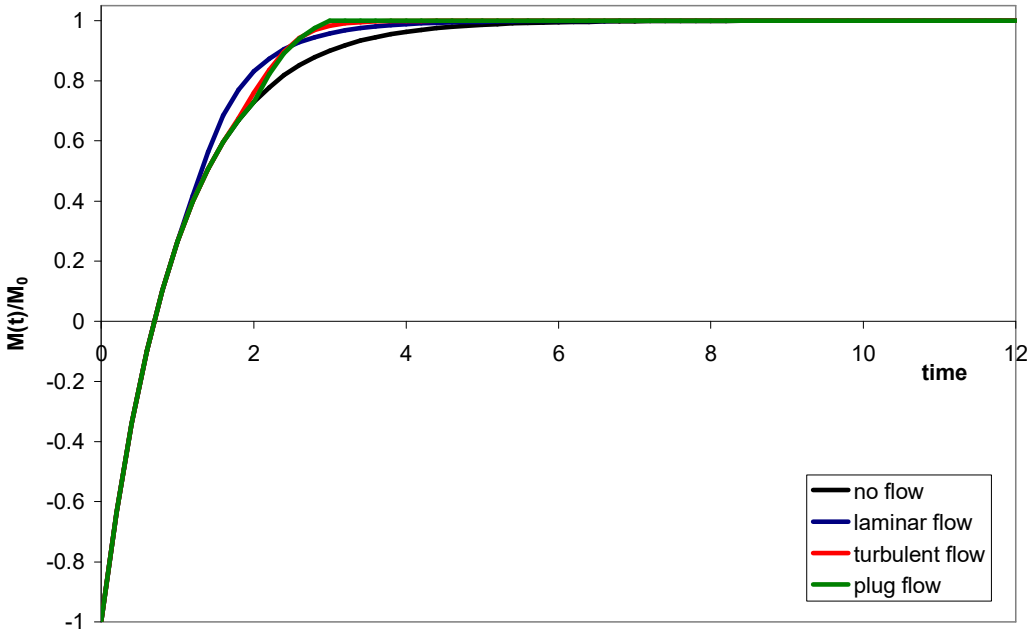

(b)

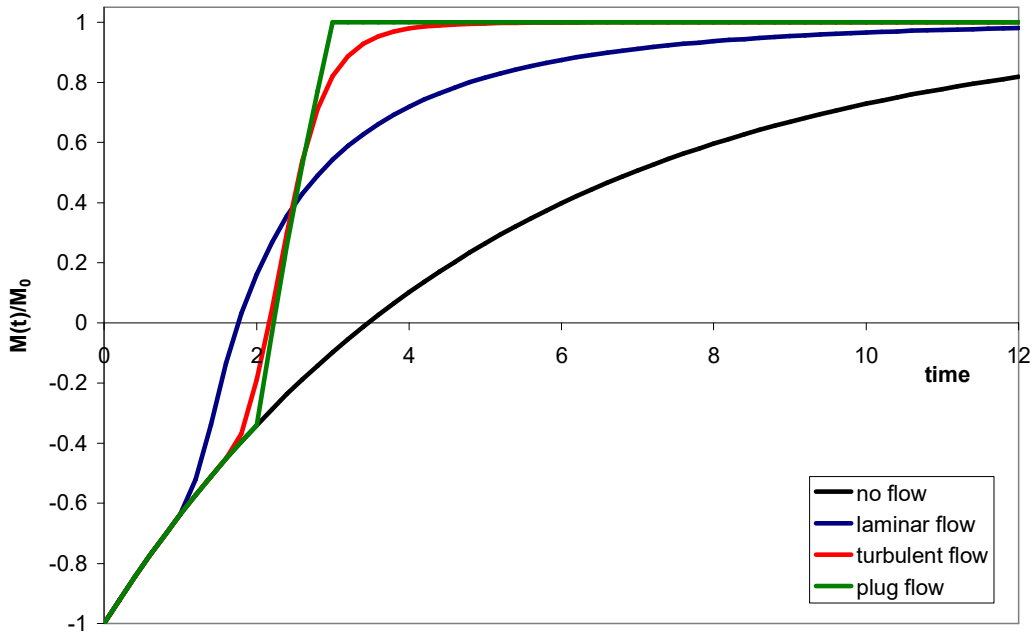

(c)

Figure 6.15 *(b)* Magnetisation recovery curve with and without flow with $T_1 = 1$, $\tau_1 = 2$ and $\tau_2 = 1$ (arb. units). The short T_1 dominates the curve for all three flow regimes.
(c) As (b) with $T_1 = 5$. The long T_1 allows the flow to dominate, so the curves resemble those seen in (a).

$$V^* = \frac{1}{2}V_i + \left(\frac{1}{2} - \frac{1}{e}\right)V_o, \tag{6.52}$$

which matched the definition in equation (6.41). For laminar flow, V^* was given by:

$$V^* = \frac{e}{4}V_i = 0.67957...V_i, \tag{6.53}$$

which disagreed with the definition but matched Lee's experimental results. Therefore, the residence-time model is again better than the exponential model at explaining the effect of flow on NMR signals.

6.3 Composition Analysis of Flowing Mixtures

The literature on NMR spectroscopy of flowing systems has not covered quantitative measurements under continuous flow conditions so far. In this section, the effect of the flow on the accuracy of quantitative composition measurements is studied, and the maximum flow rate is determined at which the composition result is reliable.

6.3.1 Experimental

Our laboratory apparatus for online NMR spectroscopy of a flowing stream consisted of a flow loop made from Viton rubber tubing (3.1 mm i.d.) and an observation cell made from a glass cylinder (length 120 mm, 4.1 mm i.d.) positioned inside a 5-mm birdcage coil in a 4.7-T superconducting magnet (figure 6.16). The liquid stream flowed downward through the magnet, so that the spins spent enough time in the magnetic field to build up a bulk magnetisation before reaching the r.f. coil. Continuous, steady flow of the liquid was produced by a peristaltic pump with a sealed bottle downstream of the pump to dampen the pulses in the flow. Viton tubing was used instead of silicone tubing to minimise the loss of the sample through the tubing. Various components (notably cyclohexane) were capable of penetrating through the rubber and evaporating from the large surface area of the tubing, causing the composition of the stream to change with time. Viton was associated with significantly less sample loss than silicone. In order to quantify the errors caused by the change in sample over time, the composition of the stream was measured without flow at regular intervals throughout the experiments.

A single-phase mixture of toluene, methanol, cyclohexane, isooctane and ethyl acetate was measured at a range of flow rates from 0 to 228 ml/min. The liquids were 99.9%

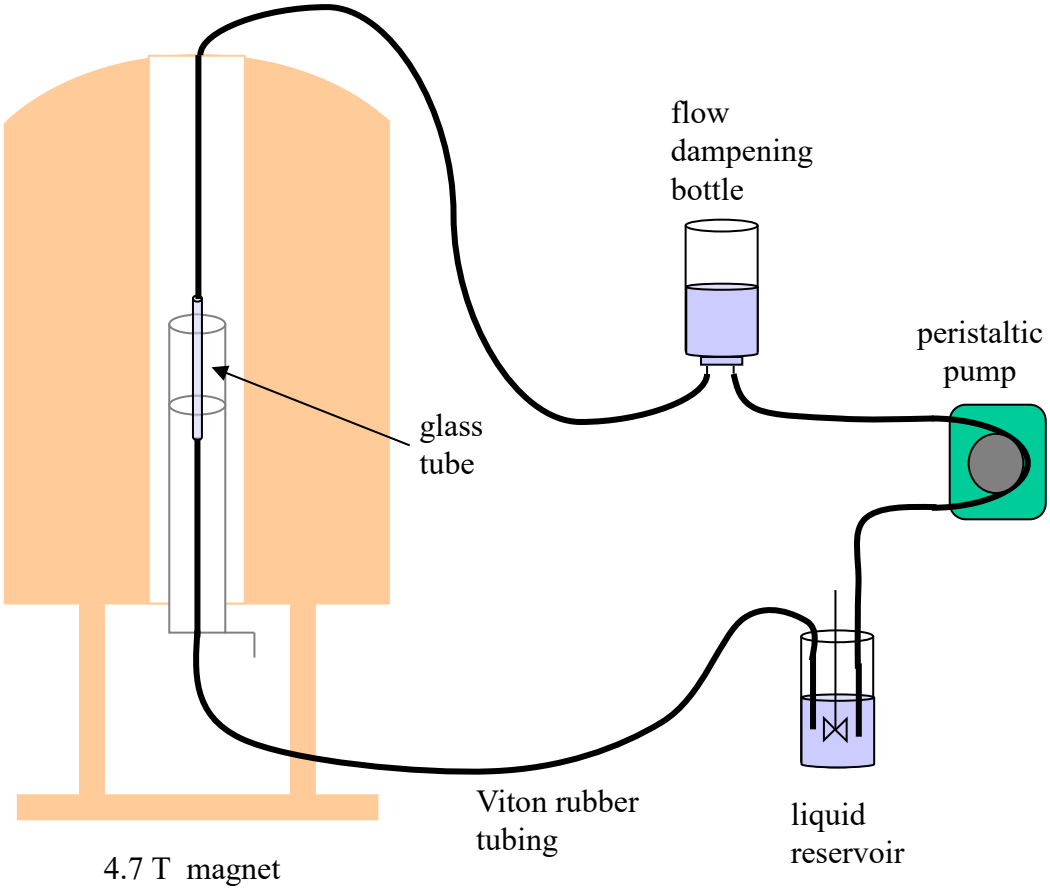

Figure 6.16 Flow loop for NMR measurements on a stream flowing through a narrow glass tube (4.1 mm i.d.) inside a 4.7 T magnet.

HPLC grade supplied by Aldrich Chemical Company and were used without further purification. The composition of the mixture at the start and the end of the experiment is shown in table 6.3. The mean change in composition due to evaporation was 1.29 mol% for the five components, with the largest change being -3.22 mol% for methanol.

The ^{1}H NMR spectra were acquired using a Bruker DMX 200 spectrometer with a 4.7 T superconducting magnet and a 5 mm micro-imaging coil tuned to a ^{1}H resonance frequency of 199.707 MHz. The ZG pulse sequence was used with a 90° excitation pulse of duration of 3.7 μs and an eight-scan phase cycle. The pre-scan delay was 143 μs, and the real and imaginary signals ware sampled simultaneously every 100 μs. For the non-flowing spectra, the receiver gain was 8, the repetition time was 30 s and the number of data points was 32768. For the flowing spectra, the receiver gain was 4 and the number of data points was reduced with increasing flow rate from 32768 to 8192. The repetition time was likewise decreased from 30 s to 1 s with increasing flow rate. The spectra were zero-filled once prior to Fourier transformation, then phase- and baseline-corrected manually. The deterioration of the resolution with increasing flow rate did not allow automated peak picking, so the peaks were assigned and integrated manually.

6.3.2 Results

Spectra of the mixture at various flow rates from 0 to 228 ml/min are shown in figure 6.17. The peak widths increased with flow rate to the extent that closely spaced peaks merged at flow rates above 40 ml/min, then became broad humps of equal width for flow rates above 60 ml/min. The active length of the r.f. coil was ~20 mm, so the observation volume was 0.264 ml. The mean residence time inside the coil decreased from 3.96 s at 4 ml/min to 0.264 s at 60 ml/min and 0.0695 s at 228 ml/min. For high flow rates (above 100 ml/min), the inverse of the peak width increased linearly with the mean residence time in the observation volume (figure 6.18(a)). At 228 ml/min, all peak widths were 14.648 Hz, whose inverse (0.0682 s) was close to the mean residence time of 0.0695 s. The agreement was not exact because the active length of the r.f. coil is not precisely known. For a series of spectra acquired with the same parameters (16384 data points, 5 s repetition time) at flow rates of 50-150 ml/min, the

Component	*Content at Start (mol%)*	*Content at End (mol%)*	*Change (mol%)*
methanol	29.39	26.17	-3.22
toluene	26.14	27.08	+0.94
cyclohexane	13.97	14.16	+0.19
isooctane	8.57	9.11	+0.54
ethyl acetate	21.92	23.49	+1.57
average			*1.29*

Table 6.3 The composition of the five-component mixture used in the flow experiments, measured under static conditions at the start and end of the experiments. The largest change in the composition was the loss of methanol due to evaporation.

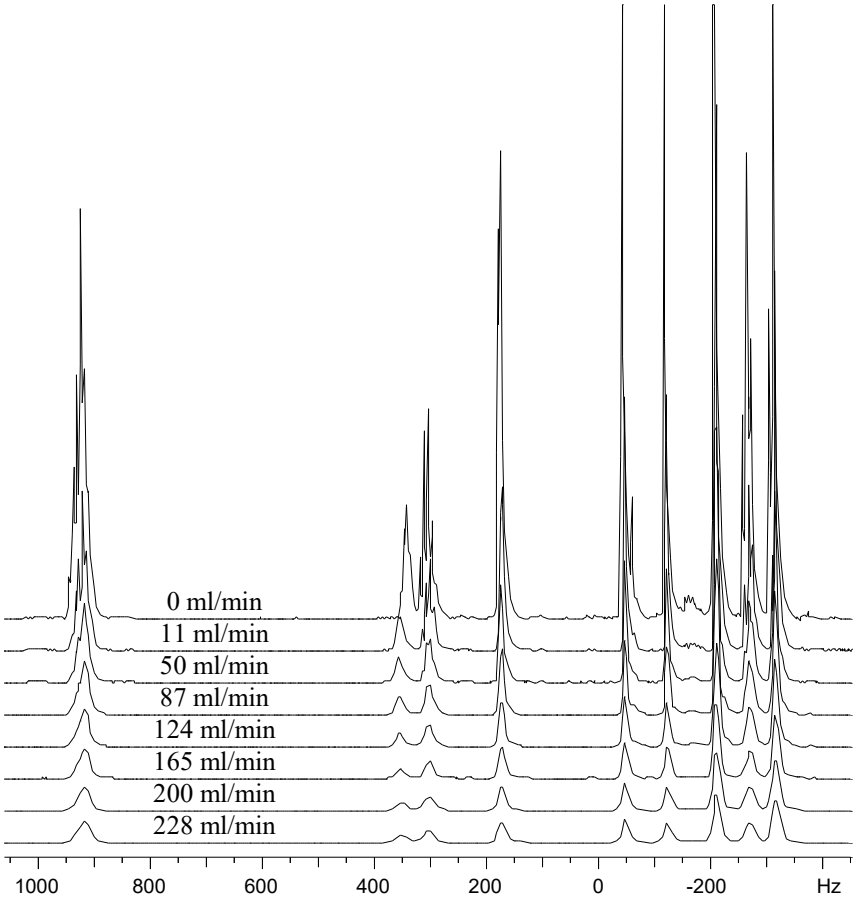

Figure 6.17 ^{1}H NMR spectra of a mixture of methanol, toluene, cyclohexane, isooctane, and ethyl acetate acquired under flowing conditions. The flow rate increases from top to bottom from 0 ml/min to 228 ml/min. The flow-induced peak broadening and intensity reduction is clearly visible. The frequency axis is in Hz instead of ppm because there was no TMS present to give a chemical shift reference.

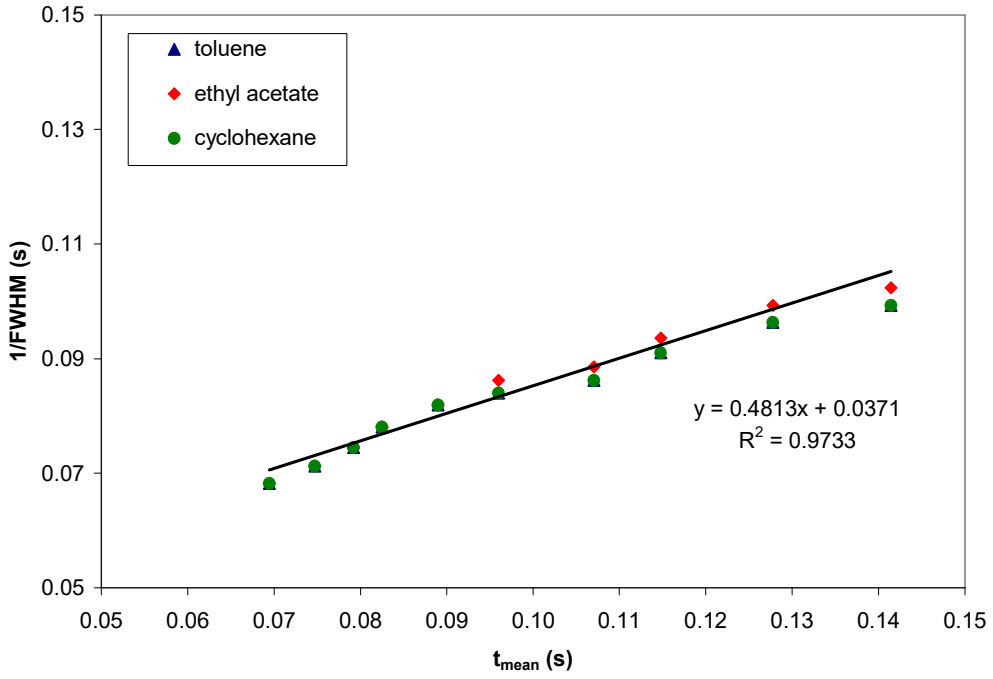

(a)

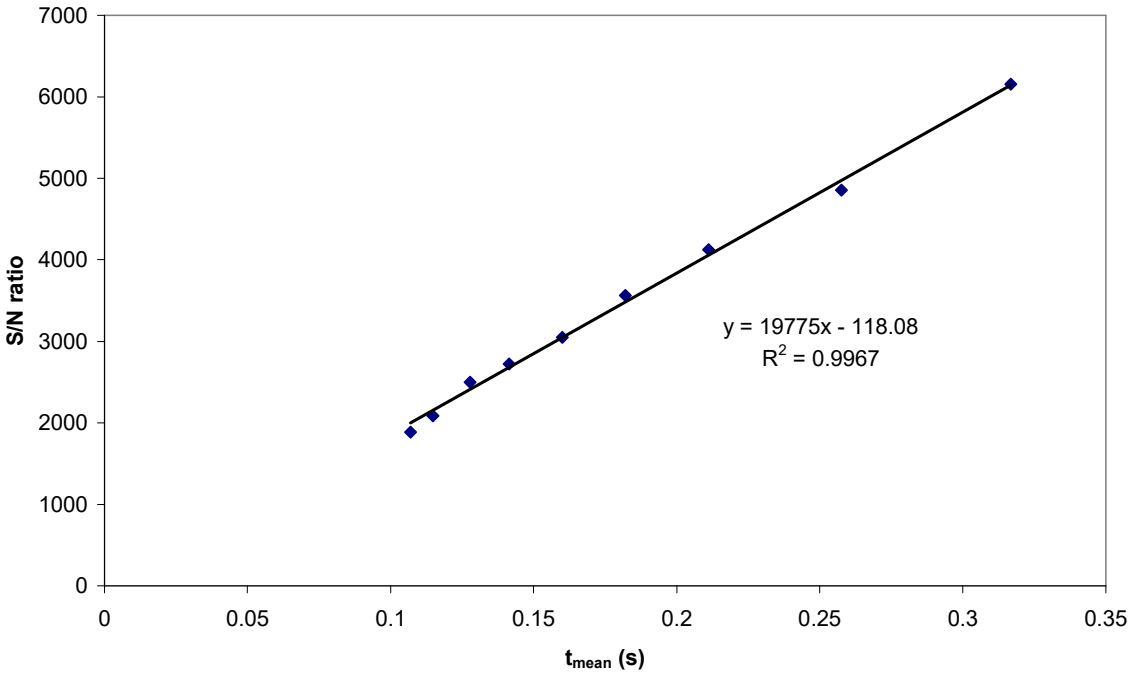

(b)

Figure 6.18 *(a)* Chart showing flow-induced broadening of NMR peaks at flow rates above 100 ml/min. The inverse of the peak width increases linearly with mean residence time in the observation coil.
(b) Chart showing the linear increase in signal-to-noise ratio with mean residence time in the observation coil for NMR spectra acquired with the same acquisition parameters.

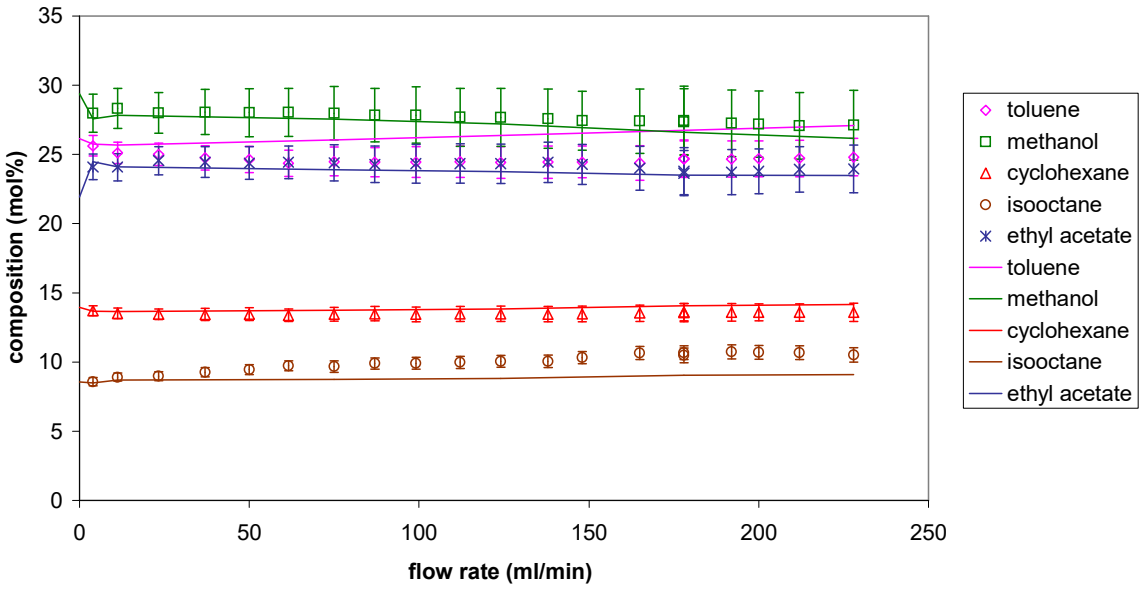

(a)

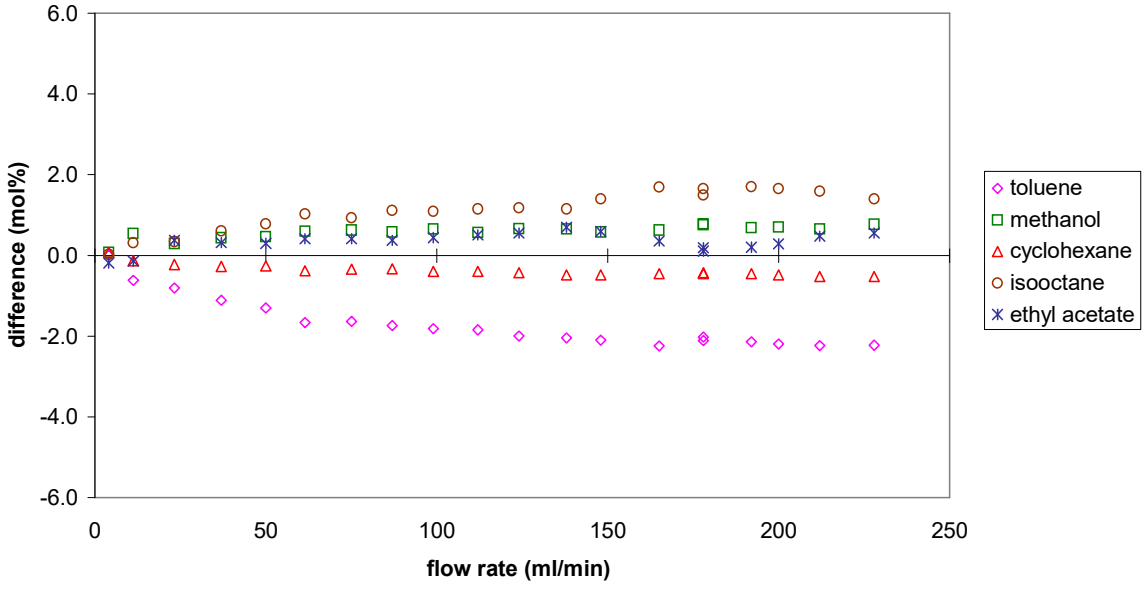

(b)

Figure 6.19 *(a)* Composition of the five-component mixture measured with (symbols) and without (lines) flow using bulk NMR spectroscopy. *(b)* Differences between the compositions measured with and without flow.

signal-to-noise ratio increased linearly with mean residence time in the coil (figure 6.18(b)).

The composition of the mixture measured under flowing conditions is shown in figure 6.19(a), along with the composition measured under static conditions over the same period. The scatter in the data was very small, even over such a vast range of flow rates, which clearly demonstrated the reproducibility of the NMR measurements. The differences between the compositions measured with and without flow increased with flow rate (figure 6.19(b)), as did the error bars on the measurements under flow. For methanol, ethyl acetate and cyclohexane, the differences were smaller than the error bars, so they were not statistically significant. Only for toluene and isooctane did the differences increase significantly with flow rate because the residence time in the magnet became too short to build up an equilibrium magnetisation. The range of T_1 values in the sample is 2 to 4 s, based on earlier measurements of similar mixtures (data not shown). For a magnetic field length of ~1 m, the maximum flow rate for a mean residence time of at least 20 s (5×4 s) upstream of the coil is 24 ml/min. In practice, higher flow rates up to 50 ml/min did not cause significant errors, but there was a clear trade-off between increasing flow rate (shorter measurement time and less exit-age averaging) and decreasing accuracy.

6.4 Volume-Selective Spectroscopy of Flowing Mixtures

The distribution of exit ages inside the detection coil means that an NMR spectrum of the entire stream gives a time-averaged composition. The extent of time averaging can be reduced by acquiring a spectrum from a smaller volume at the centre of the stream, which contains a smaller range of exit ages (section 6.2.2.1). Volume-selective spectra were acquired from flowing samples using a flow-compensated STEAM pulse sequence and the PROJSAT pulse sequence of chapter 5.

6.4.1 Flow-Compensated STEAM

6.4.1.1 Theory

When a magnetic field gradient **g** is applied, a spin at a position **r** from the gradient origin acquires a gradient-induced phase whose magnitude is given by (Pope and Yao, 1993):

$$\phi(t) = \gamma \int \mathbf{g} \cdot \mathbf{r}\, dt\,. \tag{6.54}$$

The phase depends only on the component of position that lies along the gradient direction, say x. For a spin at position x_0 at $t = 0$, moving at a steady velocity v_0 along the x direction, the phase shift relative to a stationary spin at $x = 0$ is given by:

$$\phi(t) = \gamma x_0 \int g(t)\, dt + \gamma v_0 \int g(t) \cdot t\, dt\,. \tag{6.55}$$

Equation (6.55) shows that the phase shift has a position-dependent and a velocity-dependent component, so spins at different positions or travelling at different velocities acquire different phases when the gradient is applied. These two phase components are proportional to the zeroth and first gradient moments respectively, where the n^{th} gradient moment is defined by:

$$M_n = \int_0^t g(t) \cdot t^n\, dt\,. \tag{6.56}$$

Therefore, by choosing gradient shapes with appropriate values of M_0 and M_1, one can change the sensitivity of the phase to position and velocity. In 2D imaging, a unipolar phase gradient with non-zero M_0 (figure 6.20(a)) is used so that the phase of the signal is proportional to position. In volume-resolved spectroscopy, bipolar slice selection gradients with $M_0 = 0$ (figure 6.20(b)) are used to refocus the signal from different positions in the sample. Unipolar and bipolar gradients both have non-zero M_1, so they cannot be applied to flowing samples without loss of phase coherence. This loss is caused by the distribution of velocities in the sample, since each velocity causes the spins to have a different phase. To apply imaging or volume-resolved spectroscopy to flowing samples requires flow-compensated gradients with special shapes for which $M_1 = 0$ (figure 6.20(c)). Various examples of flow-compensated gradients are given by Pope and Yao (1993).

6.4.1.2 Pulse Sequence

The STEAM pulse sequence (section 5.3) was modified to include the flow-compensated slice-selection gradients shown in figure 6.20(c). The new STEAM_FC pulse sequences for acquiring volume-selective spectra, 1D profiles and 2D images are shown in figure 6.21. Three sinc-modulated soft 90° pulses are applied in the presence of flow-compensated slice-selection gradients to select a box-shaped volume. The second slice-selection gradient is mirrored relative to the others because

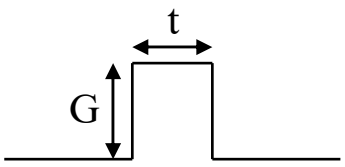

$M_0 = G\,t$
$M_1 = G\,t^2/2$

(a) Unipolar gradient

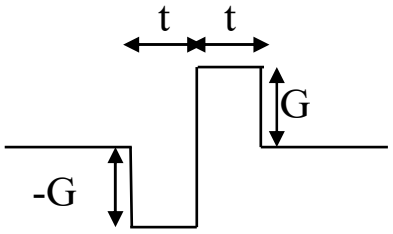

$M_0 = 0$
$M_1 = 2G\,t^2$

(b) Bipolar gradient

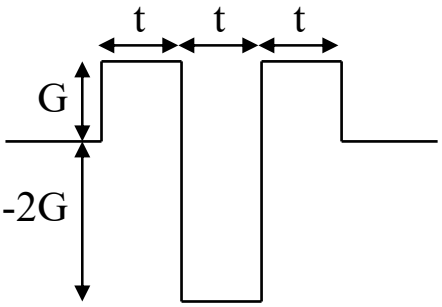

$M_0 = 0$
$M_1 = 0$

(c) Flow compensated gradient

Figure 6.20 Gradient waveforms and their moments. *(a)* A unipolar gradient used for encoding position, with both moments nonzero. *(b)* A bipolar gradient independent of position with $M_0 = 0$. *(c)* A flow compensated gradient with both moments zero.

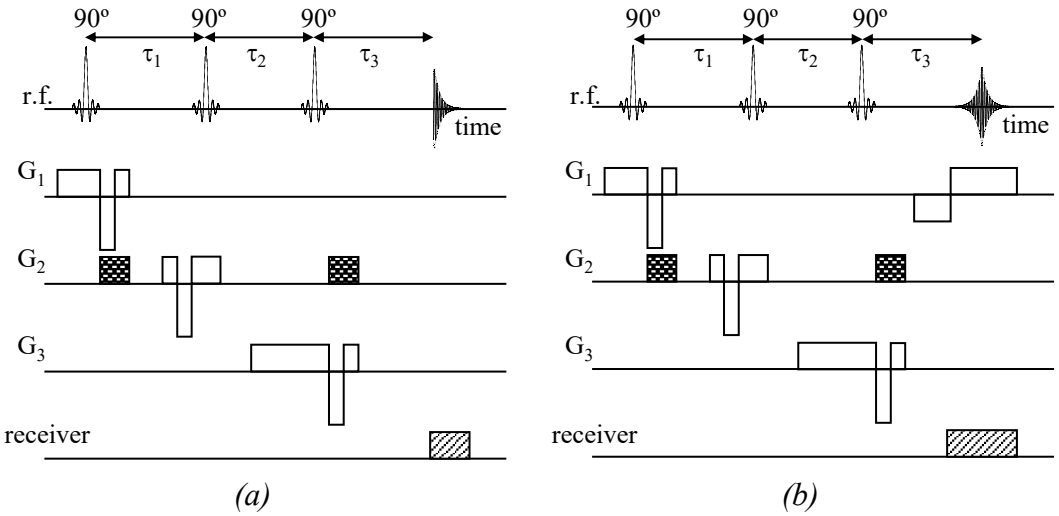

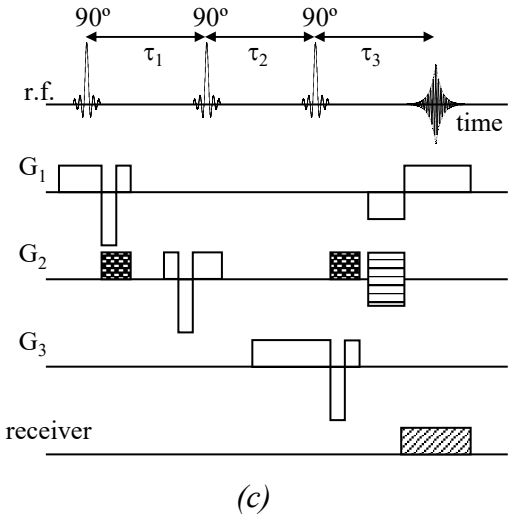

Phase Cycle																
1st 90° pulse	+x	+x	+x	+x	+x	+x	+x	+x	-x	-x	-x	-x	-x	-x	-x	-x
2nd 90° pulse	+x	+x	-x	-x	+x	+x	-x	-x	+x	+x	-x	-x	+x	+x	-x	-x
3rd 90° pulse	-x	+x	-x	+x	-y	+y	-y	+y	-x	+x	-x	+x	-y	+y	-y	+y
receiver	+x	-x	-x	+x	+y	-y	-y	+y	-x	+x	+x	-x	-y	+y	+y	-y

Figure 6.21 STEAM_FC pulse sequences for acquisition of *(a)* a spectrum, *(b)* a 1D profile, *(c)* a 2D image. Three soft 90º pulses excite a stimulated echo from a volume at the intersection of three slices. The three slice-selection gradients are flow compensated. The sixteen-scan phase cycle removes interference from unwanted echoes.

the magnetisation cannot be refocused when it is aligned along the z axis. To ensure that the gradient moments M_0 and M_1 are zero, the refocusing gradients are not trimmed. The flow-compensated gradients immediately refocus the dephased signal, so balanced homospoil gradients are added to eliminate unwanted gradient echoes. The gradient echoes cause phase twists in the spectra (figure 6.22(a)) and incorrect volume selection (figure 6.22(b)). The other gradients are unchanged. The same eight-scan phase cycle is used as for STEAM.

The signal attenuation due to diffusion (section 5.3.3.4) is less for STEAM_FC than for STEAM or STEAMQR because the flow-compensated gradients have no delay between dephasing and refocusing. The only attenuation is from the balanced homospoil gradients, which reduce the signal to $S = 0.9126\ S_0$ assuming the diffusion coefficient of water ($D = 2.0\times10^{-9}$ m^2/s). The shortest delay between the first 90° pulse and the start of acquisition is 14.07 ms for STEAM_FC and is longer than for STEAM or STEAMQR. Of this time, the magnetisation spends 8.02 ms aligned along the z axis undergoing T_1 relaxation, and 6.05 ms in the transverse plane undergoing T_2 relaxation. Therefore, STEAM_FC spectra exhibit less T_2 relaxation contrast and more T_1 relaxation contrast compared to STEAM and STEAMQR spectra. Since $T_1 > T_2$ for liquids, this implies less overall contrast for STEAM_FC.

The accuracy of volume selectivity for STEAM_FC is higher than for STEAM. The slice selection profiles are the same since the same soft pulses are used for excitation, but signal dephasing and motion losses are eliminated in STEAM_FC. The extent of signal contamination was assessed using 1D profiles of a static sample acquired with the pulse sequence shown in figure 6.21(b) and analysed as described in section 5.3.3.6. For a nominal slice thickness of 1.00 mm, the actual slice thickness was 1.02 mm along x, 1.09 mm along y and 1.02 mm along z (figure 6.23). The actual selected volume was 1.13 mm^3 and was closest to the nominal volume of 1.00 mm^3 of the three STEAM variants. The contaminant signal (13.6%) was the largest because of the smaller selection volume. When comparing profile intensities, the STEAM_FC x, y and z profiles had intensities of 1.05, 0.99 and 0.99 relative to the STEAM profiles, leading to an overall STEAM_FC signal of 1.02 relative to STEAM. Therefore, the STEAM_FC sequence is superior to STEAM even for static samples because it has better volume selection, lower diffusion attenuation, lower T_2 relaxation contrast and comparable signal intensity.

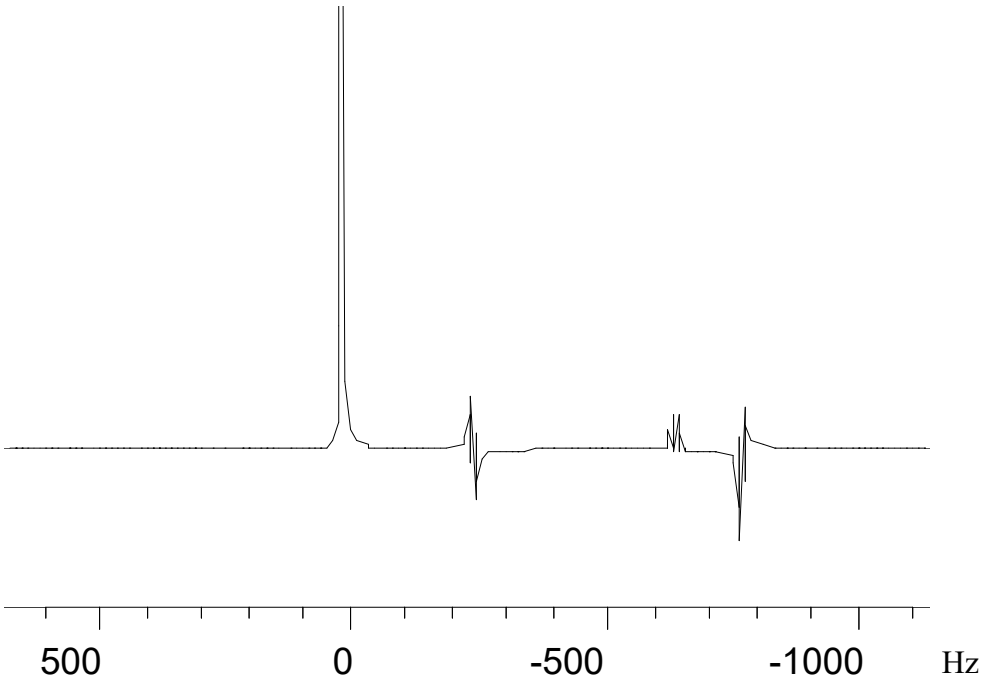

(a)

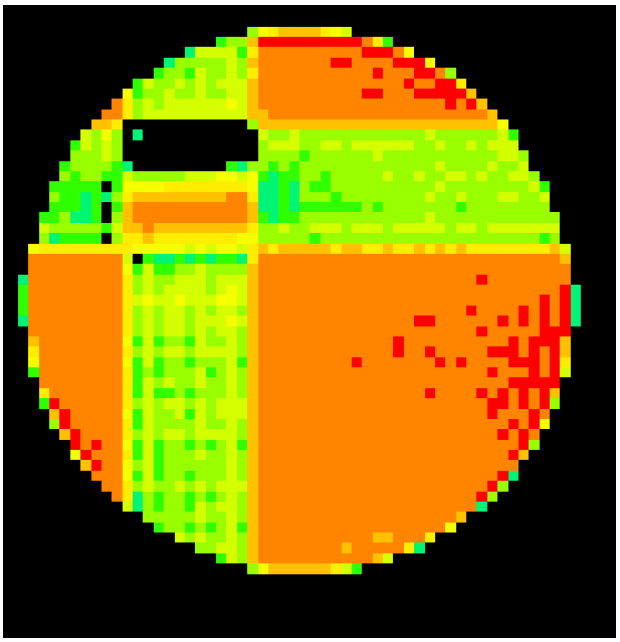

(b)

Figure 6.22 *(a)* STEAM_FC spectrum with a large phase twist caused by the refocusing of unwanted gradient echoes.

(b) STEAM_FC image showing inverted volume selection due to the refocusing of gradient echoes by the flow-compensated gradients.

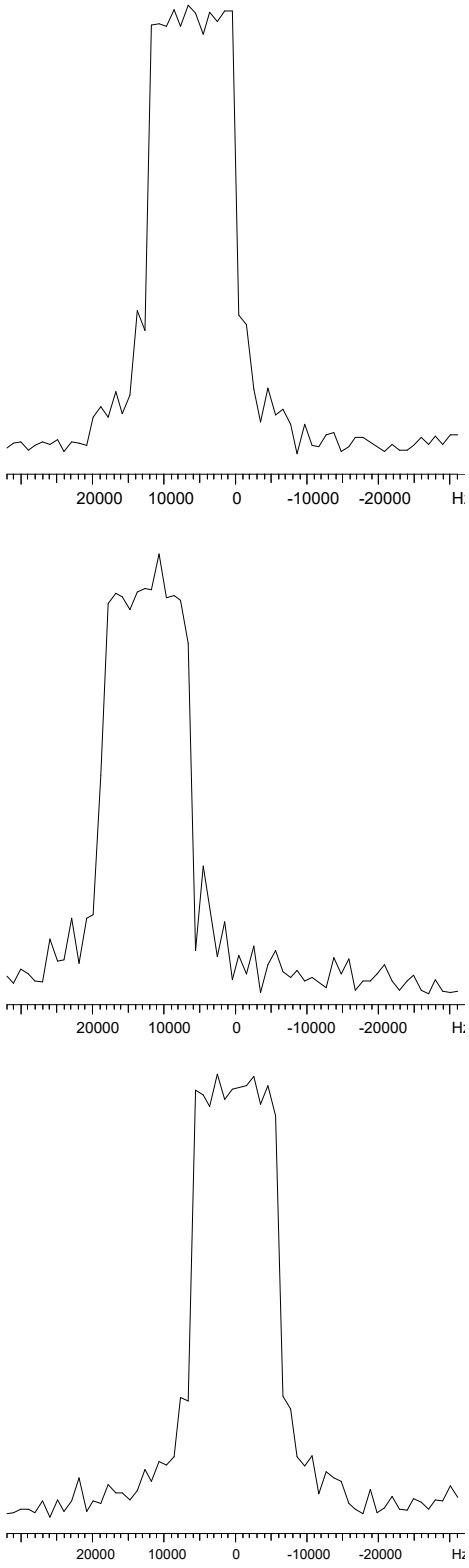

Figure 6.23 Experimental STEAM_FC profiles of ^{1}H at 200 MHz along the *x*, *y*, and *z* axes (top to bottom) for a 1×1×1 mm^3 selected volume in a four-component test sample.

Under flowing conditions, the differences between STEAM and STEAM_FC become more marked. For a water-propan-1-ol mixture flowing at 14 ml/min, the STEAM_FC *x*, *y* and *z* profiles give an overall signal 7.76 times the STEAM signal, because of flow-induced dephasing in the STEAM sequence. At a higher flow rate of 58 ml/min, the STEAM_FC signal is 9.18 times the STEAM signal. This behaviour can also be seen in the corresponding STEAM_FC spectra (figure 6.24), which have much higher signal-to-noise ratios than their STEAM equivalents.

6.4.1.3 Experimental

The composition of a non-flowing mixture of methanol (35.71 mol%), toluene (8.88 mol%), ethyl acetate (30.61 mol%) and isooctane (24.80 mol%) was measured using several STEAM_FC spectra and compared with the results from STEAM in chapter 5. The STEAM_FC acquisition parameters were: 1×1×1 mm^3 selected volume, 8 scans, 16384 data points, spectral width 5000 Hz, soft 90° pulse sinc5.1000 duration 1 ms, soft pulse power 36 dB, gradient stabilisation delay 1 ms, homospoil gradient duration 4 ms, balanced homospoil gradient duration 1.005 ms, refocusing gradient duration 0.5 ms, repetition time 15 s, receiver gain 256.

STEAM and STEAM_FC spectra were acquired of the flowing stream described in section 6.3.1. The acquisition parameters for both pulse sequences were: 1×1×10 mm^3 selected volume (*x*×*y*×*z*), 16 scans, 32768 data points, spectral width 5000 Hz, soft 90° pulse sinc5.1000 duration 1 ms, soft pulse power 36 dB, gradient stabilisation delay 1 ms, homospoil gradient duration 5 ms, refocusing gradient duration 0.5 ms, repetition time 30 s, receiver gain 128. As the flow rate was increased, the repetition time and number of data points were decreased as for the ZG spectra. The selected volume was 10 mm along the flow direction (*z*) because 1 mm was too short to observe a signal at high flow rates.

6.4.1.4 Results

The STEAM and STEAM_FC spectra of the non-flowing mixture had similar signal-to-noise ratios of ~350, and gave composition results of similar accuracy (table 6.4). The mean error for STEAM_FC was 0.97 mol%, compared to 0.96 mol% for STEAM.

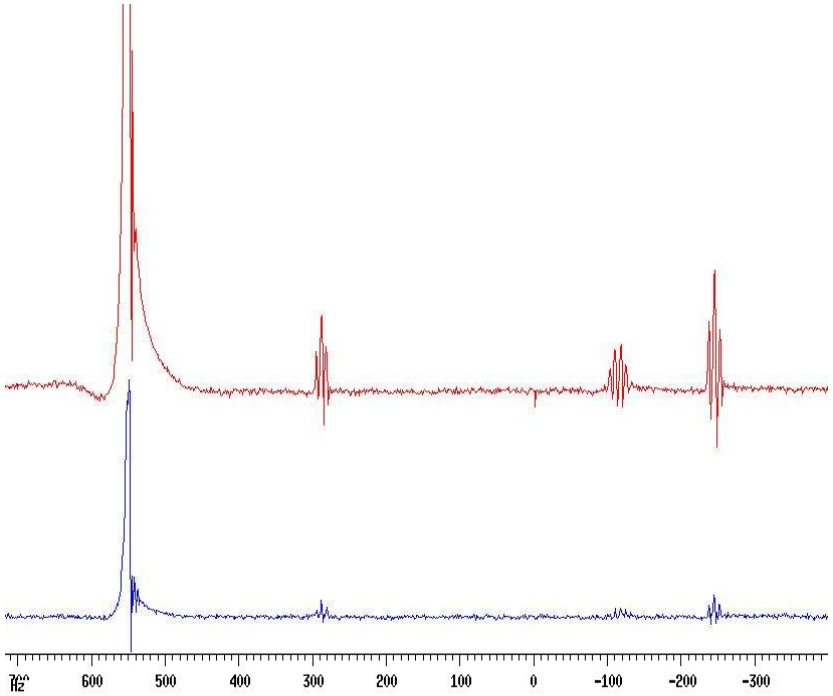

(a)

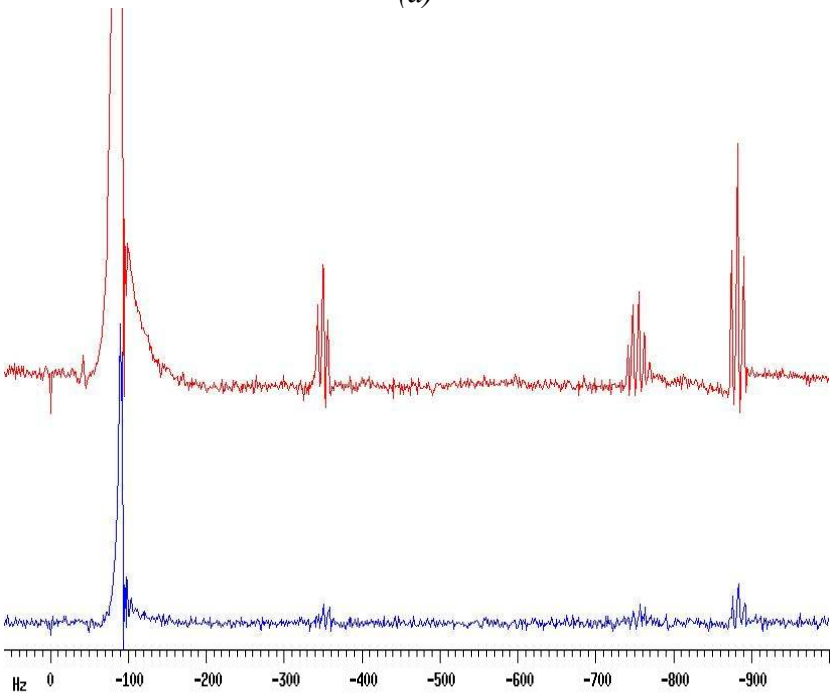

(b)

Figure 6.24 Comparison of STEAM and STEAM_FC ^{1}H NMR spectra for a mixture of water-propanol flowing at *(a)* 14 ml/min and *(b)* 58 ml/min. The red spectra were acquired using STEAM_FC and the blue spectra using STEAM. The signal-to-noise ratio is clearly higher for STEAM_FC.

Component	*Composition by weight (mol%)*	*STEAM_FC (mol%)*	*STEAM (mol%)*
methanol	35.71	37.46	36.43
toluene	8.88	7.84	7.48
ethyl acetate	30.61	30.80	31.81
isooctane	24.80	23.90	24.28
Average error	---	*0.97*	*0.96*

Table 6.4 Composition of four-component test mixture (in mol%) determined from volume-selective NMR spectra. The average error is calculated relative to the composition by weight. The uncertainty in the measured values is ±1 mol%.

STEAM and STEAM_FC spectra of the flowing sample at various flow rates from 0 to 228 ml/min are shown in figure 6.25. The flow-induced peak broadening is clearly visible. The STEAM_FC spectrum of the static sample had a narrower linewidth (0.61 Hz) than the STEAM spectrum (0.92 Hz), but for the flowing samples, the outflow effects dominated and the STEAM and STEAM_FC spectra had the same linewidths. These linewidths were larger than those found in ZG spectra at the same flow rates because the 10-mm slice along the flow direction was shorter than the length of the detection coil. For example, at 228 ml/min the linewidths were 27 Hz for STEAM and STEAM_FC, compared to 14.6 Hz for ZG.

The composition of the mixture measured under flowing conditions using STEAM and STEAM_FC is shown in figure 6.26 along with the bulk composition measured under static conditions over the same period. The scatter in the data and the error bars are larger than for the ZG data because of the lower signal-to-noise ratio and the relaxation weighting in the volume-selective spectra. The difference between the volume-selective measurements and the static bulk measurements (~2 mol%) is larger than for the ZG measurements (~1 mol%). The difference appears similar for both pulse sequences, but there is a lot of scatter in the data (figure 6.27).

In conclusion, bulk spectroscopy is more accurate than volume-selective spectroscopy for a sample with a constant composition, due to the higher signal-to-noise ratio. For a heterogeneous stream, however, volume-selective spectroscopy yields information not available by other means, as shown in section 6.5 below.

6.4.2 PROJSAT

The PROJSAT pulse sequence (section 5.4) was used to acquire volume-selective spectra of the flowing stream described in section 6.3. The gradients in the PROJSAT spectrum were not flow compensated because their purpose was to dephase the signal outside the volume of interest (VOI), so additional flow-induced dephasing would not affect the magnetisation inside the VOI. At high enough flow rates, the flow of unsaturated magnetisation into the coil during signal acquisition could lead to unwanted signal, so one aim of the experiment was to find the maximum flow rate for which PROJSAT could be used without signal contamination. The other aim was to determine the accuracy of the composition measurements using PROJSAT.

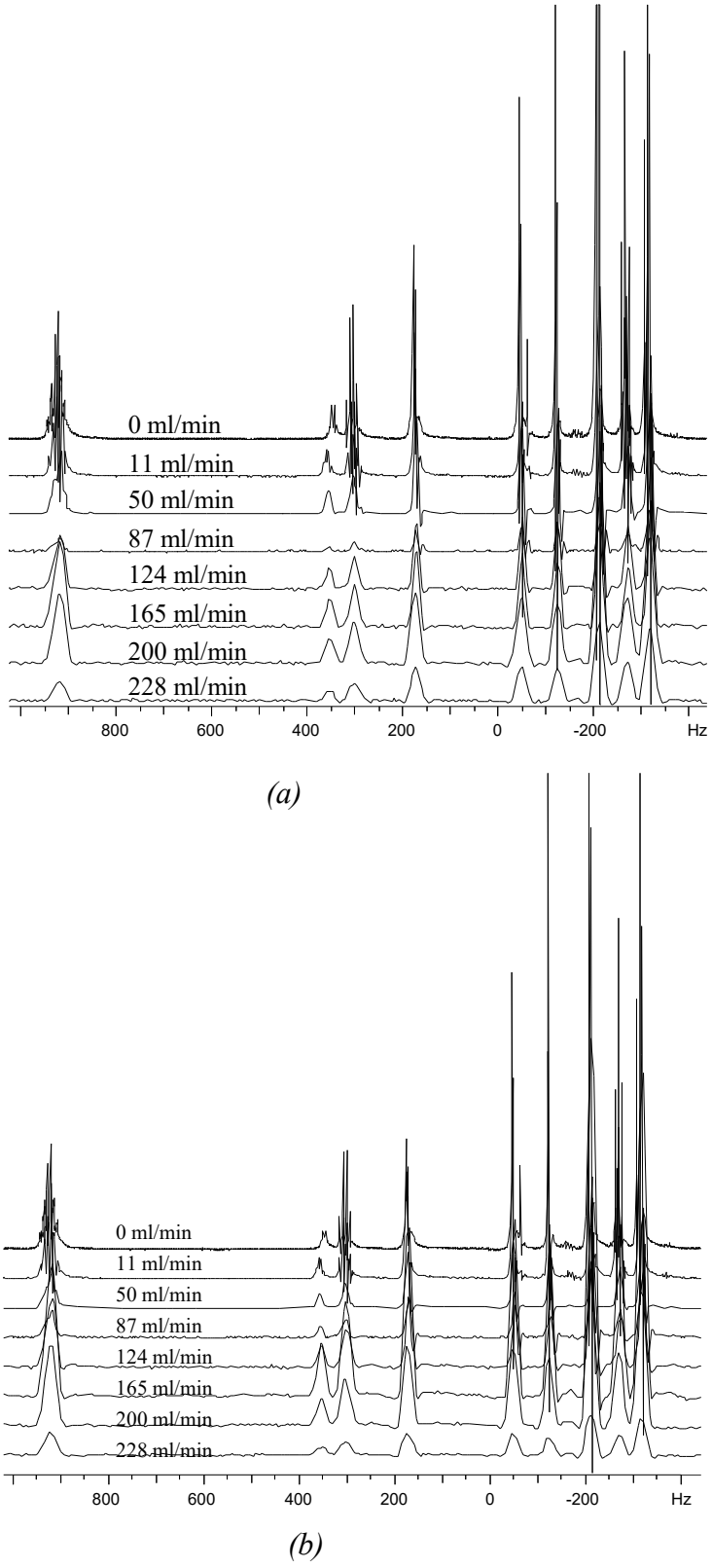

Figure 6.25 Volume-selective ^{1}H NMR spectra of a mixture of methanol-toluene-cyclohexane-isooctane-ethyl acetate flowing at 0 to 228 ml/min, acquired using *(a)* STEAM and *(b)* STEAM_FC pulse sequences. Flow-induced broadening is clearly visible in both sets of spectra.

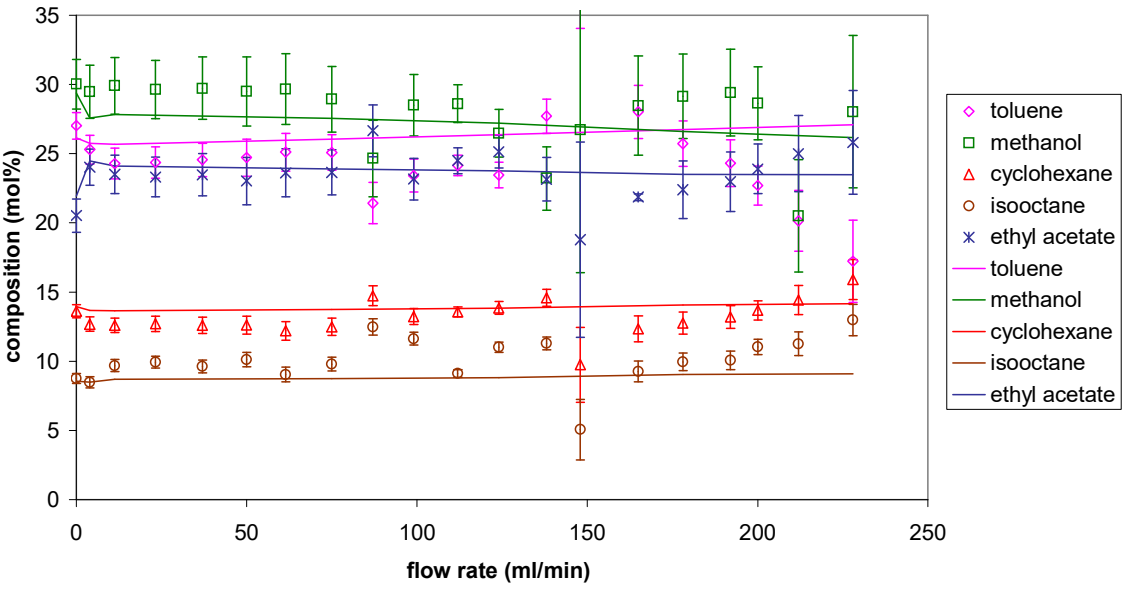

(a)

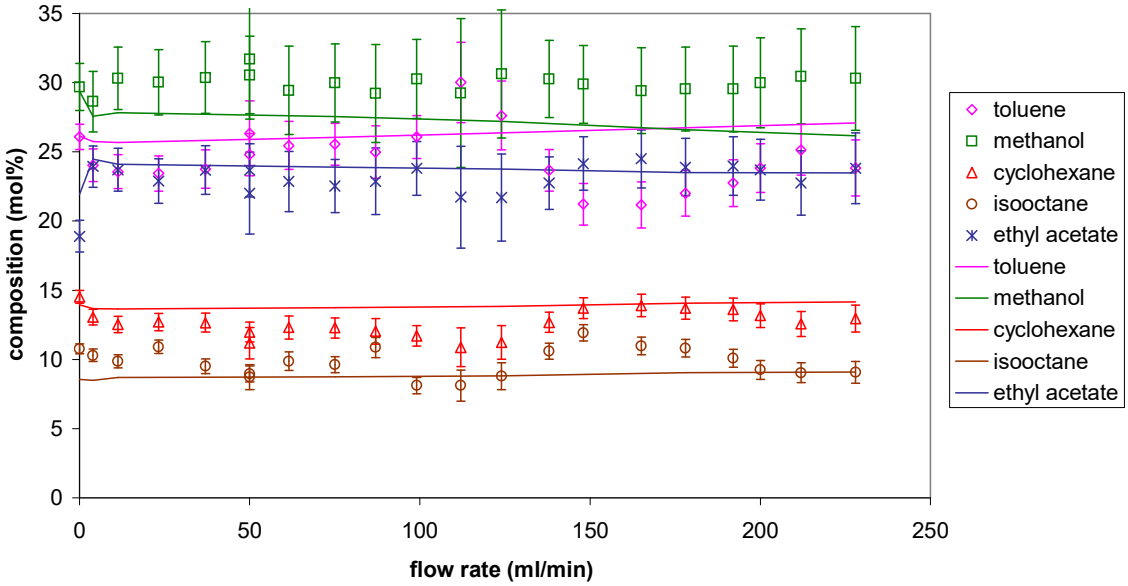

(b)

Figure 6.26 Composition of the five-component mixture flowing at various flow rates, measured inside a 1×1 ×10 mm^3 volume at the centre of the pipe using volume-selective ^1H NMR spectroscopy:
(a) using the STEAM pulse sequence,
(b) using the STEAM_FC pulse sequence.

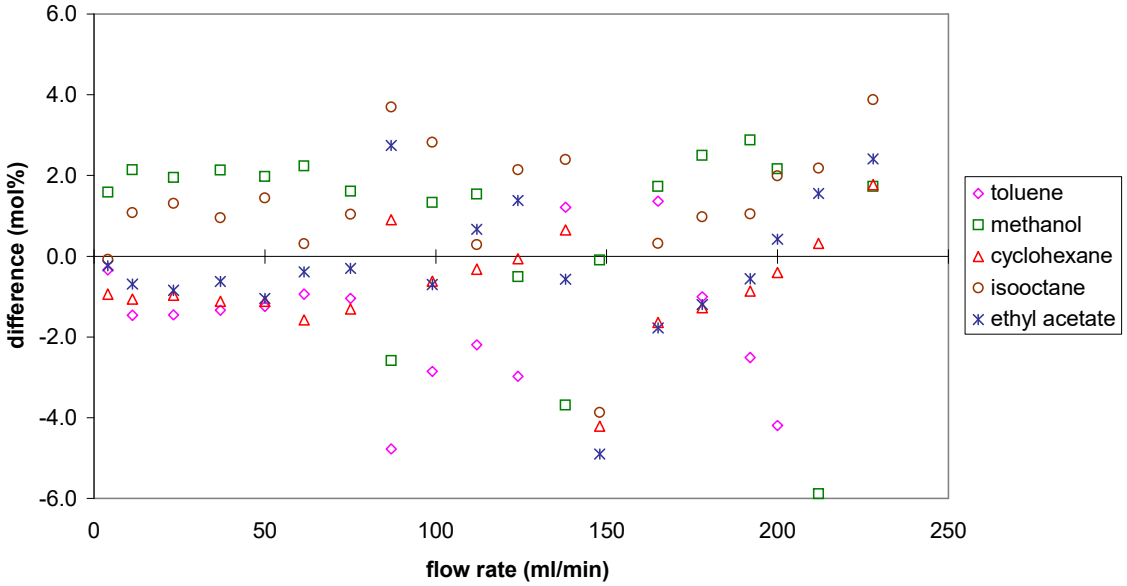

(a)

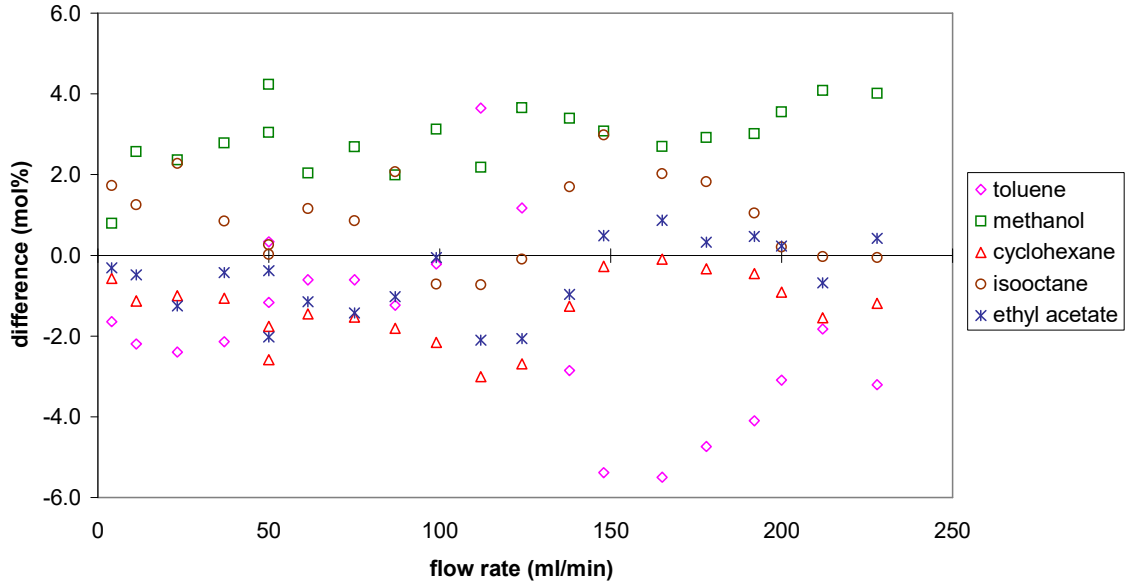

(b)

Figure 6.27 Differences between the compositions measured by static bulk ^{1}H NMR spectroscopy and by volume-selective spectroscopy in the presence of flow:
(a) using the STEAM pulse sequence,
(b) using the STEAM_FC pulse sequence.

6.4.2.1 Experimental

The modified PROJSAT pulse sequence with continuous gradients (figure 5.23) was used with the following parameters to select a 1-mm diameter cylinder at the centre of the stream: 32 "cossinc1" saturation pulses (0.5 ms each), 180° cycle, no homospoil gradients, *sp*0 = 28 dB, d2 = 0.2 ms, d3 = 0.1 ms, d4 = 2 ms, 16 scans, 32768 data points, spectral width 5000 Hz, repetition time 30 s, receiver gain 64. The spectra were processed manually due to the unusual lineshapes, and the compositions were determined from the integrals of the peaks including the high-frequency humps.

A series of longitudinal (*zx*) PROJSAT images were used to observe the inflow of unsaturated magnetisation into the coil at different flow rates. The same saturation parameters were used as above. The image parameters were: field of view 5×5 mm^2, 64×64 pixels, 10 kHz/pixel, slice thickness 1 mm, soft 90° pulse sinc5.1000 of duration 1 ms and *sp*0 = 36 dB.

6.4.2.2 Results

The PROJSAT images revealed no inflow of unsaturated magnetisation up to 100 ml/min (figure 6.28(a)). Images at higher flow rates had such low signal-to-noise ratios that no details were visible. Therefore, outer volume suppression was satisfactory and signal contamination was negligible for flow rates up to 100 ml/min.

A stacked plot of PROJSAT spectra at various flow rates between 0 and 228 ml/min is shown in figure 6.28(b). The flow-induced peak broadening is clearly visible. The composition of the mixture measured using PROJSAT under flowing conditions is shown in figure 6.29(a). The PROJSAT results were close to the ZG results, but had larger errors and more scatter, particularly at flow rates above 100 ml/min. Compared to STEAM and STEAM_FC, PROJSAT had smaller errors because of the higher signal-to-noise ratio and lower relaxation contrast. The differences between the bulk static and flowing PROJSAT measurements (figure 6.29(b)) were larger than ZG and smaller than STEAM and STEAM_FC. Therefore, PROJSAT took an intermediate position between ZG and STEAM regarding volume selectivity, signal-to-noise ratio and quantitative accuracy.

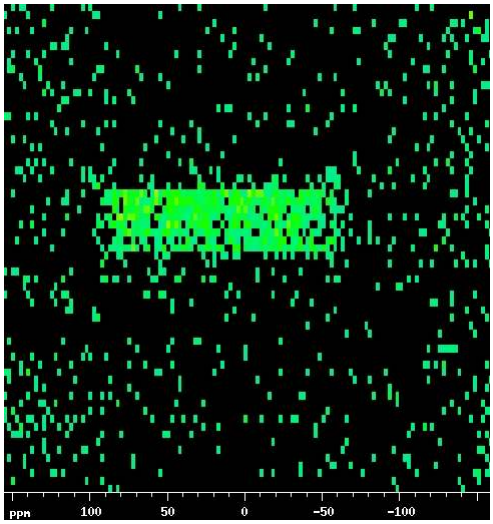

(a)

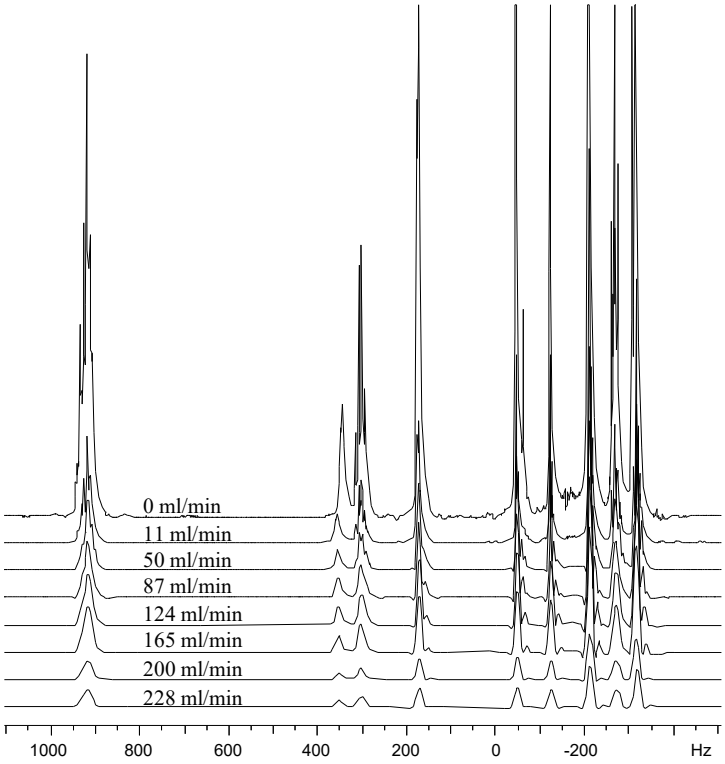

(b)

Figure 6.28 *(a)* PROJSAT image acquired along the *zy* plane of the mixture flowing at 99 ml/min. The only signal is observed in the central core, so the outer volume is still saturated in the presence of flow. *(b)* Volume-selective ^{1}H NMR spectra of a mixture of methanol-toluene-cyclohexane-isooctane-ethyl acetate flowing at 0 to 228 ml/min, acquired using PROJSAT.

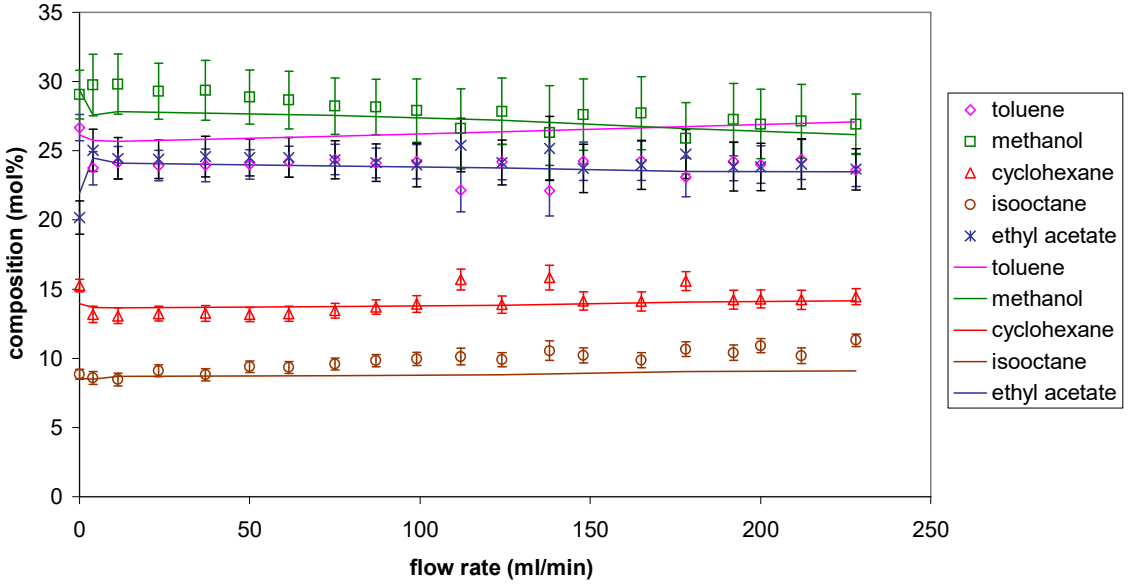

(a)

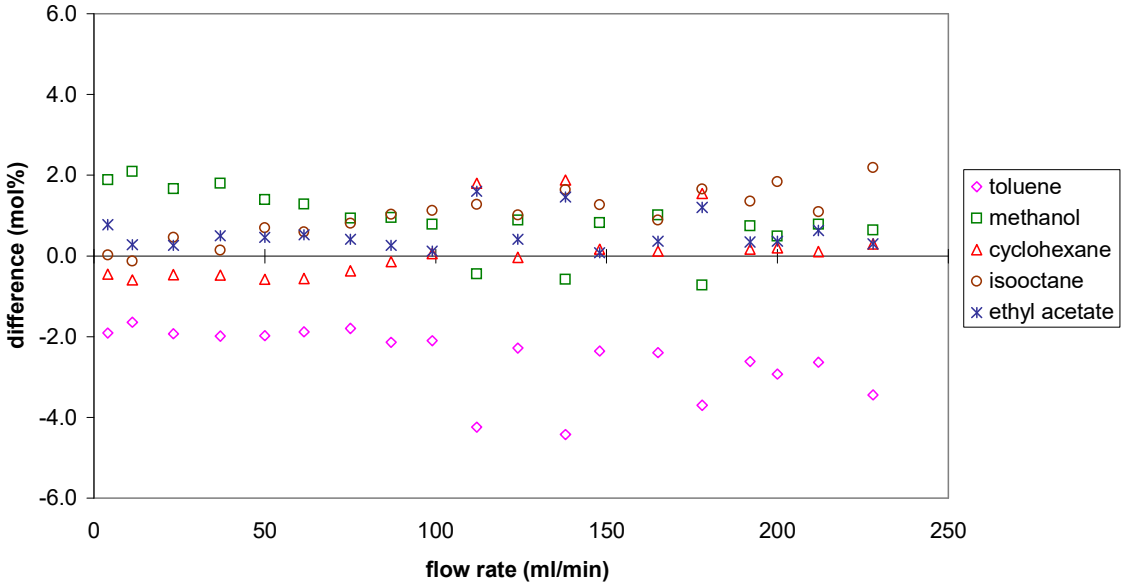

(b)

Figure 6.29 *(a)* Composition of the five-component mixture flowing at various flow rates, measured inside a 1-mm diameter cylinder at the centre of the stream using the PROJSAT pulse sequence (symbols) and compared to the static bulk composition (lines).
(b) Differences between the compositions measured by static bulk ^{1}H NMR spectroscopy and PROJSAT in the presence of flow.

6.5 Heterogeneity in Flowing Emulsions

For a more rigorous test of volume-selective spectroscopy, a spatially heterogeneous flowing stream was used consisting of an emulsion of *o*-xylene in water with Tween 40 (polyoxyethylene sorbitan monopalmitate) emulsifier. The online measurement of the droplet size distribution of this emulsion is described in detail in chapter 7. The STEAM and STEAM_FC pulse sequences were used to acquire volume-selective spectra of the flowing emulsion at different radial positions and different flow rates. The PROJSAT sequence was not used because the position of the selected volume could not easily be moved from the centre of the stream.

6.5.1 Experimental

The first emulsion consisted of 32 wt% *o*-xylene, 64 wt% water and 4 wt% Tween 40. The emulsion was prepared by preparing of solution of Tween 40 in water, then adding the *o*-xylene and stirring until it was homogeneous. The emulsion was pumped through the flow loop described in section 6.3.1, where the test section was a short 5-mm glass tube attached to Viton rubber tubing (figure 6.16). The emulsion in the reservoir was continually stirred to prevent flocculation. The ^{1}H STEAM and STEAM_FC spectra were acquired using a Bruker DMX 200 spectrometer with a 4.7 T superconducting magnet and a 5 mm micro-imaging coil tuned to a ^{1}H resonance frequency of 199.707 MHz. The acquisition parameters for STEAM and STEAM_FC were: 1×1×10 mm^3 selected volume (x×y×z), 16 scans, 16384 data points, spectral width 5000 Hz, soft 90° pulse sinc5.1000 duration 1 ms, soft pulse power 36 dB, gradient stabilisation delay 1 ms, homospoil gradient duration 5 ms, refocusing gradient duration 0.5 ms, repetition time 10 s, receiver gain 256. Spectra were acquired at nine different positions in the stream (figure 6.30) at flow rates of 20 ml/min, 43 ml/min and 78 ml/min.

The second emulsion consisted of 42 wt% *o*-xylene, 45 wt% water and 13 wt% Tween 40. The flow loop consisted of a 1.5-m glass tube of 14 mm o.d. and 11 mm i.d attached to Viton rubber tubing. The emulsion was pumped using a peristaltic pump with a sealed bottle downstream of the pump to dampen the pulses in the flow (figure 6.31). The emulsion in the reservoir was continually stirred to prevent flocculation. The ^{1}H STEAM and STEAM_FC spectra were acquired using a Bruker DMX 300 spectrometer with a 7.05 T superconducting magnet and a 15 mm micro-

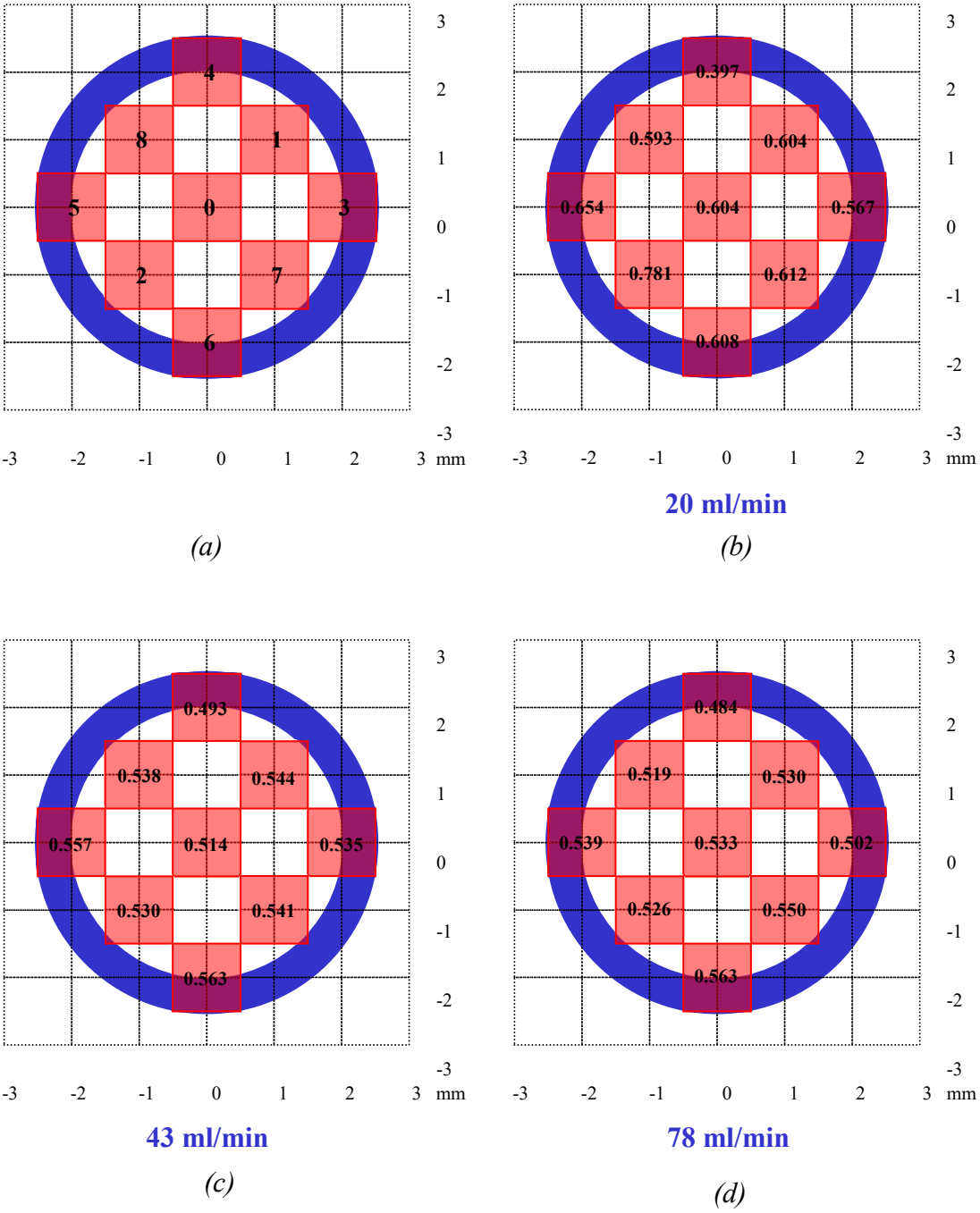

Figure 6.30 *(a)* Grid of locations used to measure the local composition of a flowing water/*o*-xylene emulsion. The blue ring represents the glass wall of the pipe and the shaded squares represent the 1×1 mm^2 cross-sections of the volumes selected using STEAM and STEAM_FC.
(b) Local ratios of *o*-xylene to water (by weight) measured using STEAM_FC for the emulsion flowing at 20 ml/min.
(c) as (b), at 43 ml/min.
(d) as (b), at 78 ml/min.

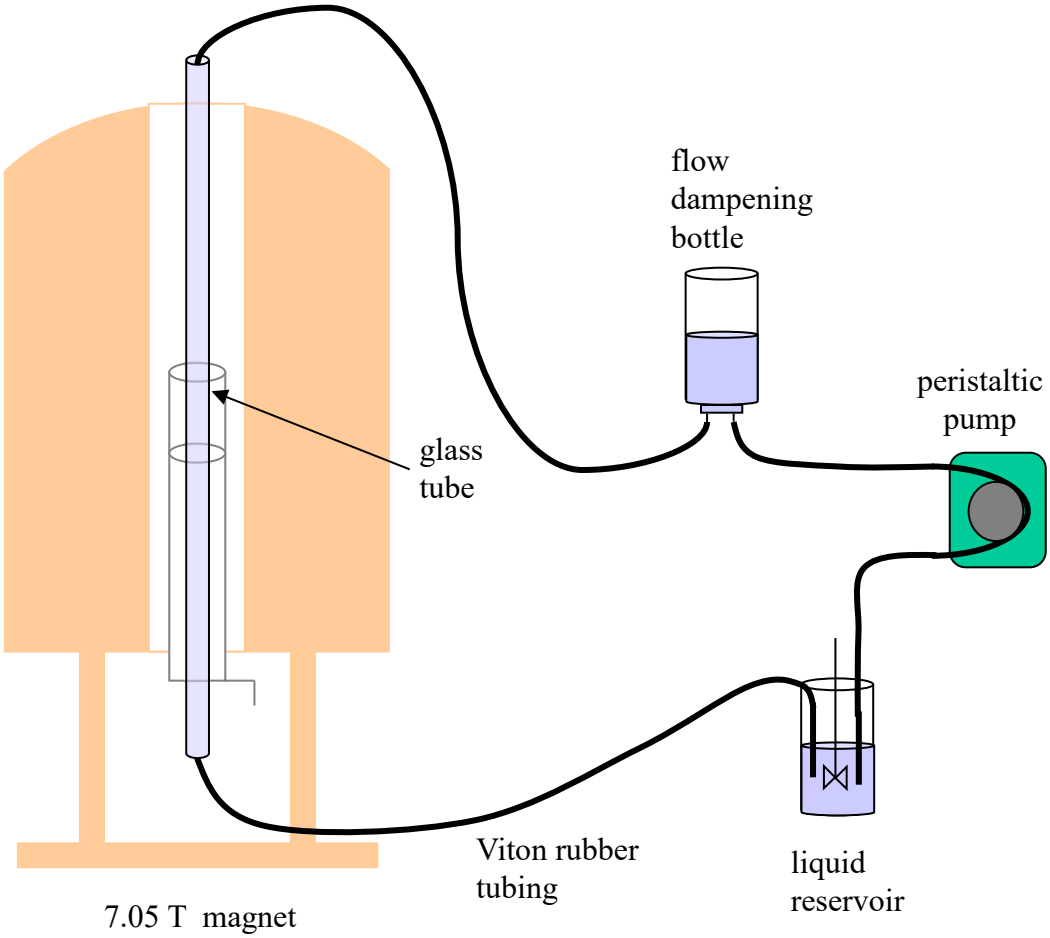

Figure 6.31 Flow loop for NMR measurements on a stream flowing through a long, wide glass tube (1.5 m length, 11 mm i.d.) inside a 7.05 T magnet.

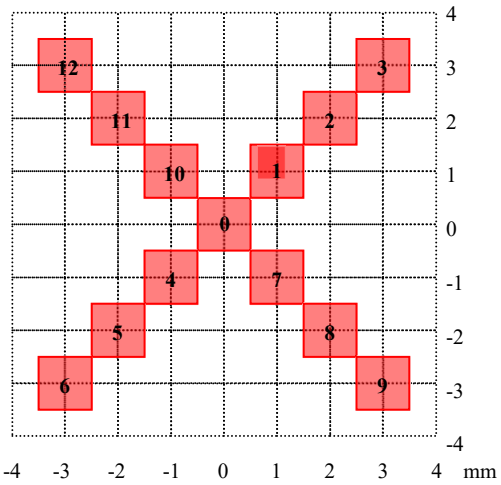

(a)

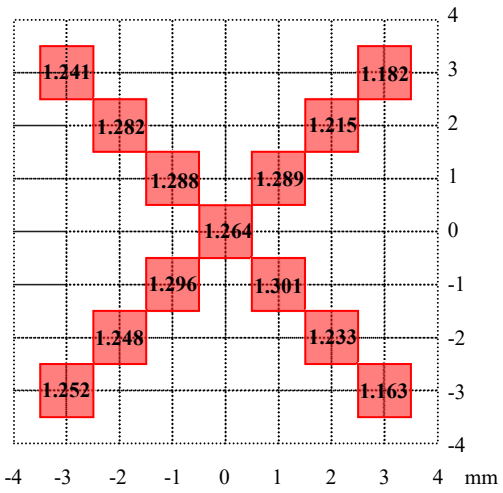

9.6 ml/min

(b)

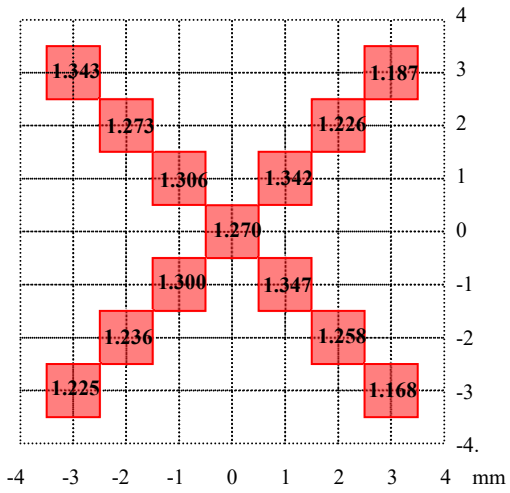

19.4 ml/min

(c)

Figure 6.32 *(a)* Grid of locations used to measure the local composition of a flowing water/*o*-xylene emulsion in a wide glass pipe. The glass wall of the pipe is out of the range of the grid. The shaded squares represent the 1×1 mm^2 cross-sections of the volumes selected using STEAM and STEAM_FC.
(b) Local ratios of *o*-xylene to water (by weight) measured using STEAM_FC for the emulsion flowing at 9.6 ml/min.
(c) as (b), at 19.4 ml/min.

imaging coil tuned to a ^{1}H resonance frequency of 300.129 MHz. The acquisition parameters for STEAM and STEAM_FC were: 1×1×10 mm^3 selected volume (x×y×z), 64 scans, 8192 data points, spectral width 20000 Hz, soft 90° pulse gauss5.1000 duration 1 ms, soft pulse power 33 dB, gradient stabilisation delay 1 ms, homospoil gradient duration 1 ms, refocusing gradient duration 0.5 ms, repetition time 5 s, receiver gain 256. Spectra were acquired in a cross pattern at thirteen different positions in the stream (figure 6.32) at flow rates of 9.6 ml/min and 19.6 ml/min.

6.5.2 Results

The measured compositions were very similar for STEAM and STEAM_FC, so only the STEAM_FC results are discussed here. In both experiments, different compositions were found at different positions in the emulsion stream. These compositions are shown graphically in figure 6.30 for the first experiment and figure 6.32 for the second experiment. The shaded squares in these figures represent the 1×1-mm^2 cross-sections of the selected volumes, while the numbers show the ratio of *o*-xylene to water by weight measured inside these volumes by STEAM_FC. The bulk ratios measured by ZG were 0.50 for the first experiment and 0.96 for the second. In both experiments, the stream contained regions of higher and lower *o*-xylene content that did not change significantly with flow rate.

The first experiment showed a region of high *o*-xylene content in the lower left of the grid – positions 5, 2 and 6 – at all three flow rates. This concentration of *o*-xylene in one part of the stream was caused by the density difference between *o*-xylene and water. While the emulsion flowed horizontally through the Viton tubing from the reservoir and through the pump, the *o*-xylene droplets rose to the top of the stream, and this structure remained as the stream flowed through the magnet.

The cross-shaped grid in the second experiment was used to test the radial symmetry of the flow of the emulsion through a wider pipe. The grid covered an area of 7×7 mm^2 inside a pipe of 11-mm i.d. The *o*-xylene-to-water ratios in the grid were all higher than the bulk ratio of 0.96, indicating that more *o*-xylene was present at the centre of the stream that at the outer edges. The same behaviour was observed within the grid, with the highest *o*-xylene content near the centre for both flow rates. The radial symmetry was also largely observed. The shear-induced migration of the

o-xylene to the centre of the stream indicated that the viscosity of the emulsion increased with *o*-xylene content.

These experiments show the ability of volume-selective NMR spectroscopy to detect differences in composition as small as 1 wt% over 1-mm length scales. This quantitative information is not available using bulk spectroscopy, which gives the average composition. Nor can it be obtained by imaging, because the signals from different chemical species are unresolved when they are acquired in the presence of a gradient. The flow-compensated pulse sequences allow online measurement of flowing systems, which enables the observation of flow effects that would be missed in a stopped-flow system.

6.6 Conclusion

The characteristics of the flow regime have a large influence on the NMR signal obtained from a flowing sample. The existence of a distribution of velocities in a flowing stream has not been appreciated by NMR spectroscopists to date, as can be seen from a number of incorrect analyses of flow NMR experiments. A new model was derived based on the residence time distributions of the flowing nuclei inside the magnetic field and the detection coil. This model was used to explain flow-induced peak broadening, sensitivity enhancement and apparent relaxation enhancement. A commonly used exponential relaxation model was shown to be invalid because it was based on incorrect assumptions and did not agree with available experimental data.

Various pulse sequences were tested for their quantitative accuracy when measuring the composition of flowing multi-component liquids. Quantitative spectroscopy under flowing conditions has not been reported previously. Spectra of the entire stream using ZG gave measurements accurate to ±1 mol% at flow rates up to 50 ml/min. This level of accuracy was similar to that of measurements without flow (chapter 2). Volume-selective spectroscopy was used to measure the composition at the centre of the stream only. The new flow-compensated STEAM pulse sequence, STEAM_FC, had better volume selectivity, less diffusion attenuation and less T_2 relaxation contrast, but more signal contamination and more T_1 relaxation contrast than STEAM. Both volume-selective pulse sequences had similar quantitative accuracy for composition measurements (±2 mol%), but were less accurate than bulk spectroscopy because of a lower signal-to-noise ratio and higher relaxation contrast.

The PROJSAT pulse sequence was also tested on a flowing sample and was intermediate between ZG and STEAM/STEAM_FC in terms of accuracy. Finally, STEAM and STEAM_FC were used to show heterogeneity in the flow of an emulsion of *o*-xylene in water, with regions of high *o*-xylene content clearly visible in the stream. Flow-compensated volume-selective NMR spectroscopy yielded unique insights not available by other means, as it combined non-invasiveness with volume selectivity and quantitative accuracy.

6.7 References

Callaghan, P.T. (1991). *Principles of Nuclear Magnetic Resonance Microscopy*. pp. 438-457. Clarendon Press, Oxford, UK.

Caprihan, A., & Fukushima, E. (1990). Flow measurements by NMR. *Physics Reports, 198*, 195-235.

Chen, R., & Bailey, J.E. (1993). Observation of aerobic, growing *Escherichia coli* metabolism using an on-line nuclear magnetic resonance spectroscopy system. *Biotechnology and Bioengineering, 42*, 215-221.

Dorn, H.C. (1996). Flow NMR. In D.M. Grant & R.K. Harris (Eds.), *Encyclopedia of Nuclear Magnetic Resonance, vol. 3*, pp. 2026-2037. John Wiley & Sons, Chichester, UK.

Fukushima, E. (1999). Nuclear magnetic resonance as a tool to study flow. *Annual Reviews of Fluid Mechanics, 31*, 95-123.

Kay, J.M., & Nedderman, R.M. (1985). *Fluid Mechanics and Transfer Processes.* pp. 142,168. Cambridge University Press, Cambridge, UK.

Kose, K., Satoh, K., Inouye, T., & Yasuoka, H. (1985). NMR flow imaging. *Journal of the Physical Society of Japan, 54*, 81-92.

Laude, D.A.Jr., Lee, R.W.K., & Wilkins, C.L. (1984). Signal enhancement of long-relaxing ^{13}C nuclei by flow NMR. *Journal of Magnetic Resonance, 60*, 453-459.

Laude, D.A.Jr., Lee, R.W.K., & Wilkins, C.L. (1985a). Analytical applications of a recycled flow nuclear magnetic resonance system: signal enhancement of slowly relaxing nuclei. *Analytical Chemisty, 57*, 1281-1286.

Laude, D.A.Jr., Lee, R.W.K., & Wilkins, C.L. (1985b). Analytical applications of a recycled flow nuclear magnetic resonance system: quantitative analysis of slowly relaxing nuclei. *Analytical Chemisty, 57*, 1286-1290.

Lee, J.H., Li, X., Sammi, M.K., & Springer, C.S.Jr. (1999). Using flow relaxography to elucidate flow relaxivity. *Journal of Magnetic Resonance, 136*, 102-113.

Levenspiel, O. (1979). *The Chemical Reactor Omnibook*. ch. 1,3,61-68. OSU Book Stores, Inc., Corvallis, Oregon, USA.

Pope, J.M., & Yao, S. (1993). Quantitative NMR imaging of flow. *Concepts in Magnetic Resonance, 5*, 281-302.

Port, S.C. (1994). *Theoretical Probability for Applications*, p. 454. Wiley-Interscience, New York, USA.

Reynolds, O. (1883). An experimental investigation of the circumstances which determine whether the motion of water shall be direct or sinuous, and the law of resistance in parallel channels. *Philosophical Transactions of the Royal Society of London, 174*, 935-982.

Sudmeier, J.L., Günther, U.L., Albert, K., & Bachovchin, W.W. (1996). Sensitivity optimization in continuous-flow FTNMR. *Journal of Magnetic Resonance Series A, 118*, 145-156.

6.8 Nomenclature

(symbol)	(description)	(unit)
Vector Variables		
g	magnetic field gradient	T m^{-1}
r	position	m
Scalar Variables		
a	radius of pipe	m
d	diameter of pipe	m
d2	delay between gradient switching and soft pulse	s
d3	duration of homospoil gradient	s
d4	dead-time between end of saturation train and 90° pulse	s
D	self-diffusion coefficient	m^2 s^{-1}
$f_1(x)$	primary probability of variable x	-
$f_2(x)$	derived probability of variable x	-
$f_{in}(r,t)$	fraction of excited spins inside coil at position r and time t	-
$f_{out}(r,t)$	fraction of excited spins that have left the coil at position r and time t	-
$F_{in}(t)$	overall fraction of excited spins in coil at time t	-
L	length of pipe section	m
M	magnetisation	J s
M_0	equilibrium magnetisation	J s
M_n	n^{th} gradient moment	T m^{-1} s^{n+1}
Q	volumetric flow rate	m^3 s^{-1}
r	radial position	m
Re	Reynolds number	-
S	time-domain signal	-
S_0	signal before diffusion attenuation	-
$sp0$	soft pulse power attenuation level	dB
t	time	s
t_F	flow decay time	s
T_1	longitudinal relaxation time constant	s
T_1^*	apparent longitudinal relaxation time constant	s
T_2	spin-spin relaxation time constant	s
T_2^*	observed transverse relaxation time constant	s
u	velocity	m s^{-1}
u_0	centreline velocity	m s^{-1}
v_0	initial velocity	m s^{-1}
V^*	effective volume	m^3

V_i	volume of inversion slice	m^3
V_o	volume of observation slice	m^3
x	position along pipe	m
x_0	initial position	m
x, y, z	Cartesian axes: z is parallel to static magnetic field $\mathbf{B_0}$	-
γ	gyromagnetic ratio	rad T^{-1} s^{-1}
λ	peak full width at half maximum	s^{-1}
μ	fluid viscosity	Pa s
ρ	fluid density	kg m^{-3}
τ	residence time	s
τ^*	centreline residence time	s
$\bar{\tau}$	mean residence time	s
ϕ	gradient-induced phase shift	rad

7 PULSED GRADIENT NMR OF FLOWING EMULSIONS

7.1 Introduction

An emulsion is a heterogeneous system where one liquid is dispersed as droplets inside another liquid (Becher, 1966). The two liquids are usually oil and water, and two common types of emulsion are oil-in-water (O/W) and water-in-oil (W/O). Emulsions are stabilised by emulsifying agents that adsorb to the interface between the two phases and lower the interfacial tension (Everett, 1988). Emulsions have many practical applications, in the food, paint and pharmaceutical industries for example. The behaviour of an emulsion depends on its droplet size distribution, and there are many techniques for measuring this distribution. A well-established technique is pulsed field gradient (PFG) NMR that measures molecular displacement, so that the droplet size is inferred from the restricted motion of the molecules in the dispersed phase. The PFG technique has been used to determine the sizes of fat globules in cheese (Callaghan *et al.*, 1983) and water droplets in margarines (Balinov *et al.*, 1994b) among others, and to study droplet coalescence over time (Lee *et al.*, 1998). The determination of the droplet size distribution is normally carried out on a non-flowing emulsion. The aim of the work presented here is to determine the droplet size distribution of a flowing emulsion using PFG NMR. The pipeline flow of emulsions has been extensively studied by Pal (Pal and Rhodes, 1989; Pal, 1993; Pal, 1996) who determined the droplet sizes off-line using photomicrographs. However, the emulsion may have a different droplet size distribution while flowing due to the shear forces present. So far, there has been no report of a droplet size distribution from a flowing emulsion.

The PFG NMR experiment measures the displacement of the molecules over a fixed time interval by using a pair of magnetic field gradient pulses to encode the positions of the nuclei before and after the interval. Any motion of the molecules during the interval causes a loss of coherence and hence a lower signal intensity, from which the molecular self-diffusion coefficient can be determined (Stejskal and Tanner, 1965). In a non-flowing emulsion, the molecular displacement of the dispersed phase is restricted to the inside of the droplets, but in a flowing emulsion there is an additional net motion of the droplets, which increases the overall displacement. The

displacement due to flow carries no information on the droplet sizes, so it must be separated from the displacement due to self-diffusion. The distribution of flow velocities causes additional dephasing of the signal, which is refocused using a flow-compensated pulse sequence.

In this chapter, the theory of PFG NMR and restricted diffusion is presented and the method for inferring droplet size distributions from the data is described. The ordinary (single echo) and flow-compensated (double echo) PFG pulse sequences based on spin echoes and stimulated echoes are presented and compared by testing them on water, for which the self-diffusion constant is well-known. Volume-selective pulse sequences are also used to restrict the measurement to a well-defined region within a large sample. The pulse sequences are applied to several emulsions, both static and flowing, to determine their droplet size distributions.

7.2 Theory

7.2.1 Pulsed Field Gradients

Consider a static sample inside a homogeneous magnetic field. If a magnetic field gradient pulse is applied with duration δ, the spins in the sample acquire a phase shift that is proportional to their position along the gradient direction (section 6.3.1). This phase shift is reversed by applying an equal and opposite gradient pulse, giving a bipolar gradient with a vanishing zeroth moment. If the second gradient pulse is not applied directly after the first, but after an interval of duration Δ, then the nuclei will have moved to new positions during this interval due to molecular self-diffusion. These nuclei will have their first phase shift only partially reversed by the second pulse, because the second phase shift is proportional to their new position and does not match the first (figure 7.1). This leads to a loss of coherence and hence to a reduction in signal intensity. This is the principle of the pulsed-field gradient (PFG) technique for measuring molecular self-diffusion that was developed by Stejskal and Tanner. They used the spin-echo pulse sequence shown in figure 7.2(a) where the 90° pulse and 180° pulse were each followed by a gradient pulse of magnitude g and duration δ, separated by a delay Δ (Stejskal and Tanner, 1965). The spin echo was used to refocus the dephasing of the transverse magnetisation during Δ due to the

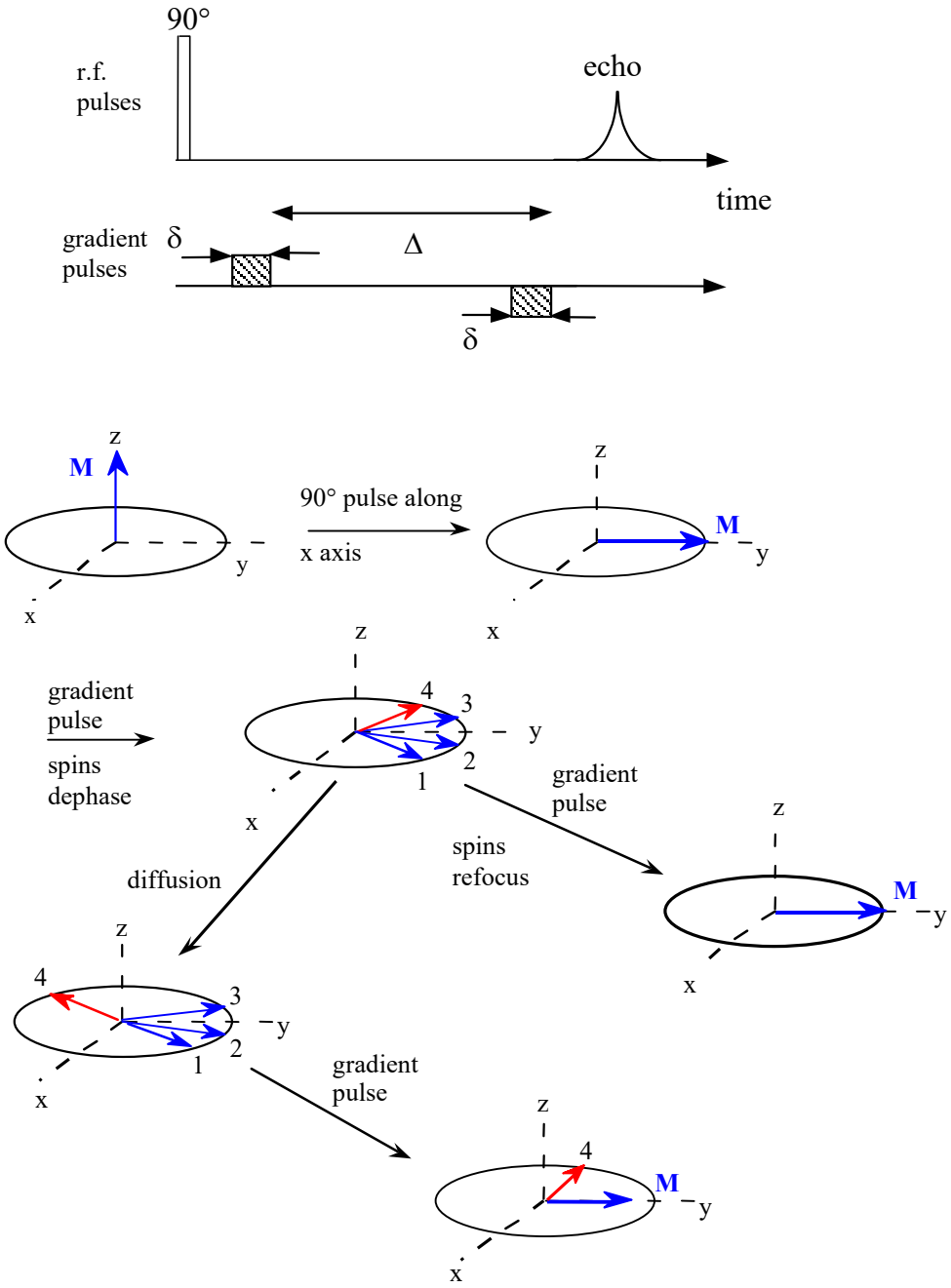

Figure 7.1 The principle of the pulsed-field gradient technique for measuring diffusion. The pulse sequence is shown in the upper diagram and the evolution of the magnetisation in the lower diagram. The nuclear spin marked in red diffuses to a new position during the interval Δ, so it is not refocused and the signal intensity is reduced.

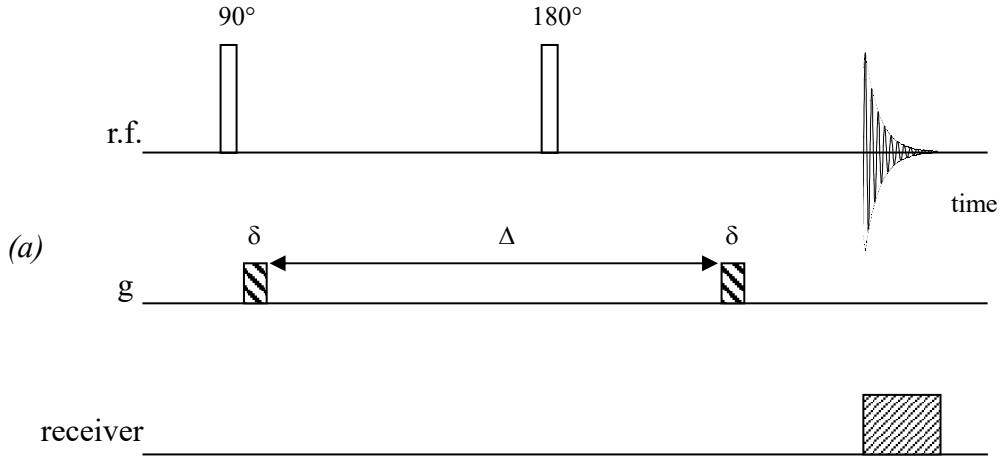

SPIN ECHO PHASE CYCLE

90° pulse	*x*	*-x*	*x*	*-x*	*x*	*-x*	*x*	*-x*
180° pulse	*y*	*y*	*y*	*y*	*y*	*y*	*y*	*y*
receiver	*x*	*-x*	*x*	*-x*	*x*	*-x*	*x*	*-x*

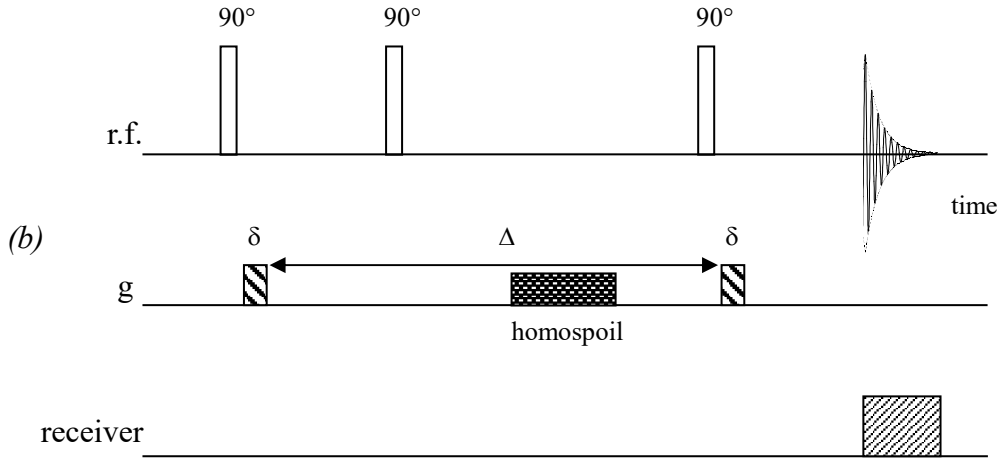

STIMULATED ECHO PHASE CYCLE

1st 90° pulse	*x*	*x*	*x*	*x*	*x*	*x*	*x*	*x*	*-x*	*-x*	*-x*	*-x*	*-x*	*-x*	*-x*	*-x*
2nd 90° pulse	*x*	*x*	*-x*	*-x*	*x*	*x*	*-x*	*-x*	*x*	*x*	*-x*	*-x*	*x*	*x*	*-x*	*-x*
3rd 90° pulse	*-x*	*x*	*-x*	*x*	*-y*	*y*	*-y*	*-y*	*-x*	*x*	*-x*	*x*	*-y*	*y*	*-y*	*-y*
receiver		*x*	*-x*	*-x*	*x*	*y*	*-y*	*-y*	*y*	*-x*	*x*	*x*	*-x*	*-y*	*y*	*y*	*-y*

Figure 7.2 The spin-echo pulse sequence of Stejskal and Tanner *(a)* and the equivalent sequence using a stimulated echo *(b)*.

magnetic field inhomogeneity. The 180° pulse inverted the phases of all the spins, so the second gradient pulse had the same sign as the first to refocus the spins.

7.2.2 Signal Attenuation

Stejskal and Tanner derived the expression for the signal attenuation due to diffusion, given by:

$$\ln\left[A(2\tau)/A(0)\right] = -\gamma^2 D\delta^2\left(\Delta - \frac{1}{3}\delta\right)g^2, \qquad (7.1)$$

where A is the signal amplitude, 2τ is the echo time, γ is the gyromagnetic ratio, D is the self-diffusion coefficient and g, δ and Δ are defined above. This result requires δ to be sufficiently short for diffusion during the gradient pulse to be neglected. A typical experiment consists of acquiring a series of spectra with different values of g while keeping δ and Δ constant. The value of D is determined from the slope of a log-linear plot of $A/A(0)$ versus $\gamma^2\delta^2(\Delta-\delta/3)g^2$, which is a straight line (figure 7.3). The experiment can also be performed at constant g and variable δ or Δ, but this changes the echo time 2τ for each spectrum, so that signal attenuation due to relaxation must also be considered. In the variable-g experiment, the attenuation due to relaxation is the same for all spectra and can be ignored.

Signal attenuation due to relaxation eventually causes the signal to vanish, so the spin-echo diffusion experiment is limited to relatively short Δ values. The diffusion experiment can be performed using a stimulated echo instead (figure 7.2(b)), so that the relaxation attenuation has a T_1 dependence instead of a T_2 dependence (Tanner, 1970). This makes it possible to study diffusion for a longer time, since T_1 is generally greater than T_2 for liquids. The signal attenuation due to diffusion is given by the same equation (7.1).

7.2.3 Restricted Diffusion

When the diffusion of the molecules is restricted to a particular region, *e.g.* inside a droplet, the echo attenuation plot deviates from a straight line. For a short diffusion time, the diffusion is apparently unrestricted because most molecules do not reach the region boundary. As the diffusion time increases, more molecules encounter the region boundary, so the apparent diffusion coefficient decreases. There is no exact

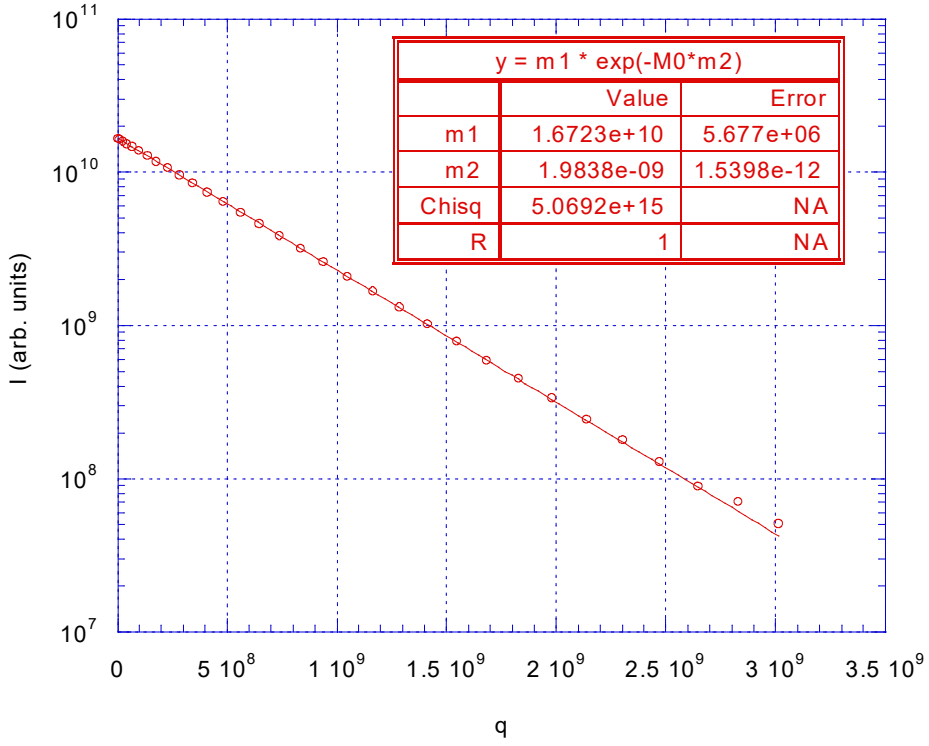

Figure 7.3 The linear echo attenuation plot resulting from a pulsed field gradient experiment on a sample of non-flowing water inside a 10-mm NMR tube. The diffusion coefficient D is obtained from the slope of the attenuation plot, which is denoted by the variable *m2* in the fit. $q = \gamma^2\delta^2(\Delta-\delta/3)g^2$.

relationship to describe the echo attenuation for restricted diffusion inside a sphere, but a commonly used approximate expression is given by (Murday and Cotts, 1968):

$$\ln\left[A(2\tau)/A(0)\right] = -2\gamma^2 g^2 \sum_{m=1}^{\infty} \frac{\left(\dfrac{2\delta}{\alpha_m^2 D} - \dfrac{2 + e^{-\alpha_m^2 D(\tau-\delta)} - 2e^{-\alpha_m^2 D\delta} - 2e^{-\alpha_m^2 D\tau} + e^{-\alpha_m^2 D(\tau+\delta)}}{\left(\alpha_m^2 D\right)^2} \right)}{\alpha_m^2 \left(\alpha_m^2 R^2 - 2\right)} \tag{7.2}$$

where R is the sphere radius and α_m is the m^{th} root of the Bessel function equation:

$$(\alpha_m R) J'_{3/2}(\alpha_m R) - \frac{1}{2} J_{3/2}(\alpha_m R) = 0\,. \tag{7.3}$$

7.2.4 Droplet Size Distributions

Equation (7.2) describes the echo attenuation when all droplets have the same radius R. Since an emulsion contains droplets of various sizes, the observed echo attenuation depends additionally on the droplet size distribution, and is given by (Packer and Rees, 1972):

$$\frac{A(2\tau)}{A(0)} = \frac{\int_0^{\infty} R^3 P(R) \dfrac{A(2\tau, R)}{A(0)} dR}{\int_0^{\infty} R^3 P(R) dR}, \tag{7.4}$$

where $A(2\tau,R)/A(0)$ is the expression in equation (7.2) and $P(R)$ is the droplet size distribution function. The algebraic form of $P(R)$ cannot be determined from the experimental data, so the common approach is to assume a particular distribution function and fit it to the data. The log-normal distribution function is often used and has given a good fit to the droplet size distributions obtained from photomicrographs (Li *et al.*, 1992; Balinov *et al.*, 1994a). This distribution is given by (Packer and Rees, 1972):

$$P(R) = \frac{e^{-\frac{(\ln(2R) - \ln(2R_m))^2}{2\sigma^2}}}{2R\sigma(2\pi)^{1/2}}, \tag{7.5}$$

where R_{m} is the mean droplet radius and σ is the standard deviation of the distribution. The parameters R_m and σ are determined by fitting equation (7.4) to the experimental attenuation data assuming a known value of D.

7.2.5 Flow Compensation

When the PFG experiment is performed on a flowing sample, the nuclei experience a bulk displacement due to the flow in addition to the random displacement due to molecular self-diffusion. This bulk displacement causes an additional phase shift that is not refocused by the bipolar gradient. If all nuclei have the same velocity, this phase shift is constant across the sample and does not attenuate the echo signal (Stejskal, 1965). However, if there is a spread of velocities across the sample, *e.g.* in laminar pipe flow, the corresponding spread of phase shifts increases the echo attenuation. This additional attenuation can be removed by using the double PFG sequence (figure 7.4(a)), where the second pair of pulsed gradients refocuses the phase shift due to flow arising from the first gradient pair (Callaghan *et al.*, 1999). The double PFG sequence is flow-compensated because zeroth and first gradient moments are both zero. The incoherent phase shift due to self-diffusion is not refocused, so in principle the double PFG sequence allows the measurement of the droplet size distribution in a flowing emulsion. The echo attenuation from the double PFG experiment is obtained by applying equation (7.1) twice to give:

$$\ln\left[A(4\tau)/A(0)\right] = -\gamma^2 D\delta^2\left(\Delta - \frac{2}{3}\delta\right)g^2 . \qquad (7.6)$$

7.3 Experimental

For a PFG experiment to give an accurate diffusion coefficient, it is usually performed on a small sample inside the homogeneous region of the gradient coil. Diffusion coefficients vary strongly with temperature and the energy released during gradient switching heats the sample, so the temperature of the sample is usually carefully controlled, typically to ±0.1°C, using heated air. However, a flowing emulsion satisfies neither of these requirements, since there is an excess of liquid outside the gradient coil and close temperature control of such a large sample is not possible. Therefore, it is necessary to study the effects of these two factors on the accuracy of the PFG experiment. This was performed by testing the pulse sequences on water because the diffusion coefficient of water (D_{water}) at various temperatures is widely available in the literature. D_{water} was reported by Stejskal and Tanner in their original article on PFG as $(2.34\pm0.08)\times10^{-9}$ m^2/s at 25.5±0.5°C (Stejskal and Tanner, 1965). For this work, the value of D_{water} at 20°C was taken to be 2.031×10^{-9} m^2/s (Holz,

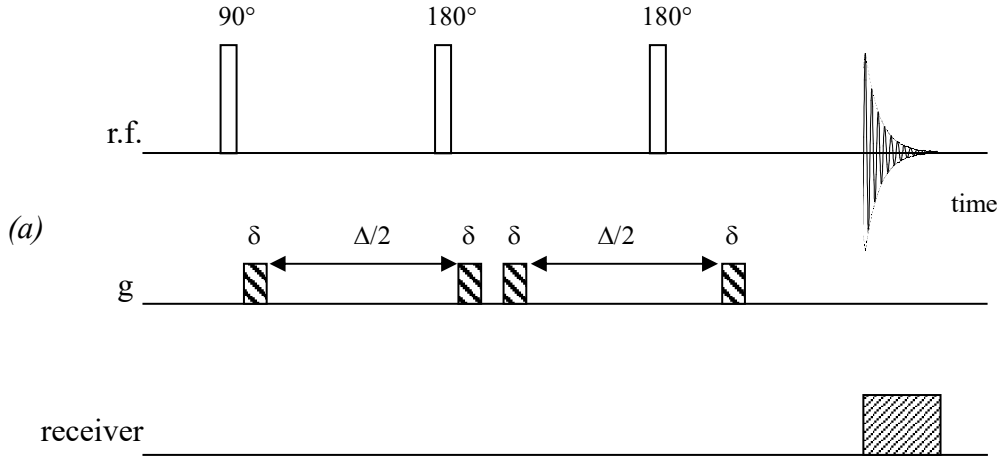

DOUBLE SPIN ECHO PHASE CYCLE

90° pulse	*x*	*-x*	*x*	*-x*	*y*	*-y*	*y*	*-y*
1st 180° pulse	*y*	*-y*	*-y*	*y*	*-x*	*x*	*x*	*-x*
2nd 180° pulse	*-y*	*y*	*y*	*-y*	*x*	*-x*	*-x*	*x*
receiver	*x*	*-x*	*x*	*-x*	*y*	*-y*	*y*	*-y*

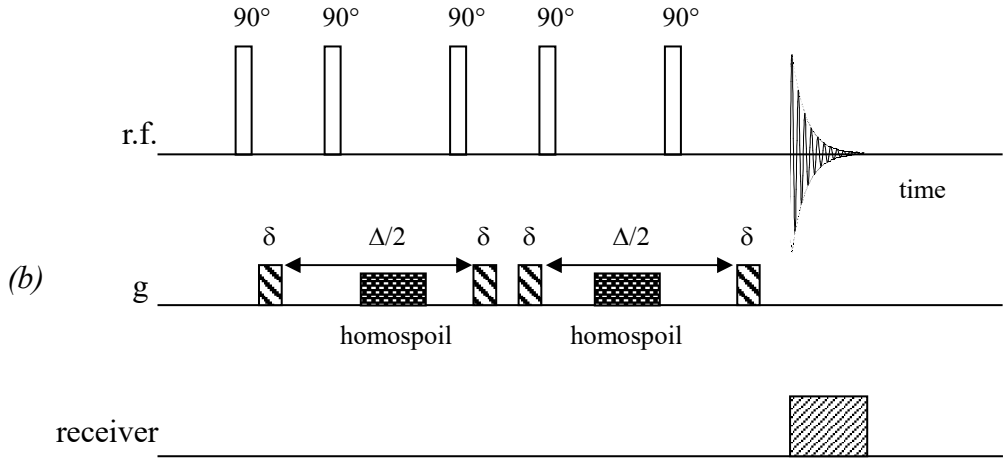

DOUBLE STIMULATED ECHO PHASE CYCLE

1st 90° pulse	[*x*] × 32 [- *x*] × 32
2nd 90° pulse	[*x* *x* *-x* *-x*] × 16
3rd 90° pulse	[*-x* *x* *-x* *x*] × 16
4th 90° pulse	[[*x*] × 8 [- *x*] × 8] × 4
5th 90° pulse	[[[*-x*] × 4 [*x*] × 4] × 2 [[*-y*] × 4 [*y*] × 4] × 2] × 2
receiver	*x -x -x x -x x x -x -x x x -x -x x x -x y -y -y y -y y y -y -y y y -y -y y y -y*
	-x x x -x x -x -x x x -x -x x x -x -x x -y y y -y y -y -y y y -y -y y y -y -y y

Figure 7.4 The flow-compensated double-echo PFG sequences using *(a)* a spin echo, *(b)* a stimulated echo.

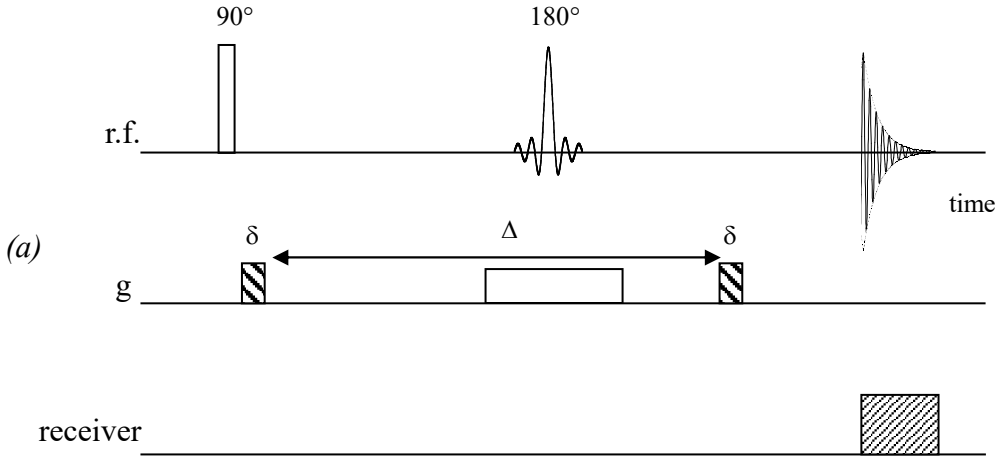

SPIN ECHO PHASE CYCLE

90° pulse	*x*	*-x*	*x*	*-x*	*x*	*-x*	*x*	*-x*
180° pulse	*y*	*y*	*y*	*y*	*y*	*y*	*y*	*y*
receiver	*x*	*-x*	*x*	*-x*	*x*	*-x*	*x*	*-x*

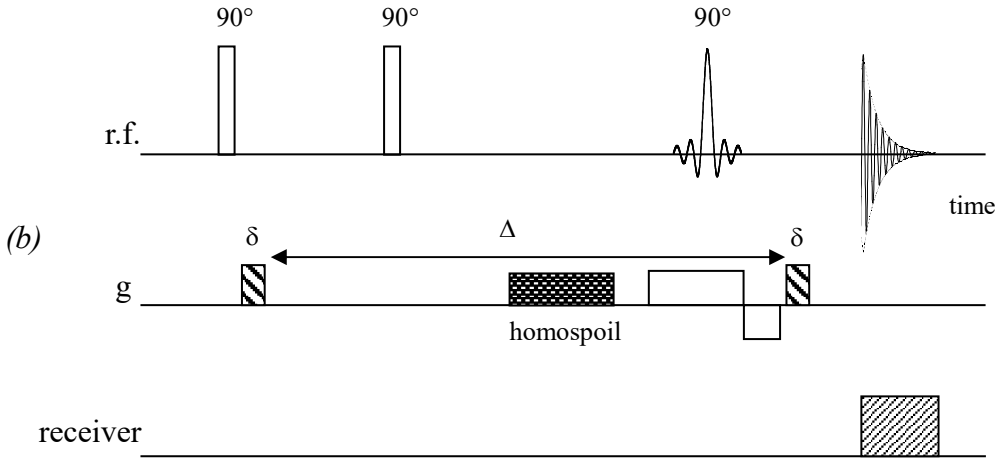

STIMULATED ECHO PHASE CYCLE

1st 90° pulse	*x*	*x*	*x*	*x*	*x*	*x*	*x*	*x*	*-x*	*-x*	*-x*	*-x*	*-x*	*-x*	*-x*	*-x*
2nd 90° pulse	*x*	*x*	*-x*	*-x*	*x*	*x*	*-x*	*-x*	*x*	*x*	*-x*	*-x*	*x*	*x*	*-x*	*-x*
3rd 90° pulse	*-x*	*x*	*-x*	*x*	*-y*	*y*	*-y*	*-y*	*-x*	*x*	*-x*	*x*	*-y*	*y*	*-y*	*-y*
receiver	*x*	*-x*	*-x*	*x*	*y*	*-y*	*-y*	*y*	*-x*	*x*	*x*	*-x*	*-y*	*y*	*y*	*-y*

Figure 7.5 Volume-selective PFG sequences using *(a)* a spin echo, *(b)* a stimulated echo.

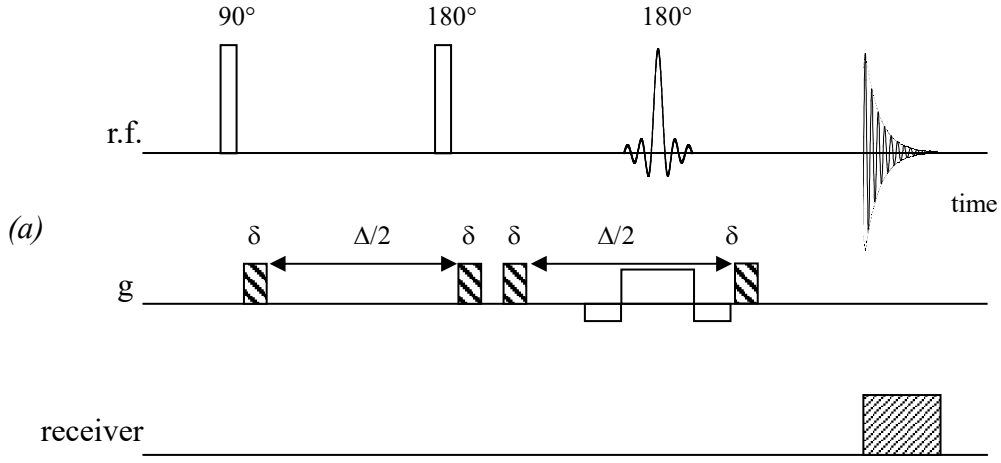

DOUBLE SPIN ECHO PHASE CYCLE

90° pulse	*x*	*-x*	*x*	*-x*	*y*	*-y*	*y*	*-y*
1st 180° pulse	*y*	*-y*	*-y*	*y*	*-x*	*x*	*x*	*-x*
2nd 180° pulse	*-y*	*y*	*y*	*-y*	*x*	*-x*	*-x*	*x*
receiver	*x*	*-x*	*x*	*-x*	*y*	*-y*	*y*	*-y*

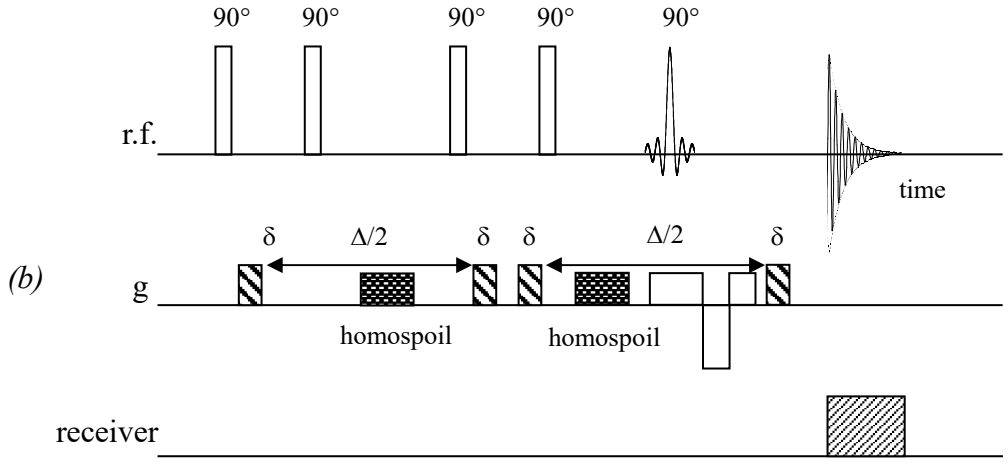

DOUBLE STIMULATED ECHO PHASE CYCLE

1st 90° pulse	[*x*] × 32 [- *x*] × 32
2nd 90° pulse	[*x* *x* *-x* *-x*] × 16
3rd 90° pulse	[*-x* *x* *-x* *x*] × 16
4th 90° pulse	[[*x*] × 8 [- *x*] × 8] × 4
5th 90° pulse	[[[*-x*] × 4 [*x*] × 4] × 2 [[*-y*] × 4 [*y*] × 4] × 2] × 2
receiver	*x -x -x x -x x x -x -x x x -x -x x x -x y -y -y y -y y y -y -y y y -y -y y y -y*
	-x x x -x x -x -x x x -x -x x x -x -x x -y y y -y y -y -y y y -y -y y y -y -y y

Figure 7.6 The flow-compensated and volume-selective PFG sequences with one slice-selective pulse using *(a)* a spin echo, *(b)* a stimulated echo.

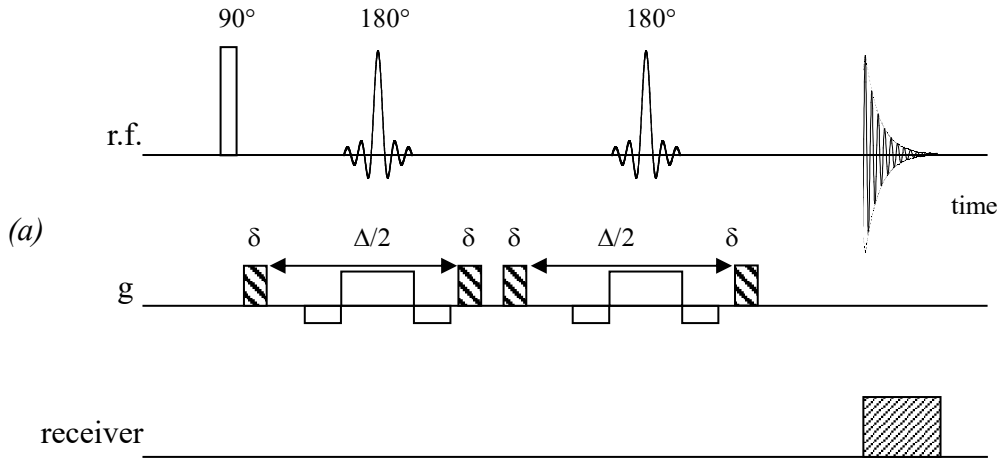

DOUBLE SPIN ECHO PHASE CYCLE

90° pulse	*x*	*-x*	*x*	*-x*	*y*	*-y*	*y*	*-y*
1st 180° pulse	*y*	*-y*	*-y*	*y*	*-x*	*x*	*x*	*-x*
2nd 180° pulse	*-y*	*y*	*y*	*-y*	*x*	*-x*	*-x*	*x*
receiver	*x*	*-x*	*x*	*-x*	*y*	*-y*	*y*	*-y*

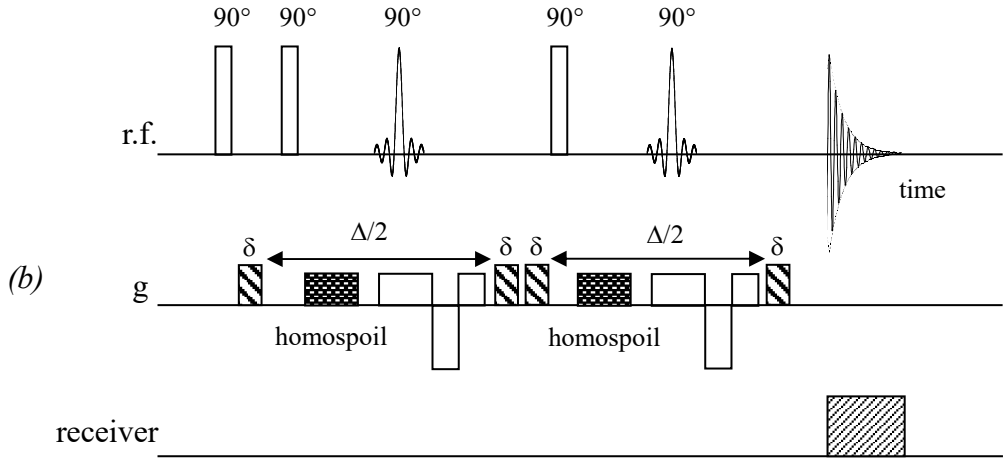

DOUBLE STIMULATED ECHO PHASE CYCLE

1st 90° pulse	[*x*] × 32 [- *x*] × 32
2nd 90° pulse	[*x* *x* *-x* *-x*] × 16
3rd 90° pulse	[*-x* *x* *-x* *x*] × 16
4th 90° pulse	[[*x*] × 8 [- *x*] × 8] × 4
5th 90° pulse	[[[*-x*] × 4 [*x*] × 4] × 2 [[*-y*] × 4 [*y*] × 4] × 2] × 2
receiver	*x -x -x x -x x x -x -x -x x x -x -x x x -x y -y -y y -y y y -y -y y y -y -y y y -y*
	-x x x -x x -x -x x x -x -x x x -x -x x -x y y -y y -y -y y y -y -y y y -y -y y

Figure 7.7 The flow-compensated and volume-selective PFG sequences with two symmetric slice-selective pulses using *(a)* a spin echo, *(b)* a stimulated echo.

1999). Since the diffusion coefficient of water is known, discrepancies in the measured values were used to assess the accuracy of the various pulse sequences.

7.3.1 Pulse Sequences

In total, ten different PFG sequences were tested. These were:

- the standard spin-echo (SE) and stimulated-echo (STE) PFG sequences (figure 7.2),
- the flow-compensated double spin echo (DSE) and double stimulated echo (DSTE) sequences (figure 7.4),
- the volume-selective spin echo (VSE) and stimulated echo (VSTE) sequences to eliminate the signal from the sample outside the homogeneous region of the magnetic field gradients (figure 7.5),
- the volume-selective, flow-compensated double spin echo (VDSE) and stimulated echo (VDSTE) sequences (figure 7.6) with one soft pulse,
- the volume-selective, flow-compensated double spin echo (VDSE2) and stimulated echo (VDSTE2) sequences with two soft pulses for symmetry (figure 7.7).

The volume-selective pulse sequences were created by replacing the last hard pulse in each sequence by a slice-selective pulse. For the double echo sequences, the slice-selection gradient was also flow compensated (Pope and Yao, 1993). Due to the large number of pulses, the stimulated-echo sequences required 16-scan phase cycles and the double stimulated-echo sequences required 64-scan phase cycles, which required very long acquisition times. The spectra acquired with only the first eight scans of the phase cycle were similar to those acquired with the full phase cycle, so all spectra were acquired with eight scans to save time.

These pulse sequences were implemented on a Bruker DMX 300 spectrometer equipped with a vertical 7.05 T superconducting magnet and a 15 mm micro-imaging coil tuned to a ^{1}H resonance frequency of 300.13 MHz. The acquisition parameters that were constant for all the pulse sequences were: 16384 data points sampled every 50 μs, hard 90° pulse duration 12 μs, hard 180° pulse duration 24 μs, gradient pulse duration (δ) 2 ms, repetition time 1 s, gradient stabilisation delay 5 ms, delay between pulse and gradient 1 ms, homospoil gradient (for STE) duration 5 ms. For the

volume-selective sequences, a 10-mm slice was selected along the *z* direction using a sinc-shaped pulse with 5 zero-crossings of 500 μs duration. The soft pulse power attenuation was 12 dB for 180° and 18 dB for 90°.

7.3.2 Diffusion of Static and Flowing Water

The ten pulse sequences listed above were compared in their ability to accurately measure the diffusion coefficient of water at room temperature in various samples, both static and flowing. Various factors were examined for their effect on the measured diffusion coefficient. They were:

- the length of the diffusion time Δ: 50, 100, 150, 250, 500, and 1000 ms;
- the orientation of the pulsed gradients along the *y* and *z* axes, i.e. perpendicular and parallel to the flow direction, to study the effectiveness of the flow compensation;
- the spin echo compared to the stimulated echo for the same values of *g*, δ and Δ;
- the effect of excess liquid, using a short sample of 18 mm, a long sample of 60 mm, and a column of 1.5 m;
- the ability of the volume-selective sequences to give accurate results in the presence of excess liquid;
- the effect of flow through an 11-mm i.d. column, at 8±1 ml/min and 16±1 ml/min.

The experiments on static water were performed on a sample of deionised water inside a 10-mm NMR tube. The flowing water experiments were performed in a flow loop consisting of a 1.5-m glass tube (o.d. 14 mm, i.d. 11 mm) attached to Viton rubber tubing that passed through a peristaltic pump, with a sealed bottle downstream of the pump to dampen the pulses in the flow (figure 6.31). The direction of flow was downwards through the magnet and a single liquid reservoir allowed continuous, steady flow.

The pulsed gradient *g* was incremented from 1.945×10^{-2} T/m to 9.238×10^{-1} T/m in 32 steps in the first experiments on the short sample using the SE and STE sequences. However, this gradient was too strong and caused the echo to decay rapidly at large Δ values, giving spectra that contained only noise at the end of the series. The gradient was halved for the short sample using the remaining eight sequences and for all

experiments on the long sample, so g was incremented from 9.724×10^{-3} T/m to 4.619×10^{-1} T/m in 32 steps. For the experiments on the column of liquid (both static and flowing), g was reduced further for large Δ values in order to minimise the number of spectra in the data series that contained only noise (table 7.1). These changes in g did not affect the measured diffusion coefficient, as can be seen from the results below.

Each series of 32 spectra was Fourier transformed and phase corrected together, and the water peaks were integrated to give the echo intensity, I. The peak integral list was exported as a text file to the KaleidaGraph spreadsheet programme, where it was plotted against the quantity $q = \gamma^2\delta^2(\Delta\text{-}\delta/3)g^2$ or $q_2 = \gamma^2\delta^2(\Delta\text{-}2\delta/3)g^2$ for the single and double echo experiments respectively. Since no echo was acquired in the absence of a gradient, both I_0 and D were determined from the least-squares fit to the data of the function:

$$I = I_0 e^{-qD} \quad \text{or} \quad I = I_0 e^{-q_2 D}, \tag{7.7}$$

for the single or double echo respectively. A sample fit for non-flowing water is shown in figure 7.3.

7.3.3 Diffusion of Static and Flowing Emulsions

The emulsion used in these experiments consisted of 37 wt% *o*-xylene, 60 wt% deionised water and 3 wt% polyoxyethylene sorbitan monopalmitate surfactant (Tween 40). The chemical structures of *o*-xylene and Tween 40 are shown in figure 7.8. The emulsion was prepared by dissolving Tween 40 in water, then adding the *o*-xylene and stirring until the emulsion was homogeneous. The emulsion was milky-white in colour, indicating the presence of droplets larger than 1 μm (Everett, 1988), but the droplet size distribution of the emulsion was not known prior to the PFG experiments. The specific gravity of *o*-xylene is 0.870, so the emulsion exhibited creaming, which is the gradual phase separation of the emulsion over time due to the density difference between the two liquids. The emulsion separated into two phases overnight if left unstirred. This emulsion was chosen because the water, oil and surfactant had non-overlapping NMR peaks, so it was easy to follow the diffusion of each phase separately. The aromatic peak of *o*-xylene was used to study the restricted diffusion inside the oil droplets.

Δ /ms	g /(T m^{-1}) for water	g /(T m^{-1}) for emulsions
50	0.03890 to 0.7172	0.01945 to 0.9238
100	0.01945 to 0.5470	0.01945 to 0.9238
150	0.01945 to 0.3586	0.01945 to 0.9238
250	0.01945 to 0.2644	0.01945 to 0.9238
500	0.01945 to 0.1702	0.01945 to 0.7354
1000	0.00972 to 0.1228	0.01945 to 0.5470

Table 7.1 Gradient strengths used in the PFG experiments on water and on the emulsions. Each gradient range was covered in 32 equal increments.

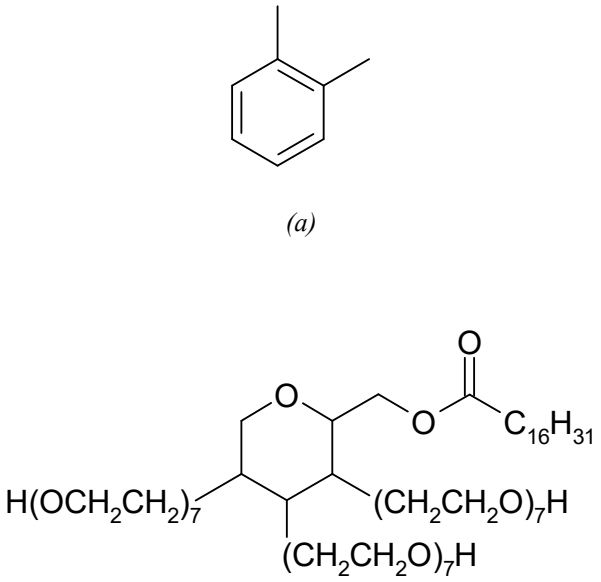

(a)

(b)

Figure 7.8 Chemical structures of *(a) o*-xylene (1,2-dimethylbenzene) and *(b)* Tween 40: polyoxyethylene(20) sorbitan monopalmitate. Tween 40 is a mixture of molecules with variable numbers of CH_2CH_2O groups. Typical values are shown.

All emulsion experiments were performed using the flow loop described above, with the emulsion in the reservoir continually stirred to prevent creaming. The tubing in the flow loop was made of Viton rubber, to minimise losses of *o*-xylene by diffusion though the tubing and evaporation from its surface. The flow rates studied were 0 (no flow), 10±1, 15±1, 27±1, and 41±1 ml/min. Only the stimulated-echo sequences were used, in order to study the long diffusion times needed to observe restricted diffusion in the larger droplets. The five pulse sequences (STE, DSTE, VSTE, VDSTE, VDSTE2) were applied with the pulsed gradients along the *y* direction, using $\delta = 2$ ms $\Delta = 50$, 100, 150, 250, 500, 1000 ms. The three flow-compensated sequences were also applied with the pulsed gradients along the *z* direction, using the same δ and Δ values. A range of Δ values was used because R_m should be independent of Δ at large Δ (Packer and Rees, 1972), but what value of Δ constitutes "large" is not known *a priori*. The gradient strengths used at each Δ value are given in table 7.1.

The concentration of *o*-xylene was varied to see if this gave a different droplet size distribution. The original emulsion contained 35±2 wt% *o*-xylene. A second series of diffusion experiments was performed one month later using the same emulsion sample flowing at 6±1, 9±1 and 14±1 ml/min, by which time the *o*-xylene content had dropped to 26±2 wt% due to evaporation. The experiments were then repeated with a more concentrated emulsion containing 41±2 wt% *o*-xylene flowing at 6±1, 9±1, 14±1 ml/min and without flow.

7.3.4 Fitting Attenuation Data for Emulsions

The diffusion coefficient of pure *o*-xylene was determined experimentally using the STE sequence with $\delta = 2$ ms and $\Delta = 50$ and 500 ms, and was found to be $(1.36\pm0.02)\times10^{-9}$ m^2/s. This value was used in determining the droplet size distributions using the approach outlined in section 7.2.4. Equation (7.4) was fitted to the echo attenuation data using a computer program originally written by Dr Michael Johns of the Magnetic Resonance Research Centre, Department of Chemical Engineering, University of Cambridge. The program searched the assigned parameter space for the values of R_m and σ that gave a simulated echo attenuation with the best least-squares fit to the experimental attenuation data. The fitting program was modified by the author to reduce its running time by changing the parameter space and reducing the number of increments. In its final form, the program searched the

range 0.5 μm ≤ R_m ≤ 100 μm in increments of 0.5 μm and 0.2 ≤ σ ≤ 1 in increments of 0.05.

7.4 Results

7.4.1 Static Water

A summary of the measured values of D_{water} is shown in table 7.2, table 7.3 and table 7.4 for the three samples of different heights (short, long, column), the ten pulse sequences and various values of Δ. The errors in the fit to the attenuation data were $\pm 0.01\times10^{-9}$ m^2/s. The reproducibility of the experiments was $\pm 0.02\times10^{-9}$ m^2/s. The results are also shown graphically in figure 7.9 and figure 7.10 with the standard value of 2.031×10^{-9} m^2/s at 20°C marked as a line on each graph. The error bars are too small to be shown.

Comparing the samples of different heights for all pulse sequences, it emerges that the short sample gave very inconsistent results, while the column of water gave the most consistent values. This trend is surprising, since it was expected that the excess liquid outside the homogeneous region of the gradient would decrease the accuracy of the measured diffusion coefficient. The short sample was designed to just fill the homogeneous gradient and r.f. region, which was measured to be 18 mm long using a one-dimensional profile. Beyond this central region, the gradient and r.f. tailed off over a further 8 mm either side. Evidently, the edges of the short sample inside the tail-off regions caused more artefacts than the excess liquid in the long sample did. The column of water gave values of D_{water} systematically lower than the long sample by ~0.1×10^{-9} m^2/s for the same pulse sequence and Δ value. This may have been caused by ~2°C difference in laboratory temperature on the days that the experiments were performed.

The pulse sequences are best compared using the D_{water} values measured on the long sample that were most consistent. In general, the spin-echo sequences were not as reliable as their stimulated-echo counterparts, particularly at larger values of Δ. This was caused by the magnetisation remaining in the transverse plane for the entire diffusion time in the SE sequences, so it was further dephased while diffusing through an inhomogeneous $\mathbf{B_0}$ field, whereas the magnetisation was placed in *z*-storage for most of the diffusion time in the STE sequences. For D_{water} measured along the *y*

D_{water} /(10^{-9} m^2/s)		Δ /ms direction	50		100		150	
			y	*z*	*y*	*z*	*y*	*z*
echo type	flow compensated	no. of soft pulses						
spin	no	0	2.0436	2.2777	2.1189	2.1821	2.2108	1.9893
		1	2.1831	2.0000	2.3682	2.0232	2.2940	1.9226
	yes	0	2.0944	2.0321	2.0286	2.0329	2.0649	2.0105
		1	2.0320	1.8489	2.1254	1.8720	2.1305	1.9526
		2	1.9356	1.7862	1.9417	1.8548	1.9515	1.8620
stimulated	no	0	2.0567	2.2040	2.1275	2.2754	2.1668	2.3210
		1	2.1707	1.6615	2.2860	1.6418	2.4527	1.6217
	yes	0	2.1812	2.2060	2.2419	2.2836	2.2053	2.3455
		1	2.0918	2.2829	2.1619	1.9304	2.1455	1.6074
		2	2.2451	2.5273	2.1189	2.3096	2.0830	2.2363

D_{water} /(10^{-9} m^2/s)		Δ /ms direction	250		500		1000	
			y	*z*	*y*	*z*	*y*	*z*
echo type	flow compensated	no. of soft pulses						
spin	no	0	2.3125	1.6062	2.3446	1.0746		
		1	2.1141	1.5673	1.5064	0.8969		
	yes	0	1.9663	1.9240	1.9396	1.5457		
		1	2.1389	1.9307	2.1297	1.7451		
		2	1.9586	1.8274	1.9295	1.8270		
stimulated	no	0	2.1619	2.3686	2.1926	2.3715	2.0879	2.2621
		1	2.5924	1.6517	2.7709	1.6220	2.8373	1.6372
	yes	0	2.3221	2.4193	2.3585	2.4430	2.1954	3.5237
		1	2.1654	1.6334	2.3629	1.7391	2.3557	1.7184
		2	2.0080	2.1831	1.9522	2.1354	1.9040	2.1056

Table 7.2 The self-diffusion coefficient of water measured in an 18-mm sample of static water inside a 10-mm (o.d.) NMR tube at room temperature. The values were obtained using ten different PFG sequences, 6 Δ values and two gradient directions. Blank entries correspond to experiments that were not performed.

D_{water} /(10^{-9} m^2/s)		Δ /ms direction	50		250		500	
			y	*z*	*y*	*z*	*y*	*z*
echo type	flow compensated	no. of soft pulses						
spin	no	0	1.9604	1.9730	1.9909	1.9488	2.0887	1.8599
		1	2.0390	2.2640	1.7525	1.8050	2.6555	1.4616
	yes	0	2.0590	2.0880	1.9417	1.7232	2.0007	1.3441
		1	2.1454	1.9066	2.0747	1.8784	2.3938	1.7797
		2	2.2100	1.9125	2.1095	1.8357	1.9231	1.7101
stimulated	no	0	1.9838	2.0815	1.9697	2.0101	1.9702	1.9523
		1	2.0196	2.0668	2.0639	2.0729	2.0824	2.0908
	yes	0	2.0497	2.1623	2.0708		2.0779	2.2085
		1	2.5091	2.6792	2.1899	2.2494	2.1957	2.1859
		2	2.4536	2.6329	2.1321	2.2655	2.0957	2.2182

D_{water} /(10^{-9} m^2/s)		Δ /ms direction	50		100		150	
			y	*z*	*y*	*z*	*y*	*z*
echo type	flow compensated	no. of soft pulses						
stimulated	no	0	1.9021	1.9727	1.8948	1.9732	1.8926	1.9817
		1	1.9162	1.9903	1.9001	1.9964	1.8973	1.9968
	yes	0	1.9106	1.9983	1.9034	2.0031	1.8997	1.9954
		1	2.3287	2.4189	2.109	2.2251	2.0346	2.1412
		2	2.3474	2.4179	2.1134	2.217	2.0527	2.1575

Table 7.3 The self-diffusion coefficient of water measured at room temperature in a 60-mm sample of static water inside a 10-mm (o.d.) NMR tube. The values were obtained using ten different PFG sequences, 6 Δ values and two gradient directions.

D_{water} /(10^{-9} m^2/s)		Δ /ms direction	250		500		1000	
			y	*z*	*y*	*z*	*y*	*z*
echo type	flow compensated	no. of soft pulses						
stimulated	no	0	1.8858	2.0149	1.8729	2.0040	1.8499	2.0802
		1	1.8886	2.0000	1.8779	2.0048	1.8573	2.0140
	yes	0	1.9028	1.9978	1.8925	1.9917	1.8749	1.9951
		1	1.9655	2.0860	1.9284	2.0456	1.8972	1.9874
		2	1.9839	2.0986	1.9427	2.0579	1.8977	2.0380

Table 7.4 The self-diffusion coefficient of water measured at room temperature in a column of static water 1.5 m long and 11-mm i.d. The values were obtained using five stimulated-echo PFG sequences, 3 Δ values and two gradient directions.

direction using the SE sequences, the values obtained using VSE were highly eccentric, while those obtained with the other four sequences were of equal accuracy ($\pm 0.2\times10^{-9}$ m^2/s). Along the z direction, the SE sequences measured D_{water} to be too low for all but the shortest Δ value, indicating lower-than-expected echo attenuation. This was probably caused by diffusion in the inhomogeneous $\mathbf{B_0}$ field further dephasing the transverse magnetisation, and dephasing due to eddy currents present after switching the gradients (Callaghan, 1991). These artefacts attenuate all echoes and result in apparently lower values of D_{water}.

Of the stimulated-echo sequences, the standard STE, flow-compensated DSTE and volume-selective VSTE gave good D_{water} values that were within 0.2×10^{-9} m^2/s of the standard value. D_{water} did not vary strongly with Δ, even up to a very long diffusion time of 1000 ms, indicating that the experiments were free of artefacts. The two volume-selective double echo sequences VDSTE and VDSTE2 gave D_{water} values that were too high by up to 0.4×10^{-9} m^2/s at short Δ, but decreased to the standard value for $\Delta \geq 250$ ms. The high values were due to the heating of the sample by 2-4°C by the large number of r.f. and gradient pulses in the sequence. For small Δ, all the energy deposited in the sample in a short time heated the sample and increased the self-diffusion, while larger Δ values required longer delays between pulses during which the heat could dissipate. D_{water} was consistently measured to be larger along the z direction than along the y direction regardless of the sequence or Δ value used. This was caused by convection in the vertical direction, and larger $\mathbf{B_0}$ inhomogeneity along z than along y.

In conclusion, the self-diffusion coefficient of static water in a long column was measured more accurately using the stimulated echo than the spin echo, and was best measured along the y direction. The excess liquid in the long sample and the column did not cause measurement errors, so there was no benefit to be gained from the volume-selective sequences. The stimulated echo sequence was accurate over a range of Δ values from 50 ms to 1000 ms.

7.4.2 Flowing Water

The self-diffusion of water in the presence of flow was measured using only the stimulated-echo sequences because they performed better than the spin-echo sequences on static water. All five STE sequences were applied with the pulsed

gradients along the *y* direction, but only the three flow-compensated sequences were applied with the pulsed gradients along the *z* (flow) direction. The phase of the water peak increased with *g*, so that each spectrum in a data series was phase-corrected separately. The resulting echo attenuation plots were linear (figure 7.11) so it was still possible to determine D_{water}. The measured D_{water} values are summarised in table 7.5 and shown graphically in figure 7.12. The D_{water} values measured along the *y* direction were independent of Δ and close to the standard value of 2.031×10^{-9} m^2/s for both flow rates. D_{water} measured using VDSTE and VDSTE2 was again too high by up to 0.4×10^{-9} m^2/s at low Δ values due to sample heating. Along the *z* direction, the correct value of D_{water} was measured by DSTE at Δ = 50 ms for both flow rates, but D_{water} increased with Δ and with flow rate, indicating incomplete flow compensation. The volume-selective sequences VDSTE and VDSTE2 did not measure D_{water} correctly along the *z* axis for any Δ due to a combination of sample heating and incomplete flow compensation.

The extent of flow compensation was studied in a separate experiment on water flowing at 30 ml/min by comparing the STE and DSTE sequences with the gradients along the *z* direction and Δ = 50 ms. STE gave $D_{water} = 5.5\times10^{-9}$ m^2/s and DSTE gave $D_{water} = 2.6\times10^{-9}$ m^2/s, indicating that the double echo refocused most of the flow-induced phase shift, but not all. The refocusing was incomplete due to the transverse diffusion of water across the velocity streamlines, so that the flow velocity of a nuclear spin was not constant over Δ and the phase shifts of the two echoes were not evenly matched. The phase mismatch was more severe at higher flow rates and longer diffusion times because there was a larger velocity difference across the sample and the transverse displacement was larger. Incomplete flow compensation may have also been caused by eddy currents or by the incomplete phase cycle.

In conclusion, the self-diffusion coefficient of water was measured accurately in the presence of flow using stimulated-echo PFG sequences with the pulsed gradients transverse to the flow direction. Flow compensation along the flow direction was only partially successful. The diffusion coefficient along *z* was measured accurately using a double echo sequence only when the flow rate was low and Δ was small. The volume-selective sequences were not useful in the presence of flow due to excess echo attenuation.

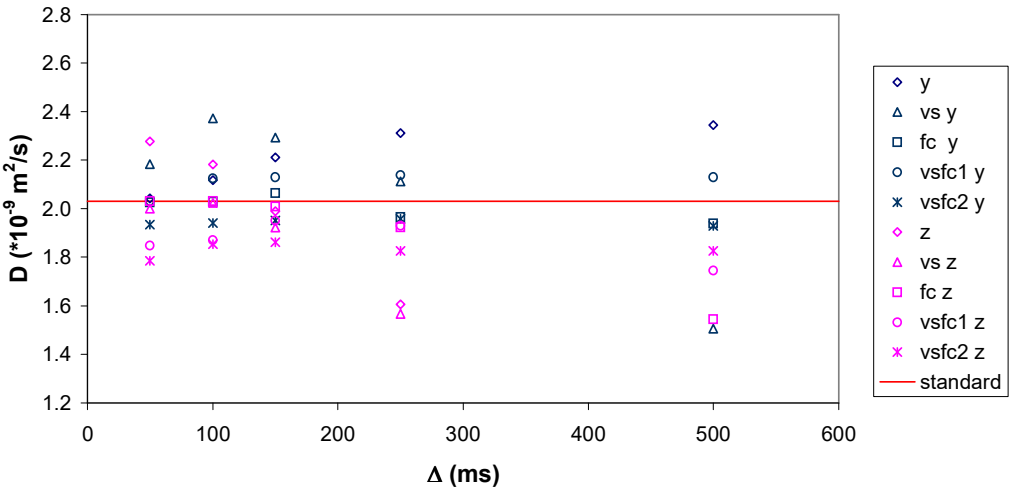

(a)

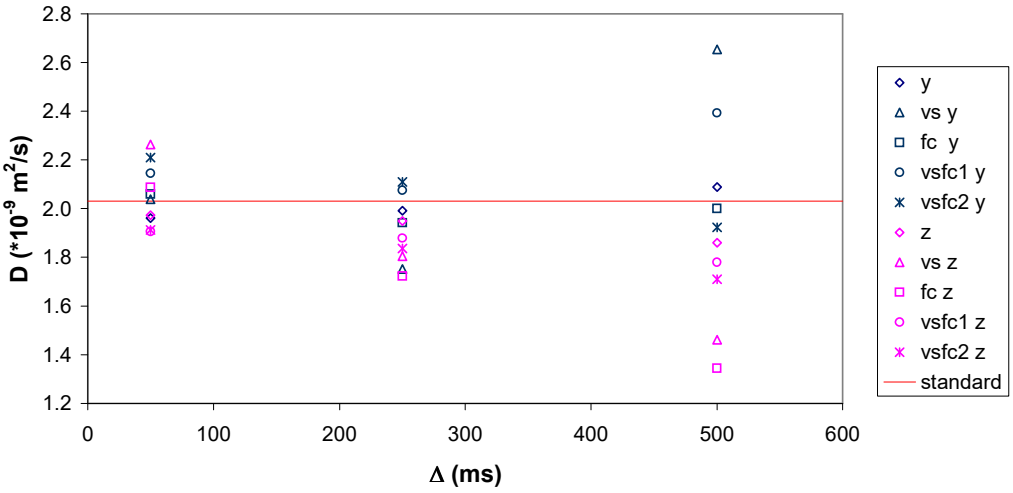

(b)

Figure 7.9 The self-diffusion coefficient of water measured at room temperature using spin-echo PFG sequences, in a static sample inside a 10-mm (o.d.) NMR tube with a liquid height of *(a)* 18 mm, *(b)* 60 mm. *vs* = volume-selective, *fc* = flow-compensated, *y, z* = gradient direction.

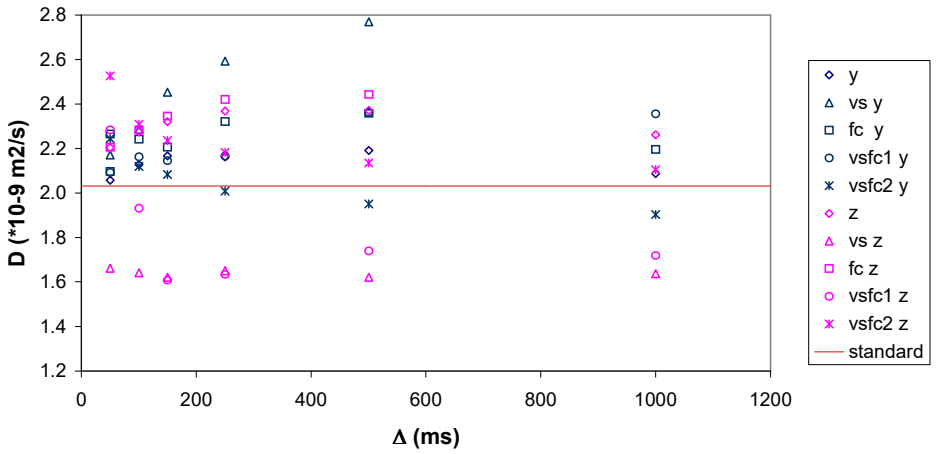

(a)

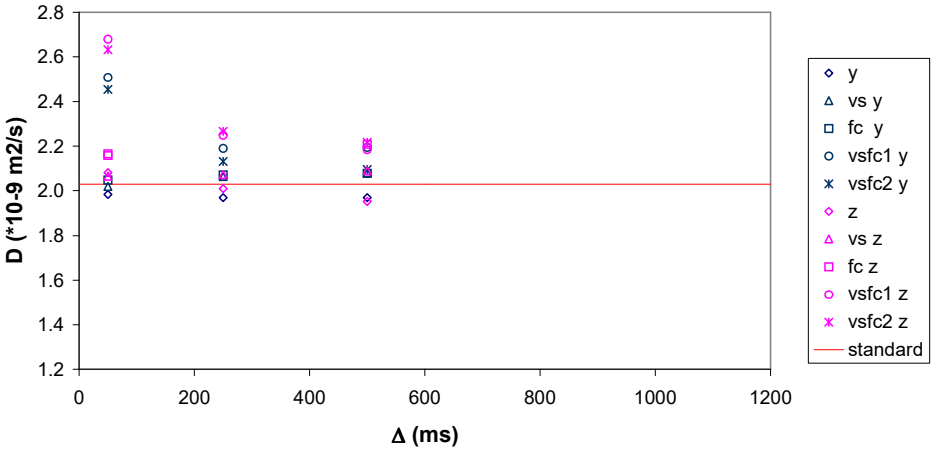

(b)

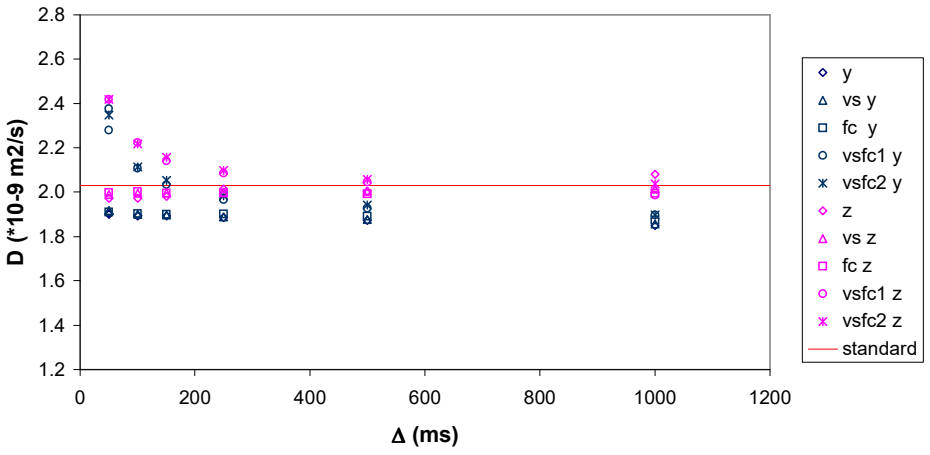

(c)

Figure 7.10 The self-diffusion coefficient of water measured at room temperature using stimulated-echo PFG sequences, in a static sample inside a 10-mm (o.d.) NMR tube with a liquid height of *(a)* 18 mm, *(b)* 60 mm, and *(c)* inside a 1.5-m column. *vs* = volume-selective, *fc* = flow-compensated, *y, z* = gradient direction.

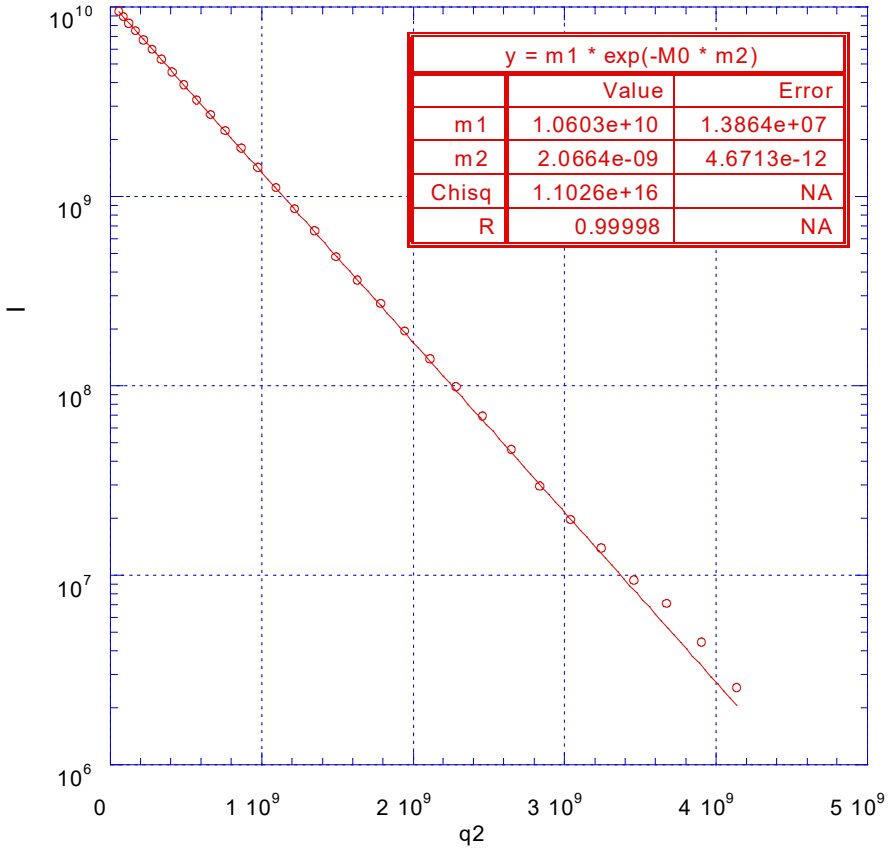

Figure 7.11 Echo attenuation plot for the self-diffusion of water flowing at 8 ml/min, acquired using the DSTE sequence with the pulsed gradients parallel to the flow direction and Δ = 500 ms. The attenuation follows a straight line and D_{water} is obtained from the fit as $2.0664\times10^{-9} \pm 4.6713\times10^{-12}$ m^2/s. $q_2 = \gamma^2\delta^2(\Delta-2\delta/3)g^2$

D_{water} /(10^{-9} m^2/s)	Δ /ms	50		250		500		1000	
	direction	*y*	*z*	*y*	*z*	*y*	*z*	*y*	*z*
flow compensated	no. of soft pulses								
no	0	2.0208		1.9956		2.0218		1.9886	
	1	2.0203		2.0197		1.9659		1.9965	
yes	0	2.0360	2.0643	1.9675	2.0578	1.9938	2.0664	2.0013	2.1808
	1	2.3650	2.6201	2.0582	2.2608	2.0388	2.2170	1.9864	2.2892
	2	2.4762	2.5979	2.0992	2.2395	2.0363	2.2073	2.0278	2.3238

(a)

D_{water} /(10^{-9} m^2/s)	Δ /ms	50		250		500		1000	
	direction	*y*	*z*	*y*	*z*	*y*	*z*	*y*	*z*
flow compensated	no. of soft pulses								
no	0	2.0825		2.1053		2.0991		2.0003	
	1	2.0680		2.0334		2.0319		2.0416	
yes	0	2.0732	2.0595	2.0434	2.1268	2.0225	2.1997	2.0271	2.4569
	1	2.4950	2.5847	2.0889	2.2660	2.0669	2.2740	2.0413	2.5482
	2	2.4495	2.5936	2.1177	2.2512	2.0307	2.3025	2.0333	2.6614

(b)

Table 7.5 The self-diffusion coefficient of water measured at room temperature in water flowing along *z* at *(a)* 8 ml/min, *(b)* 16 ml/min. The values were obtained along *y* using five stimulated-echo PFG sequences and along *z* using three flow-compensated sequences. Four different Δ values were used. Blank entries correspond to experiments that were not performed.

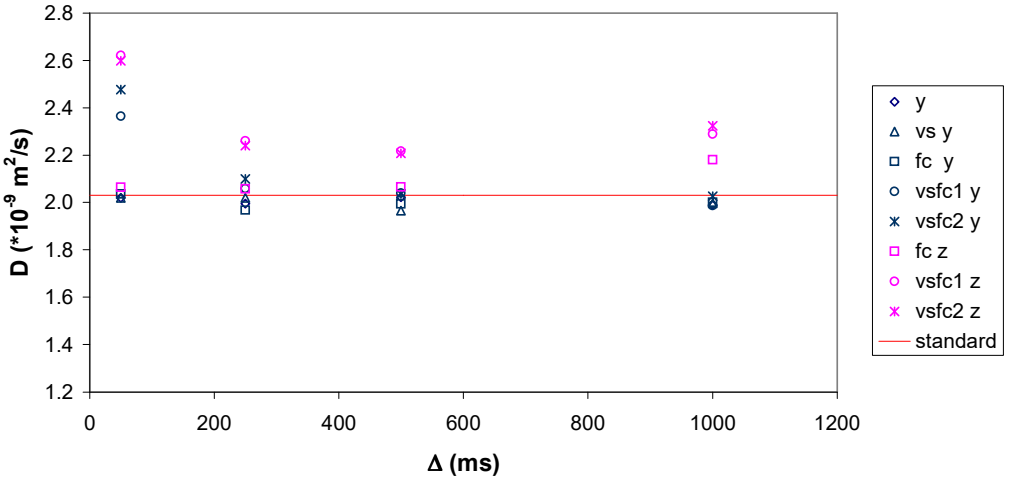

(a)

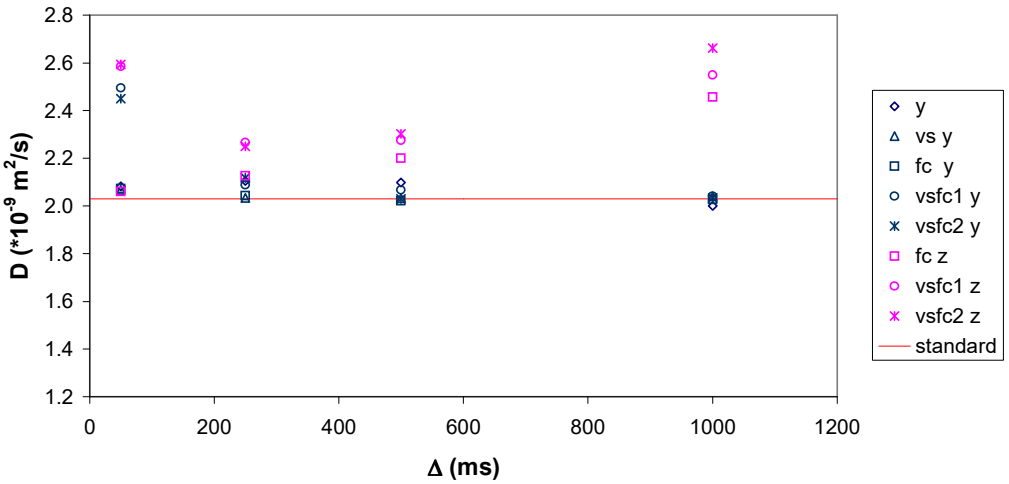

(b)

Figure 7.12 The self-diffusion coefficient of water measured at room temperature in water flowing along *z* at *(a)* 8 ml/min, *(b)* 16 ml/min using stimulated-echo PFG sequences. *vs* = volume-selective, *fc* = flow-compensated, *y, z* = gradient direction.

7.4.3 Static Emulsion

The droplet size distributions were determined for two static emulsions containing 35 wt% and 43 wt% *o*-xylene respectively. Since the distributions were not known beforehand, the reliability of the PFG results was judged based on their consistency and the performance of the pulse sequences on water. The values of R_m and σ obtained by the droplet fitting program are shown graphically in figure 7.13 and figure 7.14. The error bars are too small to be shown on the charts. They correspond to the half the search increments of the program, *viz.* ±0.25 μm for R_m and ±0.025 for σ. The charts must be interpreted with caution because they do not show how well the droplet size distributions reproduce the experimental attenuation data. Due to space constraints, it is not possible to reproduce all the attenuation data here, so only representative attenuation curves are shown.

For the 35-wt% emulsion, the experimental attenuation data were reproduced well by the log-normal droplet size distributions. The STE and VSTE sequences gave similar attenuation curves along *y* with little scatter (figure 7.15(a)) and similar droplet sizes. The best-fit values of R_m increased linearly with Δ from 16 μm to 48 μm, while σ converged to 0.40±0.05. A small increase in R_m and σ with Δ was expected since the boundaries of the larger droplets were not encountered during the shortest diffusion times, but the observed threefold increase in R_m indicated additional echo attenuation. The STE data measured along *z* were very scattered and could not be fitted to a droplet size distribution (figure 7.15(b)). The attenuation and scatter was due to creaming of the emulsion, which caused larger-than-anticipated droplet motion during a PFG experiment.

The three flow-compensated sequences DSTE, VDSTE and VDSTE2 gave attenuation data without scatter along *z*, so they were less sensitive to creaming (figure 7.15(c)). R_m and σ converged to stable values as Δ increased: $R_m = 27\pm1$ μm, $\sigma = 0.7\pm0.05$ along *y*, and $R_m = 18\pm1$ μm, $\sigma = 0.7\pm0.05$ along *z*. The smaller mean droplet size measured along *z* was caused by additional attenuation due to diffusion in an inhomogeneous $\mathbf{B_0}$ field. The fitting program used a fixed value of $D_{o\text{-}xylene}$ measured along *y*, and gave apparently smaller droplets to match the attenuation behaviour along *z*. VDSTE and VDSTE2 overestimated R_m at low Δ along *y* due to

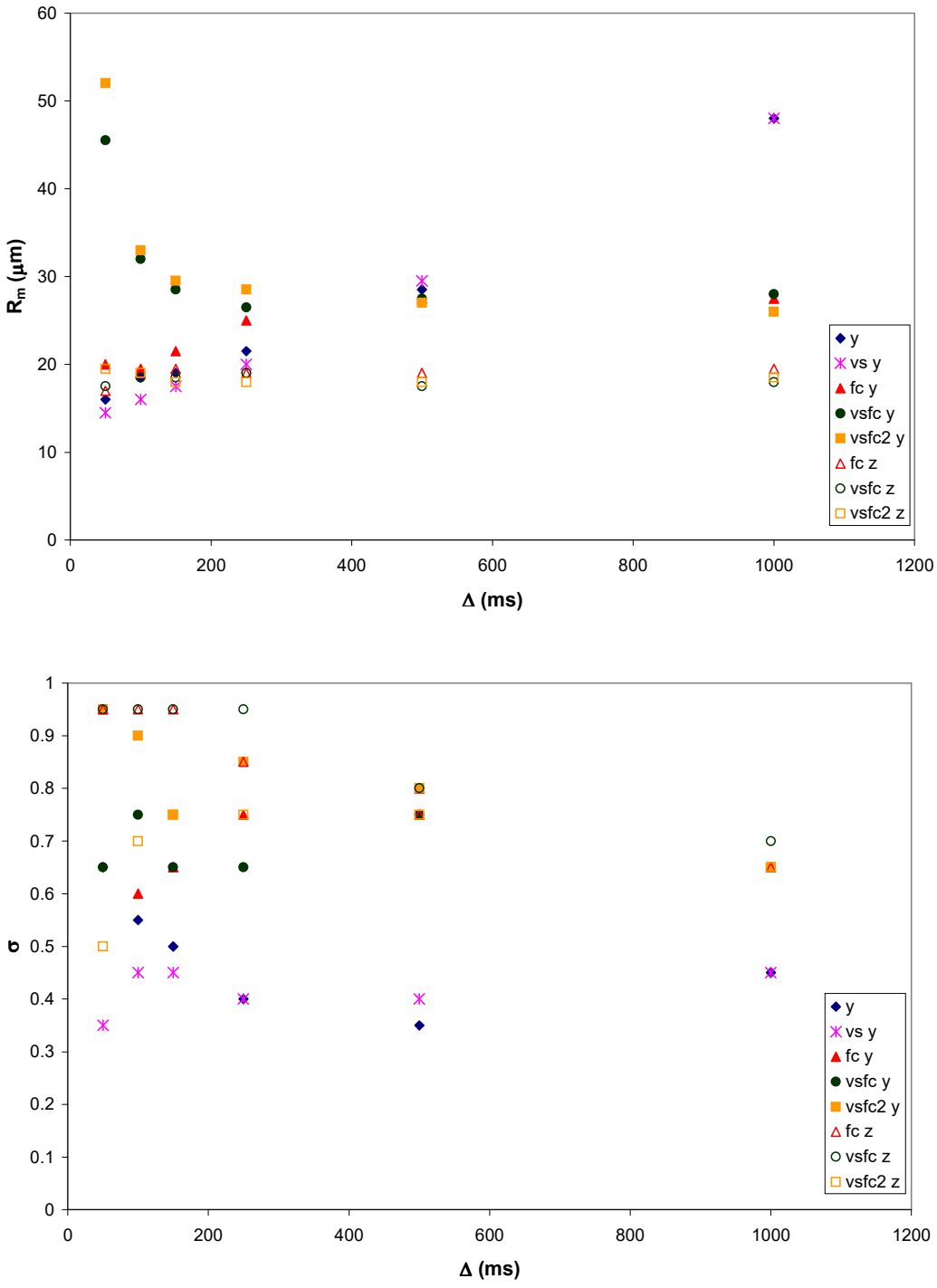

Figure 7.13 Parameters of the log-normal droplet size distribution, R_m and σ, obtained for a static emulsion containing 35 wt% *o*-xylene using five stimulated-echo PFG sequences with six different Δ values. *vs* = volume-selective, *fc* = flow-compensated, *y, z* = gradient direction.

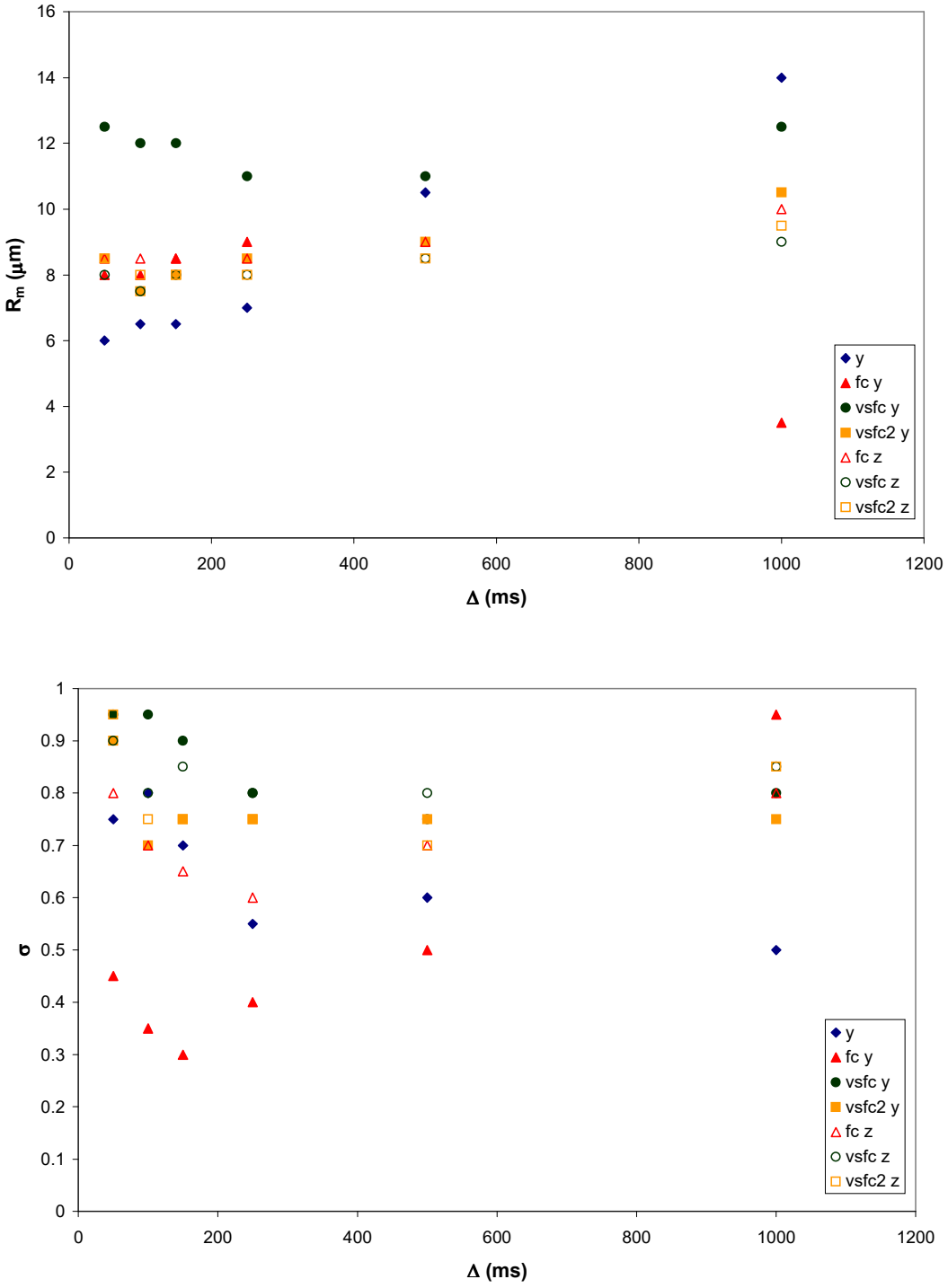

Figure 7.14 Parameters of the log-normal droplet size distribution, R_m and σ, obtained for a static emulsion containing 43 wt% *o*-xylene using five stimulated-echo PFG sequences with six different Δ values. *vs* = volume-selective, *fc* = flow-compensated, *y, z* = gradient direction.

(a)

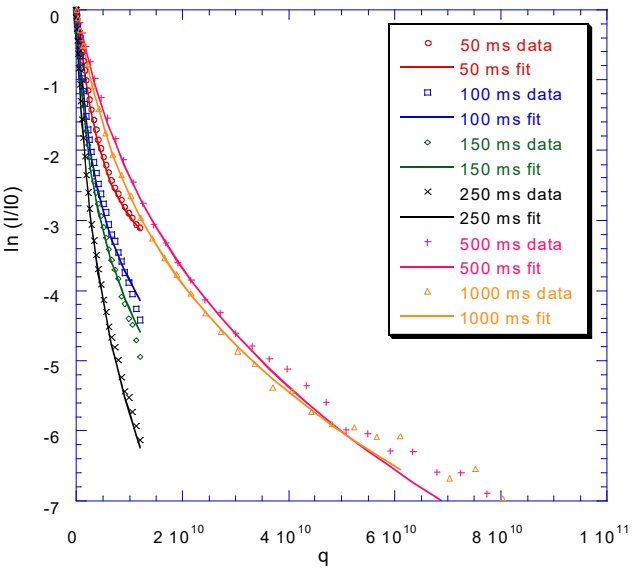

(b)

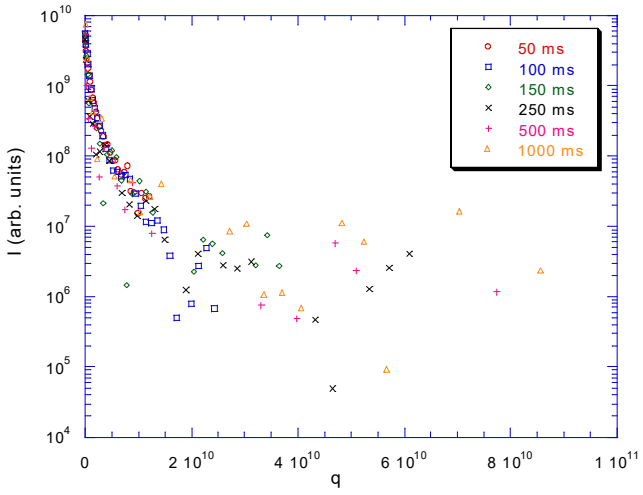

(c)

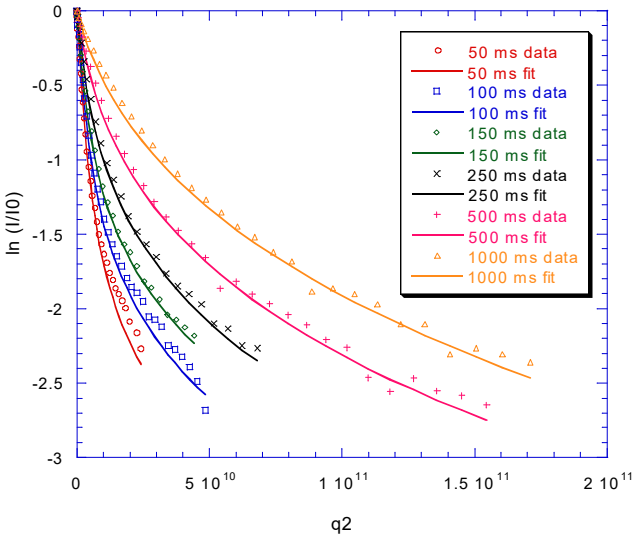

Figure 7.15 Echo attenuation plots for a static emulsion containing 35 wt% *o*-xylene, showing the experimental data (points) and the fits using log-normal droplet size distributions (lines). *(a)* STE along *y*, *(b)* STE along *z* showing a lot of scatter, *(c)* DSTE along *z* showing much less scatter than *(b)*. $q = \gamma^2\delta^2(\Delta\text{-}\delta/3)g^2$, $q_2 = \gamma^2\delta^2(\Delta\text{-}2\delta/3)g^2$.

(d)

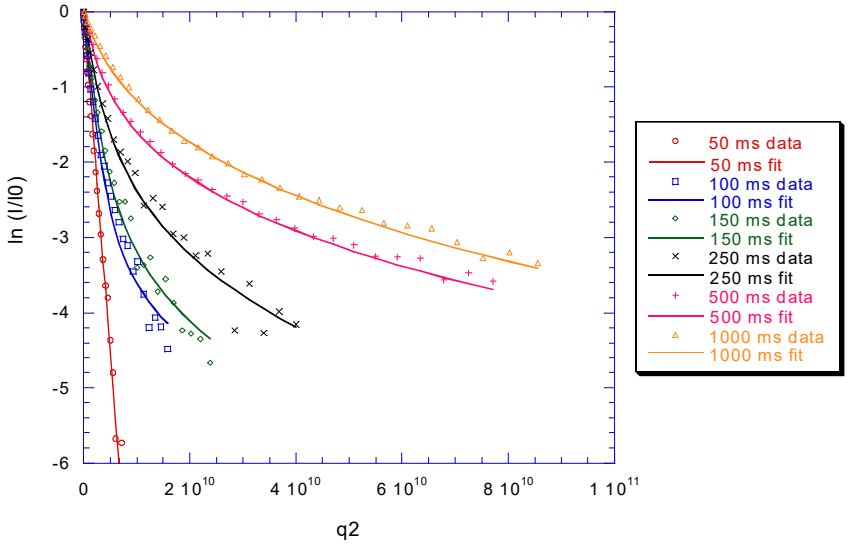

(e)

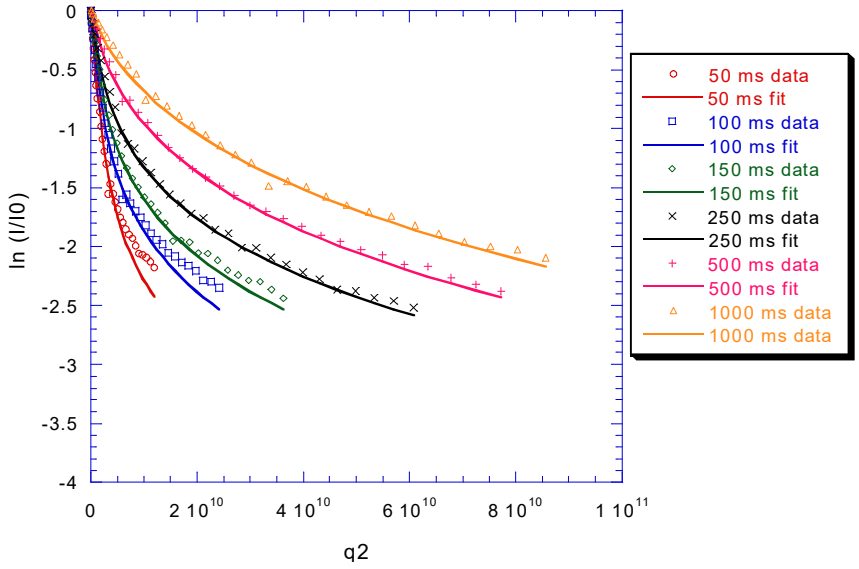

Figure 7.15 Echo attenuation plots for a static emulsion containing 35 wt% *o*-xylene, showing the experimental data (points) and the fits using log-normal droplet size distributions (lines). *(d)* VDSTE along *y* showing rapid attenuation at small Δ, *(e)* VDSTE along *z* showing less attenuation than *(d)*. $q_2 = \gamma^2\delta^2(\Delta\text{-}2\delta/3)g^2$.

very rapid echo attenuation (figure 7.15(d)) but the attenuation curves along z were normal (figure 7.15(e)). The cause of this difference is unknown.

The same effects were observed on the 43-wt% static emulsion. Most attenuation curves were close to linear and showed very little scatter (figure 7.16), indicating that σ was small (van den Enden *et al.*, 1990). STE gave R_m values that increased with Δ from 6 μm to 14 μm, while the flow-compensated sequences converged to $R_m = 10 \pm 1$ μm, $\sigma = 0.75 \pm 0.05$. The value of σ was surprisingly high in view of the attenuation data. Because the droplets were smaller, creaming was slower so the increase in R_m with Δ was smaller and the differences between the y and z measurements were smaller. The VDSTE sequence again gave excess attenuation along the y direction only.

In conclusion, the flow-compensated DSTE sequence gave the most consistent droplet sizes for a static emulsion because the single-echo sequence was sensitive to creaming and the volume-selective sequences caused additional echo attenuation. The measured droplet size distributions of the two static emulsions were clearly different: R_m was ~20 μm at 35 wt% *o*-xylene and ~10 μm at 43 wt% *o*-xylene.

7.4.4 Flowing Emulsion

The droplet size distributions were determined for three flowing emulsions containing 35 wt%, 26 wt% and 41 wt% *o*-xylene respectively. The values of R_m and σ obtained by the droplet fitting program at various flow rates are shown graphically in figure 7.17, figure 7.18 and figure 7.19. Only the results for the STE and DSTE sequences are presented, since the volume-selective sequences gave odd results on the static emulsions.

For all three emulsions, STE along y gave droplet sizes that increased with Δ and with flow rate. As for the static emulsions, these values were not representative of the real droplet sizes, but were caused by additional signal attenuation due to flow. The STE attenuation data also contained a lot of scatter (figure 7.20(a)) so some fits were poor. The 41-wt% emulsion had the best fits to the attenuation data (figure 7.20(b)).

The flow-compensated DSTE along y gave consistent results for the 35-wt% and 41-wt% emulsion. The droplet sizes varied very little with flow rate and Δ and were close to the values measured on the static emulsions. The fits to the attenuation data

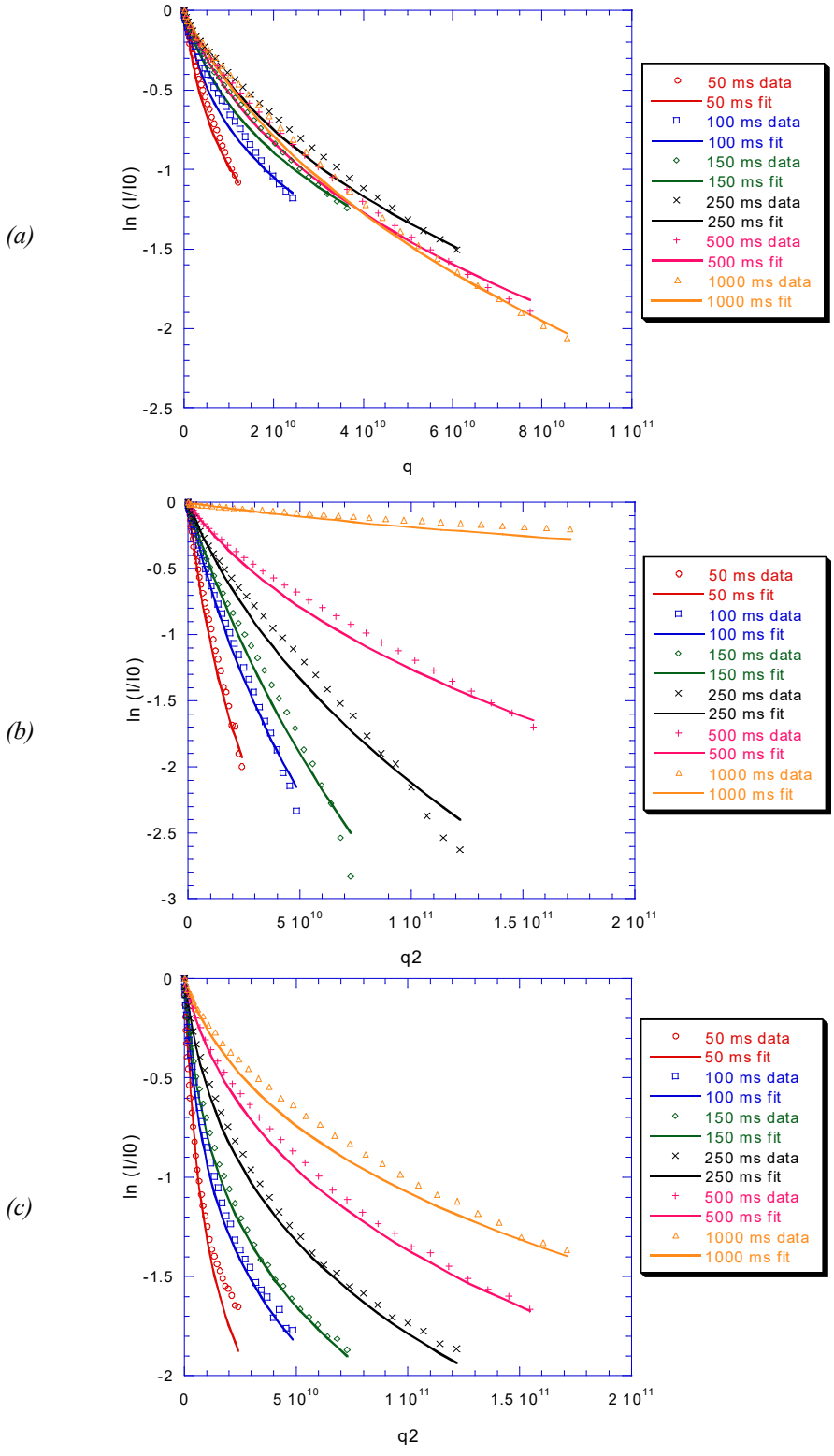

Figure 7.16 Echo attenuation plots for a static emulsion containing 43 wt% *o*-xylene, showing the experimental data (points) and the fits using log-normal droplet size distributions (lines). *(a)* STE along *y*, *(b)* DSTE along *y*, *(c)* VDSTE along *y*. $q = \gamma^2\delta^2(\Delta-\delta/3)g^2$, $q_2 = \gamma^2\delta^2(\Delta-2\delta/3)g^2$.

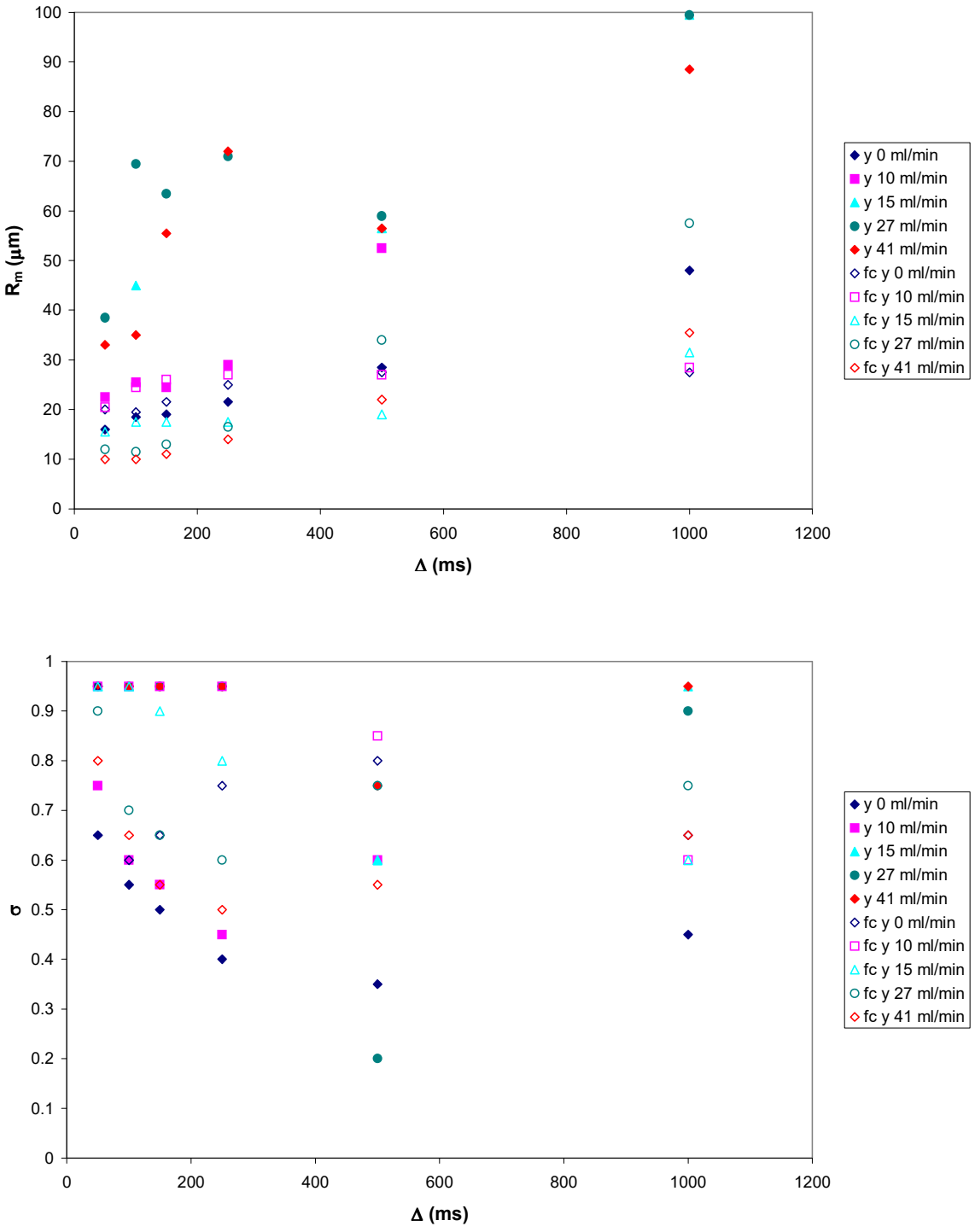

Figure 7.17 Parameters of the log-normal droplet size distribution, R_m and σ, obtained for a flowing emulsion containing 35 wt% *o*-xylene using the STE and DSTE PFG sequences with six different Δ values.

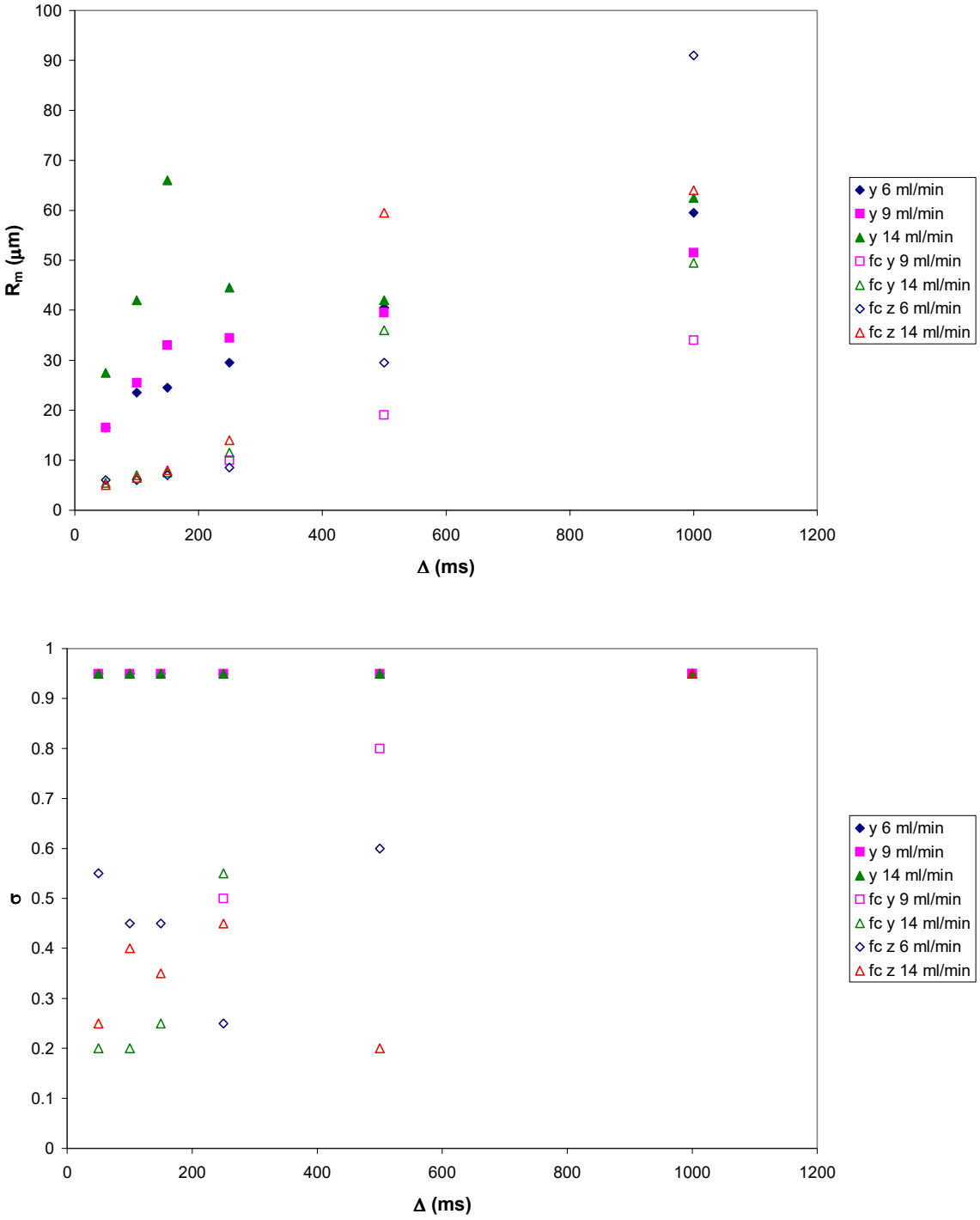

Figure 7.18 Parameters of the log-normal droplet size distribution, R_m and σ, obtained for a flowing emulsion containing 26 wt% *o*-xylene using the STE and DSTE PFG sequences with six different Δ values.

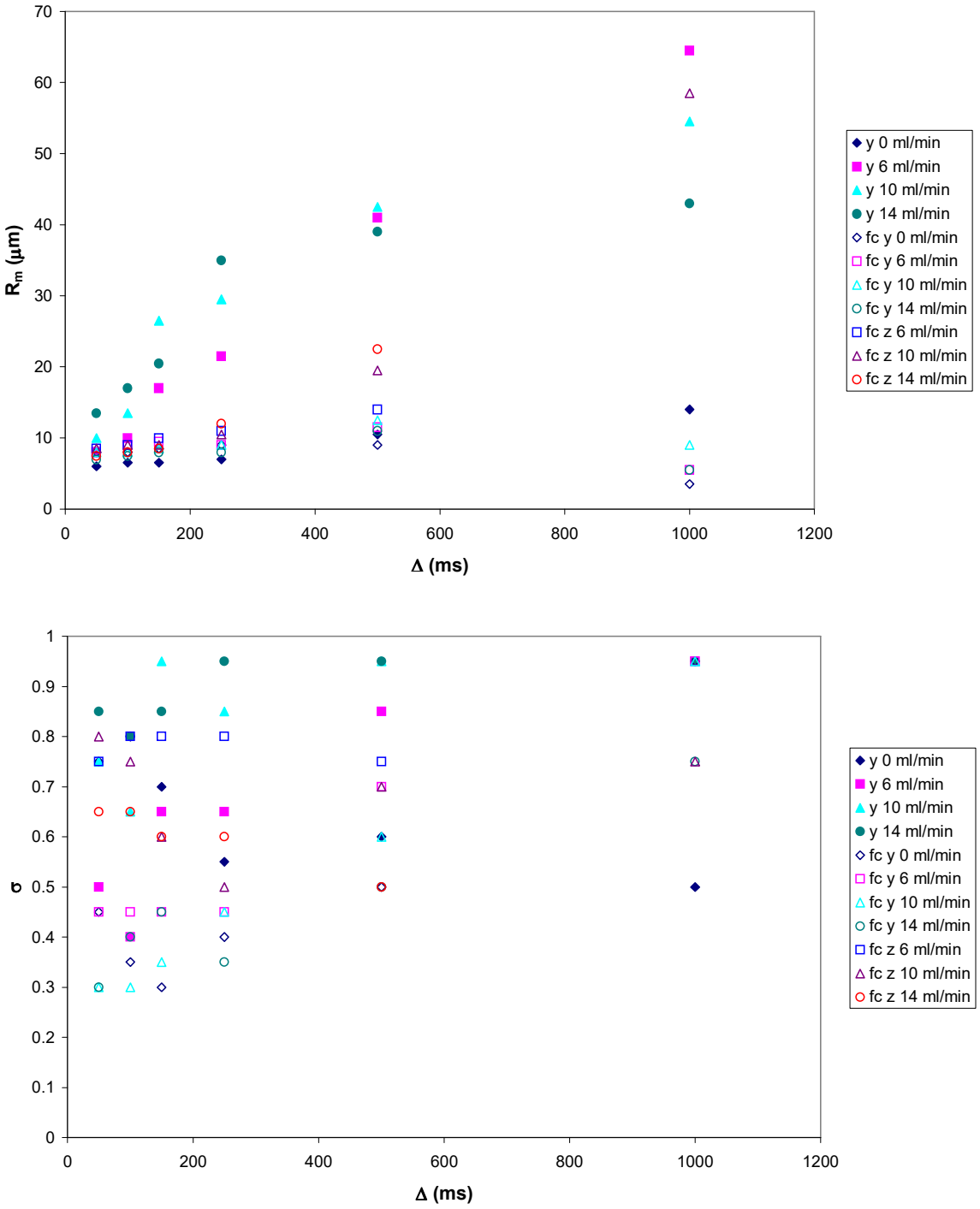

Figure 7.19 Parameters of the log-normal droplet size distribution, R_m and σ, obtained for a flowing emulsion containing 41 wt% *o*-xylene using the STE and DSTE PFG sequences with six different Δ values.

were good (figure 7.20(c)). DSTE along z gave results similar to those along y for low Δ, but then diverged dramatically at high Δ, so only the results for $\Delta \leq 250$ ms can be considered reliable.

The 26-wt% emulsion gave very odd results that could not be fitted (figure 7.21(a)). The attenuation curves at low Δ were convex and those at high Δ contained a pattern that resembled dispersive diffraction patterns (Callaghan *et al.*, 1999). The convex attenuation curves at low Δ could therefore contain the same pattern but not have reached the first minimum after 32 data points. The same patterns were present in the attenuation curves for the 41-wt% emulsion (figure 7.21(b)) but the curves for the 35-wt% emulsion were clearly concave (figure 7.20(c)). The appearance of the diffraction patterns was not related to flow rate since the strongest diffraction patterns were observed at intermediate flow rates. The patterns may have been related to droplet size or uniformity of droplet sizes, since the 35-wt% emulsion for which no diffraction was observed had the largest values of R_m and σ.

Diffraction patterns appear in PFG experiments because of correlations between spin phases and molecular position or displacement in highly ordered structures (Callaghan *et al.*, 1999). Position diffraction has been observed in a regularly spaced stack of paraffin plates (Mansfield and Grannell, 1972), and flow diffraction has been observed for a liquid flowing through a packed bed of monodisperse spheres (Seymour and Callaghan, 1996). Velocity correlation diffraction appears in a double-echo experiment for a liquid in laminar pipe flow because Taylor dispersion allows the molecules to sample the entire velocity distribution when $\Delta >> a^2/D$, where a is the pipe radius (Callagan *et al.*, 1999).

For the flowing emulsion, the *o*-xylene can only sample the velocity distribution over the width of the droplet in which it is confined, so by analogy one would expect diffraction if $\Delta >> R_m^2/D$. For $R_m = 10$ μm and $D = 1.35\times10^{-9}$ m^2/s, diffraction would occur if $\Delta >> 74$ ms, which is consistent with the appearance of diffraction patterns in the attenuation data at large Δ. For the larger droplets in the 35-wt% emulsion, taking $R_m = 20$ μm gives diffraction for $\Delta >> 296$ ms, which is again consistent with the absence of diffraction patterns in the attenuation data. If the attenuation curves are plotted using $\gamma g \delta$ as the independent variable (figure 7.22), the difference between the concave and convex attenuation curves is clearly visible. The first minimum in the

(a)

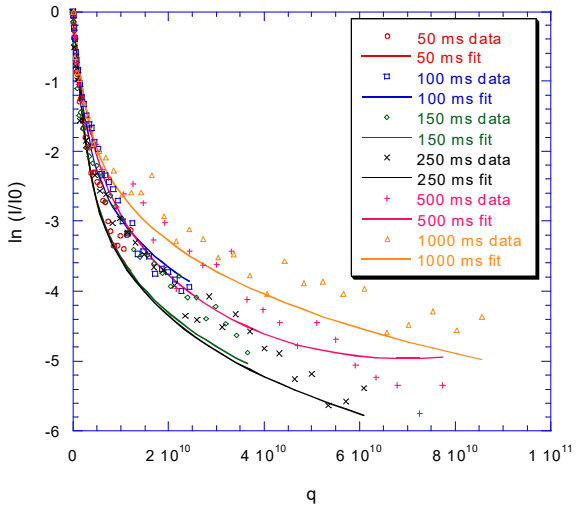

(b)

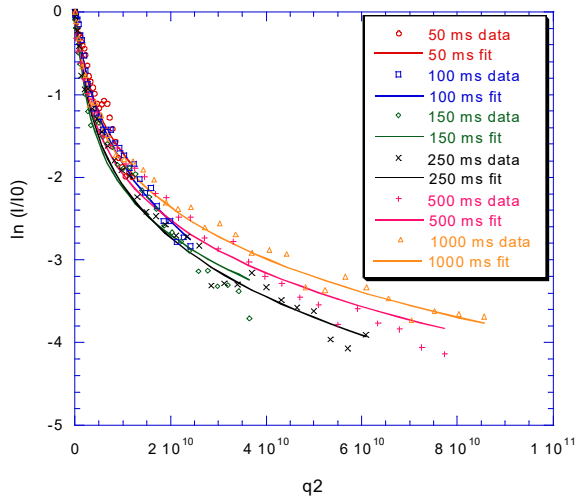

(c)

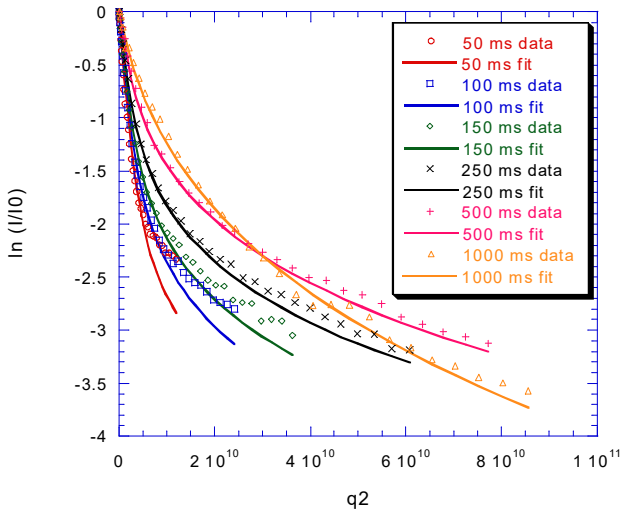

Figure 7.20 Echo attenuation plots for flowing emulsions, showing the experimental data (points) and the fits using log-normal droplet size distributions (lines). *(a)* STE along *y*, 41 ml/min, 35 wt% *o*-xylene *(b)* STE along *y*, 10 ml/min, 41 wt% *o*-xylene *(c)* DSTE along *y*, 41 ml/min, 35 wt% *o*-xylene. $q = \gamma^2\delta^2(\Delta\text{-}\delta/3)g^2$, $q_2 = \gamma^2\delta^2(\Delta\text{-}2\delta/3)g^2$.

(a)

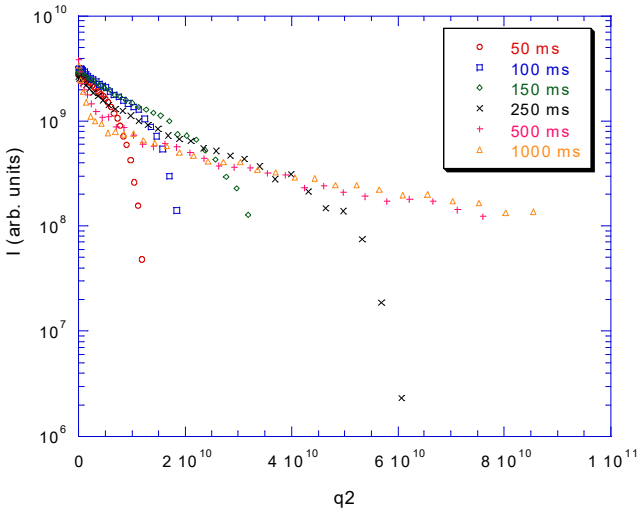

(b)

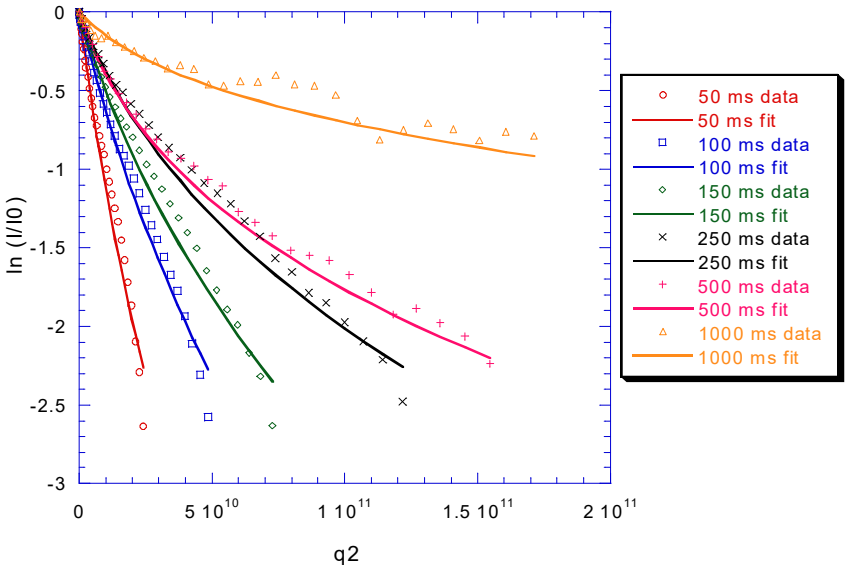

Figure 7.21 Echo attenuation plots for flowing emulsions, showing the appearance of diffraction patterns. *(a)* DSTE along *y*, 14 ml/min, 26 wt% *o*-xylene *(b)* DSTE along *y*, 10 ml/min, 41 wt% *o*-xylene. $q_2 = \gamma^2\delta^2(\Delta - 2\delta/3)g^2$.

(a)

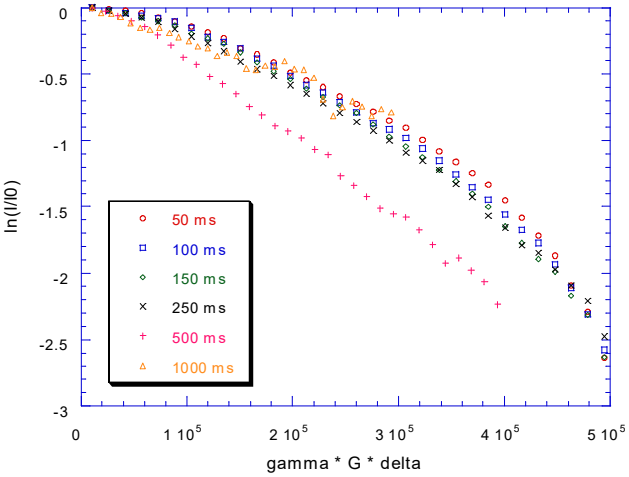

(b)

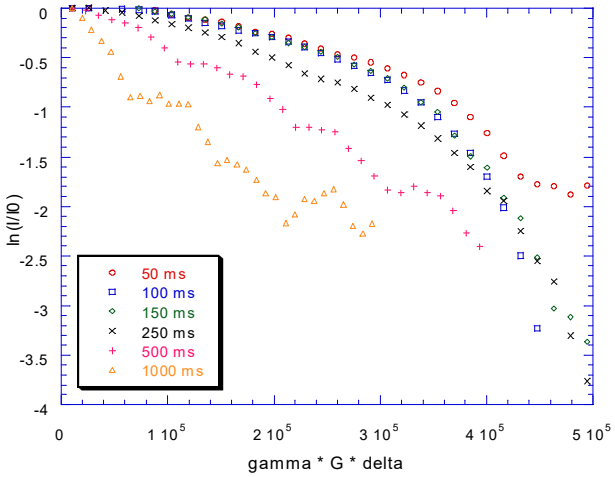

(c)

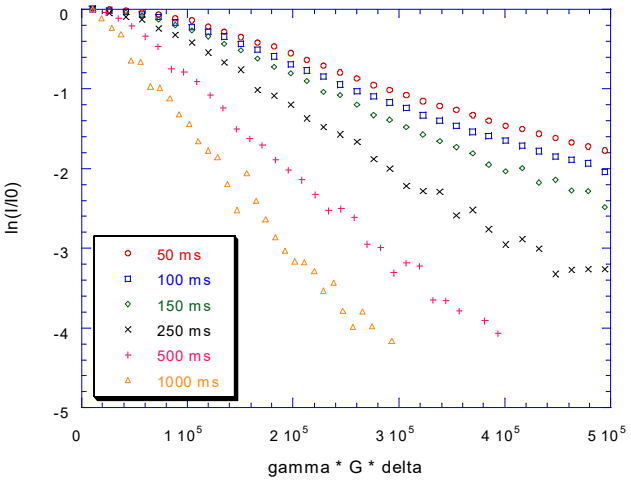

Figure 7.22 Echo attenuation plots for flowing emulsions plotted against γgδ, showing the diffraction patterns: *(a)* DSTE along *y*, 10 ml/min, 41 wt% *o*-xylene, *(b)* DSTE along *y*, 6 ml/min, 26 wt% *o*-xylene; *(c)* DSTE along *y*, 41 ml/min, 35 wt% *o*-xylene without diffraction.

diffraction pattern of the 41-wt% emulsion appears at $\gamma g\delta/2\pi = 7.96\times10^4$ m^{-1}, corresponding to a spatial dimension of 12.6 μm, which is consistent with the mean droplet size measured on the static emulsion. The diffraction pattern for the 26-wt% emulsion has different patterns for different Δ values, with first minima varying from 14 μm^{-1} at 50 ms to 97 μm^{-1} at 1000 ms.

The diffraction patterns may have been phase-twist artefacts caused by mismatched gradient pulses, as has been observed with gradient pulses of very high amplitude in slowly-diffusing systems (Price *et al.*, 1999). However, the gradient pulses used in our experiments were two orders of magnitude smaller than those used by Price, and the diffusion coefficients were four orders of magnitude larger, so the phase-twist artefacts should be dominated by the diffusive attenuation. Since the diffraction was not observed with flowing water, it was not a hardware artefact, but linked to restricted diffusion.

In conclusion, consistent droplet size distributions of flowing emulsions were measured using double-echo PFG NMR with the pulsed gradients transverse and parallel to the flow direction for short diffusion times. At longer diffusion times, flow diffraction patterns appeared in the attenuation data. The droplet size distributions of the emulsions varied with the *o*-xylene content of the emulsion, but were independent of flow rate.

7.5 Discussion

The determination of the droplet size distributions of flowing emulsions by PFG NMR contained several possible sources of experimental error. The temperature of the emulsion varied with the laboratory temperature by ~2°C, so the diffusion coefficient varied by $\pm0.1\times10^{-9}$ m^2/s, while a constant value was used in the fitting procedure. The two liquids had different magnetic susceptibilities, which could produce a background magnetic field gradient, but this was ignored in these experiments. PFG sequences exist with bipolar pulsed gradients to eliminate the background gradient (Karlicek and Lowe, 1980) but they make the pulse sequences even longer, particularly for a double echo. A new pulse sequence has been proposed recently for improved convection compensation without bipolar gradients (Sorland *et al.*, 2000).

The droplet size distributions may not have been log-normal, although this is unlikely based on the literature. The Murday-Cotts equation (7.2) was derived for a single echo, so it is not strictly speaking applicable to the flow-compensated attenuation data. However, modifying the equation for a double echo is not trivial.

7.6 Conclusion

Ten PFG pulse sequences were evaluated for their ability to determine the droplet size distributions of flowing emulsions. The standard spin-echo and stimulated-echo sequences were modified for volume selection and flow compensation. The reliability of the pulse sequences was assessed by their performance on static and flowing water, for which the diffusion coefficient was known.

Stimulated echoes gave better attenuation data for water than spin echoes because of the higher signal loss in spin echoes from transverse relaxation and diffusion in an inhomogeneous $\mathbf{B_0}$ field. The stimulated-echo sequences generally gave diffusion coefficients within 10% of the standard value. Flow compensation was only partly successful due to transverse diffusion in the flow field and incomplete phase cycling. Contrary to expectation, excess liquid outside the homogeneous region of the r.f. and gradient coils did not cause errors in the measured diffusion coefficient. The volume-selective sequences gave diffusion coefficients that were 20% too large at low Δ values.

The stimulated-echo pulse sequences were used to determine the droplet size distributions of static and flowing emulsions of *o*-xylene in water. The droplet size distributions were not known beforehand, so the reliability of the PFG results was judged based on their consistency and the results obtained for water. The creaming of the emulsions caused the single-echo data to exhibit additional attenuation and scatter that was absent in the double-echo data. Consistent droplet size distributions were obtained for static emulsions from both the single-echo and double-echo data, but for flowing emulsions only from the double-echo data at short diffusion times. The droplet size distributions varied with the *o*-xylene content of the emulsion but were independent of flow rate.

Volume-selective PFG, if successful, could provide information on the heterogeneity of flowing emulsions that is complementary to the information obtained using volume-selective spectroscopy in chapter 6. The odd results from the volume-

selective PFG sequences require further investigation. Strong echo attenuation was observed for water at low Δ values, presumably due to sample heating. Imperfect refocusing of the slice selection gradients may have caused additional attenuation. However, the strong echo attenuation at low Δ was not observed along *z* for the static emulsions, for unknown reasons.

The flow diffraction effects observed for small droplets at long diffusion times also need to be studied in more detail. They appear to limit the range of droplet sizes for which the current PFG method can give a droplet size distribution during flow. However, they may contain droplet size information in the pattern of the diffraction peaks.

7.7 References

Balinov, B., Söderman, O., & Wärnheim, T. (1994a). Determination of water droplet size in margarines and low-calorie spreads by nuclear magnetic resonance self-diffusion. *Journal of the American Oil Chemists Society, 71*, 513-518.

Balinov, B., Urdahl, O., Söderman, O., & Sjöblom, J. (1994b). Characterization of water-in-crude oil emulsions by the NMR self-diffusion technique. *Colloids and Surfaces A: Physicochemical and Engineering Aspects, 82*, 173-181.

Becher, P. (1966). Emulsification. In M.J. Schick (Ed.), *Nonionic Surfactants*, *surfactant science series volume 1*, pp. 604-605. Marcel Dekker, Basel, Switzerland.

Enden, J.C. van den, Waddington, D., Aalst, H. van, Kralingen, C.G. van, & Packer, K.J. (1990). Rapid determination of water droplet size distributions by PFG-NMR. *Journal of Colloid and Interface Science, 140*, 105-113.

Holz, M. (1999). Temperature dependence of water self-diffusivity. In *1999 Bruker Almanac*, p.72. Bruker Analytik GmbH, Rheinstetten, Germany.

Callaghan, P.T. (1991). *Principles of Nuclear Magnetic Resonance Microscopy*. pp. 470-471. Clarendon Press, Oxford, UK.

Callaghan, P.T., Codd, S.L., & Seymour, J.D. (1999). Spatial coherence phenomena arising from translational spin motion in gradient spin echo experiments. *Concepts in Magnetic Resonance, 11*, 181-202.

Callaghan, P.T., Jolley, K.W., & Humphrey, R.S. (1983). Diffusion of fat and water in cheese as studied by pulsed field gradient nuclear magnetic resonance. *Journal of Colloid and Interface Science, 93*, 521-529.

Everett, D.H. (1988). *Basic Principles of Colloid Science*. pp. 182-184. Royal Society of Chemistry, London, UK.

Karlicek, R.F. Jr., & Lowe, I.J. (1980). Modified pulsed gradient technique for measuring diffusion in the presence of large background gradients. *Journal of Magnetic Resonance, 37*, 75-91.

Lee, H.Y., McCarthy, M.J., & Dungan, S.R. (1998). Experimental characterization of emulsion formation and coalescence by nuclear magnetic resonance restricted diffusion techniques. *Journal of the American Oil Chemists Society, 75*, 463-475.

Li, X., Cox, J.C., & Flumerfelt, R.W. (1992). Determination of emulsion size distribution by NMR restricted diffusion measurement. *AIChE Journal, 38*, 1671-1674.

Mansfield, P., & Grannell, P.K. (172). NMR "diffraction" in solids? *Journal of Physics C: Solid State Physics, 6*, 422-246.

Murday, J.S., & Cotts, R.M. (1968). Self-diffusion coefficient of liquid lithium. *The Journal of Chemical Physics, 48*, 4938-4945.

Packer, K.J., & Rees, C. (1972). Pulsed NMR studies of restricted diffusion I. Droplet size distributions in emulsions. *Journal of Colloid and Interface Science, 40*, 206-218.

Pal, R. (1993). Pipeline flow of unstable and surfactant-stabilized emulsions. *AIChE Journal, 39*, 1754-1764.

Pal, R. (1996). Anomalous effects in the flow behaviour of oil-in-water emulsions. *The Chemical Engineering Journal, 63*, 195-199.

Pal, R., & Rhodes, E. (1989). Emulsion flow in pipelines. *International Journal of Multiphase Flow, 15*, 1011-1017.

Pope, J.M., & Yao, S. (1993). Quantitative NMR imaging of flow. *Concepts in Magnetic Resonance, 5*, 281-302.

Price, W.S., Hayamizu, K., Ide, H., & Arata, Y. (1999). Strategies for diagnosing and alleviating artifactual attenuation associated with large gradient pulses in PGSE NMR diffusion measurements. *Journal of Magnetic Resonance, 139*, 205-212.

Seymour, J.D., & Callaghan, P.T. (1996). "Flow diffraction" structural characterisation and measurement of hydrodynamic dispersion in porous media by PGSE NMR. *Journal of Magnetic Resonance, Series A, 122*, 90-93.

Sorland, G.H., Seland, J.G., Krane, J., & Athonsen, H.W. (2000). Improved convection compensating pulsed field gradient spin-echo and stimulated-echo methods. *Journal of Magnetic Resonance, 142*, 323-325.

Stejskal, E.O. (1965). Use of spin echoes in a pulsed magnetic-field gradient to study anisotropic, restricted diffusion and flow. *The Journal of Chemical Physics, 43*, 3597-3603.

Stejskal, E.O., & Tanner, J.E. (1965). Spin diffusion measurements: spin echoes in the presence of a time-dependent field gradient. *The Journal of Chemical Physics, 42*, 288-292.

Tanner, J.E. (1970). Use of the stimulated echo in NMR diffusion studies. *The Journal of Chemical Physics, 52*, 2523-2526.

7.8 Nomenclature

(symbol)	(description)	(unit)
Vector Variables		
$\mathbf{B_0}$	static magnetic field	T
Scalar Variables		
a	radius of pipe	m
A	signal amplitude	-
D	self-diffusion coefficient	$m^2\ s^{-1}$
g	applied gradient	$T\ m^{-1}$
I	echo intensity	-
$P(R)$	droplet size distribution function	-
q	$(\gamma g\delta)^2(\Delta-\delta/3)$	$rad\ s\ m^{-2}$
q_2	$(\gamma g\delta)^2(\Delta-2\delta/3)$	$rad\ s\ m^{-2}$
R	droplet radius	m
R_m	mean droplet radius	m
T_1	longitudinal relaxation time constant	s
T_2	transverse relaxation time constant	s
y	axis perpendicular to $\mathbf{B_0}$	-
z	axis parallel to $\mathbf{B_0}$	-
α_m	root of Bessel function equation (7.3)	-
γ	gyromagnetic ratio	$rad\ T^{-1}\ s^{-1}$
δ	duration of gradient pulse	s
Δ	diffusion time; delay between gradient pulses	s
σ	standard deviation of log-normal distribution	-
τ	delay between 90° and 180° pulse; 2τ is the echo time	s

8 FLOW IMAGING OF A LIQUID JET

8.1 Introduction

Flow imaging is a well-established application of nuclear magnetic resonance that combines imaging and pulsed field gradient techniques to give a signal that is sensitive to velocity (Caprihan and Fukushima, 1990; Pope and Yao, 1993). It allows the acquisition of velocity profiles (Xia *et al.*, 1992) and three-dimensional velocity maps (Derbyshire *et al.*, 1994) with the same spatial resolution as conventional NMR imaging. Flow imaging is used in medical applications to study blood flow and in industrial applications such as rheometry, flow of suspensions and flow in porous media (Caprihan and Fukushima, 1990; Fukushima, 1999). This chapter reports the application of NMR flow imaging to a liquid jet flowing vertically upwards into an immiscible liquid. The jet was obtained during an attempt to observe core-annular flow of two immiscible liquids. Core-annular flow is a flow regime whereby a viscous liquid flowing through the centre of a pipe is fully surrounded by a second, immiscible liquid with lower viscosity that lubricates the flow (Joseph *et al.*, 1997). Stable core-annular flow depends on the density, viscosity, surface tension, and superficial velocity of the two liquids (Marosek *et al.*, 1993) and is very difficult to achieve. In our experiments, visual observation and the flow images showed that the viscous liquid formed a jet that broke up into droplets, but core-annular flow was not achieved. A search of the Science Citation Index did not yield any reports on the flow imaging of liquid jets by NMR or other techniques, so this report is believed to be the first.

8.2 Fluid Mechanics of Liquid Jets

The available experimental data on liquid jets issuing into an immiscible liquid are restricted to visual observations and photographs, from which jet diameters have been obtained. There have been no experimental jet velocity profiles reported to date, although hydrodynamic calculations have been performed. The evolution of the shape and velocity distribution of a liquid jet has been calculated by numerically solving the equations of continuity and motion for both phases simultaneously (Duda and Vrentas, 1967; Gospodinov *et al.*, 1979; Anwar *et al.*, 1982). For a laminar jet,

the parabolic velocity profile at the nozzle exit is expected to relax downstream until it is almost flat due to the acceleration of the surface fluid by momentum exchange between the surface and the core of the jet and the action of viscous shear forces. The diameter of the jet may expand or contract, depending on the balance between the jet buoyancy and the viscous shear forces, expressed using the parameter N_j defined by (Anwar *et al.*, 1982):

$$N_j = \frac{Re}{Fr}\left(\frac{\rho_1}{\rho_2} - 1\right), \quad Re = \frac{\rho_1 u_N d_N}{\mu_1}, \quad Fr = \frac{u_N^2}{d_N g}, \tag{8.1}$$

where ρ_1 and ρ_2 are the densities of the jet and continuous phase liquid respectively, μ_1 is the viscosity of the jet liquid, u_N is the mean jet velocity at the nozzle exit, d_N is the nozzle diameter and g is the acceleration due to gravity. Anwar predicts that the jet expands if $N_j << 1$ and contracts if $N_j >> 1$ and his predictions are matched by his visual observations.

This flow pattern is very similar to that observed for a liquid flowing through an abrupt expansion, for which velocity profiles have been obtained using NMR (Xia *et al.*, 1992). The parabolic velocity profiles entering the expansion become flatter downstream of the expansion, matching the predicted behaviour of a laminar jet very closely.

8.3 NMR Flow Imaging

The NMR flow imaging technique used in these experiments is the phase-encoding method described by Callaghan (1991). This method allows accurate quantitative velocity measurements because the phase of the signal is used to encode velocity, so variations in signal intensity due to diffusion, spin density differences and relaxation weighting do not affect the velocity measurement beyond a basic requirement for a good signal-to-noise ratio. The pulse sequence (*visehs*, *v*elocity *i*maging *s*pin-*e*cho *h*ard-*s*oft) is shown in figure 8.1. A spin echo is sequence is used with read, phase and slice gradients to produce a 2D image as described in section 5.1.6. The imaging sequence is combined with a bipolar gradient that provides the velocity encoding because it has a non-zero first moment (section 6.3.1), so it induces a phase shift in the signal that is proportional to velocity and is given by (Callaghan, 1991):

$$p_s = \gamma \int_0^t \mathbf{g} \cdot \mathbf{r} dt = \gamma v g_s \delta \Delta, \tag{8.2}$$

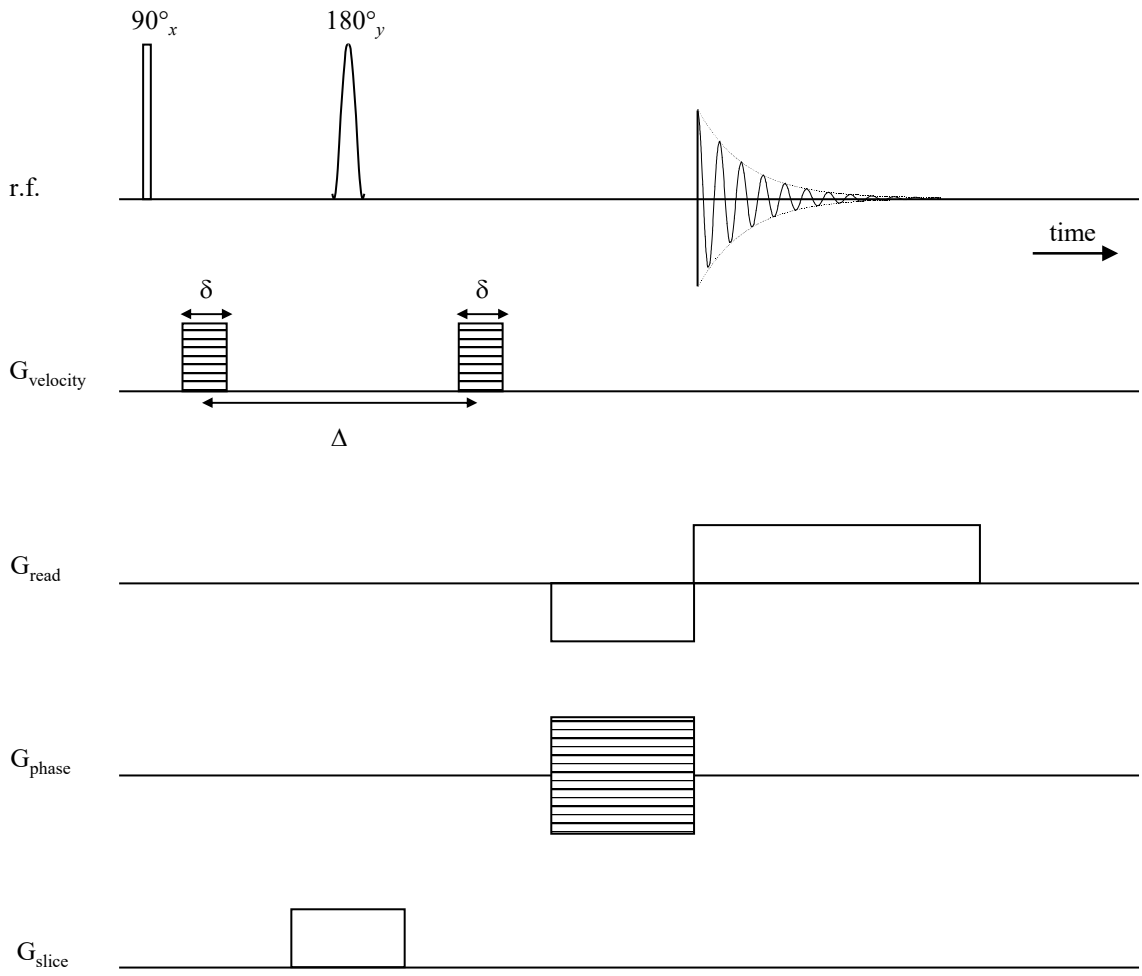

Figure 8.1 Spin-echo pulse sequence with velocity encoding (*visehs*) for acquiring a 2D velocity image of a single slice.

where p_s is the phase shift, γ is the gyromagnetic ratio of the nuclei, v is the velocity component along the gradient direction, g_s is the gradient strength, δ is the velocity encoding gradient duration and Δ is the delay between the dephasing and rephasing velocity gradients. A series of images is acquired with constant values of δ and Δ while g_s is incremented for each image, so that each images in the series has a different phase shift. The dynamic range of the measurement is restricted by the available range of phase shifts, $-\pi \leq p_s \leq +\pi$, so the maximum velocity to be observed must be estimated in order to select the appropriate velocity encoding parameters. Velocity components in different directions are measured by changing the direction in which the bipolar gradients are applied.

The velocity map is produced by Fourier transforming the time-domain data in two dimensions to give a series of 2D images, one for each value of g_s. The phase shift between successive images is calculated, and the average phase shift is used to calculate the velocity by inverting equation (8.2) to give:

$$v = \frac{p_s}{\gamma g_s \delta \Delta}. \tag{8.3}$$

To eliminate spurious phase shifts across the image caused by gradient switching, the same velocity images are acquired without flow. The "zero-velocity" images are subtracted from the phase-shifted images before applying equation (8.3).

8.4 Experimental

Two streams of flowing water and octanol were originally set up to produce core-annular flow vertically upwards in a glass column. Core-annular flow was not obtained, but a jet of octanol was observed flowing through the water. The water used was deionised tap water. The octanol ($CH_3(CH_2)_7OH$) was 99% GC grade obtained from Aldrich, and was used without further purification. The water and octanol were chosen to satisfy the requirements of core-annular flow, based on a review of the literature. Water was the obvious choice for the first liquid, and the second liquid had to satisfy the following criteria:

- It had to be immiscible with water.
- It had to have a density close to water, to reduce the effect of gravity on the flow. Octanol has a specific gravity of 0.827.

- For core-annular flow with water as the annulus liquid, the second liquid had to have a higher viscosity than water. At 20°C, octanol has a viscosity of 7.288×10^{-3} Pa s, compared to 8.565×10^{-4} Pa s for water.
- The second liquid had to have a low volatility so that evaporative losses were small. Octanol has a boiling point of 196°C, so it is less volatile than water.
- The second liquid had to be safe to handle in large quantities. Octanol is described as "irritant", but it is not harmful, toxic or flammable.
- The second liquid had to give a simple ^{1}H NMR spectrum with a few intense peaks, otherwise its signal would be lost compared to the intense water peak. The spectrum of octanol contains three peaks: one from the OH group, one from the CH_2 protons next to the OH group, and one from the other aliphatic protons. The individual peaks of the aliphatic proton groups were not resolved on our system.

The flow loop used in these experiments is shown in figure 8.2. The test section consisted of a glass column of length 1.50 m and inner diameter 11 mm (o.d. 14 mm). The inlet to the test section consisted of a T-piece to allow water entry and a narrow aluminium tube to allow separate octanol entry. The tube was positioned with the top inside the r.f. coil. The tube diameter increased from 4 mm at the bottom to 8 mm at the top. The design of the entry section was based on that of Marosek *et al.* (1993).

The liquids were pumped using two separate peristaltic pumps to allow independent control of the two flow rates. The pulsatile flow was smoothed using sealed damping bottles downstream of the pumps. The water flowed though silicone rubber tubing (i.d 4.4 mm, o.d. 6.5 mm), but flexible Viton tubing (i.d. 3.1 mm, o.d.5.8 mm) was used for octanol, because octanol penetrates through silicone rubber and evaporates from the surface.

The direction of flow was chosen to be upwards through the magnet because octanol is less dense than water. If the flow is downwards, the octanol leaving the nozzle flows back up into the water inlet and disrupts the water flow. This is contrary to Marosek's requirement that the flow should be downwards when the core fluid is less dense than the annular fluid. The two liquids left the test section at the top of the magnet and returned to a 2-l glass beaker where they separated under the influence of gravity. If the flow rates were sufficiently low, the two liquid layers in the beaker were stable and water and octanol could be drawn off separately. This enabled

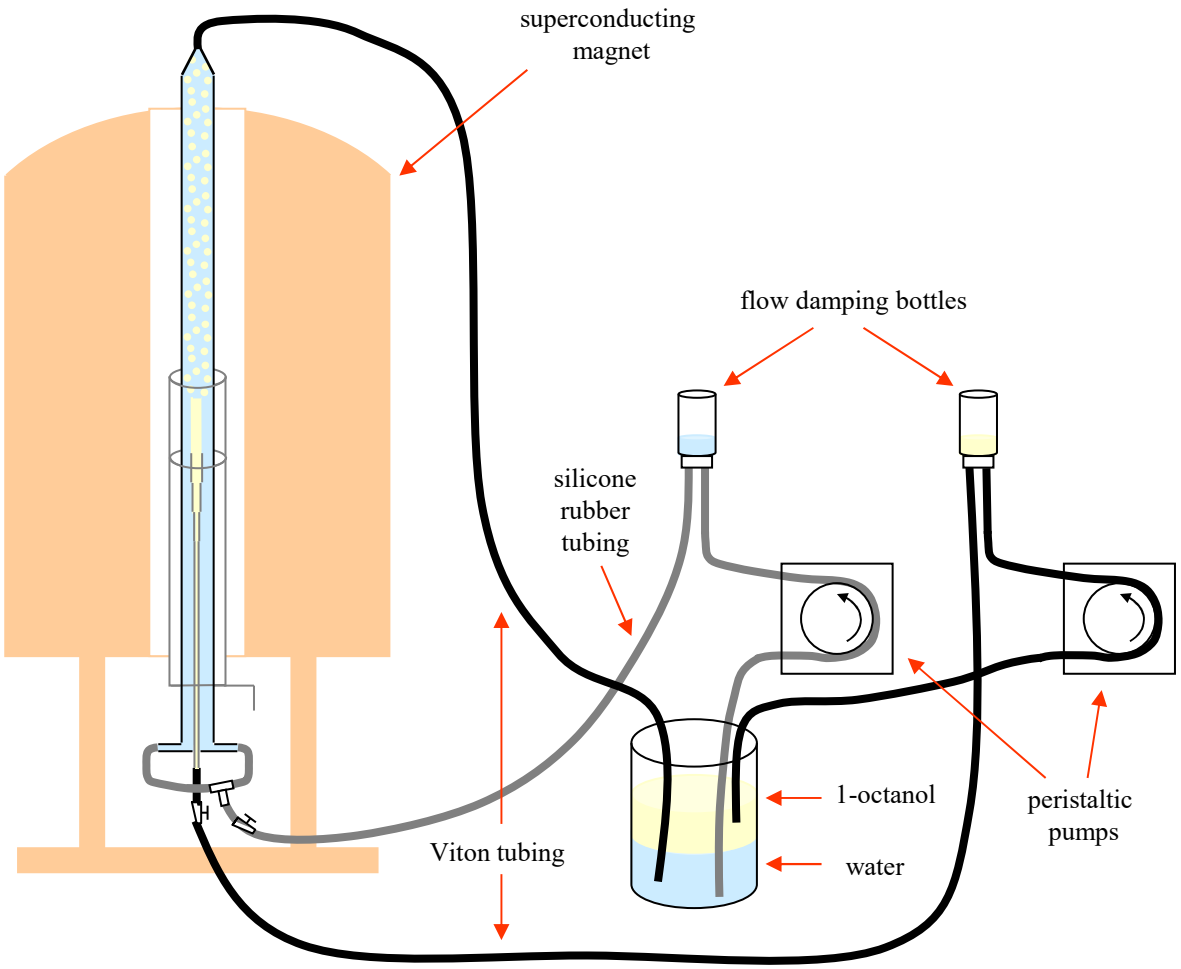

Figure 8.2 Flow loop for velocity imaging of two-phase liquid flow. The liquids are pumped from the glass beaker through the damping bottles and upwards through the magnet.

continuous operation of the flow loop. The flow rates were determined by measuring the volume of liquid flowing out of the test section in 2 minutes.

The velocity images were acquired using a Bruker DMX 300 spectrometer equipped with a 7.05 T, 89-mm bore, vertical superconducting magnet. A micro-imaging probe was used with a 25-mm birdcage coil tuned to a ^{1}H resonance frequency of 300.130 MHz. The *visehs* pulse sequence described in section 8.3 was used. Since the flow was upwards, the nuclei entered the magnetic field near the base of the magnet, then travelled upwards over the length of the probe before they reached the coil. The distance travelled inside the magnetic field was approximately 0.60 m, so the residence time in the field was too short to build up a large magnetisation before reaching the coil. Consequently, the signal intensity was low and several scans were needed for a good signal-to-noise ratio.

The velocity images were acquired in sets of six, one image for each component of the velocity (v_x, v_y, v_z) taken from a transverse and a longitudinal slice. The bulk flow was along the z direction. For the transverse images the read, phase and slice gradients were applied along the x, y and z directions respectively. The xy field of view was 12×12 mm^2 and the number of pixels was 128×128, giving a resolution of 93.75 μm/pixel. For the longitudinal images the read, phase and slice gradients were applied along the z, x and y directions respectively. The zx field of view was 60×15 mm^2 and the number of pixels was 512×128, giving a resolution of 117.19 μm/pixel. Other acquisition parameters differed per image, and their values are given in the image captions. Zero-velocity images were also acquired for each experiment, but when they were analysed later, they were found to contain unexpected phase discontinuities that were not observed in the flow images themselves. It was not possible to acquire another set of zero-velocity images at that time because the flow loop had already been dismantled. Therefore, the flow images are presented in the results without a zero-phase correction.

The phase-encoding method is based on the assumption the velocity is constant over the time Δ, so the velocity maps are only meaningful for steady flow patterns. Unsteady flow also causes additional phase shifts leading to aliasing in the image along the direction of the phase-encoding gradient, so clear images can only be obtained for steady flow. The steadiness of the jet was determined by acquiring a

quick spin-echo image without the bipolar velocity gradients. If aliasing was observed in the phase direction, then the jet was not sufficiently steady to be imaged, so the water and octanol flow rates were adjusted and another image was acquired. The position of the imaging slice relative to the nozzle exit was also varied in order to find the most stable flow pattern. The long-term stability of the jet was poor, so only four velocity encoding steps per image could be acquired.

8.5 Results

The flow patterns for the flow of water and octanol using the apparatus described above were first observed visually in the flow column before it was placed in the magnet. At low octanol flow rates (<10 ml/min), the octanol left the nozzle as droplets regardless of the water flow rate. At intermediate octanol flow rates (10-40 ml/min), the octanol leaving the nozzle narrowed to form an off-centre jet of ~3 mm diameter. The stability of the jet depended on the relative flow rates of octanol and water. If the water and octanol flow rates were low, the jet was stable over a length of ~5 cm, before breaking up into octanol droplets. If the octanol flow rate was increased relative to water, the jet would pulse along the flow direction. If the water flow rate was increased relative to octanol, the jet would flicker in the transverse direction. The behaviour of the jet resembled that of a flame in a stream of moving air. At high octanol and water flow rates (> 40 ml/min), the liquids would flow through the column separately as slugs that covered the entire column diameter, because they are immiscible. Core-annular flow was not observed, due to the low viscosity of octanol and surface tension effects.

When the column was placed inside the magnet, the water and octanol flow rates were set to the values that had given the octanol jet, since the other flow patterns (bubbles, slugs) were unsteady and could not be imaged. The stability of the jet was tested by acquiring spin-echo images of the system, and checking for aliasing. Velocity images were acquired for two stable jets at different flow rates. The first jet was at 33.5±0.81 ml/min for octanol and 12.5±0.51 ml/min for water, with the image plane 9 mm downstream of the nozzle exit. The second jet was at 21.0±0.84 ml/min for octanol and 27.0±0.55 ml/min for water with the image plane 6 mm downstream of the nozzle exit.

Twelve velocity images are shown in figures 8.3 - 8.9 showing each of the three velocity components (v_x, v_y, v_z) from a transverse and a longitudinal slice for the two observed octanol jets. A noise mask was applied to the images to set all the pixels outside the sample region to a large negative value. The phase aliasing artefacts were observed only where the jet was unsteady. They were present mainly in the noise region, and are faintly visible in the transverse images as columns of circles above and below the jet cross-section. However, their magnitude was equivalent to the noise level in the image, so they did not distort the overall velocity measurement. Since the zero-velocity images were not subtracted from the flow images, the flow images also contain some random phase variations and artefacts such as the vertical line in figure 8.4(b), but they still show very clear flow patterns.

The images in figures 8.3 - 8.5 show the three velocity components for the first jet at flow rates of 33.5±0.81 ml/min for octanol and 12.5±0.51 ml/min for water. The gaps at the bottom of the longitudinal images show the (off-centre) position of the aluminium nozzle that shields the r.f. power and produces no signal. Each image has its own colour scale because a single scale for all images was not appropriate. The v_z image (figure 8.3 (a)) shows the narrowing of the jet and the increase in octanol velocity inside the jet with distance from the nozzle, to a maximum value of 0.150 m/s. The jet parameter given by equation (8.1), $N_j = -1.100$, so if one takes the absolute value of N_j, then the contraction of the octanol jet matches Anwar's prediction. The v_z velocity profiles at different positions downstream of the nozzle exit are shown in figure 8.9. The velocity profiles are fairly flat throughout and show the narrowing and acceleration of the jet, although the predicted relaxation effect is not observed. Some profiles are asymmetric about the centre of the nozzle, in keeping with the visual observation that the jet was off-centre from the nozzle (shifted to the right in the image and profiles). The jet cross-section decreases from 5.16 mm for the first profile 0.47 mm downstream to 1.29 mm for the profile 13.36 mm downstream. The cross-section does not equal the jet diameter, because the y slice was not taken through the centre of the jet (see figure 8.3(b)), but the difference is small. We can define a jet Reynolds number given by:

$$\mathrm{Re}_{jet} = \frac{\rho_1 v_z d_{jet}}{\mu_1}, \tag{8.4}$$

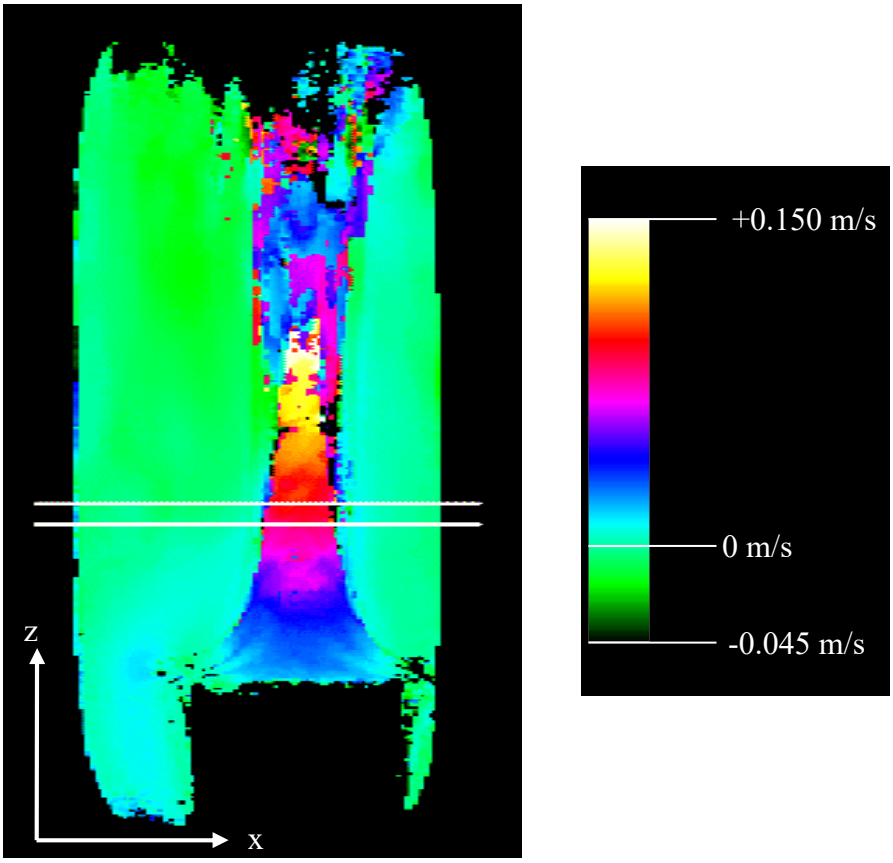

Figure 8.3 (a) Velocity image (v_z) of octanol jet (33.0±0.80 ml/min) and water (10.5 ±0.51 ml/min) co-current upward flow. Velocity encoding parameters: δ = 1 ms, Δ = 16.01 ms, g_s = 0.0097 T/m. 1 mm slice, image resolution 117.19 µm/pixel. The lines show the position of the transverse slice shown below.

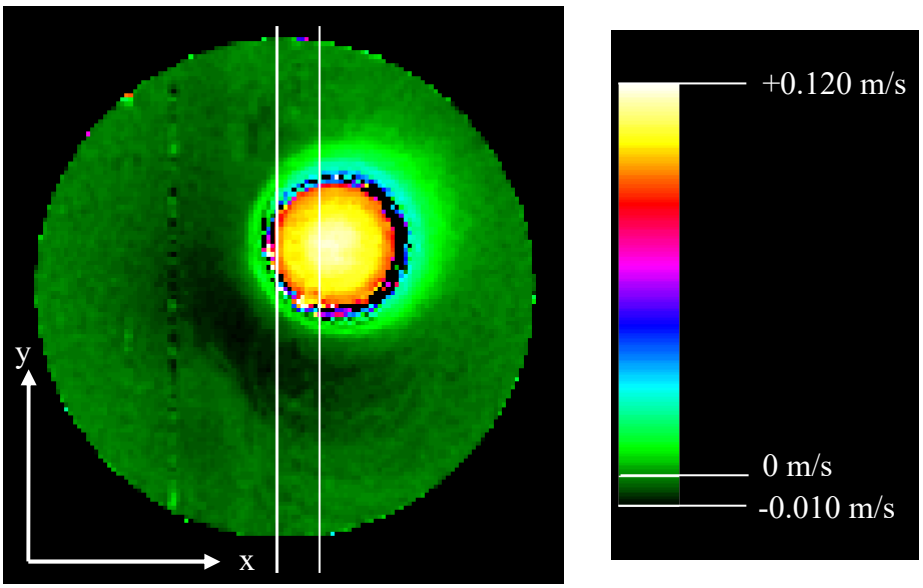

Figure 8.3 (b) Velocity image (v_z) of octanol jet (33.5±0.81 ml/min) and water (12.5 ±0.51 ml/min) co-current upward flow. Velocity encoding parameters: δ = 1 ms, Δ = 11.01 ms, g_s = 0.0097 T/m. 1 mm slice taken 9 mm downstream from nozzle, image resolution 93.75 µm/pixel. The lines show the position of the longitudinal slice shown above.

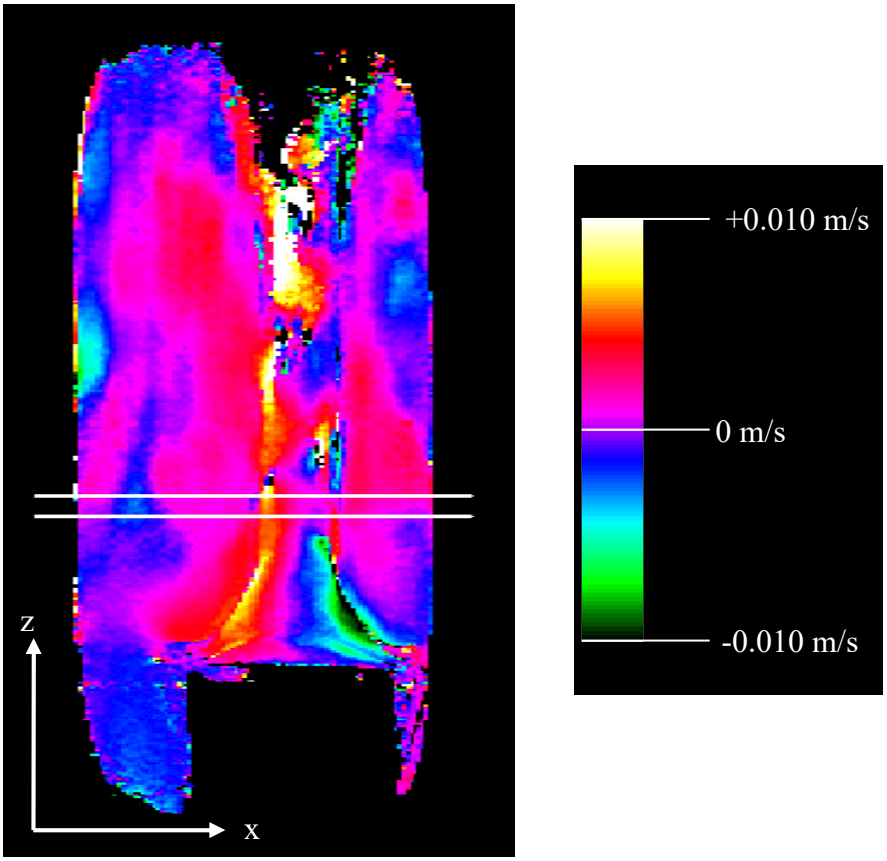

Figure 8.4 (a) Velocity image (v_x) of octanol jet (33.0±0.80 ml/min) and water (10.5 ±0.51 ml/min) co-current upward flow. Velocity encoding parameters: δ = 1 ms, Δ = 16.01 ms, g_s = 0.0194 T/m. 1 mm slice, image resolution 117.19 μm/pixel. The lines show the position of the transverse slice shown below.

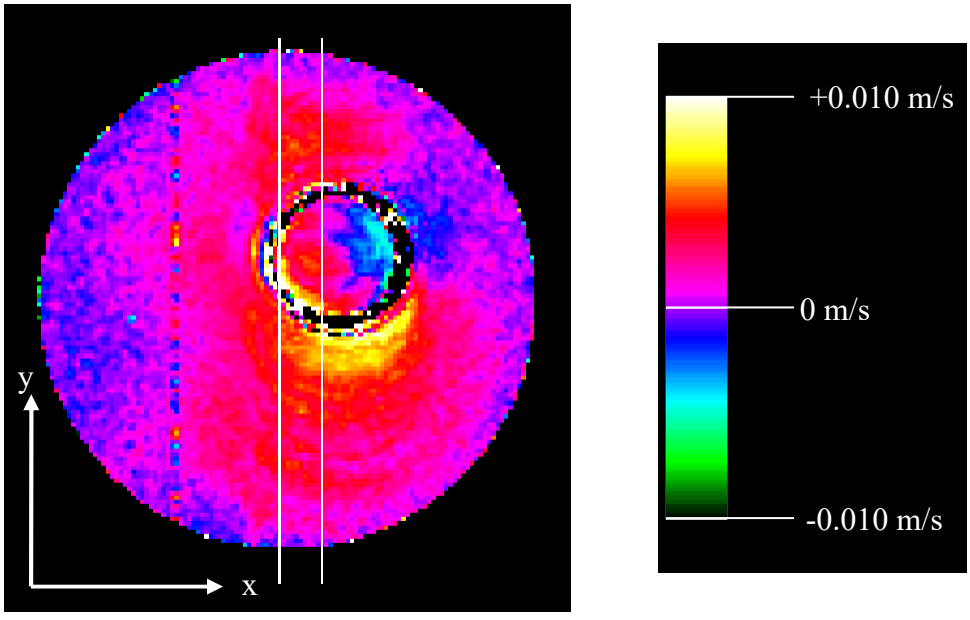

Figure 8.4 (b) Velocity image (v_x) of octanol jet (33.5±0.81 ml/min) and water (12.5 ±0.51 ml/min) co-current upward flow. Velocity encoding parameters: δ = 1 ms, Δ = 11.01 ms, g_s = 0.0194 T/m. 1 mm slice taken 9 mm downstream from nozzle, image resolution 93.75 μm/pixel. The lines show the position of the longitudinal slice shown above.

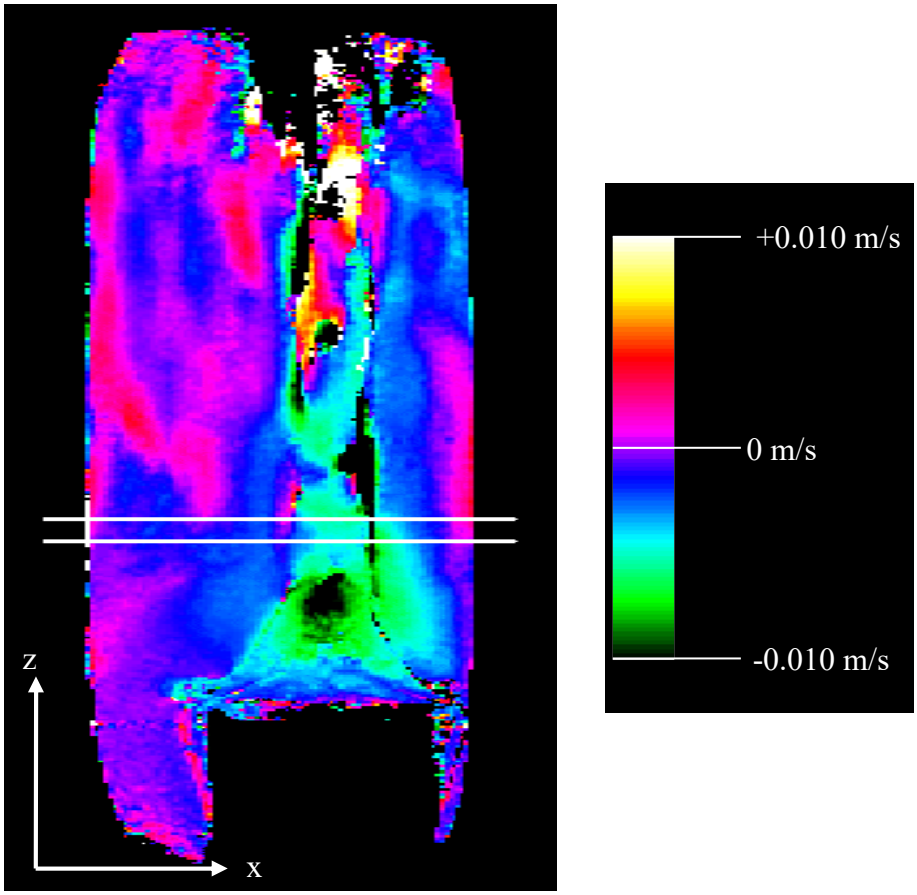

Figure 8.5 (a) Velocity image (v_y) of octanol jet (33.0±0.80 ml/min) and water (10.5 ±0.51 ml/min) co-current upward flow. Velocity encoding parameters: δ = 1 ms, Δ = 16.01 ms, g_s = 0.0194 T/m. 1 mm slice, image resolution 117.19 μm/pixel. The lines show the position of the transverse slice shown below.

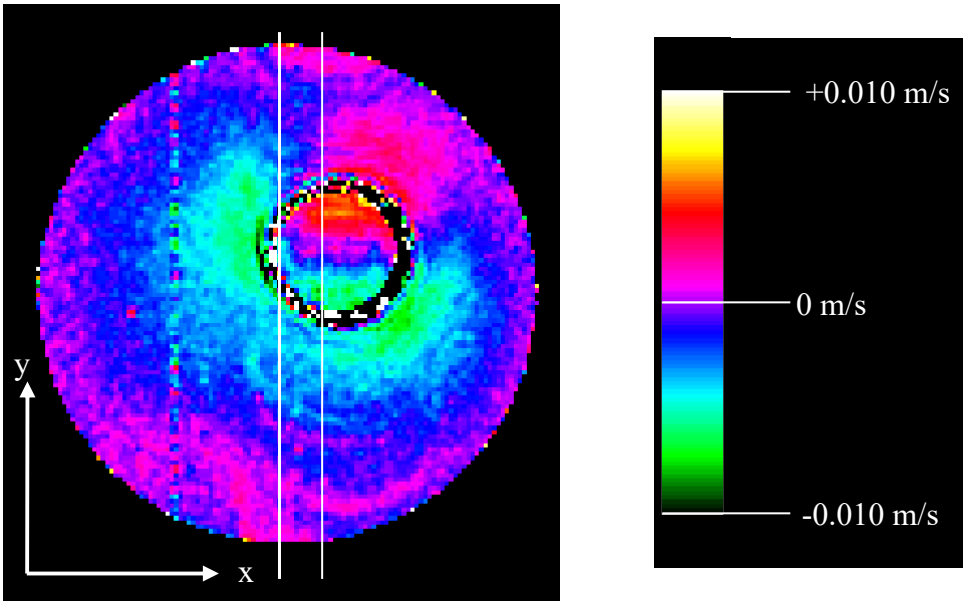

Figure 8.5 (b) Velocity image (v_y) of octanol jet (33.5±0.81 ml/min) and water (12.5 ±0.51 ml/min) co-current upward flow. Velocity encoding parameters: δ = 1 ms, Δ = 11.01 ms, g_s = 0.0194 T/m. 1 mm slice taken 9 mm downstream from nozzle, image resolution 93.75 μm/pixel. The lines show the position of the longitudinal slice shown above.

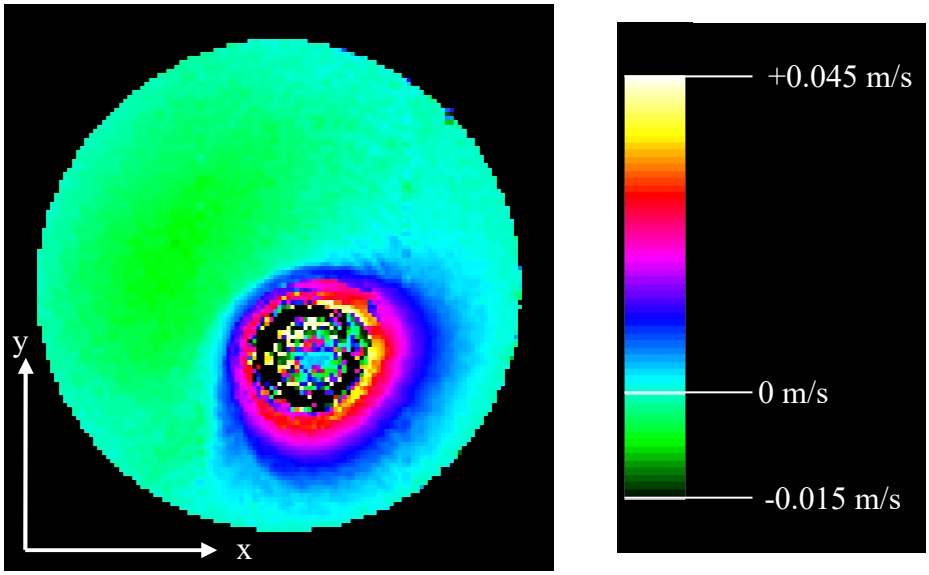

Figure 8.6 (a) Velocity image (v_z) of octanol jet (21.0±0.84 ml/min) and water (26.0 ±0.54 ml/min) co-current upward flow. Velocity encoding parameters: δ = 1 ms, Δ = 8.025 ms, g_s = 0.0486 T/m. 2 mm slice taken 6 mm downstream of nozzle, image resolution 93.75 μm/pixel.

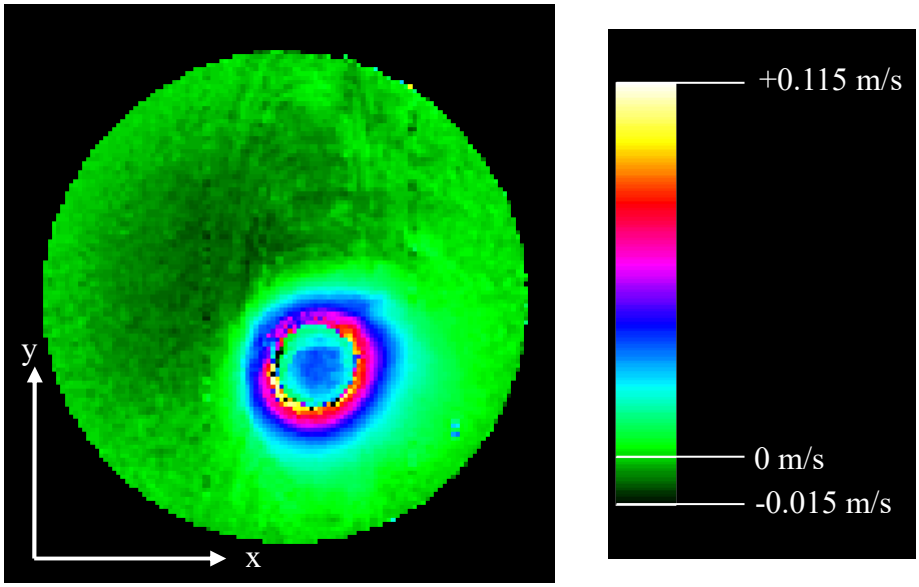

Figure 8.6 (b) Velocity image (v_z) of octanol jet (21.0±0.84 ml/min) and water (27.0 ±0.55 ml/min) co-current upward flow. Velocity encoding parameters: δ = 1 ms, Δ = 4.045 ms, g_s = 0.0389 T/m. 2 mm slice taken 6 mm downstream of nozzle, image resolution 93.75 μm/pixel.

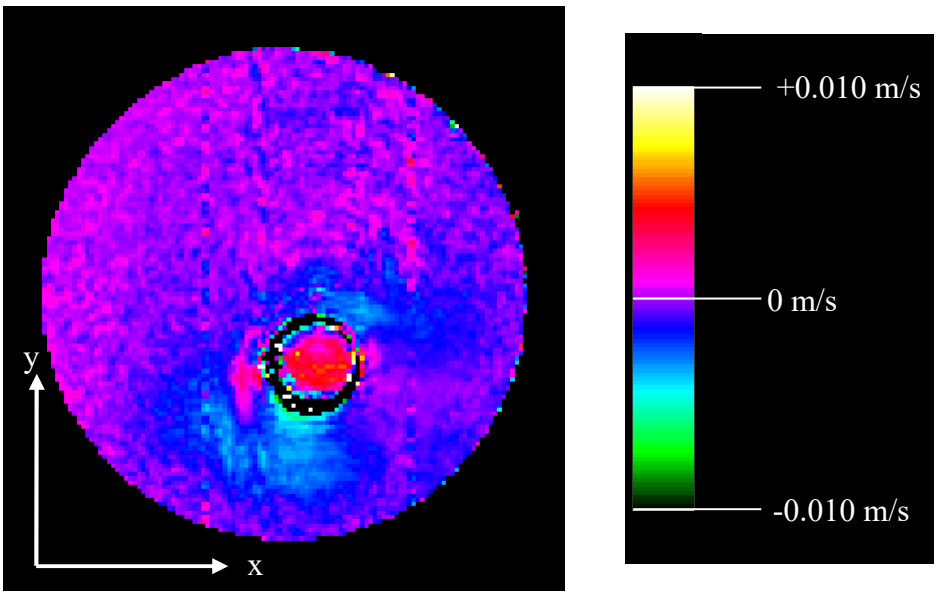

Figure 8.7 (a) Velocity image (v_x) of octanol jet (21.0±0.84 ml/min) and water (26.0 ±0.54 ml/min) co-current upward flow. Velocity encoding parameters: δ = 1 ms, Δ = 8.025 ms, g_s = 0.0486 T/m. 2 mm slice taken 6 mm downstream of nozzle, image resolution 93.75 μm/pixel.

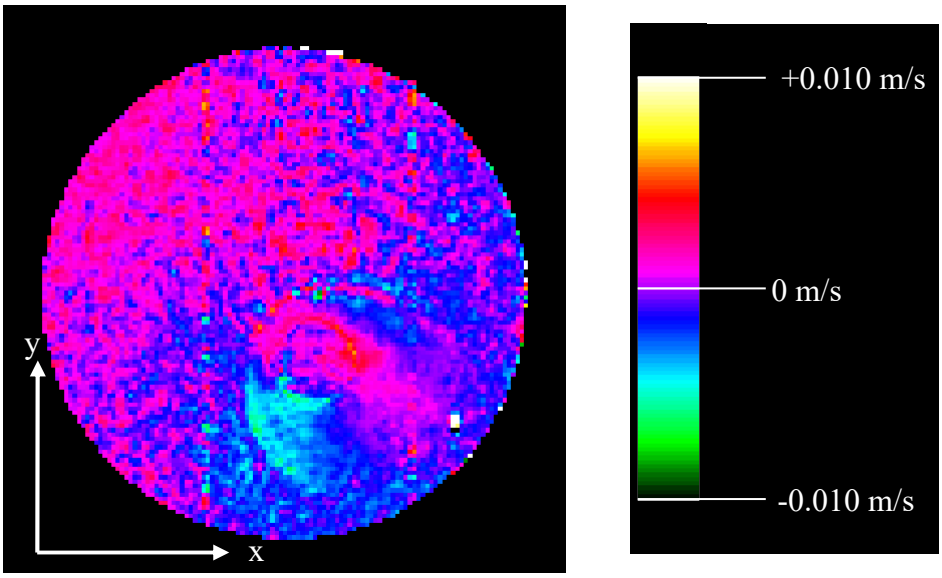

Figure 8.7 (b) Velocity image (v_x) of octanol jet (21.0±0.84 ml/min) and water (27.0 ±0.55 ml/min) co-current upward flow. Velocity encoding parameters: δ = 1 ms, Δ = 4.045 ms, g_s = 0.0389 T/m. 2 mm slice taken 6mm downstream of nozzle, image resolution 93.75 μm/pixel.

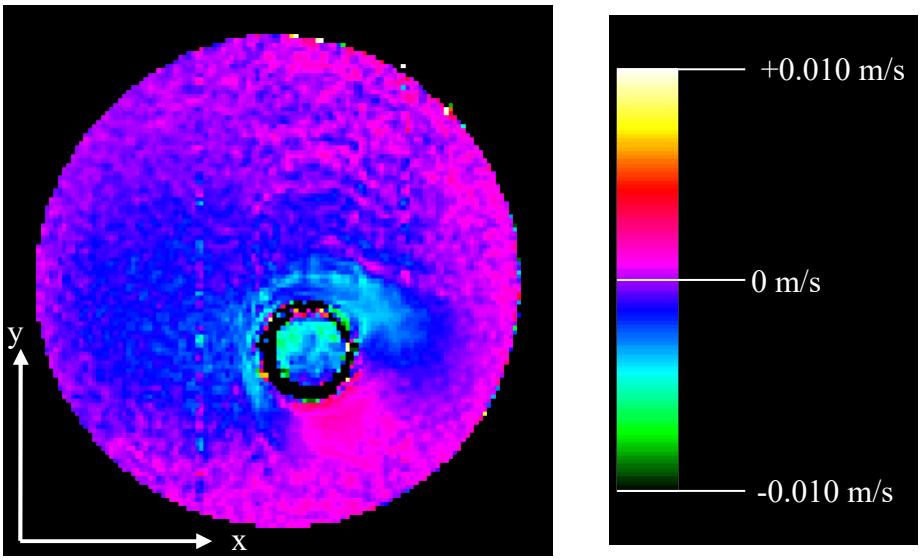

Figure 8.8 (a) Velocity image (v_y) of octanol jet (21.0±0.84 ml/min) and water (26.0 ±0.54 ml/min) co-current upward flow. Velocity encoding parameters: δ = 1 ms, Δ = 8.025 ms, g_s = 0.0486 T/m. 2 mm slice taken 6 mm downstream of nozzle, image resolution 93.75 μm/pixel.

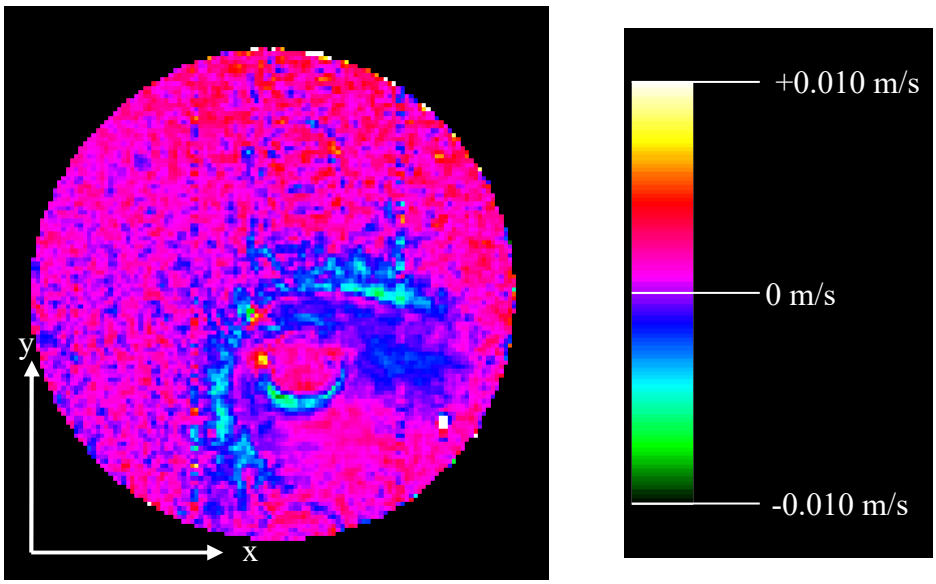

Figure 8.8 (b) Velocity image (v_y) of octanol jet (21.0±0.84 ml/min) and water (27.0 ±0.55 ml/min) co-current upward flow. Velocity encoding parameters: δ = 1 ms, Δ = 4.045 ms, g_s = 0.0389 T/m. 2 mm slice taken 6 mm downstream of nozzle, image resolution 93.75 μm/pixel.

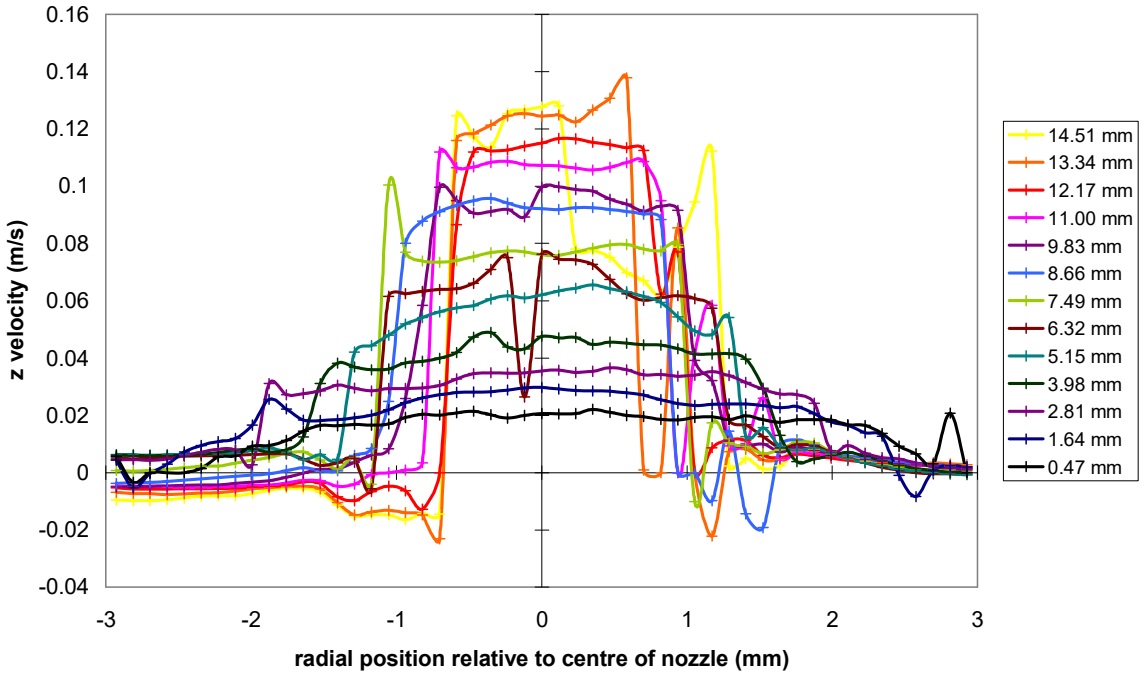

Figure 8.9 Axial velocity (v_z) profiles for an octanol jet flowing at 33.0±0.80 ml/min inside a stream of water flowing at 10.5 ±0.51 ml/min. The profiles were measured at the z positions downstream of the nozzle shown in the legend.

where ρ_1 and μ_1 are the density and viscosity of octanol respectively and d_{jet} is the jet diameter (approximated by the cross-section). Re_{jet} increases from 0.012 for the first profile to 0.019 for the last profile, but is low enough for the jet flow to be laminar until the jet becomes unsteady.

The water flow around the jet is shown in figure 8.3(a), with a region of upward flow around the left side of the nozzle and the base of the jet. Most of the flow on the right of the jet is upwards, but a large region on the left of the jet shows downward water flow, indicating a recirculation of the water. Downward water flow also occurs at the edge of the column to the right of the jet.

The image in figure 8.3(b) shows the jet and the water recirculation more clearly. The jet cross-section is circular (diameter 2.6 mm) with a radially symmetric velocity profile. The velocities inside the jet range from 0.052 m/s at the edges to 0.115 m/s at the centre. The region around the jet is devoid of signal due to the high shear rates at the edge of the jet that lead to rapid dephasing of the signal. There is an asymmetric ring of water entrained by the jet that has a higher velocity than the bulk water, with more high-velocity water on the right side of the jet. On the left of the jet, there is a region of negative water velocity showing recirculation.

The flow rates of water and octanol were calculated by multiplying the v_z values in figure 8.3(b) by the cross-sectional area of one pixel (8.789×10^{-9} m^2) then separately adding the values of the pixels containing the octanol and water flow. The calculated octanol flow rate was 33.8 ml/min, which agrees to within 1% with the measured flow rate of 33.5±0.81 ml/min. The calculated water flow rate was 0.71 ml/min, which does not agree at all with the measured flow rate of 12.5±0.51 ml/min. This is probably because rapid water flow occurred in the high shear region where the signal was lost.

The v_x image (figure 8.4(a)) shows regions of large positive (to the right) and negative (to the left) velocities as the octanol jet narrows on leaving the nozzle, meeting at the centre of the jet in a region of zero velocity. The velocity does not drop to zero after the jet stops narrowing, showing that the jet did not stabilise parallel to the z direction. The water flow around the nozzle is visible as negative velocities on the left and positive velocities on the right. The water entrained by the jet is seen clearly in figure 8.4(b) with large positive velocities near the jet and negative velocities near the edges

of the column. The region of positive water velocities almost entirely surrounds the jet, showing the rightward movement of the entrained water.

The v_y image (figure 8.5(b)) shows positive (down) and negative (up) velocities for the two halves of the jet. The water surrounding the jet is flowing towards it, with large negative velocities around most of the jet. In figure 8.5(a), most of the flow of both octanol and water has negative velocities that represent flow into the plane of the paper. Inside the jet, negative velocities are present near the nozzle and some positive velocities occur further downstream.

The transverse images in figures 8.6 - 8.8 are from the second jet, which had the nozzle in a different position and flow rates of 21.0±0.84 ml/min for octanol and 27.0±0.55 ml/min for water. The upper images were acquired with stronger velocity gradients than the lower images. The dynamic range of p_s was optimised for the lower water velocities, so the high z velocities inside the octanol jet are out of range and the apparent jet velocities in figure 8.6 should be ignored. The flow patterns in these images are largely similar to the previous experiment, with an asymmetric region of higher water velocity surrounding the jet, and negative v_z values for the rest of the water indicating recirculation. The v_x and v_y images are quite uniform, showing little transverse flow of the water. The overall entrainment of water by the jet was lower than the previous experiment because the difference between the water and octanol flow rates was smaller.

8.6 Discussion

The velocity images of the jet show clear flow patterns despite unsteady flow and lack of zero-velocity images to remove eddy current and other artefacts. The narrowing and break-up of the jet was observed, and the velocity profiles across the jet were radially symmetric and fairly uniform. The relaxation of the velocity profiles predicted by hydrodynamic calculations was not observed because the jet was unsteady and contained radial velocity components. These qualitative results can be verified by comparison with numerical simulations, *e.g.* computational fluid dynamics, but this was beyond the scope of this thesis.

The signal-to-noise ratio of the images was low and can be improved by using flow-compensated gradients for the read, phase and slice selection gradients (Pope and Yao, 1993). In the *visehs* pulse sequence used, each of these gradients led to a

velocity-dependent dephasing of the signal because of its nonzero first moment. As the velocities in this system were very large, a large amount of signal was lost. Increasing the number of scans can also increase the signal-to-noise ratio, but it was not possible in this case due to the long-term instability of the jet.

8.7 Conclusion

Two-dimensional velocity images were obtained from the upward flow of an octanol stream surrounded by flowing water, showing that the octanol stream leaving the nozzle accelerated and narrowed to form an off-centre jet that was stable for about 30 mm. The jet contained fluctuating velocity components in all three directions, so it did not flow straight upwards. The water flowed around the nozzle and some water was entrained towards the jet. The rest of the water recirculated around the base of the jet. The narrowing of the jet matched the prediction of Anwar, based on balance of jet buoyancy and viscous shear forces. The velocity profiles in the jet were fairly uniform throughout. These are believed to be the first velocity images of jet flow.

The images were obtained despite the short-term and long-term instability of the jet, but they were restricted to short experiment times and a small number of velocity encoding steps. They can be improved by using flow-compensated read, phase and slice gradients to increase the signal-to-noise ratio and reduce artefacts. For full imaging of the flow pattern, a three-dimensional imaging experiment would need to be performed, but this would only be feasible with rapid imaging techniques because of the instability of the flow.

8.8 References

Anwar, M.M., Bright, A., Das, T.K., & Wilkinson, W.L. (1982). Laminar liquid jets in immiscible liquid systems. *Transactions of the Institution of Chemical Engineers, 60*, 306-313.

Callaghan, P.T. (1991). *Principles of Nuclear Magnetic Resonance Microscopy*. pp. 337-344, 420-460. Clarendon Press, Oxford, UK.

Caprihan, A., & Fukushima, E. (1990). Flow measurements by NMR. *Physics Reports, 198*, 195-235.

Derbyshire, J.A., Gibbs, S.J., Carpenter, T.A., & Hall, L.D. (1994). Rapid three-dimensional velocimetry by nuclear magnetic resonance imaging. *AICheE Journal, 40*, 1404-1407.

Duda, J.L., & Vrentas, J.S. (1967). Fluid mechanics of laminar liquid jets. *Chemical Engineering Science, 22*, 855-869.

Fukushima, E. (1999). Nuclear magnetic resonance as a tool to study flow. *Annual Review of Fluid Mechanics, 31*, 95-123.

Gospodinov, P., Radev, S., & Penchev, I. (1979). Velocity profiles and form of a laminar jet in immiscible liquid-liquid systems. *International Journal of Multiphase Flow, 5*, 87-99.

Joseph, D.D., Bai, R., Chen, K.P., & Renardy, Y. (1997). Core-annular flows. *Annual Review of Fluid Mechanics, 29*, 65-90.

Marosek, K.W., Christy, J.R.E., Macleod, N., & Williamson, S. (1993). Development of a concurrent liquid-liquid core-annular flow column to prevent wall deposition in coagulation studies. *Chemical Engineering Science, 48*, 1061-1068.

Pope, J.M., & Yao, S. (1993). Quantitative NMR imaging of flow. *Concepts in Magnetic Resonance, 5*, 281-302.

Xia, Y., Callaghan, P.T., & Jeffrey, K.R. (1992). Imaging velocity profiles: flow through an abrupt contraction and expansion. *AIChE Journal, 38*, 1408-1420.

8.9 Nomenclature

(symbol)	(description)	(unit)
Constants		
g	acceleration due to gravity	9.81 m s^{-2}
Vector Variables		
g	applied gradient	T m^{-1}
r	position	m
Scalar Variables		
d_{jet}	diameter of jet	m
d_N	diameter of nozzle	m
Fr	Froude number	-
g_s	velocity gradient strength	T m^{-1}
N_j	jet parameter	-
p_s	phase shift of the signal with velocity gradient g_s	rad
Re	Reynolds number	-
t	time	s
u_N	mean velocity at nozzle exit	m s^{-1}
v	velocity	m s^{-1}
x, y, z	Cartesian position co-ordinate	m
γ	gyromagnetic ratio	rad T^{-1} s^{-1}
δ	duration of velocity encoding gradient	s
Δ	delay between velocity encoding gradients	s
μ	viscosity	Pa s
ρ	density	kg m^{-3}

9 CONCLUSION

9.1 Summary of Results

This thesis has discussed process applications of NMR, specifically the use of NMR for on-line measurements on flowing liquid streams. The topics covered were the quantitative accuracy of NMR spectroscopy on static and flowing samples, algorithms for automated composition analysis from NMR spectra, mathematical modelling of NMR spectra and non-Lorentzian lineshapes, quantitative volume-selective spectroscopy of static and flowing samples, the effects of flow on NMR spectroscopy, PFG NMR under flowing conditions, on-line determination of emulsion droplet size distributions and flow imaging of liquid jets.

In chapter 2, the accuracy of NMR spectroscopy for composition measurement was tested on a series of non-flowing liquid mixtures and was found to be ±0.34 mol%. The reproducibility of the measurements was ±0.08 mol%. Dilute components were measured accurately at 0.05-mol% concentration once the peaks were visible in the spectrum. The errors in the composition measurements were mainly caused by small changes in the mixture compositions due to evaporation during preparation and handling of the samples. NMR spectroscopy was therefore found to be a reliable means of determining sample composition. The chemical shifts of the peaks in the spectra of mixtures were observed to vary with composition and temperature. The polar molecules (water, methanol, toluene) exhibited larger variations than the non-polar molecules (cyclohexane, isooctane, ethyl acetate).

In chapter 3, procedures and computer algorithms were developed for automated analysis of NMR spectra of liquid mixtures, including algorithms for phase and baseline correction and peak assignment. In a departure from other workers, phase and baseline correction were performed together in two algorithms based on numerical phasing and baseline optimisation respectively. The algorithms were updated with more sophisticated baseline models and performed better than the originals at the expense of longer running times. An entirely novel algorithm was written to identify the peaks in the spectrum of a mixture based on prior knowledge of the component spectra. Peaks were assigned using their frequencies, intensities, integrals, coupling constants, separation and order in the spectrum. The peak-

assignment algorithm correctly assigned 29 out of 47 mixture spectra. The phase correction, baseline fitting and peak assignment algorithms were combined into a single program that performed the entire composition analysis in less than 4 minutes and gave a result with accuracy ±0.66 mol% for a correctly-assigned test spectrum.

In chapter 4, a new mathematical model was derived to describe the spectrum of a liquid mixture as a weighted sum of pure-component spectra. The model used a series of peak patterns instead of individual peaks to ensure that the parameters of the fit were meaningful. Fitting the model using Lorentzian lineshapes gave inaccurate composition results (±5.46 mol%) because the experimental lineshapes were non-Lorentzian. A new model lineshape was developed based on the distribution of resonance frequencies in an inhomogeneous magnetic field. The model lineshape was a convolution of a Lorentzian function with a Chebyshev series approximation of the resonance frequency distributions, and was shown to be qualitatively similar to the experimental lineshape. A least-squares fit of the model lineshape to a test peak failed to converge, so it could not be used in the model of the spectrum.

In chapter 5, two pulse sequences for volume-selective spectroscopy were presented: STEAM and PROJSAT. Both sequences were optimised for quantitative high-resolution spectroscopy, in particular the parameters for accurate localisation and minimum signal contamination. STEAM gave good localisation of the VOI with low levels of signal contamination (10%) near the edges of the VOI, but the composition measurements suffered from relaxation weighting. A modified pulse sequence, STEAMQR, with balanced homospoil gradients, was inferior to the original sequence. PROJSAT suffered from higher signal contamination (40%) than STEAM. PROJSAT spectra were not relaxation weighted but they contained very unusual lineshapes from the unsaturated magnetisation in the sample. The accuracy of the compositions of non-flowing samples determined using STEAM and PROJSAT was ±1 mol%.

In chapter 6, the flow regime was shown to have a large influence on the NMR signal obtained from a flowing sample. A new model was derived based on the residence time distributions of the flowing nuclei inside the magnetic field and the detection coil. This model was used to explain flow-induced peak broadening, sensitivity enhancement and apparent relaxation enhancement. Spectra of a flowing liquid stream using ZG gave compositions accurate to ±1 mol% at flow rates up to

50 ml/min. Volume-selective spectra were acquired from the centre of the stream using STEAM and a flow-compensated STEAM sequence, STEAM_FC. STEAM and STEAM_FC had similar quantitative accuracy for composition measurements (±2 mol%), but were less accurate than ZG because of a lower signal-to-noise ratio and higher relaxation contrast. The PROJSAT pulse sequence was also tested on a flowing sample and was intermediate between ZG and STEAM/STEAM_FC in terms of accuracy. Finally, STEAM and STEAM_FC were used to show heterogeneous flow of an emulsion of *o*-xylene in water. Flow-compensated volume-selective NMR spectroscopy yielded unique insights not available by other means, as it combined non-invasiveness with volume selectivity and quantitative accuracy.

In chapter 7, ten PFG pulse sequences were evaluated for their ability to determine the droplet size distributions of flowing emulsions. Standard spin-echo and stimulated-echo PFG sequences were modified for volume selection and flow compensation. The reliability of the pulse sequences was assessed by measuring the known diffusion coefficient of water under static and flowing conditions. The stimulated-echo sequences gave better attenuation data for water than spin echoes and gave diffusion coefficients within 10% of the standard value. Flow compensation was only partly successful due to transverse diffusion in the flow field. The volume-selective sequences gave diffusion coefficients that were 20% too large at low Δ values. The stimulated-echo pulse sequences were used to determine the droplet size distributions of static and flowing emulsions of *o*-xylene in water. Consistent results were obtained for static emulsions from both the single-echo and double-echo sequences and for flowing emulsions from the double-echo sequence at short diffusion times. The droplet size distributions varied with the *o*-xylene content of the emulsion but were independent of flow rate. Flow diffraction effects were observed for small droplets at long diffusion times.

In chapter 8, two-dimensional velocity images were obtained for the upward flow of an octanol stream surrounded by flowing water. The images showed that the octanol stream leaving the nozzle accelerated and narrowed to form an off-centre jet that was stable for about 30 mm. The jet contained fluctuating velocity components in all three directions, so it did not flow straight upwards. The water flowed around the nozzle and some water was entrained towards the jet. The rest of the water recirculated around the base of the jet. The images were obtained despite the short-

term and long-term instability of the jet, but they were restricted to short experiment times and a small number of velocity-encoding steps.

9.2 Future Work

The research described in this thesis has involved unconventional applications of NMR, among them quantitative spectroscopy of highly concentrated liquids, quantitative volume-selective spectroscopy, spectroscopy at high flow rates, and droplet size determination in the presence of flow. New computer algorithms have been written for phase and baseline correction and peak assignment. New models have been derived for NMR spectra of liquid mixtures, experimental lineshapes in inhomogeneous magnetic fields and the effects of residence time distributions on the magnetisation in a flowing stream. Consequently, there are many possible directions for future work, many of which are beyond the scope of this thesis.

For the liquid mixtures, a more systematic study can be undertaken of the shifts in resonance frequency with composition and temperature. This would yield more insights into the local chemical environments in single-phase mixtures and aid in assigning peaks in the spectra of the mixtures. The quantitative accuracy of NMR composition measurements can be assessed more precisely using mixtures containing less volatile components. The program for automated composition analysis can be speeded up using better algorithms, particularly a more sophisticated version of numerical phasing with adaptive values of σ_0/σ_1. The program can also be modified to analyse volume-selective spectra and spectra acquired under flowing conditions. Flow-induced peak broadening restricts automatic peak assignment to spectra acquired at low flow rates in which the individual peaks are resolved.

The model for the non-Lorentzian lineshape requires a better algorithm for fitting to the experimental data. Once fitted, the lineshape can be included in the model of the NMR spectrum to improve the accuracy of the composition measured from overlapping peaks. Alternatively, the lineshape model can be rewritten using a different basis set to make it easier to calculate. The lineshape model can be expanded to include spinning and flowing samples, which experience radial and axial averaging of the magnetic field respectively. The model of the NMR spectrum can be incorporated in a Bayesian analysis of the NMR data instead of the least-squares fit to the FT spectrum.

Volume-selective spectroscopy using STEAM and PROJSAT can be improved by using soft pulses with better volume selectivity than the truncated sinc pulses. The lineshape artefacts in the STEAM and PROJSAT spectra may be removed by studying the evolution of the magnetisation during the pulse sequence in more detail, and modifying the pulse and gradient shapes appropriately.

The effects of flow on NMR spectra can be studied in more detail. The predictions of the residence-time distribution model for flow-induced peak broadening and magnetisation build-up should be verified using new experimental data. It may be possible to deconvolve residence time distributions from the lineshapes observed in spectra of flowing samples.

The PFG experiments on flowing samples require follow-up studies designed to elucidate the causes of incomplete flow compensation, excess attenuation from the volume-selective sequences and the observed diffraction effects. The accuracy of the droplet size distributions measured in a flowing emulsion should be assessed with a stable emulsion that does not exhibit creaming so the NMR results can be compared with those from optical microscopy.

Flow imaging experiments of core-annular flow may be successful with a more viscous core liquid than octanol. The flow images of the liquid jets can be repeated at higher signal-to-noise ratios by acquiring more scans, and the results can be compared to numerical simulations. Images of more stable liquid jets at lower flow rates can be used to verify the hydrodynamic models already available.